University of Sheffield

Optimising P-type $Na_{0.67}Mn_{0.9}Mg_{0.1}O_2$ cathodes *via* synthesis method, doping, and phase composition

George Joseph Wilson

For the degree of Doctor of Philosophy

Supervisors: Dr Rebecca Boston
Dr Nik Reeves-McLaren

University of Sheffield

Faculty of Engineering

Department of Materials Science and Engineering

April 2023

Abstract

The shift to renewable, low-carbon energy generation creates intermittency in supply. To reduce reliance on fossil fuels, large-scale energy storage is required to store energy when it is in abundance and supply it when scarce. Sodium-ions batteries (NIBs) can enable this transition by using low-cost, sustainable materials. The P3 and P2 phases of $Na_{0.67}Mn_{0.9}Mg_{0.1}O_2$ (NMMO)are presented here are candidates for large-scale storage.

In Chapter 3, a biotemplating synthesis using naturally occurring polysaccharide dextran successfully synthesised these materials without impurities. Conventional solid state methods could not produce single phase P3-NMMO, and its initial capacity was 95 mAh g^{-1}, compared to 142 mAh g^{-1} for the biotemplated P3 phase. Biotemplating produced sharply faceted plates of P2-NMMO, with a higher initial capacity than the P2 synthesised *via* solid state methods, which has rounded plates. The biotemplated materials exhibited better rate capability than the solid state synthesised materials. These differences manifested despite synthesis methods for each phase using identical 20 h calcination regimes.

In Chapter 4, P-type NMMO was produced using only a biotemplating synthesis, with a calcination time of 2 h. This led to an increase in capacity retention for the P3 phase from 73% to 82%, but a decrease for P2 from 73% to 63%. P-type NMMO was doped with 1% and 2% Ca (NCMM) to improve the capacity retention and rate capability. This did not work in P3-NMMO, but 1% and 2% Ca doping increased the capacity retention of P2-NCMM from 63% to 73%. Initial capacity for all materials showed no significant change. The rate capability of 1% Ca P2-NCMM was better than both 0% and 2% P2-NCMM. These effects may be contributed to by the large increase in particle size of 1% Ca-P2-NCMM compared to all other samples in this chapter.

The other method of improving capacity retention and rate capability in P-type NMMO was to combine the two phases in Chapter 5. A range of biphasic samples with varying P3/P2 ratios were generated by altering the calcination temperature and compared against the same P3/P2 ratios with the P3 and P2 phases calcined separately and mixed post-synthesis. Of all the samples in this chapter, none had higher capacity or retention than the biotemplated P3-NMMO. For both preparation methods, increasing the phase fraction of P2-NMMO decreased the capacity retention. The mixed P3/P2-NMMO displayed higher capacity retention than the biphasic samples at each phase ratio. This may be because the biphases showed increased electrochemical activity of the P2 phase, leading to structural changes and more rapid degradation.

Using biotemplating to produce NIBs can significantly reduce the energy cost of production, while improving upon the performance characteristics of the material when generated *via* solid state methods. NMMO is a high capacity, low-cost cathode material that can be further optimised with further exploration of the strategies identified herein.

Acknowledgements

I would like to thank my supervisors; Dr Rebecca Boston and Dr Nik Reeves-McLaren. They have been an eternal source of support, patience, wisdom, and knowledge throughout my PhD. Thank you for dragging me, kicking and screaming, to the finish line. I wouldn't be here without you.

My gratitude also goes to Dr Rob Moorehead and all those in the XRD lab for their help setting up, troubleshooting, and optimising my many experiments. Similarly, I would like to thank all those in the Sorby Centre for their teaching and assistance in microscopy.

I would like to thank the Energy Storage CDT for the opportunity, and the EPSRC (EP/L016818/1) for the funding, to conduct this research. A huge thank you to Tracey McNeilly and Sharon Brown for organising our conferences, socials, and generally creating a welcoming research environment.

In the same vein, I would also like to thank the members of the Sustainable Oxide Processing Group, the I06 battery lab, and the Energy Storage CDT. Your expertise and generosity made for a wonderful work environment, and I can't wait to go for dinner/play squash and football with you all again soon. Special thanks to Silvija for her help in teaching me almost every technique I know, and always being available to offer advice, support, and a sympathetic ear.

Special thanks also go to Tom and Ankur for unleashing my competitive spirit over the course of many games of Catan (although Sheffield Debating can also be blamed for that). Whether it be for distraction from work or to learn more than I ever wanted to know about F1 and rugby, you both made otherwise difficult years enjoyable.

Outside of Sheffield, I would like to "thank" Jack, for convincing me that doing a PhD was a good idea. I suppose it's worth it for the sword. You, Louise, Tom, and Sofia have all helped me immensely on this journey and I'm so grateful for you always looking out for me. The same goes for the Bottle Droppers, who have humoured me as I complain at length/completely avoid talking about work over the years. Valentina has seen more of the struggles I've had over the last few years than anyone else and has always supported me. As with everyone else mentioned here, I can't express my gratitude enough.

Finally, I don't think I can properly express how much my family have helped get to this point. They have been a constant source of support, reassurance, and understanding, more than anyone could ever hope for. Whether it be Dad, Jacqueline, and Brodie giving me the space and peace to work, or Mum whisking me away for a writing retreat in the sun. There are countless examples of the support you've given me over these years, and I owe everything to you.

Contents

List of tables

List of figures

1 Introduction

1.1 Energy storage

Energy storage is an important feature of a grid, particularly one that relies more and more on renewable sources. Renewable energy is becoming increasingly prevalent in UK (Figure 1-1) [1], and indeed the world. The most common forms of renewable energy are, by capacity, wind and solar [1]. These sectors have had a lot of development in recent years, leading to cost decreases [2] and a large uptick in their deployment, but they do not produce constant, reliable power. The sun does not always shine, the wind does not always blow. Suitable methods of storing this energy for use when needed, are required.

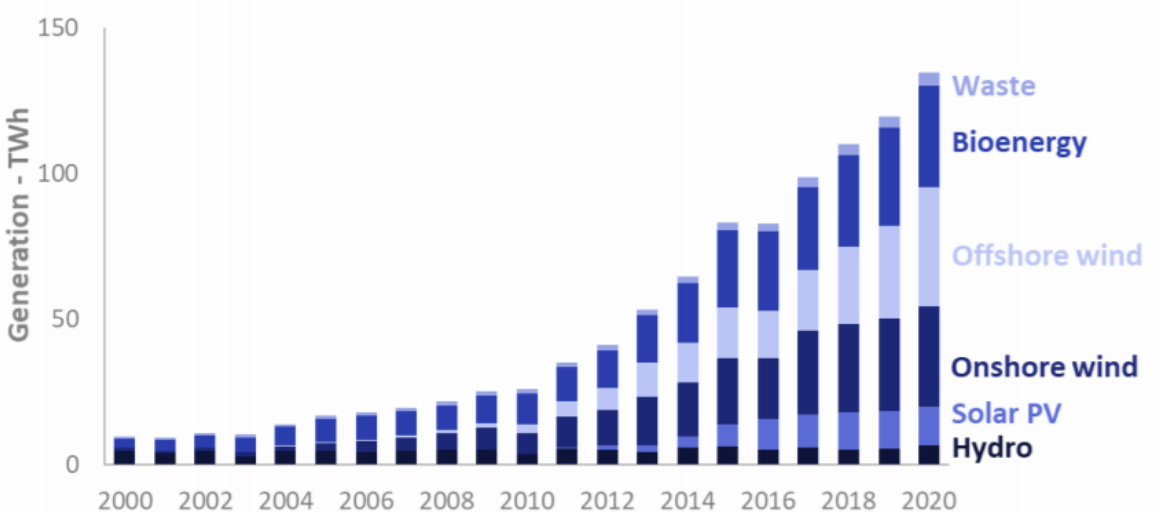

Figure 1-1: Graph showing the increasing generation from renewable sources in the UK up to 2020 [1].

Pumped-hydro storage is the most common form of large scale energy storage by capacity [3], [4]. It is a simple technology, wherein excess power supplied from the grid is used to pump water up a hill. When there is excess power demand, the water is allowed to flow down the hill to drive generators [5]. The advantages are the lifetime of the pumped-hydro stations [6], in the region of 40 years, but it requires very specific geographical conditions (of which there are very few remaining in the UK [7]) and exceedingly high capital costs – providing a significant barrier to future development.

In contrast, batteries are scalable, can be easily tailored to fit specific requirements, and can be deployed anywhere with minimal disruption to the local environment. This makes them a natural fit for a decentralised, intermittent power generation network [8].

1.1.1 Battery operation

As with all energy storage devices, batteries are a way of holding a system in a state of high potential in such a way that the energy does not immediately dissipate and can be used when needed. They comprise of two electrodes and an electrolyte that is electronically insulating but conducts (in the case of NIBs) sodium ions. During discharge,

the sodium ions are extracted from the anode and inserted into the cathode *via* the electrolyte (Figure 1-2). To balance the charge, a transition metal is reduced by electrons that have travelled through the external circuit, doing useful work. The electrodes are physically separated by a separator, an ionically conductive and electrically insulating material, often made of fibre glass or a polymer which prevents short-circuiting. This broad sequence of events holds true for all the battery systems that will be discussed herein.

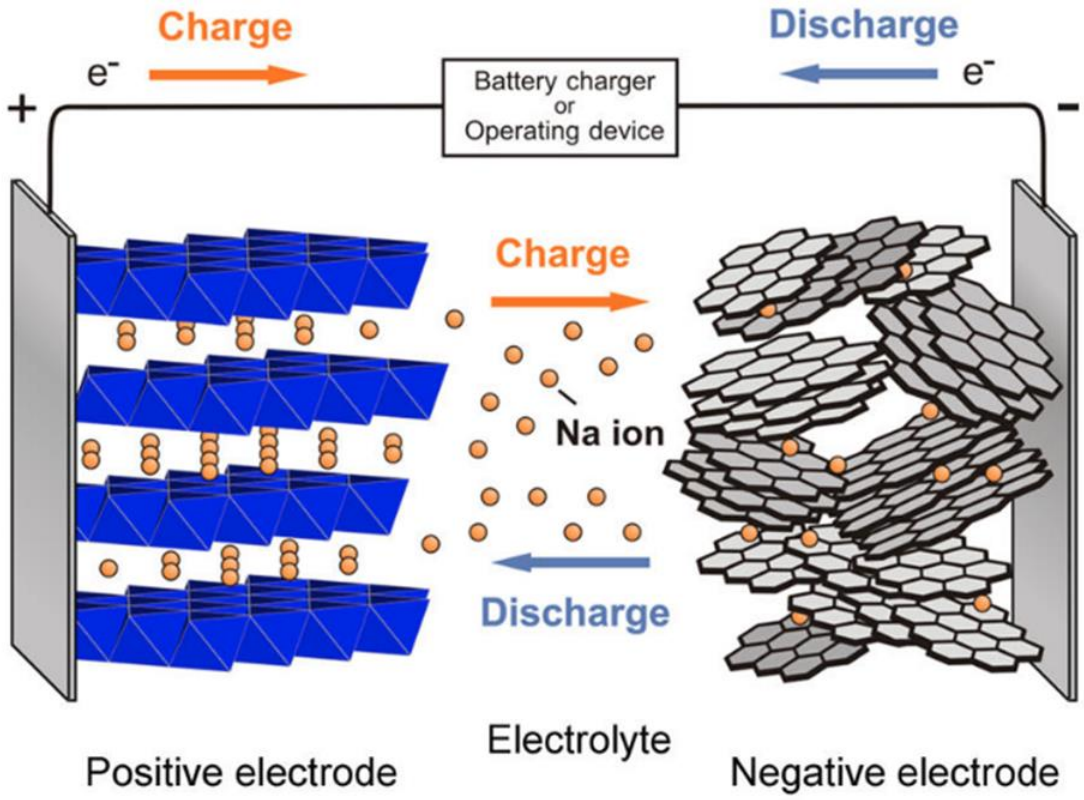

Figure 1-2: General schematic of a sodium-ion battery showing the movement of the different charged particles during charge and discharge [9].

There are several important metrics that are commonly measured to define performance in battery systems. An overview of them is given here, with a more complete discussion in Chapter 2. The first is specific capacity, measured in mAh g^{-1}. Capacity, in Ampere-hours, is a measure of the charge transferred from a material during either charge or discharge. This figure is normalised against the mass of active material to give its specific capacity. This allows the same battery materials to be compared against each other across different samples. For example, cathodes with different chemistries can be compared directly, the same materials discharged at different currents or using different voltage windows. This can also be used to compare the performance of different structures of the same material. Cells are almost exclusively tested by cycling at a constant current (galvanostatic cycling) and so specific capacity can also be thought of as the length of time a cell can discharge for at a given current.

The way current is reported is usually linked to theoretical capacity of the material. C is defined as the current needed to fully (dis)charge a battery, determined by its theoretical capacity. The current used during electrochemical testing is given as a fraction (or multiple) of C, or C-rate. 2C is the current required to fully charge or discharge in half an hour, and C/2 is the current required to charge or discharge in two hours. This is useful in comparing electrochemical performance (either capacity or capacity retention) across different samples – different materials have different capacities and will cope differently with varying currents. Using the same C-rate means that a materials capacity retention can be compared, as can be seen in Figure 1-3. Here, increasing the proportion of iron at the expense of nickel increases the capacity that can be extracted at higher discharge rates. Conversely, at low discharge rates the samples with more nickel perform better. This observation is valid as the discharge conditions are the same.

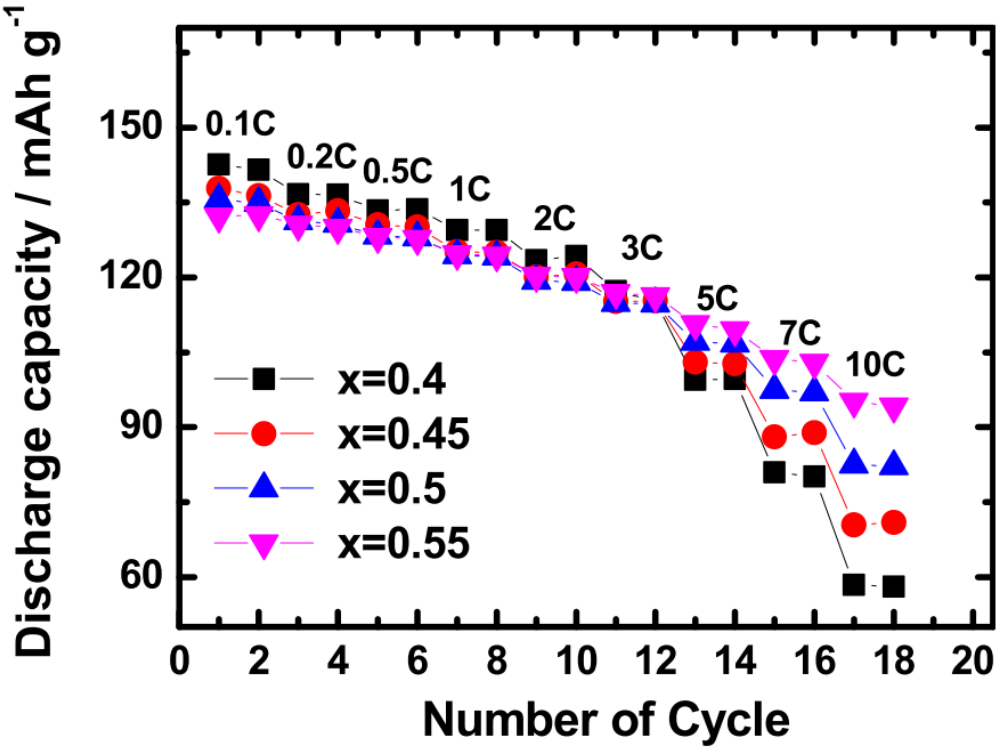

Figure 1-3: Comparison of discharge capacity of $NaNi_{0.75-x}Fe_xMn_{0.25}O_2$, charged at 0.1 C to 3.9 V vs Na and discharged at the C-rate noted on the graph [10].

Capacity retention is a measure of how well the material can reversibly change and discharge. It can be expressed as the percentage of the initial discharge capacity after a certain number of cycles. Similarly, cycle (or coulombic) efficiency is used to measure battery performance per cycle and is expressed as the discharge capacity as a percentage of the previous charge capacity. Cycle life is the number of cycles before the battery fails to meet certain criteria – usually when only 80% of its capacity can be extracted. Figure 1-4 shows the effect of the voltage window on the discharge capacity over many cycles. Larger voltage windows increase the discharge capacity as it allows more time for the

sodium to be extracted and reinserted into the cathode but can lead to more rapid capacity decay.

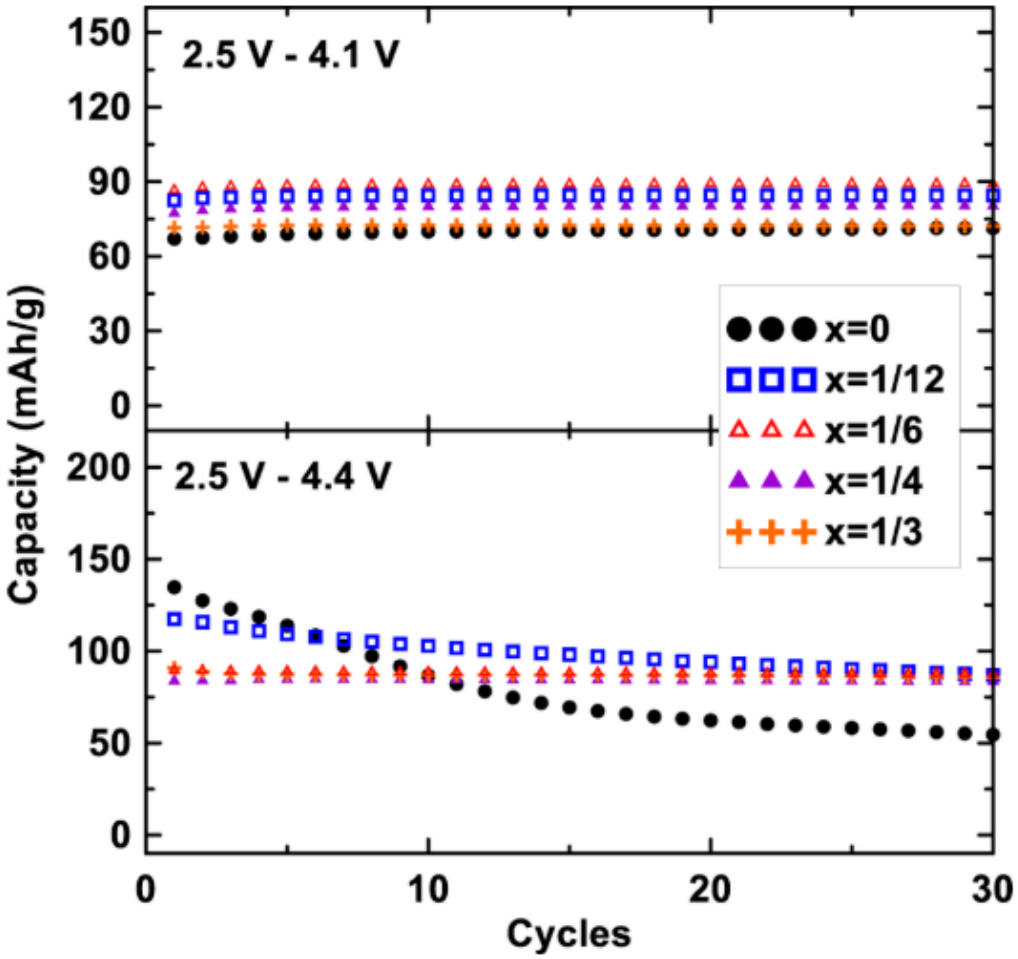

Figure 1-4: Discharge capacity over 30 cycles of $Na_{0.67}Ni_{0.33-x}Cu_xMn_{0.67}O_2$ when cycled at 1C between the given voltage windows vs *Na* [11].

1.1.2 Current battery technologies

Lithium-ion batteries have been established as a leading technology in the energy storage sector, owing to their long cycle life [12], [13], high energy density (a product of both high capacity and high operating voltage) [14], [15], and low maintenance costs [16]. Much of the recent growth in the energy storage industry has come from the development of lithium-ion batteries and their pivotal role in the development of electric vehicles (EVs) and portable electronics [13]–[15], [17], [18]. In these applications, they are a natural choice, as the performance characteristics of lithium-ion batteries lend themselves to situations where both low weight and high power are required. However, the most prevalent commercial LIB materials (like other current commercial batteries) rely on both environmentally and commercially unsustainable materials, including cobalt and lithium itself [12].

Cobalt is the redox active component of $LiCoO_2$ [13], a very widely used cathode in the battery industry [19]. It has a high capacity (theoretically 274 mAh g^{-1} [20], [21],

experimentally 215 mAh g^{-1} [19]), a long cycle life, and a high operating voltage (3.8 V vs Li/Li^+ [22]). Cobalt is frequently mined using child labour under dangerous conditions [23]. Cobalt is also toxic [24], creating further safety hazards if $LiCoO_2$ or a system such as NMC (a family of LIB containing nickel, manganese, and cobalt in varying proportions) were used at a large scale. Nickel also has supply chain concerns [25] related to its low abundance [26], as well as risks associated with toxicity [27]. Even if these hazardous materials can be avoided, the lithium is still a barrier to sustainable energy storage. The production scale of a selection of important battery materials are shown in Figure 1-5.

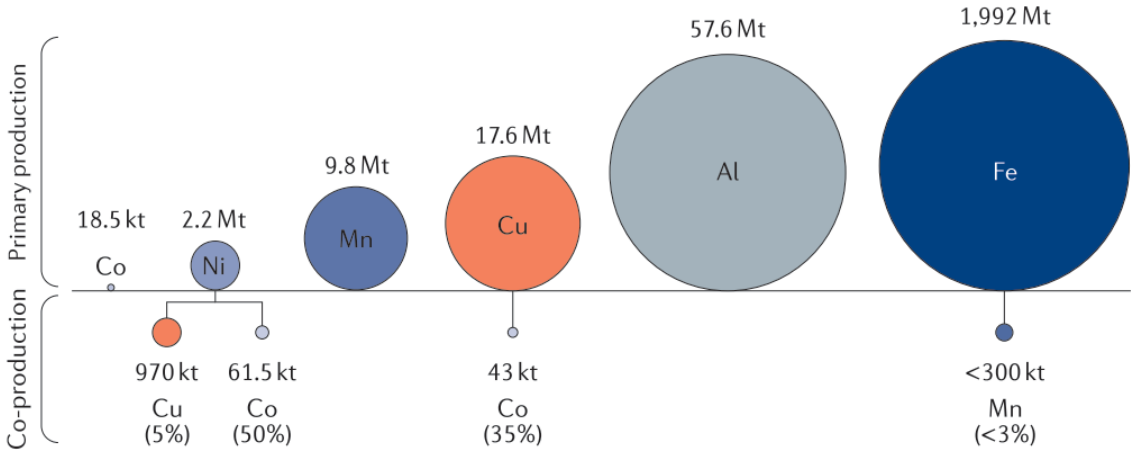

Figure 1-5: Annual production of metals from mining. Circle size is relative to their production volume, with the exception of Fe, which has been scaled down for visibility [28].

Lithium metal is mined from deposits concentrated in a small number of countries, shown in Figure 1-6 [16]. This has already led to price volatility [29], [30] and local environment disruption [31], [32]. Eventually, shortages of lithium are predicted within 100 years [33], and demand to outstrip supply possibly by 2025 [34], [35]. The geopolitical problems with countries that export oil, wherein they control the production and therefore the price of oil, are mirrored in the lithium mining industry.

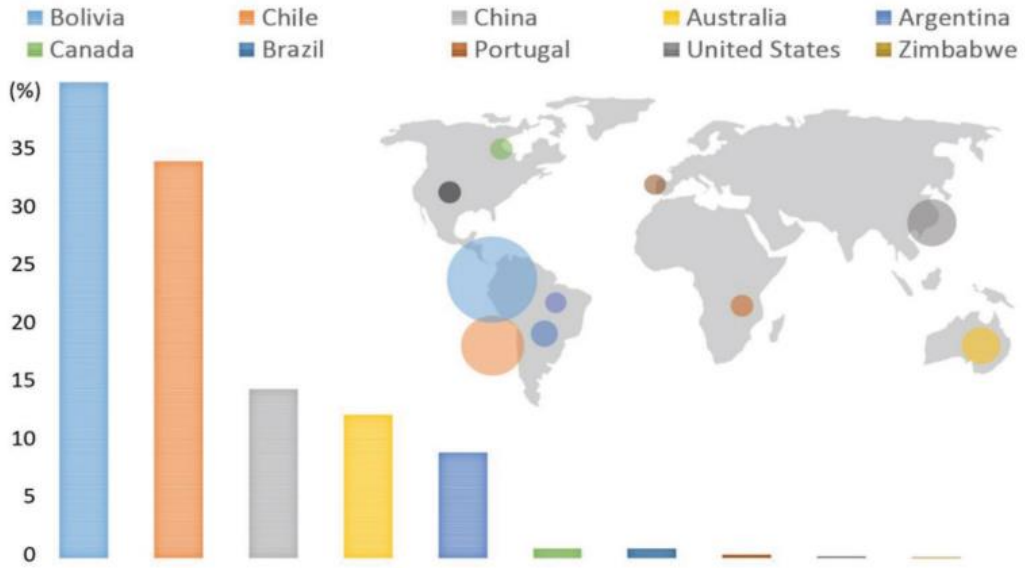

Figure 1-6: Map showing the distribution of lithium reserves across different countries [16].

There exists another notable issue with LIBs that is a barrier to large-scale usage, in that they are less safe and increase costs relative to sodium counterparts. Due to the tendency of lithium to alloy with aluminium, copper must be used as the current collector in lithium-ion battery systems [9]. As well as being more expensive than aluminium, copper is dissolved at states of high discharge [36] as it is oxidised to Cu^{2+}, when can plate onto the cathode, forming copper dendrites which can cause an internal short-circuit. sodium does not alloy with aluminium and so costs can be reduced by using aluminium as the current collector in NIBs. These are problems intrinsically tied to the lithium-ion battery industry and will always limit its potential uses when considering future sustainable energy storage technologies. Environmentally sustainable alternatives to LIBs are therefore sought to supplement global energy storage requirements.

1.1.3 Sodium-ion batteries

Sodium-ion batteries (NIBs) function essentially identically to lithium-ion batteries, except they use sodium ions to transport charge rather than lithium. Sodium is 1000 times more abundant [37] than lithium and its presence at high concentrations in sea water render its accessibility almost limitless [4]. Sodium also has the advantage of not alloying with aluminium, meaning aluminium can be used as a current collector rather than copper [9], reducing costs. NIBs can be transported whilst fully discharged, whereas lithium-ion batteries must be transported at 30% state-of-charge to prevent dissolution of the copper current collector [37] which furthers safety concerns. The difference in ionic radii between sodium ions (1.02 Å [38]) and 3d transition metal ions (the radii of Mn^{3+}, Ti^{3+}, and Ni^{2+} are 0.58 Å, 0.67 Å, and 0.70 Å, respectively) means that there is very little interlayer cation mixing [39]. As the ionic radius of Li^{+} is 0.76 Å [38], cation mixing has been reported to hinder the performance of the Ni-containing LIBs [40].

In NIBs the cathodes commonly form a layered oxide, analogous to $LiCoO_2$ in LIBs. Unlike in LIBs, these layered oxides tend to form (one of) several different structures depending (primarily) on the Na content. Layered oxides have a general formula of Na_xTMO_2, where TM is generally a transition metal, such as Co, Ni, Mn, or Fe, and x can have a range of values from $0.5 \leq x \leq 1$. Throughout this work, x is used to refer to mol fraction of Na in cathode unless stated otherwise. Structures with prismatic Na sites can be generated in a sodium off-stoichiometry condition ($0.5 \leq x \leq 0.8$) [9], [25]. The sodium ions energetically favour [41] a prismatic site in this case. This is caused in part by an expansion of the unit cell along the c axis due to a lack of shielding between negatively charged TMO_2 slabs [42]. This phenomenon means layered structures with different stacking patterns can be generated. Different stacking patterns improve various performance metrics: capacity in octahedral structures; and cycling stability, rate capability in prismatic structures [43]. As the cycling of the cell involves the insertion and extraction of Na^{+} from the cathode structure, x varies throughout a cycle. As such layered oxides can undergo several phase transitions during operation.

In general NIBs do not perform as well as their lithium counterparts, as shown in Figure 1-7. Sodium ions are heavier than lithium ions (23 g mol^{-1} and 6.94 g mol^{-1}, respectively [9]), which decreases its specific capacity compared to equivalent lithium systems. Secondly, the redox potential of Na/Na^+ vs the standard hydrogen electrode (SHE), is 2.71 V; whereas the redox potential of Li/Li^+ vs SHE is 3.04 V. This limits the energy densities that sodium-ion batteries can reach compared to lithium-ion batteries. Lastly, the size of the sodium ions means that its (de)intercalation from the host lattice leads to deleterious volume changes [44]. These volume changes are often associated with rapid capacity fading [45], [46]. Similarly, rapid capacity fading can also occur during phase transitions. These phase transitions, usually between prismatic and octahedral layered structures, are made possible only by the size of the sodium ion and its stability in a prismatic environment.

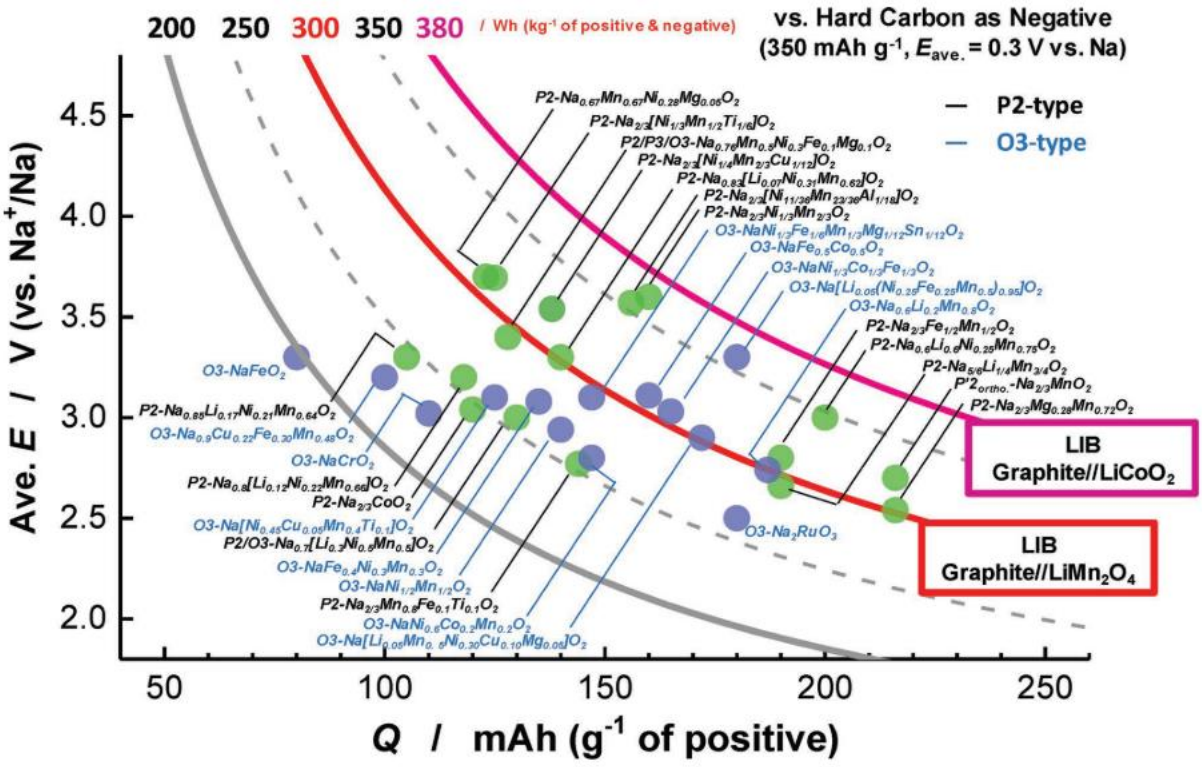

Figure 1-7: Average voltage (V) and energy density (Wh kg^{-1}) vs. gravimetric capacity (mAh g^{-1}) for selected O3 (blue circles) and P2 (green circles) sodium-ion cathode materials. The energy densities of $LiCoO_2$ and $LiMn_2O_4$ are included for comparison [39].

Given the need for sustainable energy storage technology that can operate at the scale of a national grid, sodium-ion batteries are a prime candidate for development. Having lower specific capacity is less of a problem at large scale when portability is not a consideration. In these instances, much more consideration is given to technologies that can offer cheaper and safer materials that are more sustainably sourced. Therefore, the challenge facing NIBs lies in increasing its capacity retention, and therefore its lifetime. Of course, achieving high capacities and energy densities is important, and improvements are always welcome. It is crucial to limit the starting cost of any energy storage system using NIBs to ensure its development, and this can be done by obtaining excellent

capacity and energy performance. But the overall aim is using sustainable materials that can generate cost effective, non-toxic batteries with long lifetimes, as that is the ideal technology to deploy as the energy storage system at a large scale.

One final consideration in battery development is the energy cost of synthesis. The processing of materials, particularly cathode materials, represents a significant energy cost using the current standard techniques. There are potential methods that can vastly reduce these costs, enabling several important steps to commercialisation: rapid prototyping, optimisation, and scale up of production. The cheaper and faster the synthesis of materials can be made, the easier the above processes will be. The knock-on effect of this will hopefully be the faster adoption of the sodium-ion battery technology and smoother transition to a renewable energy world.

1.2 Sodium-ion battery cathodes

The layered oxide structure, with generic formula Na_xMO_2, ($0.6 \leq x \leq 1$) has been used with great success in the development of sodium-ion batteries [39], [47], [48]. Initially, research focussed on materials with only one transition metal (e.g. $NaCrO_2$, $NaMnO_2$, etc) and $x = 1$ in the early 1980s [49]. These materials had poor specific capacities and capacity retention, owing partly to the lack of optimisation of various elements such as the electrolyte and equipment [48]. One driving force behind the research is the mitigation of these initial problems (low reversible capacity, low operating voltage, etc) by doping the electrochemically active transition metals with other metal ions – either other transition metals, or electrochemically inactive metals, e.g. titanium [50] or magnesium [51].

This has led to a great degree of variation in the body of layered oxide work, as groups combine different metals to achieve different aims. For example, doping the transition metal layer with magnesium is common in manganese [51]–[54] systems as it mitigates the Jahn-Teller distortions that arise during cycling as Mn^{3+} is oxidised to Mn^{4+} and *vice versa* when charging and discharge, respectively. Without the magnesium doping, the Na_xMnO_2 cathode undergoes several structural distortions [55], seen in the charge/discharge profile as steps in the voltage [56]. After enough time, the continual distortion of the material leads to the formation of cracks, disconnecting it from the current collector. It becomes electrochemically inactive, resulting in a capacity decrease. This is shown in Figure 1-8 as particle cracking.

The structural distortions in NIBs are commonly layer glides as the as the structure transitions between (typically) prismatic and octahedral sodium geometries and cation/vacancy ordering (discussed further in Section 1.2.1), although the identity of the changes themselves are not always identified [51].

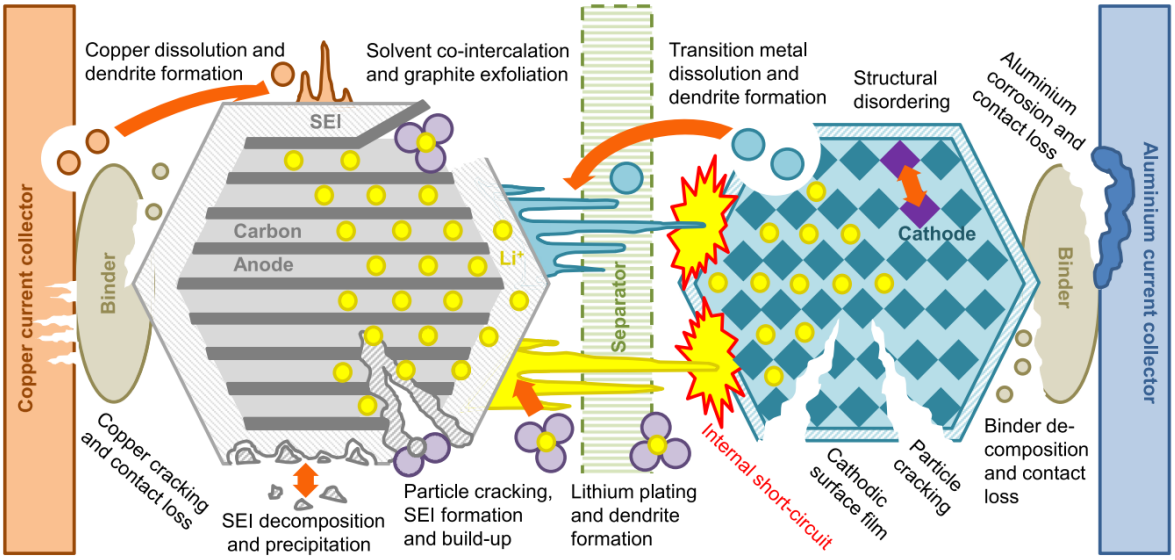

Figure 1-8: Schematic of the degradation mechanisms in lithium-ion batteries [57].

Another example is combining two redox active metal, such as manganese and iron [58], where both metals undergo redox but at different potentials. This allows capacity to be extracted from the battery with a wider voltage window. In this study, the additional capacity meant the energy density of the binary system was higher than both unary systems, despite the additional capacity being extracted at a lower potential, as shown in Figure 1-9.

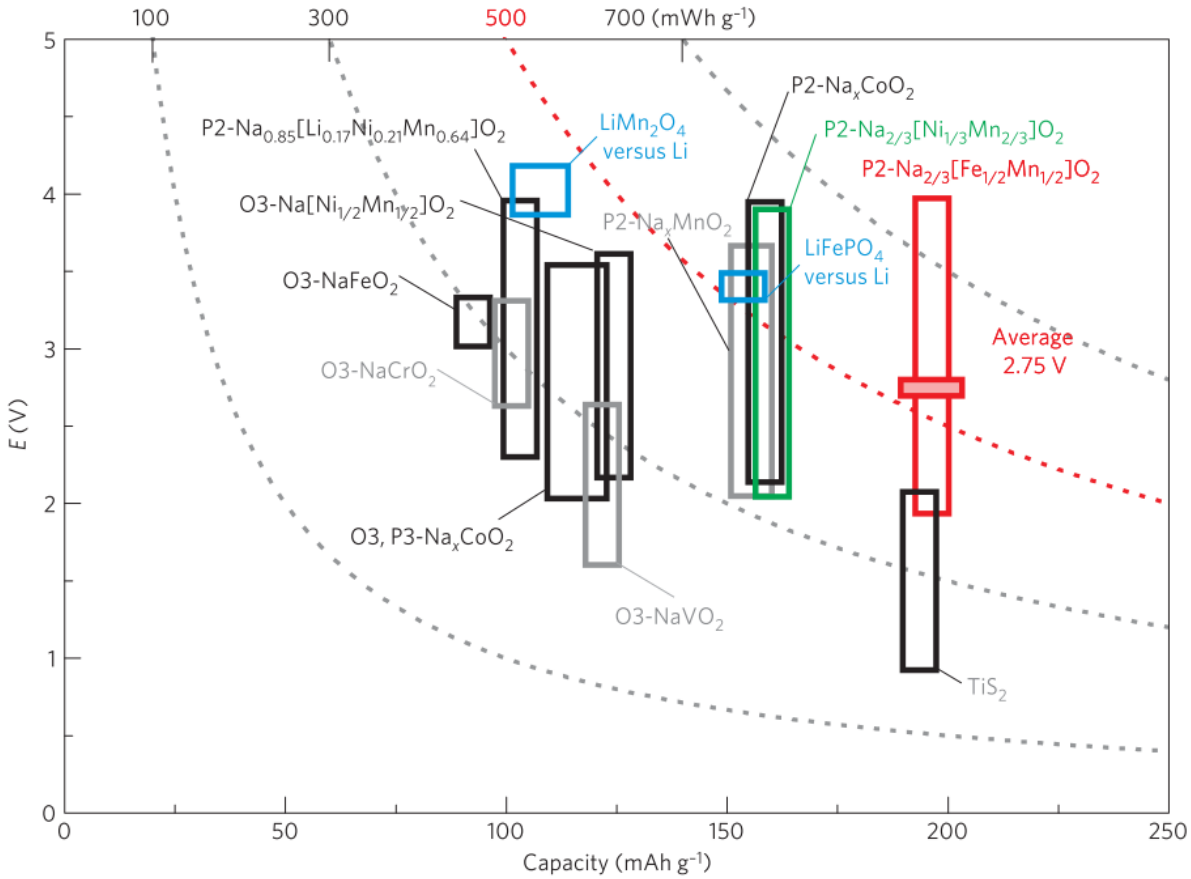

Figure 1-9: Capacity vs *potential window of several battery systems. Dotted lines indicate energy density* [58].

1.2.1 Phases of layered oxides

Layered oxides in NIB cathodes can form different phases. Unlike in lithium layered oxides which remain in the same octahedral structure during cycling, sodium layered oxides alternate between octahedral and prismatic structures depending on the sodium content and the synthesis conditions. This is due to the size of the sodium ion, which stabilises the prismatic sites between the MO_2 layers. Layered oxides can be separated into subgroups according to their crystal structure as defined by Delmas et al [49], grouping crystals into discrete phases by (a) the coordination of the Na ion by oxygen in the metal oxide layer, and (b) the number of distinct metal oxide layers in each repeating unit. The oxygen coordination in Na-ion cathodes is most commonly either octahedral (O) or trigonal prismatic (P) [9], and there are generally either 2 or 3 layers per repeating unit. These combine to give the most common types of cathode phases: O3 (space group: *R*-3*m*) and P2 (SG: $P6_3/mmc$) [59], and the P3 (SG: *R*3*m*) phase has also been observed [60], [61]. Furthermore, distortions of these phases can occur and are denoted with a prime symbol (P'2 or O'3, for example) [62], [63], or multiple if there are multiple distortions (P''3) [64].

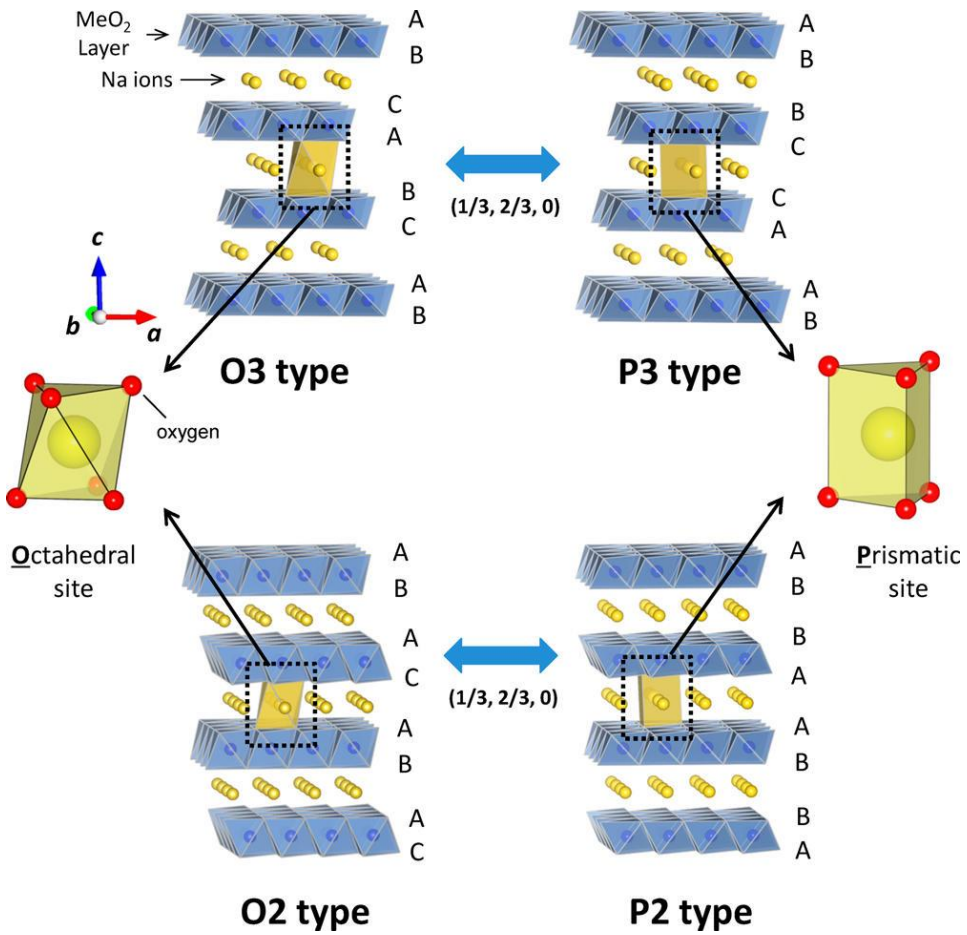

Figure 1-10: Schematic of the common phases of layered oxides in sodium-ion batteries [9].

Typically, O-type stacking is favoured at high Na content since the positive charge of the Na ion disrupts the repulsion between negatively charged metal oxide layers. For example, O3-$NaFe_{0.5}Co_{0.5}O_2$ [65] and O3-$NaNi_{0.5}Mn_{0.5}O_2$ [66], both of which form a P3 phase during desodiation [67], [68]. Although the capacities of these materials are high, 160 mAh g^{-1} [65] and 185 mAh g^{-1} [66], respectively, poor Na diffusion kinetics and structural changes lead to significant capacity fade over time [69]. O3-$NaFe_{0.5}Co_{0.5}O_2$ [65] loses 15% of capacity over 50 at 12 mA g^{-1} (C/20, a low current density). O3-$NaNi_{0.5}Mn_{0.5}O_2$ [66] only delivers 20 mAh g^{-1} after 27 cycles, even at C/30. The primary reason for this is the high upper voltage limit of 4.5 V vs Na/Na^+. When lowered to 3.8 V vs Na/Na^+ the capacity retention is greatly improved (69% over 50 cycles at 48 mA g^{-1}, or C/5), although the initial capacity is lowered to 130 mAh g^{-1}. The reason for this difference is that at high voltage (low Na^+ content) the cathode forms a P3'' with a very large interslab distance (the distance between adjacent TMO_2 layers). This distorted phase incorporates solvent molecules in between TMO_2 layers, which reduces the amount of Na^+ that can be reversibly inserted back into it [66].

Generally, P-type stacking is more open, as the oxygen ions are stacked on top of each other, increasing the electrostatic repulsion between layers which creates larger diffusion channels [70], [71]. Larger channels enable Na ions move more easily through the structure, leading to an increase in structural stability and rate capabilities. P2-

$Na_{0.67}Ni_{0.33}Mn_{0.67}O_2$, for example, is a well-studied cathode material [72]. It has a high average operating voltage (3.6 V) as a result of the Ni^{2+}/Ni^{4+} redox couple [43], reversibility [73], and theoretical capacity of 173 mAh g^{-1} [73]. This has translated into measured capacities as high as 160 mAh g^{-1}, [74], [75]. At high potentials, ~4.2 V, the sodium content is low and cannot stabilise the prismatic sites within the cathode structure and so the structure adopts an octahedral geometry. This can either be in the form of an O2 phase, or an OP4 phase (which has alternating prismatic-octahedral geometry). The P2↔O2 phase transition is harmful to capacity retention and poor performance of P2 materials can be attributed to its occurrence [44], [74]. The reason for this that when the transition occurs there are two layer glides that can result in an O2 phase [74], shown in Figure 1-11, and since both are possible it causes stacking faults occur in the cathode. It also causes a large (20%) volume change that can lead to exfoliation [75].

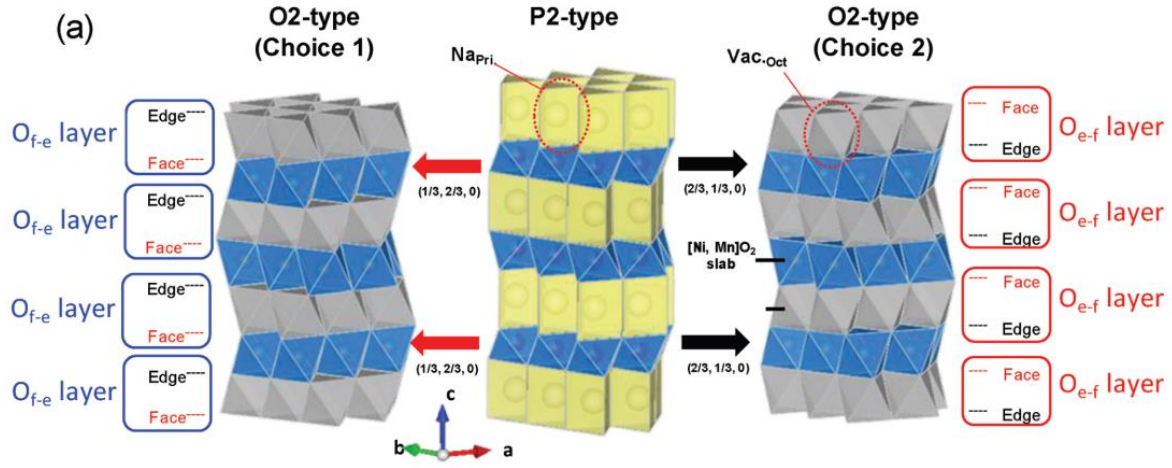

Figure 1-11: Schematic showing the two ways that the P2 phase can transition to the O2 phase [39].

The P3 phase, like P2, is synthesised in a Na deficient condition ($x \approx 0.67$). As such, it shares the prismatic Na sites and higher Na diffusion than O-types as the P2 phase [76]. The octahedral Na sites in O-type phases are separated by interstitial tetrahedral sites, meaning a more tortuous path and increased energy barrier for Na migration than in P-type phases (Figure 1-12). This translates to excellent rate capability [65]. The capacity of P3 phases does not fade as quickly as in P2 when considering the phase transitions, as the P3↔O3 transition is highly reversible [77], [78], unlike P2↔O2. It is still a source of capacity fading, as phase transitions require an overpotential which leads to voltage hysteresis. The transition also results in large volume changes [79], resulting in particle cracking and loss of active material. However, the same techniques that are used to mitigate phase transitions in other phases are used to explore the potential of P3 phases. Furthermore, the formation of P3 phases occurs at a lower temperature to P2 phases [39], [80], which is promising for the increased sustainability of cathode production as it reduces the energy demand of calcination.

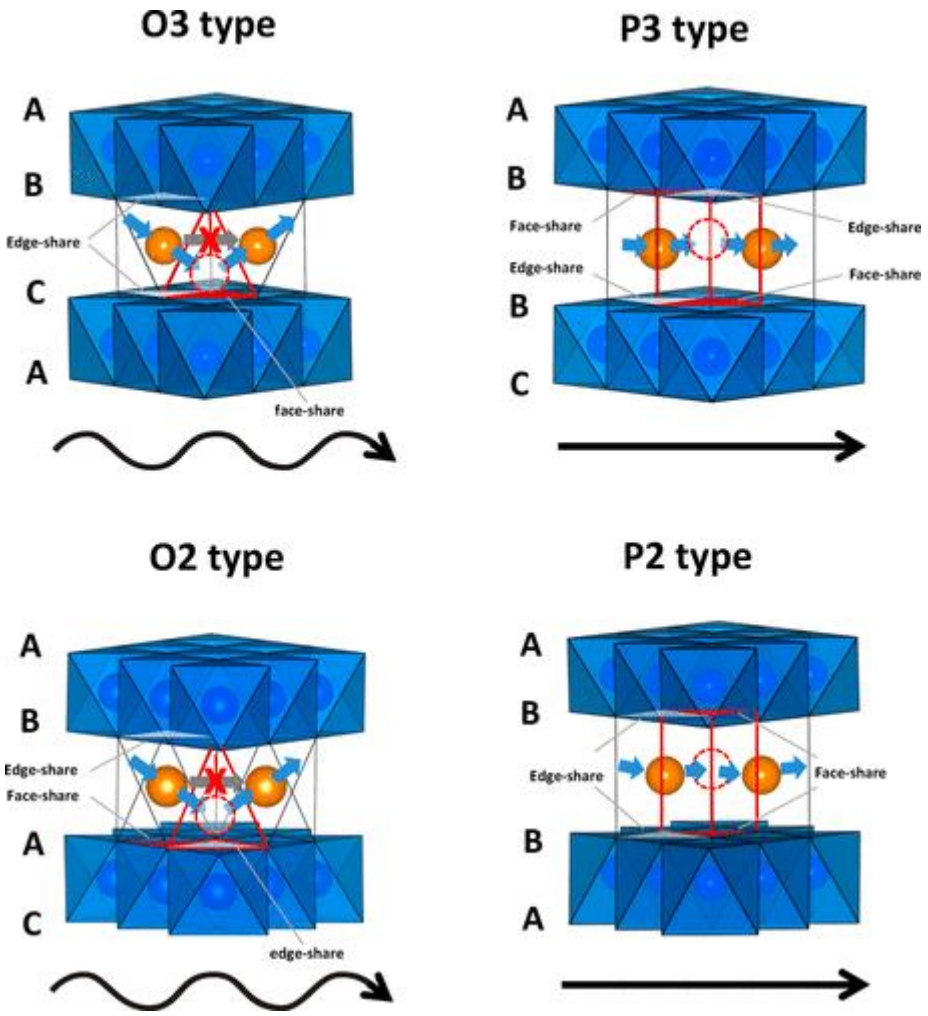

Figure 1-12: Schematic of the Na migration pathways in the common layered oxide structures [81].

P2-$Na_{0.67}Ni_{0.33}Mn_{0.67}O_2$ exhibited an initial discharge capacity of 160 mAh g^{-1} when cycled between 2.0- 4.5 V at 10 mA g^{-1} (~C/20), with a capacity retention of 50% after 50 cycles. with 1% Mg doping, encouraging the P2↔OP4 phase transition to occur instead of P2↔O2, the initial capacity dropped to 113 mAh g^{-1}, with a capacity retention of 98% in the same test parameters. As such, work on these systems is often focussed on either preventing the phase transition or encouraging the less harmful P2↔OP4 transition instead [44], [73], [82]–[84].

A similar phase transition occurs in O3 systems. For O3-$Na_xMn_{0.25}Fe_{0.25}Co_{0.25}Ni_{0.25}O_2$ [85], the P3 phase is dominant at potentials above ~2.7 V. Below ~2.7 V, the O3 phase is dominant as the sodium content gets progressively higher, approaching x = 1. This P3↔O3 transition has been observed from $x \approx 0.9$ [86] to $x \approx 0.67$ [87]. The O3 phase is formed at both high and low potentials here. At potentials >3.7 the Na^+ present in the material ($x \approx 0.33$) cannot stabilise the prismatic sites, as with the P2 phase. At potentials <2.7 or high Na content ($x \approx 0.8$) the Na^+ disrupts the repulsion between neighbouring TMO_2 layers and allows them to shift back to an octahedral geometry. The value of x at

which the P3↔O3 phase transition occurs depends on the identity and therefore electropositivity of the transition metal in the TMO_2 layer [88].

The fluidity of the phases *in operando* is apparent in Figure 1-13, where the phase transitions are tracked using *operando* XRD. O3-$Na_xMn_{0.25}Fe_{0.25}Co_{0.25}Ni_{0.25}O_2$ [85] displays an initial capacity of 180 mAh g^{-1} when cycled at C/10, with a capacity retention of 86% after 20 cycles. The ways phase transitions affect performance must always be considered when evaluating a cathodes performance. A more complex phase diagram does not necessarily lead to worse capacity retention (and *vice versa*), and often a lower initial discharge capacity leads to improved capacity retention.

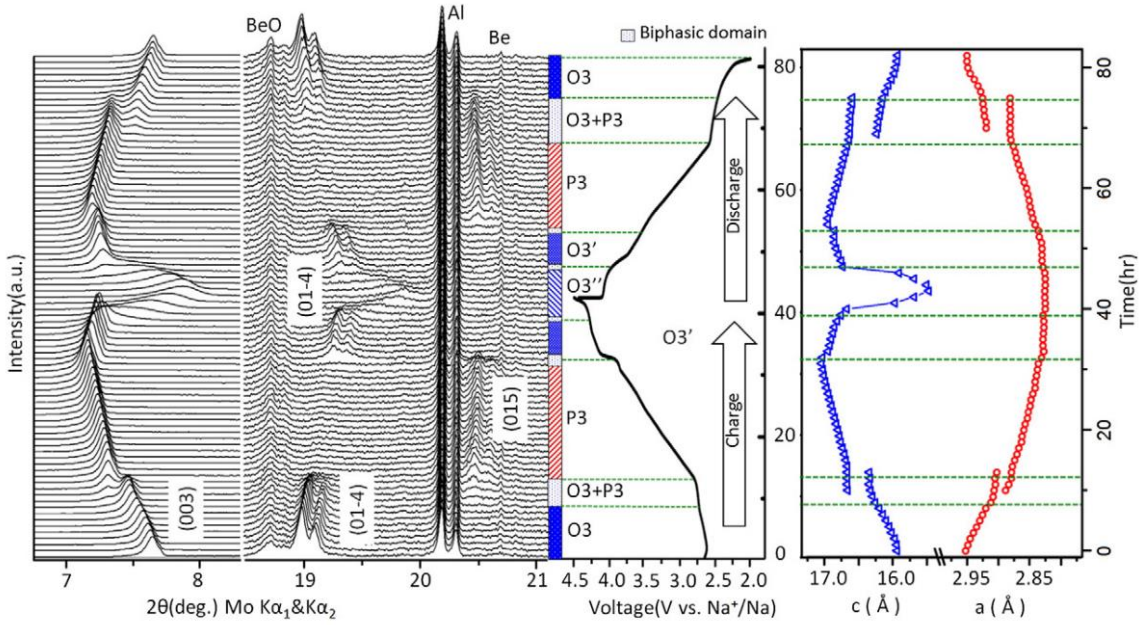

Figure 1-13: Operando *XRD of characteristic* hkl *peaks of* $Na_xMn_{0.25}Fe_{0.25}Co_{0.25}Ni_{0.25}O_2$ *(left), corresponding to the* in situ *galvanostatic charge and discharge profiles at C/50 rate (middle), and corresponding lattice parameter evolution (right). Double peaks for (01–4) and (015) peaks are from the* $K\alpha_1$ *and* $K\alpha_2$ *emissions in the Mo X-ray source* [85].

The above results demonstrate the relationship between the intercalation of sodium ions and structural modification [89]. The transition is triggered by a change in the sodium content, rather than occurring at specific potentials, as the potential of the cell at the transition is affected by the resistivity of the electrolyte and the current. Shown in Figure 1-14 are some typical phase transitions that cathodes can undergo, the selected P2 cathode materials generally undergo fewer phase transitions than O3 cathodes, and LIB cathodes undergo fewer than NIB cathodes. The Z phase listed in Figure 1-14 is referred to in the literature [90], [91]. It has been identified as an intermediate intergrowth structure as the P2 phase transitions to the O2 phase *via* the OP4 structure [92]. As Na is extracted from the P2 structure, some layers will reach a Na content where it is favourable to shift to an octahedral geometry before others. A schematic is shown in Figure 1-15.

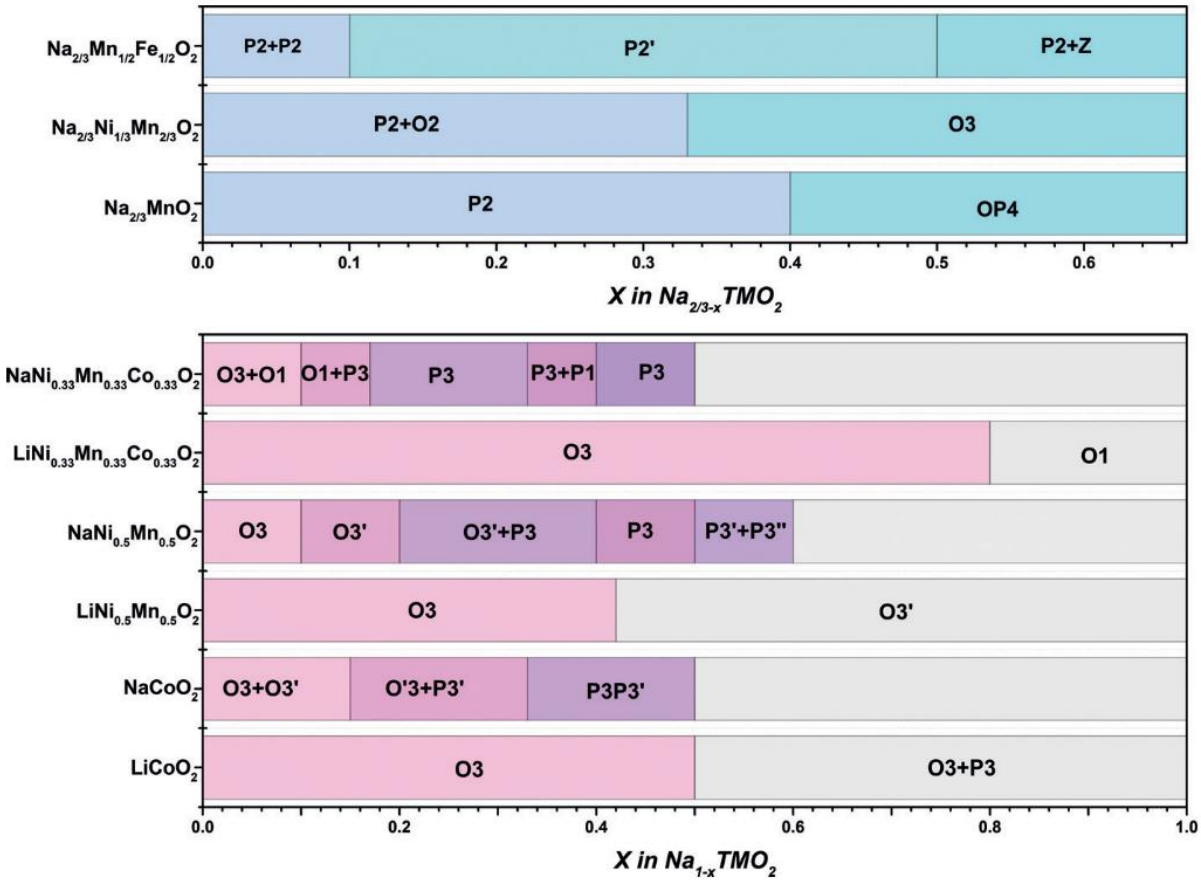

Figure 1-14: Phase behaviour of different Li layered oxides ($LiCoO_2$, $LiNi_{0.5}Mn_{0.5}O_2$, $LiNi_{0.33}Mn_{0.33}Co_{0.33}O_2$) and sodium layered oxides. Mainly P2-type materials ($Na_{2/3}MnO_2$, $Na_{2/3}Ni_{1/3}Mn_{2/3}O_2$, $Na_{2/3}Mn_{1/2}Fe_{1/2}O_2$) are shown on top, mainly O3-type materials ($NaCoO_2$, $NaNi_{0.5}Mn_{0.5}O_2$, $NaNi_{0.33}Mn_{0.33}Co_{0.33}O_2$) are shown at the bottom [24].

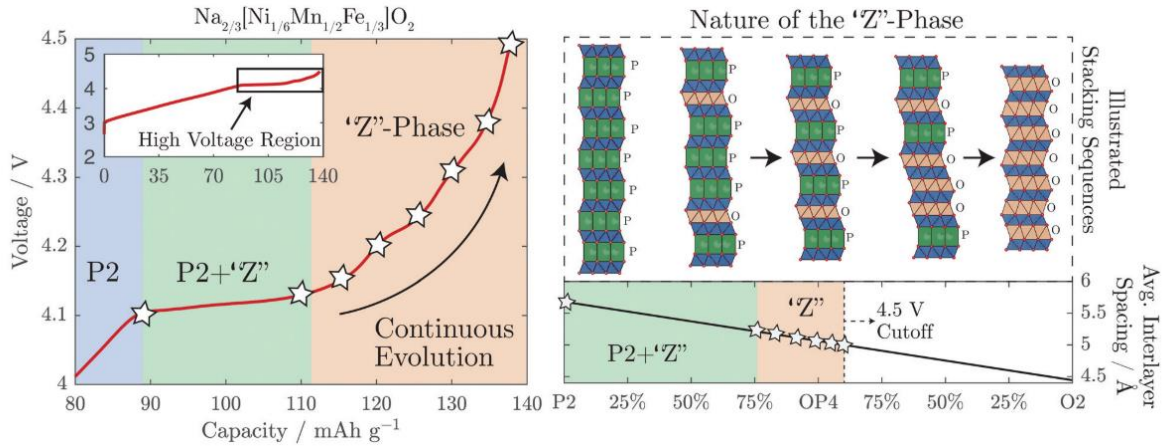

Figure 1-15: A summary of the proposed phase transformation mechanism for the Z-phase is shown. Above 4.1 V, Na is extracted via *the introduction of O-type stacking faults into the P2 structure decreasing the average interlayer spacing of the structure. The inset on the top left shows the whole charging curve, highlighting the high voltage region to which the main plot relates.*

The two P-type phases, P2 and P3, perform differently too. The main difference between the two, other than the number of TMO_2 layers in the unit cell, is the environment of the Na. For P2, there are two Na sites present. One is face-sharing (Na^I) with the two neighbouring TMO_2 octahedra, meaning it feels more electrostatic repulsion and is a higher energy site. The other is edge-sharing (Na^{II}) with neighbouring TMO_2 octahedra, which can have a higher occupancy than Na^I as it is energetically favourable electrostatically [93]. This results in two redox couples during cycling [53]. The Na site in P3 structures is edge-sharing on one side and face-sharing on the other, and so the sites are equivalent. Since P2 and P3 phases should have the same composition, the two have the same capacity in the same material but this is not usually the case; P2 has been shown to have higher capacity [94], or capacity retention [91], or both [80]. This is not always the case, as will be shown in Section 1.2.2.1, where P3 cathodes can display a higher capacity than the P2 phase of the same material. As will be discussed there, the difference between the two depends on the processes active in the cathode, such as phase transitions and other redox active species.

These and other transitions can be interpreted from the voltage profile of the material [56], [74]. The voltage profile of a material will have up to 3 distinct features: plateaux, linear change, and steps. These can be resolved into specific steps: two-phase regions, solid solutions, and unique (or "peculiar") compositions, respectively. This is demonstrated in an investigation into Na_xCoO_2 [95], using *in situ* XRD to track changes in the unit cell structure and lattice parameters. This work discharged Na_xCoO_2 using the galvanostatic intermittent titration technique (GITT) to observe the structure as close as possible to the thermodynamic equilibrium (Figure 1-16). The mode of operation in GITT is to discharge (or charge) the cell at fixed current intermittingly, rather than constantly. During the time when no current flows, the potential of the cell settle to an equilibrium value, at which point an XRD pattern is obtained. This allowed them to observe voltage drops and plateaux with better resolution than charging and discharging under a constant current.

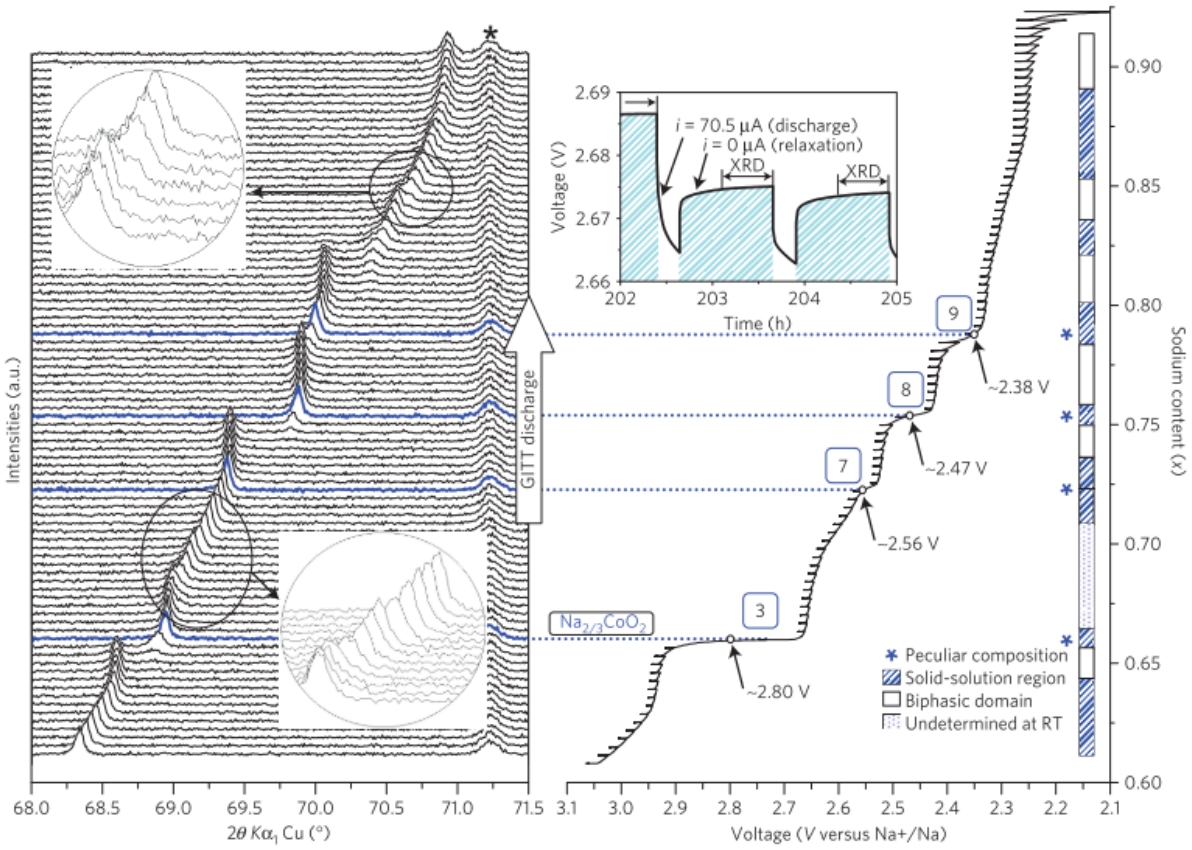

Figure 1-16: In situ *XRD patterns, corresponding the potential of P2-Na_xCoO_2. The XRD scan is conducted during the relaxation step of the GITT experiment* [95].

Notably, the features of the charge and discharge profiles of this material are similar, showing the reversibility of the intercalation process. When cycling the material, there is a drop in the number of re-intercalated sodium ions after the first charge, owing to electrolyte oxidation above 3.0 V. Charging only up to 3.1 V, the authors obtain a detailed description of the changes in structure the Na_xCoO_2 cathode undergoes during cycling. The accuracy with which they can do this is based on how reliably they can obtain a given composition. The value of x in the pristine Na_xCoO_2 cathode can be accurately estimated as Na_xCoO_2 is a well-defined material, as its potential at certain Na content values (e.g. x = 0.67) is well-known (2.8 V).

The authors demonstrate that features of the voltage profile correspond to events within the cathode structure. A phase transition, such as P3↔O3, or P2↔O2, is represented by a voltage plateau. The potential between the two electrode remains constant but sodium ions are still extracted/inserted. Voltage steps are points in the cycle where the cathode has reached a unique composition, e.g. $Na_{0.67}CoO_2$, where the material can form a superstructure *via* sodium ordering. When this happens during discharge, the ordering stabilises the structure, so the potential of the cell is lowered without sodium ions being inserted. The third feature of the voltage profile is linear sloping regions. These are simple solid solution regions, where sodium is inserted into the cathode without its structure changing, aside from a contraction of the unit cell along the *c* axis.

The implication of this work is that it is possible to predict the phases that are generated *in situ* by interpreting the voltage profile. In many cases, the voltage profile contains many steps and plateaux, and so identification of specific phase transitions is difficult. Similarly, there are many potential phase transitions that are possible, beyond the transition between prismatic and octahedral phases, such as the formation of distorted phases. The effects of specific phase transitions and what can be done to mitigate them has been mentioned already, such as doping or altering voltage ranges. They will be discussed in greater detail in Section 1.2.2.

Phase transitions are driven by an overpotential [96]. When discharging, sodium ions are inserted into the lattice which is followed by phase stabilisation and a decrease in energy as the transition metal accepts electrons into the *d* orbital [56] of the transition metal. During charge, however, the reverse of this process requires a promotion from lower energy states. The result of this is a difference between the charge and discharge voltage profiles, or voltage hysteresis, centred around the equilibrium potential for the phase transition Figure 1-17. This outcome is not limited to phase transitions: it occurs during solid-solution regions too, but phase transitions are the result of a higher overpotential.

A battery has an internal resistance, R_b, to the ionic current, I_i. So, the discharge voltage will be lower than the (equilibrium) open-circuit voltage V_{OC} by a polarisation, $\eta = I_{dis}.R_b$, just as the charge voltage will be increased by a polarisation, $\eta = I_{ch}.R_b$, to reverse the chemical reaction [18]. The polarisation is equal to the overpotential needed to induce a phase transition and leads to reductions in energy efficiency in a cell. Sometimes, the polarisation is small and leads to only small drops in efficiency, but that is not always the case. In particular, the P2↔O2 transition leads to a large polarisation, and overpotentials are highly pronounced at higher C-rates. In fact, higher rates of discharge can lead to formation of intermediate phase that aren't observed at lower rates [97].

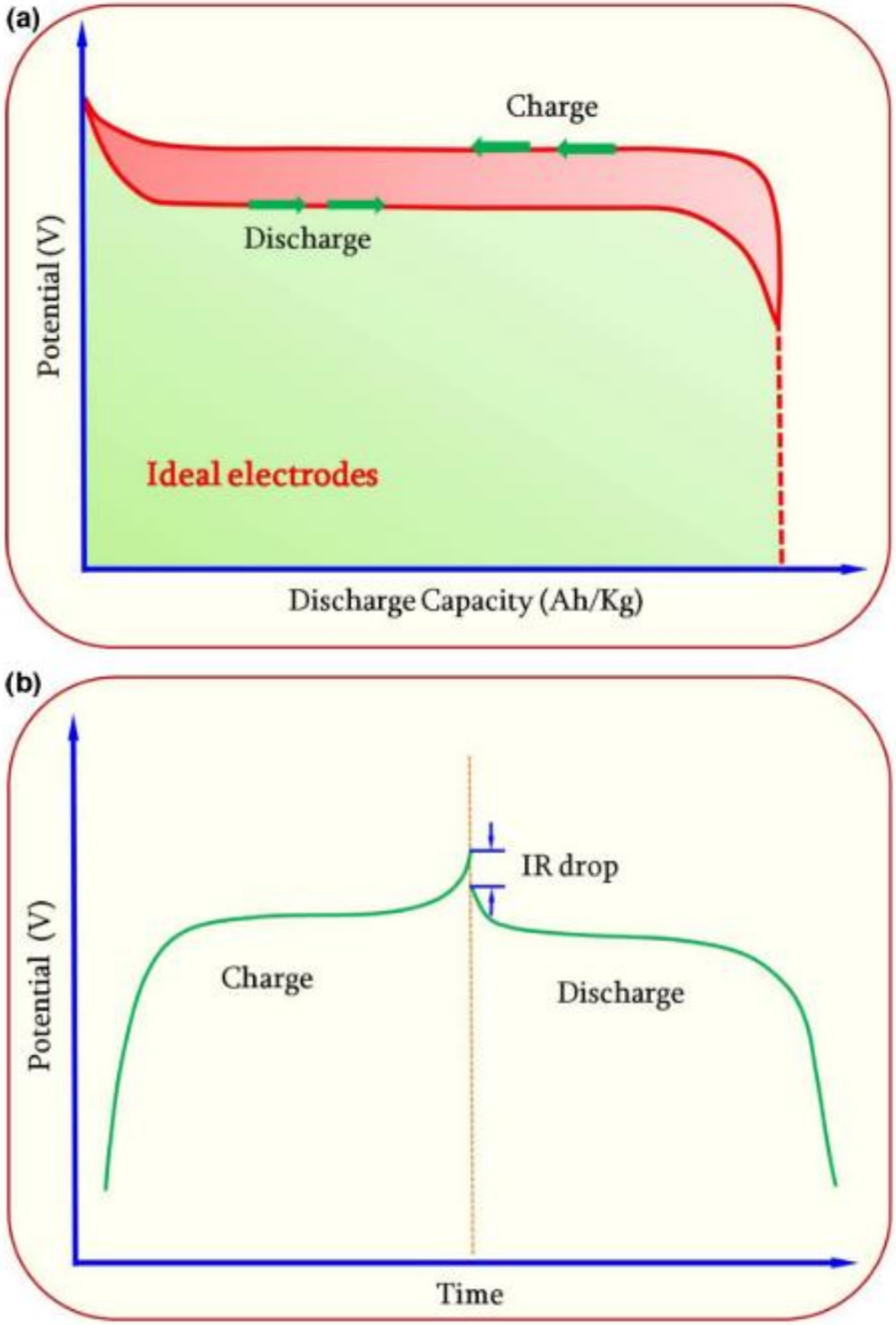

Figure 1-17: (a) the potential hysteresis (red) in the voltage profile of an electrode, and (b) the IR drop between charge and discharge [56].

1.2.2 Layered oxide development

1.2.2.1 High capacity

Since specific discharge capacity is a measure of simple how many Na^+ are reversibly inserted into the cathode relative to its mass, higher capacities can be achieved by simply reducing the mass of the cathode. This can be most easily done by using lighter redox active transition metals. High capacities have been achieved by using manganese, either as a redox active transition metal [51]–[54], [91], [98], [99], or as a lightweight redox inactive species [73], [100]–[105]. The initial discharge capacities of a selection these and similar materials are given in Table 1-1. The capacities of these materials range from 125 mAh g^{-1} to 210 mAh g^{-1}, which is approximately the same capacity range for LIB intercalation cathodes [22]. This highlights the competitiveness of NIBs in reaching higher capacities but does not consider the voltage range used, or its effect on the capacity retention. For further context, Figure 1-18 shows the voltage range and capacity of several NIB cathodes, with the majority delivering 100-150 mAh g^{-1}.

Table 1-1: Initial discharge capacity and C-rate for a range Mn-rich NIB cathodes.

Sample	Initial discharge capacity/mAh g^{-1}	C-rate	Reference
P2-$Na_{0.67}Mn_{0.9}Mg_{0.1}O_2$	175	C/15	[51]
P2-$Na_{0.67}Mn_{0.95}Mg_{0.0.5}O_2$	175	C/2	[52]
P2-$Na_{0.67}Mn_{0.89}Mg_{0.11}O_2$	150	C/15	[53]
P2-$Na_{0.67}Mn_{0.8}Mg_{0.2}O_2$	127[1]	C/2	[54]
P2-$Na_{0.67}Mn_{0.9}Mg_{0.1}O_2$	125	C/10	[91]
P3-$Na_{0.67}Mn_{0.9}Cu_{0.1}O_2$	138	C/20	[98]
P3-$Na_{0.67}Mn_{0.8}Mg_{0.2}O_2$	140	C/20	[99]
P2-$Na_{0.67}Ni_{0.33}Mn_{0.67}O_2$	138	C/5	[72]
P3-$Na_{0.67}Ni_{0.33}Mn_{0.67}O_2$	210	C/10	[100]
P2-$Na_{0.67}Ni_{0.33}Mn_{0.67}O_2$	155	C/10	[102]
O3-$NaNi_{1/3}Fe_{1/3}Mn_{1/3}O_2$	130	C/10	[104]
P3-$Na_{0.5}Ni_{0.25}Mn_{0.75}O_2$	130	C/20	[105]
O3-$NaNi_{0.5}Mn_{0.5}O_2$	148	C/10	[106]
O3-$NaNi_{0.45}Mn_{0.55}O_2$	200	C/20	[107]

[1] Data taken from second cycle.

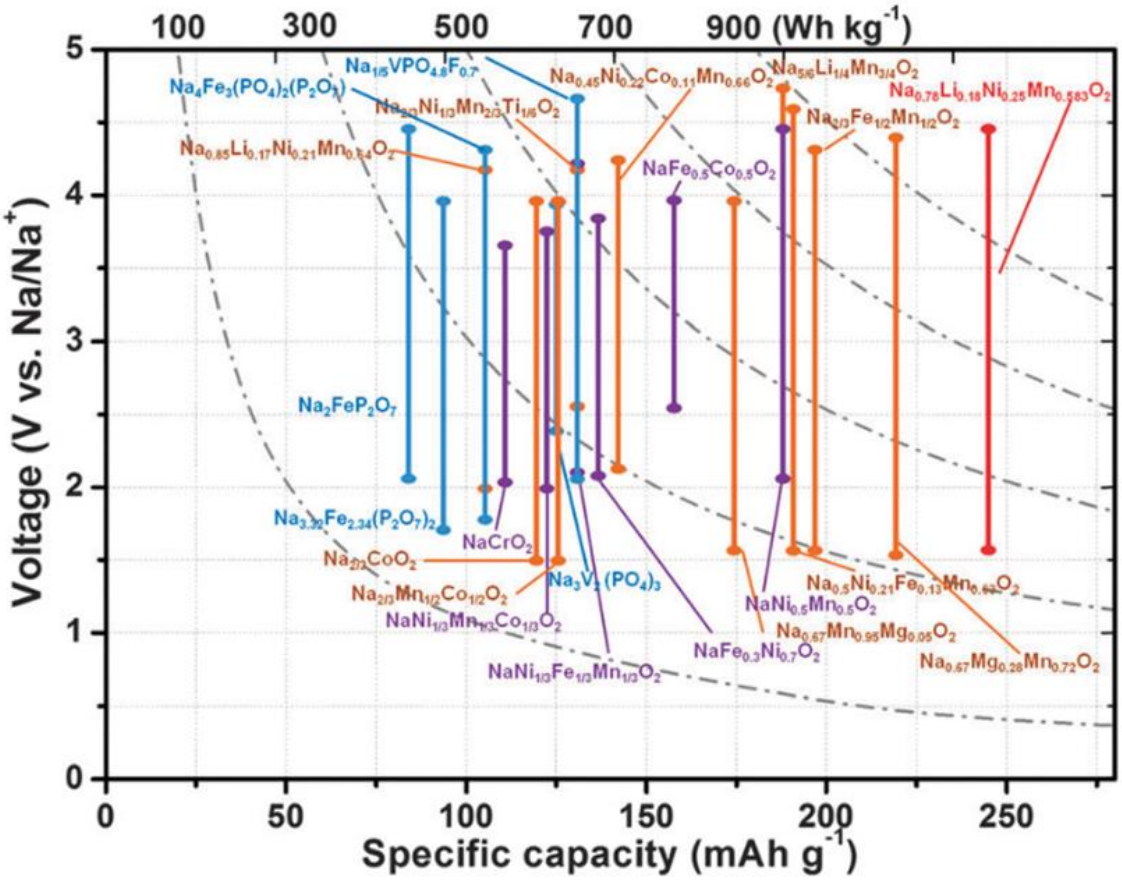

Figure 1-18: Graph comparing the discharge capacities and voltage windows of a range of sodium-ion cathode materials and structures [68].

As a lightweight transition metal, Mn-rich cathodes will necessarily have a higher specific capacity per sodium ion that can be reversibly extracted than, for example $NaCoO_2$. Indeed, it does have a high capacity, but due to the Jahn-Teller activity present (from the Mn^{3+} ion) the capacity retention of undoped O3-$NaMnO_2$ and P2-$Na_{0.67}MnO_2$ is limited: 72% after 20 cycles between 2.0 – 3.8 V at C/10 and 59% after 61 cycles between 2.0-4.1 V at C/15, respectively [55], [82]. However, reducing the fraction of manganese in the material can be done without sacrificing its capacity; either by substituting manganese with another electrochemically active transition metal (e.g. Ni [108], Co [109], Fe [110]), or an inactive element (e.g. Mg [51], [52]).

$Na_{0.67}Ni_{0.33}Mn_{0.67}O_2$

When combining manganese with nickel, excellent performance can be achieved. P2-$Na_{0.67}Ni_{0.33}Mn_{0.67}O_2$ exhibits high capacities, with 0.67 mol of sodium able to be extracted because of the Ni^{2+}/Ni^{4+} redox couple. Fully extracting all 0.67 mol sodium from the host material can be done reversibly and means a theoretical capacity of 173 mAh g^{-1}, which is considered high. This is commonly reported [44], [60], [61], [74], [75], [93], [111]–[113] almost as a standard cathode material, with a wide variety of alterations to the starting material (e.g. doping, varying the nickel/manganese ratio [93], [114], different

synthesis techniques, etc). The work done by a selection of these groups is detailed below and summarised in Table 1-2.

Table 1-2: Several approaches to improving performance of P2-$Na_{0.67}Ni_{0.33}Mn_{0.67}O_2$. Initial capacity is given in mAh g^{-1}, capacity retention is given after 50 cycles.

Strategy	Synthesis	Cycling test	Initial capacity	Capacity retention	Ref.
10% Mg doping	Solid state	2.0-4.5 V C/15	128	95%	[93]
20% Mg doping	Solid state	1.5 – 4.2 V C/5	130	92%	[114]
Al_2O_3 surface coating	Solid state	2.5 – 4.3 V C/2	150	88%	[75]
1% Sn doping	Co-precipitation	1.5 – 4.5 V 1C	175	74%	[111]
FEC additive, shorter voltage range	Sol-gel	2.0 – 4.0 V C/10	95	100%	[113]

As was shown for $Na_{0.67}MnO_2$, doping P2-$Na_{0.67}Ni_{0.33}Mn_{0.67}O_2$ with 10% Mg (replacing 0.1 mol Ni) increases the capacity retention [93]; increasing the discharge capacity from 55 mAh g^{-1} to 122 mAh g^{-1}after 50 cycles at 12 mA g^{-1} (C/15), as well as at 400 mA g^{-1} (2.3C). *In situ* XRD and the differential capacity plots of the material reveal no evidence of the P2↔O2 transition, but instead the OP4 phase is formed at high voltage. The avoidance of the O2 phase is credited for the increase in capacity retention, and the high capacity at elevated discharge currents is due to the increased Na mobility in the structure. The Mg is theorised to reduce the length of the TM-O bonds, increasing the interlayer spacing, lowering the energy barrier to Na^+ diffusion. Similar logic is applied when discussing the difference in Na^+ mobility in P-type and O-type cathodes [43], [69]. Later work shows that Mg^{2+} disrupts Na^+ ordering in the material [44] and leads to more gradual structural changes during cycling.

Increasing the Mg^{2+} doping level in P2-$Na_{0.67}Ni_{0.33}Mn_{0.67}O_2$ to 20% causes 5% Mg to occupy the Na layer, with the remaining 15% Mg in the TMO_2, which causes a contraction in the *c* lattice parameter [114]. This causes a pillar effect, often seen when doping layered materials with Ca^{2+} [115]–[118] which is discussed in greater detail in Chapter 4. This materials shows O redox activity above 4.0 V, but oxygen loss is prevented by the presence of Mg, which has a stabilising effect on oxygen [119]. Raising the lower voltage limit to 2.5 V led to a capacity retention of 75% over 1000 cycles at 1C between 2.5 – 4.2 V, with an initial capacity of 75 mAh g^{-1}. At 25C, the cathode delivers 55 mAh g^{-1}.

A 12 nm coating of Al_2O_3 was used to provide external mechanical support for P2-$Na_{0.67}Ni_{0.33}Mn_{0.67}O_2$ during the phase transition to O2, rather than avoid it [75] as the phase transition involves a large (20%) volume change. The effect of this is to increase

the capacity retention of the material: the coated P2-$Na_{0.67}Ni_{0.33}Mn_{0.67}O_2$ delivers 115 mAh g^{-1}after 300 cycles between 2.5 – 4.3 V at C/2, compared to just 43 mAh g^{-1} for the uncoated material. The coating does hinder Na^+ by increasing the contact resistance, which means that the coated P2-$Na_{0.67}Ni_{0.33}Mn_{0.67}O_2$ delivers almost 0 mAh g^{-1} at 5C, compared to 20 mAh g^{-1} for uncoated P2-$Na_{0.67}Ni_{0.33}Mn_{0.67}O_2$. The coated material recovers to 140 mAh g^{-1} after cycling at C/10, because the high current does not degrade the material, but high impedance causes the potential to drop significantly. The Al_2O_3 coating also changes the SEI formation mechanism, and suppresses a side reaction that occurs at 4.4 V.

Doping with 1% Sn [111] causes the particle size of P2-$Na_{0.67}Ni_{0.33}Mn_{0.67}O_2$ to be reduced from micron-sized flakes to spherical particles that are <0.5 μm in size. It also causes a P3 phase to form, as Sn^{4+} decreases the pH of the mixture solution, which favours P3 formation [86]. When cycled at C/10 between 1.5 – 4.5 V during a rate capability test, the $Na_{0.67}Ni_{0.33}Mn_{0.67}Sn_{0.01}O_2$ delivers 245 mAh g^{-1}, far exceeding its theoretical capacity. Using this voltage range at 1C, the discharge capacity is 175 mAh g^{-1}. The capacity fades to 130 mAh g^{-1} for 50 cycles, however. When only cycled between 2.0 – 4.2 V the capacity is instead 90 mAh g^{-1} but remains very steady – a capacity retention of 100% after 50 cycles at 1C. The additional capacity in this material is a result of oxygen redox activity. High capacity and low capacity retention are common in materials that use O redox [120]–[122], which is due to subsequent O loss from the structure [119]. The capacity retention appears worse at C/10 than 1C, which may be because of the large voltage hysteresis associated with O redox, so less O redox occurs at 1C, leading to improved capacity retention.

Through selection of voltage limits and electrolyte additives, P2-$Na_{0.67}Ni_{0.33}Mn_{0.67}O_2$ was successfully cycled at 10C for 1200 cycles, with an initial capacity of 66 mAh g^{-1} and capacity retention of 71% [113]. The voltage range used to obtain these results was 2.0 – 4.0 V, but if the upper limit is raised to 4.5 V or the lower limit is lowered to 1.5 V, the P2↔O2 phase transition occurs, causing much lower capacity retention. The high capacity retention is also caused by the addition of fluoroethylene carbonate (FEC). This is an electrolyte additive [123] that suppresses electrolyte decomposition and enhances the reversibility of metallic Na deposition and dissolution.

The average capacity of the cathodes discussed so far is 150 mAh g^{-1} ± 30 mAh g^{-1}, which is high compared to the average state-of-the-art NIB [124]. There have been attempts to increase the capacity further by increasing the fraction of sodium that can be extracted. This was achieved using O3-$NaNi_{0.5}Mn_{0.5}O_2$ [66]. This high sodium content means that the material forms an O3 phase instead of P2. The capacity available from this material is high, 185 mAh g^{-1}, corresponding to 1 mol of sodium being extracted, but suffers from significant capacity fading; only 25 mAh g^{-1} capacity remaining after 26 cycles at C/30. The upper voltage limit required to extract sodium is likely decomposing the electrolyte. Capacity retention can be improved by lowering the cut-off voltage on charge from 4.5 V to 3.8 V, at the cost of reducing the discharge capacity to 125 mAh g^{-1}. This corresponds

to 0.5 mol sodium being reversibly extracted. This is achieved at a low discharge current, C/30. Longer term cycling, conducted at C/5 for 50 cycles, exhibits an initial discharge capacity of 115 mAh g^{-1}, which decreases to 90 mAh g^{-1}. As will be discussed later, the group later improve the capacity retention by using 2% v/v FEC as an electrolyte additive. Doping O3-$NaNi_{0.5}Mn_{0.5}O_2$ with 1% Ca (replacing 0.02 mol Na) stabilises the high upper voltage limit [103]. An initial capacity of 198 mAh g^{-1}, with a capacity retention of 75% after 100 cycles at C/2 between 2.0 – 4.3 V. Ca^{2+} mitigates the volume change when the O-type to P-type phase transition occurs. O redox is not mentioned but may play a role, given the high capacity.

Work has also been done in exploring new phases and synthesis [61] techniques to increase capacity of $Na_{0.67}Ni_{0.33}Mn_{0.67}O_2$. Biotemplating, discussed in greater depth in Section 1.3.5, was used to generate cathode particles that were an order of magnitude smaller than those synthesised *via* solid state methods, and formed as a P3 phase rather than P2. The effect of this was to increase the capacity by 20 mAh g^{-1}, dramatically reduce the calcination temperature and time, and to smooth the charge and discharge voltage profiles. A direct comparison of the P2 and P3 phases was not performed here, meaning the specific differences in performance of the two structures cannot be fully elucidated, nor can the changes in performance be related back to the synthesis methods used.

Nickel has been used to successfully obtain high (>150 mAh g^{-1}) capacities in sodium-ion batteries. However due to its low abundance, leading cost and supply concerns, and toxicity [25]–[27] it is unlikely to be a feasible candidate for large-scale storage. Instead, researchers have turned their attention to manganese, which fares better on both metrics while still delivering high capacity.

$Na_{0.67}Mn_{0.9}Mg_{0.1}O_2$

The aim of sodium-ion batteries is to increase the sustainability of the energy storage industry, then using a cathode material utilising nickel [125] is inappropriate. Success has been achieved by using P2-type Mn-rich oxides [45], [51]–[53], [58], [70], [119], [126]–[130] (summarised in Table 1-3) as the electrochemically active element in the system to increase the sustainability of the system, given the relative abundance of manganese compared to other transition metals [39].

In initial investigations [45], it was found that P2-$Na_{0.6}MnO_2$ could achieve discharge capacities of 150 mAh g^{-1}. The material soon degraded, losing 50% of its capacity by the end of 10 cycles, even within a limited voltage window and a current density of 0.1 mA cm^{-2} (approximately C/10). It can be seen from the voltage profiles that both the charge and discharge processes involved several steps as they are not smooth, and there are several distinct peaks in the differential capacity plot. These data point to several structural changes occurring in the cathode, primarily ordering of the sodium ions. The authors suggest that it is due to the inflexibility of the host structure, and it is unable to withstand the strain and distortion from the continual insertion and extraction of sodium ions before eventually collapsing. Given the relative infancy of this area of research, it is

reasonable that some of this can be explained by the lack of optimisation of the experimental set up. However, it cannot be denied that P2-$Na_{0.6}MnO_2$ suffers from severe capacity fade, but does exhibit a high discharge capacity, considering the sustainability of the constituent materials.

Table 1-3: Several approaches to improving performance of P2-$Na_{0.67}MnO_2$. Initial capacity is given in mAh g^{-1}, capacity retention is given after 50 cycles.

Strategy	Synthesis	Cycling test	Initial capacity	Capacity retention	Ref.
20% Mg doping	Solid state	1.5 – 4.2 V C/15	150	97%[2]	[51]
Combining P2 (95%) and O3 (5%) phases	Solid state	1.5 – 4.2 V C/10	125	76%	[70]
1:1 Mn and Fe	Solid state	1.5 – 4.3 V C/20	190	79%[3]	[58]
11% Al doping	Liquid state	2.0 – 4.0 V C/10	130	96%	[130]

One method to improve the performance of P2-$Na_{0.6}MnO_2$ is to use single crystalline nanoplates [126], which delivers 164 mAh g^{-1} (near the theoretical capacity of 170 mAh g^{-1}) – comparable to the high capacity cathode P2-$Na_{0.67}Ni_{0.33}Mn_{0.67}O_2$. The capacity remains high, with 110 mAh g^{-1} of reversible capacity available after 50 cycles at 40 mA g^{-1} (approximately C/4) even when charging to 4.5 V. The authors highlight the importance of the (100) plane as it allows for facile sodium ion insertion and extraction, and how this is achieved *via* nanosizing. They synthesise their material using a hydrothermal method, with a 6 h calcination at 220 °C. This temperature is significantly lower than all solid state synthesis due to the nature of the hydrothermal synthesis. The XRD patterns and Rietveld analysis presented does agree with the conclusion that they successfully synthesised a P2 phase. This study reinforces the importance of particle size in the development of batteries with long cycle lives and high capacities.

One high capacity material of note that involves the Mn^{3+}/Mn^{4+} redox couple is P2-$Na_{0.67}Fe_{0.5}Mn_{0.5}O_2$ [58]. Its initial discharge capacity is a remarkably high 190 mAh g^{-1} and remains high (150 mAh g^{-1}) after 30 cycles at C/20. Its performance suffers at higher C-rates, however. At 4C, it can only deliver 60 mAh g^{-1}. It also involves the Fe^{3+}/Fe^{4+} redox couple, but from X-ray absorption spectroscopy it appears that most of the charge compensation is driven by manganese redox, at least below 3.8 V. Between 3.8 V and 4.2 V, the Fe^{3+}/Fe^{4+} redox couple is active, as can be seen in the extended X-ray absorption fine structure (EXAFS) spectra where the radial distribution around the iron ions changes noticeably. Specifically, the Fe-O distance is shortened after charging to 4.2 V, and not

[2] Retention after 25 cycles.
[3] Retention after 30 cycles.

before charging to 3.8 V. The effect of this is to increase the average operating voltage of the cell. Another point to note in this study is the reversibility of the material despite repeatedly charging to 4.2 V. The authors detail how upon charging beyond 3.8 V an OP4 phase is obtained, as opposed to an O2 phase. The authors do not comment on why this transition is favoured in the P2-$Na_{0.67}Fe_{0.5}Mn_{0.5}O_2$. Studies [93], [102] have suggested that it is a function of dopants; certain dopants supress the formation of the O2 phase or stabilise the OP4 phase. It may also be that the OP4 phase is an intermediate phase [131] in between the P2 and O2 phases – sodium is extracted preferentially from octahedral sites upon partial layer shearing. The dopants may be acting to stabilise the P2 phase and delay O2 formation in this case. Prismatic sites are destabilised by sodium extraction and so are extracted from newly formed octahedral layers instead.

These materials, though they exhibit high specific capacities, exhibit voltage profiles with several features. This is particularly common in systems using manganese; it has many steps and short plateaux. There are two problems with this:

1) It makes practical applications for these materials harder as the power output is harder to predict and the state of charge is harder to estimate.
2) It indicates various structural transitions occurring during cycling, which can be responsible for capacity fading over time.

This makes routes to commercialisation difficult, as the performance and health of the battery cannot be reliably estimated. If the state of charge is uncertain there is a risk of over-charging or -discharging the battery, which leads to degradation. Large-scale energy storage installations must have long lifetimes to be economically viable, so degradation (either *via* improper charging or discharging, or structural transitions) limit this, and therefore its uptake.

As mentioned earlier, one cause of this in manganese systems is the presence of Jahn-Teller distortions caused by Mn^{3+}. It also causes distortions after calcination, where two phases (the ideal P2 structure hexagonal *P6₃/mmc* space group and the distorted P2 structure orthorhombic *Cmcm*) can be observed in undoped samples. Billaud *et al*. [51] successfully generate the ideal P2 structure with the *P*6₃/*mmc* space group *via* two mechanisms: slow cooling and doping with Mg^{2+}. This study highlights several important considerations when developing battery cathodes: synthesis conditions and dopants have a significant effect on the phase transitions that materials undergo when cycling; and the phase transitions that are undergone have significant (and often negative) effects on the cycle life of said materials. Specifically, magnesium doping and slow cooling results in a smoother voltage profile. The effect of magnesium doping is more pronounced in the samples that are quenched. In terms of phase transitions, the undoped $Na_{0.67}MnO_2$ displays a voltage plateau at 3.5 V, which is identified by the authors to be a P2-OP4 transition. This plateau is much less pronounced in the slow cooled samples at each magnesium doping level and decreases in length as the level of magnesium doping increases. Although the (reduced) plateau is still present in the slow cooled, doped samples there is no trace of the new phase in the post-charge XRD, which the authors

suggest is indicative of a small nucleus of this OP4 phase having a significant effect on the voltage features of the material.

Overall, there is a trend of increasing the level of magnesium doping leading to a drop in capacity as seen in Figure 1-19 (from 175 mAh g^{-1} in the undoped sample, to 150 mAh g^{-1} in P2-$Na_{0.67}Mn_{0.8}Mg_{0.2}O_2$) and an increase in capacity retention (130 mAh g^{-1} after 25 cycles in the undoped sample, 145 mAh g^{-1} in P2-$Na_{0.67}Mn_{0.8}Mg_{0.2}O_2$). The equivalent trend can be seen when comparing the quenched and slow cooled samples. The origin of this trend lies in the fraction of (Jahn-Teller active) Mn^{3+} in the material. When doping, two Mn^{3+} ions are replaced by one Mg^{2+} ion and one Mn^{4+} ion. Similarly, slow cooling leads to more manganese vacancies, and to balance the charge of the material, more manganese ions must be in the +4 oxidation state. This results in there being fewer Mn^{3+} ions in the material in its reduced (discharged, Na-rich state) and so fewer sodium ions can be extracted from the material (or fewer ions can be oxidised) during charge, leading to a reduction in the capacity of the material and an increase in capacity retention as fewer phase distortions/transitions occur. Similar effects have been found several times [52], [53].

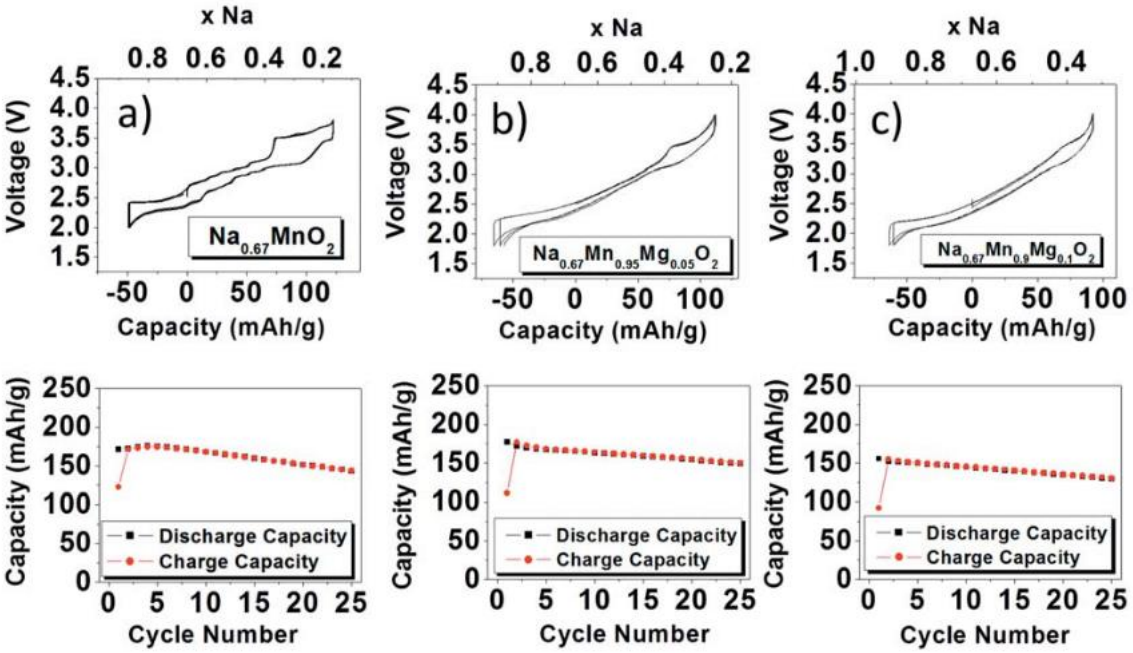

Figure 1-19: Voltage profiles and capacity over 25 cycles for quenched P2-$Na_{0.67}Mn_{1-x}Mg_xO_2$ cycled at 12 mA g^{-1} vs Na. (a) x = 0, 2.0 – 3.6 V, (b) x = 0.05, 1.75 – 4.0 V, (c) x = 0.1, 1.75 – 4.0 V [51].

There have been, however, reports using the same material with a higher level of magnesium doping that achieves a very high capacity of 220 mAh g^{-1}: P2-$Na_{0.67}Mn_{0.72}Mg_{0.28}O_2$ [119], [127]. This capacity is beyond the theoretical capacity of the material when only considering the Mn^{3+}/Mn^{4+} redox couple. The extra capacity comes from the redox activity of the oxide ions but is not stable: the material loses 27% of its capacity in the first 30 cycles. As with nickel, cobalt, and lithium cathodes in general, this

is not conducive with our desire to develop sustainable energy storage materials, however this group demonstrates that the same phenomenon can be achieved by doping with magnesium.

The high capacity observed in this material is obtained when charging to 4.4 V. There is a voltage plateau at 4.2 V which is maintained over at least 5 cycles at a rate of 10 mA g^{-1} (C/26). After 30 cycles at this rate, the capacity drops steadily to ~160 mAh g^{-1}. This is still high, but the rate of decline is concerning. Structural analysis *via* synchrotron XRD (λ = 0.5 Å) shows a peak at 6.6 °2Θ that matches to a (1/3 1/3 0) superlattice plane that is still visible after charging to 4.4 V, indicating that in-plane cation ordering is retained throughout cycling. Further chemical analysis suggests that magnesium is not being extracted from the host structure. The authors note that there is evidence of a P2↔O2 transition in the broadening of XRD diffraction peaks on repeated cycling. This broadening is due to the introduction of stacking faults that follows the O2↔P2 transition and could be the cause of the capacity fade. It could also be, as the authors suggest, a result of a unit cell volume change of 15% during the P2↔O2 phase transition.

A later study on the same material [119] observed no oxygen loss occurring due to the interaction of Mg^{2+} with the O 2*p* orbital. No such interactions take place when the dopant is an alkali metal ion, such as in $LiNi_{0.2}Li_{0.2}Mn_{0.6}O_2$ [132], and so oxygen loss does occur. Several drawbacks of the material are noted in this study: the potential at which oxygen redox occurs is close to the stability limit for current electrolytes, and that there is significant voltage hysteresis, which is posited to be a result of the transition from O2 back to P2.

A study into oxygen redox in sodium-ion batteries looked at $Na_{0.6}Li_{0.2}Mn_{0.8}O_2$ [121], as in the pristine material the manganese should be in the +4 oxidation state, and so should not be further oxidised during charge. Here, the formation of peroxo-like dimers occurs, which would ordinarily lead to oxygen gas *via* a series of thermodynamically favourable steps. However, in this case it does not. The size of the sodium prismatic site is too large for the manganese or lithium to migrate into, and so rearrangement of the structure is prevented, and the peroxo-like dimer is preserved. The material does undergo rapid capacity fading at low currents (0.1 C), but this improves when it is increased to 2.0 C. the capacity fade is attributed to the P2↔O2 phase transition, so it is possible that the higher C-rate increases the polarisation to the extent that the transition is not fully complete by the time the cut-off voltage is reached, and so its reversibility is improved – even if initial discharge capacity is reduced.

These studies highlight a key consideration: chasing higher capacities often risks sacrificing capacity retention. The solutions to achieving both high capacity and good capacity retention likely lie in some of the same techniques discussed above: doping, tailoring phase fraction, improving electrolyte performance; using synthesis methods that generate smaller particles so that more sodium can be reversibly extracted; and exploring phases that have more reversible transitions at high potentials.

1.2.2.2 Improving cycle life

Improving the cycle life is a crucial performance metric to improve in NIBs if they are to replace LIBs [125]. As mentioned previously, a common source of capacity fade in sodium-ion batteries is the phase transitions in P2 materials, particularly to the O2 phase as it induces stacking faults and exfoliation P2 can be engineered to transform reversibly to the OP4 phase, an intergrowth intermediate between P2 and O2. As seen earlier [51], the OP4 does still have a harmful effect on the capacity and performance of the cell, even though the transition is more reversible. When the transition is less reversible it increases the polarisation of the cell, so the voltage required to charge the cell is higher than the voltage supplied when discharging the cell. Since the voltage limits are fixed, this translates to lower capacity too. Even if the capacity extracted is the same, the energy efficiency of the cell is lower.

There are ways that the P2 phase transition can be avoided. There have been several examples of doping the sodium layer with calcium [102], [115]–[118], which acts as a pillar and prevents the layers from gliding across each other. This does limit the amount of sodium that can reside in the layer, for every 1 mol Ca^{2+}, 2 mol Na^{+} are displaced. The Ca ions occupy the Na layer (Figure 1-20) because of the similar ionic radii of the two ions (1.00 Å and 1.02 Å, respectively [38]). The effect of Ca/F doping P2-$Na_{0.67-x}Ca_xNi_{0.33}Mn_{0.67}O_{2-2x}F_{2x}$ (x = 0.03) is to reduce initial capacity by 5 mAh g^{-1} to 83 mAh g^{-1}, but to increase the capacity retention over 500 cycles at 1C between 2.0 – 4.3 V from 29% to 87%.

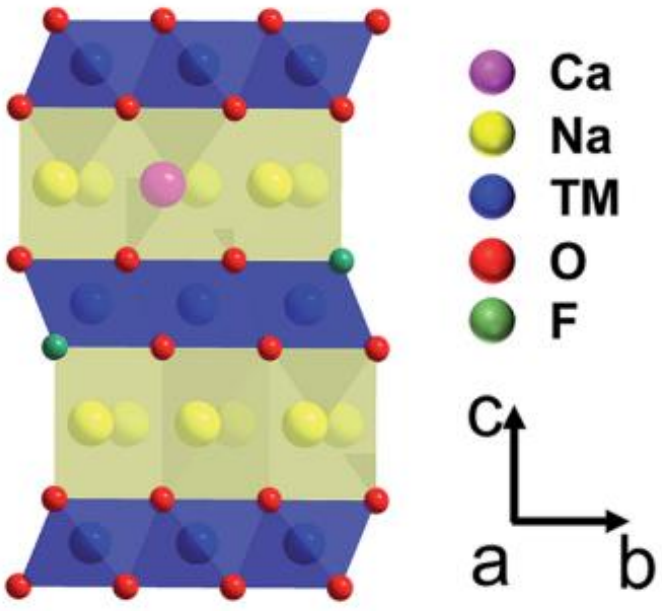

Figure 1-20: Schematic of P2-$Na_{0.67-x}Ca_xNi_{0.33}Mn_{0.67}O_{2-2x}F_{2x}$, doped with Ca (occupying Na sites) and F (occupying O sites) [102].

In one study, P3-$Na_{0.9}Ni_{0.5}Mn_{0.5}O_2$ [86] displays excellent capacity retention: 78% of the capacity is retained over 500 cycles at 1 C, even within a wide voltage window of 1.5 V –

4.5 V. *Operando* XRD reveals that phase transitions do occur near the end of both charge and discharge, forming the O3 phase. This transition is like the P2↔O2 transition, but more reversible, and evidently leads to lower capacity fading. The sodium ions stabilise the prismatic sites between the transition metal oxide layers, and so when it is extracted during charge the layers glide to form octahedral sites around the resultant vacancies. During discharge, this process is reversed, but when too much sodium is inserted into the structure, it disrupts the repulsion between transition metal oxide layers, and so an octahedral environment is more favourable at high sodium contents.

In this study, the voltage profile when charging to 4.5 V has few steps and plateaux and becomes smoother after ~10 cycles, as shown in Figure 1-21. This smoothing does not occur when only charging to 4.0 V. The authors posit that this is a result of side reactions between the electrode material and the electrolyte. Examining the long-term cycling data, when cycling in a lower voltage window (1.5 – 4.0 V) the capacity retention increases from 95% over 547 cycles to 99%, although the capacity drops from 102 mAh g^{-1} to 92 mAh g^{-1}. Furthermore, it can be observed that the polarisation between charge and discharge profiles is low, although the authors do not quantify this. These results suggest that the P3 phase is a promising structure for long-term cycling stability and consistent specific energy output and efficiency.

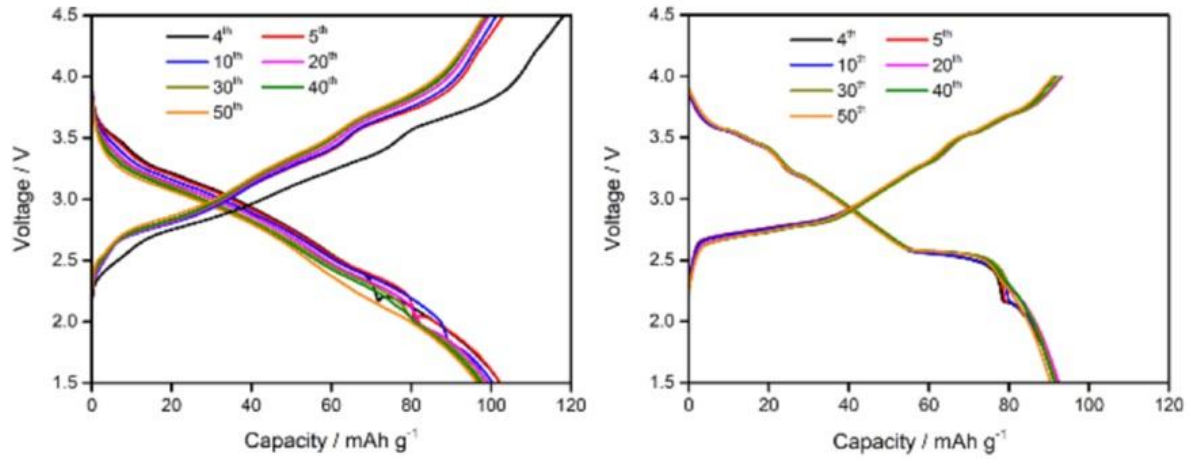

Figure 1-21: Voltage profiles of P3-$Na_{0.9}Ni_{0.5}Mn_{0.5}O_2$ when cycled at 1C between 1.5 – 4.5 V (left) and 1.5 – 4.0 V (right) vs *Na. The sample has much smoother profile after 10 cycles* [86].

Investigating P2- and P3-$Na_xNi_{0.22}Co_{0.11}Mn_{0.67}O_2$ [80] had less success. The P3 material showed a higher initial discharge capacity than the P2 (147 mAh g^{-1} and 130 mAh g^{-1}, respectively), but a much more rapid capacity fade. After 200 cycles at 0.1 C between 2.1 V – 4.3 V, the discharge capacities were 86 mAh g^{-1} and 100 mAh g^{-1}, respectively (Figure 1-22). At every cycle, the coulombic efficiency of the P2 material was higher than P3. The explanation given was related to particle size: the authors identify a trend in their samples that those with smaller particle sizes (the P3 phase and an intergrowth P2/P3 phase) degraded faster. It is suggested this could be a result of manganese dissolution that occurs *via* the tetrahedral sites on the O-type phase generated *in situ* [81]. This runs

counter to some of the research where smaller particles have exhibited greater performance [61]. Again, the electrolyte may be an issue: PC solvent has been shown to be unstable above 4.0 V [86], below the voltage limits in this study. Of course, each sample uses the same electrolyte solvent, but it likely that the deleterious effects of the solvent are more pronounced with smaller particles, as there will be greater contact between the electrode and electrolyte. Indeed, comparing the performance of the P2 samples with differing particle sizes, the P2 sample with the smaller particle sizes has better rate capability [80].

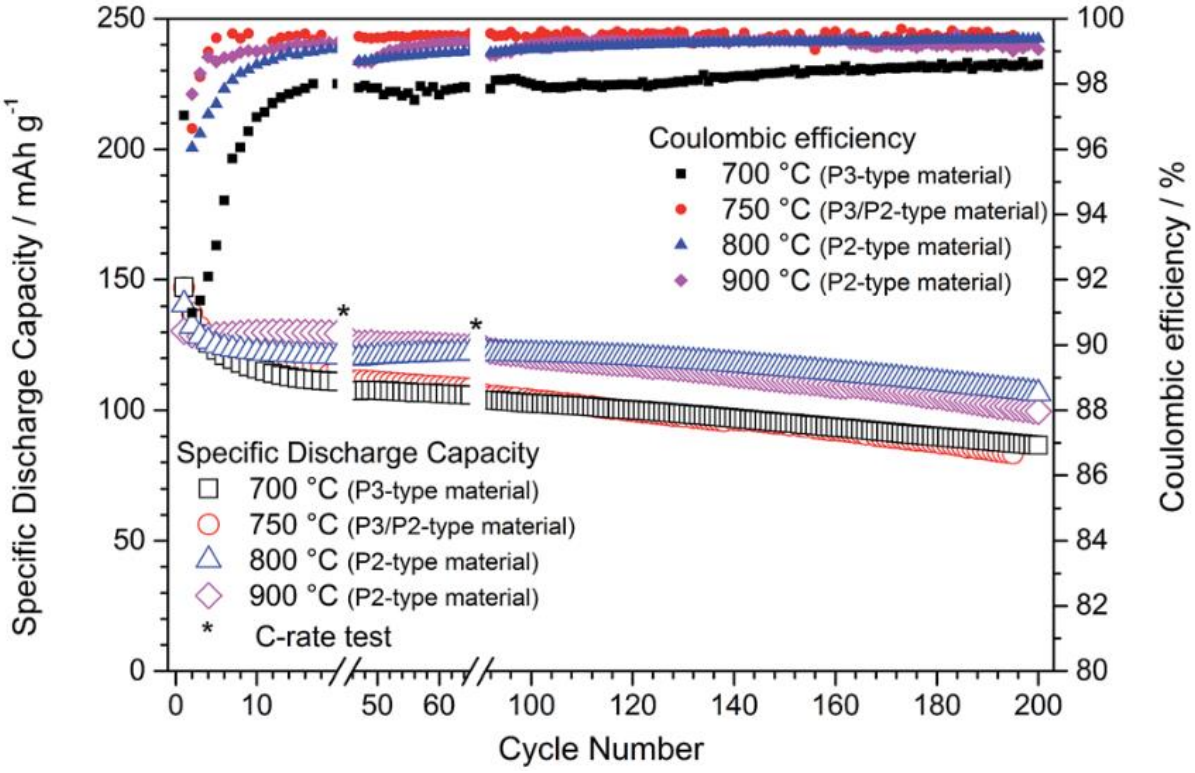

Figure 1-22: Capacity retention and coulombic efficiency of P-type $Na_xNi_{0.22}Co_{0.11}Mn_{0.67}O_2$ over 200 cycles. Except for the C-rate test cycles, the cell was cycled at 0.1 C between 2.1 – 4.3 V vs Na [80].

1.2.2.3 Rate capability

Increasing a materials capacity generally decreases its cycle life, usually because the additional capacity originates from an irreversible phase transition or redox process. However, approaches to materials that improve cycle life often increase the materials capacity at high C-rates. The reason for this is that the method of increasing capacity retention is the mitigation of harmful phase transitions – these cause voltage hysteresis that reduces capacity due to fixed voltage limits which is more pronounced at higher C-rates.

One paper directly compares the P2 against the P3 phase [94], using $Na_xTi_{0.37}Cr_{0.63}O_2$. It shows that by all metrics they test (capacity, capacity retention, rate capability testing) the P2 phase performs better. These materials are being tested as anode materials in the voltage range 0.15 – 2.5 V. This means that these materials operate at high sodium

content ($0.6 \leq x \leq 1$), whereas the cathode materials studied here are at lower sodium contents and operate at higher voltage ranges. It is unclear from their analysis whether these outcomes will hold true for cathode materials. Their study finds no evidence for a P2↔O2 or P3↔O3 transition. It also finds that the diffusion coefficient of the sodium ions changes depending on the sodium content of the crystal, as it changes during cycling as per GITT measurements. It is, therefore, unclear from this work how P3 compares to the P2 phase when used as cathodes as the voltage ranges have little overlap.

When phase transitions can be prevented [69] the capacity retention and rate capability improve noticeably. When cycling at 0.5 C, the capacity of the undoped sample is initially 73 mAh g^{-1} and drops to 47 mAh g^{-1} after 300 cycles (Figure 1-23). The cobalt doped sample, under the same conditions, starts at 82 mAh g^{-1} and drops to only 73 mAh g^{-1}. It also greatly reduces voltages hysteresis, thus increasing energy efficiency. 10% cobalt doping into O3-$Na_{0.8}Ni_{0.4}Ti_{0.6}O_2$ to generate O3-$Na_{0.8}Ni_{0.3}Co_{0.1}Ti_{0.6}O_2$ [69] led to nickel migration into the sodium layer, which is a common but harmful occurrence in lithium-ion batteries. It is estimated that 53% – 65% of the nickel migrates. The nickel bonds strongly with the oxygen in the transition metal oxide layers, and prevents them from gliding across each other, acting as a pillar. This is a similar technique to the Ca^{2+} and Mg^{2+} doping studies and will be discussed further in Chapter 4.

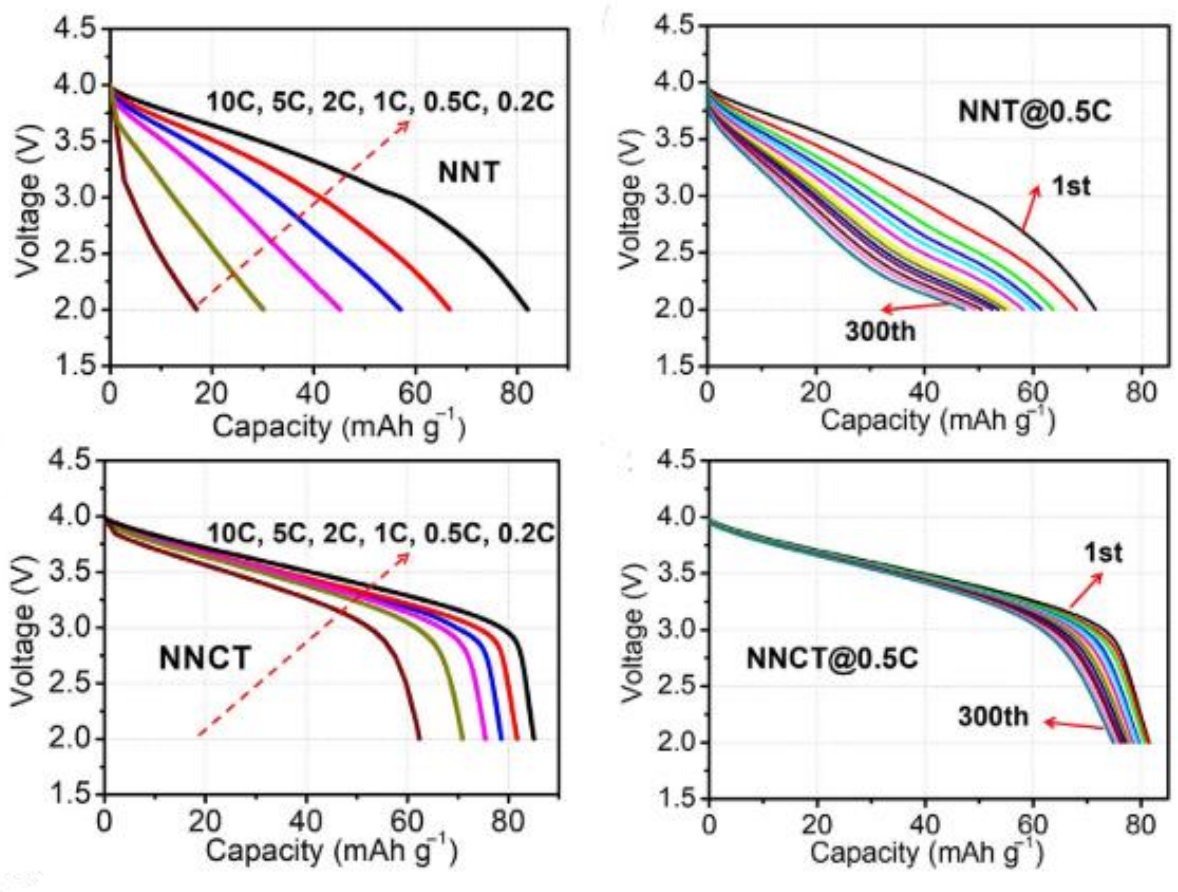

Figure 1-23: Voltage profiles between 2.0 – 4.0 V of (top left) $Na_{0.8}Ni_{0.4}Ti_{0.6}O_2$ (NNT) at the indicated C-rates, (top right) NNT at 0.5C for 300 cycles, (bottom left) $Na_{0.8}Ni_{0.3}Co_{0.1}Ti_{0.6}O_2$ (NNCT) at the indicated C-rates, (bottom right) NNCT at 0.5 C for 300 cycles [69].

The particle size for both $Na_{0.8}Ni_{0.4}Ti_{0.6}O_2$ (NNT) and $Na_{0.8}Ni_{0.4}Ti_{0.6}O_2$ (NNCT) is in the region of 1 – 2 μm. these improvements are likely the result of no longer requiring an overpotential to drive a phase transition, rather than changing particle size. This suggests that preventing transitions altogether may be ideal. It may be the case that there are other procedures available to reduce the voltage hysteresis and the energy efficiency. For example, if the particle size can be reduced further or if there are other materials that can better mitigate or accommodate phase transitions.

Similar improvements in capacity retention have been replicated by mixing P2 and P3 phases materials [109]. Biphasic P2/P3-$Na_{0.67}Co_{0.5}Mn_{0.5}O_2$ cycling at 5 C between 1.5 V – 4.3 V shows an initial capacity of 126 mAh g^{-1}, and 98 mAh g^{-1} after 100 cycles, which is excellent capacity retention at such a C-rate. It references work mentioned above [80] in which a P2/P3 biphasic material performs less well than the pure P2-$Na_xNi_{0.2-2}Co_{0.11}Mn_{0.67}O_2$. Increasing the C-rate of P2/P3-$Na_xNi_{0.22}Co_{0.11}Mn_{0.67}O_2$ led to raising the voltage plateaux at which phase transitions occurred, until they were above the cut-off voltage. This meant a sharp decrease in capacity, as the P to O transition is the rate determining the sodium (de)intercalation process. In biphasic P2/P3-$Na_{0.67}Co_{0.5}Mn_{0.5}O_2$ no phase transitions are observed *via in situ* XRD, even when the cell is charged to 4.3 V

at 1 C, lending further credence to the idea that capacity retention and rate capability are improved by preventing phase transitions altogether. It may be the case that this material specifically is stable in a sodium deficient P2/P3 state and that is why no phase transition occur, or that the Co^{3+}/Co^{4+} has a high redox potential *vs* Na/Na^{+} and so sodium extraction only occurs at high potentials, delaying the P2↔O2 transition. Combining multiple phases into intergrowth structures is discussed further in Chapter 5.

Phase transitions occur at certain sodium contents related to the identity of the constituent metals, not at specific voltages. For example, P2↔O2 in $Na_xNi_{0.33}Mn_{0.67}O_2$ occurs at $x \approx 0.33$, which usually coincides with a voltage of 4.2 V. This is highlighted in a study into P2-$Na_{0.77}Cu_{0.22}Fe_{0.11}Mn_{0.67}O_2$ [133], which is a relatively sodium-rich material compared to other P2 materials, which generally have a sodium content of $x = 0.67$. Here the authors show that P2-$Na_{0.77}Cu_{0.22}Fe_{0.11}Mn_{0.67}O_2$ [133] can be cycled to 4.2 V reversibly without converting P2 to O2, because at 4.2 V the sodium content is only $x \approx 0.4$, corresponding to a capacity of ~89 mAh g^{-1} when cycling at 0.1 C between 2.5 – 4.2 V. When cycling at 1 C for 150 cycles in the same voltage range, the capacity only falls from 69 to 60 mAh g^{-1}. This material also displayed good rate capability, with a capacity 51 mAh g^{-1} at 2 C, compared to 90 at 0.1 C. Overall, the capacity of this material is quite low, compared to other materials, but the technique of avoiding phase transitions to improve capacity retention and rate capability is invaluable for the push to commercialise sodium-ion batteries.

These results indicate that a major source of degradation and poor performance at high C-rates in sodium-ion batteries is a result of phase transitions. In particular, the P2↔O2 transition is harmful for long term battery cycling, and performance improves dramatically when it is avoided. There are several techniques that are available for this: doping the sodium layer, where the dopants can act as a pillar to prevent layer gliding; mechanical barriers to transition, such as other phases or coatings; and finding materials that are stable in a sodium-deficient state.

1.3 Synthesising cathode materials

Synthesis technique and conditions have a significant effect on the performance of cathode materials. Even without changing the structure, altering the calcination time or temperature of a certain material can affect its capacity retention and rate capability by controlling the size of the particles [61], [134]–[137]. The size of the particle determines the diffusion path length for sodium ions in the cathode and so how quickly capacity can be extracted. This is particularly important at high C-rates – when the rate of diffusion becomes the limiting factor. Similarly, smaller particles have a greater surface area in contact with the electrolyte and so may suffer from more rapid degradation, [138], [139].

There are other factors besides size to consider too. For example, the orientation of the exposed face. If the particles are all of one shape (e.g. plates, needles), then one plane will be exposed more than the others. If this plane runs perpendicular to the sodium ion layer,

then the diffusion path length of sodium ions out of the particles is shorter even if the particle size remains large [126], [134].

The synthesis for layered oxides can be performed multiple ways but temperatures exceeding 800 °C are common, as are calcination times of up to 15 hours. This represents a significant energy requirement, which can be reduced to further improve the sustainability of layered oxide-based energy storage systems.

1.3.1 Solid state methods

Solid state is the most common synthesis method for making inorganic materials [140]. It involves the mixing of powdered reagents, usually oxides or carbonates, and then heating them together. This method is very effective and, given that it is so widely used, there are a lot of examples of oxide syntheses using this technique. This means that there are many studies into battery materials that can be used as a guide for synthesis.

The powders may be pressed into a pellet beforehand, to bring the particles physically closer together. The mixing of powders creates a large surface area of interactions between the reagent and increases the likelihood of the formation of a product nucleus. The nucleus formation is a balance between the negative free energy of formation and its positive surface energy. If the nucleus is too small, then it will disintegrate. Therefore, enough energy must be put into the system to form a nucleus large enough to overcome the surface energy of the nuclei. This energy is large because of the number of ions that must all come together – the nucleus must be tens of angstroms across, and so contain many tens of ions, which takes a lot of energy.

Although the reagents in solid state synthesis are powdered, and so heterogenous on relative to the particle sizes, they are homogenous on the atomic scale. At the interface, the product will be formed *via* diffusion of ions. As the new crystal grows, the further the ions must travel to react with the others and so the reaction slows as it progresses. This leads to long (>10 hour) calcination times [44], [52], [72], [102], [112], [119], [141], [142], which is a potential source of contamination [140].

Beyond these intrinsic considerations with solid state synthesis, there are practical problems to overcome too. For example, some starting materials will evaporate before reacting (especially since long times at high temperatures are required). This can change the stoichiometry of the reagents if a reagent volatilises so the formula of the product cannot be reliably predicted. This is not conducive to making reliable, reproducible structures. Reagents must also be dried prior to weighing and mixing, further increasing the energy cost of production.

1.3.2 Co-precipitation

Co-precipitation is another widely-used method [52], [53], [76], [114], [143]–[147] for generating battery materials. A schematic of a co-precipitation synthesis is shown in Figure 1-24. It involves dissolving salts of the constituent cations, adding a precipitating agent until a precursor is formed and precipitates out of solution. This precipitate is dried

and calcined to form the product. The reagents are dissolved, ensuring atomic-level mixing of cations. In this case, however, they cations must come together first to form a hydroxide, carbonate, or sometimes oxalate precursor. The formation of this precursor is not guaranteed, as the two salts must precipitate out of solution at the same time to ensuring good dispersion of the cations.

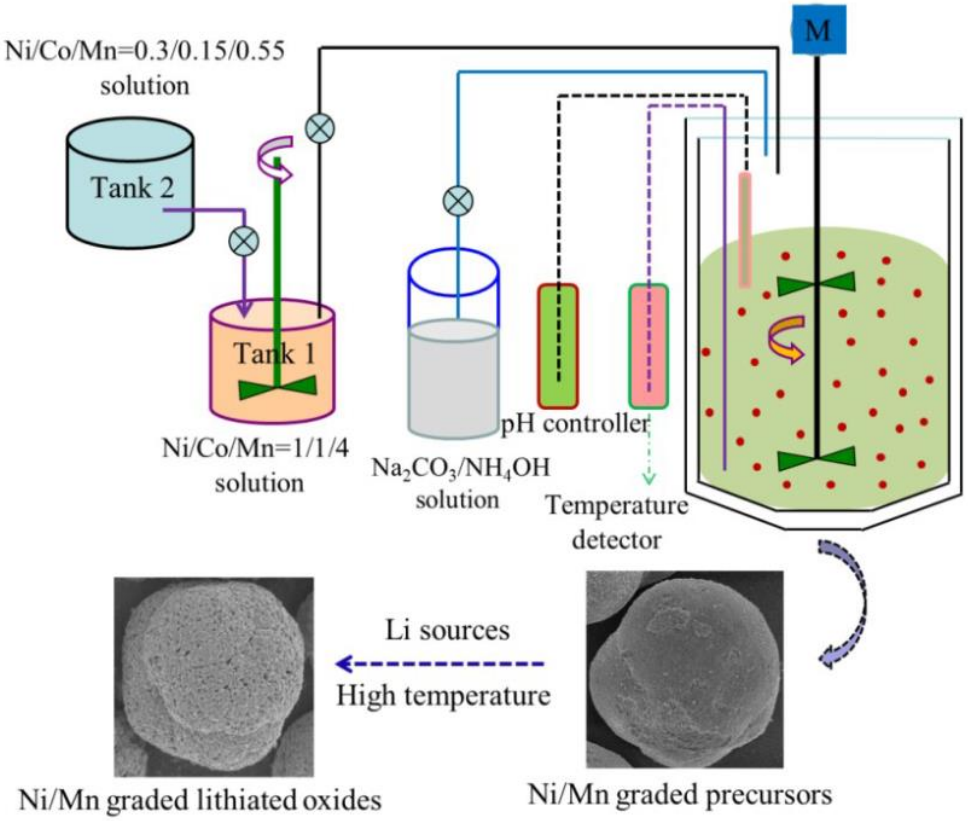

Figure 1-24: Schematic of the synthesis of Ni/Mn graded $Li_{1.16}Ni_{0.138}Co_{0.138}Mn_{0.564}O_2$ *via co-precipitation. The manganese-rich solution in Tank 1 is fed into a continuously stirred tank reactor (CSTR). Before this is completed, the relative nickel-rich solution in Tank 2 is continuously fed into Tank 1. The solution in Tank 1, which still feeds the CSTR, becomes more nickel-rich and so the precursors have an increasing nickel gradient at the edges of the particles* [148].

The technique is often combined with solid state methods: a hydroxide precursor is generated made of the transition metals desired and mixed with Na_2CO_3 and undergoes a final calcination step. This final mixing can be done in solution, to ensure the two reagents are mixed. So, the process can ensure excellent homogeneity with respect to dopant dispersal through the transition metal layer, but it still requires the long calcination times and several processing steps of solid state methods.

1.3.3 Hydrothermal synthesis

Hydrothermal synthesis is also used to generate cathode materials, though only rarely. It involves heating the reagents in high pressure and temperature water (and/or other solvents), which acts both as a solvent and as a medium for transmitting pressure. The sealed reaction vessel is placed in an oven and heated until the water is supercritical.

Although an autoclave is needed to obtain high pressures, much lower temperatures [126], [149], [150] are needed, compared to solid state. For example, P2-$Na_{0.7}MnO_2$ [126] is synthesised at 220 °C for 6 h using a hydrothermal method *vs* 900 °C for 15 h for a solid state synthesis state of P2-$Na_{0.67}MnO_2$ [51].

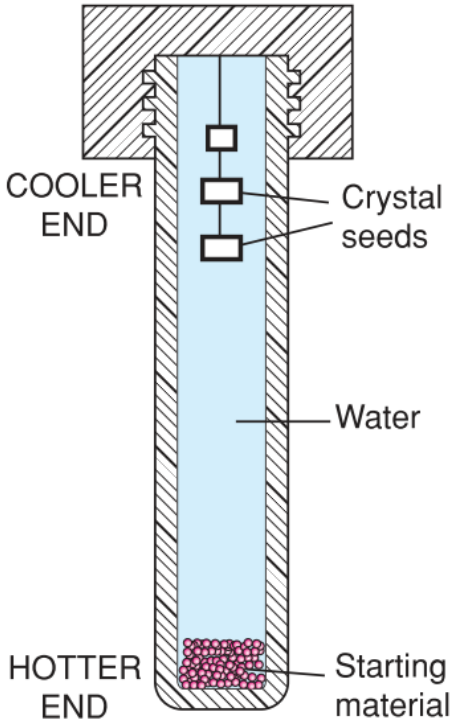

Figure 1-25: Schematic of a hydrothermal PTFE reaction vessel [140].

There are two potential reasons for the limited application of hydrothermal synthesis: equipment requirements, and ingress of water into the cathode structure. Hydrothermal syntheses require an autoclave to generate supercritical water. Water ingress is a major concern in cathode synthesis as they are generally hydroscopic [9], [43], [64], [133], [151]–[153]. Best practice is to store layered oxides under an argon atmosphere or vacuum soon after calcination. Water will intercalate into the sodium layer, causing the structure to collapse. Some materials such as $Na_{0.67}Ni_{0.33}Mn_{0.67}O_2$ [74] are more resistant to water ingress, but others such as $Na_{0.67}Co_{0.33}Mn_{0.67}O_2$ or $Na_{0.67}Mn_{0.6}Fe_{0.25}Co_{0.15}O_2$ [154] are not.

1.3.4 Sol-gel synthesis

The sol-gel method involves the dissolution of cationic reagents to form a colloidal suspension (sol) by hydrolysis of alkoxides, which dries to form a solid (gel). This has several benefits over solid state methods. Chiefly the level of mixing, meaning that the lengths ions must diffuse to form the correct structure is much lower. When this is the case, the prolonged heating at high temperatures is avoidable. This heating regime in solid state syntheses is a source of contamination, from container materials and the furnace atmosphere. The greater level of mixing also increases the homogeneity of the

material – increasing the understanding of its properties and their reliance on composition or dopants. When dopants or other constituent ions are not homogenously spread throughout a material, it is not possible to validly attribute an effect on a materials property to a specific feature.

A common adaptation of this method used in sodium-ion battery research [71], [101], [155]–[157] is the citrate gel method. This involves the solution of metal ions, a chelating agent (commonly citric acid) to form complexes in solution. This prevents the hydrolysis of the metal ions, allowing time for the solvent to evaporate and leaving a glassy gel [158]. This solution is dried to form the gel before a calcination step to remove the chelating agent and leave only the product. The metal salts used are often (though not always) nitrates, which are hazardous to use and other synthesis methods with similar benefits exist that will allow for safer reagents to be used.

1.3.5 Biotemplating

Biotemplating synthesis is a technique is based on the Pechini [61], [158]–[161] process, in the family of sol-gel syntheses. The difference between the sol-gel process and he Pechini process is the addition of a polyalcohol, such as ethylene glycol. This causes an esterification reaction between the polyalcohol and the carboxylic acid group of the citrate, creating linkages between them. This creates stable complexes over a wide pH range, allowing for easy synthesis of complex oxides.

Biotemplating allows a Pechini-like process to be process in one step by using a long chain biopolymer. Phase-pure syntheses of layered oxide cathodes using dextran as a biotemplate has been achieved with the level of homogeneity of the sol-gel and hydrothermal processes, but with vastly reduced calcination times and fewer steps in the process [61], [100]. This way rapid prototyping can be done on a range of samples and the route to scaling up production becomes much more viable: it is less labour intensive, and the energy requirements are reduced significantly. Generally, the biopolymers used as templates are polysaccharides, such as dextran or sodium alginate. These contain up to four hydroxyl groups per monomer unit and are water-soluble. It is postulated that the hydroxyl groups can coordinate to metal cations in an aqueous solution, binding them into the organic matrix after a drying step. This forms a large, disordered metal-organic complex in an egg-box structure [162] (Figure 1-26). Upon heating the template undergoes thermal decomposition to leave only the oxide structure behind.

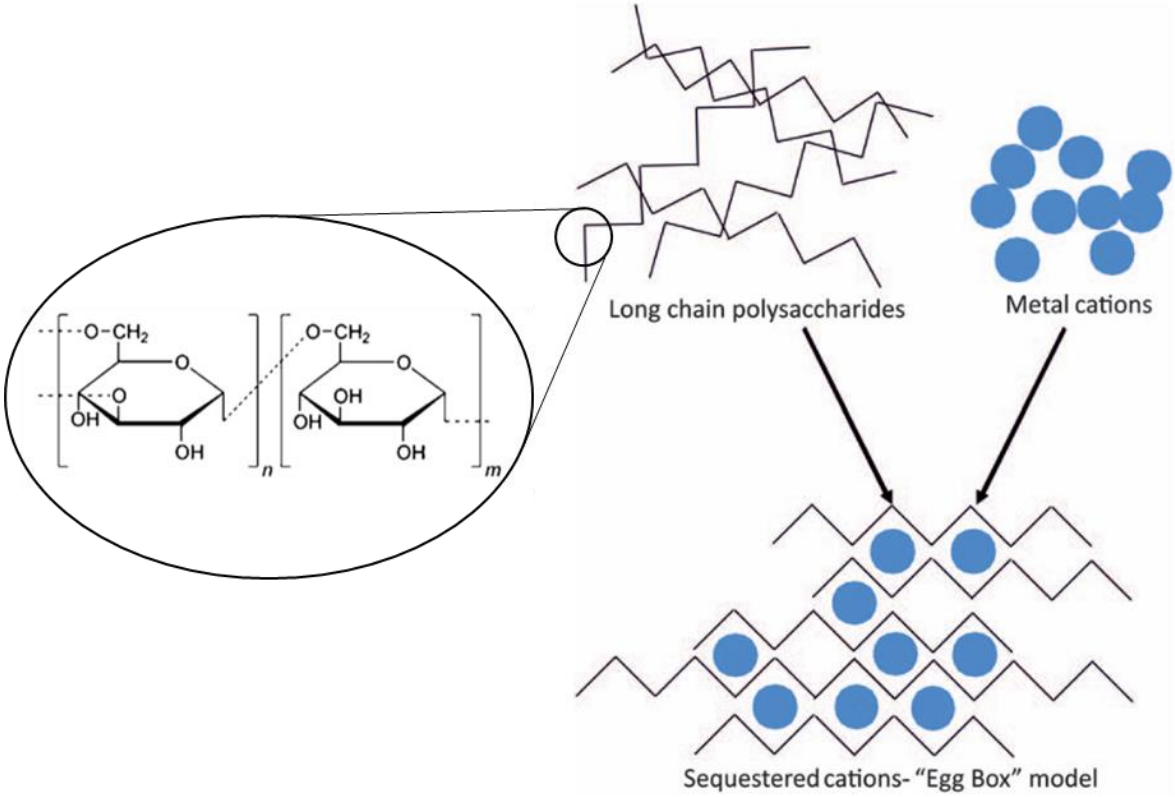

Figure 1-26: Schematic of dextran [158] *and the "egg box" model: metal cations coordinated to negative regions along a polysaccharide* [163].

A range of biotemplates have been used previously to generate inorganic compounds. Chitosan has been used in the production of superconductor $YBa_2Cu_3O_8$ (Y124) with high critical temperature (T_c) [164]. The presence of chitosan matrix prevents sintering of the nucleated nanoparticles, which are sites of subsequent outgrowth for nanowires. The formation of this specific morphology, made possible using the chitosan matrix, leads directly to the high T_c of the material.

Another biotemplate that is often used in the production of nanoparticles is ammonium or sodium alginate [165], [166]. Like chitosan, sodium alginate was shown to prevent sintering in the production of $La_{0.67}Sr_{0.33}MnO_3$ [167], resulting in nanoparticles. In this case, *in situ* formation of Na_2CO_3 prevents sintering of crystalline phases and acts as a flux when melting at 764 °C and leads to the formation of nanowires. If ammonium alginate is used instead, the same synthesis produced nanoparticles. Further, if sodium ascorbate (chemically identical to sodium alginate) is used, sodium doping does not occur. This is suggested to be because the sodium alginate gel prevents aggregation of particles and increase solubility of the precursor phases. the differences in particle morphology highlight the effect that selection of template can have since this can directly influence the performance of a material.

Further examples of the effect that subtle changes can have on the morphology and performance of materials can be seen in $YBa_2Cu_3O_{7-\delta}$ (Y123) [168]. A range of oligosaccharides was used to determine which would generate plate-like crystallites, as

this leads to preferred grain boundary orientation and increased critical current density (J_c). This work found that using longer-chain oligosaccharides (4-6 glucose monomers) leads to a higher fraction of plate-like crystallites in the final material. Conversely, shorter-chained oligosaccharides lead to a reduction in phase purity.

A mixed oxide of praseodymium, barium, copper, and iron (PrBCFO) [169] was prepared *via* this route of dextran coordinating to the metal ions in solution, and a phase-pure sample was achieved after annealing for two hours. This phase had not previously been synthesised *via* the sol-gel process. The dextran prevented the formation of impurity phases by sequestering all the metal cations in solution. This produced phase pure PrBCFO, whereas the synthesis that did not use dextran contained a $BaPrO_3$ impurity. Any impurity phases that did form were only at the nanoscale and able to react completely to form the final phase in the presence of CO_2. The final material produced was porous, which would be expected to produce quality cathodes [170], [171].

Dextran has also been used to successfully synthesise Y123 [172]–[174]. Dextran templating was used to obtain a sponge-like architecture [172] by calcining in air, which foamed the dextran. This controlled crystal growth and overall morphology. Platelets of $YBa_2Cu_3O_7$ (YBCO) can be obtained instead [173] by sodium doping with NaCl, or *via* selection of biotemplate [168]. The amount of dextran in the synthesis varied here, and results in different morphologies in the final product. YBCO mostly forms as a platelet, with CuO present as an impurity on the sample surface, at low dextran amounts. Increasing the amount of dextran increased the size of the platelets. With an excess of dextran, the YBCO formed as a porous structure with clusters of platelets depending on the exposure to NaCl. This demonstrates the flexibility of dextran-templated syntheses regarding the morphology of the product, and the effect that dextran can have on particle size.

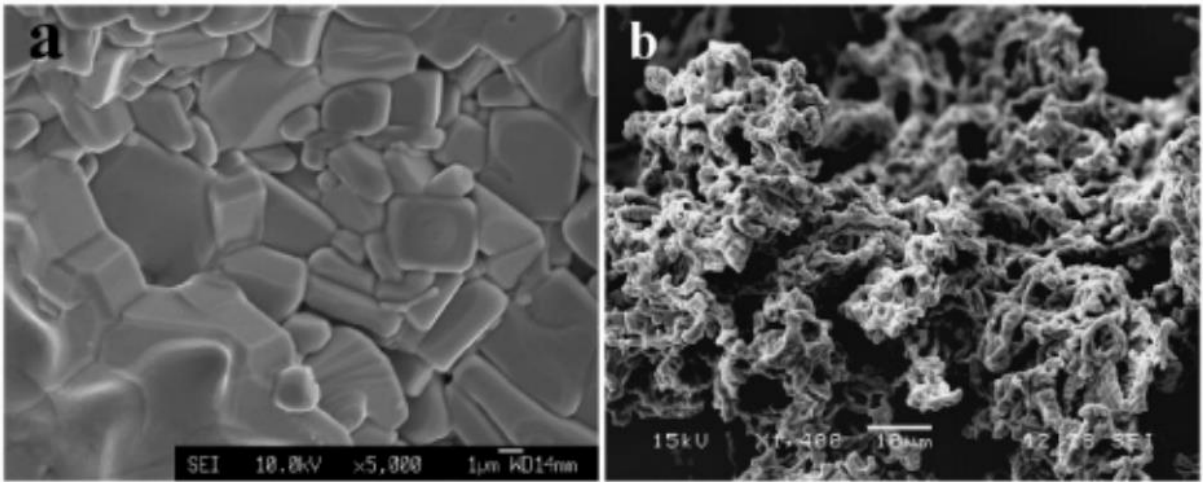

Figure 1-27: SEM images of (a) commercially available Y123 showing an average particle size of 5 μm, and (b) dextran-templated Y123 with a sponge-like architecture [172].

In a final example of the dextran-templated synthesis of Y123, the dextran used has its morphology transferred over to the Y123 product [174]. Carboxylated spherical dextran

(CM-Sephadex®) leads to the synthesis of hollow Y123 spheres by spatially separating the ions that form impurity phases early in the synthesis. In this case, barium ions are separated *via* the utilisation of preferential chelation sites which, as the template carbonises, remain spatially separated. This prevents the growth of a barium carbonate crystal.

In each of these cases, the product is formed after only a two hour calcination. Along with a significant reduction in the energy requirements of synthesis, this leads to greater oxygen content within the structure, as the high surface area enables easier oxygen uptake from the atmosphere. This also reduces the potential for oxygen loss during syntheses at high temperature [163]. In layered oxides, this would increase the reliability and robustness of synthesis.

Battery performance can be improved by controlling the size and morphology of the cathode particles. The diffusion lengths from the material bulk phase to the electrolyte, conductive elements are made shorter in smaller particles, meaning that reducing these distances increases the capacity that can be extracted from the cathode at a given C-rate. Although this also exposes the material to degradation *via* the electrolyte [80], improved characteristics have been achieved by reducing particle size in a range of materials [61], [80], [126], including *via* biotemplating.

The homogenous nature of the gel precursor means the calcination times are much lower and once formed particle size can be manipulated by increasing the calcination time. Biotemplating offers significant control of the particle size and thus the performance of the battery.

1.3.6 Other techniques used for Na-ion cathode materials

Spray pyrolysis [60] is a rarely used in the synthesis of cathode materials. As with most non-solid state techniques, it results in the excellent mixing of reagents. It achieves this through aerosolising the aqueous reagent solution, which flows into a furnace. Although it is simple and easily scaled up [140], it requires specialised equipment and is not suited to laboratory-scale experiments.

Combustion synthesis [175] is used in a small number of examples. As the name suggests, it involves the combustion of the reagents, which becomes self-sustaining and generate temperatures beyond 800 °C. If the reagents cannot fulfil the role themselves, a fuel such as glycine or tetraethylene glycol [91] is used, and nitrates of the constituent metal ions are used as the oxidant. In one study found to use the combustion synthesis, the nitrate reagents are dissolved in water, followed by the addition of glycine. The dispersion of the ions in the crystal is not commented on, but their capacity of P2-$Na_xMn_{0.5}Fe_{0.5}O_2$ is lower than the same material reported using solid state (and a wider voltage window), 145 mAh g^{-1} and 190 mAh g^{-1}, respectively. The authors posit that it is due to the larger particle size they generated – the combustion synthesis required two extra calcination steps, one at 700 °C for 20 h in air, and another at 1000 °C for 5 h in oxygen. There are more energy

efficient ways of achieving dopant or transition metal dispersal that also allow greater control over particle size.

1.3.7 Synthesis method comparisons

Comparing the effects of synthesis method will always be challenging unless direct studies are performed– there are currently very few. Researchers do not always report the same metrics or test in directly comparable ways. But there have been several instances of the same or similar materials reported by different groups who have used different synthesis methods. As mentioned before, P2-$Na_{0.67}Ni_{0.33}Mn_{0.67}O_2$ is a very commonly studied cathode material, and so there are examples of its synthesis using a range of techniques, although unfortunately the relatively unexplored biotemplating technique has not been reported to generate P2-$Na_{0.67}Ni_{0.33}Mn_{0.67}O_2$.

As summarised in Table 1-4 there are a range of different techniques that can be used. Each study will have slightly different experimental parameters, but several techniques involve several calcination steps, and all calcination times are above 12 h, up to 24 h. except for one anomalously high capacity, the capacity limit seems to be ~150 mAh g^{-1} when cycling at C/10. The effect of phase, particle size, and voltage window undoubtedly has a role to play in the accessible capacity, and in the retention and rate capability.

Table 1-4: Summary of $Na_{0.67}Ni_{0.33}Mn_{0.67}O_2$ cathodes with the synthesis method, calcination regime, initial capacity, C-rate, and voltage window.

Material	Synthesis method	Calcination regime	Initial capacity	Ref.
P2-$Na_{0.67}Ni_{0.33}Mn_{0.67}O_2$	Solid state	900 °C for 15 h	145 mAh g^{-1} ~C/15 2.0 – 4.4 V	[176]
P2-$Na_{0.67}Ni_{0.33}Mn_{0.67}O_2$	Solid state	850 °C for 12 h	80 mAh g^{-1} ~C/15 2.0 – 4.2 V	[61]
P2-$Na_{0.67}Ni_{0.33}Mn_{0.67}O_2$	Co-precipitation	500 °C for 5 h, then 900 °C for 24 h	151 mAh g^{-1} C/10 1.5 – 3.75 V	[147]
P2-$Na_{0.5}Ni_{0.25}Mn_{0.75}O_2$	Sol-gel	400 °C for 5 h, then 900 °C for 12 h	210 mAh g^{-1} C/10 1.5 – 4.4 V	[157]
P2-$Na_{0.67}Ni_{0.33}Mn_{0.67}O_2$	Spray pyrolysis	800 °C pyrolysis, then 900 °C for 12 h	86 mAh g^{-1} C/10 2.0 – 4.0 V	[60]

There is a link between higher capacity and an increased voltage window – which is intuitive. However, different potentials correlate to different processes, so the capacity extracted will vary. Furthermore, the extension of the voltage window may have negative side effects for the health of the battery – charging to potential that is too high can degrade the electrolyte, and overextraction of sodium ions can lead to unwanted phase changes. This has been discussed in Section 1.2.2.

There are also differences in the formulations of these materials. The material prepared *via* sol-gel methods had a slightly higher proportion of manganese, and a lower proportion of nickel and so was $Na_{0.5}Ni_{0.25}Mn_{0.75}O_2$, rather than $Na_{0.5}Ni_{0.33}Mn_{0.67}O_2$ [157]. This has a few effects. First the material is lighter, as it contains less sodium and has a higher proportion of manganese compared to the heavier nickel. This alone will not produce this large an increase in capacity.

Also, the authors note that from the differential capacity curve there is evidence of Mn^{3+}/Mn^{4+} redox activity. Ordinarily in $Na_{0.5}Ni_{0.33}Mn_{0.67}O_2$ the manganese ion is in the +4 oxidation state and is not redox active. It is likely that during discharge, more sodium is being inserted into the cathode that the 0.5 mol of sodium that was initially there. This could cause the manganese redox activity seen at low potentials, and the increase in capacity compared to P2-$Na_{0.67}Ni_{0.33}Mn_{0.67}O_2$ material. Manganese redox is credited with 70 mAh g^{-1} of capacity when a lower voltage window [147] is used in $Na_{0.67}Ni_{0.33}Mn_{0.67}O_2$. It is likely in both scenarios more sodium is being inserted into the cathode on discharge than was present in the pristine material.

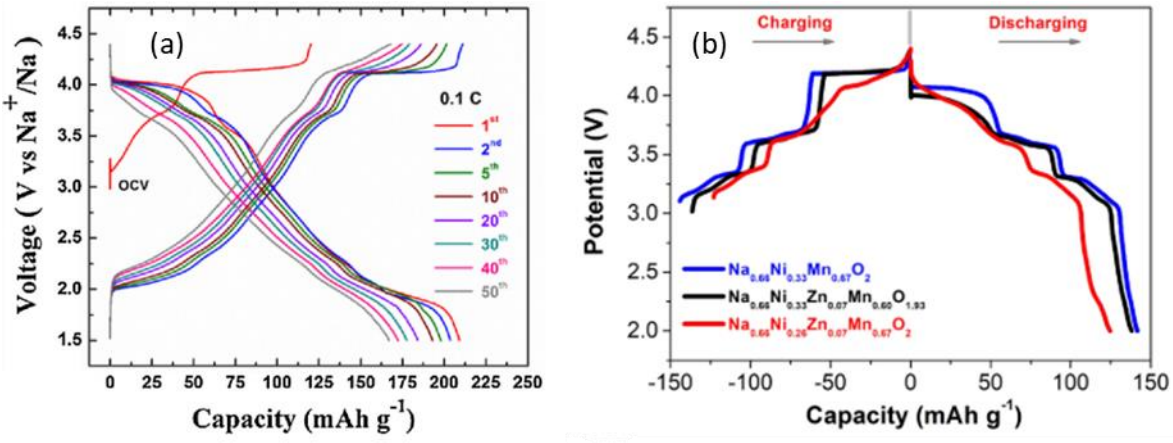

Figure 1-28: Voltage profile of (a) P2-$Na_{0.5}Ni_{0.25}Mn_{0.75}O_2$ [157] *and (b) P2-$Na_{0.67}Ni_{0.33}Mn_{0.67}O_2$* [176].

As seen in Figure 1-28, the sol-gel sample has a much smoother voltage profile than the solid state sample (especially below 3.8 V), as well as a much higher capacity. In both samples, the particles are 3 µm in size. P2-$Na_{0.5}Ni_{0.25}Mn_{0.75}O_2$ [157] has a plate-like morphology with plates >5 µm across, compared to 2 µm in P2-$Na_{0.67}Ni_{0.33}Mn_{0.67}O_2$ [176]. The authors do not credit the size or morphology of the particles to the anomalously high

capacity of the material. It may be possible that the large particle size acts as a mechanical support for the material, similarly to the Al_2O_3 coating [75] discussed in Section 1.2.2. It is claimed by the authors that the voltage plateau at 4.1 V is caused by the P2↔O2 phase transition. If that is the case, it is remarkably well preserved. It may be more likely that it is caused by O redox (possibly simultaneously) as this would be the source of additional capacity, as seen in other $Na_{0.67}Ni_{0.33}Mn_{0.67}O_2$ materials [111]. In this case, the large size of the particles could prevent the loss of oxygen from the structure, leading to the high capacity retention for this material at this capacity and voltage range.

Overall, the comparison of synthesis methods in the literature is limited. Even when the same, commonly reported cathode material is used there are different C-rates, voltage windows and electrolytes used. This affects the initial discharge capacity and influences the capacity retention of the battery. High C-rates and phase changes cause the material to degrade faster over time (although the specific phase changes will influence how much). Higher voltage cut-offs will cause more rapid electrolyte degradation which further decreases capacity retention. Even in studies where the same material is synthesised in multiple ways [51] there is no comment on the difference between the various methods with respect to the performance of the material. The difficulties in using solid state synthesis to form homogenously doped samples were explained above, whereas aqueous synthesis routes allow comparatively easy doping, alongside shorter, lower temperature calcinations.

The lack of comparison of the effect of synthesis method on the performance of cathode materials makes evaluating their efficacy challenging. There are obvious differences, such as the ability to dope materials, or the energy costs of long, high temperature calcinations that are inherent to the syntheses themselves. Beyond that, however, there is little data. This could be because the effect on performance is negligible, so if the right formulation is reached with a reasonable particle size, then any method can be chosen. If this was the case, then arguments in favour of syntheses such as biotemplating are clear. But there is little evidence one way or another, and so if there are methods that offer unique benefits over the others, then it should be explored.

1.4 Aims and thesis structure

The work presented in this thesis builds on the body of work presented here. Many of the current NIB cathodes in development that offer exceptional capacity, cycle life, or power, rely on starting materials or process that are unsustainable. Cobalt, lithium, and nickel are low in natural abundance, causing them to be vulnerable to price increases, supply chain issues, and extraction methods that are opposed to the sustainable values upon which tomorrow's world should rest. Similarly, the production methods of cathode materials currently involve long, high temperature calcinations, where lower temperature, shorter calcinations could be used to produce even better cathode performance, and finer control over particle size.

The goal of the work in this thesis is to increase the feasibility and sustainability of NIBs, to be more competitive with LIBs. To areas of potential improvement have been identified: reducing the energy cost of the cathode production process and increasing the capacity retention of the cathode materials. Cathode production relies on solid state synthesis. If biotemplating can maintain or improve on performance metrics (capacity, capacity retention, rate capability) while reducing the energy cost of production, then it could be more widely adopted in a research and industrial setting. Capacity retention is the biggest barrier to penetration of NIBs into the energy storage market. Here techniques are used to improve the capacity retention of what is already a high-capacity, low-cost material, $Na_{0.67}Mn_{0.9}Mg_{0.1}O_2$ (NMMO) [52], [131], but suffers from capacity fade due to the phase transitions and distortions the cathode undergoes during cycling. By preventing phase transitions, the capacity fading of P-type NMMO should be reduced; fewer distortions and therefore cracks in the particle surface should occur. This should lead to less surface passivation and dissolution of active material. As it has already been shown to successfully produce $Na_{0.67}Ni_{0.33}Mn_{0.67}O_2$ cathodes using a 2 h synthesis [61], [100], as well as its non-toxicity and high natural abundance, dextran is used as the template in the biotemplating syntheses.

The work is split into three chapters, each with its own introduction. Chapter 3 of this thesis details work done to elucidate the differences between the P3 and P2 phases of NMMO, a cathode material with high capacity and using more abundant materials than $Na_{0.67}Ni_{0.33}Mn_{0.67}O_2$. The two phases were synthesised *via* a solid state and biotemplating synthesis, meaning that a four-way comparison can be conducted between the two synthesis methods and the two phases. The materials are characterised *via* XRD and SEM. Voltage profiles, capacity, and rate capability of the materials are used to evaluate the performance. The calcination regime of the biotemplating synthesis mirrors that of the solid state so that the comparisons between the two methods are only change one variable.

For Chapter 4 and Chapter 5, a biotemplating synthesis only is used to produce P3- and P2-NMMO. For these, the calcination regimes used follow other reported dextran biotemplating syntheses. The idea for these two chapters is to apply techniques that have been successful in increasing capacity retention and rate capability in previous NIB cathodes to NMMO, namely Ca doping and using multiphase composites.

For Chapter 4, the two P-type phases are doped with 1% and 2% Ca to minimise the phase transitions that occur *in situ* and increase the capacity retention of the material. Due to the similar ionic radii, Ca^{2+} should be inserted into the Na layer of the NMMO cathode. Its greater charge density should create a pillaring effect, preventing adjacent TMO_2 layers from gliding across one another. Cycling tests and characterisation techniques are the same as in Chapter 3.

For Chapter 5, the P3- and P2-NMMO phases are combined. Intergrowth phases have highlighted so far here already as a promising avenue of research to enhance capacity retention and rate capability. P3- and P2-NMMO are combined using a one-pot

biotemplating synthesis through a mid-point calcination temperature. The two phases are also produced separately and mixed, to test whether any changes or performance improvements are caused by the synthesis method, not just the P3/P2 ratio. The biphasic structure, like Ca^{2+} pillaring, should prevent phase transitions by providing an external barrier to layer gliding,

1.5 References

[1] BEIS, "Digest of UK Energy Statistics Annual data for UK, 2020," no. July, 2021.

[2] IRENA, "Renewable Power Generation Costs in 2021," 2021.

[3] DOE, "Global Energy Storage Database." Accessed: Sep. 03, 2021. [Online]. Available: https://www.sandia.gov/ess-ssl/global-energy-storage-database-home/

[4] D. Larcher and J.-M. Tarascon, "Towards greener and more sustainable batteries for electrical energy storage," *Nature Chemistry*, vol. 7, no. 1. pp. 19–29, 2015. doi: 10.1038/nchem.2085.

[5] S. Rehman, L. M. Al-Hadhrami, and M. M. Alam, "Pumped hydro energy storage system: A technological review," *Renew. Sustain. Energy Rev.*, vol. 44, pp. 586–598, 2015, doi: 10.1016/j.rser.2014.12.040.

[6] B. Zakeri and S. Syri, "Electrical energy storage systems: A comparative life cycle cost analysis," *Renew. Sustain. Energy Rev.*, vol. 42, pp. 569–596, 2015, doi: 10.1016/j.rser.2014.10.011.

[7] P. J. R. Torrealba, "The Benefits of Pumped Storage Hydro to the UK," no. August 2016, pp. 1–49, 2016, doi: 10.13140/RG.2.2.18778.13768/1.

[8] M. Aneke and M. Wang, "Energy storage technologies and real life applications – A state of the art review," *Applied Energy*, vol. 179. 2016. doi: 10.1016/j.apenergy.2016.06.097.

[9] N. Yabuuchi, K. Kubota, M. Dahbi, and S. Komaba, "Research development on sodium-ion batteries," *Chem. Rev.*, vol. 114, no. 23, pp. 11636–11682, 2014, doi: 10.1021/cr500192f.

[10] J. Y. Hwang, S. T. Myung, D. Aurbach, and Y. K. Sun, "Effect of nickel and iron on structural and electrochemical properties of O3 type layer cathode materials for sodium-ion batteries," *J. Power Sources*, vol. 324, pp. 106–112, 2016, doi: 10.1016/j.jpowsour.2016.05.064.

[11] L. Zheng, J. Li, and M. N. Obrovac, "Crystal Structures and Electrochemical Performance of Air-Stable $Na_{2/3}Ni_{1/3-x}Cu_xMn_{2/3}O_2$ in Sodium Cells," *Chem. Mater.*, vol. 29, no. 4, pp. 1623–1631, 2017, doi: 10.1021/acs.chemmater.6b04769.

[12] G. E. Blomgren, "The Development and Future of Lithium Ion Batteries," *J. Electrochem. Soc.*, vol. 164, no. 1, 2017, doi: 10.1149/2.0251701jes.

[13] D. Deng, "Li-ion batteries: Basics, progress, and challenges," *Energy Sci. Eng.*, vol. 3, no. 5, pp. 385–418, 2015, doi: 10.1002/ese3.95.

[14] J.-M. Tarascon and M. Armand, “Issues and challenges facing rechargeable lithium batteries,” *Nature*, vol. 414, no. 6861, pp. 359–367, 2001, doi: 10.1038/35104644.

[15] V. Etacheri, R. Marom, R. Elazeri, G. Salitra, and D. Aurbach, “Challenges in the development of advanced Li-ion batteries: a review,” *Energy Environ. Sci.*, vol. 4, pp. 3243–3262, 2011, doi: 10.1039/c1ee01598b.

[16] X. Zeng, M. Li, D. Abd El-Hady, W. Alshitari, A. S. Al-Bogami, J. Lu, and K. Amine, “Commercialization of Lithium Battery Technologies for Electric Vehicles,” *Adv. Energy Mater.*, vol. 9, no. 27, pp. 1–25, 2019, doi: 10.1002/aenm.201900161.

[17] M. R. Palacín, “Recent advances in rechargeable battery materials: a chemist’s perspective,” *Chem. Soc. Rev.*, vol. 38, no. 9, p. 2565, 2009, doi: 10.1039/b820555h.

[18] J. B. Goodenough and K. S. Park, “The Li-ion rechargeable battery: A perspective,” *J. Am. Chem. Soc.*, vol. 135, no. 4, pp. 1167–1176, 2013, doi: 10.1021/ja3091438.

[19] J. Qian, L. Liu, J. Yang, S. Li, X. Wang, H. L. Zhuang, and Y. Lu, “Electrochemical surface passivation of $LiCoO_2$ particles at ultrahigh voltage and its applications in lithium-based batteries,” *Nat. Commun.*, vol. 9, no. 1, 2018, doi: 10.1038/s41467-018-07296-6.

[20] S. Kalluri, M. Yoon, M. Jo, S. Park, S. Myeong, J. Kim, S. X. Dou, Z. Guo, and J. Cho, “Surface Engineering Strategies of Layered LiCoO2 Cathode Material to Realize High-Energy and High-Voltage Li-Ion Cells,” *Adv. Energy Mater.*, vol. 7, no. 1, 2017, doi: 10.1002/aenm.201601507.

[21] J. I. Lee, E. H. Lee, J. H. Park, S. Park, and S. Y. Lee, “Ultrahigh-energy-density lithium-ion batteries based on a high-capacity anode and a high-voltage cathode with an electroconductive nanoparticle shell,” *Adv. Energy Mater.*, vol. 4, no. 8, pp. 1–9, 2014, doi: 10.1002/aenm.201301542.

[22] N. Nitta, F. Wu, J. T. Lee, and G. Yushin, “Li-ion battery materials: Present and future,” *Mater. Today*, vol. 18, no. 5, pp. 252–264, 2015, doi: 10.1016/j.mattod.2014.10.040.

[23] S. Kara, *Cobalt Red: How the Blood of the Congo Powers Our Lives*. St. Martin’s Press, 2023.

[24] P. K. Nayak, L. Yang, W. Brehm, and P. Adelhelm, “From Lithium-Ion to Sodium-Ion Batteries: Advantages, Challenges, and Surprises,” *Angew. Chemie - Int. Ed.*, vol. 57, no. 1, pp. 102–120, 2018, doi: 10.1002/anie.201703772.

[25] M. Titirici, P. Adelhelm, and Y. Hu, *Sodium-Ion Batteries: Materials, Characterization, and Technology, Volume 1*, vol. 23, no. 8. Wiley, 2022. doi: 10.1002/9783527825769.

[26] R. S. Carmichael, *Practical Handbook of Physical Properties of Rocks and Minerals (1988)*. Boca Raton: CRC Press, 2017. doi: 10.1201/9780203710968.

[27] N. Ortiz-Vitoriano, N. E. Drewett, E. Gonzalo, and T. Rojo, “High performance manganese-based layered oxide cathodes: Overcoming the challenges of sodium ion batteries,” *Energy Environ. Sci.*, vol. 10, no. 5, pp. 1051–1074, 2017, doi: 10.1039/c7ee00566k.

[28] C. Vaalma, D. Buchholz, M. Weil, and S. Passerini, “A cost and resource analysis of sodium-ion batteries,” *Nat. Rev. Mater.*, vol. 3, 2018, doi: 10.1038/natrevmats.2018.13.

[29] P. Desai and M. Nguyen, “Shortages flagged for EV materials lithium and cobalt,” Reuters. Accessed: Sep. 03, 2021. [Online]. Available: https://www.reuters.com/business/energy/shortages-flagged-ev-materials-lithium-cobalt-2021-07-01/

[30] “Lithium carbonate prices have nearly doubled in 2021: Benchmark,” Mining Journal. [Online]. Available: https://www.mining-journal.com/energy-minerals-news/news/1406529/lithium-carbonate-prices-have-nearly-doubled-in-2021-benchmark

[31] I. Penn and E. Lipton, “Lithium Gold Rush: Inside the Race to Power Electric Vehicles,” The New York Times. Accessed: Sep. 03, 2021. [Online]. Available: https://www.nytimes.com/2021/05/06/business/lithium-mining-race.html

[32] T. Riofrancos, “The rush to ‘go electric’ comes with a hidden cost: destructive lithium mining,” The Guardian. Accessed: Sep. 03, 2021. [Online]. Available: https://www.theguardian.com/commentisfree/2021/jun/14/electric-cost-lithium-mining-decarbonasation-salt-flats-chile

[33] P. Greim, A. A. Solomon, and C. Breyer, “Assessment of lithium criticality in the global energy transition and addressing policy gaps in transportation,” *Nat. Commun.*, vol. 11, no. 1, pp. 1–11, 2020, doi: 10.1038/s41467-020-18402-y.

[34] D. Runkevicius, “As Tesla Booms, Lithium Is Running Out,” Forbes. Accessed: Sep. 03, 2021. [Online]. Available: https://www.forbes.com/sites/danrunkevicius/2020/12/07/as-tesla-booms-lithium-is-running-out/?sh=5cc62d861a44

[35] M. Gallucci, “EVs Will Drive A Lithium Supply Crunch,” IEEE Spectrum.

[36] L. Zhang, Y. Ma, X. Cheng, C. Du, T. Guan, Y. Cui, S. Sun, P. Zuo, Y. Gao, and G. Yin, “Capacity fading mechanism during long-term cycling of over-discharged LiCoO2/mesocarbon microbeads battery,” *J. Power Sources*, vol. 293, pp. 1006–1015, 2015, doi: 10.1016/j.jpowsour.2015.06.040.

[37] Z. Dai, U. Mani, H. T. Tan, and Q. Yan, “Advanced Cathode Materials for Sodium-Ion Batteries: What Determines Our Choices?,” *Small Methods*, vol. 1, no. 5, p. 1700098, 2017, doi: 10.1002/smtd.201700098.

[38] R. D. Shannon and C. T. Prewitt, “Effective ionic radii in oxides and fluorides,” *Acta Crystallogr. Sect. B Struct. Crystallogr. Cryst. Chem.*, vol. 25, no. 5, pp. 925–946, 1969, doi: 10.1107/S0567740869003220.

[39] K. Kubota, S. Kumakura, Y. Yoda, K. Kuroki, and S. Komaba, “Electrochemistry and Solid-State Chemistry of $NaMeO_2$ (Me = 3d Transition Metals),” *Advanced Energy Materials*, vol. 8, no. 17. Wiley-VCH Verlag, Jun. 15, 2018. doi: 10.1002/aenm.201703415.

[40] E. Rossen, C. D. W. Jones, and J. R. Dahn, “Structure and electrochemistry of $Li_xMn_yNi_{1-y}O_2$,” *Solid State Ionics*, vol. 57, no. 3–4, pp. 311–318, 1992, doi:

10.1016/0167-2738(92)90164-K.

[41] J. Y. Hwang, S. T. Myung, and Y. K. Sun, “Sodium-ion batteries: Present and future,” *Chem. Soc. Rev.*, vol. 46, no. 12, pp. 3529–3614, 2017, doi: 10.1039/c6cs00776g.

[42] M. H. Han, E. Gonzalo, N. Sharma, J. M. López Del Amo, M. Armand, M. Avdeev, J. J. Saiz Garitaonandia, and T. Rojo, “High-Performance P2-Phase $Na_{2/3}Mn_{0.8}Fe_{0.1}Ti_{0.1}O_2$ Cathode Material for Ambient-Temperature Sodium-Ion Batteries,” *Chem. Mater.*, vol. 28, no. 1, pp. 106–116, 2016, doi: 10.1021/acs.chemmater.5b03276.

[43] P. F. Wang, Y. You, Y. X. Yin, and Y. G. Guo, “Layered Oxide Cathodes for Sodium-Ion Batteries: Phase Transition, Air Stability, and Performance,” *Adv. Energy Mater.*, vol. 8, no. 8, pp. 1–23, 2018, doi: 10.1002/aenm.201701912.

[44] N. Tapia-Ruiz, W. M. Dose, N. Sharma, H. Chen, J. Heath, J. W. Somerville, U. Maitra, M. S. Islam, and P. G. Bruce, “High voltage structural evolution and enhanced Na-ion diffusion in P2-$Na_{2/3}Ni_{1/3-x}Mg_xMn_{2/3}O_2$ ($0 \le x \le 0.2$) cathodes from diffraction, electrochemical and *ab initio* studies,” *Energy Environ. Sci.*, vol. 11, no. 6, pp. 1470–1479, 2018, doi: 10.1039/c7ee02995k.

[45] A. Caballero, L. Hernán, J. Morales, L. Sánchez, J. Santos Peña, and M. A. G. Aranda, “Synthesis and characterization of high-temperature hexagonal P2-$Na_{0.6}MnO_2$ and its electrochemical behaviour as cathode in sodium cells,” *J. Mater. Chem.*, vol. 12, no. 4, pp. 1142–1147, 2002, doi: 10.1039/b108830k.

[46] H. Yoshida, N. Yabuuchi, K. Kubota, I. Ikeuchi, A. Garsuch, M. Schulz-Dobrick, and S. Komaba, “P2-type $Na_{2/3}Ni_{1/3}Mn_{2/3-x}Ti_xO_2$ as a new positive electrode for higher energy Na-ion batteries,” *Chem. Commun.*, vol. 50, no. 28, pp. 3677–3680, 2014, doi: 10.1039/C3CC49856E.

[47] E. Gonzalo, M. Zarrabeitia, N. E. Drewett, J. M. López del Amo, and T. Rojo, “Sodium manganese-rich layered oxides: Potential candidates as positive electrode for Sodium-ion batteries,” *Energy Storage Mater.*, vol. 34, no. September 2020, pp. 682–707, 2021, doi: 10.1016/j.ensm.2020.10.010.

[48] M. H. Han, E. Gonzalo, G. Singh, and T. Rojo, “A comprehensive review of sodium layered oxides: Powerful cathodes for Na-ion batteries,” *Energy Environ. Sci.*, vol. 8, no. 1, pp. 81–102, 2015, doi: 10.1039/c4ee03192j.

[49] C. Delmas, C. Fouassier, and P. Hagenmuller, “Structural classification and properties of the layered oxides,” *Phys. B+C*, vol. 99, no. 1–4, pp. 81–85, 1980, doi: 10.1016/0378-4363(80)90214-4.

[50] Y. Tsuchiya, K. Takanashi, T. Nishinobo, A. Hokura, M. Yonemura, T. Matsukawa, T. Ishigaki, K. Yamanaka, T. Ohta, and N. Yabuuchi, “Layered $Na_xCr_xTi_{1-x}O_2$ as bifunctional electrode materials for rechargeable sodium batteries,” *Chem. Mater.*, vol. 28, no. 19, pp. 7006–7016, 2016, doi: 10.1021/acs.chemmater.6b02814.

[51] J. Billaud, G. Singh, A. R. Armstrong, E. Gonzalo, V. Roddatis, M. Armand, T. Rojo, and P. G. Bruce, “$Na_{0.67}Mn_{1-x}Mg_xO_2$ ($0 \le x \le 0.2$): a high capacity cathode for sodium-ion batteries,” *Energy Environ. Sci.*, vol. 7, no. 4, pp. 1387–1391, 2014, doi: 10.1039/C4EE00465E.

[52] R. J. Clément, J. Billaud, A. Robert Armstrong, G. Singh, T. Rojo, P. G. Bruce, and C. P. Grey, "Structurally stable Mg-doped P2-$Na_{2/3}Mn_{1-y}Mg_yO_2$ sodium-ion battery cathodes with high rate performance: insights from electrochemical, NMR and diffraction studies," *Energy Environ. Sci.*, vol. 9, no. 10, pp. 3240–3251, 2016, doi: 10.1039/C6EE01750A.

[53] D. Buchholz, C. Vaalma, L. G. Chagas, and S. Passerini, "Mg-doping for improved long-term cyclability of layered Na-ion cathode materials - The example of P2-type $Na_xMg_{0.11}Mn_{0.89}O_2$," *J. Power Sources*, vol. 282, pp. 581–585, 2015, doi: 10.1016/j.jpowsour.2015.02.069.

[54] N. Sharma, N. Tapia-Ruiz, G. Singh, A. R. Armstrong, J. C. Pramudita, H. E. A. Brand, J. Billaud, P. G. Bruce, and T. Rojo, "Rate Dependent Performance Related to Crystal Structure Evolution of $Na_{0.67}Mn_{0.8}Mg_{0.2}O_2$ in a Sodium-Ion Battery," *Chem. Mater.*, vol. 27, no. 20, pp. 6976–6986, 2015, doi: 10.1021/acs.chemmater.5b02142.

[55] X. Ma, H. Chen, and G. Ceder, "Electrochemical Properties of Monoclinic $NaMnO_2$," *J. Electrochem. Soc.*, vol. 158, no. 12, p. A1307, 2011, doi: 10.1149/2.035112jes.

[56] C. Liu, Z. G. Neale, and G. Cao, "Understanding electrochemical potentials of cathode materials in rechargeable batteries," *Mater. Today*, vol. 19, no. 2, pp. 109–123, 2016, doi: 10.1016/j.mattod.2015.10.009.

[57] C. R. Birkl, M. R. Roberts, E. McTurk, P. G. Bruce, and D. A. Howey, "Degradation diagnostics for lithium ion cells," *J. Power Sources*, vol. 341, pp. 373–386, 2017, doi: 10.1016/j.jpowsour.2016.12.011.

[58] N. Yabuuchi, M. Kajiyama, J. Iwatate, H. Nishikawa, S. Hitomi, R. Okuyama, R. Usui, Y. Yamada, and S. Komaba, "P2-type $Na_x[Fe_{1/2}Mn_{1/2}]O_2$ made from earth-abundant elements for rechargeable Na batteries," *Nat. Mater.*, vol. 11, no. 6, pp. 512–517, 2012, doi: 10.1038/nmat3309.

[59] X. Xiang, K. Zhang, and J. Chen, "Recent advances and prospects of cathode materials for sodium-ion batteries," *Adv. Mater.*, vol. 27, no. 36, pp. 5343–5364, 2015, doi: 10.1002/adma.201501527.

[60] S. Y. Lee, J. H. Kim, and Y. C. Kang, "Electrochemical properties of P2-type $Na_{2/3}Ni_{1/3}Mn_{2/3}O_2$ plates synthesized by spray pyrolysis process for sodium-ion batteries," *Electrochim. Acta*, vol. 225, pp. 86–92, 2017, doi: 10.1016/j.electacta.2016.11.141.

[61] S. Zilinskaite, A. J. R. Rennie, R. Boston, and N. Reeves-McLaren, "Biotemplating: a sustainable synthetic methodology for Na-ion battery materials," *J. Mater. Chem. A*, vol. 6, no. 13, pp. 5346–5355, 2018, doi: 10.1039/C7TA09260A.

[62] S. Kumakura, Y. Tahara, S. Sato, K. Kubota, and S. Komaba, "P′2-$Na_{2/3}Mn_{0.9}Me_{0.1}O_2$ (Me = Mg, Ti, Co, Ni, Cu, and Zn): Correlation between Orthorhombic Distortion and Electrochemical Property," *Chem. Mater.*, vol. 29, no. 21, pp. 8958–8962, Nov. 2017, doi: 10.1021/acs.chemmater.7b02772.

[63] Y. Lei, X. Li, L. Liu, and G. Ceder, "Synthesis and stoichiometry of different layered sodium cobalt oxides," *Chem. Mater.*, vol. 26, no. 18, pp. 5288–5296, 2014, doi: 10.1021/cm5021788.

[64] M. H. Han, E. Gonzalo, M. Casas-Cabanas, and T. Rojo, "Structural evolution and electrochemistry of monoclinic $NaNiO_2$ upon the first cycling process," *J. Power Sources*, vol. 258, pp. 266–271, 2014, doi: 10.1016/j.jpowsour.2014.02.048.

[65] H. Yoshida, N. Yabuuchi, and S. Komaba, "$NaFe_{0.5}Co_{0.5}O_2$ as high energy and power positive electrode for Na-ion batteries," *Electrochem. commun.*, vol. 34, pp. 60–63, 2013, doi: 10.1016/j.elecom.2013.05.012.

[66] S. Komaba, N. Yabuuchi, T. Nakayama, A. Ogata, T. Ishikawa, and I. Nakai, "Study on the reversible electrode reaction of $Na_{1-x}Ni_{0.5}Mn_{0.5}O_2$ for a rechargeable sodium-ion battery," *Inorg. Chem.*, vol. 51, no. 11, pp. 6211–6220, 2012, doi: 10.1021/ic300357d.

[67] S. Guo, P. Liu, H. Yu, Y. Zhu, M. Chen, M. Ishida, and H. Zhou, "A layered P2- and O3-type composite as a high-energy cathode for rechargeable sodium-ion batteries," *Angew. Chemie - Int. Ed.*, vol. 54, no. 20, pp. 5894–5899, 2015, doi: 10.1002/anie.201411788.

[68] H. Liu, J. Xu, C. Ma, and Y. S. Meng, "A new O3-type layered oxide cathode with high energy/power density for rechargeable Na batteries," *Chem. Commun.*, vol. 51, no. 22, pp. 4693–4696, 2015, doi: 10.1039/C4CC09760B.

[69] S. Guo, Y. Sun, P. Liu, J. Yi, P. He, X. Zhang, Y. Zhu, R. Senga, K. Suenaga, M. Chen, and H. Zhou, "Cation-mixing stabilized layered oxide cathodes for sodium-ion batteries," *Sci. Bull.*, vol. 63, no. 6, pp. 376–384, 2018, doi: 10.1016/j.scib.2018.02.012.

[70] M. Bianchini, E. Gonzalo, N. E. Drewett, N. Ortiz-Vitoriano, J. M. Lopez Del Amo, F. J. Bonilla, B. Acebedo, and T. Rojo, "Layered P2-O3 sodium-ion cathodes derived from earth abundant elements," *J. Mater. Chem. A*, pp. 3552–3559, 2018, doi: 10.1039/C7TA11180K.

[71] X. Song, X. Zhou, Y. Deng, J. Nan, D. Shu, Z. Cai, Y. Huang, and X. Zhang, "Synthesis of $Na_xMn_{0.54}Ni_{0.13}Fe_{0.13}O_2$ with P2-type hexagonal phase as high-performance cathode materials for sodium-ion batteries," *J. Alloys Compd.*, vol. 732, pp. 88–94, 2018, doi: 10.1016/j.jallcom.2017.10.131.

[72] J. Sun, J. Shen, and T. Wang, "Electrochemical study of $Na_{0.66}Ni_{0.33}Mn_{0.67-x}Mo_xO_2$ as cathode material for sodium-ion battery," *J. Alloys Compd.*, vol. 709, pp. 481–486, 2017, doi: 10.1016/j.jallcom.2017.02.200.

[73] P. F. Wang, Y. You, Y. X. Yin, Y. S. Wang, L. J. Wan, L. Gu, and Y. G. Guo, "Suppressing the P2–O2 Phase Transition of $Na_{0.67}Mn_{0.67}Ni_{0.33}O_2$ by Magnesium Substitution for Improved Sodium-Ion Batteries," *Angew. Chemie - Int. Ed.*, vol. 55, no. 26, pp. 7445–7449, 2016, doi: 10.1002/anie.201602202.

[74] Z. Lu and J. R. Dahn, "*In Situ* X-Ray Diffraction Study of P2-$Na_{2/3}[Ni_{1/3}Mn_{2/3}]O_2$," *J. Electrochem. Soc.*, vol. 148, no. 11, p. A1225, 2001, doi: 10.1149/1.1407247.

[75] Y. Liu, X. Fang, A. Zhang, C. Shen, Q. Liu, H. A. Enaya, and C. Zhou, "Layered P2-$Na_{2/3}[Ni_{1/3}Mn_{2/3}]O_2$ as high-voltage cathode for sodium-ion batteries: The capacity decay mechanism and Al_2O_3 surface modification," *Nano Energy*, vol. 27, pp. 27–34, 2016, doi: 10.1016/j.nanoen.2016.06.026.

[76] E. Lee, J. Lu, Y. Ren, X. Luo, X. Zhang, J. Wen, D. Miller, A. DeWahl, S. Hackney, B. Key, D. Kim, M. Slater, and C. S. Johnson, "Layered P2/O3 intergrowth cathode: Toward high power Na-ion batteries," *Adv. Energy Mater.*, vol. 4, no. 17, pp. 1–8, 2014, doi: 10.1002/aenm.201400458.

[77] S. Y. Zhang, Y. J. Guo, Y. N. Zhou, X. D. Zhang, Y. Bin Niu, E. H. Wang, L. B. Huang, P. F. An, J. Zhang, X. A. Yang, Y. X. Yin, S. Xu, and Y. G. Guo, "P3/O3 Integrated Layered Oxide as High-Power and Long-Life Cathode toward Na-Ion Batteries," *Small*, vol. 17, no. 10, 2021, doi: 10.1002/smll.202007236.

[78] P. F. Wang, H. R. Yao, X. Y. Liu, J. N. Zhang, L. Gu, X. Q. Yu, Y. X. Yin, and Y. G. Guo, "Ti-Substituted $NaNi_{0.5}Mn_{0.5-x}Ti_xO_2$ Cathodes with Reversible O3–P3 Phase Transition for High-Performance Sodium-Ion Batteries," *Adv. Mater.*, vol. 29, no. 19, pp. 1–7, 2017, doi: 10.1002/adma.201700210.

[79] Y. Shi, Z. Zhang, P. Jiang, A. Gao, K. Li, Q. Zhang, Y. Sun, X. Lu, D. Cao, and X. Lu, "Unlocking the potential of P3 structure for practical Sodium-ion batteries by fabricating zero strain framework for Na^+ intercalation," *Energy Storage Mater.*, vol. 37, no. February, pp. 354–362, 2021, doi: 10.1016/j.ensm.2021.02.020.

[80] L. G. Chagas, D. Buchholz, C. Vaalma, L. Wu, and S. Passerini, "P-type $Na_xNi_{0.22}Co_{0.11}Mn_{0.66}O_2$ materials: linking synthesis with structure and electrochemical performance," *J. Mater. Chem. A*, vol. 2, no. 47, pp. 20263–20270, 2014, doi: 10.1039/C4TA03946G.

[81] N. Yabuuchi and S. Komaba, "Recent research progress on iron- and manganese-based positive electrode materials for rechargeable sodium batteries," *Sci. Technol. Adv. Mater.*, vol. 15, no. 4, 2014, doi: 10.1088/1468-6996/15/4/043501.

[82] W. Zuo, J. Qiu, X. Liu, B. Zheng, Y. Zhao, J. Li, H. He, K. Zhou, Z. Xiao, Q. Li, G. F. Ortiz, and Y. Yang, "Highly-stable P2–$Na_{0.67}MnO_2$ electrode enabled by lattice tailoring and surface engineering," *Energy Storage Mater.*, vol. 26, no. November 2019, pp. 503–512, Apr. 2020, doi: 10.1016/j.ensm.2019.11.024.

[83] Y. N. Zhou, P. F. Wang, Y. Bin Niu, Q. Li, X. Q. Yu, Y. X. Yin, S. Xu, and Y. G. Guo, "A P2/P3 composite layered cathode for high-performance Na-ion full batteries," *Nano Energy*, vol. 55, no. September 2018, pp. 143–150, 2019, doi: 10.1016/j.nanoen.2018.10.072.

[84] D. Pahari and S. Puravankara, "On controlling the P2-O2 phase transition by optimal Ti-substitution on Ni-site in P2-type $Na_{0.67}Ni_{0.33}Mn_{0.67}O_2$ (NNMO) cathode for Na-ion batteries," *J. Power Sources*, vol. 455, no. February, p. 227957, 2020, doi: 10.1016/j.jpowsour.2020.227957.

[85] X. Li, D. Wu, Y. N. Zhou, L. Liu, X. Q. Yang, and G. Ceder, "O3-type $Na(Mn_{0.25}Fe_{0.25}Co_{0.25}Ni_{0.25})O_2$: A quaternary layered cathode compound for rechargeable Na ion batteries," *Electrochem. commun.*, vol. 49, pp. 51–54, 2014, doi: 10.1016/j.elecom.2014.10.003.

[86] T. Risthaus, L. Chen, J. Wang, J. Li, D. Zhou, L. Zhang, D. Ning, X. Cao, X. Zhang, G. Schumacher, M. Winter, E. Paillard, and J. Li, "P3 $Na_{0.9}Ni_{0.5}Mn_{0.5}O_2$ Cathode Material for Sodium Ion Batteries," *Chem. Mater.*, vol. 31, no. 15, pp. 5376–5383, 2019, doi: 10.1021/acs.chemmater.8b03270.

[87] C. Y. Yu, J. S. Park, H. G. Jung, K. Y. Chung, D. Aurbach, Y. K. Sun, and S. T. Myung, "$NaCrO_2$ cathode for high-rate sodium-ion batteries," *Energy Environ. Sci.*, vol. 8, no. 7, pp. 2019–2026, 2015, doi: 10.1039/c5ee00695c.

[88] S. Mariyappan, Q. Wang, and J. M. Tarascon, "Will Sodium Layered Oxides Ever Be Competitive for Sodium Ion Battery Applications?," *J. Electrochem. Soc.*, vol. 165, p. A3714, 2018, doi: 10.1149/2.0201816jes.

[89] Y. Takeda, K. Nakahara, M. Nishijima, N. Imanishi, and O. Yamamoto, "Sodium deintercalation from sodium iron oxide," *Mater. Res. Bull.*, vol. 29, no. 6, pp. 659–666, 1994, doi: 10.1016/0025-5408(94)90122-8.

[90] B. Mortemard de Boisse, D. Carlier, M. Guignard, L. Bourgeois, and C. Delmas, "P2-$Na_xMn_{1/2}Fe_{1/2}O_2$ Phase Used as Positive Electrode in Na Batteries: Structural Changes Induced by the Electrochemical (De)intercalation Process," *Inorg. Chem.*, vol. 53, no. 20, pp. 11197–11205, Oct. 2014, doi: 10.1021/ic5017802.

[91] B. Sambandam, M. H. Alfaruqi, S. Park, S. Lee, S. Kim, J. Lee, V. Mathew, J. Y. Hwang, and J. Kim, "Validating the structural (In)stability of P3- and P2-$Na_{0.67}Mg_{0.1}Mn_{0.9}O_2$-Layered cathodes for sodium-ion batteries: A time-decisive approach," *ACS Appl. Mater. Interfaces*, vol. 13, no. 45, pp. 53877–53891, 2021, doi: 10.1021/acsami.1c15394.

[92] J. W. Somerville, A. Sobkowiak, N. Tapia-Ruiz, J. Billaud, J. G. Lozano, R. A. House, L. C. Gallington, T. Ericsson, L. Häggström, M. R. Roberts, U. Maitra, and P. G. Bruce, "Nature of the 'Z'-phase in layered Na-ion battery cathodes," *Energy Environ. Sci.*, vol. 12, no. 7, pp. 2223–2232, 2019, doi: 10.1039/C8EE02991A.

[93] G. Singh, N. Tapia-Ruiz, J. M. Lopez Del Amo, U. Maitra, J. W. Somerville, A. R. Armstrong, J. Martinez De Ilarduya, T. Rojo, and P. G. Bruce, "High Voltage Mg-Doped $Na_{0.67}Ni_{0.3-x}Mg_xMn_{0.7}O_2$ (x = 0.05, 0.1) Na-Ion Cathodes with Enhanced Stability and Rate Capability," *Chem. Mater.*, vol. 28, no. 14, pp. 5087–5094, 2016, doi: 10.1021/acs.chemmater.6b01935.

[94] S. Guo, Y. Sun, J. Yi, K. Zhu, P. Liu, Y. Zhu, G. Zhu, M. Chen, M. Ishida, and H. Zhou, "Understanding sodium-ion diffusion in layered P2 and P3 oxides *via* experiments and first-principles calculations: a bridge between crystal structure and electrochemical performance," *NPG Asia Mater.*, vol. 8, p. e266, 2016, doi: 10.1038/am.2016.53.

[95] R. Berthelot, D. Carlier, and C. Delmas, "Electrochemical investigation of the P2–Na_xCoO_2 phase diagram," *Nat. Mater.*, vol. 10, no. 1, pp. 74–80, 2011, doi: 10.1038/nmat2920.

[96] M. Tang, W. C. Carter, and Y.-M. Chiang, "Electrochemically Driven Phase Transitions in Insertion Electrodes for Lithium-Ion Batteries: Examples in Lithium Metal Phosphate Olivines," *Annu. Rev. Mater. Res.*, vol. 40, no. 1, pp. 501–529, Jun. 2010, doi: 10.1146/annurev-matsci-070909-104435.

[97] Y. N. Zhou, J. L. Yue, E. Hu, H. Li, L. Gu, K. W. Nam, S. M. Bak, X. Yu, J. Liu, J. Bai, E. Dooryhee, Z. W. Fu, and X. Q. Yang, "High-Rate Charging Induced Intermediate Phases and Structural Changes of Layer-Structured Cathode for Lithium-Ion Batteries," *Adv. Energy Mater.*, vol. 6, no. 21, Nov. 2016, doi:

10.1002/aenm.201600597.

[98] S. F. Linnell, A. G. Manche, Y. Liao, M. Hirsbrunner, S. Imada, A. B. Naden, J. T. S. Irvine, L. C. Duda, and A. R. Armstrong, "Effect of Cu substitution on anion redox behaviour in P3-type sodium manganese oxides," *JPhys Energy*, vol. 4, no. 4, 2022, doi: 10.1088/2515-7655/ac95cc.

[99] E. J. Kim, L. A. Ma, D. M. Pickup, A. V. Chadwick, R. Younesi, P. Maughan, J. T. S. Irvine, and A. R. Armstrong, "Vacancy-enhanced oxygen redox reversibility in P3-type magnesium-doped sodium manganese oxide $Na_{0.67}Mg_{0.2}Mn_{0.8}O_2$," *ACS Appl. Energy Mater.*, vol. 3, no. 11, pp. 10423–10434, 2020, doi: 10.1021/acsaem.0c01352.

[100] S. Zilinskaite, N. Reeves-McLaren, and R. Boston, "Xanthan gum as a water-based binder for P3-$Na_{2/3}Ni_{1/3}Mn_{2/3}O_2$," *Front. Energy Res.*, vol. 10, no. August, pp. 1–11, Aug. 2022, doi: 10.3389/fenrg.2022.909486.

[101] D. Yuan, W. He, F. Pei, F. Wu, Y. Wu, J. Qian, Y. Cao, X. Ai, and H. Yang, "Synthesis and electrochemical behaviors of layered $Na_{0.67}[Mn_{0.65}Co_{0.2}Ni_{0.15}]O_2$ microflakes as a stable cathode material for sodium-ion batteries," *J. Mater. Chem. A*, vol. 1, no. 12, pp. 3895–3899, 2013, doi: 10.1039/c3ta01430d.

[102] Q. Mao, Y. Yu, J. Wang, L. Zheng, Z. Wang, Y. Qiu, Y. Hao, and X. Liu, "Mitigating the P2-O2 transition and Na^+/vacancy ordering in $Na_{2/3}Ni_{1/3}Mn_{2/3}O_2$ by anion/cation dual-doping for fast and stable Na+insertion/extraction," *J. Mater. Chem. A*, vol. 9, no. 17, pp. 10803–10811, 2021, doi: 10.1039/d1ta01433a.

[103] T. Y. Yu, J. Kim, J. Y. Hwang, H. Kim, G. Han, H. G. Jung, and Y. K. Sun, "High-energy O3-$Na_{1-2x}Ca_x[Ni_{0.5}Mn_{0.5}]O_2$ cathodes for long-life sodium-ion batteries," *J. Mater. Chem. A*, vol. 8, no. 27, pp. 13776–13786, 2020, doi: 10.1039/d0ta04847j.

[104] L. Sun, Y. Xie, X. Z. Liao, H. Wang, G. Tan, Z. Chen, Y. Ren, J. Gim, W. Tang, Y. S. He, K. Amine, and Z. F. Ma, "Insight into Ca-Substitution Effects on O3-Type $NaNi_{1/3}Fe_{1/3}Mn_{1/3}O_2$ Cathode Materials for Sodium-Ion Batteries Application," *Small*, vol. 14, no. 21, pp. 1–7, 2018, doi: 10.1002/smll.201704523.

[105] J. Liu, C. Didier, M. Sale, N. Sharma, Z. Guo, V. K. Peterson, and C. D. Ling, "Elucidation of the high-voltage phase in the layered sodium ion battery cathode material P3-$Na_{0.5}Ni_{0.25}Mn_{0.75}O_2$," *J. Mater. Chem. A*, vol. 8, no. 40, pp. 21151–21162, 2020, doi: 10.1039/d0ta06600a.

[106] T. Y. Yu, H. H. Ryu, G. Han, and Y. K. Sun, "Understanding the Capacity Fading Mechanisms of O3-Type $Na[Ni_{0.5}Mn_{0.5}]O_2$ Cathode for Sodium-Ion Batteries," *Adv. Energy Mater.*, vol. 10, no. 37, pp. 1–8, 2020, doi: 10.1002/aenm.202001609.

[107] L. Zheng and M. N. Obrovac, "Investigation of O3-type $Na_{0.9}Ni_{0.45}Mn_xTi_{0.55-x}O_2$ ($0 \leq x \leq 0.55$) as positive electrode materials for sodium-ion batteries," *Electrochim. Acta*, vol. 233, pp. 284–291, 2017, doi: 10.1016/j.electacta.2017.03.033.

[108] S. Komaba, W. Murata, T. Ishikawa, N. Yabuuchi, T. Ozeki, T. Nakayama, A. Ogata, K. Gotoh, and K. Fujiwara, "Electrochemical Na insertion and solid electrolyte interphase for hard-carbon electrodes and application to Na-ion batteries," *Adv. Funct. Mater.*, vol. 21, no. 20, pp. 3859–3867, 2011, doi: 10.1002/adfm.201100854.

[109] X. Chen, X. Zhou, M. Hu, J. Liang, D. Wu, J. Wei, and Z. Zhou, "Stable layered P3/P2

$Na_{0.66}Co_{0.5}Mn_{0.5}O_2$ cathode materials for sodium-ion batteries," *J. Mater. Chem. A*, vol. 3, no. 41, pp. 20708–20714, 2015, doi: 10.1039/c5ta05205j.

[110] Y. Bai, L. Zhao, C. Wu, H. Li, Y. Li, and F. Wu, "Enhanced Sodium Ion Storage Behavior of P2-Type $Na_{2/3}Fe_{1/2}Mn_{1/2}O_2$ Synthesized *via* a Chelating Agent Assisted Route," *ACS Appl. Mater. Interfaces*, vol. 8, no. 4, pp. 2857–2865, Feb. 2016, doi: 10.1021/acsami.5b11848.

[111] J. Li, T. Risthaus, J. Wang, D. Zhou, X. He, N. Ehteshami, V. Murzin, A. Friesen, H. Liu, X. Hou, M. Diehl, E. Paillard, M. Winter, and J. Li, "The effect of Sn substitution on the structure and oxygen activity of $Na_{0.67}Ni_{0.33}Mn_{0.67}O_2$ cathode materials for sodium ion batteries," *J. Power Sources*, vol. 449, no. November 2019, p. 227554, 2020, doi: 10.1016/j.jpowsour.2019.227554.

[112] H. Wang, B. Yang, X. Z. Liao, J. Xu, D. Yang, Y. S. He, and Z. F. Ma, "Electrochemical properties of P2-$Na_{2/3}[Ni_{1/3}Mn_{2/3}]O_2$ cathode material for sodium ion batteries when cycled in different voltage ranges," *Electrochim. Acta*, vol. 113, pp. 200–204, 2013, doi: 10.1016/j.electacta.2013.09.098.

[113] Q. Liu, Z. Hu, M. Chen, C. Zou, H. Jin, S. Wang, Q. Gu, and S. L. Chou, "P2-type $Na_{2/3}Ni_{1/3}Mn_{2/3}O_2$ as a cathode material with high-rate and long-life for sodium ion storage," *J. Mater. Chem. A*, vol. 7, no. 15, pp. 9215–9221, 2019, doi: 10.1039/c8ta11927a.

[114] Q. C. Wang, J. K. Meng, X. Y. Yue, Q. Q. Qiu, Y. Song, X. J. Wu, Z. W. Fu, Y. Y. Xia, Z. Shadike, J. Wu, X. Q. Yang, and Y. N. Zhou, "Tuning P2-Structured Cathode Material by Na-Site Mg Substitution for Na-Ion Batteries," *J. Am. Chem. Soc.*, vol. 141, no. 2, pp. 840–848, 2019, doi: 10.1021/jacs.8b08638.

[115] L. Zheng, J. C. Bennett, and M. N. Obrovac, "Stabilizing $NaCrO_2$ by Sodium Site Doping with Calcium," *J. Electrochem. Soc.*, vol. 166, no. 10, pp. A2058–A2064, 2019, doi: 10.1149/2.1041910jes.

[116] R. Zhou, X. Guo, Z. Li, S. Luo, and M. Luo, "More Ca^{2+}, Less Na^{+}: Increase the Desalination Capacity and Performance Stability of $Na_xCa_yCoO_2$," *ACS Sustain. Chem. Eng.*, vol. 7, no. 17, pp. 14561–14568, 2019, doi: 10.1021/acssuschemeng.9b02157.

[117] S. C. Han, H. Lim, J. Jeong, D. Ahn, W. B. Park, K. S. Sohn, and M. Pyo, "Ca-doped Na_xCoO_2 for improved cyclability in sodium ion batteries," *J. Power Sources*, vol. 277, pp. 9–16, 2015, doi: 10.1016/j.jpowsour.2014.11.150.

[118] Y. Ishado, H. Hasegawa, S. Okada, M. Mizuhata, H. Maki, and M. Matsui, "An experimental and first-principle investigation of the Ca-substitution effect on P3-type layered Na_xCoO_2," *Chem. Commun.*, vol. 56, no. 58, pp. 8107–8110, 2020, doi: 10.1039/d0cc01675f.

[119] U. Maitra, R. A. House, J. W. Somerville, N. Tapia-Ruiz, J. G. Lozano, N. Guerrini, R. Hao, K. Luo, L. Jin, M. A. Pérez-Osorio, F. Massel, D. M. Pickup, S. Ramos, X. Lu, D. E. McNally, A. V. Chadwick, F. Giustino, T. Schmitt, L. C. Duda, *et al.*, "Oxygen redox chemistry without excess alkali-metal ions in $Na_{2/3}[Mg_{0.28}Mn_{0.72}]O_2$," *Nat. Chem.*, vol. 10, no. 3, pp. 288–295, 2018, doi: 10.1038/nchem.2923.

[120] Z. Q. Deng and A. Manthiram, "Influence of Cationic Substitutions on the Oxygen

Loss and Reversible Capacity of Lithium-Rich Layered Oxide Cathodes," *J. Phys. Chem. C*, vol. 115, no. 14, pp. 7097–7103, Apr. 2011, doi: 10.1021/jp200375d.

[121] X. Rong, J. Liu, E. Hu, Y. Liu, Y. Wang, J. Wu, X. Q. Yu, K. Page, Y. S. Hu, W. Yang, H. Li, X. Q. Yang, L. Chen, and X. Huang, "Structure-Induced Reversible Anionic Redox Activity in Na Layered Oxide Cathode," *Joule*, vol. 2, no. 1, pp. 125–140, 2018, doi: 10.1016/j.joule.2017.10.008.

[122] E. J. Kim, K. Mofredj, D. M. Pickup, A. V. Chadwick, J. T. S. Irvine, and A. R. Armstrong, "Activation of anion redox in P3 structure cobalt-doped sodium manganese oxide via introduction of transition metal vacancies," *J. Power Sources*, vol. 481, no. September 2020, p. 229010, 2021, doi: 10.1016/j.jpowsour.2020.229010.

[123] S. Komaba, T. Ishikawa, N. Yabuuchi, W. Murata, A. Ito, and Y. Ohsawa, "Fluorinated ethylene carbonate as electrolyte additive for rechargeable Na batteries," *ACS Appl. Mater. Interfaces*, vol. 3, no. 11, pp. 4165–4168, 2011, doi: 10.1021/am200973k.

[124] A. Mauger and C. M. Julien, "State-of-the-Art Electrode Materials for Sodium-Ion Batteries," *Materials (Basel).*, vol. 13, no. 16, p. 3453, Aug. 2020, doi: 10.3390/ma13163453.

[125] J. Peters, D. Buchholz, S. Passerini, and M. Weil, "Life cycle assessment of sodium-ion batteries," *Energy Environ. Sci.*, vol. 9, no. 5, pp. 1744–1751, 2016, doi: 10.1039/c6ee00640j.

[126] D. Su, C. Wang, H. J. Ahn, and G. Wang, "Single Crystalline $Na_{0.7}MnO_2$ Nanoplates as Cathode Materials for Sodium-Ion Batteries with Enhanced Performance," *Chem. - A Eur. J.*, vol. 19, no. 33, pp. 10884–10889, 2013, doi: 10.1002/chem.201301563.

[127] N. Yabuuchi, R. Hara, K. Kubota, J. Paulsen, S. Kumakura, and S. Komaba, "A new electrode material for rechargeable sodium batteries: P2-type $Na_{2/3}[Mg_{0.28}Mn_{0.72}]O_2$ with anomalously high reversible capacity," *J. Mater. Chem. A*, vol. 2, no. 40, pp. 16851–16855, 2014, doi: 10.1039/C4TA04351K.

[128] M. S. Kwon, S. G. Lim, Y. Park, S. M. Lee, K. Y. Chung, T. J. Shin, and K. T. Lee, "P2 Orthorhombic $Na_{0.7}[Mn_{1-x}Li_x]O_{2+y}$ as Cathode Materials for Na-Ion Batteries," *ACS Appl. Mater. Interfaces*, vol. 9, no. 17, pp. 14758–14768, 2017, doi: 10.1021/acsami.7b00058.

[129] A. Mendiboure, C. Delmas, and P. Hagenmuller, "Electrochemical intercalation and deintercalation of NaxMnO2 bronzes," *J. Solid State Chem.*, vol. 57, no. 3, pp. 323–331, 1985, doi: 10.1016/0022-4596(85)90194-X.

[130] W. L. Pang, X. H. Zhang, J. Z. Guo, J. Y. Li, X. Yan, B. H. Hou, H. Y. Guan, and X. L. Wu, "P2-type Na2/3Mn1-xAlxO2cathode material for sodium-ion batteries: Al-doped enhanced electrochemical properties and studies on the electrode kinetics," *J. Power Sources*, vol. 356, pp. 80–88, 2017, doi: 10.1016/j.jpowsour.2017.04.076.

[131] R. J. Clément, P. G. Bruce, and C. P. Grey, "Review—Manganese-Based P2-Type Transition Metal Oxides as Sodium-Ion Battery Cathode Materials," *J. Electrochem. Soc.*, vol. 162, no. 14, pp. A2589–A2604, 2015, doi: 10.1149/2.0201514jes.

[132] A. R. Armstrong, M. Holzapfel, P. Novák, C. S. Johnson, S. H. Kang, M. M. Thackeray, and P. G. Bruce, "Demonstrating oxygen loss and associated structural

reorganization in the lithium battery cathode Li[Ni0.2Li0.2Mn 0.6]O2," *J. Am. Chem. Soc.*, vol. 128, no. 26, pp. 8694–8698, 2006, doi: 10.1021/ja062027+.

[133] Y. Li, Z. Yang, S. Xu, L. Mu, L. Gu, Y. S. Hu, H. Li, and L. Chen, "Air-Stable Copper-Based P2-$Na_{7/9}Cu_{2/9}Fe_{1/9}Mn_{2/3}O_2$ as a New Positive Electrode Material for Sodium-Ion Batteries," *Adv. Sci.*, vol. 2, no. 6, pp. 1–7, 2015, doi: 10.1002/advs.201500031.

[134] C. Bischoff, O. Fitz, C. Schiller, H. Gentischer, D. Biro, and H.-M. Henning, "Investigating the Impact of Particle Size on the Performance and Internal Resistance of Aqueous Zinc Ion Batteries with a Manganese Sesquioxide Cathode," *Batteries*, vol. 4, no. 3, p. 44, 2018, doi: 10.3390/batteries4030044.

[135] C. H. Lu and S. W. Lin, "Influence of the particle size on the electrochemical properties of lithium manganese oxide," *J. Power Sources*, vol. 97–98, pp. 458–460, 2001, doi: 10.1016/S0378-7753(01)00637-1.

[136] T. Drezen, N. H. Kwon, P. Bowen, I. Teerlinck, M. Isono, and I. Exnar, "Effect of particle size on $LiMnPO_4$ cathodes," *J. Power Sources*, vol. 174, no. 2, pp. 949–953, 2007, doi: 10.1016/j.jpowsour.2007.06.203.

[137] A. Kraytsberg and Y. Ein-Eli, "Conveying Advanced Li-ion Battery Materials into Practice The Impact of Electrode Slurry Preparation Skills," *Adv. Energy Mater.*, vol. 6, no. 21, 2016, doi: 10.1002/aenm.201600655.

[138] J. Li, S. Jeong, R. Kloepsch, M. Winter, and S. Passerini, "Improved electrochemical performance of $LiMO_2$ (M=Mn, Ni, Co)-Li_2MnO_3 cathode materials in ionic liquid-based electrolyte," *J. Power Sources*, vol. 239, pp. 490–495, 2013, doi: 10.1016/j.jpowsour.2013.04.015.

[139] L. G. Chagas, D. Buchholz, L. Wu, B. Vortmann, and S. Passerini, "Unexpected performance of layered sodium-ion cathode material in ionic liquid-based electrolyte," *J. Power Sources*, vol. 247, pp. 377–383, 2014, doi: 10.1016/j.jpowsour.2013.08.118.

[140] A. R. West, *Solid state chemistry and its applications*. Wiley, 2014. doi: 10.1107/s0108768185002476.

[141] N. Yabuuchi, H. Yoshida, and S. Komaba, "Crystal Structures and Electrode Performance of Alpha-$NaFeO_2$ for Rechargeable Sodium Batteries," *Electrochemistry*, vol. 80, no. 10, pp. 716–719, 2012, doi: 10.5796/electrochemistry.80.716.

[142] D. Baster, K. Dybko, M. Szot, K. Świerczek, and J. Molenda, "Sodium intercalation in Na_xCoO_{2-y} - Correlation between crystal structure, oxygen nonstoichiometry and electrochemical properties," *Solid State Ionics*, vol. 262, pp. 206–210, 2014, doi: 10.1016/j.ssi.2013.11.040.

[143] J. Li, J. Wang, X. He, L. Zhang, A. Senyshyn, B. Yan, M. Muehlbauer, X. Cao, B. Vortmann-Westhoven, V. Kraft, H. Liu, C. Luerenbaum, G. Schumacher, E. Paillard, M. Winter, and J. Li, "P2-Type $Na_{0.67}Mn_{0.8}Cu_{0.1}Mg_{0.1}O_2$ as a new cathode material for sodium-ion batteries: Insights of the synergetic effects of multi-metal substitution and electrolyte optimization," *J. Power Sources*, vol. 416, no. December 2018, pp. 184–192, 2019, doi: 10.1016/j.jpowsour.2019.01.086.

[144] S. Maddukuri, P. Valerie, and V. V. Upadhyayula, “Synthesis and Electrochemical Study of New P3 Type Layered $Na_{0.6}Ni_{0.25}Mn_{0.5}Co_{0.25}O_2$ for Sodium-Ion Batteries,” *ChemistrySelect*, vol. 2, no. 20, pp. 5660–5666, 2017, doi: 10.1002/slct.201700376.

[145] P. Hou, J. Yin, X. Lu, J. Li, Y. Zhao, and X. Xu, “A stable layered P3/P2 and spinel intergrowth nanocomposite as a long-life and high-rate cathode for sodium-ion batteries,” *Nanoscale*, vol. 10, no. 14, pp. 6671–6677, 2018, doi: 10.1039/c8nr00650d.

[146] D. Kim, E. Lee, M. Slater, W. Lu, S. Rood, and C. S. Johnson, “Layered $Na[Ni_{1/3}Fe_{1/3}Mn_{1/3}]O_2$ cathodes for Na-ion battery application,” *Electrochem. commun.*, vol. 18, no. 1, pp. 66–69, 2012, doi: 10.1016/j.elecom.2012.02.020.

[147] Y. Wen, B. Wang, G. Zeng, K. Nogita, D. Ye, and L. Wang, “Electrochemical and structural study of layered P2-type $Na_{2/3}Ni_{1/3}Mn_{2/3}O_2$ as cathode material for sodium-ion battery,” *Chem. - An Asian J.*, vol. 10, no. 3, pp. 661–666, 2015, doi: 10.1002/asia.201403134.

[148] F. Li, Y. Wang, S. Gao, P. Hou, and L. Zhang, “Mitigating the capacity and voltage decay of lithium-rich layered oxide cathodes by fabricating Ni/Mn graded surface,” *J. Mater. Chem. A*, vol. 5, no. 47, pp. 24758–24766, 2017, doi: 10.1039/c7ta07659b.

[149] S. Guo, H. Yu, Z. Jian, P. Liu, Y. Zhu, X. Guo, M. Chen, M. Ishida, and H. Zhou, “A high-capacity, low-cost layered sodium manganese oxide material as cathode for sodium-ion batteries,” *ChemSusChem*, vol. 7, no. 8, pp. 2115–2119, 2014, doi: 10.1002/cssc.201402138.

[150] N. Hassanzadeh, S. K. Sadrnezhaad, and G. Chen, “In-situ hydrothermal synthesis of $Na_3MnCO_3PO_4$/rGO hybrid as a cathode for Na-ion battery,” *Electrochim. Acta*, vol. 208, pp. 188–194, 2016, doi: 10.1016/j.electacta.2016.05.028.

[151] I. Saadoune, A. Maazaz, M. Ménétrier, and C. Delmas, “On the $Na_xNi_{0.6}Co_{0.4}O_2$ system: Physical and electrochemical studies,” *J. Solid State Chem.*, vol. 122, no. 1, pp. 111–117, 1996, doi: 10.1006/jssc.1996.0090.

[152] Y. Wang, J. Tang, X. Yang, and W. Huang, “A study on electrochemical properties of P2-type Na-Mn-Co-Cr-O cathodes for sodium-ion batteries,” *Inorg. Chem. Front.*, vol. 5, no. 3, pp. 577–584, 2018, doi: 10.1039/c7qi00778g.

[153] Y. Zhang, R. Zhang, and Y. Huang, “Air-stable Na_xTMO_2 cathodes for sodium storage,” *Front. Chem.*, vol. 7, no. MAY, pp. 1–15, 2019, doi: 10.3389/fchem.2019.00335.

[154] C. Marino, E. Marelli, S. Park, and C. Villevieille, “Impact of water-based binder on the electrochemical performance of P2-$Na_{0.67}Mn_{0.6}Fe_{0.25}Co_{0.15}O_2$ electrodes in Na-ion batteries,” *Batteries*, vol. 4, no. 4, pp. 1–12, 2018, doi: 10.3390/batteries4040066.

[155] Z. Y. Li, R. Gao, L. Sun, Z. Hu, and X. Liu, “Designing an advanced P2-$Na_{0.67}Mn_{0.65}Ni_{0.2}Co_{0.15}O_2$ layered cathode material for Na-ion batteries,” *J. Mater. Chem. A*, vol. 3, no. 31, pp. 16272–16278, 2015, doi: 10.1039/C5TA02450A.

[156] M. Sathiya, K. Hemalatha, K. Ramesha, J.-M. Tarascon, and A. S. Prakash, “Synthesis, structure, and electrochemical properties of the layered sodium insertion cathode

material: $NaNi_{1/3}Mn_{1/3}Co_{1/3}O_2$," *Chem. Mater.*, vol. 24, no. 10, pp. 1846–1853, 2012, doi: 10.1021/cm300466b.

[157] P. Manikandan, D. Ramasubramonian, and M. M. Shaijumon, "Layered P2-type $Na_{0.5}Ni_{0.25}Mn_{0.75}O_2$ as a high performance cathode material for sodium-ion batteries," *Electrochim. Acta*, vol. 206, pp. 199–206, 2016, doi: 10.1016/j.electacta.2016.04.138.

[158] Z. Schnepp, "Biopolymers as a flexible resource for nanochemistry," *Angew. Chemie - Int. Ed.*, vol. 52, no. 4, pp. 1096–1108, 2013, doi: 10.1002/anie.201206943.

[159] B. L. Cushing, V. L. Kolesnichenko, and C. J. O'Connor, "Recent Advances in the Liquid-Phase Syntheses of Inorganic Nanoparticles," *Chem. Rev.*, vol. 104, no. 9, pp. 3893–3946, 2004, doi: 10.1021/cr030027b.

[160] D. Walsh, L. Arcelli, T. Ikoma, J. Tanaka, and S. Mann, "Dextran templating for the synthesis of metallic and metal oxide sponges," *Nat. Mater.*, vol. 2, no. 6, pp. 386–390, 2003, doi: 10.1038/nmat903.

[161] J. F. Carneiro, J. R. Silva, R. S. Rocha, J. Ribeiro, and M. R. V. Lanza, "Morphological and Electrochemical Characterization of $Ti/M_xTi_ySn_zO_2$ (M = Ir or Ru) Electrodes Prepared by the Polymeric Precursor Method," *Adv. Chem. Eng. Sci.*, vol. 06, no. 04, pp. 364–378, 2016, doi: 10.4236/aces.2016.64037.

[162] G. T. Grant, E. R. Morris, D. A. Rees, P. J. C. Smith, and D. Thom, "Biological interactions between polysaccharides and divalent cations: The egg-box model," *FEBS Lett.*, vol. 32, no. 1, pp. 195–198, 1973, doi: 10.1016/0014-5793(73)80770-7.

[163] R. Boston, *Chapter 1. Bioinspired Synthesis: History, Fundamentals and Outlook*, no. 4. 2019. doi: 10.1039/9781788015806-00001.

[164] S. R. Hall, "Biomimetic Synthesis of High-T_c, Type-II Superconductor Nanowires," *Adv. Mater.*, vol. 18, no. 4, pp. 487–490, 2006, doi: 10.1002/adma.200501971.

[165] K. Wang, Y. Liu, D. Li, A. Zhang, P. Mo, J. Liu, Y. Wang, and Y. Chen, "Electrodeposited Alginate-Based Green Synthesis of CuS Nanoparticles and Nanocomposite Films for Electrochemical and Colorimetric Detection," *Macromol. Mater. Eng.*, vol. 307, no. 8, pp. 1–9, 2022, doi: 10.1002/mame.202200090.

[166] N. H. Mohd Kaus, S. S. Imam, A. W. Aziz, H. L. Lee, R. Adnan, M. L. Ibrahim, and S. Yudha S, "Controlled growth of $BiFeO_3$ nanoparticles in the presence of alginate template for adsorptive removal of different dyes," *Colloids Surfaces A Physicochem. Eng. Asp.*, vol. 615, no. February, p. 126294, 2021, doi: 10.1016/j.colsurfa.2021.126294.

[167] Z. Schnepp, S. C. Wimbush, S. Mann, and S. R. Hall, "Alginate-mediated routes to the selective synthesis of complex metal oxide nanostructures," *CrystEngComm*, vol. 12, no. 5, pp. 1410–1415, 2010, doi: 10.1039/b923543b.

[168] S. R. Hall, S. C. Wimbush, Y. Shida, and W. Ogasawara, "Biotemplated synthesis of superconducting plate-like $YBa_2Cu_3O_{7-\delta}$ using oligosaccharides," *Chem. Phys. Lett.*, vol. 507, no. 1–3, pp. 144–150, 2011, doi: 10.1016/j.cplett.2011.03.071.

[169] J. L. Konne, S. A. Davis, S. Glatzel, and S. R. Hall, "Synthesis of phase pure

praseodymium barium copper iron oxide," *Chem. Commun.*, vol. 49, no. 48, pp. 5477–5479, 2013, doi: 10.1039/c3cc42462f.

[170] Y. Liu, Y. Xu, X. Han, C. Pellegrinelli, Y. Zhu, H. Zhu, J. Wan, A. C. Chung, O. Vaaland, C. Wang, and L. Hu, "Porous Amorphous $FePO_4$ Nanoparticles Connected by Single-Wall Carbon Nanotubes for Sodium Ion Battery Cathodes," *Nano Lett.*, vol. 12, no. 11, pp. 5664–5668, 2012, doi: 10.1021/nl302819f.

[171] Q. Wang, B. Zhao, S. Zhang, X. Gao, and C. Deng, "Superior sodium intercalation of honeycomb-structured hierarchical porous $Na_3V_2(PO_4)_3$/C microballs prepared by a facile one-pot synthesis," *J. Mater. Chem. A*, vol. 3, no. 15, pp. 7732–7740, 2015, doi: 10.1039/c5ta00765h.

[172] D. Walsh, S. C. Wimbush, and S. R. Hall, "Use of the Polysaccharide Dextran as a Morphological Directing Agent in the Synthesis of High-T_c Superconducting $YBa_2Cu_3O_{7-\delta}$ Sponges with Improved Critical Current Densities," *Chem. Mater.*, vol. 19, no. 4, pp. 647–649, 2007, doi: 10.1021/cm0626684.

[173] Z. Zhang, S. C. Wimbush, A. Kursumovic, H. Suo, and J. L. MacManus-Driscoll, "Detailed study of the process of biomimetic formation of YBCO platelets from nitrate salts in the presence of the biopolymer dextran and a molten NaCl flux," *Cryst. Growth Des.*, vol. 12, no. 11, pp. 5635–5642, 2012, doi: 10.1021/cg301143r.

[174] R. Boston, A. Carrington, D. Walsh, and S. R. Hall, "Synthesis of spherical superconductors," *CrystEngComm*, vol. 15, no. 19, p. 3763, 2013, doi: 10.1039/c3ce40269j.

[175] B. Mortemard De Boisse, D. Carlier, M. Guignard, and C. Delmas, "Structural and Electrochemical Characterizations of P2 and New O3-$Na_xMn_{1-y}Fe_yO_2$ Phases Prepared by Auto-Combustion Synthesis for Na-Ion Batteries," *J. Electrochem. Soc.*, vol. 160, no. 4, pp. A569–A574, 2013, doi: 10.1149/2.032304jes.

[176] W. Zuo, J. Qiu, C. Hong, X. Liu, J. Li, G. F. Ortiz, Q. Li, S. Zheng, G. R. Zheng, and Y. Yang, "Structure-Performance Relationship of Zn^{2+} Substitution in P2-$Na_{0.66}Ni_{0.33}Mn_{0.67}O_2$ with Different Ni/Mn Ratios for High-Energy Sodium-Ion Batteries," *ACS Appl. Energy Mater.*, vol. 2, no. 7, pp. 4914–4924, 2019, doi: 10.1021/acsaem.9b00614.

2 Methodology

2.1 Cathode material preparation

2.1.1 Synthesis methods

The cathode materials investigated were P3- and P2-$Na_{0.67}Mn_{0.9}Mg_{0.1}O_2$ (NMMO) produced *via* two synthesis methods: solid state and biotemplating. Biotemplating is used in each Results chapter, whereas a solid state synthesis is only used in Results 1.

Solid state synthesis is a simple and very commonly used method in cathode material preparation [1]–[5]. The basic procedure involves drying, milling, and pressing powder reactants into pellets, and calcining them [6]. Mixing the powders together only mixes them on the scale of particle sizes. This means that for the individual ions to mix in the correct stoichiometry and form a product, they must diffuse across long distances, typically ≤ 1 µm [7]. The diffusion pathways get longer as the new crystal grows, and the reactant ions must travel further to reach other ions to react with to form new product crystal (Figure 2-1). This often leads to long calcination times; times of at least 12 h are common [8]–[11].

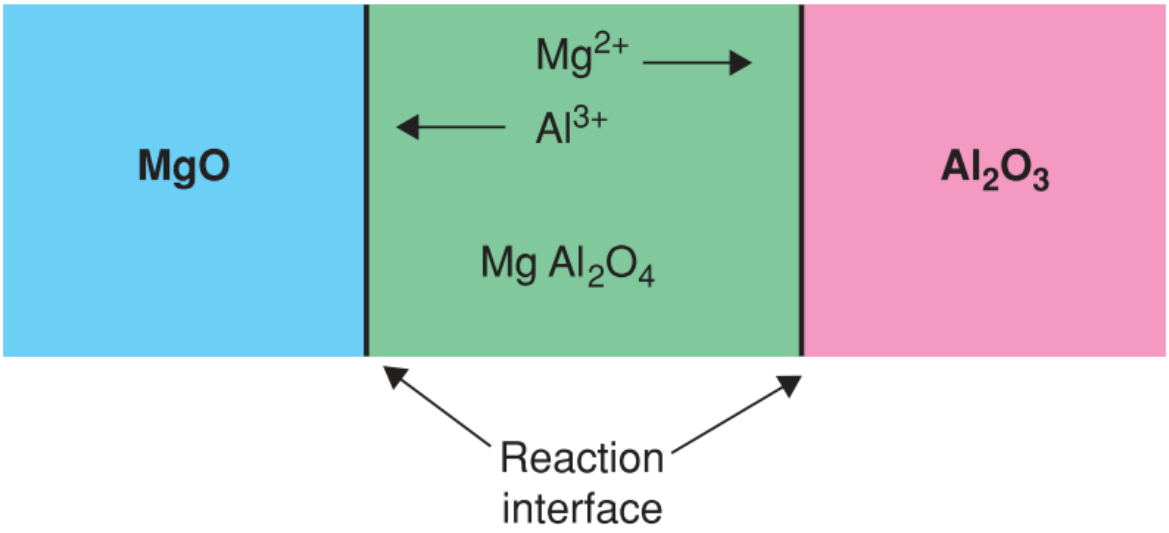

Figure 2-1: Schematic of a solid state reaction between MgO and Al_2O_3 to form $MgAl_2O_4$ [7].

In contrast, biotemplating dissolves the metal cations in solution. Adapted from the Pechini process which uses citric acid [12], a long-chain biopolymer is used to prevent agglomeration of cations in solution. Dextran has been used in biotemplating syntheses before [13]–[15], including in cathode preparation [16], [17]. The metal cations are dissolved into an aqueous solution before the addition and dissolution of dextran (Figure 21 in Section 2.4.5). Once the dextran is dissolved, the solution is dried and calcined. The biotemplate thermally decomposes, leaving the product to leave the oxide structure. The level of mixing here is significantly greater than solid state, owing to the dissolution step; the cation mixing is on an atomic level, as opposed to micron. This means shorter

calcination times are often used in biotemplating syntheses [14], [18], and lower temperature phases can be accessed more readily [16], [17].

2.1.2 Chapter 3: P3- and P2-$Na_{0.67}Mn_{0.9}Mg_{0.1}O_2$

To produce NMMO *via* solid state synthesis (referred to as solid state P3- or P2-NMMO), Na_2CO_3 (Sigma Aldrich, UK, ≥ 99.5%), MnO_2 (Sigma Aldrich, UK, ≥ 99%), and MgO (Sigma Aldrich, UK, ≥ 99%) were dried and subsequently mixed in stoichiometric amounts (with a 10% excess of Na to counteract Na volatility during calcination [19]–[22]) *via* ball milling for 8 h in isopropyl alcohol, and dried at 80 °C in air. The mixture was sieved through a 250 µm aperture sieve and uniaxially pressed into 10 mm pellets using approximately 0.112 MPa to bring particles closer together pre-calcination.

For the biotemplated samples, CH_3COONa (Sigma Aldrich, UK, ≥ 99%), $(CH_3COO)_2Mn.4H_2O$ (Alfa, ≥ 22% Mn content by assay), $(CH_3COO)_2Mg.4H_2O$ (Sigma Aldrich, UK, ≥ 98 %) were dissolved in distilled water in stoichiometric amounts (with 10% excess of CH_3COONa to counteract Na volatility during calcination). Dextran (Sigma Aldrich, UK, M_r = 70 000) was added to this solution in a 1:10 by weight ratio with the water. This translated to a metal ion to template ratio of 2:3 by mass. Once dissolved, the solution was dried in air in muffle furnace at 80 °C to produce a hard organic-inorganic composite.

The calcination temperatures were determined through a combination of high-temperature XRD (HTXRD) and iterative development that will be discussed in the chapter itself. The heating protocols for both solid state and biotemplated samples were kept consistent for each phase. All calcinations in this chapter lasted 20 h in air, with a 5 °C min^{-1} ramp rate and held at 200 °C post-calcination to avoid water absorption. The 20 h calcination time was chosen to allow the solid state reaction to reach completion, although there were still starting materials apparent in XRD patterns of the P3 sample synthesised *via* solid state. The resultant powders were ground in air using an agate pestle and mortar and dried in a 120 °C vacuum oven for at least 8 h to remove any water absorbed by the structure prior to transferral into an Ar-filled glovebox.

2.1.3 Chapter 4: $Na_{0.67-2x}Ca_xMn_{0.9}Mg_{0.1}O_2$

A range of Ca^{2+}-doped P3- and P2-$Na_{0.67-2x}Ca_xMn_{0.9}Mg_{0.1}O_2$ (x = 0, 0.01, 0.02) (NCMM) samples were generated using a biotemplated synthesis. CH_3COONa (Sigma Aldrich, UK, ≥ 99%), $(CH_3COO)_2Ca.H_2O$ (Sigma Aldrich, UK, ≥ 98 %) $(CH_3COO)_2Mn.4H_2O$ (Alfa, ≥ 22 % Mn content by assay), $(CH_3COO)_2Mg.4H_2O$ (Sigma Aldrich, UK, ≥ 98 %) were dissolved in distilled water in stoichiometric amounts. A stoichiometric excess of Na was not used here: the shortened calcination times mitigated the volatility of the Na, and the presence of excess Na when doping with another alkali metal made prediction of the final stoichiometry more challenging. Dextran (Sigma Aldrich, UK, M_r = 70 000) was added to this solution in a 1:10 by weight ratio with the water. Once dissolved, the solution was dried at 80 °C to produce a hard organic-inorganic composite.

The calcination times temperatures used to generate P2 and P3 phases were adapted from previous dextran biotemplating studies [13]–[17]. P3-NCMM was generated *via*

calcination at 650 °C for 2 h, in line with other P3 materials, using a 10 °C min^{-1} ramp rate. Similar for P2-NCMM with a 900 °C calcination temperature. Samples were held at 200 °C post-calcination. Calcination times used here, 2 h, are much closer to the times that have been used in previous dextran biotemplating studies [13]–[17], as a comparison to the solid state synthesis is not the focus of this chapter. The resultant powders were ground in air using an agate pestle and mortar and stored in a 120 °C vacuum oven for at least 8 h to remove any water absorbed by the structure prior to transferral into an Ar-filled glovebox.

2.1.4 Chapter 5: P3/P2-$Na_{0.67}Mn_{0.9}Mg_{0.1}O_2$

A range of composite P3-NMMO and P2-NMMO (referred to as P3/P2-NMMO) structures were formed *via* biotemplating synthesis. The ratio of P3 to P2 phase was controlled with the calcination temperature used to obtain each layered structure. The ratios aimed for, and the calcination temperature used are detailed in Table 2-1. This was investigated and compared to a phase-pure biotemplated P3 and P2 phase, and a physical mixture of the P3 and P2 phases in the same phase ratio as the intergrowth structures.

As a control, P3 and P2 mixtures were produced by grinding the appropriate ratios of P3- and P2-NMMO powders together post-calcination. The temperature used to generate the intergrowth structure, determined by HTXRD, aimed to result in a 1:1 by mass mix of the P3 and P2 phases, as determined by Rietveld refinements. Samples were held at 200 °C post-calcination. The resultant powders were ground in air and stored in a 120 °C vacuum oven for at least 8 h to remove any water absorbed by the structure prior to transferral into an Ar-filled glovebox.

Table 2-1: Calcination regimes of each phase of $Na_{0.67}Mn_{0.9}Mg_{0.1}O_2$ by synthesis method

P3 to P2 ratio (%)	Calcination temperature (°C)
100:0	650
90:10	720
70:30	730
50:50	770
30:70	800
10:90	820
0:100	900

2.2 X-ray Diffraction

2.2.1 Fundamentals

X-ray diffraction (XRD) is a technique used to examine long-range order in crystalline materials. The cathode materials used herein have crystalline structures, and as such are

made up of repeating patterns of ions that make up the crystal lattice. The smallest repeating unit of the lattice is the unit cell.

Unit cells are used to describe the symmetry within the crystal. And can be grouped into seven different systems, detailed in Table 2-2. Rhombohedral is a subset of the trigonal system but is often thought of as distinct. Unit cells can be further described by its body type: primitive (P), body-centred (I), face-centred (F), C-centred (C). It was shown in 1850 by Bravais [23] that there are 14 possible lattice types. Within a crystal lattice, not all symmetry operations are allowed to appear together. As such there are only a certain number of combinations possible between the Bravais lattices and symmetry operations, forming 230 space groups.

Table 2-2: Crystal systems

Crystal system	Unit cell axis lengths	Unit cell angles	Possible lattices
Cubic	$a = b = c$	$\alpha = \beta = \gamma = 90°$	P, I, F
Hexagonal	$a = b \neq c$	$\alpha = \beta = 90°$ $\gamma = 120°$	P
Tetragonal	$a = b \neq c$	$\alpha = \beta = \gamma = 90°$	P, I
Trigonal	$a = b \neq c$	$\alpha = \beta = 90°$ $\gamma = 120°$	R
(Rhombohedral)	$(a = b = c)$	$(\alpha = \beta = \gamma)$	
Orthorhombic	$a \neq b \neq c$	$\alpha = \beta = \gamma = 90°$	P, C, I, F
Monoclinic	$a \neq b \neq c$	$\alpha = \gamma = 90°$ $\beta > 90°$	P, C
Triclinic	$a \neq b \neq c$	$\alpha \neq \beta \neq \gamma$	P, I, F

There are an infinite number of planes in the unit cell, and they can be described by a Miller index, (*hkl*), which describe the fraction of the unit cell axis where the plane and axis meet. The plane (*hkl*) will intercept the unit cell x-axis at $\left(\frac{1}{h}\right)\overline{a}$, *y*-axis at $\left(\frac{1}{k}\right)\overline{b}$, and the *z*-axis at $\left(\frac{1}{l}\right)\overline{c}$. Here $\overline{a}, \overline{b}, \overline{c}$ are the unit cell vectors. From the relationship between the unit cell vectors and the Miller indices, the spacing of each plane, d_{hkl}, are derived.

Across the crystal lattice, planes correspond to repeating planes of atoms. When the X-ray beam hits these planes, it is reflected, with the angle of reflection equal to the angle of incidence. The existence of these planes and the separation between them depends on

the motif of the unit cell. XRD exploits the spacing, *d*, between planes to build up a picture of the unit cell.

For a powder sample, the volume of powder that can be examined is large enough that it can contain crystallites in every possible orientation. Meaning that when the sample is irradiated, it will re-emit that radiation in all directions. This also means that many Miller planes present in the crystal will be positioned to reflect the X-ray beam into the detector as it and the X-ray source sweep through the 2θ range.

As shown in Figure 2-2, an X-ray beam (denoted as 1) will hit a Miller plane at some angle of incidence, θ. It will be elastically scattered by the first plane of atoms in every direction, and so some will be reflected towards the detector (1'). Another beam (2) passes through the first plane and undergoes the same process but is scattered by an atom in the second layer of atoms. When second X-ray beam reaches the detector, it will have travelled an extra distance, *xyz*, further than the first. For constructive interference to occur, *xyz* must be equal to $n\lambda$, where *n* is the order of diffraction (and thus always an integer) and λ is the X-ray beam wavelength.

The Bragg condition is satisfied when the reflected beams (1' and 2') are in-phase with one another and constructive interference will occur. For the two beams to be in-phase, the extra distance travelled by 2', *xyz*, must be equal to an integer number of wavelengths, $n\lambda$. Since the planes are parallel, we can use this information and some geometry to calculate *d* of a given Miller plane using the following equation:

$$n\lambda = xyz = 2xy \qquad \textit{Equation 1}$$

$$d\ sin\theta = xy = \frac{n\lambda}{2} \qquad \textit{Equation 2}$$

$$d = \frac{n\lambda}{2sin\theta} \qquad \textit{Equation 3}$$

Rearranging this gives us the Bragg equation:

$$n\lambda = 2d\ sin\theta \qquad \textit{Equation 4}$$

As the incident X-ray beams sweep through a range of 2θ values, constructive interference will occur at specific *d* spacings (or 2θ values, referred to as Bragg angles) relating to different Miller planes. The constructive interference manifests itself in the XRD pattern as peaks. The positions of these peaks are interpreted and used to identify the structure of the unit cell.

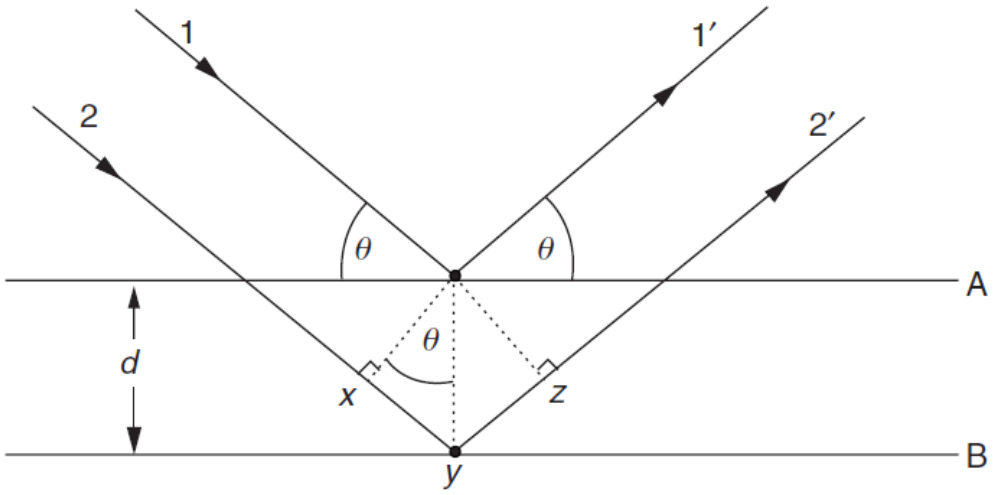

Figure 2-2: Schematic showing the interaction of an X-ray beam with two planes of a crystal structure. Annotated with the geometries that satisfy the Bragg condition [7].

This identification process in this thesis is initially done *via* phase matching using the ICDD PDF4+ Sieve+ software [24]. The phases of interest, P2 and P3, are distinct and well-established as common phases in the sodium-ion cathode literature, so are also identified *via* qualitative comparisons to patterns in previously published work.

Unit cells with the same structure will have similar XRD patterns, except for shifts in the peak position according to contractions or expansions of the unit cell, perhaps caused by Na^+ content or the transition metal ions present. Therefore, the calculation of lattice parameters, phase fractions, and confirmation of the phases present was done *via* Rietveld refinements.

2.2.2 Rietveld refinement

The exact determination of the unit cell parameters was done *via* Rietveld refinement using HighScore (Panalytical) [25]. Rietveld refinements are a full profile fitting of the expected XRD pattern against the observed pattern. The refinement program then allows variations of the parameters defining the sample *via* a least-squares fit method to minimise Δ in the following equation [26]:

$$\Delta = \sum_i w_i \{Y_{O,i} - Y_{C,i}\}^2 \qquad \textit{Equation 5}$$

Where Y_i is the intensity value at each 2θ value for the observed ($Y_{O,i}$) and calculated ($Y_{C,i}$) datasets, and w_i is the weighting of each observation. The weighting is related to the error, σ, attributed to each observation:

$$w_i = \frac{1}{\sigma[Y_{O,i}]^2} \qquad \textit{Equation 6}$$

And so:

$$\sigma = \frac{1}{w_i[Y_{O,i}]^2} \qquad \textit{Equation 7}$$

From the HighScore documentation, the estimation of standard errors is calculated only from statistical randomness in counting and are too small. This is of particular importance with "noisy" data, where a poorly defined background will result in better fitting metrics. To counter this, the data from the XRD experiments must be of high quality, even though this may worsen the fitting metrics.

Using the weighting, more consideration is given to intense peaks, and less to the background. From here, several metrics that are used to evaluate the fit can be derived: the weight-profile *R*-factor (R_{wp}), the expected *R*-factor, or "best possible R_{wp}" (R_{exp}), χ^2, and the Goodness of Fit parameter (GOF):

$$R_{wp} = \left(\frac{\sum_i w_i(Y_{O.i} - Y_{C,i})^2}{\sum_i w_i Y_{O,i}^2}\right)^{\frac{1}{2}} \qquad \textit{Equation 8}$$

$$R_{exp} = \left(\frac{N - P + C}{\sum_i w_i Y_{O,i}^2}\right)^{\frac{1}{2}} \qquad \textit{Equation 9}$$

$$\chi^2 = \left(\frac{R_{wp}}{R_{exp}}\right)^2 \qquad \textit{Equation 10}$$

$$GOF = \chi = \left(\frac{R_{wp}}{R_{exp}}\right) \qquad \textit{Equation 11}$$

Where *N* is the number of data points, *P* is the number of varied least-squares parameters (or degrees of freedom), and *C* is the number of constraints. $N - P + C \approx N$, given the number of data points measured is sufficiently large. R_{wp} and R_{exp} are both multiplied by 100 to represent them at a percentage. For this work, the values for R_{wp} and GOF are used to evaluate the fit. In general, $R_{wp} < 10\%$ and $1 < GOF < 2$ is taken to indicate a close fit [27]. The materials under investigation (layered oxide sodium cathodes) have well-defined and understood structures, and so the likelihood that the structure model is incorrect is low, increasing the confidence that a close fit is accurate.

Rietveld was used to measure unit cell parameters. The sample parameters (space group, unit cell parameters, atomic positions, occupancy) used were taken initially from a previous study of P2 and P3 NIB [16], [28] materials. For more accurate determinations of unit cell parameters, the material was mixed with a Si standard (estimated 10% by weight to give comparable peak intensities) to calibrate the peak positions and account for sample height displacement. After refinements to determine the background, the sample height was corrected for using the Si standard. From here the unit cell parameters could be refined, and the Rietveld refinement continued as normal. These unit cell parameters were used in subsequent refinements.

During the Rietveld refinements, manganese and magnesium occupancies were set to sum to 1. The background was fitted to the sample pattern using a Shifted Chebyshev I method with up to 10 terms or until the simulated background qualitatively matched the observed background. The unit cell parameters were then refined, followed by refinements of the Caglioti parameters and the peak shape parameters. This was followed by refinements of atomic position and site occupancy.

The width of the peaks is affected by the single crystalline domain size in the materials. Constructive interference occurs at the Bragg angle, when the additional path length travelled by the x-ray beam reflected by lower lattice planes is an integer multiple of the wavelength, λ. Deviations away from the Bragg angle lead to the x-ray beams being out-of-phase.

For example, if the angle of incidence, θ, was increased so that the additional path length travelled by the beam reflected by the second lattice plane was equal to 1.1 λ, then the additional path length travelled by the beam reflected by the sixth plane would be 5.5 λ. Being 0.5 λ out-of-phase with the beam reflected by the first plane leads to destructive interference. Therefore, in this scenario destructive interference will occur between beams separated by five planes.

As θ approaches the Bragg angle, destructive interference will occur between pairs of lattice planes that are continually further apart. If the additional distance travelled by the x-ray reflected by the second plane is equal to 1.0001 λ, then destructive interference will occur between beams separated by 5000 planes instead. The closer θ gets to the Bragg angle, the more the planes separating completely out-of-phase x-ray beams.

For smaller crystallites, the planes that will cause this destructive interference will not be present. As such, smaller crystallites will allow more deviations from the Bragg angle before destructive interference occurs. Reducing the crystallite size increases the width (and consequently reduces the peak height) of the reflection peaks, as defined by the Scherrer equation [29],

$$B(2\theta) = \frac{K\lambda}{L\ cos\theta} \qquad \textit{Equation 12}$$

Where $B(2\theta)$ is the additional broadening (radians) at a given value of 2θ, K is the Scherrer constant (dimensionless), λ is the wavelength of the radiation (Å), L is the apparent crystallite size (Å), and θ is the Bragg angle (radians). The value of the Scherrer constant was 0.9 as most particles had a roughly spherical shape, although this may mean losing size data if the particle shape changes between samples.

When the instrument and its parameters remain the same across XRD patterns of different samples, the broadness of the peaks in the pattern are used to qualitatively compare crystallite sizes. The factors affecting peak broadening are obtained during the refinement and fit into the following equation:

$$H_k{}^2 = W + V\ tan\theta\ + U\ tan^2\theta$$ *Equation 13*

Where H_k is the Caglioti function, and W, V, and U are the parameters that define it. U and W are the parameters that can inform crystallite size and microstrain broadening. Without the use of a line-broadening standard, these results are unreliable, and so crystallite size measurements are obtained using scanning electron microscopy (SEM).

2.2.3 Experimental setup

2.2.3.1 Reflection

All powder XRD conducted to identify and characterise phases were done so using a Cu Kα radiation source (λ = 1.5406 Å). Experiments were conducted using one of three instruments: a D2 Phaser (Bruker), an X'Pert^3 (Panalytical), and an Aeris (Panalytical). The D2 Phaser was used only for phase identification. The XRD patterns from the X'Pert^3 and Aeris were used in Rietveld refinements due to their superior detector which allowed for greater resolution of peaks. This means more accurate determination *d* spacing and unit cell parameters. Crystal structure visualisations were generated using CrystalMaker®: a crystal and molecular structures program for Mac and Windows. CrystalMaker Software Ltd, Oxford, England (www.crystalmaker.com).

Powders were mounted in a standard Bruker PMMA holder of 25 mm diameter and 1 mm depth. The D2 Phaser does not use a monochromator. The beam energy settings were 10 mA, 30 kV. The X'Pert^3 powder samples were held in a back-loaded stainless steel powder sample holder, 16 mm in diameter and 2.4 mm thick. The beam energy settings were 40 mA, 45 kV. All samples examined in the Aeris used beam energy settings of 15 mA, 40 kV. The Aeris used the same sample holders as the X'Pert^3 and was exclusively used to examine cathode materials, containing manganese, and so a reduced fluorescence scan setting was used.

Most samples were examined in the 10 – 80 °2θ range, in some cases where Rietveld refinements were conducted the range was increased to 10 – 120 °2θ and this will be indicated on the individual XRD patterns. 10 – 80 °2θ is sufficient to capture the largest peak, (002) or (003) are ~16 °2θ, and other characteristic peaks that can be used to identify both P3 and P2 structures. A 10 – 100 °2θ range was used with the Aeris.

Step time was varied when using the D2 Phaser depending on laboratory conditions, but was commonly set to 0.400 s, which gave peak intensities that allowed for satisfactory phase identification and preliminary Rietveld analysis. Given the aim of the XRD patterns obtained using the D2 Phaser is phase analysis, the variation of step time does not adversely affect the validity of the conclusions that can be drawn. Using the X'Pert^3 step time was set at 118.32 s. This gave sufficient peak intensities to conduct Rietveld refinements.

2.2.3.2 High temperature XRD

The progression of a reaction was monitored using XRD while increasing the temperature within the machine. High temperature XRD (HTXRD) was used to determine reaction

progression and confirm the presence of any intermediate phases. Lattice parameter expansions or contractions can be observed in HTXRD experiments. However, the process of heating causes the sample holder and the sample itself to expand. Due to the uncertainty this introduces, quantitative analysis of lattice parameters was not conducted. Rietveld analyses were used only to estimate phase fractions. These results were used to guide calcination temperatures for P2/P3 biphase generation.

HTXRD was conducted on the X'Pert^3 using a HTK1200N furnace attachment (Anton Paar). Sample was mounted in an alumina sample holder with 15 mm diameter and 1 mm depth. Temperature and ramp rate was chosen to reflect the synthesis method. XRD patterns were measured every 25 °C from 10 – 80 °2θ with a step size of 0.013 °2θ and a step time of 67.34 s.

The sample height was adjusted to using the automatic Stage Mover Program (Anton Paar). The largest peak in the XRD of the sample was calibrated to its expected value before running the non-ambient program. The lack of XRD standard in the sample was necessary to ensure that the reaction was not affected, and so sample displacement may occur during the HTXRD program. This uncertainty in the peak positions means that derived lattice parameters will not be reliable.

2.3 Scanning electron microscopy

2.3.1 Fundamentals

Scanning electron microscopy (SEM) is a technique used to examine particle size and morphology. It involves a beam of electrons interacting with the surface of a material which are scattered, or release electrons from the surface. These electrons are collected by an electron detector and used to create an image of the sample. The electrons are fired from the electron gun and focussed through various lenses and apertures. The electron beam scans across the sample surface in a raster pattern. An image is generated *via* either the backscattered electrons (BSE) or secondary electrons (SE) that interact with the detector.

Backscattered electrons (BSE) are reflected off the surface of the sample *via* Rutherford scattering. This process is elastic and arises because of the electrostatic interaction between incident electrons and the nuclei within the sample. Atoms with higher atomic numbers have a greater likelihood of scattering electrons, so BSE can be used to indicate compositional contrast in materials: higher BSE counts will arise from higher atomic numbers.

Inelastic scattering occurs when the incident electron transfers some of its energy to the electrons in the sample. If the energy transferred to an electron is sufficient for it to escape the sample, then it is termed a SE. SE that are formed directly from the incident beam (i.e., electrons that are released from the sample and do not undergo other interactions before reaching the detector) are known as SE1 and have a very high spatial resolution as the escape area is highly localised to the incident beam.

The escape area of the electrons is what determines the resolution of the image, and can be affected by the beam diameter, shape, and energy. The energy of the beam depends on the incident beam voltage, so increasing this creates more SE (improving the signal intensity) but will widen the interaction volume and decrease the resolution. A compromise between the two must be found.

2.3.2 Experimental setup

SEM images were obtained using either an Inspect F (FEI), or an Inspect F50 (FEI) if energy-dispersive X-ray spectroscopy (EDX) was needed. The two machines are almost identical, as is the data quality that they can extract. The electron beam used had a voltage of either 10 or 15 kV and a spot size of 3.0 or 3.5. This allowed for good resolution up to 80,000*x* magnification for measuring particle sizes. A small amount (~10 mg) of sample powder was deposited on a carbon tab affixed to an SEM stub and sputtered with a thin layer of gold to aid electron conductivity on the surface. Energy-dispersive analysis of X-rays (EDX) was conducted using Aztec (Oxford instruments). Determinations of particle size were conducted using ImageJ [30]. Measurements of at least 500 individual particles were taken along the longest visible dimension.

2.4 Electrochemistry

2.4.1 Fundamentals

The electrochemistry tests herein determined the performance of the materials under investigation. The materials were tested using two procedures: galvanostatic cycling and rate capability testing. The derivative of the galvanostatic cycling curve allowed further examination electrochemical process. The tests were conducted within a set voltage range, where the (open circuit) voltage, V_{OC}, of the cell is given by:

$$V_{OC} = \frac{\mu_A - \mu_C}{e} \qquad \textit{Equation 14}$$

Where μ_A and μ_C the chemical potentials are the anode and cathode, respectively, and e is the magnitude of electronic charge [31], [32]. Galvanostatic cycling was conducted by withdrawing a constant current from the cell, within a set voltage window. The length of time taken to reach these limits (the lower limit on discharge, and vice versa), combined with the mass of active material and the specific capacity of the material returned the specific capacity. The theoretical specific capacity of the material was calculated using the following equation:

$$Q_O = \frac{nF}{3.6 \times M_r} \qquad \textit{Equation 15}$$

Where Q_O is the theoretical specific capacity in mAh g^{-1}, n is the mol of electrons transferred during charge/discharge per mol of active material, M_r is the molar mass of the active material in g mol^{-1}, F is the Faraday constant, 96 485 As mol^{-1}. 3.6 converts the Faraday constant from As to mAh. For this material, n was taken as 0.67. This gave a theoretical capacity of 184 mAh g^{-1}.

Based on theoretical capacity, the current needed to fully charge or discharge the cell in 1 h, C, was 184 mA g^{-1}. Typically, the current at which the cell is charged and discharged is a given as a fraction (or multiple) of C (C-rate). The actual current was obtained by multiplying the coefficient of C by the mass of active material. The discharge capacity of the material is given by:

$$Q = \frac{It}{m} \qquad \textit{Equation 16}$$

Where Q is the measured specific capacity in mAh g^{-1}, I is the discharge current in mA, t is the time taken for the cell to discharge in h, and m is mass of active material in g.

At the end of the charging step, the cell was held at the upper voltage limit. The current during this time should fall to 0 A, and the cell would be at equilibrium. In practice, a current cut-off of C/10 was used. The two charging modes are referred to as constant current (CC) and constant voltage (CV) charging, and constant current-constant voltage (CCCV) charging altogether. Discharge only used a CC mode. In between the charge and discharge steps, a 10 min rest period was used to allow the cell to fully equilibrate before the next step.

The differential capacity graph was generated by taking the derivative of the voltage curve. Due to the data collection during the galvanostatic cycling, there are consecutive data points in which the change in voltage was very small. This led to very noisy data. To offset this, the data was cleaned after the test procedure was completed; stripping data points where the change in voltage was less than 20 mV. The CV section of the charge step was also removed from the dataset for the same reason. Since the component of interest is the cathode, rather than the full cell, the differential capacity graph was preferable to cyclic voltammetry [33]. It offered superior resolution, a consistent IR drop, and full access to the capacity of the cell during the cycle.

Rate capability testing was similar to galvanostatic testing. Cells were cycled five times at a given current using the same galvanostatic procedure, after which the C-rate was increased. This was done several times to generate capacities and voltage curves for the material at a range of C-rates. This resulted in increased polarisation within the battery, specifically the ohmic polarisation. This is also known as the *IR* drop [32], and is proportional to the (dis)charge current, *I*. Therefore, as the current is increased, the cells were pushed further from theoretical equilibrium, and voltage and capacity decreased as a result. The capacity decreased in part because of the lower voltage from increased polarisation, but also due to more rapid fall in the battery voltage. The battery voltage after (dis)charging is given by the Armand equation [34]:

$$E_{cell} = {E^0}_{cell} - \frac{nRT}{F}\ln\left(\frac{y}{1-y}\right) + ky \qquad \textit{Equation 17}$$

Here, E_{cell} is the new potential of the cell, E^0_{cell} is the standard potential, R is the molar gas constant, 8.314 J $K^{-1}mol^{-1}$, T is the absolute temperature, y is the sodium occupancy, and ky is the effect of interactions between sodium ions on the battery voltage. There are

factors that directly influence *y* and *k*, such as diffusion, phase transitions, electrode particle size, temperature, electrolyte characteristics, and porosity. As the C-rate is increased, the rate of transfer of ions across the electrode/electrolyte boundary becomes diffusion-limited [35], and the discharge curves get lower and smoother.

2.4.2 Electrochemical testing

Galvanostatic cycling measurements were taken to determine the capacity of the cathodes under investigation. Unless stated otherwise, cells were cycled at C/5 [36] (1C = 184 mA g^{-1}) between 1.5 – 4.0 V [37] for 50 cycles. Charge cycles used a constant current, constant voltage procedure [38], [39]; after reaching 4.0 V, the cell was held at 4.0 V until the current dropped to C/10. This was followed by a 10 min rest period before constant current discharge, and another 10 min rest step before the next cycle. These test parameters were selected optimise performance of the cathode material (with respect to discharge capacity and capacity retention), while obtaining results quickly. Performance of each material was further examined rate capability testing. The C-rates used were C/10, C/5, C/2, 1C, 2C, and 5C. After cycling at 5C, cells were cycled at C/10 for a final 5 cycles to determine their ability to regain the capacity.

2.4.3 Cathode preparation

In an Ar-filled glovebox, an 8:1:1 (w/w) mixture of active material, C65 (MTI), and polyvinylidene fluoride (PVDF) (MTI) were ground together in an agate pestle and mortar. C65 and PVDF were both dried in an 80 °C vacuum oven overnight prior to transferral into the glovebox. This powder was combined with approximately 2.2 mL per gram of powder mixture of *N*-methyl-2-pyrrolidone (NMP) (99.5%, Sigma Aldrich) in a Thinkymixer. A smooth, viscous slurry was formed by mixing the powder and NMP until a smooth, viscous slurry formed. Usually this was done by mixing for 20 min at 2000 rpm, followed by a defoaming step for 30 s at 2200 rpm. This procedure was adapted from an outline by Talaie *et al*. [33] *via* an iterative process.

In a fume hood, the slurry was cast onto carbon-coated aluminium foil (MTI) at a thickness of 250 µm, and dried in air at 120 °C for approximately 90 min [40], [41]. These conditions generated cathodes with an active material loading of approximately 4 mg cm^{-2} [6], [16], [42] .The cast slurry was cured overnight in a vacuum oven at 80 °C [6], [43], [44], then calendared to 50% of the initial slurry thickness to densify the cathode slurry and improve electrochemical performance. Calendaring to 50% thickness was shown to achieve this and was used through to maintain consistency. 12 mm discs were punched from it and dried again in an 80 °C vacuum oven overnight [45] and transferred back to the Ar-filled glovebox.

2.4.4 Cell assembly

Stainless steel 2032 coin cells were assembled using a stainless steel wave spring, a 0.5 mm stainless steel spacer, a sodium metal (99.8%, Alfa Aesar) electrode to act as both the counter and reference electrode, a glass microfibre (Whatman GF/6) separator dried overnight in an 80 °C vacuum oven, and the cathode discs (Figure 2-3). Separator was wetted with 1 M $NaPF_6$ in a 1:1 by volume solution of ethylene carbonate (EC) and diethyl

carbonate (DEC) (Fluorochem) electrolyte (0.85 mL) during assembly. These were sealed with a pressure of 100 kg cm^{-2} using a gas-driven crimper (MTI). Cells were allowed to rest for 12 hours before cycling to allow the electrolyte to fully soak the separator.

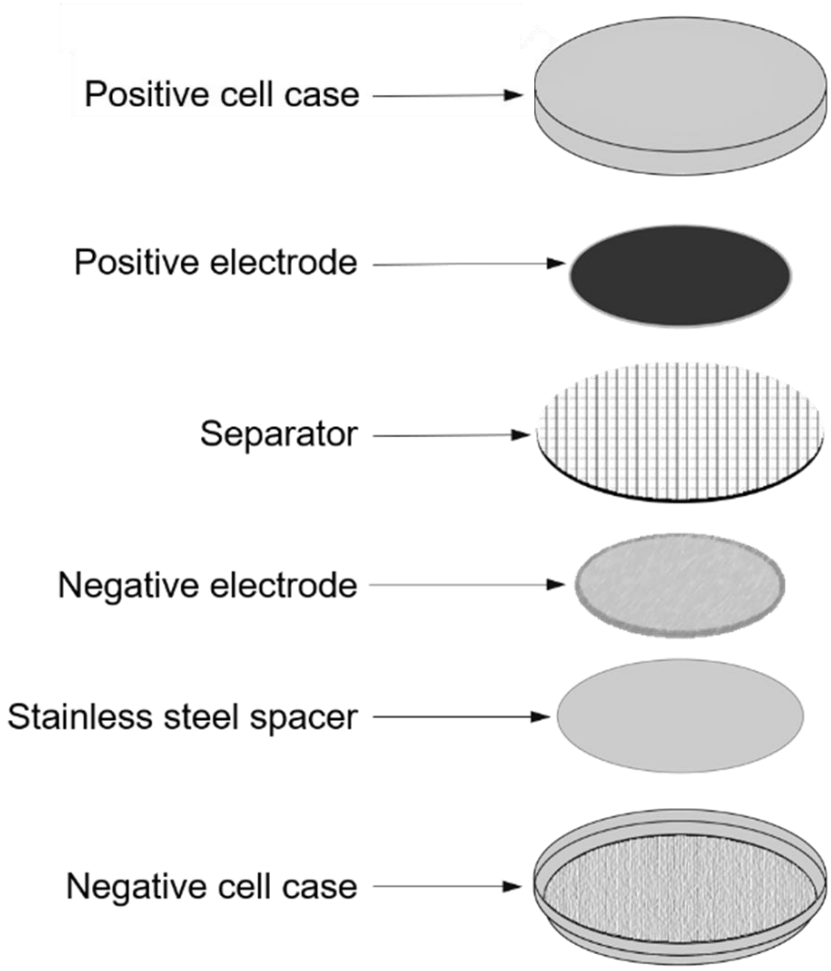

Figure 2-3: Schematic showing an exploded view of a coin cell. Spring not shown.

2.5 Conclusion

This chapter details the steps taken to produce, characterise, and test P3- and P2-NMMO and its derivatives. The synthesis methods involved either a conventional solid state reaction or biotemplating using the polysaccharide dextran as the template. Materials were characterised using XRD and SEM and tested using a standard array of electrochemical techniques: galvanostatic testing and rate capability testing. These methods produce reliable results that will inform on the crystal structure, particle size and morphology, and performance of each material under investigation, respectively.

2.6 References

[1] A. K. Rai, L. T. Anh, J. Gim, V. Mathew, and J. Kim, "Electrochemical properties of Na_xCoO_2 (x~0.71) cathode for rechargeable sodium-ion batteries," *Ceram. Int.*, vol. 40, no. 1 PART B, pp. 2411–2417, 2014, doi: 10.1016/j.ceramint.2013.08.013.

[2] D. Kim, E. Lee, M. Slater, W. Lu, S. Rood, and C. S. Johnson, "Layered $Na[Ni_{1/3}Fe_{1/3}Mn_{1/3}]O_2$ cathodes for Na-ion battery application," *Electrochem. commun.*, vol. 18, no. 1, pp. 66–69, 2012, doi: 10.1016/j.elecom.2012.02.020.

[3] J. J. Ding, Y. N. Zhou, Q. Sun, X. Q. Yu, X. Q. Yang, and Z. W. Fu, "Electrochemical properties of P2-phase $Na_{0.74}CoO_2$ compounds as cathode material for rechargeable sodium-ion batteries," *Electrochim. Acta*, vol. 87, pp. 388–393, 2013, doi: 10.1016/j.electacta.2012.09.058.

[4] B. Dong, R. Jarkaneh, S. Hull, N. Reeves-McLaren, J. J. Biendicho, and A. R. West, "Synthesis, structure and electrical properties of N-doped Li_3VO_4," *J. Mater. Chem. A*, vol. 4, no. 4, pp. 1408–1413, 2015, doi: 10.1039/c5ta07823g.

[5] X. Wang, M. Tamaru, M. Okubo, and A. Yamada, "Electrode properties of P2-$Na_{2/3}Mn_yCo_{1-y}O_2$ as cathode materials for sodium-ion batteries," *J. Phys. Chem. C*, vol. 117, no. 30, pp. 15545–15551, 2013, doi: 10.1021/jp406433z.

[6] J. Billaud, G. Singh, A. R. Armstrong, E. Gonzalo, V. Roddatis, M. Armand, T. Rojo, and P. G. Bruce, "$Na_{0.67}Mn_{1-x}Mg_xO_2$ ($0 \le x \le 0.2$): a high capacity cathode for sodium-ion batteries," *Energy Environ. Sci.*, vol. 7, no. 4, pp. 1387–1391, 2014, doi: 10.1039/C4EE00465E.

[7] A. R. West, *Solid state chemistry and its applications*. Wiley, 2014. doi: 10.1107/s0108768185002476.

[8] X. Wu, J. Guo, D. Wang, G. Zhong, M. J. McDonald, and Y. Yang, "P2-type $Na_{0.66}Ni_{0.33-x}Zn_xMn_{0.67}O_2$ as new high-voltage cathode materials for sodium-ion batteries," *J. Power Sources*, vol. 281, pp. 18–26, 2015, doi: 10.1016/j.jpowsour.2014.12.083.

[9] J. Zhai, H. Ji, W. Ji, R. Wang, Z. Huang, T. Yang, C. Wang, T. Zhang, Z. Chen, W. Zhao, A. Tayal, L. Jin, J. Wang, and Y. Xiao, "Suppressing the irreversible phase transition from P2 to O2 in sodium-layered cathode *via* integrating P2- and O3-type structures," *Mater. Today Energy*, vol. 29, p. 101106, 2022, doi: 10.1016/j.mtener.2022.101106.

[10] C. Chen, W. Hang, Y. Li, M. Zhang, K. Nie, J. Wang, W. Zhao, R. Qi, C. Zuo, Z. Li, H. Yi, and F. Pan, "P2/O3 biphasic Fe/Mn-based layered oxide cathode with ultrahigh capacity and great cyclability for sodium ion batteries," *Nano Energy*, vol. 90, no. PA, p. 106504, 2021, doi: 10.1016/j.nanoen.2021.106504.

[11] M. Matsui, F. Mizukoshi, and N. Imanishi, "Improved cycling performance of P2-type layered sodium cobalt oxide by calcium substitution," *J. Power Sources*, vol. 280, pp. 205–209, 2015, doi: 10.1016/j.jpowsour.2015.01.044.

[12] B. L. Cushing, V. L. Kolesnichenko, and C. J. O'Connor, "Recent Advances in the Liquid-Phase Syntheses of Inorganic Nanoparticles," *Chem. Rev.*, vol. 104, no. 9, pp. 3893–3946, 2004, doi: 10.1021/cr030027b.

[13] D. Walsh, S. C. Wimbush, and S. R. Hall, "Use of the Polysaccharide Dextran as a Morphological Directing Agent in the Synthesis of High-T_c Superconducting $YBa_2Cu_3O_{7-\delta}$ Sponges with Improved Critical Current Densities," *Chem. Mater.*, vol.

19, no. 4, pp. 647–649, 2007, doi: 10.1021/cm0626684.

[14] R. Boston, A. Carrington, D. Walsh, and S. R. Hall, “Synthesis of spherical superconductors,” *CrystEngComm*, vol. 15, no. 19, p. 3763, 2013, doi: 10.1039/c3ce40269j.

[15] Z. Zhang, S. C. Wimbush, A. Kursumovic, H. Suo, and J. L. MacManus-Driscoll, “Detailed study of the process of biomimetic formation of YBCO platelets from nitrate salts in the presence of the biopolymer dextran and a molten NaCl flux,” *Cryst. Growth Des.*, vol. 12, no. 11, pp. 5635–5642, 2012, doi: 10.1021/cg301143r.

[16] S. Zilinskaite, A. J. R. Rennie, R. Boston, and N. Reeves-McLaren, “Biotemplating: a sustainable synthetic methodology for Na-ion battery materials,” *J. Mater. Chem. A*, vol. 6, no. 13, pp. 5346–5355, 2018, doi: 10.1039/C7TA09260A.

[17] S. Zilinskaite, N. Reeves-McLaren, and R. Boston, “Xanthan gum as a water-based binder for P3-$Na_{2/3}Ni_{1/3}Mn_{2/3}O_2$,” *Front. Energy Res.*, vol. 10, no. August, pp. 1–11, Aug. 2022, doi: 10.3389/fenrg.2022.909486.

[18] D. Walsh, L. Arcelli, T. Ikoma, J. Tanaka, and S. Mann, “Dextran templating for the synthesis of metallic and metal oxide sponges,” *Nat. Mater.*, vol. 2, no. 6, pp. 386–390, 2003, doi: 10.1038/nmat903.

[19] S. Guo, Y. Sun, P. Liu, J. Yi, P. He, X. Zhang, Y. Zhu, R. Senga, K. Suenaga, M. Chen, and H. Zhou, “Cation-mixing stabilized layered oxide cathodes for sodium-ion batteries,” *Sci. Bull.*, vol. 63, no. 6, pp. 376–384, 2018, doi: 10.1016/j.scib.2018.02.012.

[20] S. Guo, H. Yu, P. Liu, Y. Ren, T. Zhang, M. Chen, M. Ishida, and H. Zhou, “High-performance symmetric sodium-ion batteries using a new, bipolar O3-type material, $Na_{0.8}Ni_{0.4}Ti_{0.6}O_2$,” *Energy Environ. Sci.*, vol. 8, no. 4, pp. 1237–1244, 2015, doi: 10.1039/c4ee03361b.

[21] R. Berthelot, D. Carlier, and C. Delmas, “Electrochemical investigation of the P2–Na_xCoO_2 phase diagram,” *Nat. Mater.*, vol. 10, no. 1, pp. 74–80, 2011, doi: 10.1038/nmat2920.

[22] D. Baster, K. Dybko, M. Szot, K. Świerczek, and J. Molenda, “Sodium intercalation in Na_xCoO_{2-Y} - Correlation between crystal structure, oxygen nonstoichiometry and electrochemical properties,” *Solid State Ionics*, vol. 262, pp. 206–210, 2014, doi: 10.1016/j.ssi.2013.11.040.

[23] Z. Dauter and M. Jaskolski, “How to read (and understand) Volume A of International Tables for Crystallography: An introduction for nonspecialists,” *J. Appl. Crystallogr.*, vol. 43, no. 5 PART 2, pp. 1150–1171, 2010, doi: 10.1107/S0021889810026956.

[24] S. Gates-Rector and T. Blanton, “The Powder Diffraction File: a quality materials characterization database,” *Powder Diffr.*, vol. 34, no. 4, pp. 352–360, 2019, doi: 10.1017/S0885715619000812.

[25] T. Degen, M. Sadki, E. Bron, U. König, and G. Nénert, "The HighScore suite," *Powder Diffr.*, vol. 29, no. August, pp. S13–S18, 2014, doi: 10.1017/S0885715614000840.

[26] B. H. Toby, " R factors in Rietveld analysis: How good is good enough? ," *Powder Diffr.*, vol. 21, no. 1, pp. 67–70, 2006, doi: 10.1154/1.2179804.

[27] A. Clearfield, J. H. Reibenspies, and N. Bhuvanesh, *Principles and Applications of Powder Diffraction*. Wiley-Blackwell, 2008. doi: 10.1002/9781444305487.

[28] Z. Lu, R. A. Donaberger, and J. R. Dahn, "Superlattice ordering of Mn, Ni, and Co in layered alkali transition metal oxides with P2, P3, and O3 structures," *Chem. Mater.*, vol. 12, no. 12, pp. 3583–3590, 2000, doi: 10.1021/cm000359m.

[29] J. I. Langford and A. J. C. Wilson, "Scherrer after sixty years: A survey and some new results in the determination of crystallite size," *J. Appl. Crystallogr.*, vol. 11, no. 2, pp. 102–113, Apr. 1978, doi: 10.1107/S0021889878012844.

[30] J. Schindelin, C. T. Rueden, M. C. Hiner, and K. W. Eliceiri, "The ImageJ ecosystem: An open platform for biomedical image analysis," *Mol. Reprod. Dev.*, vol. 82, no. 7–8, pp. 518–529, 2015, doi: 10.1002/mrd.22489.

[31] L. X. Yuan, Z. H. Wang, W. X. Zhang, X. L. Hu, J. T. Chen, Y. H. Huang, and J. B. Goodenough, "Development and challenges of $LiFePO_4$ cathode material for lithium-ion batteries," *Energy Environ. Sci.*, vol. 4, no. 2, pp. 269–284, 2011, doi: 10.1039/c0ee00029a.

[32] C. Liu, Z. G. Neale, and G. Cao, "Understanding electrochemical potentials of cathode materials in rechargeable batteries," *Mater. Today*, vol. 19, no. 2, pp. 109–123, 2016, doi: 10.1016/j.mattod.2015.10.009.

[33] E. Talaie, P. Bonnick, X. Sun, Q. Pang, X. Liang, and L. F. Nazar, "Methods and protocols for electrochemical energy storage materials research," *Chem. Mater.*, vol. 29, no. 1, pp. 90–105, 2017, doi: 10.1021/acs.chemmater.6b02726.

[34] J.-K. Park, *Principles and Applications of Lithium Secondary Batteries*. Wiley, 2012. [Online]. Available: https://ebookcentral.proquest.com/lib/sheffield/detail.action?docID=943094.

[35] J. B. Goodenough and K. S. Park, "The Li-ion rechargeable battery: A perspective," *J. Am. Chem. Soc.*, vol. 135, no. 4, pp. 1167–1176, 2013, doi: 10.1021/ja3091438.

[36] S. Chu, C. Zhang, H. Xu, S. Guo, P. Wang, and H. Zhou, "Pinning Effect Enhanced Structural Stability toward a Zero-Strain Layered Cathode for Sodium-Ion Batteries," *Angew. Chemie*, vol. 133, no. 24, pp. 13478–13483, 2021, doi: 10.1002/ange.202100917.

[37] R. J. Clément, J. Billaud, A. Robert Armstrong, G. Singh, T. Rojo, P. G. Bruce, and C. P. Grey, "Structurally stable Mg-doped P2-$Na_{2/3}Mn_{1-y}Mg_yO_2$ sodium-ion battery cathodes with high rate performance: insights from electrochemical, NMR and diffraction studies," *Energy Environ. Sci.*, vol. 9, no. 10, pp. 3240–3251, 2016, doi: 10.1039/C6EE01750A.

[38] H. Yoshida, N. Yabuuchi, K. Kubota, I. Ikeuchi, A. Garsuch, M. Schulz-Dobrick, and S. Komaba, "P2-type $Na_{2/3}Ni_{1/3}Mn_{2/3-x}Ti_xO_2$ as a new positive electrode for higher energy Na-ion batteries," *Chem. Commun.*, vol. 50, no. 28, pp. 3677–3680, 2014, doi: 10.1039/C3CC49856E.

[39] C. Bischoff, O. Fitz, C. Schiller, H. Gentischer, D. Biro, and H.-M. Henning, "Investigating the Impact of Particle Size on the Performance and Internal Resistance of Aqueous Zinc Ion Batteries with a Manganese Sesquioxide Cathode," *Batteries*, vol. 4, no. 3, p. 44, 2018, doi: 10.3390/batteries4030044.

[40] D. Buchholz, C. Vaalma, L. G. Chagas, and S. Passerini, "Mg-doping for improved long-term cyclability of layered Na-ion cathode materials - The example of P2-type $Na_xMg_{0.11}Mn_{0.89}O_2$," *J. Power Sources*, vol. 282, pp. 581–585, 2015, doi: 10.1016/j.jpowsour.2015.02.069.

[41] T. Risthaus, L. Chen, J. Wang, J. Li, D. Zhou, L. Zhang, D. Ning, X. Cao, X. Zhang, G. Schumacher, M. Winter, E. Paillard, and J. Li, "P3 $Na_{0.9}Ni_{0.5}Mn_{0.5}O_2$ Cathode Material for Sodium Ion Batteries," *Chem. Mater.*, vol. 31, no. 15, pp. 5376–5383, 2019, doi: 10.1021/acs.chemmater.8b03270.

[42] J. J. Ding, Y. N. Zhou, Q. Sun, and Z. W. Fu, "Cycle performance improvement of $NaCrO_2$ cathode by carbon coating for sodium ion batteries," *Electrochem. commun.*, vol. 22, no. 1, pp. 85–88, 2012, doi: 10.1016/j.elecom.2012.06.001.

[43] X. Song, X. Zhou, Y. Deng, J. Nan, D. Shu, Z. Cai, Y. Huang, and X. Zhang, "Synthesis of $Na_xMn_{0.54}Ni_{0.13}Fe_{0.13}O_2$ with P2-type hexagonal phase as high-performance cathode materials for sodium-ion batteries," *J. Alloys Compd.*, vol. 732, pp. 88–94, 2018, doi: 10.1016/j.jallcom.2017.10.131.

[44] Y. Wang, J. Tang, X. Yang, and W. Huang, "A study on electrochemical properties of P2-type Na-Mn-Co-Cr-O cathodes for sodium-ion batteries," *Inorg. Chem. Front.*, vol. 5, no. 3, pp. 577–584, 2018, doi: 10.1039/c7qi00778g.

[45] T. Marks, S. Trussler, A. J. Smith, D. Xiong, and J. R. Dahn, "A Guide to Li-Ion Coin-Cell Electrode Making for Academic Researchers," *J. Electrochem. Soc.*, vol. 158, no. 1, p. A51, 2011, doi: 10.1149/1.3515072.

3 Solid state and biotemplating synthesis of P3- and P2-$Na_{0.67}Mn_{0.9}Mg_{0.1}O_2$

3.1 Introduction

The work in this chapter, currently undergoing publication, is a comparison of the P3 and P2 phases of the cathode material, $Na_{0.67}Mn_{0.9}Mg_{0.1}O_2$ (NMMO), generated *via* two different synthesis routes. The two synthesis methods used are a conventional solid state method and a biotemplating synthesis using dextran, resulting in a four-way study. 10% Mg doping is used here, as this is a well-studied cathode material (Table 3-1) for both the P2 and P3 phases. Although it has been shown to have a lower capacity than the 5% Mg doped material [1], its capacity retention is higher than both the 5% and 0% Mg doped materials.

P2-NMMO is a low-cost [2] battery material with a high specific discharge capacity based on the Mn^{3+}/Mn^{4+} redox couple and consists of metals that are comparatively more sustainable and safer than more conventional cathode metals such as lithium, nickel, and cobalt. Due to the Jahn-Teller activity of Mn^{3+}, this is ordinarily associated with structural distortions [3] or changes [4], and manganese dissolution [5]–[8], leading to capacity fading. Doping with Mg^{2+} alleviates this and has resulted in increased capacity retention, meaning that despite a decrease in initial capacity, the capacity after 25 cycles is higher in the doped material.

A summary of the pre-existing work on P-type $Na_{0.67}Mn_{1-x}Mg_xO_2$ ($0 \leq x \leq 0.33$) cathodes is given in Table 3-1. They show an initial capacity commonly of 150 mAh g^{-1}, and higher where the upper voltage cut-off is higher than 4.0 V vs Na/Na^+. With a voltage 1.5 – 4.0 V vs Na/Na^+, for example, the predominant source of capacity in both P3 and P2 phases is the Mn^{3+}/Mn^{4+} redox couple. In P3-type cathodes, the reversible P3↔O3 phase transition occurs within this range, concurrent with Mn^{3+}/Mn^{4+} redox. Charging to > 4.0 V generally results in greater capacity, but also worse capacity retention. At these potentials, processes such as the P2↔O2 phase transition occur, as well as oxygen redox activity. The O redox activity in particular is when leads to the rapid capacity fade [9], reportedly owing to its poor kinetics [10].

There are exceptions to this: the P2-NMMO reported by Sambandam *et al*. [11] shows a capacity retention of 80% after 270 cycles despite charging to 4.5 V. Here the initial capacity is lower than the other materials listed, and *operando* XRD of the P2 material reveals no phase transitions. There is some evidence of anionic redox above 4.0 V, but it ceases after the 2nd cycle. From examination of the voltage profile, little to no capacity is extracted from the material above 4.0 V after the 2nd cycle. This is possibly due to large internal resistance, as during discharge the voltage falls immediately from 4.5 V to 3.5 V before capacity is extracted. The irreversible phase transitions and O redox activity may be pushed to a higher potential and not occur within the voltage window used, resulting in a lower but steady capacity.

Table 3-1: Synthesis method, cycling parameters, and electrochemical performance of P-type NMMO cathodes.

Cathode material	Synthesis method	C-rate	Voltage range (vs Na/Na^+)	Initial capacity /mAh g^{-1}	Capacity retention
P2-$Na_{0.67}MnO_2$ [3]	Sol-gel	~C/10	2.0 – 3.8 V	150	40% after 10 cycles
P2-$Na_{0.7}MnO_2$ [12]	Hydrothermal	~C/5	2.0 – 4.5 V	165	67% after 50 cycles
P2-$Na_{0.67}MnO_2$ [1]	Co-precipitation	C/15	1.5 – 4.0 V	175	75% after 25 cycles
P2-$Na_{0.67}Mn_{0.95}Mg_{0.05}O_2$ [1]	Co-precipitation	C/15	1.5 – 4.2 V	180	70% after 25 cycles
P2-$Na_{0.67}Mn_{0.9}Mg_{0.1}O_2$ [1]	Co-precipitation	C/15	1.5 – 4.2 V	170	85% after 25 cycles
P2-$Na_{0.67}Mn_{0.72}Mg_{0.28}O_2$ [9]	Solid state	C/20	1.5 – 4.4 V	220	70% after 30 cycles
P2-$Na_{0.67}Mn_{0.89}Mg_{0.11}O_2$ [5]	Co-precipitation	C/15	1.5 – 4.4 V	150	65% after 200 cycles
P2-$Na_{0.67}Mn_{0.8}Mg_{0.2}O_2$ [13]	Co-precipitation	1C	2.0 – 4.2 V	60	>100% after 500 cycles
P2-$Na_{0.67}Mn_{0.9}Mg_{0.1}O_2$ [11]	Combustion	C/10	2.0 – 4.5 V	125	80% after 260 cycles
P3-$Na_{0.67}Mn_{0.67}Mg_{0.33}O_2$ [14]	Solid state	C/10	1.6 – 4.4 V	200	70% after 30 cycles
P3-$Na_{0.67}Mn_{0.8}Mg_{0.2}O_2$ [15]	Co-precipitation	C/20	1.8 – 3.8 V	155	97% after 25 cycles
P3-$Na_{0.67}Mn_{0.8}Mg_{0.2}O_2$ [15]	Co-precipitation	C/20	1.8 – 4.3 V	185	81% after 25 cycles
P3-$Na_{0.67}Mn_{0.9}Mg_{0.1}O_2$ [11]	Combustion	C/10	2.0 – 4.5 V	150	40% after 240 cycles
P3-$Na_{0.67}Mn_{0.9}Mg_{0.1}O_2$ [16]	Co-precipitation	C/20	1.8 – 4.3 V	165	75% after 40 cycles

Similarly, P2-NMMO [5] exhibits high capacity retention despite a high upper voltage limit of 4.4 V. Again, evidence of O redox and a P2↔O2 phase transition are (mostly) absent. Instead, the capacity loss is argued to come from loss of active material: Mn^{2+} dissolution, generated by Mn^{3+} disproportionation upon cycling [5]. In this case, a high internal resistance could be caused by the hydrated phase in the layered material. The high capacity retention could be due to prevention of irreversible process that occur when the magnesium content is higher. The avoidance of the P2↔O2 transition is likely a product of high internal resistance: the potential at which the transition occurs is pushed above the upper voltage limit.

There is a correlation between the lower capacity materials and higher capacity retention (e.g. Li *et al*. [13]) and *vice versa* (e.g. Yabuuchi *et al*. [9] and Song *et al*. [14]). The higher capacity comes from processes that occur at high voltages but are irreversible (O redox leading to loss of O_2 from the structure). The activation of O redox occurs at higher magnesium contents (28% and 33%, respectively) [5]. P3 materials with higher Mg^{2+} content ($x \approx 0.33$) also exhibit higher capacity due to the activation of O redox in the material [14] with a similarly deleterious effect on capacity retention compared to samples that do not undergo O redox. Lower magnesium content (≤ 20%) leads to improvements in capacity retention over the undoped samples *via* an increase in average oxidation state of the manganese, thus reducing the amount of Mn^{3+} in the sample. Since Mn^{3+} is Jahn-Teller active, it causes distortions of the crystal structure when it is oxidised and causes capacity fading in the cathode material [1], [17]. However, oxidation of Mn^{3+} to Mn^{4+} is necessary for Na^+ extraction, and so reducing the amount of Mn^{3+} also leads to a loss of initial capacity.

Na^+ is extracted from both P-type materials at ~2.2 V, which can be seen as a peak in a cyclic voltammetry (CV) or differential capacity graph. A second CV peak is seen in the P2 material at ~3.0 V, also corresponding to Na^+ extraction. The existence of two peaks occurs because there are two sites that Na^+ can occupy in the P2 structure. One site is face-sharing with the TMO_2 octahedra either side of it, and Na^+ is extracted from it at ~2.2 V. The second is edge-sharing with the TMO_2 and the Na^+ is extracted from there at the higher potential. The Na^+ in the face-sharing site is at a higher energy because of the repulsion from the TMO_2 cations compared to the edge-sharing site [5].

The P3 phase is less commonly reported for sodium cathodes, nor is it often compared to the P2 phase [18]. Reported P3 cathodes (other than NMMO) are shown to have lower capacities than those listed in Table 3-1. Initial capacities range from 100-150 mAh g^{-1} [19]–[24], with those with higher capacities suffering from more rapid capacity fade. One study [11] into the electrochemical performance of P3-NMMO reports initial capacities of 150 mAh g^{-1} at 0.1 C, compared to 125 mAh g^{-1} for the P2 material. The capacity of the P3 phase fades rapidly, compared to the P2 phase: after 25 cycles it falls below the P2 phase and reaches 60 mAh g^{-1} after 241 cycles (40% retention).

The P2 phase still maintains 100 mAh g^{-1} (80%) after 262 cycles [11]. This effect is more pronounced at 0.5 C. The P2 phase also exhibits lower polarisation – which the authors a

to its greater stability and relatively higher structural order, respectively. Upon examination using *operando* XRD between 2.0 V – 4.5 V, no evidence of a phase transition is observed in the P2 material as no new planes appear during cycling, nor is there a shift in (00*l*) peak. Therefore, the cathode structure changes very little during cycling in this study. As explained, phase transitions are harmful to cycle life as they have an associated energy cost and (particularly P2↔O2) lead to material degradation. This is because there are multiple ways for the O2↔P2 transition to occur (Figure 3-1), which leads to stacking faults in the structure (identified *via operando* XRD) [25]. The presence of these faults leads to micro-cracks in the material which increases capacity fade since the surface area of the material increases. As the surface area increases, as does the chance for redox active material so dissolve into the electrolyte, and for solid-electrolyte interphase (SEI) formation.

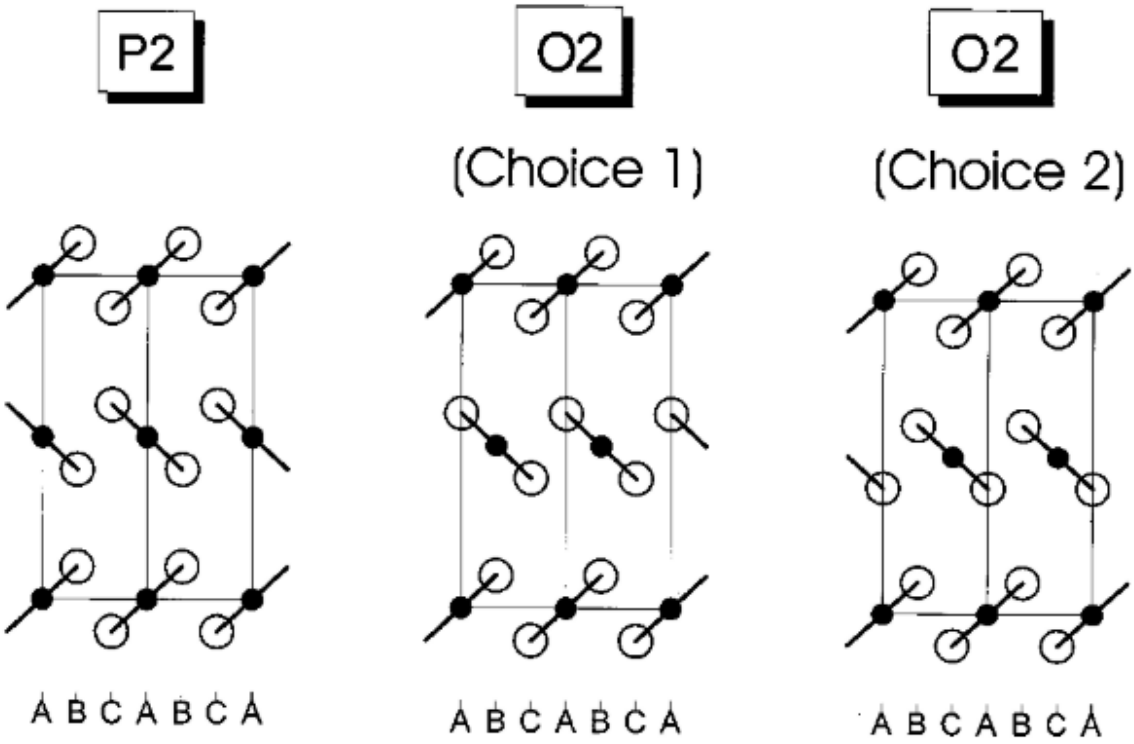

Figure 3-1: Projection of the P2 phase and the two O2 phases that can be formed by gliding of the middle layer. ● = transition metal ions, ○ = oxide ions. [25]

The authors [11] also suggested that the higher initial capacity of the P3-NMMO phase is due to the anion redox reaction at 4.2 V. This anion redox activity is short-lived, as the plateau corresponding to it in the discharge voltage curve is greatly diminished in the 2nd cycle, and not present in the 100th cycle. Other P3 and O3 materials exhibit a P3↔O3 transition at approximately 2 V. Indeed, in the above study we see the beginning of it, but since the voltage range used was 2.0 – 4.5 V, the transition is not completed.

The other studies of P3-$Na_{0.67}Mn_xMg_{1-x}O_2$ (x = 0.1, 0.2) mostly have lower capacity retention (in terms of proportion of capacity lost per cycle) than the P3-NMMO reported by Sambandam *et al*. [11]. The highest capacity retention is P3-$Na_{0.67}Mn_{0.8}Mg_{0.2}O_2$ [15],

which is limited to an upper voltage limit of 3.8 V – highlighting the selection of appropriate voltage limits as an important factor in maximising cathode performance. Part of the reason for the high capacity retention is the additional Mg^{2+} in the sample, which would normally lead to a reduction in capacity [1], [17]. However, it delivers the same initial discharge capacity as P3-NMMO reported by Sambandam *et al*. [11], possibly because of a relative lowering of the lower voltage limit from 2.0 V to 1.8 V.

Little work has been conducted exploring the effect that synthesis method has on cathodes, and specifically P-type $Na_{0.67}Mn_{1-x}Mg_xO_2$ ($0 \leq x \leq 0.33$). Several methods have been used to generate it with no comment as to the effect on its capacity or longevity. A study into this was conducted P3- and P2-$Na_{0.66}Ni_{0.33}Mn_{0.67}O_2$ [26]. P3-$Na_{0.66}Ni_{0.33}Mn_{0.67}O_2$ (containing 1.1% P2-$Na_{0.66}Ni_{0.33}Mn_{0.67}O_2$) was synthesised *via* a biotemplating method using dextran as a template, but the same calcination procedure using a solid state method resulted in P2-$Na_{0.66}Ni_{0.33}Mn_{0.67}O_2$. The study found that the biotemplating synthesised P3 phase exhibited an improved initial discharge capacity of 140 mAh g^{-1} compared to P2-$Na_{0.66}Ni_{0.33}Mn_{0.67}O_2$ synthesised *via* solid state methods (81 mAh g^{-1}). The capacity of biotemplated P3-$Na_{0.66}Ni_{0.33}Mn_{0.67}O_2$ falls rapidly over two cycles to 86 mAh g^{-1}, and then remains steady over ten cycles. The capacity of P3-$Na_{0.66}Ni_{0.33}Mn_{0.67}O_2$ was further improved by reducing the calcination temperature and time. After 10 cycles, P3-$Na_{0.66}Ni_{0.33}Mn_{0.67}O_2$ calcined at 650 °C for 2 h delivered 99 mAh g^{-1}, and calcining at 550 °C for 12 h delivered 100 mAh g^{-1}. However, the values given do not give an estimate of the spread so it's not possible to say whether the capacity of the materials changes with particle size.

The differences in capacity between these materials are likely a result of the particle sizes of each sample. SEM of the samples shows an increase in particle with calcination time and temperature (Table 3-2). The data suggest that there exists a relationship between discharge capacity and particle size; with smaller particle sizes having higher capacities. This cannot be confirmed however without knowing the spread of capacity values. This work shows the importance of optimising synthesis, as it can be used to increase the capacity extracted from cathode materials.

Table 3-2: Synthesis conditions, particle size, and discharge capacity after 10 cycles for P-type $Na_{0.66}Ni_{0.33}Mn_{0.67}O_2$ [26].

Synthesis	Temperature/°C	Time/h	Particle size/nm	Capacity after 10 cycles/mAh g^{-1}
Biotemplating	550	12	124 ± 21	103
Biotemplating	650	2	115 ± 25	99
Biotemplating	650	5	119 ± 32	92
Biotemplating	650	12	167 ± 41	87
Biotemplating	750	12	309 ± 98	87
Biotemplating	850	12	553 ± 253	86
Solid state	850	12	1740 ± 742	81

As will be shown in this chapter, conventional solid state synthesis struggles with generating low temperature phases, and requires long calcinations to complete reactions due to the large particle sizes of the reactants [27]. However, biotemplating synthesis mixes cathode metal cations at an atomic level *via* an aqueous dissolution step, allowing lower temperature phases to be accessed and shorter calcination times to be used [28]–[31]. In this chapter, the same calcination regimes were used for each sample to keep calcination conditions consistent across synthesis technique.

3.2 Aims

This study is used as the basis for this chapter, aims of which are to determine the differences in performance that arise through selection of synthesis method. The two P3- and P2-NMMO cathode materials are generated using a solid state synthesis and a biotemplating synthesis using dextran as the template. The performance (capacity and cycle life) of the synthesis methods and the two phases are compared to determine primarily effect of synthesis method on the behaviour and performance of the materials, and the differences in performance between the two phases directly. Similarly, very little work has focussed on the explicit differences in performance of P2 and P3 cathodes, particularly of the same material. This can be seen in this work and the previous example of P3-NMMO [11], in which solid state synthesis and a combustion synthesis struggle to produce phase-pure materials.

The synthesis of the P3- and P2-NMMO *via* solid state and biotemplating is outlined in greater detail in Chapter 2, Section 2.1.2. The heating protocols were kept the same during the synthesis of each polymorph to be able to compare the method only – not allowing changes in particle size from shorter or lower temperature calcinations. The 10% excess Na source and calcination time were the same across all samples. Although biotemplating can reduce reaction times by at least 75% (8 h to 2 h), thus reducing the energy costs as well as granting more control over the particle size [32], it was necessary to compare the subtle differences in the two techniques that would have been overshadowed by factors like reduced particle size. P3-NMMO in each case was calcined for 20h at 580 °C, P2-NMMO was calcined for 20h at 900 °C. These temperatures were determined *via* combination of HTXRD and *ex situ* calcinations. P3- and P2-NMMO materials were also synthesised *via* biotemplating with calcination temperatures and times closer to previous studies [26], [33]–[36] as part of a later results chapter. Data from these materials will be compared against the results here too.

In this chapter, the sample powders are synthesised and examined by XRD three times, examined by SEM once, and one sample powder is used to make the cathode material. From the cathode material, three cells are made to test the discharge capacity over 50 cycles, and one is used to test the rate capability.

3.3 Results and discussion

3.3.1 XRD

3.3.1.1 HTXRD

To determine the calcination temperatures that would generate the P3 and P2 phases at the same temperature in both biotemplating and solid state syntheses, HTXRD was conducted for both methods. Examining the HTXRD solid state synthesised P2-NMMO (Figure 3-2), starting materials (most visibly MnO_2 by peak height) are present in the material up to 600 °C. The peaks associated with them progressively diminish up to this point. P3-NMMO is visible from 500 °C and persists until approximately 800 °C. P2-NMMO begins to appear at 700 °C and is present at least until up to 1000 °C, where the experiment stopped. The identity of these two phases was confirmed *via* phase matching [37].

Between 500 °C and 850 °C, a phase emerges and disappears that can be indexed to $Na_{0.44}MnO_2$ (space group: *Pbam*). This material is a known cathode material and can be synthesised *via* solid state methods at 750 °C [38]. The material has a tunnel-like structure through which Na^+ can migrate, leading to its electrochemical activity. Because of this impurity phase, it is not possible to synthesis phase pure P3-NMMO *via* solid state synthesis.

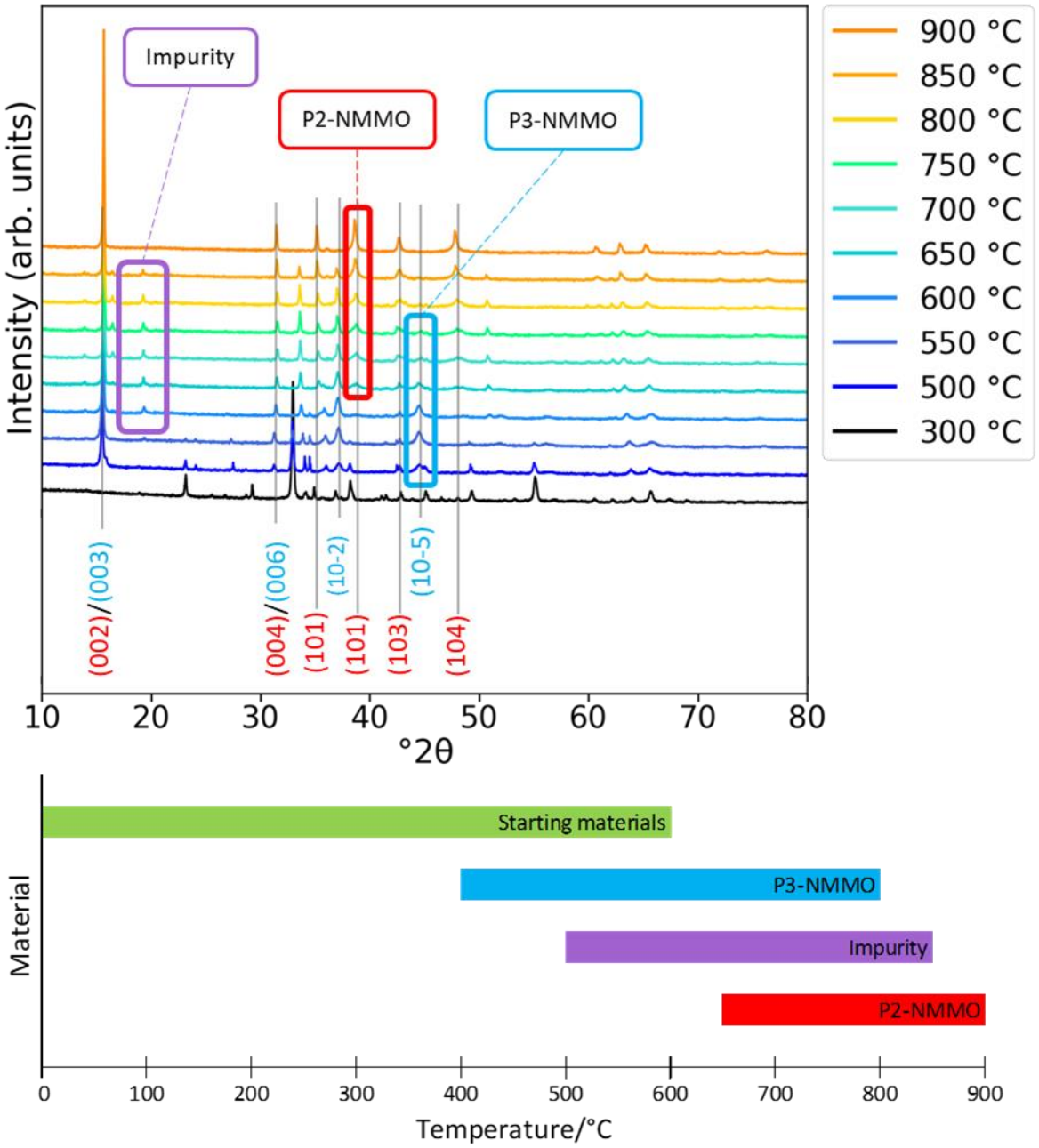

Figure 3-2: The XRD patterns at each temperature with selected peaks of the phases present highlighted, and a schematic of phases present during formation of P2-NMMO via *solid state synthesis. Major peaks associated with the P2 and P3 phases are labelled in red and blue, respectively.*

Synthesis of P2-NMMO *via* biotemplating follows a similar pattern in HTXRD: P3-NMMO forms first, at lower temperatures, followed by formation of P2-NMMO and the subsequent disappearance of the P3-NMMO phase. The phase progression is displayed in Figure 3-3. However, there is no evidence of an impurity phase during this transition, although there is a phase visible at 300 °C. This phase, designated as Proto P3-NMMO shares some but not all peaks with the P3 phase, and so may be the P3-NMMO phase before it is fully formed. In this synthesis, P3-NMMO is again visible as low as 500 °C and is present until 800 °C. P2-NMMO appears at 750 °C and persists until the end of the

heating protocol. The P2-NMMO is visible later in the HTXRD of the biotemplated NMMO than in the solid state NMMO. This may be a result of the smaller intensities of the biotemplated sample. This can be seen in the peak to noise ratio of the XRD patterns, which are lower than in the solid state sample, which is likely to be caused by using incorrect discriminator settings. It is likely that the presence of the impurity phase $Na_{0.44}MnO_2$ affects the formation of the layered structures. In this case, the lack of $Na_{0.44}MnO_2$ could cause the P3-NMMO to be present in the biotemplated sample in greater proportions in the solid state one, delaying the onset of P2-NMMO formation.

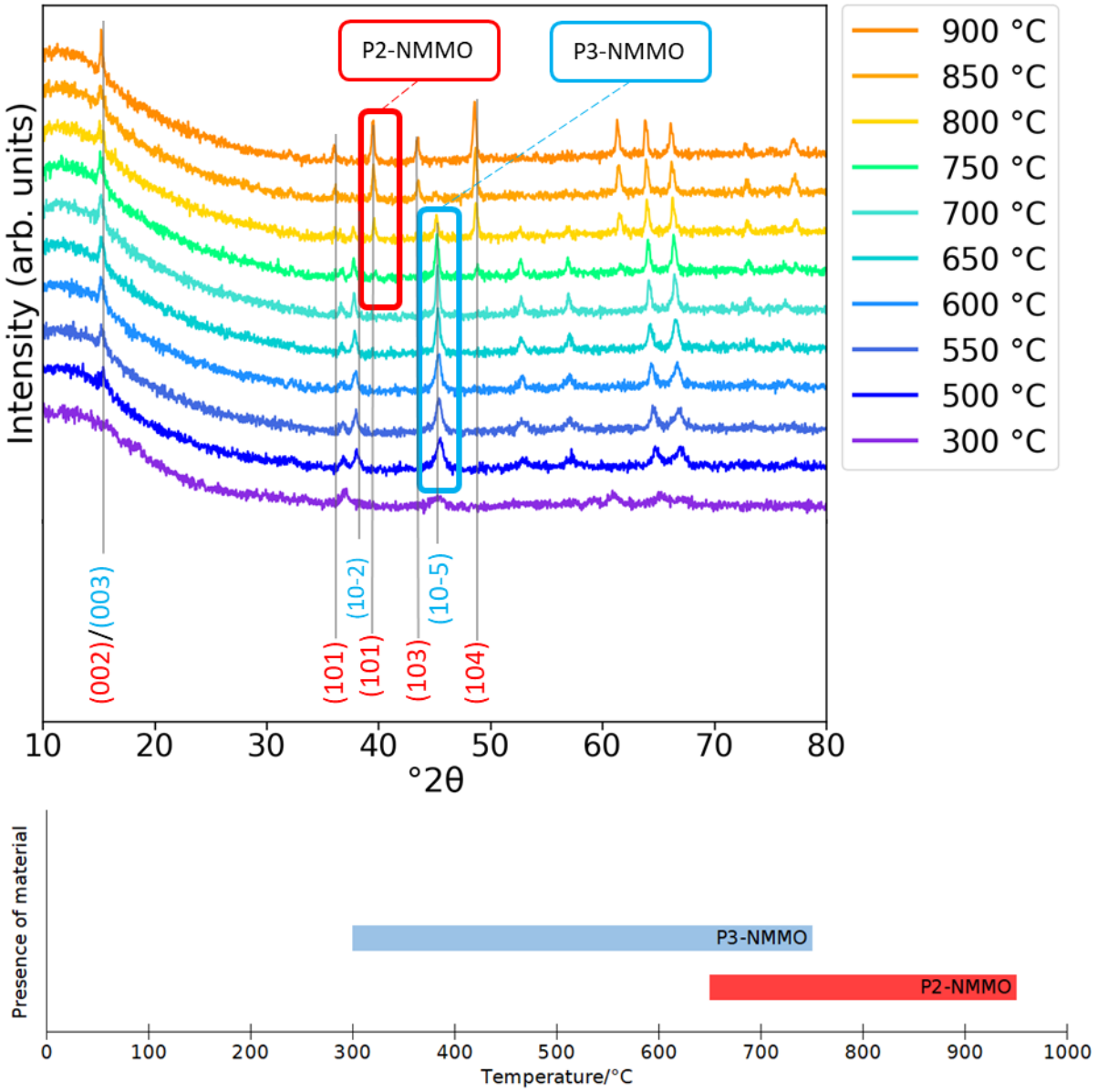

Figure 3-3: The XRD patterns at each temperature with selected peaks of the phases present highlighted, and a schematic of phases present during formation of P2-NMMO via *biotemplating. Major peaks associated with the P2 and P3 phases are labelled in red and blue, respectively.*

HTXRD results show that synthesis of phase-pure P3-NMMO *via* solid state synthesis is not possible, and so calcination conditions were chosen to minimise the unwanted

phases: starting material and $Na_{0.44}MnO_2$. A calcination regime of 580 °C for 20 h was found to achieve this and could also be used to produce phase-pure P3-NMMO *via* biotemplating. For this chapter, P3-NMMO was calcined at 580 °C for 20 h, and P2-NMMO was calcined at 900 °C for 20 h for both syntheses.

3.3.1.2 Room temperature XRD

Using the calcination parameters as determined by HTXRD, P3- and P2-NMMO samples were generated *via* both solid state and biotemplating synthesis. Using XRD, these samples were examined, and their lattice parameters determined. Phase-pure solid state P2-NMMO and biotemplated P2- and P3-NMMO samples could be successfully synthesised. Solid state P3-NMMO contained several impurity phases. The XRD patterns and Rietveld refinements of each sample are displayed in Figure 3-4. Further Rietveld detail can be found in the Appendix.

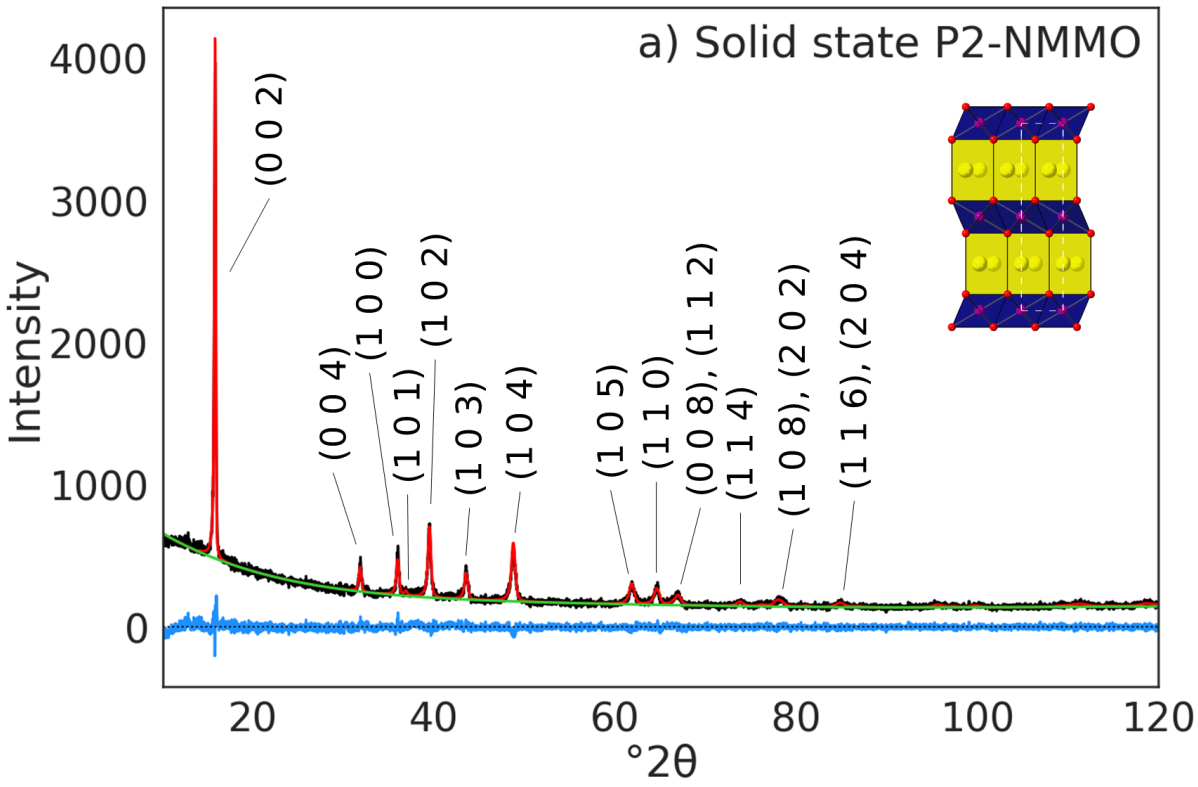
a) Solid state P2-NMMO
Intensity
°2θ
(0 0 2)
(0 0 4)
(1 0 0)
(1 0 1)
(1 0 2)
(1 0 3)
(1 0 4)
(1 0 5)
(1 1 0)
(0 0 8), (1 1 2)
(1 1 4)
(1 0 8), (2 0 2)
(1 1 6), (2 0 4)

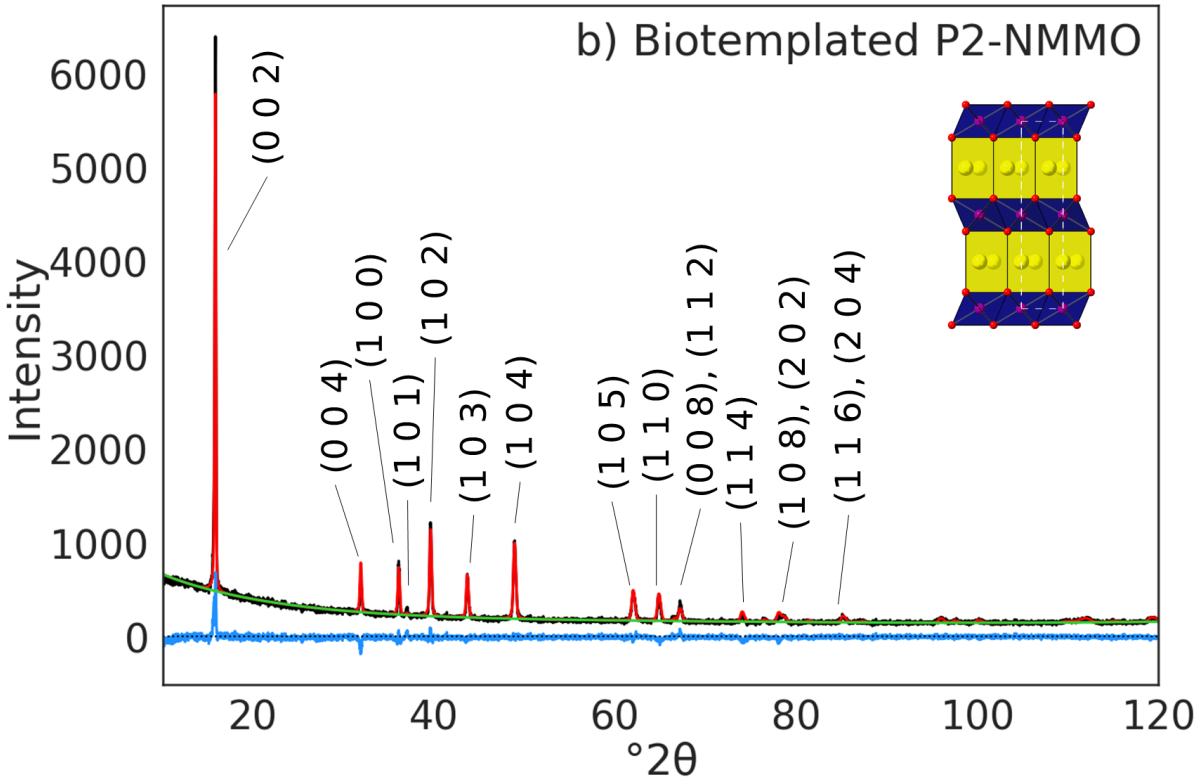
b) Biotemplated P2-NMMO
Intensity
°2θ
(0 0 2)
(0 0 4)
(1 0 0)
(1 0 1)
(1 0 2)
(1 0 3)
(1 0 4)
(1 0 5)
(1 1 0)
(0 0 8), (1 1 2)
(1 1 4)
(1 0 8), (2 0 2)
(1 1 6), (2 0 4)

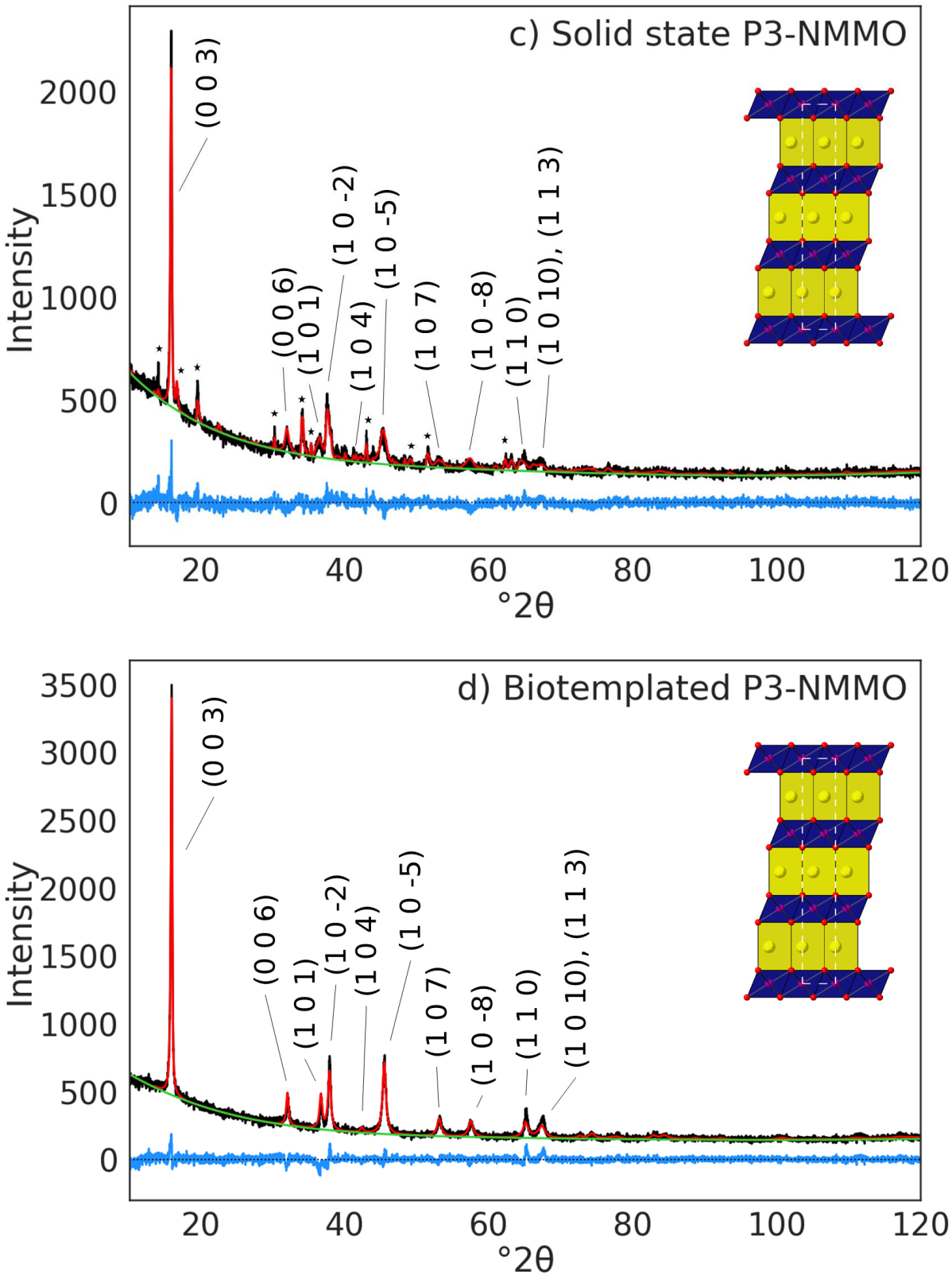

Figure 3-4: XRD pattern (black), Rietveld refinement (red), background (green), and difference pattern (blue) of P2-NMMO synthesised via *(a) solid state methods, and (b) biotemplating, and P3-NMMO synthesised* via *(c) solid state methods, and (d) biotemplating. * = $Na_{0.44}MnO_2$. Inset with a schematic of the (a, b) P2 and (c, d) P3 crystal structure.*

Both P2-NMMO structures refine well to the ideal *P6$_3$/mmc* space group, with lattice parameters (Table 3-3) in line with previous studies [1], [5], [17], [39]. The lattice parameters of biotemplated P2-NMMO are smaller: Δa = 0.010 Å, Δc = 0.025 Å. The lattice parameters of the layered structures vary with Na content, and this difference could be the result of 5% more Na in the biotemplated sample than the solid state P2-NMMO [40].

Similar for both P3-NMMO structures (Figure 3-4c and d), which instead refine well to the *R3m* space group [21], [22], [24], [41], [42]. Table 3-3 shows the results of the Rietveld refinement for each sample. the occupancies of the P3-NMMO synthesised *via* solid state are not likely to vary too much from the single phase samples.

The elemental composition of the impurity phase was not determined, but if it can be assumed to be $Na_{0.44}MnO_2$, then the Rietveld refinement results suggest that the P3-NMMO contains less than 0.67 mol Na per mole of P3-NMMO. Presence of MgO may mean that the material contains less Mg^{2+} than expected, but this is difficult to confirm without knowing the elemental composition of the tunnel-like phase as it is likely that it can be doped with Mg along with the P3-NMMO. Even if this is the case, (further) Na deficiency should not affect the electrochemical behaviour or performance of the layered material, as Na metal is used as the counter electrode and so beyond the first charge cycle Na deficiency does not matter. The change in Mg content may affect the performance of P3-NMMO. The presence of MgO suggests that the P3 phase will have less Mg than expected, and this will be manifest in the electrochemical data as higher capacity, faster capacity fading, and more features in the voltage profile and differential capacity plot.

Table 3-3: Rietveld refinement results from the XRD patterns of each sample.

Sample	Space group	*a* (Å)	*c* (Å)	R_{wp} (%)	GOF
Solid state P2	*P6$_3$/mmc*	2.8885(5)	11.270(1)	6.92	1.05
Biotemplated P2	*P6$_3$/mmc*	2.8785(1)	11.245(2)	7.77	1.21
Solid state P3	*R3m*	2.8736(3)	16.835(1)	7.08	1.06
Biotemplated P3	*R3m*	2.8683(3)	16.824(5)	6.98	1.08

The solid state synthesised P3-NMMO impurity phases include unreacted starting material (MgO and Na_2CO_3) and $Na_{0.44}MnO_2$ [38], [43], identified *via* phase matching. As seen in HTXRD (Figure 3-2), the co-existence of only $Na_{0.44}MnO_2$ and P3-NMMO is possible. Therefore, the presence of starting material in the XRD pattern indicates that the reaction is incomplete. Phase ratios from the Rietveld refinements show that the phase fractions of P3-NMMO, $Na_{0.44}MnO_2$, Na_2CO_3, and MgO are 64%, 17%, 14%, 5%, respectively). A schematic of $Na_{0.44}MnO_2$ is shown in Figure 3-5, and shows the presence of sodium ion channels within the crystal lattice. The tunnel-type structure is a known cathode material that operates using these channels.

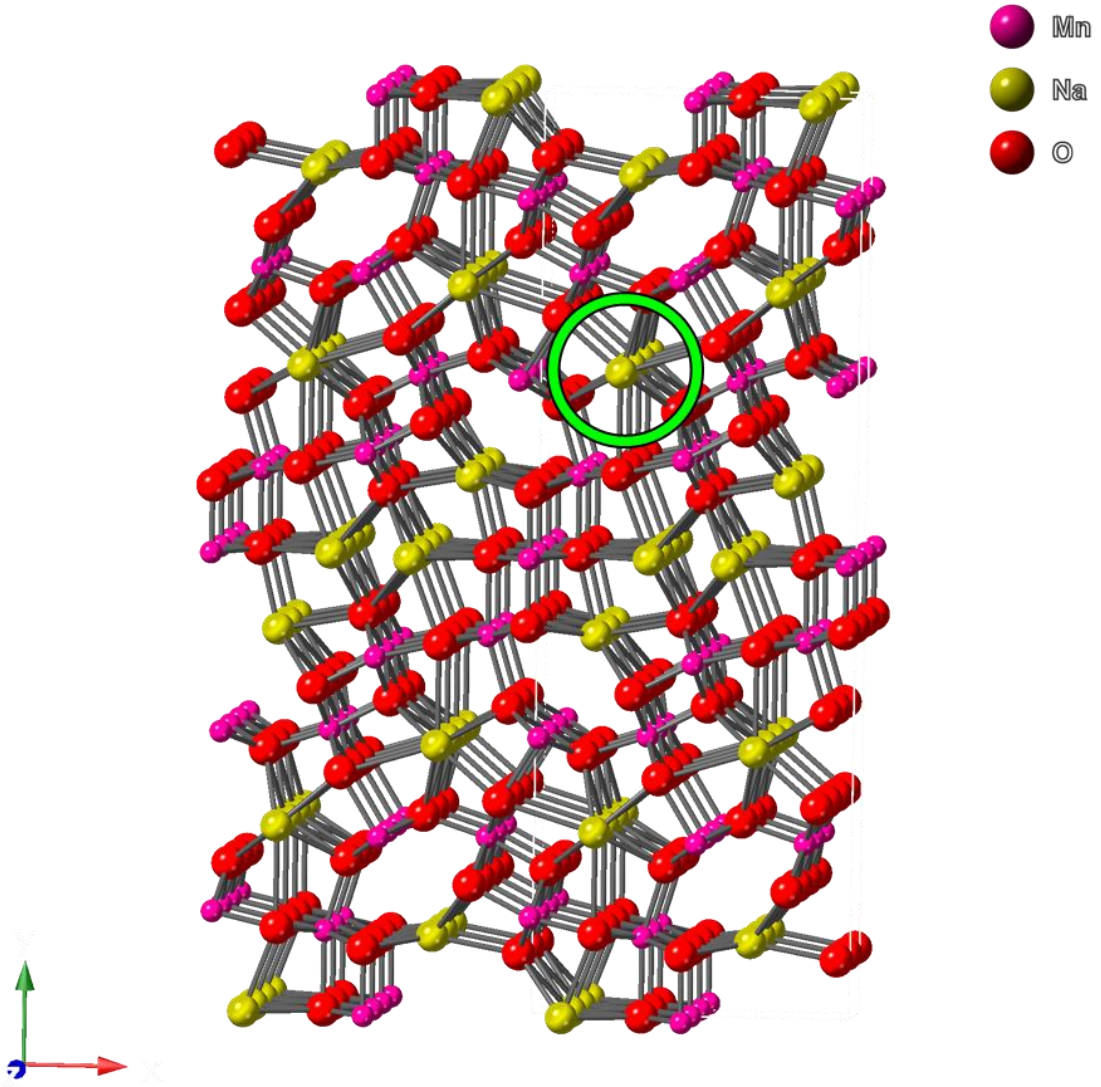

Figure 3-5: Representation of impurity phase, $Na_{0.44}MnO_2$, generated in CrystalMaker X. Na^+ channel highlighted.

The purpose of the XRD is primarily to determine the crystal structure of the cathodes, which was successfully done and independent of the Na content of the material. The lattice parameters for each cathode phase match well with previous reports of similar materials [1], [11], [17] but the nature of these layered oxides is to have variable *c* and *a* lattice parameters with changing sodium ion content. Variation in Na content is expected, owing to Na volatility during calcination – this is the rationale behind the 10% Na excess. The refinement values detailed fixed the Na content at $x = 0.67$, and the refinement still fits well. When allowed to refine, the Na content refines to $x \approx 0.43$ – this is less than the nominal value but is unlikely to reflect the real value. The Na^+ can migrate throughout the interslab layer, and so their position in the sample is not fixed. The low atomic mass and high mobility of the Na^+ makes its occupancy challenging to determine *via* Rietveld refinement [44].

The Na content is still likely to be higher than $x = 0.43$. A biotemplated sample of P3-NMMO calcined at 700 °C for 2 h was examined with inductively coupled plasma-optical emission spectroscopy (ICP-OES). Assuming the Mn and Mg occupancies sum to 1, the molar ratios of the cations in the sample were 0.61 Na, 0.91 Mn, 0.09 Mg. Given the single phase nature of the biotemplated samples (and assuming that there is no amorphous material present), this indicates that the target stoichiometry has been achieved. Rietveld refinement of this sample resulted in similar Na content values, and so it can be assumed that Na content was close to $x = 0.61$ in the sample in this chapter. Regardless, variation in Na content is acceptable in these experiments as the cathodes will be cycled *vs*. an "infinite" source of sodium.

The sodium layer in layered oxide materials is necessarily going to allow a large degree of sodium freedom – if sodium ions were not free to move throughout the layer, or if the activation energy for sodium diffusion was higher it would make layered oxides unsuitable for battery materials. Therefore, it can be assumed that sodium ions, particularly in sodium-deficient materials, are in any one position within the layer. Another consideration is the mass of the sodium ion: it is a lightweight element and thus its scattering factor will be low. These factors contribute to the errors in the Rietveld and mean that refined values obtained for sodium content are unlikely to be reliable, so Na content was not refined.

From these results, biotemplating synthesis can be used to produce phase-pure P3- and P2-NMMO, whereas solid state synthesis only produces phase-pure P2-NMMO. Both synthesis methods produce the ideal crystal structures of the P3 and P2 phases: *R3m* and $P6_3/mmc$, respectively.

3.3.2 SEM

While the XRD results reveal the crystal structure of the cathode materials, which determine the phase transitions they will undergo and so the shape of the voltage curves, it can only hint at particle shapes and sizes. SEM can reveal this information which has consequences for the capacity and cycle life of the material [21], [26].

SEM images of solid state P2-NMMO are displayed in Figure 3-6. The average size of the particles here is 2.71µm ± 2.27 µm, typical of the P2 phase [21], [45], [46]. The sample is made up of 2 populations of crystallites: the larger population (> 1.0 µm) are plate-like particles with a thickness of approximately 1.0 µm, with the average longest dimension measuring 3.69 µm ± 2.04 µm. The second is smaller particles (< 1.0 µm) dispersed on the surface of larger particles with an average size of 0.45 µm ± 0.22 µm, giving them a rough appearance – seen in work on similar materials [13], [47], [48]. Solid state P2-NMMO does not appear to have any other major features with respect to shape and appear as rounded plate-like particles.

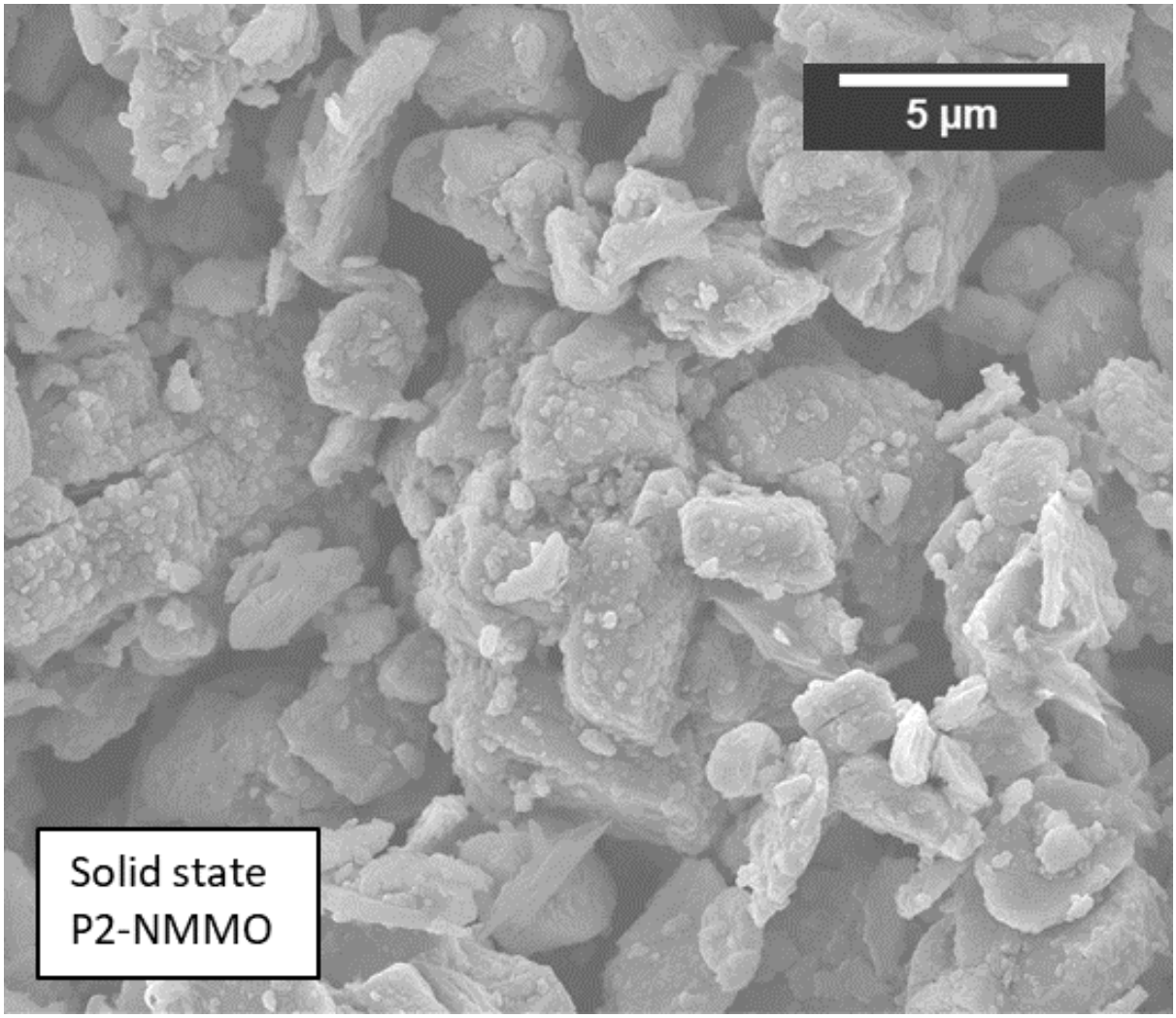

Figure 3-6: SEM image of P2-NMMO synthesised by solid state.

Biotemplated P2-NMMO (Figure 3-7) is similar the solid state sample: it is made up of two population sizes with sizes 0.48 µm ± 0.20 µm and 3.39 µm ± 2.04 µm, with an overall average size of 2.00 µm ± 2.07 µm. Unlike solid state P2-NMMO, however, there are clear examples of particles with sharply faceted crystallites with clearly defined, measurable angles of 120°. Since both P2-NMMO samples underwent identical calcination procedures and processing post-calcination: grinding in an agate pestle and mortar and drying at 120 °C in a vacuum. This suggests that biotemplating promotes growth of particles in this fashion. There is also evidence of the crystal structure growing in layers: steps in the particle surface with the same hexagonal angles. Like the solid state sample, it is covered in smaller particles/growths but has a generally smoother surface. In neither sample is there any evidence of a secondary crystalline phase in the XRD results, these particles are unlikely to be an impurity or secondary phase but are in fact P2-NMMO.

The origin of the smaller (<1.0 µm) particles in the two samples is unclear. It could be caused by grinding of the sample breaking the particles up, but this is unlikely given the forces used in hand grinding. It could be new crystallites forming on the surface of the particles, although there should not be many new crystallites growing after 20 h. It has been proposed that they are particles of $NaOH/Na_2CO_3$ forming on the surface as Na is

expelled from the structure during exposure to air [48]. There is no evidence of any impurities in the XRD patterns of either biotemplated or solid state samples. Again, given the availability of Na in the electrochemical test is practically unlimited, the effect of these imperfections on the surface should be limited to increased resistance on the cell. In future, this can be combatted by greater vigilance in reducing contact of the sample with air. The larger lattice parameters of solid state P2-NMMO was suspected to be a result of varying Na content. The formation of less $NaOH/Na_2CO_3$ on the material surface could indicate better air stability of the biotemplated sample, possibly related to morphology of the particles formed.

The sizes of the P2-NMMO samples are in line with previous studies [1], [21], [48]–[51]. The average size of the biotemplated P2-NMMO is smaller than solid state P2-NMMO but due to error overlap this difference is unlikely to be meaningful. The hexagonal shape of the biotemplated P2-NMMO plates here has been observed in other materials [18], [52]–[57]. None mention the effect that hexagonal shape has specifically, but suggest instead that regular morphology contributes to excellent electrochemical performance [18], which is the case for biotemplating P2-NMMO rather than using solid state synthesis [26].

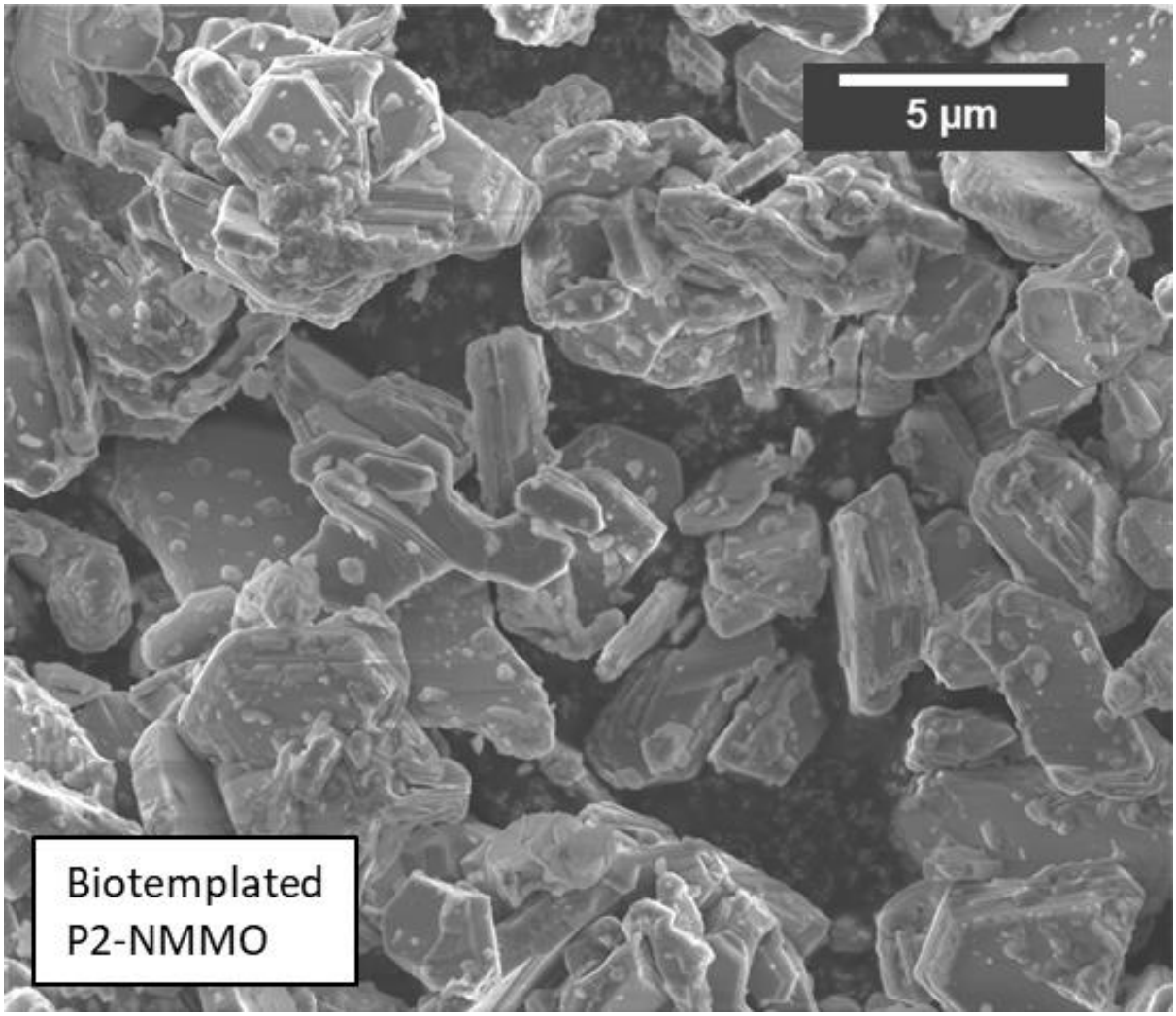

Figure 3-7: SEM image of P2-NMMO synthesised by biotemplating.

P3-NMMO samples are both approximately an order of magnitude smaller than P2-NMMO. In both instances the particles are less well-defined than the P2-NMMO. The solid state P3 phase (Figure 3-8) had an average of 0.36 μm ± 0.30 μm. From the XRD, it contains several impurities: $Na_{0.44}MnO_2$, Na_2CO_3, MgO. $Na_{0.44}MnO_2$ generally takes the form of nanorods or nanowires [58], but it can also form nanofibres and nanoribbons [59]. There are fibre-like structures in the solid state P3-NMMO with lengths of 1-2 μm, whereas $Na_{0.44}MnO_2$ typically has lengths of 5-10 μm [60]–[63]. The fibres are also present in the biotemplated P3-NMMO sample (Figure 3-9) so it is more likely that is some impurity picked up post-calcination.

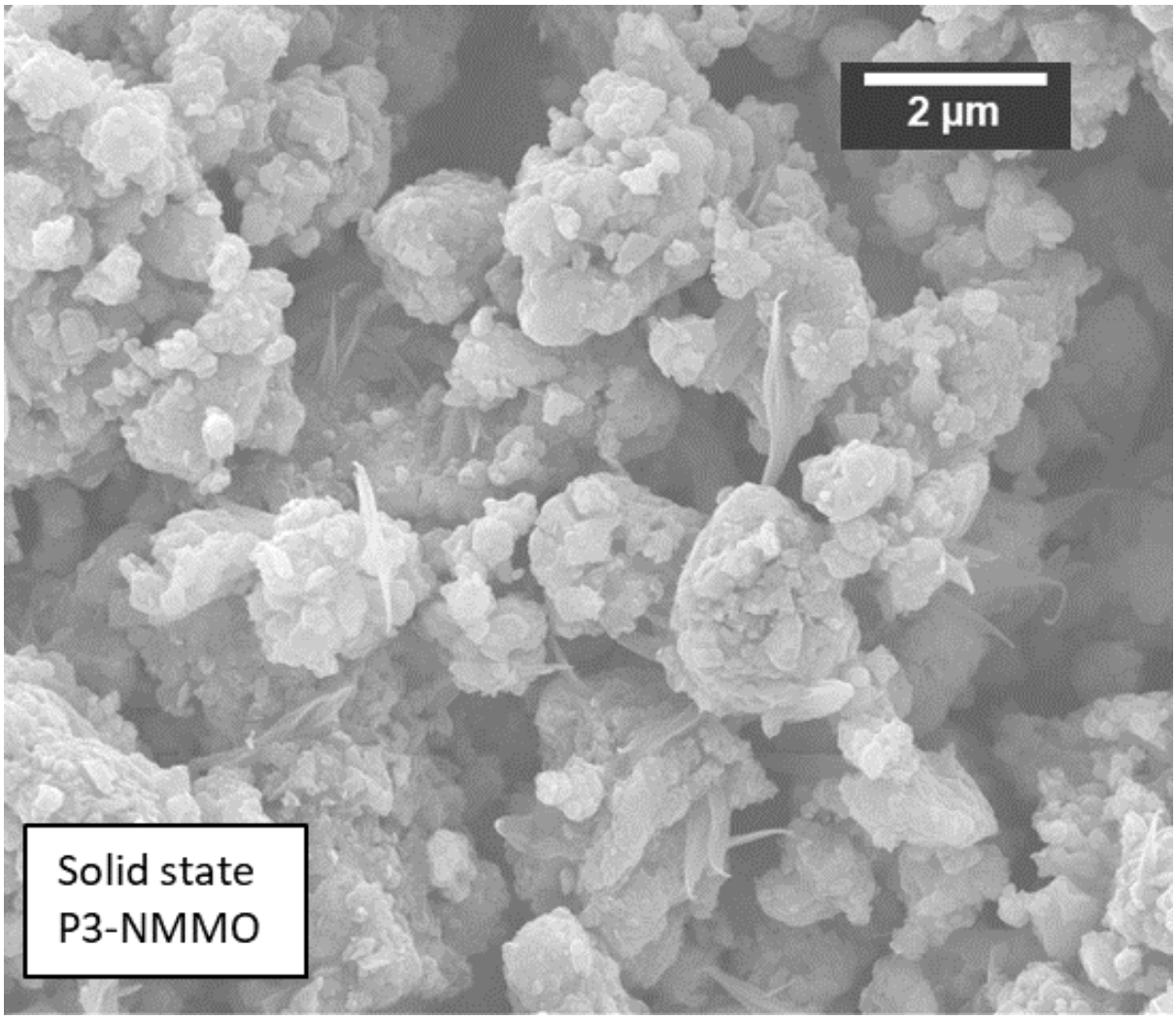

Figure 3-8: SEM image of P3-NMMO synthesised by solid state.

Biotemplated P3-NMMO (Figure 3-9) has an average crystallite size of 0.21 μm ± 0.11 μm. The size of these particles (and those of solid state P3-NMMO) is in line with other P3 materials synthesised *via* biotemplating and sol-gel methods [22], [26]. They show the same fibres as the solid state P3-NMMO, but the XRD pattern of the biotemplated P3-NMMO shows no evidence of any impurity phases, nor does the HTXRD. This suggests that the identity of these fibres is not $Na_{0.44}MnO_2$, or the other impurities present in solid state P3-NMMO. As will be shown in the electrochemical examination of the P3 materials, there is no evidence of $Na_{0.44}MnO_2$ in biotemplated P3-NMMO, yet there is in solid state

P3-NMMO. Further, the fibres do not appear to be separate from the other particles in either sample, and in fact seem to grow from other particles. The fibres then are most likely a different polymorph of P3-NMMO, perhaps made possible by the relatively low calcination temperature and/or longer calcination time. Indeed, this morphology is absent from the biotemplated P3-NMMO samples synthesised at 650 °C for 2 h, shown in later chapters.

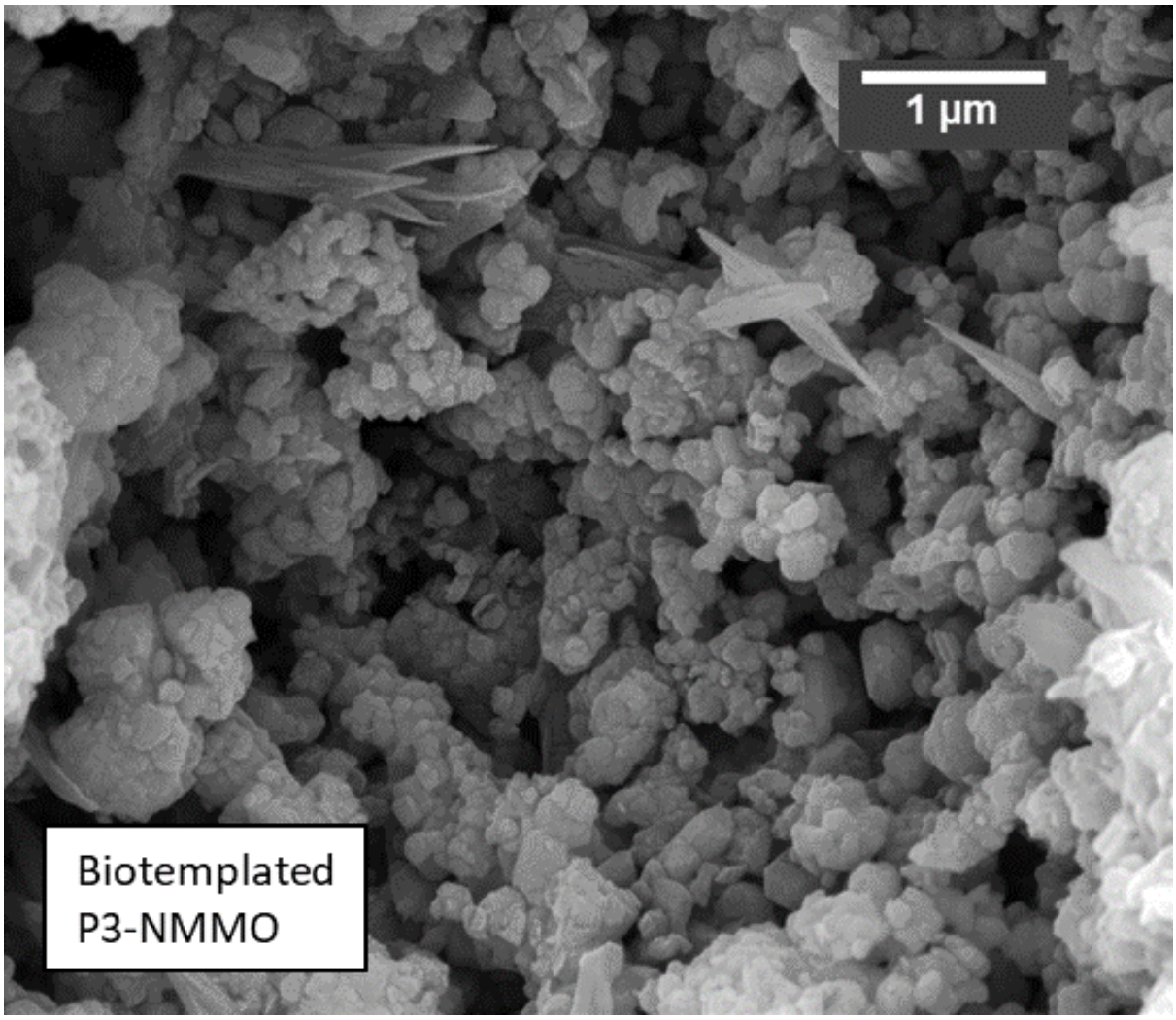

Figure 3-9: SEM image of P3-NMMO synthesised by biotemplating.

Figure 3-10 shows a clear difference in particle size between the P3- and P2-NMMO samples. As expected, higher the calcination temperature generates larger particles. If particles <1.0 µm in the P2-NMMO samples are indeed $NaOH/Na_2CO_3$ [48], the average size of solid state P2-NMMO sample is 3.686 µm, with the biotemplated P2-NMMO 0.3 µm smaller. The thickness of the plates varies between particles, but both samples have plate thickness between 0.5-1 µm. The size difference is small compared to the range of particle size which leads to large errors in determining the average size. As such the two samples can be considered to be the same size. However, the morphology is different: both have plate-like particles but the biotemplated P2-NMMO particles have sharply defined facets absent in solid state P2-NMMO. The solid state P2-NMMO particles are rounded, with angles that are much less well-defined. The difference in particle morphology is likely to

be a direct result of the synthesis method used. The effect of morphology on performance could be to improve Na^+ storage performance, seen in a study by Lee *et al*. [18]. This study only remarks on the regularity of the particles and does not decouple the effect of morphology from other differences between the materials studied, such as size and charge-transfer resistances. Other studies into morphology note more significant differences between two samples than the existence of facets on similarly sized plates [64]–[67].

SEM reveals few size or morphological differences between solid state and biotemplated P3-NMMO. P3-NMMO have much smaller particle sizes overall, approximately an order of magnitude smaller than the P2 phase. The sizes have a smaller spread than P2-NMMO. Again, the solid state synthesis yields a wider spread of particle sizes than biotemplating, as well as a smaller average size. Both contain a fibre- or ribbon-like phase that, given the absence of impurities in the XRD pattern of biotemplated P3-NMMO, is likely to be a different morphology of the P3 phase. It is notable that this morphology is generated *via* both synthesis methods but isn't present in later examples of biotemplated P3-NMMO calcined at 650 °C for 2 h, rather than 580 °C for 20 h, nor is it present in the P2-NMMO samples which were calcined at 900 °C.

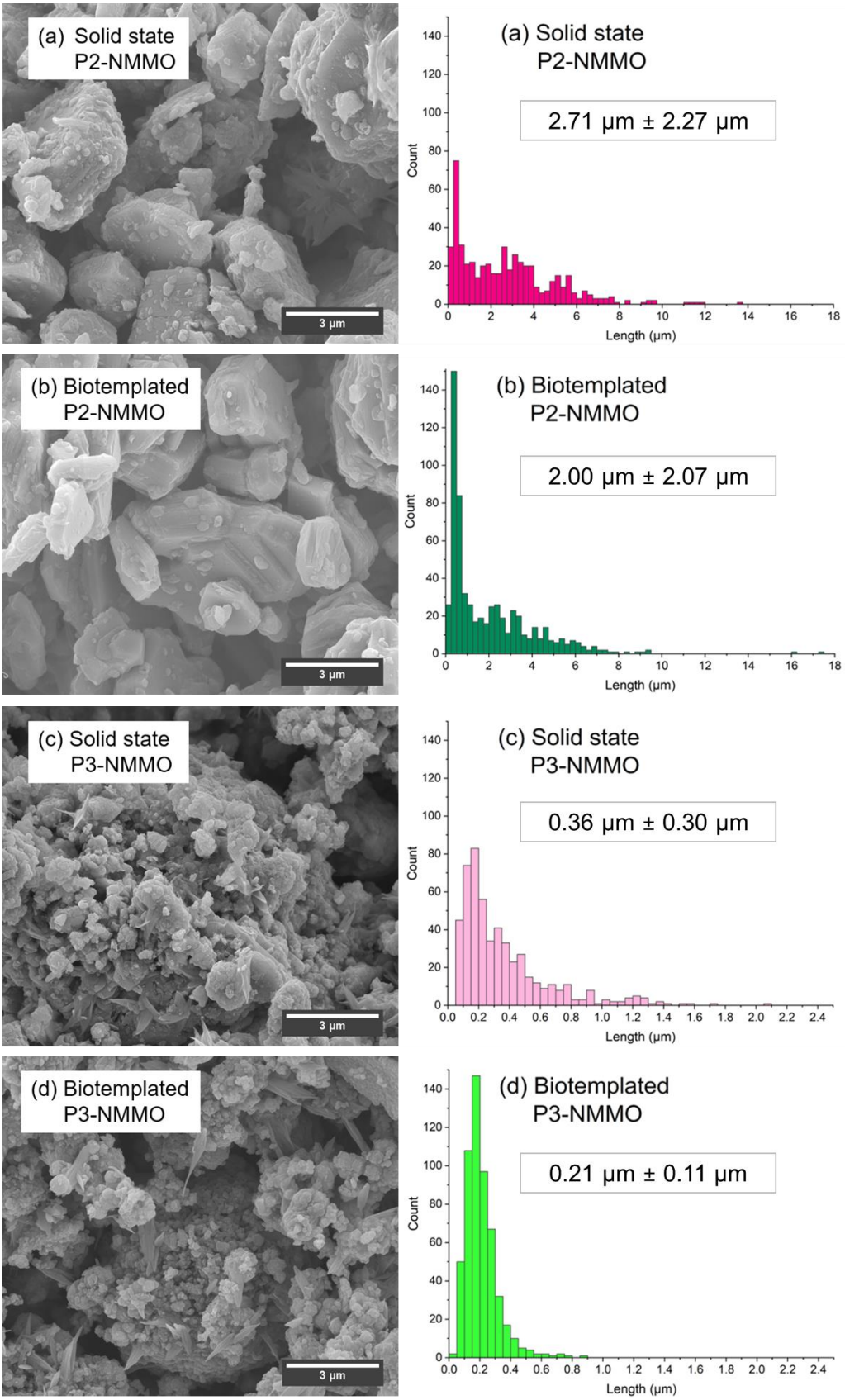

Figure 3-10: SEM images and histograms of particle sizes of P2-NMMO synthesised via *(a) solid state, and (b) biotemplating, and P3-NMMO synthesised* via *(c) solid state, and (d) biotemplating. Note the differences in x-axis scale between P2- and P3-NMMO samples.*

3.3.3 Electrochemistry

This section investigates and compares the electrochemical properties of the four samples. Galvanostatic cycling using a C-rate of (37 mA g^{-1}), and a voltage range of 1.5 – 4.0 V vs Na/Na^+ was used to test the discharge capacities of each material. Discharging to 1.5 V allows the P3-NMMO cathodes to undergo the (reversible) P3↔O3 phase transition [68], enhancing its specific capacity. The P3↔O3 transition can be recognised by the characteristic long plateau in the voltage profile. An upper voltage limit of 4.0 V vs Na/Na^+ is applied to improve the cycle life of the material by avoiding (irreversible) P2↔O2 phase transition.

Several other electrochemical tests were conducted, including a rate capability test to observe the performance of the materials at different C-rates: C/10, C/5, C/2, 1C, 2C, 5C. Solid state P2-NMMO was tested with different voltage ranges; 1.5 – 3.8 V vs Na/Na^+ and 2.0 – 4.0 V vs Na/Na^+, and at 0.05C as well as C/5 in these voltage ranges to provide a baseline.

3.3.3.1 Determining the voltage range

To determine an optimal potential window for both phases, solid state P2-NMMO and biotemplated P3-NMMO were examined under different conditions. These two were used as an initial exploration into the experimental parameters as they were available and gave sufficient insight into the performance. For solid state P2-NMMO, three voltage ranges were tested: 1.5 – 3.8 V vs Na/Na^+, 2.0 – 4.0 V vs Na/Na^+, and 1.5 – 4.0 V vs Na/Na^+. The poor performance of the 1.5 – 3.8 V range in solid state P2-NMMO meant that it was not used when testing the biotemplated P3-NMMO. Thus, for biotemplated P3-NMMO, only two voltage ranges were tested: 2.0 – 4.0 V and 1.5 – 4.0 V. Unless stated otherwise, a current of C/5 was used and cells were cycled 50 times, and the voltage measured vs Na/Na^+.

Solid state P2-NMMO delivered a capacity of 93 mAh g^{-1} initially when cycled between 1.5 – 3.8 V (Table 3-4). The capacity drops to 83 mAh g^{-1} by the 10^{th} cycle, and then falls to 71 mAh g^{-1} after 50 cycles, displaying a lower capacity retention when compared with the other examined voltage ranges but only marginally. For every cycle the capacity is lower than the cells cycled between 2.0 – 4.0 V and 1.5 – 4.0 V. This would be expected initially as the voltage range is narrower, and wider voltage range can extract more Na^+ which leads to higher capacity. What can be seen here is that increasing the upper voltage limit (1.5 – 4.0 V) increased the capacity while also increasing capacity retention. Below 1.9 V, the potential of the cell falls rapidly with respect to capacity; more rapidly than when the potential was >1.9 V. This may be indicative of an ordering step within the cathode [69], [70].

The cell cycled between 2.0 – 4.0 V (Table 3-4) avoids this step. It delivers an initial capacity of 125 mAh g^{-1}, falling to 113 mAh g^{-1} after 10 cycles. This is a greater drop in capacity than when cycled between 1.5 – 3.8 V, but after 50 cycles the capacity remains at 100 mAh g^{-1}: 29 mAh g^{-1} higher than 1.5 – 3.8 V. There is no apparent difference in the electrochemical processes in these cells beyond avoiding the voltage drop present in the

1.5 – 3.8 V cell. This confirms that raising the upper voltage limit from 3.8 V to 4.0 V increases the capacity of the material by approximately 20 mAh g^{-1}. There is little obvious performance difference between the 2.0 – 4.0 V and 1.5 – 4.0 V potential windows. The similar levels of capacity fading also suggest that no additional degradation occurs between 1.5 V and 2.0 V. The reason for the lower capacity of solid state P2-NMMO when cycling between 1.5 – 3.8 V compared to 1.5 – 4.0 V or 2.0 – 4.0 V is that the upper voltage limit was lower. Little capacity can be extracted below 2.0 V due to the voltage drop at this point, but can be extracted above 3.8 V.

It has been mentioned that there are two Na sites in P2 phases, and Na ions are extracted from the structure at different potentials as a result. The Na ions extracted from the edge-sharing site at higher potentials may have a higher overpotential associated with it and extraction may be incomplete when charging to 3.8 V. This would mean that stopping charge causes lower capacity on the subsequent discharge step and following cycles.

Extending the voltage range to 1.5 – 4.0 V does not lead to a significant drop in capacity retention. Capacity retention in the 1.5 – 4.0 V range was 3% lower than in the 2.0 – 4.0 V range, which is too small a difference to be meaningful. Performance of different cells is affected by binder distribution, electrolyte penetration, and cell pressure. Thus a ±5% variation in capacity retention is allowed for variation between cells.

Table 3-4: Discharge capacities of solid state P2-NMMO cycled at C/5 in different voltage ranges.

Voltage range (vs Na/Na^+)	Discharge capacity/mAh g^{-1}			Capacity retention after 50 cycles
	1^{st} cycle	10^{th} cycle	50^{th} cycle	
1.5 – 3.8 V	93	83	71	76%
1.5 – 4.0 V	124	110	95	77%
2.0 – 4.0 V	124	112	101	80%

Cycling the biotemplated P3-NMMO between 2.0 – 4.0 V vs Na/Na^+ yielded a capacity of 70 mAh g^{-1}. While the capacity over the 50 cycles (shown in Table 3-5) remains steady, even when cycled at C/5, the capacity is far lower than expected of this material. The reason for this is the that much of the capacity in P3-NMMO is extracted below 2.0 V, during Mn^{3+}/Mn^{4+} redox [5], [11], [71]. This redox couple is associated with a voltage plateau that is indicative of a phase transition [69], [70], [72], likely of P3↔O3 [19], [73]–[75]. Other P3- $Na_{0.67}Mn_{1-x}Mg_xO_2$ ($0 \leq x \leq 0.33$) materials exhibit higher capacity than biotemplated P3-NMMO cycled between 2.0 – 4.0 V, even when the lower voltage limit is 2.0 V. It's possible that the cells used here had a high internal resistance that lowered the potential at which Mn^{3+}/Mn^{4+} redox occurred during discharge. $NaOH/Na_2CO_3$ is thought to cover the surface of the P2-NMMO particles, the same is likely to be true for P3-NMMO, but not seen in the SEM analysis because of the similarity in size and morphology between P3-NMMO and $NaOH/Na_2CO_3$.

Biotemplated P3-NMMO delivers over 140 mAh g^{-1} when cycled between 1.5 – 4.0 V vs Na/Na^+. The capacity fades over 10 cycles to 135 mAh g^{-1}. Compared to the 2.0 – 4.0 V vs Na/Na^+ cell the capacity fading is much more severe in this case but even after 50 cycles the cell is still able to deliver over 100 mAh g^{-1} at C/5. Of the voltage ranges tested, 1.5 – 4.0 V vs Na/Na^+ allows the maximum capacity to be extracted from both P2- and P3-NMMO without risking electrolyte degradation or irreversible P2↔O2 phase transitions. As such this voltage range was used throughout the rest of the work. Although the capacity is higher when cycled in this voltage range, the capacity retention is much lower (73%) than when cycled between 2.0 – 4.0 V vs Na/Na^+ (94%). Again, this is evidence of the suppression of a phase transition when the voltage limit is raised to 2.0 V; fewer defects in the cathode will appear as a single phase is maintained.

Table 3-5: Discharge capacities of biotemplated P3-NMMO cycled at C/5 in different voltage ranges.

Voltage range (vs Na/Na^+)	Discharge capacity/mAh g^{-1}			Capacity retention after 50 cycles
	1st cycle	10th cycle	50th cycle	
1.5 – 4.0 V	142	133	103	73%
2.0 – 4.0 V	72	70	68	94%

3.3.3.2 Galvanostatic testing

P2-NMMO

The results from galvanostatic testing of both solid state and biotemplated P2-NMMO are displayed in Table 3-6. After 10 cycles, 110 mAh g^{-1} and 119 mAh g^{-1} can be extracted from each material, respectively. At the end of 50 cycles, this falls to 95 mAh g^{-1} and 98 mAh g^{-1}, respectively. This difference in capacity is unlikely to be meaningful, as a variation of ±5 % is allowed for changes in cell construction parameters. This is lower than previous reports (Table 3-1), which use different electrolytes, voltage limits, synthesis techniques, and often lower discharge currents which accounts for some of the differences. From cycle 20 to cycle 50 biotemplated P2-NMMO loses 10 mAh g^{-1} of capacity, whereas solid state P2-NMMO loses 15 mAh g^{-1}, showing better stability at discharge rate of C/5 when using biotemplating synthesis here. The difference is again not large but suggests that biotemplated P2-NMMO may stabilise after 20 cycles. Cycling beyond 50 cycles may yield higher capacity retention. This correlates with a plateau which is visible in the voltage profile of biotemplated P2-NMMO that slowly shortens until it is barely visible after 20 cycles.

Table 3-6: Discharge capacities of solid state and biotemplated P2-NMMO over 50 cycles at C/5 between 1.5 – 4.0 V vs Na/Na^+.

P2-NMMO sample	Discharge capacity/mAh g^{-1}			Capacity retention after 50 cycles
	1st cycle	10th cycle	50th cycle	

Solid state	124	110	95	77%
Biotemplated	134	119	98	73%

The voltage profiles and differential capacity graphs (Figure 3-11) reveal more features of the voltage profile. With respect to peak position, both P2-NMMO samples are similar, with three redox pairs: 2.1/2.2 V, 2.7/3.0 V, and 3.1/3.5 V vs Na/Na^+. The first two correspond to the extraction of Na^+ from the crystal structure. There are two Na^+ environments in the P2 crystal: one edge-sharing and one face-sharing with the MeO_2 octahedra [76]. Na^+ extraction is accompanied by Mn^{3+} oxidation to Mn^{4+} [47], and Jahn-Teller distortions [17]. The first redox pair, 2.1 V/2.2 V, is barely visible absent in the voltage profile of solid state P2-NMMO and is clearer in biotemplated P2-NMMO but disappears after 20 cycles. in the differential capacity plot this can be seen as the oxidation peak of this redox pair is greatly attenuated in the solid state P2-NMMO, compared to biotemplated P2-NMMO. Both shift to higher potentials (2.2 V to 2.4 V). Shortening of the plateau is observed in $Na_{0.67}Mn_{0.89}Mg_{0.11}O_2$ [5] and is attributed here to Mn^{2+} dissolution [4], [6], [77] into the electrolyte following Mn^{3+} disproportionation. The oxidation peak in both samples at 3.5 V is known to be caused by the P2↔OP4 phase transition [1], [25], [78]. Below 1.9 V, the potential of the cell falls rapidly with respect to capacity; more rapidly than when the potential was >1.9 V. This may be indicative of an ordering step within the cathode [69], [70].

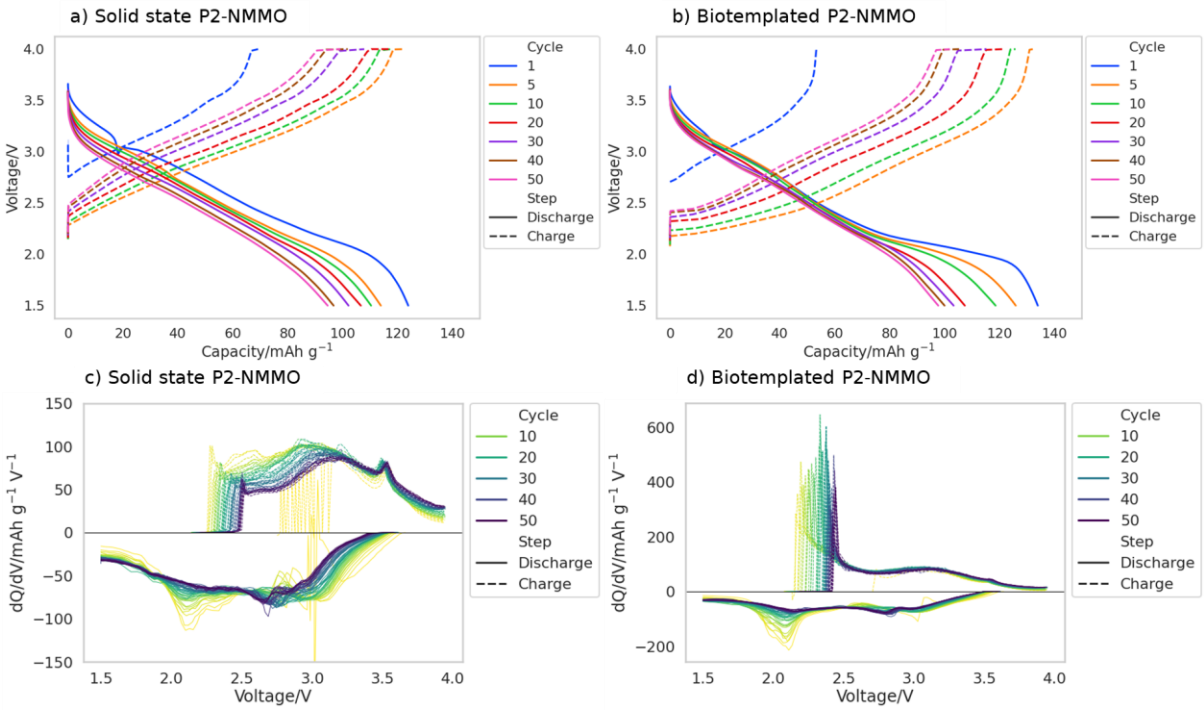

Figure 3-11: Galvanostatic cycling of P2-NMMO synthesised via *(a) solid state methods, and (b) biotemplating. The plateau at the top of each charge step is when the cell was held at a constant voltage. Differential capacity plots of P2-NMMO synthesised* via *(c) solid state methods, and (d) biotemplating. Line colour shifts from yellow to green to blue as cycle number increases. Cycled at C/5 between 1.5 – 4.0 V vs Na/Na^+ for 50 cycles.*

P3-NMMO

The capacity of solid state and biotemplated P3-NMMO is shown in Table 3-7. The solid state P3-NMMO exhibits 93 mAh g^{-1} after 10 cycles, and 89 mAh g^{-1} after 50 cycles. Conversely, biotemplated P3-NMMO displays 133 mAh g^{-1} and 103 mAh g^{-1} after 10 and 50 cycles, respectively. The extra capacity in the biotemplated P3-NMMO is due to the presence of a voltage plateau at 2.1 V. The redox couple corresponding to it is apparent in the voltage profiles and differential capacity graphs of both materials (Figure 3-12) but the intensity of the 2.1 V/2.2 V redox peaks in the solid state P3-NMMO are approximately 10-20% the intensity of the peak in the biotemplated P3-NMMO sample. This pair is associated with the P3↔O3 phase transition [19], [73], [79], [80]. The capacity of the solid state P3-NMMO will be lower than the other samples in this chapter naturally, as it contains several impurity phases, but the theoretical capacity was not adjusted, and neither was the C-rate used.

Table 3-7: Discharge capacities of solid state and biotemplated P3-NMMO over 50 cycles at C/5 between 1.5 – 4.0 V vs Na/Na⁺.

P3-NMMO sample	Discharge capacity/mAh g^{-1}			Capacity retention after 50 cycles
	1st cycle	10th cycle	50th cycle	
Solid state	94	93	89	95%
Biotemplated	142	133	103	73%

The presence of a smaller peak in solid state P3-NMMO suggests that the transition occurs but to a lesser extent than the biotemplated P3-NMMO. The high capacity retention could be a result of this, as there would be less structural degradation. The suppression of the P3↔O3 transition may be caused by the presence of $Na_{0.44}MnO_2$, akin to the suppression of P2↔O2 or P2↔OP4 transitions in biphasic intergrowth structures [21], [46], [81], [82]. The presence of secondary phases suppressing phase transitions and improving capacity retention is well known and forms the basis of Results 3.

The initial measured discharge capacity of biotemplated P3-NMMO (142 mAh g^{-1}) compares well with other P3 materials [11], [19], [83], due to the relatively low molecular mass of the cathode and the optimised voltage range. However, its capacity is lower than that of previously reported P3-NMMO materials (Table 3-1). The P3-NMMO tested here are cycled at C/5, whereas the others are tested at C/10 or lower, and still exhibits comparable capacity retention on a per cycle basis. The capacity retention of P3-$Na_{0.67}Mn_{0.8}Mg_{0.2}O_2$ [15] is much higher (97% after 25 cycles) but also includes an additional 10% Mg doping which improves capacity retention.

The voltage plateau gradually fades over 25 cycles, resulting in a drop in capacity and appears instead as a slope due to degradation within the cathode. Full cell degradation can be ruled out as it is not replicated in the solid state P3-NMMO samples. Degradation of the cathode leads to increasing internal resistance and higher overpotentials for electrochemical processes [84], [85], and decreasing capacity. The 2.1 V/2.2 V redox pair

in biotemplated P3-NMMO becomes increasingly polarised throughout cycling (Figure 3-12d). Capacity fading could also be due to Mn^{2+} dissolution, as with P2-NMMO. Since the capacity fading is more pronounced in the biotemplated P3-NMMO it is more likely that it arises from degradation from the P3↔O3 transition. The particle sizes of the two P3-NMMO samples are comparable, and so more rapid degradation owing to this is unlikely. The high capacity retention then likely comes from the impurity $Na_{0.44}MnO_2$ phase suppressing phase transformations in solid state P3-NMMO.

The result is a reduction in capacity and a change in the discharge curve from plateau to slope, after which the capacity becomes stable. The P3↔O3 transition is reportedly sluggish and there is a great deal of strain between the two phases [41]. This strain will cause the loss of active material and the increased internal resistance will increase the overpotential of any phase change. This manifests itself as increased polarisation, which can be observed in the differential capacity graph in Figure 3-12d. As seen in investigations into $Na_{0.67}MnO_2$ [47], the smoothing of a voltage profile and reduction of capacity can be caused by the growth of a passivating layer on the surface of the electrode. The P3 and O3 structures have different unit cell sizes since the Na layers have different spacing. This mismatch causes the strain on the cathode material. If the strain between P3 and O3 structures causes cracks in the material this would provide a larger surface area for any passivating layer to form and worsen any overpotential increases. Increasing the overpotential means that less capacity is extracted from the cathode before the voltage cut offs (both upper and lower) are reached.

Solid state P3-NMMO undergoes several additional redox processes compared to biotemplated P3-NMMO, seen in the differential capacity graph (Figure 3-12c). It is suggested that the cause of these redox process is the impurity phase, $Na_{0.44}MnO_2$. Its crystal structure contains Na^+ channels, shown in Figure 3-5, and so Na^+ diffusion through the crystal may be possible, utilising the Mn^{3+}/Mn^{4+} redox. The average oxidation state of the Mn in the material should be +3.42. Excluding impurity phases, there are few differences between solid state and biotemplated P3-NMMO, so it is possible that the impurity phase undergoes several redox processes while supressing the P3↔O3 transition.

Suppression of phase transitions is a common tactic [41], [86]–[93] for improving capacity retention. Often this is accomplished through doping the transition metal layer, by stabilising the prismatic sodium ion environment. It is also prevalent in cathodes dependent on the Mn^{3+}/Mn^{4+} redox couple, where Jahn-Teller activity leads to distortions, cracks, and capacity fading. Here the capacity retention of the solid state P3-NMMO is very high, indicating that phase transitions are being suppressed. It is possible in that case that the impurities are stabilising the prismatic structure from outside the cathode structure, rather than within. This could be *via* preventing contraction of the unit cell, by increasing the structural rigidity of the cathode if it is dispersed throughout the sample. O*perando* XRD would be used to confirm the phase progression of the sample, including any changes in the lattice parameters of either layered or tunnel structure, and how it compares with the biotemplated P3-NMMO sample [94], [95].

Given that there is only 64% P3-NMMO (and 17% $Na_{0.44}MnO_2$ that appears redox active) in the cathode due to impurities, the capacity per unit mass of active material of solid state P3-NMMO (and $Na_{0.44}MnO_2$) is 116 mAh g^{-1}.

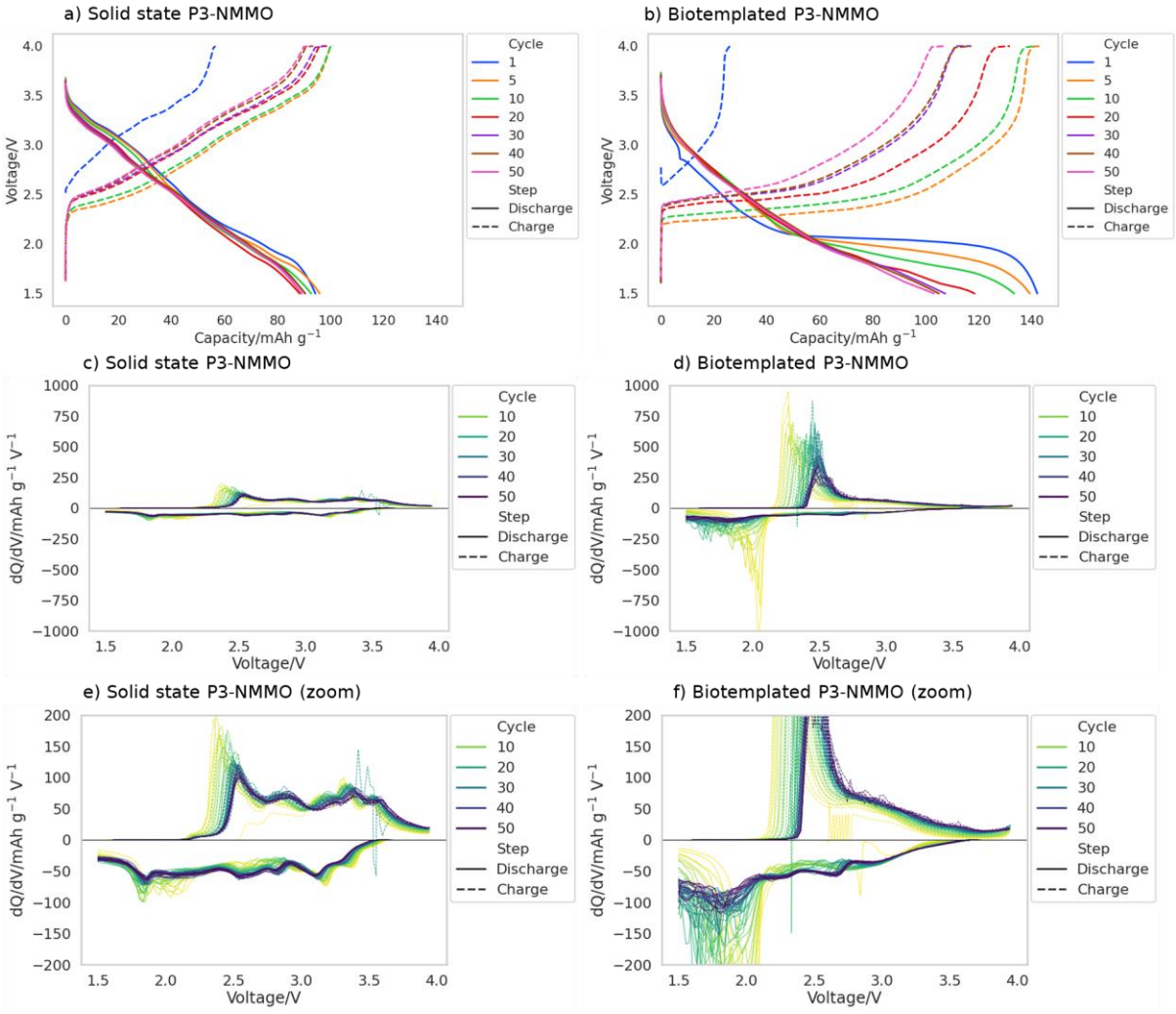

Figure 3-12: Galvanostatic cycling of P3-NMMO synthesised via (a) solid state methods, and (b) biotemplating. The plateau at the top of each charge step is when the cell was held at a constant voltage. Differential capacity plots of P3-NMMO synthesised via (c) solid state methods, and (d) biotemplating. (e, f) show the differential capacity plots on the same y-axis scale. Line colour shifts from yellow to green to blue as cycle number increases. Cycled at C/5 between 1.5 – 4.0 V vs Na/Na⁺ for 50 cycles.

A comparison of all four cathode materials is displayed in Figure 3-13. It shows that biotemplated P3-NMMO delivers a greater capacity than both P2-NMMO samples, as well as solid state P3-NMMO. P2 phases have either been shown to outperform P3 phases [83], [96], or the capacity decay of P3 phase is such that it falls below the P2 phase after 15 cycles [11]. In these studies, the lower voltage cut-off is 2.0 V which inhibits the P3↔O3 transition and much of the capacity of the P3 phase. This highlights both the importance of the selection of voltage limits to optimise performance, and the use of synthesis methods to control material production.

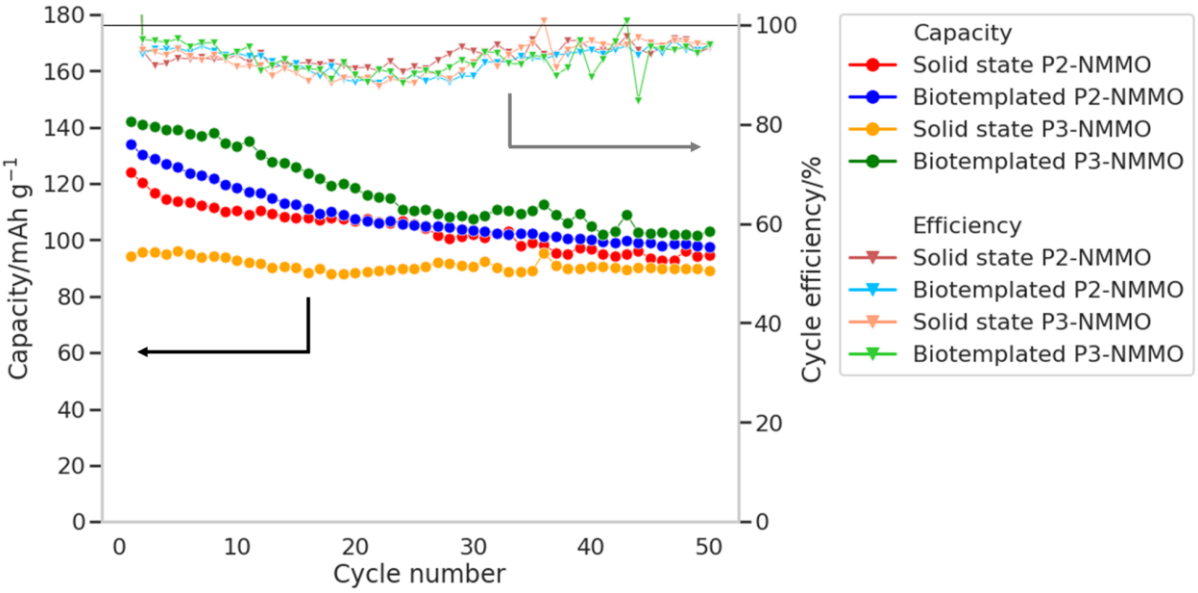

Figure 3-13: Discharge capacity and cycle efficiency of all four samples. Cycled between 1.5 – 4.0 V at C/5 for 50 cycles.

The average discharge capacity of the last cycle of the three cells tested for each sample was taken. The average and standard deviation can be seen in Table 3-8. It shows that the spreads of capacities do not overlap with each other. Thus, the differences in capacity shown here (particularly that biotemplated P3-NMMO displays the highest capacity and solid state P3-NMMO the lowest) are significant. Biotemplated P2-NMMO has a higher capacity than solid state P2-NMMO and, although the difference is small, the errors do not overlap.

Table 3-8: Average discharge capacity of the 50th cycle of each sample and the standard deviation.

Sample	Average 50th discharge capacity (mAh g^{-1})	Standard deviation (mAh g^{-1})
Solid state P2-NMMO	94.3	2.3
Biotemplated P2-NMMO	99.5	1.6
Solid state P3-NMMO	88.2	2.4
Biotemplated P3-NMMO	107.7	3.5

The cycle efficiencies of all four samples are approximately equal and follow the same trend; starting at 95% initially, it falls steadily until cycle 30. At this point, the efficiency increases and remains steady (with some fluctuations) at 95%. Most capacity degradation is seen in the first 30 cycles, leading to lower efficiencies. The likelihood of Mn^{2+} dissolution from the cathode into the electrolyte has been discussed and could be the cause of low (<98%) efficiencies [97]. Both P2-NMMO samples have a lower capacity than biotemplated P3-NMMO.

However, these results show the biotemplated P3-NMMO sample exhibits the highest initial capacity of the four samples examined. Here the differences between the

biotemplating and solid state syntheses are more apparent. Solid state generates impurities in the material that suppress the phase transitions that would otherwise occur. While this leads to a much improved capacity retention, the initial capacity is 48 mAh g^{-1} lower. Further cycling may reveal that the capacity of biotemplated P3-NMMO continues to fall after 50 cycles to below solid state P3-NMMO. In the test procedure used here, however, the biotemplated P2-NMMO outperforms solid state P3-NMMO.

Biotemplated P3-NMMO also delivers a higher capacity than both P2-NMMO samples. This may be a result of the smaller particle size of the P3-NMMO; this is a phenomenon that has been observed before [26] when comparing biotemplating against solid state synthesis. Smaller particle size means that more Na^+ can be inserted into/extracted from the layered structure at a given C-rate. It can also harm capacity retention of this material by allowing more Mn^{2+} dissolution, although the capacity retention of the biotemplated P3-NMMO is similar to the P2-NMMO samples. It is possible that P3-NMMO is less susceptible to Mn^{2+} dissolution than P2-NMMO. Mg^{2+} dissolution occurs through migration *via* the Na layer. In P2 phases, there are Na sites with lower energy than the Na sites in P3, because they are edge-sharing on both sides. This may make it easier for Mn^{2+} to migrate into the Na layer and dissolve into the electrolyte. As will be discussed in greater depth in later chapters, the capacity retention of biotemplated P2-NMMO when calcined for only 2 h, with a particle size of 0.54 µm ± 0.55 µm, has an initial capacity of 147 mAh g^{-1} (higher than when calcined for 20 h), but a retention of only 63% after 50 cycles with the same test parameters. Here the P2-NMMO both have the same particle size, and so their performance is similar, with any differences between it and the solid state P2-NMMO indistinguishable from variation between like cells.

3.3.3.3 Rate capability

Finally, the rate capability of each material was tested, and the results are displayed in Figure 3-14. These results further highlight the higher capacity of the biotemplated P3-NMMO cathode. As with cycling at C/5 (37 mA g^{-1}), it displays capacities that are higher than each of the other samples at each C-rate.

All four samples do exhibit a steep capacity drop as the C-rate is increased. The high polarisation of the cells and how that implies a high internal resistance has been discussed and manifests here as poor performance at high C-rate. For each phase, the biotemplated cathodes perform better than their solid state counterparts. Both biotemplated NMMO cathodes deliver approximately 40 mAh g^{-1} at 5C, compared to 10 mAh g^{-1} and 20 mAh g^{-1} for solid state P3- and P2-NMMO, respectively. These capacities at 5C signify a large drop off in performance overall [17], [39], [98], but there are studies with similar rate capabilities [46], [99]. All four samples recover their initial capacity when cycling again at C/10 after the rate capability test, indicating that the capacity loss at high current is not due to material degradation. This shows the materials stability at high C-rates and suggests that that the drop in capacity results from a relatively high internal resistance [88], which can be improved with further development and optimisation.

When comparing between phases, it can be argued that in the case of P3-NMMO the smaller particle sizes [26], [69], [100] of the biotemplated material improves its performance over the solid state sample. The smaller particle size means that sodium ions have more surface area from which they diffuse into the cathode. This is the same reason for its higher capacity overall. In the case of solid state P3-NMMO, the presence of a secondary phase forming an intergrowth would be thought to improve rate capability [92], especially $Na_{0.44}MnO_2$ with reportedly high rate capability [63], [101]. This does not happen here, as the capacity of the two solid state samples becomes lower than the biotemplated samples as the current is increased. There are visible impurities in the solid state P3-NMMO from the unreacted starting material. As mentioned when discussing the growths on the P2-NMMO particles, this can lead to increased internal resistances [48]. This becomes more detrimental at higher C-rates, as the overpotential that drives the processes in the cell is a product of the current and the resistance [69], [85].

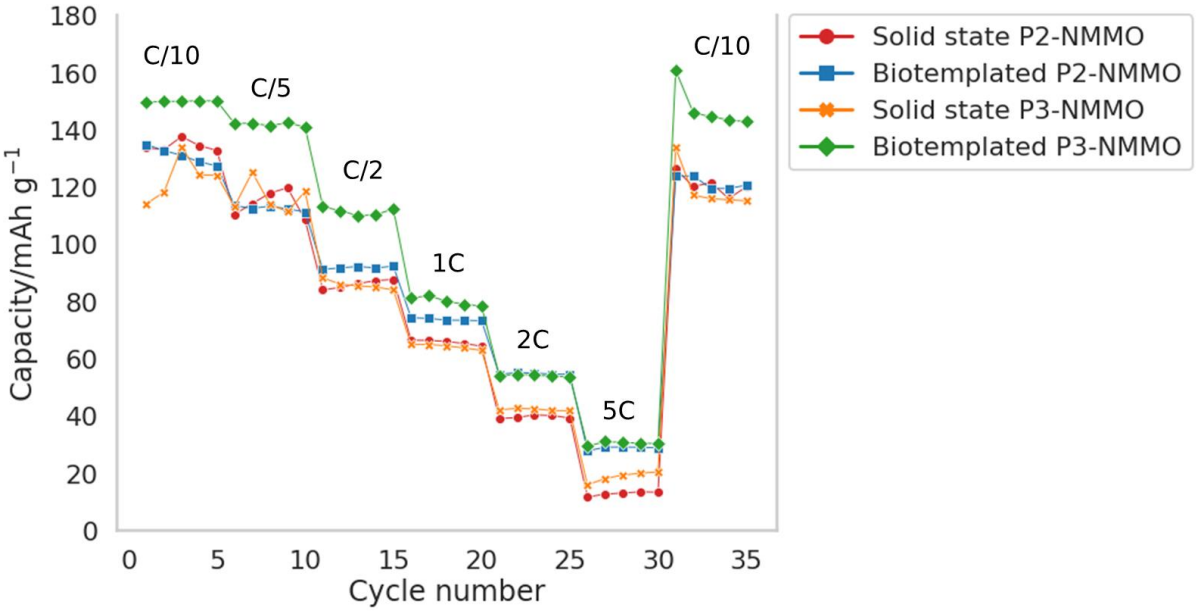

Figure 3-14: Discharge capacity graph of all four samples. Cycled between 1.5 – 4.0 V at a given C-rate as marked on the graph for 5 cycles each.

For P2-NMMO, the biotemplated cathode again exhibits higher capacity than solid state P2-NMMO at high C-rates. Since the particles of both P2-NMMO samples are almost identical, the particle size is unlikely to be a factor in the improved performance. The main difference between the two P2-NMMO samples is the faceted appearance of the biotemplated P2-NMMO, compared to the rounded plates of solid state P2-NMMO. These facets could expose a face in the crystal structure that facilitates faster Na^+ extraction and insertion. The faceted particles are also likely to have greater surface area than round particles of the same size, leading to faster Na^+ extraction and insertion. A proposal for the confirmation of this hypothesis is discussed in 3.5 Further work.

3.4 Conclusion

The results here indicate that the P3-NMMO cathode material can outperform its P2 counterpart with respect to discharge capacity. This is the opposite to most research into

P3 cathodes, in which they are typically shown to have lower capacities than the P2 equivalent [11], [96]. For P-type $Na_{0.67}Mn_{1-x}Mg_xO_2$ ($0 \leq x \leq 0.33$), the capacity of both P3 and P2 phases ranges from typically 150-200 mAh g^{-1}, with higher capacity resulting from the activation of O redox by higher Mg^{2+} content. The biotemplated materials presented here display a capacity of up to 150 mAh g^{-1} when cycled at C/10, which compares well with the previous studies summarised in Table 3-1. Beyond that, the capacity retention of biotemplated P3-NMMO means that even after cycling at C/5 its capacity remains higher than the P2-NMMO, regardless of the P2 synthesis method. The likely reason for this is the high surface area of the P3 material, and due to the likely resistance to Mn^{2+} dissolution of the P3 phase.

All four materials studied showed rapid capacity fading from increasing C-rate, but a good capacity recovery after cycling again at C/10. This shows all four materials did not suffer structural degradation at high currents and suggests that poor rate capability is a result of high internal resistance. The two biotemplated samples displayed 10-15 mAh g^{-1} higher capacity at high (5C) currents than the solid state samples. Biotemplated P3-NMMO likely displays better rate capability because of its lower particle size and higher surface area than the P2-NMMO. Solid state P3-NMMO also has a higher surface area but may be encumbered by high resistance from unreacted starting material in the cathode. The faceted appearance of biotemplated P2-NMMO likely increases its surface area relative to solid state P2-NMMO, explaining its superior performance at high C-rates.

The synthesis of a high capacity material at comparatively low temperatures (580 °C for P3 and 900 °C for P2) promises a sustainable option for large-scale energy storage. Biotemplating means that the P3 phase can be accessed much more reliably than using the more common solid state synthesis method. This highlights the strength of biotemplating a technique for accessing low temperature phases, as well as its ability to incorporate dopants into the structure.

The results for biotemplated and solid state P2-NMMO cathodes being similar indicate that the biotemplating synthesis returns generally the same characteristics as the solid state material. There are some differences between the two, such as the presence of a prominent voltage plateau, that have not been fully explored yet. The differences between the two cathodes tend to favour biotemplating as the synthesis method, owing to the slower degradation of the cell and resultant slower capacity fade.

The initial capacities of the two biotemplated NMMO phases (P3: 142 mAh g^{-1}, P2: 134 mAh g^{-1}) rank low in comparison with the capacities of previous work into NMMO (detailed in Table 3-1). All samples tested, in particular solid state P3-NMMO, compare well with the literature with respect to capacity retention – with some exceptions where authors have achieved excellent capacity retention. The average here (not counting exceptions already mentioned) is approximately 0.5% capacity loss per cycle, while in the literature is approximately 1% per cycle.

However, the aim of the study was to compare them against the solid state P2-NMMO under the same conditions, where they perform favourably. This is on top of further benefits to using biotemplating, such as reduced processing time, and (shown in later

chapters) reduced calcination time. This chapter also details the differences in performance of the P2 and P3 phases of the NMMO material, while direct comparisons of between phases are rare. The reasons for the lower capacity could be caused by several factors, such as the cathode material being exposed to water or O_2 in the air during processing or characterisation. These imperfections and sources of error in cell production mean that the focus of this chapter (and later chapters) is comparison to the samples tested, rather than previous work. However, it must be recognised that improvements can be made in the cell production process, as proven by the literature discussed.

There are additional benefits to the biotemplating synthesis. These include easier synthesis with fewer steps to produce a phase pure product – particularly useful in producing P3-NMMO. It also allows the cathode material to be produced faster, calcining for only 2 h, rather than the 20 h needed here and with a faster ramp rate (10 °C min^{-1} rather than 5 °C min^{-1}), which will be shown in the next two chapters. Including the time taken for the furnace to reach temperature and cool, a P2-NMMO at 900 °C would take one third the time to calcine. This allows for faster prototyping and testing, which can be invaluable at the laboratory stage, and mean significant cost savings at larger scale production.

3.5 Further work

There are two main causes of poor performance in this work: Mn^{2+} dissolution leading to capacity fade; and high internal resistance meaning lower capacity, particularly pronounced at high C-rates.

Strategies to prevent Mn^{2+} dissolution could be increasing the particle size of the P2-NMMO phase with higher calcination temperatures, coating the particles with a conductive additive, or the use of electrolyte additives. However, there is also an argument for reducing the particle size of the biotemplated materials as this will increase the available Na^+ in the material that can be reversibly inserted and extracted. Coating the material in this case may lead to higher, more stable capacities. Electrolyte choice can also impact capacity fading. Ionic liquids have been used with great success to minimise Mn^{2+} dissolution [6], as has the electrolyte additive fluorinated ethylene carbonate (FEC) [102]. These could be tested independently and should improve the capacity retention of the all materials (except maybe solid state P3-NMMO).

High internal resistance may be caused by $NaOH/Na_2CO_3$ impurities arising from contact with air. Work can be done to ensure minimal contact between cathode materials and air, as this is likely to have increased the internal resistance of the cells. This could be investigated for P2-NMMO using SEM, determining how many outgrowths appear on the particle surface after different exposures to air. This could be corroborated by testing these materials electrochemically to see if capacity or rate capability is increased. Coating the particles with carbon [103] or Al_2O_3 [53], [104] could also reduce the internal resistance.

The reasons for biotemplated P2-NMMO having a higher capacity at elevated C-rates than solid state P2-NMMO must be proven. To confirm that biotemplated P2-NMMO has a higher surface area than solid state P2-NMMO nitrogen sorption can be used. More complex analysis is needed to confirm the difference in exposed crystal faces of the faceted biotemplated P2-NMMO particles, compared to the rounded particles of solid state P2-NMMO. TEM could be used to confirm this and would reveal whether the exposed faces of the biotemplated P2-NMMO particles are perpendicular to the Na^+ channels in P2-NMMO. if this is the case it could lead to faster Na^+ diffusion into the crystal structure at higher C-rates, and thus higher capacity.

3.6 References

[1] J. Billaud, G. Singh, A. R. Armstrong, E. Gonzalo, V. Roddatis, M. Armand, T. Rojo, and P. G. Bruce, "$Na_{0.67}Mn_{1-x}Mg_xO_2$ ($0 \leq x \leq 0.2$): a high capacity cathode for sodium-ion batteries," *Energy Environ. Sci.*, vol. 7, no. 4, pp. 1387–1391, 2014, doi: 10.1039/C4EE00465E.

[2] H. Liu, W. Deng, X. Gao, J. Chen, S. Yin, L. Yang, G. Zou, H. Hou, and X. Ji, "Manganese-based layered oxide cathodes for sodium ion batteries," *Nano Sel.*, vol. 1, no. 2, pp. 200–225, 2020, doi: 10.1002/nano.202000030.

[3] A. Caballero, L. Hernán, J. Morales, L. Sánchez, J. Santos Peña, and M. A. G. Aranda, "Synthesis and characterization of high-temperature hexagonal P2-$Na_{0.6}MnO_2$ and its electrochemical behaviour as cathode in sodium cells," *J. Mater. Chem.*, vol. 12, no. 4, pp. 1142–1147, 2002, doi: 10.1039/b108830k.

[4] X. Ma, H. Chen, and G. Ceder, "Electrochemical Properties of Monoclinic $NaMnO_2$," *J. Electrochem. Soc.*, vol. 158, no. 12, p. A1307, 2011, doi: 10.1149/2.035112jes.

[5] D. Buchholz, C. Vaalma, L. G. Chagas, and S. Passerini, "Mg-doping for improved long-term cyclability of layered Na-ion cathode materials - The example of P2-type $Na_xMg_{0.11}Mn_{0.89}O_2$," *J. Power Sources*, vol. 282, pp. 581–585, 2015, doi: 10.1016/j.jpowsour.2015.02.069.

[6] L. G. Chagas, D. Buchholz, L. Wu, B. Vortmann, and S. Passerini, "Unexpected performance of layered sodium-ion cathode material in ionic liquid-based electrolyte," *J. Power Sources*, vol. 247, pp. 377–383, 2014, doi: 10.1016/j.jpowsour.2013.08.118.

[7] J. Li, S. Jeong, R. Kloepsch, M. Winter, and S. Passerini, "Improved electrochemical performance of $LiMO_2$ (M=Mn, Ni, Co)-Li_2MnO_3 cathode materials in ionic liquid-based electrolyte," *J. Power Sources*, vol. 239, pp. 490–495, 2013, doi: 10.1016/j.jpowsour.2013.04.015.

[8] M. M. Thackeray, "Manganese oxides for lithium batteries," *Prog. Solid State Chem.*, vol. 25, no. 1–2, pp. 1–71, 1997, doi: 10.1016/S0079-6786(97)81003-5.

[9] N. Yabuuchi, R. Hara, K. Kubota, J. Paulsen, S. Kumakura, and S. Komaba, "A new electrode material for rechargeable sodium batteries: P2-type $Na_{2/3}[Mg_{0.28}Mn_{0.72}]O_2$ with anomalously high reversible capacity," *J. Mater. Chem.*

A, vol. 2, no. 40, pp. 16851–16855, 2014, doi: 10.1039/C4TA04351K.

[10] G. Assat, D. Foix, C. Delacourt, A. Iadecola, R. Dedryvère, and J.-M. Tarascon, "Fundamental interplay between anionic/cationic redox governing the kinetics and thermodynamics of lithium-rich cathodes," *Nat. Commun.*, vol. 8, no. 1, 2017, doi: 10.1038/s41467-017-02291-9.

[11] B. Sambandam, M. H. Alfaruqi, S. Park, S. Lee, S. Kim, J. Lee, V. Mathew, J. Y. Hwang, and J. Kim, "Validating the structural (In)stability of P3- and P2-$Na_{0.67}Mg_{0.1}Mn_{0.9}O_2$-Layered cathodes for sodium-ion batteries: A time-decisive approach," *ACS Appl. Mater. Interfaces*, vol. 13, no. 45, pp. 53877–53891, 2021, doi: 10.1021/acsami.1c15394.

[12] D. Su, C. Wang, H. J. Ahn, and G. Wang, "Single Crystalline $Na_{0.7}MnO_2$ Nanoplates as Cathode Materials for Sodium-Ion Batteries with Enhanced Performance," *Chem. - A Eur. J.*, vol. 19, no. 33, pp. 10884–10889, 2013, doi: 10.1002/chem.201301563.

[13] J. Li, J. Wang, X. He, L. Zhang, A. Senyshyn, B. Yan, M. Muehlbauer, X. Cao, B. Vortmann-Westhoven, V. Kraft, H. Liu, C. Luerenbaum, G. Schumacher, E. Paillard, M. Winter, and J. Li, "P2-Type $Na_{0.67}Mn_{0.8}Cu_{0.1}Mg_{0.1}O_2$ as a new cathode material for sodium-ion batteries: Insights of the synergetic effects of multi-metal substitution and electrolyte optimization," *J. Power Sources*, vol. 416, no. December 2018, pp. 184–192, 2019, doi: 10.1016/j.jpowsour.2019.01.086.

[14] B. Song, E. Hu, J. Liu, Y. Zhang, X. Q. Yang, J. Nanda, A. Huq, and K. Page, "A novel P3-type $Na_{2/3}Mg_{1/3}Mn_{2/3}O_2$ as high capacity sodium-ion cathode using reversible oxygen redox," *J. Mater. Chem. A*, vol. 7, no. 4, pp. 1491–1498, 2019, doi: 10.1039/c8ta09422e.

[15] E. J. Kim, L. A. Ma, D. M. Pickup, A. V. Chadwick, R. Younesi, P. Maughan, J. T. S. Irvine, and A. R. Armstrong, "Vacancy-enhanced oxygen redox reversibility in P3-type magnesium-doped sodium manganese oxide $Na_{0.67}Mg_{0.2}Mn_{0.8}O_2$," *ACS Appl. Energy Mater.*, vol. 3, no. 11, pp. 10423–10434, 2020, doi: 10.1021/acsaem.0c01352.

[16] S. F. Linnell, A. G. Manche, Y. Liao, M. Hirsbrunner, S. Imada, A. B. Naden, J. T. S. Irvine, L. C. Duda, and A. R. Armstrong, "Effect of Cu substitution on anion redox behaviour in P3-type sodium manganese oxides," *JPhys Energy*, vol. 4, no. 4, 2022, doi: 10.1088/2515-7655/ac95cc.

[17] R. J. Clément, J. Billaud, A. Robert Armstrong, G. Singh, T. Rojo, P. G. Bruce, and C. P. Grey, "Structurally stable Mg-doped P2-$Na_{2/3}Mn_{1-y}Mg_yO_2$ sodium-ion battery cathodes with high rate performance: insights from electrochemical, NMR and diffraction studies," *Energy Environ. Sci.*, vol. 9, no. 10, pp. 3240–3251, 2016, doi: 10.1039/C6EE01750A.

[18] S. Y. Lee, J. H. Kim, and Y. C. Kang, "Electrochemical properties of P2-type $Na_{2/3}Ni_{1/3}Mn_{2/3}O_2$ plates synthesized by spray pyrolysis process for sodium-ion batteries," *Electrochim. Acta*, vol. 225, pp. 86–92, 2017, doi: 10.1016/j.electacta.2016.11.141.

[19] T. Risthaus, L. Chen, J. Wang, J. Li, D. Zhou, L. Zhang, D. Ning, X. Cao, X. Zhang, G.

Schumacher, M. Winter, E. Paillard, and J. Li, "P3 $Na_{0.9}Ni_{0.5}Mn_{0.5}O_2$ Cathode Material for Sodium Ion Batteries," *Chem. Mater.*, vol. 31, no. 15, pp. 5376–5383, 2019, doi: 10.1021/acs.chemmater.8b03270.

[20] S. Maddukuri, P. Valerie, and V. V. Upadhyayula, "Synthesis and Electrochemical Study of New P3 Type Layered $Na_{0.6}Ni_{0.25}Mn_{0.5}Co_{0.25}O_2$ for Sodium-Ion Batteries," *ChemistrySelect*, vol. 2, no. 20, pp. 5660–5666, 2017, doi: 10.1002/slct.201700376.

[21] L. G. Chagas, D. Buchholz, C. Vaalma, L. Wu, and S. Passerini, "P-type $Na_xNi_{0.22}Co_{0.11}Mn_{0.66}O_2$ materials: linking synthesis with structure and electrochemical performance," *J. Mater. Chem. A*, vol. 2, no. 47, pp. 20263–20270, 2014, doi: 10.1039/C4TA03946G.

[22] X. Chen, X. Zhou, M. Hu, J. Liang, D. Wu, J. Wei, and Z. Zhou, "Stable layered P3/P2 $Na_{0.66}Co_{0.5}Mn_{0.5}O_2$ cathode materials for sodium-ion batteries," *J. Mater. Chem. A*, vol. 3, no. 41, pp. 20708–20714, 2015, doi: 10.1039/c5ta05205j.

[23] Y. Shi, Z. Zhang, P. Jiang, A. Gao, K. Li, Q. Zhang, Y. Sun, X. Lu, D. Cao, and X. Lu, "Unlocking the potential of P3 structure for practical Sodium-ion batteries by fabricating zero strain framework for Na^+ intercalation," *Energy Storage Mater.*, vol. 37, no. February, pp. 354–362, 2021, doi: 10.1016/j.ensm.2021.02.020.

[24] M. Kalapsazova, G. F. Ortiz, J. L. Tirado, O. Dolotko, E. Zhecheva, D. Nihtianova, L. Mihaylov, and R. Stoyanova, "P3-Type Layered Sodium-Deficient Nickel-Manganese Oxides: A Flexible Structural Matrix for Reversible Sodium and Lithium Intercalation," *Chempluschem*, vol. 80, no. 11, pp. 1642–1656, 2015, doi: 10.1002/cplu.201500215.

[25] Z. Lu and J. R. Dahn, "*In Situ* X-Ray Diffraction Study of P2-$Na_{2/3}[Ni_{1/3}Mn_{2/3}]O_2$," *J. Electrochem. Soc.*, vol. 148, no. 11, p. A1225, 2001, doi: 10.1149/1.1407247.

[26] S. Zilinskaite, A. J. R. Rennie, R. Boston, and N. Reeves-McLaren, "Biotemplating: a sustainable synthetic methodology for Na-ion battery materials," *J. Mater. Chem. A*, vol. 6, no. 13, pp. 5346–5355, 2018, doi: 10.1039/C7TA09260A.

[27] A. R. West, *Solid state chemistry and its applications*. Wiley, 2014. doi: 10.1107/s0108768185002476.

[28] D. Walsh, S. C. Wimbush, and S. R. Hall, "Use of the Polysaccharide Dextran as a Morphological Directing Agent in the Synthesis of High-T_c Superconducting $YBa_2Cu_3O_{7-\delta}$ Sponges with Improved Critical Current Densities," *Chem. Mater.*, vol. 19, no. 4, pp. 647–649, 2007, doi: 10.1021/cm0626684.

[29] S. R. Hall, S. C. Wimbush, Y. Shida, and W. Ogasawara, "Biotemplated synthesis of superconducting plate-like $YBa_2Cu_3O_{7-\delta}$ using oligosaccharides," *Chem. Phys. Lett.*, vol. 507, no. 1–3, pp. 144–150, 2011, doi: 10.1016/j.cplett.2011.03.071.

[30] Z. Schnepp, "Biopolymers as a flexible resource for nanochemistry," *Angew. Chemie - Int. Ed.*, vol. 52, no. 4, pp. 1096–1108, 2013, doi: 10.1002/anie.201206943.

[31] R. Boston, *Chapter 1. Bioinspired Synthesis: History, Fundamentals and Outlook*, no.

4. 2019. doi: 10.1039/9781788015806-00001.

[32] B. L. Cushing, V. L. Kolesnichenko, and C. J. O'Connor, "Recent Advances in the Liquid-Phase Syntheses of Inorganic Nanoparticles," *Chem. Rev.*, vol. 104, no. 9, pp. 3893–3946, 2004, doi: 10.1021/cr030027b.

[33] S. Zilinskaite, N. Reeves-McLaren, and R. Boston, "Xanthan gum as a water-based binder for P3-$Na_{2/3}Ni_{1/3}Mn_{2/3}O_2$," *Front. Energy Res.*, vol. 10, no. August, pp. 1–11, Aug. 2022, doi: 10.3389/fenrg.2022.909486.

[34] R. Boston, A. Carrington, D. Walsh, and S. R. Hall, "Synthesis of spherical superconductors," *CrystEngComm*, vol. 15, no. 19, p. 3763, 2013, doi: 10.1039/c3ce40269j.

[35] D. Walsh, L. Arcelli, T. Ikoma, J. Tanaka, and S. Mann, "Dextran templating for the synthesis of metallic and metal oxide sponges," *Nat. Mater.*, vol. 2, no. 6, pp. 386–390, 2003, doi: 10.1038/nmat903.

[36] S. R. Hall, "Biomimetic Synthesis of High-T_c, Type-II Superconductor Nanowires," *Adv. Mater.*, vol. 18, no. 4, pp. 487–490, 2006, doi: 10.1002/adma.200501971.

[37] Z. Lu, R. A. Donaberger, and J. R. Dahn, "Superlattice ordering of Mn, Ni, and Co in layered alkali transition metal oxides with P2, P3, and O3 structures," *Chem. Mater.*, vol. 12, no. 12, pp. 3583–3590, 2000, doi: 10.1021/cm000359m.

[38] X. Ju, H. Huang, H. Zheng, P. Deng, S. Li, B. Qu, and T. Wang, "A facile method to hunt for durable high-rate capability $Na_{0.44}MnO_2$," *J. Power Sources*, vol. 395, no. May, pp. 395–402, 2018, doi: 10.1016/j.jpowsour.2018.05.086.

[39] Q. C. Wang, J. K. Meng, X. Y. Yue, Q. Q. Qiu, Y. Song, X. J. Wu, Z. W. Fu, Y. Y. Xia, Z. Shadike, J. Wu, X. Q. Yang, and Y. N. Zhou, "Tuning P2-Structured Cathode Material by Na-Site Mg Substitution for Na-Ion Batteries," *J. Am. Chem. Soc.*, vol. 141, no. 2, pp. 840–848, 2019, doi: 10.1021/jacs.8b08638.

[40] N. Sharma, N. Tapia-Ruiz, G. Singh, A. R. Armstrong, J. C. Pramudita, H. E. A. Brand, J. Billaud, P. G. Bruce, and T. Rojo, "Rate Dependent Performance Related to Crystal Structure Evolution of $Na_{0.67}Mn_{0.8}Mg_{0.2}O_2$ in a Sodium-Ion Battery," *Chem. Mater.*, vol. 27, no. 20, pp. 6976–6986, 2015, doi: 10.1021/acs.chemmater.5b02142.

[41] S. Guo, Y. Sun, P. Liu, J. Yi, P. He, X. Zhang, Y. Zhu, R. Senga, K. Suenaga, M. Chen, and H. Zhou, "Cation-mixing stabilized layered oxide cathodes for sodium-ion batteries," *Sci. Bull.*, vol. 63, no. 6, pp. 376–384, 2018, doi: 10.1016/j.scib.2018.02.012.

[42] D. Buchholz, L. G. Chagas, C. Vaalma, L. Wu, and S. Passerini, "Water sensitivity of layered P2/P3-$Na_xNi_{0.22}Co_{0.11}Mn_{0.66}O_2$ cathode material," *J. Mater. Chem. A*, vol. 2, no. 33, pp. 13415–13421, 2014, doi: 10.1039/c4ta02627f.

[43] M. S. Chae, A. Chakraborty, S. Kunnikuruvan, R. Attias, S. Maddukuri, Y. Gofer, D. T. Major, and D. Aurbach, "Vacancy-Driven High Rate Capabilities in Calcium-Doped $Na_{0.4}MnO_2$ Cathodes for Aqueous Sodium-Ion Batteries," *Adv. Energy Mater.*, vol. 10,

no. 37, pp. 1–7, 2020, doi: 10.1002/aenm.202002077.

[44] Y. Wang, A. Huq, and W. Lai, “Insight into lithium distribution in lithium-stuffed garnet oxides through neutron diffraction and atomistic simulation: $Li_{7-x}La_3Zr_{2-x}Ta_xO_{12}$ (x = 0-2) series,” *Solid State Ionics*, vol. 255, no. 230, pp. 39–49, 2014, doi: 10.1016/j.ssi.2013.11.017.

[45] M. Keller, D. Buchholz, and S. Passerini, “Layered Na-Ion Cathodes with Outstanding Performance Resulting from the Synergetic Effect of Mixed P- and O-Type Phases,” *Adv. Energy Mater.*, vol. 6, no. 3, pp. 1–11, 2016, doi: 10.1002/aenm.201501555.

[46] M. Bianchini, E. Gonzalo, N. E. Drewett, N. Ortiz-Vitoriano, J. M. Lopez Del Amo, F. J. Bonilla, B. Acebedo, and T. Rojo, “Layered P2-O3 sodium-ion cathodes derived from earth abundant elements,” *J. Mater. Chem. A*, pp. 3552–3559, 2018, doi: 10.1039/C7TA11180K.

[47] X. Wang, M. Tamaru, M. Okubo, and A. Yamada, “Electrode properties of P2-$Na_{2/3}Mn_yCo_{1-y}O_2$ as cathode materials for sodium-ion batteries,” *J. Phys. Chem. C*, vol. 117, no. 30, pp. 15545–15551, 2013, doi: 10.1021/jp406433z.

[48] B. Mortemard De Boisse, D. Carlier, M. Guignard, and C. Delmas, “Structural and Electrochemical Characterizations of P2 and New O3-$Na_xMn_{1-y}Fe_yO_2$ Phases Prepared by Auto-Combustion Synthesis for Na-Ion Batteries,” *J. Electrochem. Soc.*, vol. 160, no. 4, pp. A569–A574, 2013, doi: 10.1149/2.032304jes.

[49] J. Zhao, J. Xu, D. H. Lee, N. Dimov, Y. S. Meng, and S. Okada, “Electrochemical and thermal properties of P2-type $Na_{2/3}Fe_{1/3}Mn_{2/3}O_2$ for Na-ion batteries,” *J. Power Sources*, vol. 264, pp. 235–239, 2014, doi: 10.1016/j.jpowsour.2014.04.048.

[50] X. Wu, J. Guo, D. Wang, G. Zhong, M. J. McDonald, and Y. Yang, “P2-type $Na_{0.66}Ni_{0.33-x}Zn_xMn_{0.67}O_2$ as new high-voltage cathode materials for sodium-ion batteries,” *J. Power Sources*, vol. 281, pp. 18–26, 2015, doi: 10.1016/j.jpowsour.2014.12.083.

[51] Y. S. Wang, R. Xiao, Y. S. Hu, M. Avdeev, and L. Chen, “P2-$Na_{0.6}[Cr_{0.6}Ti_{0.4}]O_2$ cation-disordered electrode for high-rate symmetric rechargeable sodium-ion batteries,” *Nat. Commun.*, vol. 6, pp. 1–9, 2015, doi: 10.1038/ncomms7954.

[52] J. Chen, S. Zhong, X. Zhang, J. Liu, S. Shi, Y. Hu, and L. Wu, “High performance of hexagonal plates P2-$Na_{2/3}Fe_{1/2}Mn_{1/2}O_2$ cathode material synthesized by an improved solid-state method,” *Mater. Lett.*, vol. 202, pp. 21–24, 2017, doi: 10.1016/j.matlet.2017.05.084.

[53] Y. Liu, X. Fang, A. Zhang, C. Shen, Q. Liu, H. A. Enaya, and C. Zhou, “Layered P2-$Na_{2/3}[Ni_{1/3}Mn_{2/3}]O_2$ as high-voltage cathode for sodium-ion batteries: The capacity decay mechanism and Al_2O_3 surface modification,” *Nano Energy*, vol. 27, pp. 27–34, 2016, doi: 10.1016/j.nanoen.2016.06.026.

[54] G. Singh, N. Tapia-Ruiz, J. M. Lopez Del Amo, U. Maitra, J. W. Somerville, A. R. Armstrong, J. Martinez De Ilarduya, T. Rojo, and P. G. Bruce, “High Voltage Mg-Doped $Na_{0.67}Ni_{0.3-x}Mg_xMn_{0.7}O_2$ (x = 0.05, 0.1) Na-Ion Cathodes with Enhanced

Stability and Rate Capability," *Chem. Mater.*, vol. 28, no. 14, pp. 5087–5094, 2016, doi: 10.1021/acs.chemmater.6b01935.

[55] C. Y. Yu, J. S. Park, H. G. Jung, K. Y. Chung, D. Aurbach, Y. K. Sun, and S. T. Myung, "$NaCrO_2$ cathode for high-rate sodium-ion batteries," *Energy Environ. Sci.*, vol. 8, no. 7, pp. 2019–2026, 2015, doi: 10.1039/c5ee00695c.

[56] H. Yoshida, N. Yabuuchi, K. Kubota, I. Ikeuchi, A. Garsuch, M. Schulz-Dobrick, and S. Komaba, "P2-type $Na_{2/3}Ni_{1/3}Mn_{2/3-x}Ti_xO_2$ as a new positive electrode for higher energy Na-ion batteries," *Chem. Commun.*, vol. 50, no. 28, pp. 3677–3680, 2014, doi: 10.1039/C3CC49856E.

[57] N. Tapia-Ruiz, W. M. Dose, N. Sharma, H. Chen, J. Heath, J. W. Somerville, U. Maitra, M. S. Islam, and P. G. Bruce, "High voltage structural evolution and enhanced Na-ion diffusion in P2-$Na_{2/3}Ni_{1/3-x}Mg_xMn_{2/3}O_2$ ($0 \leq x \leq 0.2$) cathodes from diffraction, electrochemical and *ab initio* studies," *Energy Environ. Sci.*, vol. 11, no. 6, pp. 1470–1479, 2018, doi: 10.1039/c7ee02995k.

[58] Q. Liu, Z. Hu, M. Chen, Q. Gu, Y. Dou, Z. Sun, S. Chou, and S. X. Dou, "Multiangular rod-shaped $Na_{0.44}MnO_2$ as cathode materials with high rate and long life for sodium-ion batteries," *ACS Appl. Mater. Interfaces*, vol. 9, no. 4, pp. 3644–3652, 2017, doi: 10.1021/acsami.6b13830.

[59] G. Ma, Y. Zhao, K. Huang, Z. Ju, C. Liu, Y. Hou, and Z. Xing, "Effects of the starting materials of $Na_{0.44}MnO_2$ cathode materials on their electrochemical properties for Na-ion batteries," *Electrochim. Acta*, vol. 222, pp. 36–43, 2016, doi: 10.1016/j.electacta.2016.11.048.

[60] M. Xu, Y. Niu, C. Chen, J. Song, S. Bao, and C. M. Li, "Synthesis and application of ultra-long $Na_{0.44}MnO_2$ submicron slabs as a cathode material for Na-ion batteries," *RSC Adv.*, vol. 4, no. 72, pp. 38140–38143, 2014, doi: 10.1039/c4ra07355j.

[61] F. Sauvage, L. Laffont, J. M. Tarascon, and E. Baudrin, "Study of the insertion/deinsertion mechanism of sodium into $Na_{0.44}MnO_2$," *Inorg. Chem.*, vol. 46, no. 8, pp. 3289–3294, 2007, doi: 10.1021/ic0700250.

[62] E. Hosono, T. Saito, J. Hoshino, M. Okubo, Y. Saito, D. Nishio-Hamane, T. Kudo, and H. Zhou, "High power Na-ion rechargeable battery with single-crystalline $Na_{0.44}MnO_2$ nanowire electrode," *J. Power Sources*, vol. 217, pp. 43–46, 2012, doi: 10.1016/j.jpowsour.2012.05.100.

[63] K. Dai, J. Mao, X. Song, V. Battaglia, and G. Liu, "$Na_{0.44}MnO_2$ with very fast sodium diffusion and stable cycling synthesized *via* polyvinylpyrrolidone-combustion method," *J. Power Sources*, vol. 285, pp. 161–168, Jul. 2015, doi: 10.1016/j.jpowsour.2015.03.087.

[64] Q. Wang, B. Zhao, S. Zhang, X. Gao, and C. Deng, "Superior sodium intercalation of honeycomb-structured hierarchical porous $Na_3V_2(PO_4)_3$/C microballs prepared by a facile one-pot synthesis," *J. Mater. Chem. A*, vol. 3, no. 15, pp. 7732–7740, 2015, doi: 10.1039/c5ta00765h.

[65] J. Y. Hwang, S. M. Oh, S. T. Myung, K. Y. Chung, I. Belharouak, and Y. K. Sun, "Radially aligned hierarchical columnar structure as a cathode material for high energy density sodium-ion batteries," *Nat. Commun.*, vol. 6, pp. 1–9, 2015, doi: 10.1038/ncomms7865.

[66] X. Xiang, K. Zhang, and J. Chen, "Recent advances and prospects of cathode materials for sodium-ion batteries," *Adv. Mater.*, vol. 27, no. 36, pp. 5343–5364, 2015, doi: 10.1002/adma.201501527.

[67] N. Bucher, S. Hartung, A. Nagasubramanian, Y. L. Cheah, H. E. Hoster, and S. Madhavi, "Layered Na_xMnO_{2+z} in Sodium Ion Batteries–Influence of Morphology on Cycle Performance," *ACS Appl. Mater. Interfaces*, vol. 6, no. 11, pp. 8059–8065, Jun. 2014, doi: 10.1021/am406009t.

[68] X. Li, D. Wu, Y. N. Zhou, L. Liu, X. Q. Yang, and G. Ceder, "O3-type $Na(Mn_{0.25}Fe_{0.25}Co_{0.25}Ni_{0.25})O_2$: A quaternary layered cathode compound for rechargeable Na ion batteries," *Electrochem. commun.*, vol. 49, pp. 51–54, 2014, doi: 10.1016/j.elecom.2014.10.003.

[69] C. Liu, Z. G. Neale, and G. Cao, "Understanding electrochemical potentials of cathode materials in rechargeable batteries," *Mater. Today*, vol. 19, no. 2, pp. 109–123, 2016, doi: 10.1016/j.mattod.2015.10.009.

[70] R. Berthelot, D. Carlier, and C. Delmas, "Electrochemical investigation of the P2–Na_xCoO_2 phase diagram," *Nat. Mater.*, vol. 10, no. 1, pp. 74–80, 2011, doi: 10.1038/nmat2920.

[71] S. F. Linnell, M. Hirsbrunner, S. Imada, G. Cibin, A. B. Naden, A. V. Chadwick, J. T. S. Irvine, L. C. Duda, and A. R. Armstrong, "Enhanced Cycling Stability in the Anion Redox Material P3-Type Zn-Substituted Sodium Manganese Oxide," *ChemElectroChem*, vol. 9, no. 11, 2022, doi: 10.1002/celc.202200240.

[72] S. Kumakura, Y. Tahara, S. Sato, K. Kubota, and S. Komaba, "P′2-$Na_{2/3}Mn_{0.9}Me_{0.1}O_2$ (Me = Mg, Ti, Co, Ni, Cu, and Zn): Correlation between Orthorhombic Distortion and Electrochemical Property," *Chem. Mater.*, vol. 29, no. 21, pp. 8958–8962, Nov. 2017, doi: 10.1021/acs.chemmater.7b02772.

[73] S. Komaba, N. Yabuuchi, T. Nakayama, A. Ogata, T. Ishikawa, and I. Nakai, "Study on the reversible electrode reaction of $Na_{1-x}Ni_{0.5}Mn_{0.5}O_2$ for a rechargeable sodium-ion battery," *Inorg. Chem.*, vol. 51, no. 11, pp. 6211–6220, 2012, doi: 10.1021/ic300357d.

[74] T. Y. Yu, J. Kim, J. Y. Hwang, H. Kim, G. Han, H. G. Jung, and Y. K. Sun, "High-energy O3-$Na_{1-2x}Ca_x[Ni_{0.5}Mn_{0.5}]O_2$ cathodes for long-life sodium-ion batteries," *J. Mater. Chem. A*, vol. 8, no. 27, pp. 13776–13786, 2020, doi: 10.1039/d0ta04847j.

[75] S. Kumakura, Y. Tahara, K. Kubota, K. Chihara, and S. Komaba, "Sodium and Manganese Stoichiometry of P2-Type $Na_{2/3}MnO_2$," *Angew. Chemie - Int. Ed.*, vol. 55, no. 41, pp. 12760–12763, 2016, doi: 10.1002/anie.201606415.

[76] J. Y. Hwang, S. T. Myung, and Y. K. Sun, "Sodium-ion batteries: Present and future,"

Chem. Soc. Rev., vol. 46, no. 12, pp. 3529–3614, 2017, doi: 10.1039/c6cs00776g.

[77] Y. Terada, Y. Nishiwaki, I. Nakai, and F. Nishikawa, "Study of Mn dissolution from $LiMn_2O_4$ spinel electrodes using *in situ* total reflection X-ray fluorescence analysis and fluorescence XAFS technique," *J. Power Sources*, vol. 97–98, pp. 420–422, Jul. 2001, doi: 10.1016/S0378-7753(01)00741-8.

[78] N. Yabuuchi, M. Kajiyama, J. Iwatate, H. Nishikawa, S. Hitomi, R. Okuyama, R. Usui, Y. Yamada, and S. Komaba, "P2-type $Na_x[Fe_{1/2}Mn_{1/2}]O_2$ made from earth-abundant elements for rechargeable Na batteries," *Nat. Mater.*, vol. 11, no. 6, pp. 512–517, 2012, doi: 10.1038/nmat3309.

[79] N. Yabuuchi, H. Yoshida, and S. Komaba, "Crystal Structures and Electrode Performance of Alpha-$NaFeO_2$ for Rechargeable Sodium Batteries," *Electrochemistry*, vol. 80, no. 10, pp. 716–719, 2012, doi: 10.5796/electrochemistry.80.716.

[80] J. J. Ding, Y. N. Zhou, Q. Sun, and Z. W. Fu, "Cycle performance improvement of $NaCrO_2$ cathode by carbon coating for sodium ion batteries," *Electrochem. commun.*, vol. 22, no. 1, pp. 85–88, 2012, doi: 10.1016/j.elecom.2012.06.001.

[81] J. Zhai, H. Ji, W. Ji, R. Wang, Z. Huang, T. Yang, C. Wang, T. Zhang, Z. Chen, W. Zhao, A. Tayal, L. Jin, J. Wang, and Y. Xiao, "Suppressing the irreversible phase transition from P2 to O2 in sodium-layered cathode *via* integrating P2- and O3-type structures," *Mater. Today Energy*, vol. 29, p. 101106, 2022, doi: 10.1016/j.mtener.2022.101106.

[82] C. Chen, W. Hang, Y. Li, M. Zhang, K. Nie, J. Wang, W. Zhao, R. Qi, C. Zuo, Z. Li, H. Yi, and F. Pan, "P2/O3 biphasic Fe/Mn-based layered oxide cathode with ultrahigh capacity and great cyclability for sodium ion batteries," *Nano Energy*, vol. 90, no. PA, p. 106504, 2021, doi: 10.1016/j.nanoen.2021.106504.

[83] Y. N. Zhou, P. F. Wang, Y. Bin Niu, Q. Li, X. Q. Yu, Y. X. Yin, S. Xu, and Y. G. Guo, "A P2/P3 composite layered cathode for high-performance Na-ion full batteries," *Nano Energy*, vol. 55, no. September 2018, pp. 143–150, 2019, doi: 10.1016/j.nanoen.2018.10.072.

[84] M. Tang, W. C. Carter, and Y.-M. Chiang, "Electrochemically Driven Phase Transitions in Insertion Electrodes for Lithium-Ion Batteries: Examples in Lithium Metal Phosphate Olivines," *Annu. Rev. Mater. Res.*, vol. 40, no. 1, pp. 501–529, Jun. 2010, doi: 10.1146/annurev-matsci-070909-104435.

[85] C. Bischoff, O. Fitz, C. Schiller, H. Gentischer, D. Biro, and H.-M. Henning, "Investigating the Impact of Particle Size on the Performance and Internal Resistance of Aqueous Zinc Ion Batteries with a Manganese Sesquioxide Cathode," *Batteries*, vol. 4, no. 3, p. 44, 2018, doi: 10.3390/batteries4030044.

[86] P. F. Wang, Y. You, Y. X. Yin, Y. S. Wang, L. J. Wan, L. Gu, and Y. G. Guo, "Suppressing the P2–O2 Phase Transition of $Na_{0.67}Mn_{0.67}Ni_{0.33}O_2$ by Magnesium Substitution for Improved Sodium-Ion Batteries," *Angew. Chemie - Int. Ed.*, vol. 55, no. 26, pp. 7445–7449, 2016, doi: 10.1002/anie.201602202.

[87] J. Y. Hwang, S. T. Myung, D. Aurbach, and Y. K. Sun, "Effect of nickel and iron on structural and electrochemical properties of O3 type layer cathode materials for sodium-ion batteries," *J. Power Sources*, vol. 324, pp. 106–112, 2016, doi: 10.1016/j.jpowsour.2016.05.064.

[88] J. Sun, J. Shen, and T. Wang, "Electrochemical study of $Na_{0.66}Ni_{0.33}Mn_{0.67-x}Mo_xO_2$ as cathode material for sodium-ion battery," *J. Alloys Compd.*, vol. 709, pp. 481–486, 2017, doi: 10.1016/j.jallcom.2017.02.200.

[89] H. Yoshida, N. Yabuuchi, and S. Komaba, "$NaFe_{0.5}Co_{0.5}O_2$ as high energy and power positive electrode for Na-ion batteries," *Electrochem. commun.*, vol. 34, pp. 60–63, 2013, doi: 10.1016/j.elecom.2013.05.012.

[90] L. Zheng, J. Li, and M. N. Obrovac, "Crystal Structures and Electrochemical Performance of Air-Stable $Na_{2/3}Ni_{1/3-x}Cu_xMn_{2/3}O_2$ in Sodium Cells," *Chem. Mater.*, vol. 29, no. 4, pp. 1623–1631, 2017, doi: 10.1021/acs.chemmater.6b04769.

[91] L. Zheng and M. N. Obrovac, "Investigation of O3-type $Na_{0.9}Ni_{0.45}Mn_xTi_{0.55-x}O_2$ ($0 \leq x \leq 0.55$) as positive electrode materials for sodium-ion batteries," *Electrochim. Acta*, vol. 233, pp. 284–291, 2017, doi: 10.1016/j.electacta.2017.03.033.

[92] Q. Wang, S. Chu, and S. Guo, "Progress on multiphase layered transition metal oxide cathodes of sodium ion batteries," *Chinese Chem. Lett.*, vol. 31, no. 9, pp. 2167–2176, 2020, doi: 10.1016/j.cclet.2019.12.008.

[93] J. Xu, D. H. Lee, R. J. Clément, X. Yu, M. Leskes, A. J. Pell, G. Pintacuda, X.-Q. Yang, C. P. Grey, and Y. S. Meng, "Identifying the Critical Role of Li Substitution in P2–$Na_x[Li_yNi_zMn_{1-y-z}]O_2$ ($0 < x, y, z < 1$) Intercalation Cathode Materials for High-energy Na-Ion Batteries," *Chem. Mater.*, vol. 26, no. 2, pp. 1260–1269, Jan. 2014, doi: 10.1021/cm403855t.

[94] L. Yu, Z. Cheng, K. Xu, Y. X. Chang, Y. H. Feng, D. Si, M. Liu, P. F. Wang, and S. Xu, "Interlocking biphasic chemistry for high-voltage P2/O3 sodium layered oxide cathode," *Energy Storage Mater.*, vol. 50, no. May, pp. 730–739, 2022, doi: 10.1016/j.ensm.2022.06.012.

[95] A. Kulka, C. Marino, K. Walczak, C. Borca, C. Bolli, P. Novák, and C. Villevieille, "Influence of Na/Mn arrangements and P2/P′2 phase ratio on the electrochemical performance of Na_xMnO_2 cathodes for sodium-ion batteries," *J. Mater. Chem. A*, vol. 8, no. 12, pp. 6022–6033, 2020, doi: 10.1039/c9ta12176e.

[96] S. Guo, Y. Sun, J. Yi, K. Zhu, P. Liu, Y. Zhu, G. Zhu, M. Chen, M. Ishida, and H. Zhou, "Understanding sodium-ion diffusion in layered P2 and P3 oxides *via* experiments and first-principles calculations: a bridge between crystal structure and electrochemical performance," *NPG Asia Mater.*, vol. 8, p. e266, 2016, doi: 10.1038/am.2016.53.

[97] J. Ma, S. H. Bo, L. Wu, Y. Zhu, C. P. Grey, and P. G. Khalifah, "Ordered and disordered polymorphs of $Na(Ni_{2/3}Sb_{1/3})O_2$: Honeycomb-ordered cathodes for Na-ion batteries," *Chem. Mater.*, vol. 27, no. 7, pp. 2387–2399, 2015, doi: 10.1021/cm504339y.

[98] W. Zuo, J. Qiu, X. Liu, F. Ren, H. Liu, H. He, C. Luo, J. Li, G. F. Ortiz, H. Duan, J. Liu, M. S. Wang, Y. Li, R. Fu, and Y. Yang, "The stability of P2-layered sodium transition metal oxides in ambient atmospheres," *Nat. Commun.*, vol. 11, no. 1, pp. 1–12, 2020, doi: 10.1038/s41467-020-17290-6.

[99] M. Kalapsazova, P. Markov, K. Kostov, E. Zhecheva, D. Nihtianova, and R. Stoyanova, "Controlling at Elevated Temperature the Sodium Intercalation Capacity and Rate Capability of P3-$Na_{2/3}Ni_{1/2}Mn_{1/2}O_2$ through the Selective Substitution of Nickel with Magnesium," *Batter. Supercaps*, vol. 3, no. 12, pp. 1329–1340, 2020, doi: 10.1002/batt.202000137.

[100] X. Liu, X. Wang, A. Iyo, H. Yu, D. Li, and H. Zhou, "High stable post-spinel $NaMn_2O_4$ cathode of sodium ion battery," *J. Mater. Chem. A*, vol. 2, no. 36, pp. 14822–14826, 2014, doi: 10.1039/C4TA03349C.

[101] P. Zhan, S. Wang, Y. Yuan, K. Jiao, and S. Jiao, "Facile Synthesis of Nanorod-like Single Crystalline $Na_{0.44}MnO_2$ for High Performance Sodium-Ion Batteries," *J. Electrochem. Soc.*, vol. 162, no. 6, pp. A1028–A1032, 2015, doi: 10.1149/2.0891506jes.

[102] S. Komaba, T. Ishikawa, N. Yabuuchi, W. Murata, A. Ito, and Y. Ohsawa, "Fluorinated ethylene carbonate as electrolyte additive for rechargeable Na batteries," *ACS Appl. Mater. Interfaces*, vol. 3, no. 11, pp. 4165–4168, 2011, doi: 10.1021/am200973k.

[103] C. H. Mi, X. B. Zhao, G. S. Cao, and J. P. Tu, "*In Situ* Synthesis and Properties of Carbon-Coated $LiFePO_4$ as Li-Ion Battery Cathodes," *J. Electrochem. Soc.*, vol. 152, no. 3, p. A483, 2005, doi: 10.1149/1.1852438.

[104] W. Zuo, J. Qiu, X. Liu, B. Zheng, Y. Zhao, J. Li, H. He, K. Zhou, Z. Xiao, Q. Li, G. F. Ortiz, and Y. Yang, "Highly-stable P2–$Na_{0.67}MnO_2$ electrode enabled by lattice tailoring and surface engineering," *Energy Storage Mater.*, vol. 26, no. November 2019, pp. 503–512, Apr. 2020, doi: 10.1016/j.ensm.2019.11.024.

4 Ca-doped P3- and P2-$Na_{0.67-2x}Ca_xMn_{0.9}Mg_{0.1}O_2$

4.1 Introduction

In this chapter, NMMO is doped with Ca^{2+} with the aim of improving cycle life and capacity retention. Due to the similar ionic radii of the Ca^{2+} and Na^+ ions [1], the Ca^{2+} has been shown to insert into the Na-layer of the cathode material [2], [3]. Ca^{2+} is divalent, and so has a greater charge density than the Na^+ and causes a pillaring effect: making it harder for the TMO_2 layers to glide across one another and form new phases. Phase transitions are often harmful to capacity retention [4]–[12], and much research has been dedicated to minimising phase transitions and improve battery life. Ca^{2+} doping has become a well-known technique to achieve this and extend the cycle life of NIB cathode materials.

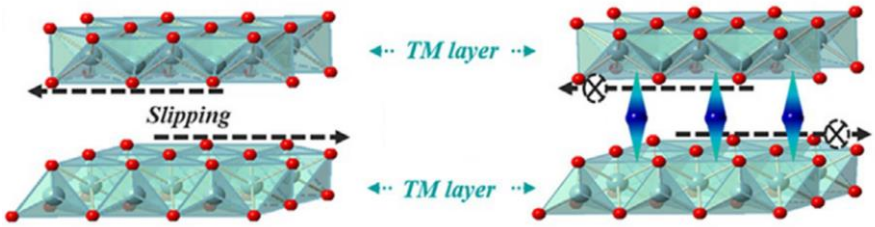

Figure 4-1: A schematic of the pillaring in layered materials. The TMO_2 layer is preventing from slipping after the addition of Ca^{2+} (dark blue balls) [13].

Transition metal migration into the alkali metal layer has been shown to improve cathode performance *via* the same pillaring mechanism, e.g. migration of Ni into the Na layer, induced by the addition of Co, in O3-$Na_{0.8}Ni_{0.3}Co_{0.1}Ti_{0.6}O_2$ [4]. The mechanism of this may be a result of the creation of Na-free layers due to random desodiation [14]. This is in contrast to Li-ion cathodes, particularly in Ni-containing materials [15], and other Na-ion cathodes [16] where cation-mixing is detrimental to the health of the battery. Induced by Co-doping, Ni migrates to the Na layer during the transition of the initial O3-$Na_{0.8}Ni_{0.3}Co_{0.1}Ti_{0.6}O_2$ to the P3 phase and prevents the reverse from occurring. This means that in the voltage range under examination, after the first charge the P3 phase is maintained throughout the rest of the procedure with no other obvious phase transformations (visible *via* XRD).

The outcome of the suppression of phase transitions is a reduction in lattice strain between charged and discharge states, with variations along the *a* and *c* axes between states equal to 0.7% and 0.08%, respectively. This variation is lower than even a "zero-strain" material [17]. Another aspect of the P3↔O3 phase transition being prevented is the reduced overpotential in the material. Overpotential is the driving force behind phase transitions [18]–[21], and so since no phase transitions occur, the overpotential is reduced which increases the energy efficiency of the cathode from 75% – 80% to 93%. It also greatly improves the rate capability and capacity retention (both at C/20 and C/2). After 300 cycles between 2.0 – 4.0 V vs Na/Na^+ at C/2, the capacity of the Co-doped

material falls from 83 mAh g^{-1} to 74 mAh g^{-1}, whereas the undoped sample falls from 72 mAh g^{-1} to 48 mAh g^{-1} within the same test parameters.

Similarly, Fe^{3+} has been used in P2-$Na_{0.67}Mn_{0.5}Co_{0.4}Fe_{0.1}O_2$ to prevent TMO_2 slabs from gliding across one another, preventing phase transitions [13]. 10% Fe doping increased the capacity retention from 69% for P2-$Na_{0.67}Mn_{0.5}Co_{0.5}O_2$ to 90% for P2-$Na_{0.67}Mn_{0.5}Co_{0.4}Fe_{0.1}O_2$. This is an example of how the reduction in lattice variation and eliminating phase transitions improves the capacity retention of battery materials. The reduction in lattice variation reduces the strain on the material, and greatly improves long term cycling performance [22]–[24]. Lattice strain does not always result in poor capacity retention, as there are several strategies to reduce capacity loss. However, in materials where phase transitions occur, lattice strain also occurs and causes capacity fade [9], [25]–[28]. Preventing it has a positive effect on capacity retention [17], [29]. A summary of the research into Ca doping is presented in Table 4-1.

Table 4-1: A summary of Ca doping papers. The samples were chosen based on the best performance in each study with respect to capacity and capacity retention. Initial capacity is given in mAh g^{-1}, capacity retention is calculated after 50 cycles.

Sample	Cycling regime (V vs Na/Na^+)	Initial capacity	Capacity retention	Ref.
P2-$Na_{0.6}Ca_{0.07}CoO_2$	2.0 – 4.0 V C/10	105	97%	[2]
P2-$Na_{0.625}Ca_{0.042}CoO_2$	2.0 – 4.0 C C/2	105	100%	[3]
P2-$Na_{0.62}Ca_{0.025}Ni_{0.33}Mn_{0.67}O_2$	2.0 – 4.2 V ~ C/3	130	69%	[30]
NASICON $Na_{2.79}Ca_{0.07}K_{0.07}V_2(PO_4)_3/C$	2.5 – 4.0 V 1C	99	91%	[31]
P2-$Na_{0.61}Ca_{0.03}Ni_{0.33}Mn_{0.67}O_{1.94}F_{0.06}$	2.0 – 4.3 V C/5	105	79%	[32]
O3-$Na_{0.93}Ca_{0.035}CrO_2$	1.5 – 3.8 V 10C	115	74%[1]	[33]
O3-$Na_{0.9}Ca_{0.05}CrO_2$	2.0 – 3.7 V C/5	124	90%	[34]
O3-$Na_{0.98}Ca_{0.01}Ni_{0.5}Mn_{0.5}O_2$	2.0 – 4.3 V C/2	198	88%	[35]
O3-$Na_{0.9}Ca_{0.05}Ni_{0.33}Fe_{0.33}Mn_{0.33}O_2$	2.0 – 4.0 V 1C	115	99%	[36]
P3-$Na_{0.52}Ca_{0.04}Ni_{0.33}Mn_{0.33}Co_{0.33}O_2$	2.5 – 4.2 V ~1C	140	87%	[37]
P3-$Na_{0.69}Ca_{0.04}CoO_2$	2.0 – 4.0 V N/A[2]	109	87%	[38]
P3-$Na_{0.69}Ca_{0.04}CoO_2$	2.0 – 3.7 V 1C	81	90%	[39]

Han *et al*. [2] show that improvements can be made to the capacity retention of P2-$Na_{0.73}CoO_2$ with as little as 2% Ca doping. The best results, however, came from increasing the mole fraction of Ca^{2+} in the host material to 7%. This led to a *c*-axis length of 10.8695 Å, reduced from 10.8807 Å in the undoped material; a reduction of 0.0112 Å. Previous reports of P2-$Na_{0.73}CoO_2$ found the c-axis length to be 10.8970 Å [40], so the significance

[1] Almost all the capacity fade occurs in the first 5 cycles. Capacity retention for cycles 5-55 is 95%.
[2] Likely 1C based on similar work [39].

of this difference is not clear. The Ca^{2+} were found, *via* Rietveld refinement, to occupy Na^{+} sites that are edge-sharing (2d Wyckoff site, or Na2) with the TMO_2 octahedra and thus there is less electrostatic repulsion between the two metal ions. Another effect of 7% Ca doping is the formation of 5 μm wide well-defined hexagonal pillars composed of 0.1 μm platelets, as opposed to rough, sphere-like 2 μm sized particles. This difference is caused by Ca^{2+} ions creating an increase in attractive forces between adjacent TMO_2 slabs.

Regarding the electrochemical performance, the voltage steps become more sloped with increasing Ca content, with smaller steps being diminished entirely. The molar fraction of Na^{+} that can be extracted decreases after 5% Ca doping. The differential capacity plots show peaks (correlating to voltage plateaux) decreasing in intensity/broadening, but not shifting in position, indicating that any structural changes/ordering steps occur at the same Na^{+} (+ Ca^{2+}) content, although they have been suppressed. In fact, *ex situ* XRD revealed a reduction in superlattice peaks at ~ 28 °2θ for the 7% Ca doped sample, showing the disruption of Na^{+}/vacancy ordering with increased Ca^{2+} content. The initial discharge capacity of the samples was 105-110 mAh g^{-1}, except the 10% Ca doped sample which had an initial capacity of 96 mAh g^{-1}. Over 60 cycles between 2.0 – 4.0 V vs Na/Na^{+} at C/10, the capacity of undoped P2-$Na_{0.73}CoO_2$ fell from 109 mAh g^{-1} to 74 mAh g^{-1}. For the sample doped with 2% Ca, the capacity after 60 cycles was 89 mAh g^{-1}. The capacity retention for both the 7% and 10% Ca samples was high: a capacity fade of 4 mAh g^{-1}. The 7% Ca sample also showed improved capacity over the undoped sample at 2C; 47 mAh g^{-1} compared to 7 mAh g^{-1}. The capacity recovery when resuming cycling at C/10 was also improved, showing little capacity decay. The high rate performance is likely due to the higher average diffusion coefficient of the Na^{+} in the 7% Ca-doped material than the undoped material (0.3 – 0.5 x 10^{-11} cm^2 s^{-1} and 0.07 – 0.3 x 10^{-11} cm^2 s^{-1}, respectively), facilitated by the absences caused by additional vacancies caused by divalent Ca^{2+} ions.

Another early example of Ca^{2+} pillaring in NIB cathodes is from Matsui *et al*. [3], in which P2-$Na_{0.67-2x}Ca_xCoO_2$ is doped *via* a solid-state reaction with 16.7%, 8.3%, and 4.2% Ca^{2+}, and compared to P2-$Na_{0.74}CoO_2$. The doped samples also show a drop in discharge capacity, as the molar fraction of Na^{+} that can be extracted is reduced because it is replaced by Ca^{2+} which are immobile. The doped samples also show a higher overpotential, as the Ca^{2+} in the alkali metal layer can hinder the diffusion of the Na^{+}, which is compounded by a shorter *c* lattice parameter. A side effect of this is to smoothen the voltage profile. The plateaux and steps in the voltage profile are caused by phase transitions and Na^{+}/vacancy ordering at specific sodium contents [41]. The ordering steps are disrupted because there are fewer sites the Na^{+} can occupy. The solid solution regions are expanded because the Ca-O bonds are stronger than Na-O, preventing large volume changes or layer gliding. Consequently, many of the steps and plateaux shrink or are smoothed out.

While the initial discharge capacities of the Ca-doped samples are lower, it retains its capacity much better than the undoped samples at higher currents. At a discharge charge current of 11 mA g^{-1} (C/20, 1C = 235 mA g^{-1}), the capacities of the undoped P2-$Na_{0.74}CoO_2$

and P2-$Na_{0.625}Ca_{0.042}CoO_2$ were 134 mAh g^{-1} and 124 mAh g^{-1}, respectively. At 1C, the capacity of the undoped sample begins to fall relative to the Ca-doped one. This is even more pronounced at 2.5C, wherein the capacity of the Ca-doped sample becomes higher than the undoped sample, after 115 cycles total. Cycling again at C/20, the doped sample delivered 94% of its original capacity, compared to 77% for the undoped sample. This shows the stability that Ca^{2+} doping lends the cathode; its structure is not degraded by cycling at high C-rates. An inactive sodium-poor phase is theorised to form during cycling, which limits to the capacity of the undoped sample and isn't present in the Ca-doped sample. The formation of a second phase creates interfacial stress from a lattice mismatch which reduces stability of the active material long term [42]. The addition of Ca^{2+} reduces the formation of this phase and hence the improved cycling performance. The cycling performance of the other samples was not shown or discussed, possibly because the reduction in capacity was too large in exchange for the capacity retention gained.

There are other mechanisms that increase the cycle life of cathode materials using Ca doping. A side-effect of preventing P2↔O2 phase transitions is that transition metal ion migration can be avoided. Although there is an example of Ni migration assisting with capacity retention [4], it generally has a negative impact on cathode performance. Ca doping is shown to prevent TM migration in P2-$Na_{0.67-2x}Ca_xNi_{0.33}Mn_{0.67}O_2$ when doped with x = 2.5% and 5% Ca^{2+} [30]. The migration occurs during the high voltage, low-Na transition to the O2 phase since Ni prefers octahedral environments and more Na^+ vacancies exist. A trade-off occurs here, with Ca doping leading to a reduction in capacity, particularly from the shortening of a voltage plateau above 4.1 V vs Na/Na^+ related to O redox – this is the result of Ca^{2+} altering the Ni-O bond hybridisation. The Ni *3d* and O *2p* orbitals shifts to lower energy, making the high-voltage reactions less accessible. Thus, the capacity at high voltages available in Ca-doped P2-$Na_{0.67-2x}Ca_xNi_{0.33}Mn_{0.67}O_2$ is lower, but both the capacity retention and rate capability are improved. After 50 cycles at 50 mA g^{-1} between 2.0 – 4.2 V, the undoped sample delivered 85 mAh g^{-1}, down from 140 mAh g^{-1}. The 2.5% Ca-doped sample delivered 90 mAh g^{-1}, down from 130 mAh g^{-1} with the same test parameters.

In this case, doping with Ca is combined with Mg to produce further benefits and illustrates that Mg/Ca co-doping is possible *via* a solid state reaction. The same has been shown with Ca/K co-doping [31] and Ca/F co-doping [32]. In the case of the former, the K^+ replaces the Na^+, just as the Ca^{2+} does, in $Na_3V_2(PO_4)_3$. For the latter, the F^- replaces the O^{2-} in the TMO_2 layer in P2-$Na_{0.67-x}Ca_xNi_{0.33}Mn_{0.67}O_{2-2x}F_{2x}$. In this material, the capacity retention and rate capability improvements are a result of maintaining the P2 phase throughout charging up to 4.3 V vs Na/Na^+ and avoiding the P2↔O2 phase transition, and lessening *c* axis expansion upon charging. Even 1% Ca/F co-doping improved the discharge capacity after 500 cycles at 1C from 25 mAh g^{-1} to 45 mAh g^{-1}. 3% and 5% both had discharge capacities of *ca.* 75 mAh g^{-1} after 500 cycles. All three doped samples performed similarly in rate capability testing: delivering 65 mAh g^{-1} at 5C. This shows that capacity retention and rate capability do not continually increase with higher levels

of doping, and that even 1% Ca/F doping can have a marked effect on the material performance, as can only Ca doping[43].

The examples so far have primarily focussed on P2-type cathodes. Ca^{2+} are stable in the P2 structure as the Na layer contains sites that are edge-sharing with the TMO_2 octahedra; therefore, divalent Ca^{2+} experiences less electrostatic repulsion from the neighbouring multivalent TM than if it occupied a face-sharing site. There are examples of both O3 and P3 phase materials that have been doped with Ca^{2+}. Ca doping of 3.5% of O3-$NaCrO_2$ [33] showed a reduction in TM migration into the Na layer and a subsequent improvement in capacity retention, even though there are no significant differences between the Ca-doped and undoped material visible in *operando* XRD. In both materials, the charge-discharge results in phase transitions from O3↔O'3↔P'3. This builds on similar work by Zheng *et al*. [34] which shows a reduction in interlayer distance with 5% Ca doping – which is mirrored in the work by Lee *et al*. [33].

The benefits seen repeatedly from Ca doping (enhanced capacity retention and rate capability) are seen with doping levels as low as x = 0.01, 0.02, and 0.03 at C/2 (based on 1C = 150 mA g^{-1}) between 2.0 – 4.3 V vs Na/Na^+ in O3-$Na_{1-2x}Ca_xNi_{0.5}Mn_{0.5}O_2$ [35]. The discharge capacity of these doped samples after 100 cycles is 145 mAh g^{-1}, 135 mAh g^{-1}, and 125 mAh g^{-1} respectively. In contrast, the discharge capacity of the undoped O3-$NaNi_{0.5}Mn_{0.5}O_2$ falls to 62 mAh g^{-1} under the same conditions. This material goes through a number of phase transitions; O3 (at 2.0 V vs Na/Na^+)↔O'3↔P3↔P'3 (at 4.0 V vs Na/Na^+)↔O3'↔O3'' (at 4.3 V vs Na/Na^+) [44]. As seen in previous studies, the volume changes in the material throughout cycling are lessened due to the Ca doping; 13.24% to 8.20%. Further, at the end of charge the ratio of O3' to O3'' in the doped ($x \approx 0.04$) material is less than in the undoped material (1:7 *vs* 1:4, respectively). There is a large disparity in *c* lattice parameter between these two phases, and since Ca doping suppresses that phase transition that increases the capacity retention of the doped material compared to the undoped one.

The effect of Ca doping of layered materials is often to reduce the interlayer distance, because the Ca-O bond is stronger than the Na-O bond [45], and the ionic radii are similar. However, in O3-$Na_{1-2x}Ca_xNi_{0.33}Fe_{0.33}Mn_{0.33}O_2$ the interslab distance (the size of the Na^+ layer) increases [36]. The authors note the increase in the lattice d spacing of the (101) as evidence of Ca^{2+} doping into the material bulk. In this study, 2.5% and 5% Ca doping is achieved, but the effects of 2.5% on the capacity retention are minor compared to other studies detailed here: after 200 cycles at 1C between 2.0 – 4.0 V vs Na/Na^+ the discharge capacity is 90 mAh g^{-1} rather than 82 mAh g^{-1} in the undoped material, down from 120 mAh g^{-1} and 122 mAh g^{-1}, respectively. 5% doping instead yielded much better capacity retention; 107 mAh g^{-1}, although the initial discharge capacity is 7 mAh g^{-1} lower than the undoped material. There are few differences between any of the materials in the rate capability testing. At the higher C-rate, 10C, the 5% Ca-doped cathode delivered 87 mAh g^{-1}, whereas both the undoped and 2.5% Ca-doped material both delivered 84 mAh g^{-1}. This is likely to be due to the high Na^+ diffusion coefficient of the undoped materials,

which Ca doping does not appear to significantly affect. The phase progression seen in *operando* XRD (Figure 4-2) shows only an O3 and a P3 phase, with a voltage plateau when the two phases coexist. The 2.5% Ca-doped sample showed a wider voltage range in which the P3 was present than the undoped sample.

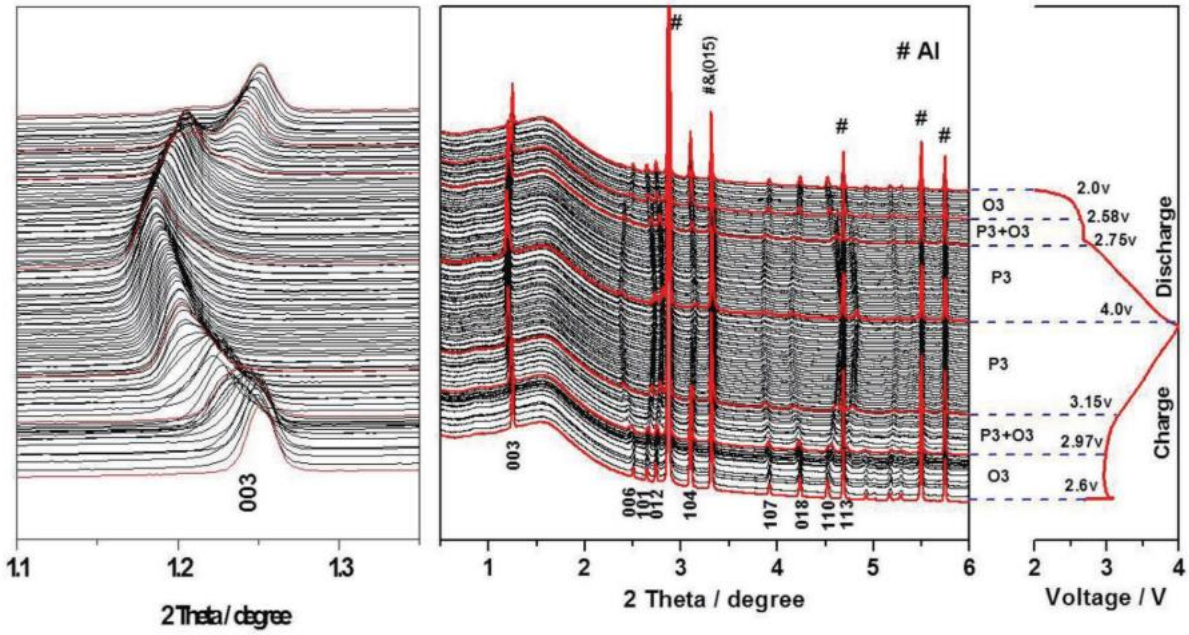

Figure 4-2: Operando *XRD patterns collected during the charge/discharge cycle of O3-$Na_{0.9}Ca_{0.05}Ni_{0.33}Fe_{0.33}Mn_{0.33}O_2$, cycled between 2.0 – 4.0 V at C/10* [36].

There are several examples of the P3 phase being doped with Ca in which the same benefits are seen as in other layered oxide structures. P3-$Na_{0.6-x}Ca_xNi_{0.33}Mn_{0.33}Co_{0.33}O_2$ (x = 0.02, 0.04, 0.08) has been reported to show enhanced capacity retention during cycling, enhanced Na^+ mobility and the suppression of the irreversible O'3→O1 phase transition [37]. Notably, the P3 material had crystallites making up agglomerates of size 5 – 10 µm, much larger than other layered materials, particularly P3-type. This may be caused by the long calcination (36 h at 350 °C under O_2) and the large particle size of the hydroxide precursor. In this study [37], doping with 8% Ca led to the formation of a NiO impurity due to the slow diffusion of Ca^{2+} during the reaction. The Ca doping in general also leads to lattice expansion because of the extra Ca^{2+}-TM repulsion. This does not occur in P2 structures due to the Ca^{2+} occupying a prismatic site that is edge-sharing on both ends with the TMO_2 octahedra. This site does not exist in P3 structures, where all the prismatic sites are face-sharing on one end and edge-sharing on the other (Figure 4-3). The effect of the lattice expansion may be a decrease in hysteresis in the charge-discharge profiles, as the Na^+ migration barrier is suppressed.

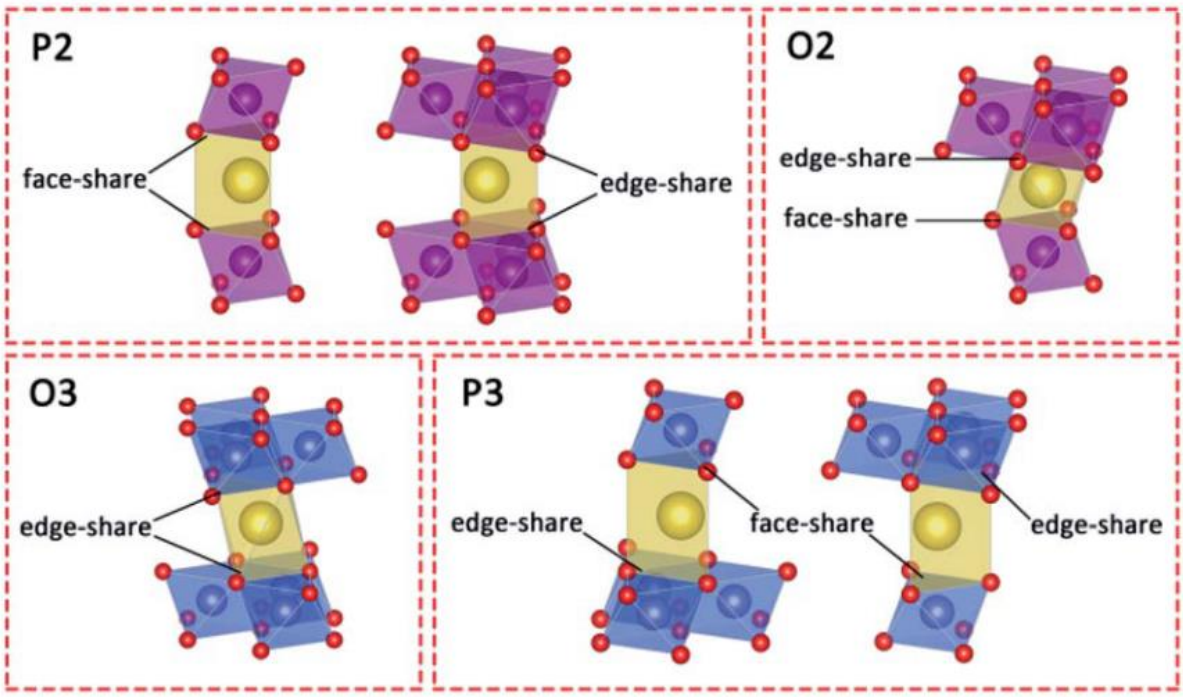

Figure 4-3: Schematic of the different Na sites in P-type and O-type layered oxide structures [30].

This system phase transitions from P3 into O'3 at approximately 4.4 V vs Na/Na^+, then O1 at 4.5 V vs Na/Na^+ during charge. During discharge, the P3 is reformed *via* the O'3 phase, and eventually an O3 phase is seen at 2.2 V vs Na/Na^+. 4% Ca doping suppresses the formation of the O1 phase, and in doing so improves the capacity retention after 100 cycles between 2.5 – 4.2 V vs Na/Na^+ at 200 mA g^{-1} (1C ≈ 175 mA g^{-1}) from 68% to 77% (177 mAh g^{-1} to 121 mAh g^{-1}, and 173 mAh g^{-1} to 134 mAh g^{-1}, respectively). It also improves the discharge capacity above 400 mAh g^{-1}, but below this (10 mA g^{-1} – 200 mA g^{-1}) the undoped material has a higher capacity.

A study into P3-$Na_{0.81}CoO_2$ *vs* P3-$Na_{0.69}Ca_{0.04}CoO_2$ [38] showed that 4% Ca doping drastically improved capacity retention. The undoped material has an initial discharge capacity of 138 mAh g^{-1}, which is higher than the Ca-doped material (131 mAh g^{-1}). After 100 cycles between 2.0 – 4.0 V vs Na/Na^+ the materials delivered 25.6% and 80.8%, respectively, of their initial capacities. The capacity loss is mitigated in P3-$Na_{0.81}CoO_2$ by lowering the upper voltage limit to 3.7 V vs Na/Na^+ which is proposed to avoid the P'3 to O'3 transitions. The Ca-doped material also shows a lower hysteresis from the expanded *c* lattice parameter, as seen in other Ca-doped P3 materials. The O'3 phase is present in the Ca-doped material but does not suffer the same capacity loss. The reason for this may be the suppression of this transition, as well as suppression of O1 formation by Ca^{2+} pinning the TMO_2 slabs. Later work from the same group [39] show that Na^+ extraction and the subsequent P'3↔O'3 transition in P3-$Na_{0.81}CoO_2$ results in Co ions migrating into the alkali metal layer and form Co_3O_4. This is suppressed when the alkali layer contains Ca^{2+} because it repels the Co ions, and so migration is prevented.

The research thus far demonstrates an effective strategy to improve the capacity retention of NIBs, often at the temporary expense of discharge capacity. The cathodes investigated use unsustainable materials. As discussed in Chapter 1 Introduction, cobalt and nickel are expensive due to their low abundance [46] which will affect supply (or has already) [47], and chromium is toxic [48]. These issues mean that despite the success of Ca doping the cathodes developed are unlikely to be ideal candidates for large scale storage. The constituent ions in P-type $Na_{0.67}Mn_{0.9}Mg_{0.1}O_2$ (NMMO) are more abundant than cobalt, nickel, and chromium [48] and have shown to produce high capacity cathodes. Therefore, an investigation into enhancing the capacity retention of P-type NMMO is warranted. From the outcome of Chapter 3, Ca doping should be attempted in both P2- and P3-NMMO as both displayed high capacities.

Also identified in Chapter 3 is that biotemplating is an effective way to generate both the P2 and P2 structures of layered oxide cathodes. All samples here are synthesised *via* biotemplating. Part of the reasoning for this is the performance and phase purity of the biotemplated samples in comparison to solid state synthesised NMMO, shown in Chapter 3. Another consideration was the ease of generating several samples with different doping levels; biotemplating synthesis includes a dissolution step which can encourage good dispersion of any dopants and so the pillaring effect of the Ca^{2+} is spread throughout the crystal structure, particularly at low levels. Given that long calcination times are required to produce the layered oxide structure to allow time for diffusion of ions to occur, it may be difficult to ensure good dispersion of Ca throughout the sample. Even if good dispersion can be obtained, phase pure P3-NMMO cannot be synthesised *via* solid state synthesis.

4.2 Aims

In Chapter 3, we identified that biotemplating can generate phase pure P3 and P2-NMMO with high capacities. However, both materials suffered from capacity loss of 73% over 50 cycles at C/5. These capacity retention figures are in line with other reported NMMO samples, but less than (most of) the Ca-doped samples listed in Table 4-1. Here, we test the effect of Ca^{2+} doping, the host NMMO material, prepared by substituting $2x$ mol Na^+ with x mol Ca^{2+}. The stoichiometric ratio accounts for the difference in charge between Na^+ and Ca^{2+}, and maintains the charge balance, average oxidation state of the Mn, and the prismatic structure. The result of this should be an increase in the *c* lattice parameter of the material for the P3 material [37], but a decrease for the P2-type [2]. In terms of electrochemical properties there should be a reduced hysteresis in the charge-discharge profiles, translating to increased rate capability [33]. Finally, the capacity retention of the materials should increase as phase transitions are suppressed [32] – which should be reflected in the differential capacity graphs.

The aim of NIB development is the increased sustainability of the energy sector, the possibility of reduced calcination times (and thus lower energy requirements) can be realised with biotemplating. To this end, the calcination of P3- and P2-$Na_{0.67}$-

$_{2x}Ca_xMn_{0.9}Mg_{0.1}O_2$ (NCMM) was shortened to 2 h with a ramp rate of 10 °C min^{-1} [49]–[53]. P3-NCMM was calcined at 650 °C [50], [52], and P2-NCMM at 900 °C. This results in a total heat treatment time of 4 h and 5 h, respectively. 50% and 40% of the total heat treatment time was spent at the final heat treatment temperature. Doping levels of Ca^{2+} were selected at 0%, 1%, and 2 (atomic) %. All Ca % quoted here refer to atomic fraction.

In this chapter, the sample powders are synthesised and examined by XRD once, examined by SEM once, and one sample powder is used to make the cathode material. From the cathode material, three cells are made to test the discharge capacity over 50 cycles, and one is used to test the rate capability.

4.3 Results and discussion

4.3.1 XRD

4.3.1.1 P3-NCMM

P3-NCMM samples are successfully synthesised *via* biotemplating at 650 °C for 2 h. The structures form their ideal *R*3*m* space group, as confirmed by XRD and Rietveld refinements. Shown in Figure 4-4a and b, the 0% and 1% P3-NCMM phases form without impurities, indicating that the biotemplating synthesis successfully forms the P3 layered structure. In the 2% Ca-doped sample, the P3-NCMM also forms. There are minor peaks, marked *, which may correspond to $Ca_2Mn_3O_8$ [54]. These impurities suggest that there is a solution limit to the Ca doping of P3-NMMO. Since doping NCMM with 2% Ca starts to lead to impurities, doping beyond this point was not examined electrochemically. There are no significant changes with respect to peak broadening, heights, or positions. The difference that Ca doping makes to the unit cell appears minimal is borne out in the Rietveld refinement results displayed in Table 4-2. Further Rietveld detail can be found in the Appendix.

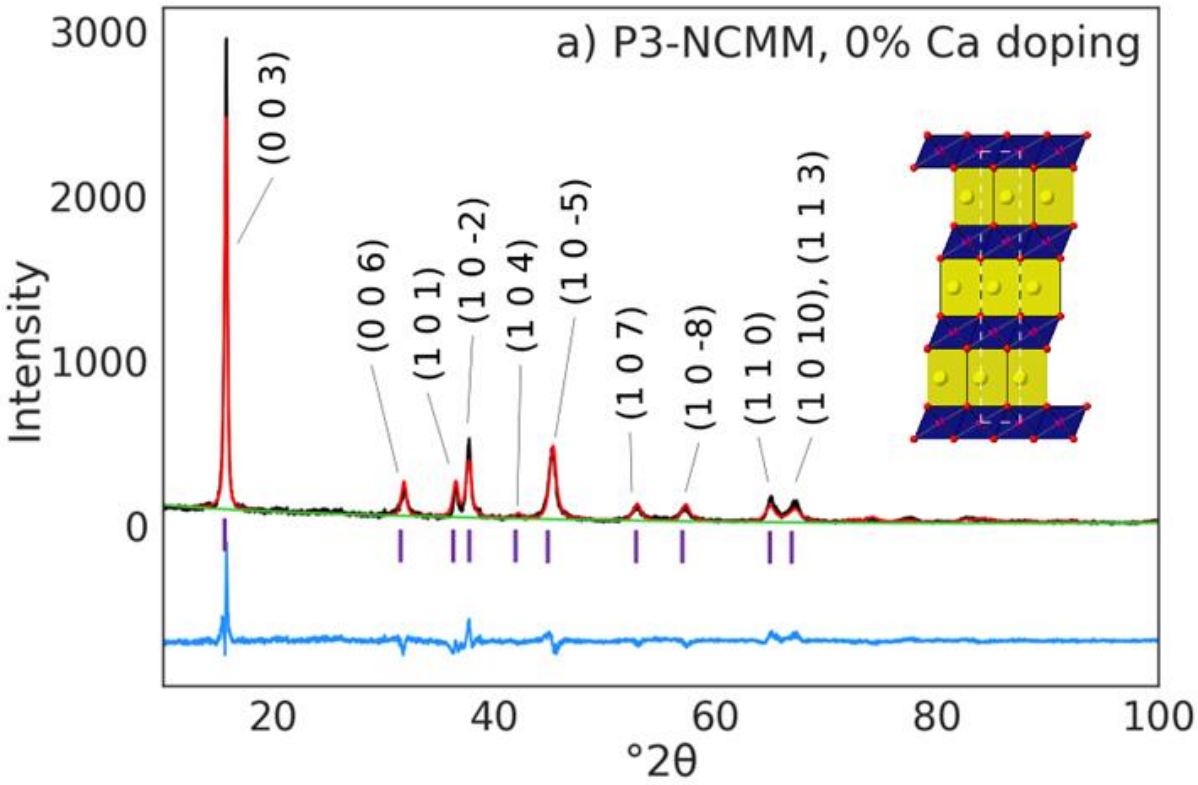
a) P3-NCMM, 0% Ca doping
Intensity
°2θ
(0 0 3)
(0 0 6)
(1 0 1)
(1 0 -2)
(1 0 4)
(1 0 -5)
(1 0 7)
(1 0 -8)
(1 1 0)
(1 0 10), (1 1 3)

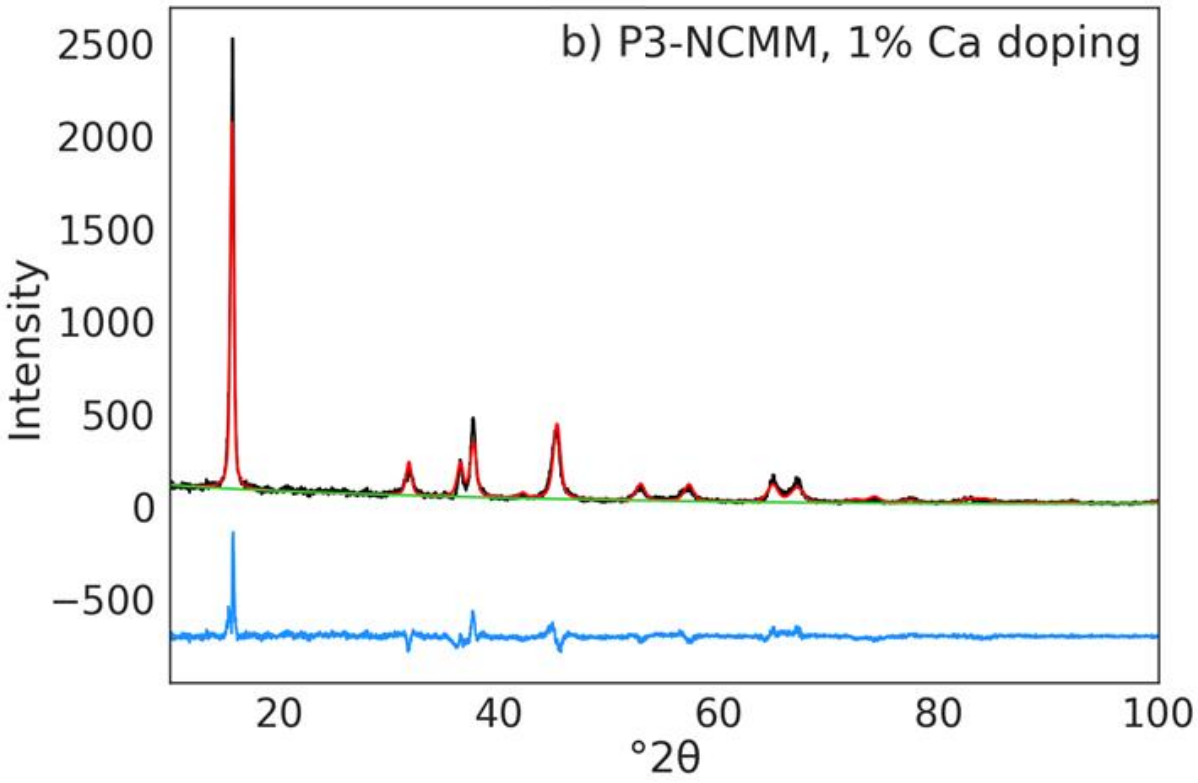
b) P3-NCMM, 1% Ca doping
Intensity
°2θ

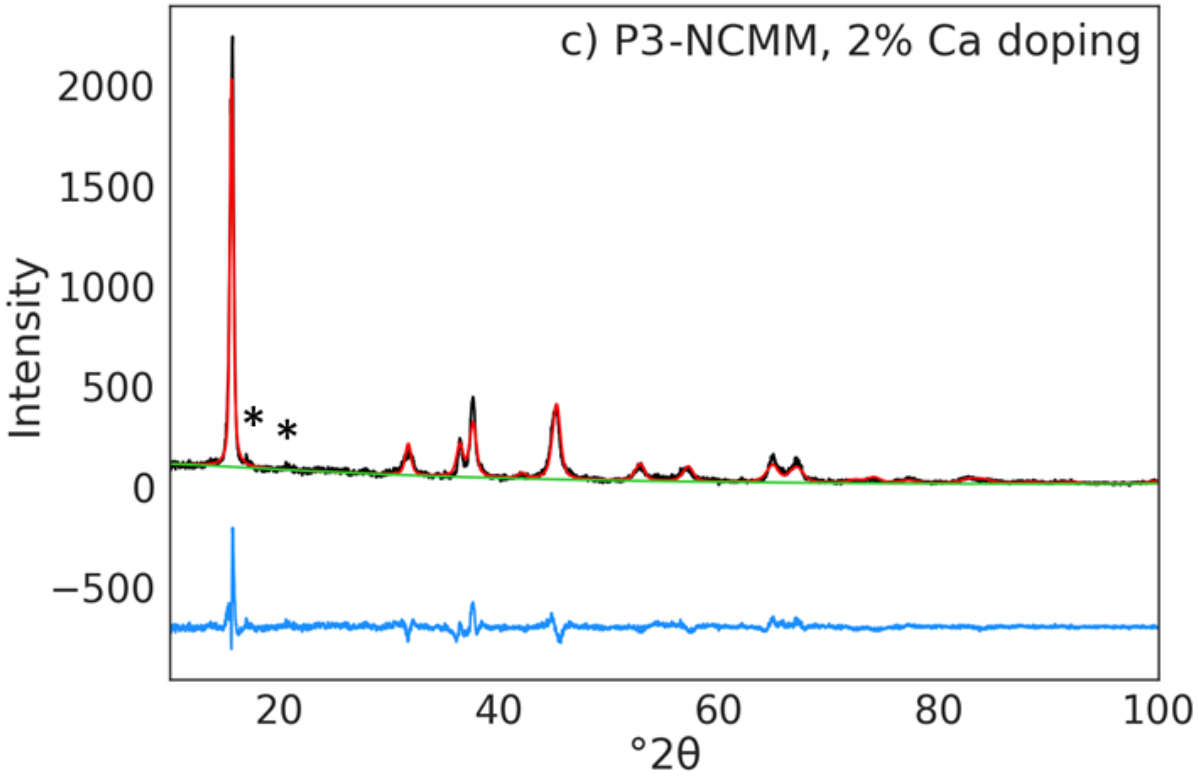

*Figure 4-4: XRD pattern (black), Rietveld refinement (red), background (green), and difference pattern (blue) of P3-NCMM doped with (a) 0% Ca, (b) 1% Ca, and (c) 2% Ca. Inset with a schematic of the crystal structure. Impurity peaks marked with *.*

Table 4-2: Refined structural parameters of each P3-NCMM sample.

Sample	Space group	*a* (Å)	*c* (Å)	R_{wp} (%)	GOF
0% Ca P3-NCMM	*R*3*m*	2.867(1)	16.843(5)	17.3	1.48
1% Ca P3-NCMM	*R*3*m*	2.868(1)	16.856(6)	18.7	1.60
2% Ca P3-NCMM	*R*3*m*	2.871(2)	16.898(7)	18.7	1.59

There is then a pattern of increasing *c* lattice parameters as Ca doping is increased for P3-NCMM. However, the increases are small. There are no significant changes (greater than 3 standard deviations) in either the *a* or *c* lattice parameter. A similar investigation into an O3-type material found that 5% Ca doping resulted in a 0.2 Å increase in the lattice spacing of the (101) plane, according to the research group [36]. Here the increases in the (101) for the P3 material are 0.0016 Å (0% → 1%) and 0.0062 Å (0% → 2%), not likely to indicate Ca doping into the alkali layer. A difference in *d* spacing two orders of magnitude higher would be more likely to indicate Ca doping the Na site.

The doubled electrostatic attraction between Ca^{2+}-O^{2-} compared to Na^{+}-O^{2-}, with only a minor change in effective ionic radii (1.00 Å *vs* 1.02 Å [1], respectively), causes the *c* lattice

parameter to decrease in P2-type and O3-type materials [2], [3], [35]. It is shown in P3-type $Na_{0.6-x}Ca_xNi_{0.33}Mn_{0.33}Co_{0.33}O_2$ [37] that the *c* lattice parameter actually increases with Ca doping. In that instance, 2% Ca doping increased the *c* lattice parameter by 0.007 Å, whereas in this work the increase is 0.064 Å. It is posited [35] that an increase in lattice parameter would occur if the Ca^{2+} replaced a transition metal (TM) layer ion, rather than the Na^+, for example, if the Ca^{2+} replaced the Mg^{2+}, Mn^{3+}, or Mn^{4+} (1.00 Å *vs* 0.72 Å [1], 0.58 Å, and 0.54 Å, respectively).

The increasing lattice parameters therefore suggest that the Ca^{2+} is doping the layered structure, but not in the Na layer. To determine where the Ca^{2+} is in the crystal, its position was allowed to refine freely in Rietveld refinements. Ca^{2+} was found to refine to either $z = 0.05(2)$ or $z = 0.32(2)$, depending on its initial value. This puts the Ca^{2+} approximately in the TM layer, which has not been observed before. Schematics of the 2% Ca P3-NCMM are shown in Figure 4-5. Figure 4-5a shows the Ca^{2+} when its coordinates are constrained to be equal to Na^+: occupies the sodium site. When $z = 0.05$ (Figure 4-5b) the Ca^{2+} sits on the boundary between the TM and Na^+ site. The final option is $z = 0.32(2)$, where the Ca^{2+} occupies a tetragonal site in between the $Mn^{3+/4+}$- and Mg^{2+}-occupied octahedra. This position makes more physical sense than the having the Ca^{2+} positioned within the O^{2-} layer, as it is too close to the other metal cations.

The position of the Ca^{2+} does not meaningfully affect the Rietveld R_{wp} or GOF output. Table 4-3 shows the Rietveld refinements of each P3-NCMM sample when the Ca^{2+} is constrained to the Na^+ site, and the fit matches well with the observed data. Although the R_{wp} is high (> 10%), the GOF is good [55]. The effect of the different Ca^{2+} positions has a negligible effect on either of these parameters.

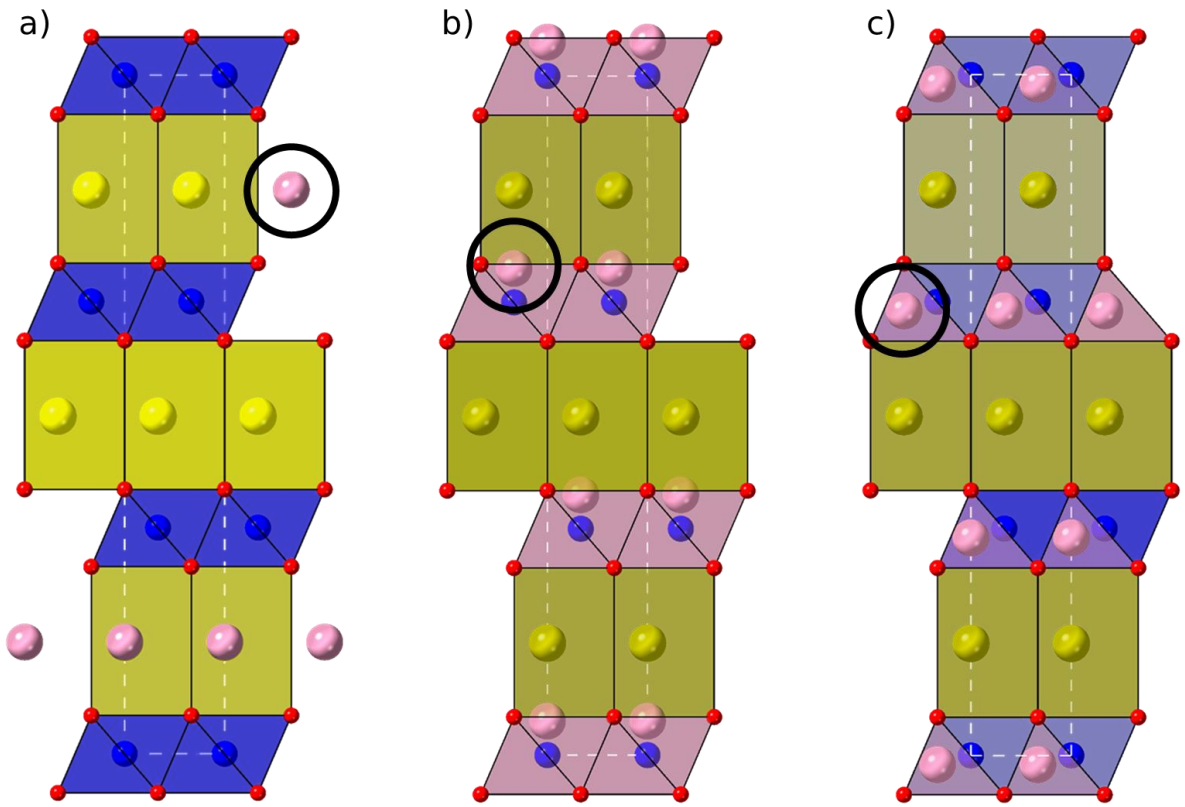

Figure 4-5: Crystal structures of 2% Ca P3-NCMM with the Ca^{2+} in different z coordinates. (a) Ca^{2+} on the Na^{+} site (z = 0.1645(6)), (b) Ca^{2+} at z = 0.05(2), (c) Ca^{2+} at z = 0.32(2). Ca^{2+} is highlighted by a black circle. Na^{+} are shown as yellow spheres, $Mn^{3+/4+}$ and Mg^{2+} are represented by blue spheres. O^{2-} are represented by red spheres and which have been resized for visibility.

From these data, and the XRD data showing an increase in lattice parameter of the P3-NCMM, suggests that the Ca^{2+} is not replacing Na^{+}. The unit cell parameters should increase with Ca^{2+} doping, but it is unlikely it would increase to this degree if this were the case. It suggests that the Ca^{2+} is being incorporated into the TM layer instead. From the three crystal structures derived from Rietveld refinements, the Ca^{2+} in the tetrahedral interstitial site seems to be the best fit; it has the lowest GOF and R_{wp} values. The previous research into Ca doping of P3 materials does not report a problem with Ca^{2+} position within the P3 structure. There have only been two unique P3 Ca-doped formulations reported, and so it's possible that difficulties with Ca^{2+} in the P3 structure have not been fully identified.

Similarly, the Ca^{2+} may be incompatible with the NMMO material. In $Na_{0.67-2x}Ca_xMn_{0.9}Mg_{0.1}O_2$ the Mn has an average oxidation state of 3.48. Mn^{3+} is Jahn-Teller active, which causes distortions in the cathode during cycling [56]. It's possible that the distortions of Mn^{3+} in the TMO_2 octahedra create a stable site for the Ca^{2+} to occupy. The distortion in Jahn-Teller active Mn^{3+} is shown in Figure 4-6. The solid solution limit for layered materials varies too. For some materials the limit is below 2% [35], and for others, at least 10% Ca doping is achievable [34]. The incorporation of the Ca^{2+} is not

guaranteed, but the changes in lattice parameter suggest that the lattice is changing, but not necessarily in line with previous research.

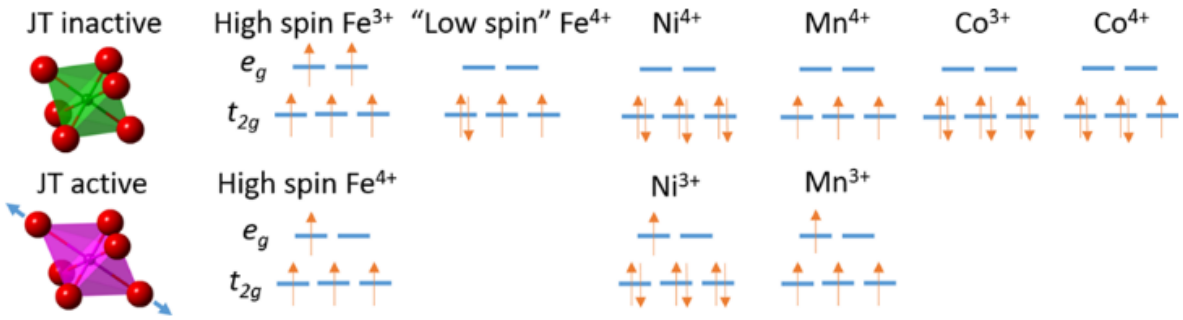

Figure 4-6: Schematic showing the Jahn-Teller distortion in TMO_2 octahedra [56].

The Ca^{2+} position has implications for the electrochemical performance. The divalent nature of the ion when in the Na^+ layer should cause it to pin the TM layer. This in turn discourages phase transitions, where the TM layers glide over each other to change the Na^+ environment from prismatic to octahedral (or *vice versa*) [57]. The data suggest that the Ca^{2+} residing in a tetrahedral site in the TM layer. This will likely mean that it is not going to achieve this pillaring effect, as the Ca^{2+} will be too far from the adjacent TMO_2 layer to stop it from gliding. Ideally, Ca^{2+} is positioned between the two layers to form Ca-O bonds with adjacent layers, but the closer Ca^{2+} moves towards one layer, the bonds with the oxide ions in the other layer get weaker and there will be interference from shielding from other nearby ions.

Table 4-3: Refined structural parameters of 1% Ca and 2% Ca P3-NCMM samples, for three different Ca^{2+} positions.

Sample	Ca^{2+} position	*a* (Å)	*c* (Å)	R_{wp} (%)	GOF
1% Ca P3-NCMM	*z* = 0.16 (Na^+ site)	2.868(1)	16.857(6)	18.7	1.60
1% Ca P3-NCMM	*z* = 0.05	2.868(1)	16.856(6)	18.3	1.57
1% Ca P3-NCMM	*z* = 0.33	2.868(1)	16.855(6)	18.3	1.56
2% Ca P3-NCMM	*z* = 0.16 (Na^+ site)	2.871(1)	16.899(7)	18.7	1.59
2% Ca P3-NCMM	*z* = 0.05	2.869(1)	16.873(6)	18.1	1.54
2% Ca P3-NCMM	*z* = 0.32	2.869(1)	16.865(3)	18.0	1.52

4.3.1.2 P2-NCMM

P2-NCMM is successfully synthesised *via* biotemplating at 900 °C for 2 h. In all cases, 0%, 1%, and 2% Ca, the NCMM forms the ideal $P6_3/mmc$ space group (Figure 4-7). Further Rietveld detail can be found in the Appendix. The 0% Ca and 1% Ca P2-NCMM do not

show any impurity phases in the XRD, as with the P3-NCMM, although there is a minor peak at 22 °2θ that likely corresponds to superstructure ordering [58]. At 2% an impurity phase becomes visible. The impurity peaks, marked *, match with a *Pbam* tunnel structure seen in $Na_{0.44}MnO_2$ [59]–[61], similar to the impurity phase seen in P3-NMMO synthesised *via* a solid state reaction in Chapter 3. This material is used as a cathode and is electrochemically active. *Via* Rietveld, the phase fraction of this impurity is 1.4%. It's possible that the impurity is a Ca-doped analogue of $Na_{0.4}MnO_2$. Although a different impurity to that seen in 2% Ca P3-NCMM, it shows that the doping of the host NMMO material is not trivial, regardless of whether the P3 or P2-type structure is investigated.

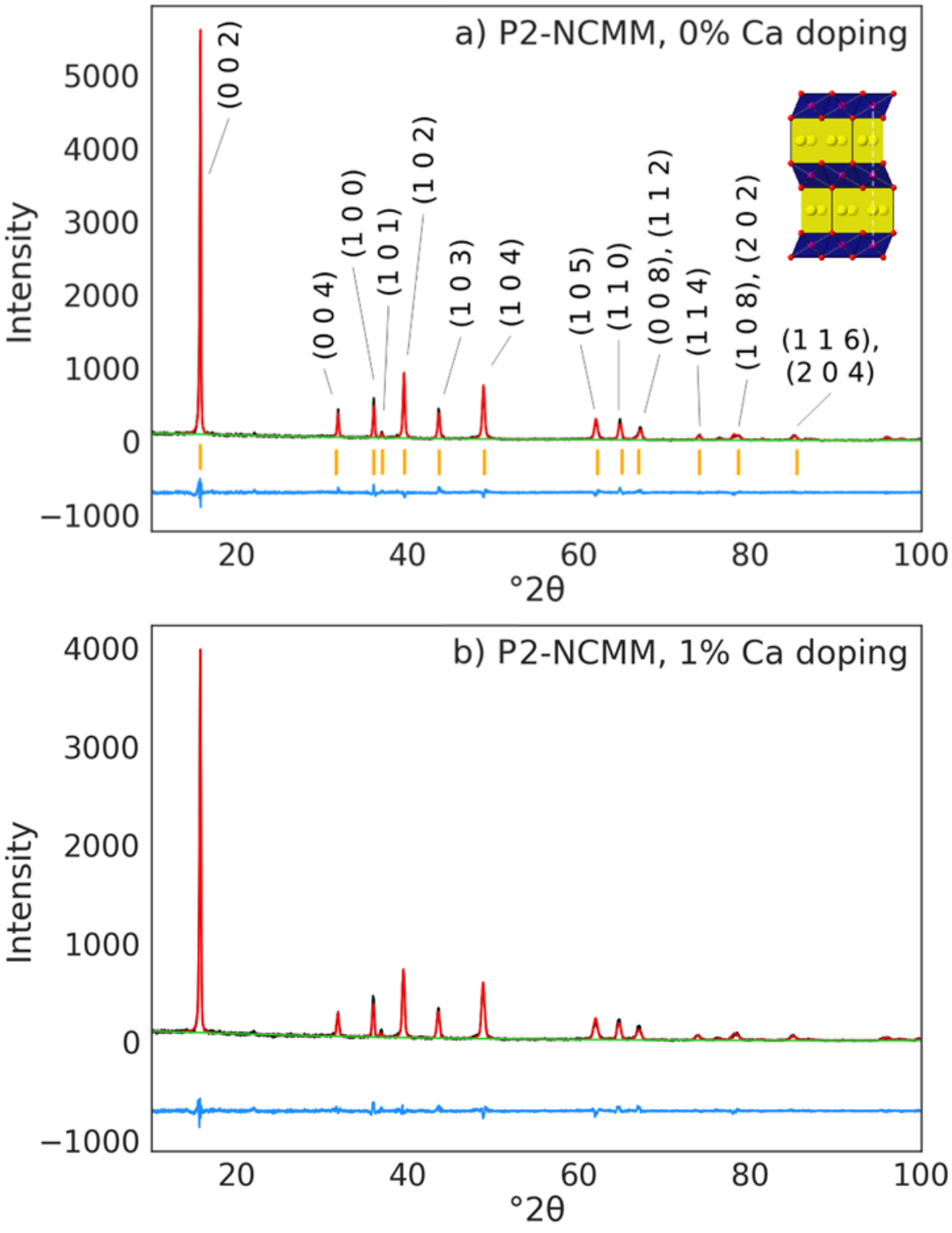
a) P2-NCMM, 0% Ca doping
(0 0 2)
(0 0 4)
(1 0 0)
(1 0 1)
(1 0 2)
(1 0 3)
(1 0 4)
(1 0 5)
(1 1 0)
(0 0 8), (1 1 2)
(1 1 4)
(1 0 8), (2 0 2)
(1 1 6), (2 0 4)
Intensity
°2θ
b) P2-NCMM, 1% Ca doping
Intensity
°2θ

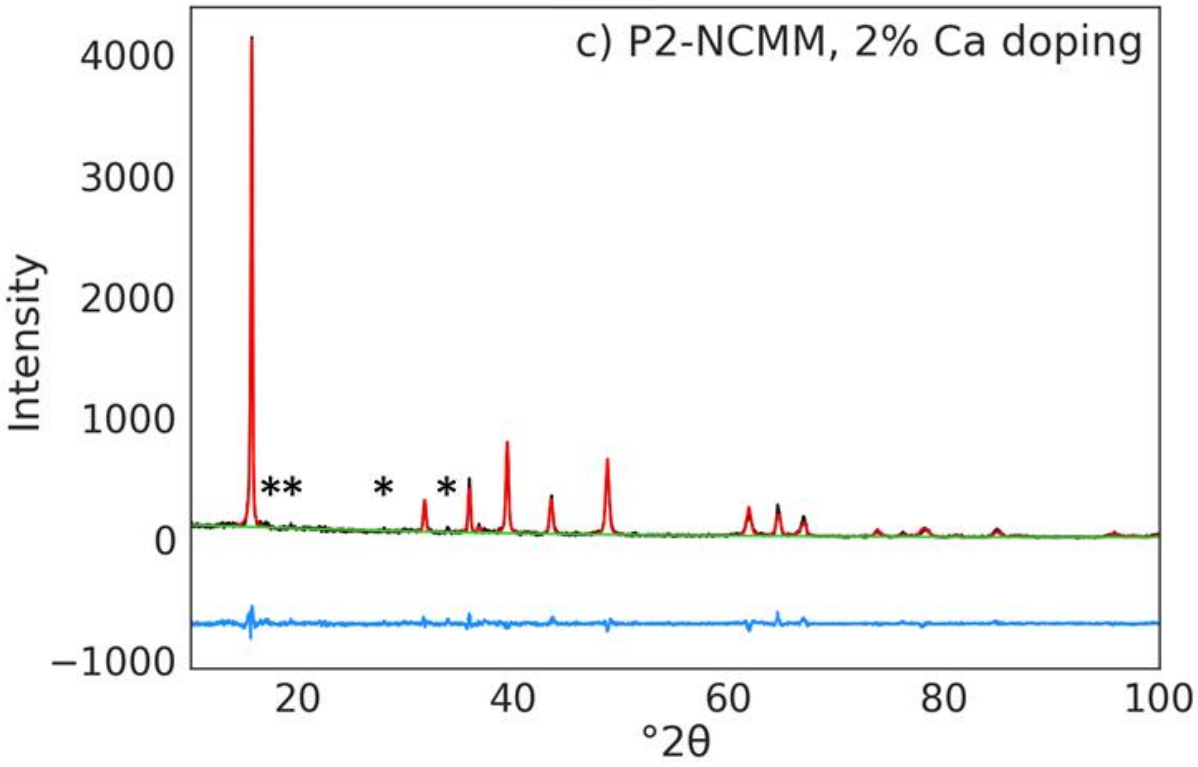

*Figure 4-7: XRD pattern (black), Rietveld refinement (red), background (green), and difference pattern (blue) of P2-NCMM doped with (a) 0% Ca, (b) 1% Ca, and (c) 2% Ca. Inset with a schematic of the crystal structure. Impurity peaks marked with *.*

To verify the identity of this impurity phase, a 5% Ca P2-NCMM sample was synthesised. The impurity is assumed to have a formula of $Na_{0.44}MnO_2$, as with the impurity phase in Chapter 3. Here, the impurity has a 28% phase fraction of the tunnel-type structure by Rietveld refinement, shown in Figure 4-8. The original $P6_3/mmc$ still forms in these conditions, but a 28% impurity with only 5% doping level suggests that the Ca^{2+} disrupts the formation of the P2 phase in favour of the tunnel-type one. Further, the lattice parameters of the P2 structure are a = 2.8803(2) Å and c = 11.2305(7) Å, values which are very close to the 2% Ca P2-NCMM sample, evidence that little further Ca^{2+} incorporation is occurring beyond 2% Ca doping. As such, a maximum of 2% Ca doping was used throughout.

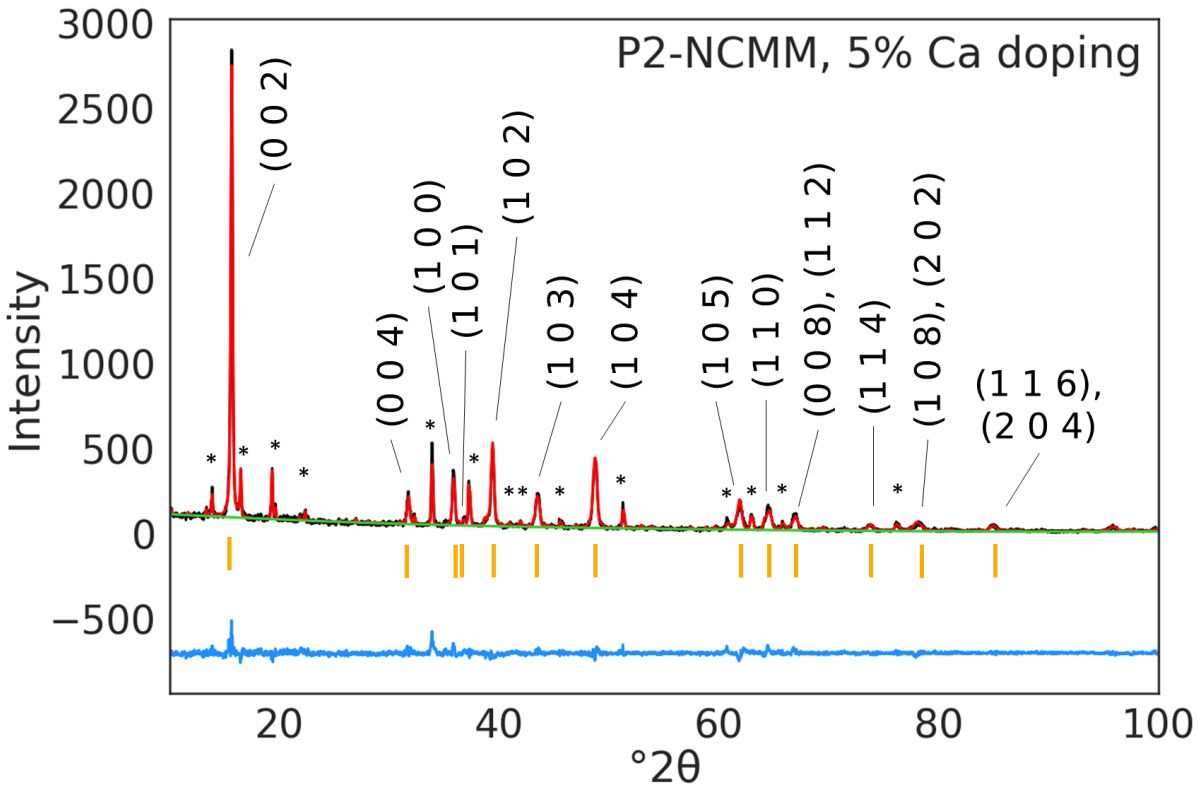

Figure 4-8: XRD pattern (black), Rietveld refinement (red), background (green), and difference pattern (blue) of P2-NCMM doped with 5% Ca. Pbam *impurity marked with *.*

Although the *c* parameter increases in the P3-NCMM samples with Ca doping, the pattern is not expected to repeat in the P2-NCMM. This is typical of P2-type materials; there are two possible Na^+ sites the Ca^{2+} can occupy. One is edge-sharing with TMO_2 octahedra and the other is face-sharing with the octahedra. The Ca^{2+} preferentially occupies the edge-sharing site to minimise the electrostatic repulsion upon it. The Ca^{2+} in the edge-sharing Na site forms a stronger bond with the neighbouring oxide ions than Na^+ would, and so the interlayer distance shortens in P2-type materials upon Ca doping. In P3-type materials, the repulsion between Ca^{2+} and the nearby TM causes an increase in the interlayer distance.

The unit cell parameters (given in Table 4-4) for the P2-NCMM do not increase with Ca doping. The *c* parameters of the P2-NCMM samples have a range of only 0.0041 Å, compared to the increases of 0.013 Å and 0.014 Å in the *c* parameter for 1% and 2% Ca P3-NCMM, respectively. The decrease in the *c* lattice parameter for P2-NCMM from 0% → 1% Ca doping is 0.0041 Å, and for 0% → 2% it is only 0.0009 Å. Overall, there is no significant change in the *c* lattice parameter across the doping range, but the *a* lattice parameter is significantly smaller in 0% Ca P2-NCMM than the 1% and 2% doped samples. One example of Ca doping of P2-type $Na_{0.71-x}Ca_xCoO_2$ by Zhou *et al.* [43] showed a decrease of 0.0074 Å (0% → 1%) and 0.0216 Å (0% → 3%), which is an almost linear increase with Ca doping. The change in lattice parameter from 0% → 1% in these cases is similar – the change is almost half as large in P2-NCMM as the values reported in P2-$Na_{0.71-x}Ca_xCoO_2$. The *c* lattice parameter decreases from 0% → 2% Ca doping in P2-NCMM

is 24 times smaller than 0% → 3% Ca in P2-$Na_{0.71-x}Ca_xCoO_2$, suggesting that additional Ca doping in P2-NCMM may in fact disrupt the Ca insertion into the P2 structure.

Table 4-4: Refined structural parameters of each P2-NCMM sample.

Sample	Space group	*a* (Å)	*c* (Å)	R_{wp} (%)	GOF
0% Ca P2-NCMM	$P6_3/mmc$	2.8760(1)	11.2316(5)	16.4	1.37
1% Ca P2-NCMM	$P6_3/mmc$	2.8800(2)	11.2275(6)	15.1	1.24
2% Ca P2-NCMM	$P6_3/mmc$	2.8797(2)	11.2307(6)	16.5	1.37

If the Ca^{2+} is not inserted into the structure it could instead be forming the impurity phase that is visible in the XRD. P2-NCMM made with 5% Ca^{2+} doping clearly showed an impurity phase, with a higher calculated phase fraction than the level of Ca doping. The P2 may then not be incorporating the Ca^{2+} into the P2 structure when the doping level is above 1%, and the impurity phase is formed that is visible in the 2% Ca-doped sample.

The way to confirm this will be through the examination of the electrochemical data. The outcome of Ca^{2+} incorporation into the layered structure (both P3 and P2) is usually increased rate capability and capacity retention [13]. For P3 samples a lower hysteresis may be observed [37], [38] as Na interlayer distance increases, making diffusion through the crystal structure easier, but the reverse is true for the P2 samples [3].

As may be the case for the P3 sample, if the Ca^{2+} is in a tetrahedral site then the pillaring effect will most likely not occur. This is because the distance between the Ca^{2+} and the next nearest TMO_2 layer is too far to prevent layer gliding. The effect on the electrochemistry of Ca doping is unlikely to be what has previously been seen in Ca doping. Instead, the P3 samples are likely to show no improvement at different levels of Ca doping.

The 1% Ca P2-NCMM shows evidence of incorporation of Ca^{2+} into the layered structure because the lattice parameters decrease to a degree similar to previous studies. In this case, the increased rate capability and capacity retention would be expected. However, for the 2% Ca P2-NCMM would be less likely to exhibit these benefits because the evidence (much smaller change in *c* lattice parameter from 0% → 2%), appearance of an impurity phase) suggests that Ca^{2+} is not incorporated into the structure in the same way as for the 1% Ca P2-NCMM.

4.3.2 SEM

The particle size and morphology of each sample was examined *via* scanning electron microscopy (SEM). In the previous chapter, the 20 h calcination times and difference in temperature between P3 and P2 samples of 320 °C led to large differences in particle sizes, and some differences in shape. This chapter uses much shorter calcination times (2

h) and the P3 samples are calcined at 650 °C, rather than 580 °C, to bring it more in line with other biotemplating studies into P3-type materials [50], [52]. This will affect the particle size and will in turn affect the electrochemistry and comparisons between samples.

The 2 h calcination is common among biotemplated samples and is sufficient for the formation of a well crystallised sample. In some cases, it even leads to improvement in the capacity of the material ($Na_{0.66}Ni_{0.33}Mn_{0.67}O_2$) compared to solid state synthesis, due to a reduction in particle size [50]. In this chapter, the doping of the host material in both P3- and P2-NCMM does not result in a meaningful change in particle size except for 1% Ca P2-NCMM, echoing the increase seen by Han *et al*. [2].

In general, the particle sizes (detailed in Table 4-5) of P3- and P2-NCMM are less than 1 µm in size. This is common for P3 materials [29], [62] but P2 materials are typically larger, 1-4 µm in size [63]–[65]. Samples have also formed larger agglomerates no more than 10 µm across and do not have an obvious shape. The exception here is 1% Ca P2-NCMM, which has formed particles of approximately 2-3 µm in size. They seem visually much more like the particles that were calcined at 900 °C for 20 h, rather than the other samples here, calcined for 2 h, in that they have a more plate-like shape.

Table 4-5: The average size and standard deviation of each NCMM sample (µm).

Sample	Average size (µm)	Standard deviation (µm)
0% P3-NCMM	0.65	0.41
1% P3-NCMM	0.84	0.62
2% P3-NCMM	0.42	0.21
0% P2-NCMM	0.54	0.55
1% P2-NCMM	2.57	0.98
2% P2-NCMM	0.42	0.25

The reason for the different particle size and shapes between 1% Ca P2-NCMM and the other samples is unclear. It is possible that the Ca doping allows the layered structure to form more rapidly than the undoped samples, but this would not explain why the same phenomenon does not occur in the P3-NCMM samples, or the 2% Ca P2-NCMM. The consistency in size and shape of the P3-NCMM, 0% Ca P2-NCMM, and 2% Ca P2-NCMM samples suggests that the results for the 1% Ca P2-NCMM are an outlier.

The analysis of the XRD and Rietveld suggests that the P3-NCMM is forming with the Ca^{2+} in an interstitial site in the MO_2 layer, rather than the Na^+ layer. As such the Ca^{2+} does not lead to any stabilisation of the layered structure as it forms. This could be the case with 1% Ca P2-NCMM, as it appears that the Ca^{2+} does reside in the Na^+ layer. This means that the Ca^{2+} should lead to a pillaring effect that causes the P2-NCMM to form more easily. As the 2% Ca P2-NCMM forms with an impurity phase, this impurity phase may disrupt the

formation of the layered structure, causing it to form more slowly than in the 1% Ca P2-NCMM sample.

As a result of the different particle shape and size (shown in Figure 4-9), we would expect 1% Ca P2-NCMM to display different electrochemical properties to the other P2-NCMM. One reason for this expectation builds on the analysis of the XRD: the Ca^{2+} is more likely to be in the Na layer in the 1% Ca P2-NCMM and instead forms an impurity in 2% Ca P2-NCMM. Another reason is that different particle sizes perform differently in electrochemical testing. In Chapter 3 smaller particle sizes were shown to lead to improvements in electrochemical performance: in that case, the size difference was 3-4 μm for the P2-NMMO samples, and 0.2 μm for the P3-NMMO. This led to the biotemplated P3-NMMO samples having a higher discharge capacity at C/5 than both P2-NMMO samples over the course of 50 cycles. We also saw that the biotemplated P2-NMMO at higher C-rates (2C and 5C) delivered the same capacity as biotemplated P3-NMMO. However, the dependence of the NCMM material on the Mn^{3+}/Mn^{4+} redox couple means that the cathode is liable to Mn^{2+} dissolution, resulting in capacity fading [63], [66]–[69].

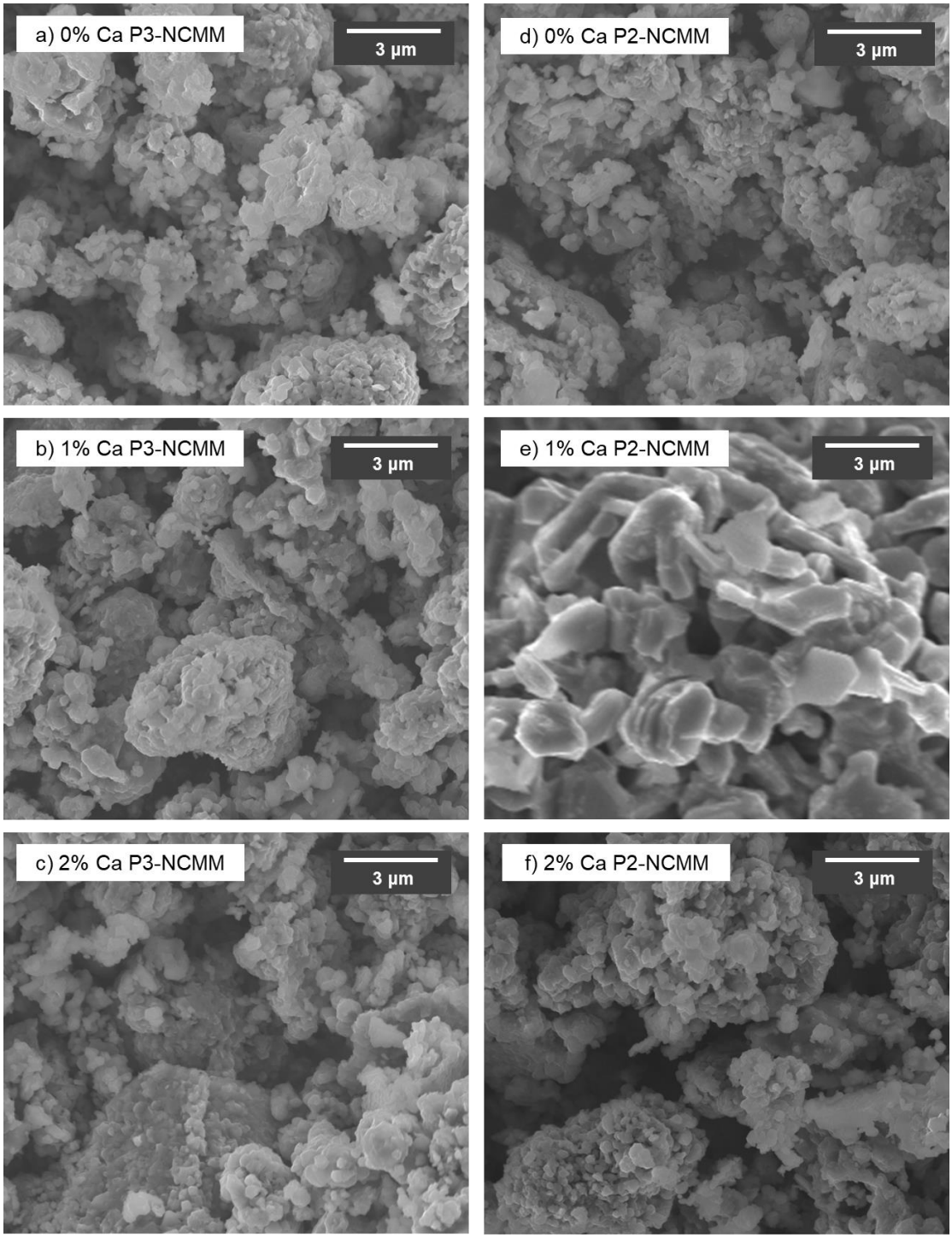

Figure 4-9: SEM images of (a) 0% Ca, (b) 1% Ca, and (c) 2% Ca P3-NCMM, and (d) 0% Ca, (e) 1% Ca, and (f) 2% Ca P2-NCMM. Note the different scale used for (e) 1% Ca P2-NCMM.

The implication for the electrochemistry here is that the 1% Ca P2-NCMM would be expected to perform worse than the other samples, at least with respect to the initial discharge capacity. This is what happened when comparing biotemplated P2-NMMO and P3-NMMO. P2-NMMO, with an average particle size of 2-4 µm had a lower initial capacity than biotemplated P3-NMMO, with an average particle size of 0.3 µm.

4.3.3 Electrochemistry

4.3.3.1 P3-NCMM

The samples under study were assembled into half-cells and cycled at C/5 (1C = 184 mA g^{-1}). The discharge capacities of the samples are displayed in Table 4-6. The range of the initial capacities of the P3-NCMM materials is 5 mAh g^{-1}, which can be attributed to variation between cathode materials. The capacity retentions of the samples are similar, although there is an improvement from 0% → 1% Ca doping of P3-NCMM. The range of the capacity retention of these samples is 6%, which is unlikely to be significant and caused by Ca doping – especially since the 2% Ca P3-NCMM capacity retention is lower than the 0% Ca P3-NCMM.

Table 4-6: Discharge capacities of the 1st, 10th, and 50th cycle of Ca-doped P3-NCMM.

P3-NCMM	Discharge capacity/mAh g^{-1}				Capacity retention over 50 cycles
	1st cycle	10th cycle	50th cycle	Avg. 50th cycle and std. dev.	
0% Ca	139	134	114	111.3 ∓ 2.2	82%
1% Ca	141	144	121	119.1 ∓ 2.3	86%
2% Ca	136	131	109	110.5 ∓ 1.3	80%

The discharge capacities and cycle efficiency over 50 cycles are shown in Figure 4-10. In the 1% Ca and 2% Ca P3-NCMM, much of the capacity loss appears to occur between cycle 20 and cycle 30. 1% Ca P3-NCMM drops from 140 mAh g^{-1} to 123 mAh g^{-1}, and 2% Ca P3-NCMM drops from 123 mAh g^{-1} to 111 mAh g^{-1}. This is accompanied by fluctuations in the discharge capacity, which increases and decreases by up to 7 mAh g^{-1} per cycle. This would suggest that the material is unstable, perhaps. However, these fluctuations occur at similar cycle numbers. There is a decrease in capacity at cycle 30 for both 1% Ca (5 mAh g^{-1}) and 2% Ca (7 mAh g^{-1}), and an increase at 40 and 41 for 1% Ca (5 mAh g^{-1}) and 2% Ca (5 mAh g^{-1}), respectively. It is therefore also possible that an external factor was affecting the discharge capacity of both these cells, but not the 0% Ca P3-NCMM. This factor may be temperature as the drops in capacity generally (though not always) occur when discharging at night. Steps were taken to mitigate changing temperatures in the lab, such as wrapping in electric tape and being covered by polythene bags. Since the cells are still exposed to temperature changes outside, some cells may feel the changes in temperature more than others.

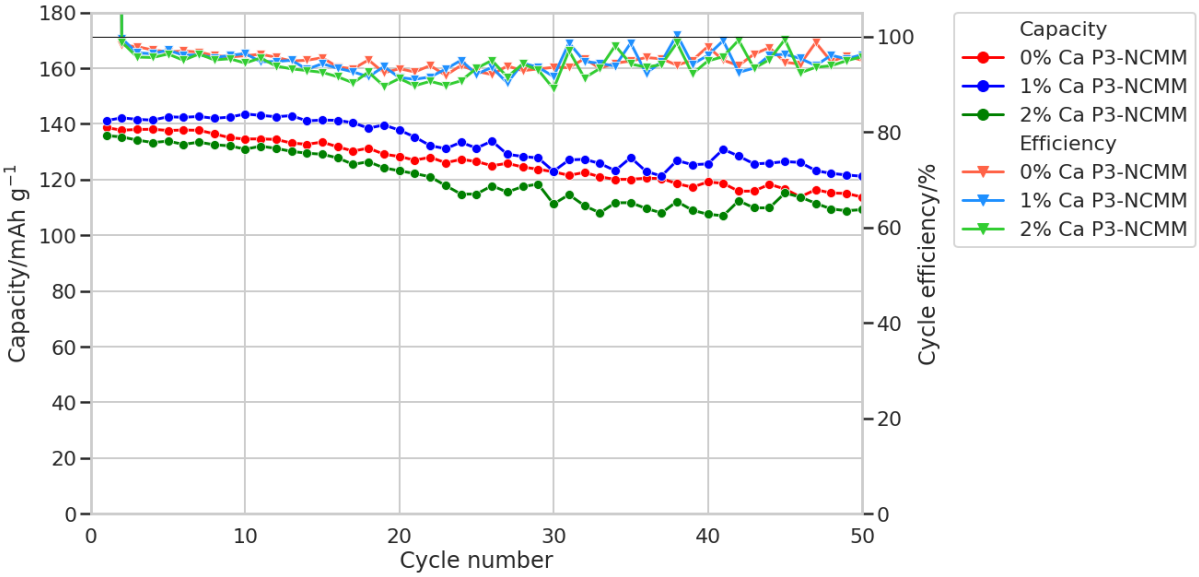

Figure 4-10: Discharge capacities of 0% (red), 1% (blue) and 2% (green) Ca P3-NCMM.

As expected, P3-NMMO (from Chapter 3) has an identical crystal structure to 0% Ca P3-NCMM, with a shorter calcination time used in the Ca doped samples. As discussed, all P3-NCMM samples have the ideal *R*3*m* space group. With this information, much of the same electrochemical analysis of the P3-NCMM samples can be used here.

The voltage profiles and differential capacity graphs are shown in Figure 4-11. During charge, there is a long voltage plateau at 2.2 V vs Na/Na^+ (rising to 2.4 V vs Na/Na^+ steadily over the course of the test procedure), followed by a steady, linear increase in voltage with respect to capacity. At approximately 3.5 V vs Na/Na^+, there is a step in the voltage, from 3.5 V to 4.0 V vs Na/Na^+. This occurs during discharge too, but due to a degree of hysteresis, the same processes occur at a lower voltage. This description holds for each P3-NCMM sample across the Ca doping range.

As cycling continues, the features of the voltage profiles become less distinct; the plateau shortens and becomes more slope-like, as does the voltage step at the end of charge. This is the effect of degradation of the cell over time. It is more pronounced during discharge; the voltage plateau in the first cycle persists for approximately 70 mAh g^{-1}. By the 50th cycle, it is more of a shallow slope than a plateau. It seems that degradation of the plateau is where much of the capacity loss occurs. The plateau coincides with the Mn^{3+}/Mn^{4+} redox potential [70]–[72], and is simultaneously associated with biphasic domains characteristic of first-order transitions [41], [73]. The plateau is thus likely to be a result of a P-type to O-type transition, such as P3↔O3 [35], [74]–[76].

The increasingly slope-like (i.e. the gradient of the discharge curve increases) character of the plateau suggests that the Mn^{3+}/Mn^{4+} redox is occurring less as cycling progresses. A reason for this is Mn^{2+} dissolution into the electrolyte, as suggested during analysis of the SEM. Mn^{2+} originates from Mn^{3+}, which can disproportionate into Mn^{2+} and Mn^{4+}. The lower cycle efficiency may be explained by this. During cycling, cracks may appear in the cathode particles as the crystal structure undergoes volume expansion/contraction

during phase transitions. The increased surface area allows greater Mn^{2+} dissolution and capacity fading. This should be prevented, or at least mitigated, by Ca doping. However, as there is little evidence of Ca pillaring in the material, the Mn^{2+} dissolution continues. The capacity fade seems to slow after 40 cycles, possibly because there is less Mn^{3+} available near to cathode surface.

The differential capacity graphs in Figure 4-11 show the presence of the redox pair at 2.10 V/2.20 V vs Na/Na^+, marking the voltage plateau. It shows degradation over time as the redox peaks attenuate: the charge peaks shift to higher potentials, and *vice versa* for the discharge peaks, and represents the increasing gradient of the plateaux. Beyond this, there are few visible features of the differential capacity graph that indicate other electrochemical process; although the sharp increase in potential between 3.5 V – 4.0 V vs Na/Na^+ suggests an ordering step is occurring.

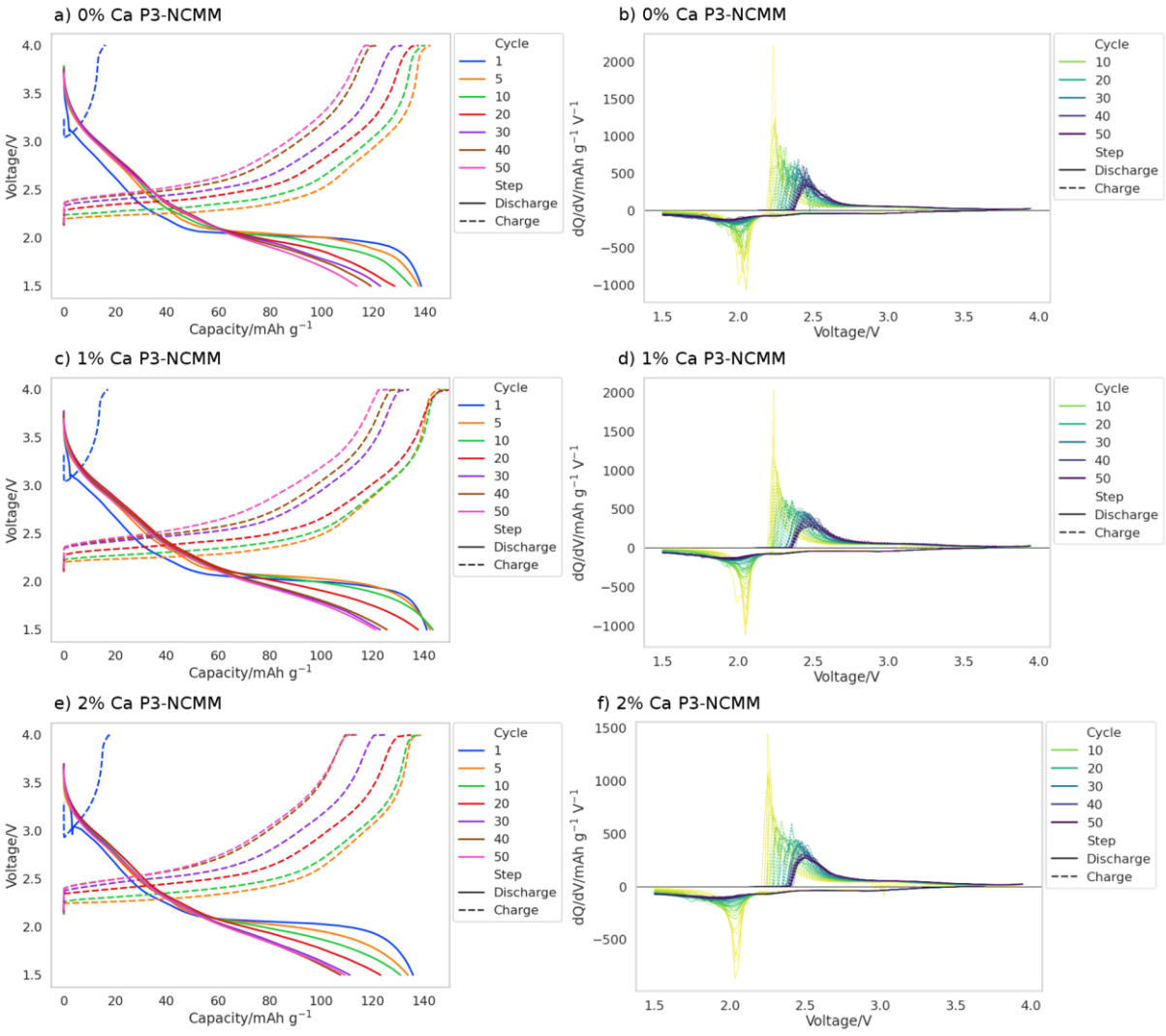

Figure 4-11: Galvanostatic cycling of (a) 0% Ca, (c) 1%, and (e) 2% Ca P3-NCMM. The plateau at the top of each charge step is when the cell was held at a constant voltage. Differential capacity plots of (b) 0% Ca, (d) 1%, and (f) 2% Ca P3-NCMM. Line colour shifts

from yellow to green to blue as cycle number increases. Cycled at C/5 between 1.5 – 4.0 V for 50 cycles.

A more detailed picture of the differential capacity graphs is shown in Figure 4-12. When zooming in, there are other process that can be observed that are dwarfed by major redox pair. Most visible is a peak in the discharge plot at 2.25 V vs Na/Na^+. There are also two very small peaks in the discharge plot at 2.75 V and 2.90 V vs Na/Na^+. In the charge plot, the second two peaks are mirrored at 2.85 V and 3.10 V vs Na/Na^+. There is also evidence of a final peak at 3.50 V vs Na/Na^+ in the charge curve, with no clear pair during discharge, in 0% P3-NCMM. This peak is less intense in the following two samples. The identities of these minor redox have not been confirmed, in part due to their low intensities relative to the 2.1 V/2/2 V vs Na/Na^+ pair. This makes them almost invisible in the voltage profiles, as well as difficult to separate from the background of the differential capacity graphs. It is likely that they are the result of minor phase transformations, such as the formation of distorted P3, or P'3 [77]. They do not appear to affect the electrochemistry of the cell: they do not contribute much capacity, nor do they fade or shift appreciably.

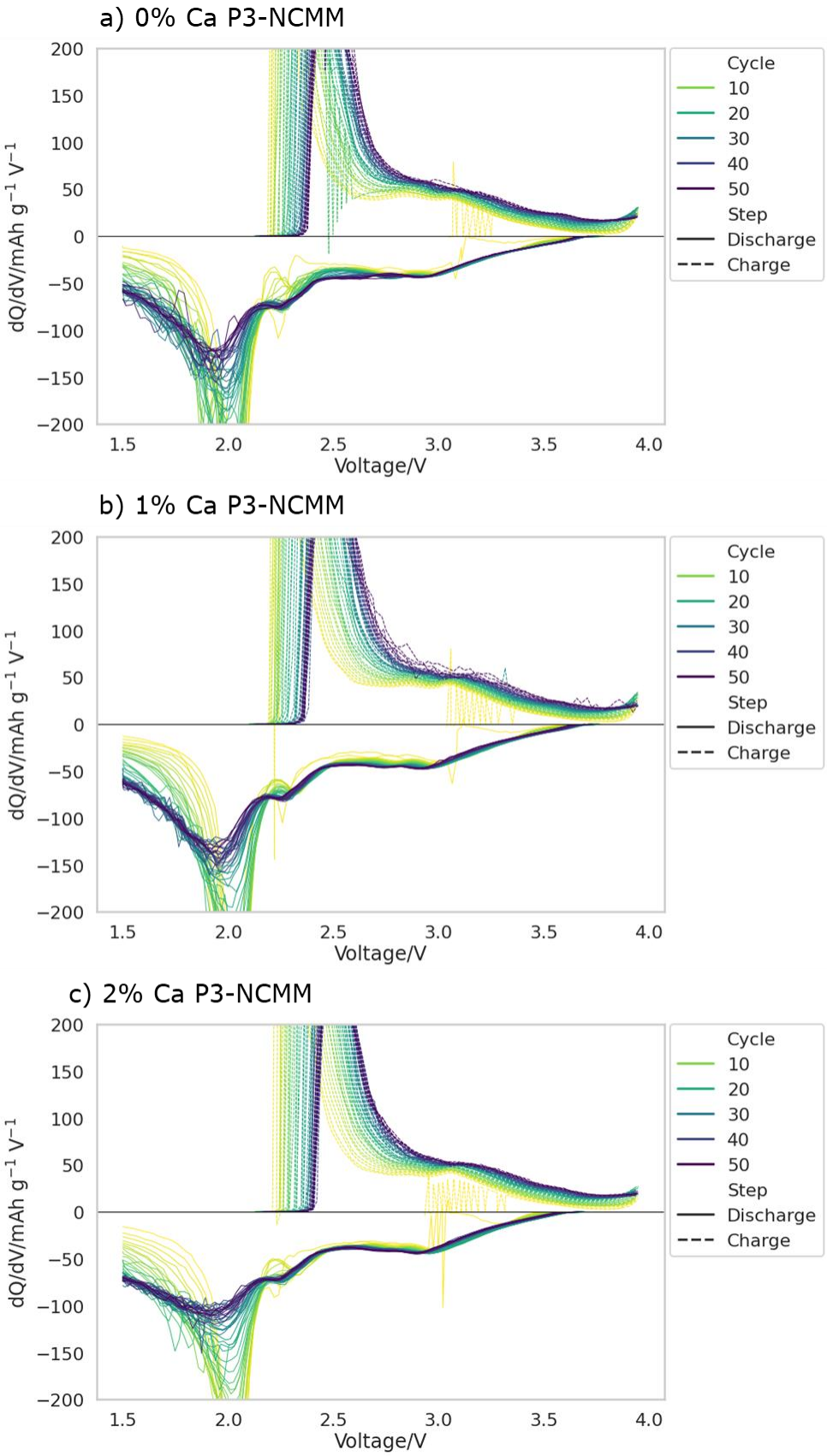

Figure 4-12: Differential capacity plots of (a) 0% Ca, (b) 1%, and (c) 2% Ca P3-NCMM. Line colour shifts from yellow to green to blue as cycle number increases. Cycled at C/5 between 1.5 – 4.0 V vs Na/Na⁺ for 50 cycles.

It is apparent how little the electrochemistry changes as the Ca doping level increases, corroborating the hypothesis that pillaring is not occurring. 1% Ca doping can increase the capacity from 25 mAh g^{-1} to 50 mAh g^{-1} after 500 cycles [32], and 2% Ca doping can increase it from 74 mAh g^{-1} to 90 mAh g^{-1} after 60 cycles [2]. There are cases where even 5% doping does not show as significant improvement in capacity [36], but doping to that degree in this material leads to impurities and so is not a promising avenue of experimentation. The similarities in discharge capacity after 50 cycles further supports the theory that Ca^{2+} is not influencing the crystal structure through pillaring. XRD suggests that the Ca^{2+} is in the P3 structure, but in the tetrahedral sit of the MO_2 layer which would was predicted not to affect the electrochemistry.

The similarity of the voltage profiles, combined with the similarities between the initial and final capacities of the material, confirms that the Ca^{2+} is not being inserted into the Na^{+} site, and is not causing a pillaring effect. As determined *via* Rietveld refinement, the changes in *c* lattice parameter were larger than previously seen in Ca-doped P3 structures, The starting capacities range from 141 mAh g^{-1} to 136 mAh g^{-1}, and 121 mAh g^{-1} to 109 mAh g^{-1} after 50 cycles. 1% Ca doping increased the discharge capacity of the host P3 structure by 7 mAh g^{-1} and 2% Ca doping lowers it by 5 mAh g^{-1}. The range of these values is not significant enough to suggest any change by Ca^{2+} pillaring, expect perhaps in 1% Ca P3-NCMM. In the case of this sample, the increase in capacity and capacity retention lies outside of the range of values of the other two samples, suggesting that something has caused an improvement in performance. It may be Ca^{2+} doping into the structure, but the improvements are small compared to literature and are not maintained. It is possible that the improvement is not caused by Ca^{2+} doping alone.

There is no clear pattern to the variation in capacity between the P3 samples. These levels of Ca doping have improved capacity retention in other materials to a much greater extent, and so from these data it appears to have to effect on electrochemical performance.

4.3.3.2 P2-NCMM

In the range of P2-NCMM samples, we see a different pattern to the P3 in the discharge capacity values across the cycling regime. These results are shown in The capacity and efficiency per cycle are displayed in Figure 4-13. When the P2-NMMO with 1% Ca, the capacity at the 50th cycle increases by 19 mAh g-1. Doping with 2% Ca increases it by 16 mAh g-1. This is a greater increase than seen in the P3-NCMM samples and suggests that there is some increase in capacity retention caused by Ca2+ pillaring in the P2-NCMM. After 20 cycles there is an increase in noise in the capacity and cycle efficiency of the 1% and 2% Ca P2-NCMM, also seen in the 1% and 2% Ca P3-NCMM which were run at the same time, in the same conditions.

Table 4-7. Unlike the P3-NCMM samples, which show only an increase in capacity retention of 4% when going from 0% to 1% Ca doping, the capacity retention of the P2-NCMM increases by 10%. This is indicative of Ca doping improving the structural stability

of the material, which was indicated by the Rietveld and SEM analysis of 1% Ca P2-NCMM. Further Ca doping does not improve the capacity retention, although the capacity decreases by 3-4 mAh g^{-1}.

The capacity and efficiency per cycle are displayed in Figure 4-13. When the P2-NMMO with 1% Ca, the capacity at the 50th cycle increases by 19 mAh g^{-1}. Doping with 2% Ca increases it by 16 mAh g^{-1}. This is a greater increase than seen in the P3-NCMM samples and suggests that there is some increase in capacity retention caused by Ca^{2+} pillaring in the P2-NCMM. After 20 cycles there is an increase in noise in the capacity and cycle efficiency of the 1% and 2% Ca P2-NCMM, also seen in the 1% and 2% Ca P3-NCMM which were run at the same time, in the same conditions.

Table 4-7: Discharge capacities of the 1st, 10th, and 50th cycle of Ca-doped P2-NCMM.

P2-NCMM	Discharge capacity/mAh g^{-1}				Capacity retention over 50 cycles
	1st cycle	10th cycle	50th cycle	Avg. 50th cycle and std. dev.	
0% Ca	147	127	93	94.6 ∓ 0.9	63%
1% Ca	153	142	112	107.1 ∓ 3.6	73%
2% Ca	149	137	109	106.2 ∓ 1.9	73%

Different levels of Ca doping in the literature can show improvements in performance; 2.5% [30], 3% [32], 4% [38], [39], 5% [34], [36], and 7% [2], summarised in Table 4-1. However, these Ca doping values are for different materials, and it was shown that doping with 5% Ca cannot be done (Figure 4-8). The doping limit of P2-NMMO with Ca is between 1% and 2%. Even at these levels, the effect is smaller than the other Ca-doped materials.

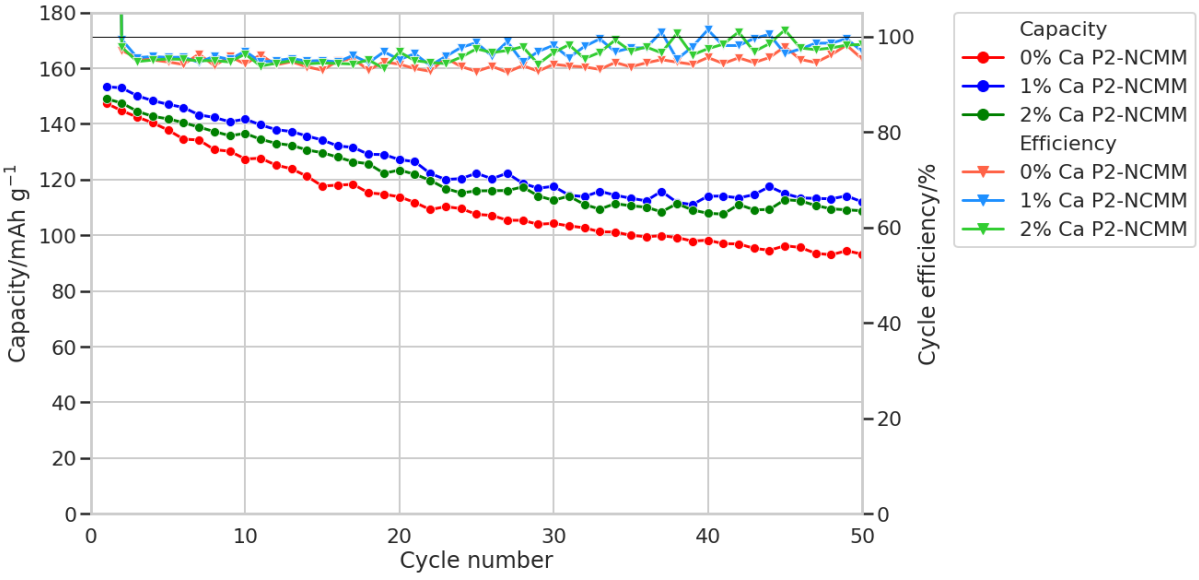

Figure 4-13: Discharge capacities of 0% (red), 1% (blue) and 2% (green) Ca P2-NCMM.

Shown in the XRD analysis, 2% Ca doping leads to impurity phases that are not apparent in 1% Ca P2-NCMM. This suggests that there is a solid solution limit for Ca^{2+} in the P2 structure. The difference in capacity between 1% Ca and 2% Ca across the test procedure is consistently 3-4 mAh g^{-1}. If the solid solution limit is between 1-2% Ca, then the 2% Ca P2-NCMM is showing a reduced capacity because the mass of active material has been overestimated, leading to a higher current being used in the test procedure and a lower capacity as a result. The capacity retention is the same in both samples, which may be because the solution limit is close to 1%. There is no evidence of doping the alkali layer in P-type NMMO previously, and so the doping limits are unexplored.

From the earlier, the 2% Ca P2-NCMM is not expected to contain Ca in the structure. The lattice parameters showed little difference to the 0% Ca P2-NCMM, as with the particle size. Unlike the 1% P2-NCMM which does show a change – particularly in the particle size.

XRD analysis showed that 1% Ca doping led to a contraction of the *c* lattice parameter, indicating Ca^{2+} incorporation into the alkali layer. This should be visible in the voltage profiles and differential capacity graphs as structural changes are suppressed. The voltage profiles show little variation in the behaviour of P2-NCMM as Ca doping increases, beyond the slower fall in capacity – the plateau at 2.2 V vs Na/Na^{+} does not shorten as rapidly as in the 0% Ca P2-NCMM (Figure 4-14).

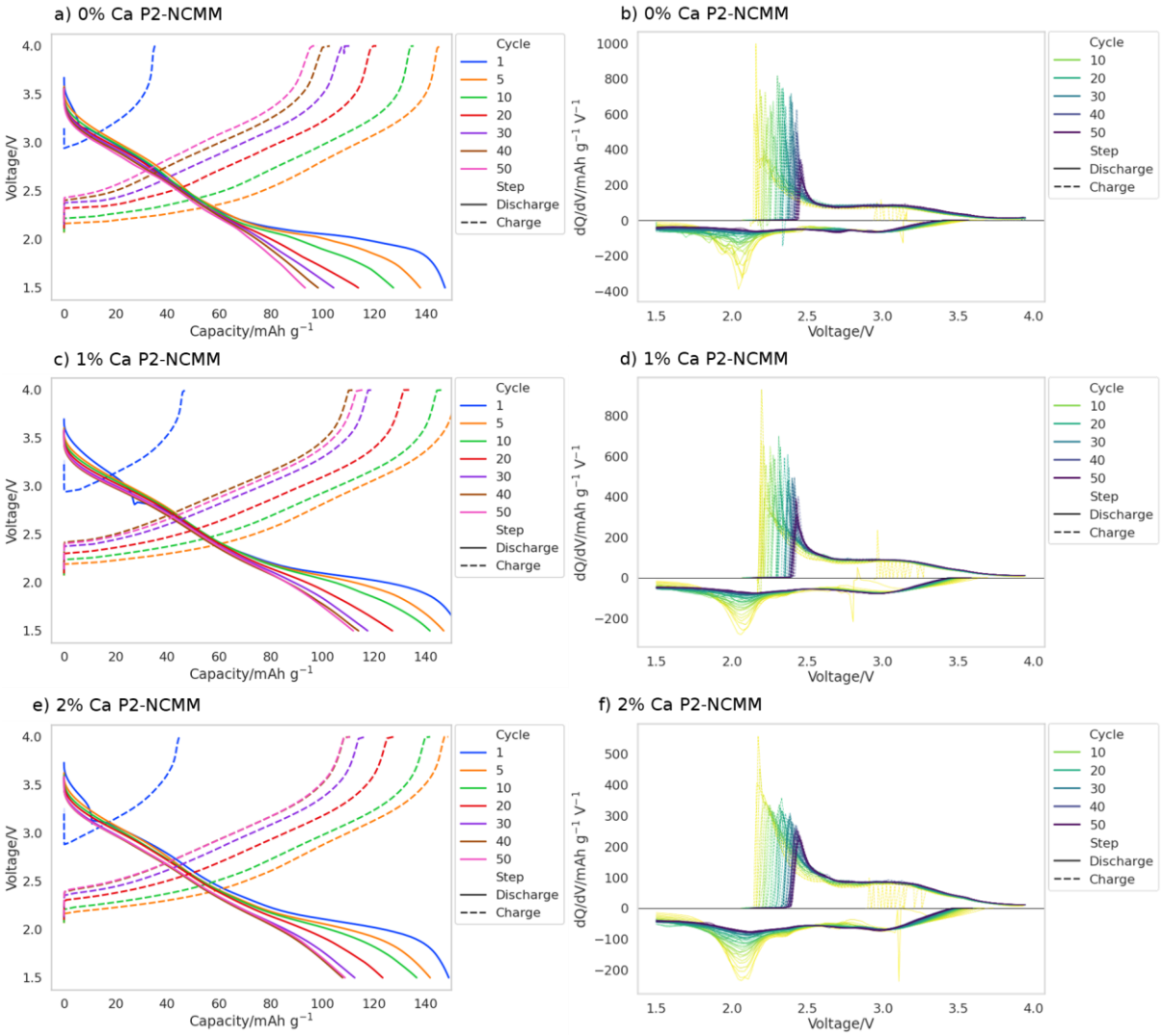

Figure 4-14: Galvanostatic cycling of (a) 0% Ca, (c) 1%, and (e) 2% Ca P2-NCMM. The plateau at the top of each charge step is when the cell was held at a constant voltage. Differential capacity plots of (b) 0% Ca, (d) 1%, and (f) 2% Ca P2-NCMM. Line colour shifts from yellow to green to blue as cycle number increases. Cycled at C/5 between 1.5 – 4.0 V vs Na/Na^+ for 50 cycles.

Typical of P2-NMMO [20], [70], there is a major peak at 2.1 V/2.2 V vs Na/Na^+ in the differential capacity graph, which becomes broader and more polarised over time: 2.1 V/2.5 V vs Na/Na^+ by the 50th cycle. This could be evidence of Mn^{2+} dissolution [66], [78], [79], as broadening and polarisation have been mentioned as indications of transition metal migration [30].

The peak during the discharge step also attenuates during cycling. There is also a very broad peak at 2.9 V/3.1 V vs Na/Na^+. These two couples correspond to the extraction of Na^+ from P2-NCMM. The appearance of two redox couples is a result of the two Na^+ sites present in the P2 structure [70].

As with the P3-NCMM samples, information is lost owing to the intensity of the main redox pair. For example, in Figure 4-14 there is little evidence of a P2↔OP4 transition at

3.5 V vs Na/Na^+ in the charge step [20]. However, as the graph is enlarged in Figure 4-15, there is some evidence of a peak in this position. This peak is maintained throughout the doping series.

One major difference between the doped and undoped samples is the electrochemical behaviour at 2.65 V vs Na/Na^+ on discharge. The peak in 0% Ca P2-NCMM shifts throughout cycling and develops with no obvious oxidation counterpart. It is entirely absent in the 1% P2-NCMM and may reappear in 2% P2-NCMM but much less clearly. The presence of this peak in 0% P2-NCMM may explain its more rapid degradation compared to the doped samples, as the three differential capacity graphs appear almost identical.

This would then provide further evidence for the Ca^{2+} being incorporated into the 1% Ca P2-NCMM structure, in contrast to the P3-NCMM where there is little evidence of any Ca^{2+} in the alkali layer. It suggests that the Ca^{2+} is preventing some crystal structure transformation or degradation reaction.

In fact, this peak at 2.65 V seems to slowly emerge in the discharge step, not fully forming until approximately the 30^{th} cycle. This could be evidence of Na^+/vacancy ordering beginning to occur, but the presence of Ca^{2+} pillaring in the Na^+ layer prevents the reordering step from taking place [33], [34]. This could be confirmed by *operando* XRD, which would show superstructure peaks in the obtained patterns.

The particle sizes of the samples are also relevant here. 0% and 2% Ca P2-NCMM both have particle sizes of approximately 0.5 – 1.0 μm, whereas the 1% Ca P2-NCMM particles are 1.0 – 3.0 μm. If the dominant capacity fading mechanism of NCMM is Mn^{2+} dissolution, as seen with NMMO, then larger particle sizes should improve capacity retention because it reduces the surface area/volume ratio. However, the capacity retentions of the 1% Ca and 2% Ca P2-NCMM are the same. The XRD and SEM of 2% Ca P2-NCMM both suggest that there is little difference between it and the 0% Ca P2-NCMM. The electrochemistry shows that its performance is more like the 1% Ca P2-NCMM, which does have evidence of Ca doping.

Because the characterisation of 2% Ca P2-NCMM does not reveal any Ca doping, it may be the case that a different factor is improving the capacity retention. In Chapter 3, an impurity phase was seen in the solid state synthesised P3-NMMO with a similar crystal structure to the impurity seen in 2% Ca and 5% Ca P2-NCMM. That tunnel-like structure shows some electrochemical activity that is not observed here, but a capacity retention of 95% within the same test parameters as the cells here. There are examples of multiphasic structures having improved capacity retention than single phases [80]–[82], which can be obtained *via* doping [83]. This will be explored in more detail in the next chapter, but a minor phase in a composite structure can prevent phase transitions and improve capacity retention. This could be the mechanism by which the cycle life of 2% Ca P2-NCMM is improved, rather than inserting Ca^{2+} into the Na layer. This way, the lattice parameters and particle would be expected to be the same in both 0% and 2% Ca P2-NCMM but perform differently electrochemically.

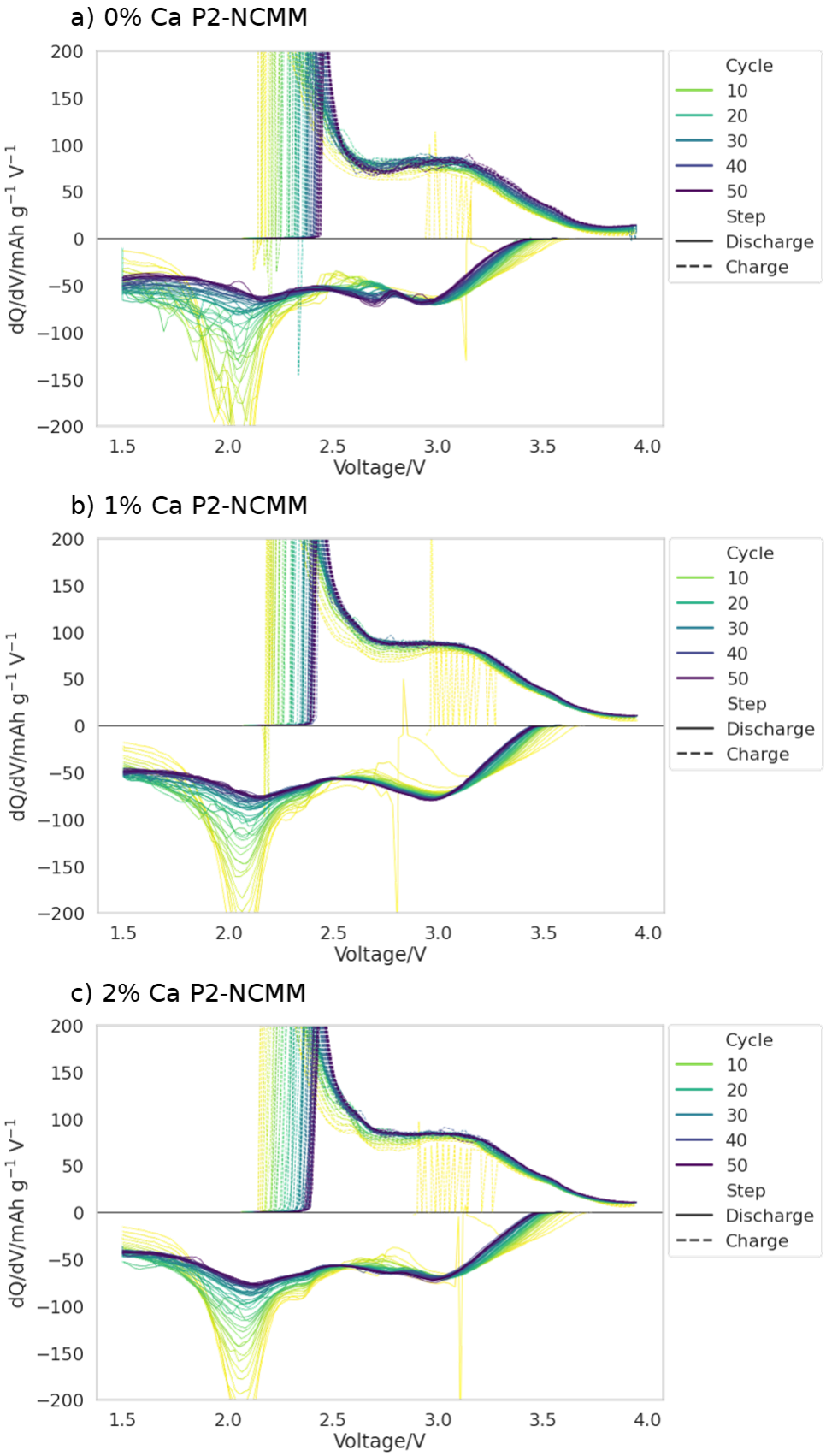

Figure 4-15: Differential capacity plots of (a) 0% Ca, (b) 1%, and (c) 2% Ca P2-NCMM. Line colour shifts from yellow to green to blue as cycle number increases. Cycled at C/5 between 1.5 – 4.0 V vs Na/Na⁺ for 50 cycles.

As seen in the comparison between biotemplating and solid state syntheses, the P3-NCMM has a generally higher capacity than P2-NCMM after 50 cycles at C/5, despite the lower initial discharge capacity. The higher initial capacity of P2-type materials has been observed before [84]–[86], but the higher capacity retention has not. One reason for the low capacity retention in the P2 material, particularly the 0% Ca P2-NCMM, may be the particle size. P2 materials often have particle sizes of ~2 μm, whereas in this work the size is <1 μm. P2-NMMO analysed in Chapter 3 was calcined for 20 h, rather than 2 h, hence the different sizes. This increases the surface area for Mn^{2+} dissolution and speeds up capacity fade. In the previous chapter, biotemplated P2-NMMO (calcined for 20 h) had a capacity retention of 83%, 20% higher than the 0% Ca P2-NCMM (also biotemplated, calcined for 2 h). The P2-NMMO material calcined for 20 h had larger particle sizes than all Ca-doped P2-NCMM samples.

This indicates that surface area is a significant contributor to capacity retention in P2-NCMM. The capacity retention gains in 1% Ca P2-NCMM may be a result of increased structural stability or suppressed phase transitions, but they may also be caused by the increased particle size. However, it is likely that the increase particle size is caused by the Ca^{2+} doping of the alkali layer [2].

The capacity retention of the P3-NCMM is higher than the P2-NCMM but varies less with Ca doping. The P3-NCMM may simply be less susceptible to Mn^{2+} dissolution than the P2 phase, perhaps owing to the lack of edge-sharing sites for the Mn^{2+} to occupy and diffuse through. Overall, the addition of Ca^{2+} did not have a significant impact on the capacity or capacity retention of the P3 material. The differences in the capacity values are likely due to variation between cells rather than an effect of Ca doping. None of the results here suggest that Ca is doping the alkali layer. The XRD shows an increase in the *c* lattice parameter, but to a higher degree than expected from previous work into Ca doping of P3 materials.

4.3.3.3 Rate capability testing

As it commonly shows improvement with Ca doping, the rate capability of each material was tested to investigate its impact on the performance of P3- and P2-NCMM. The evidence has indicated that the P3-NCMM does not incorporate the Ca^{2+} into the Na^{+} layer, as was attempted, and this continues here. As shown in Figure 4-16, the 1% Ca P3-NCMM fares the worst of the three samples under high discharge currents, with it delivering the lowest capacity for each rate. The difference between the samples fluctuates too; at 1C the difference between 0% Ca and 1% Ca P3-NCMM is approximately 10 mAh g^{-1}, whereas it is 20 mAh g^{-1} at both C/5 and 5C.

After cycling at 5C, the samples are cycled again at C/10. While all three regain the lost capacity at this point, the 1% Ca and 2% Ca P3-NCMM both suffer rapid capacity fade over the final five cycles. This points to structural degradation of the material after cycling at high C-rates. So far it has been supposed that Ca^{2+} is occupying a tetrahedral site in the TMO_2 layer, rather than a prismatic site in the Na layer, because of the expanding *c* lattice

parameter. As such it is expected not to affect the electrochemistry of the material, which was argued when examining the capacity and voltage profiles. The data from the rate capability testing support this, because the difference between samples is not significant enough to disprove this hypothesis – especially when comparing it to the results of the P2-NCMM rate capability test.

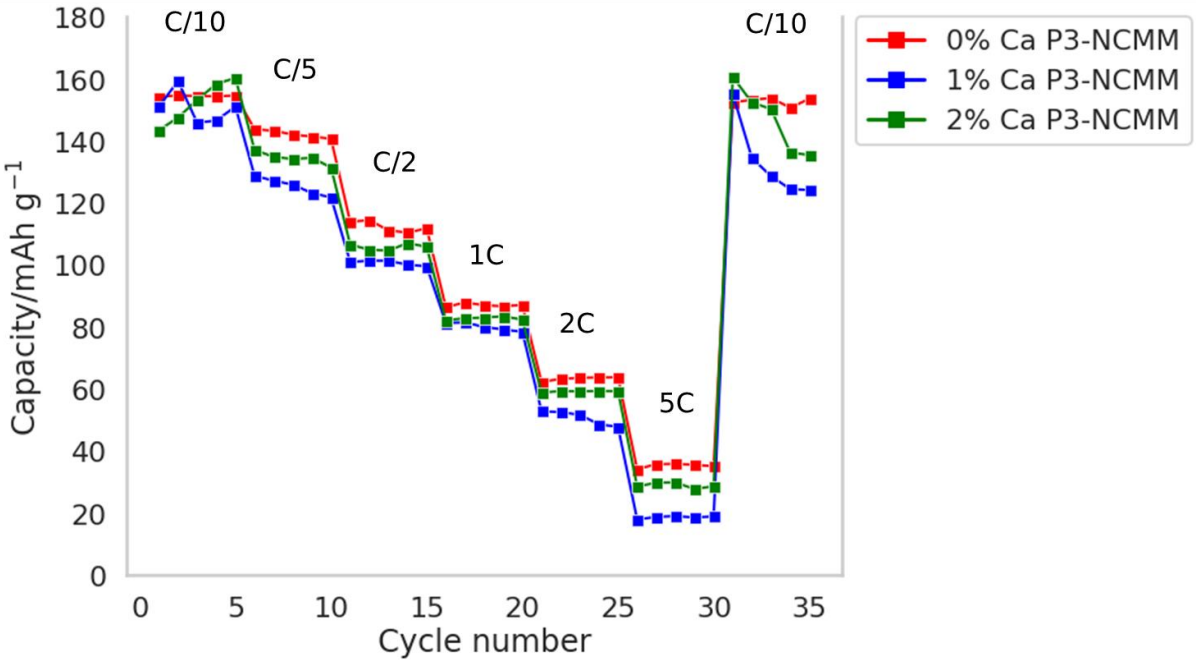

Figure 4-16: Discharge capacity of each P3-NCMM sample. Cycled between 1.5 – 4.0 V at a given C-rate as marked on the graph for 5 cycles each.

By comparison, the difference between capacities for the P2-NCMM samples is much larger (Figure 4-17). Consistently, the 2% Ca P2-NCMM delivers the lowest capacity of the three samples here, approximately 40 mAh g^{-1} lower when cycled at 2C. The 1% Ca P2-NCMM instead offers greater capacity at each C-rate. The 1% Ca P2-NCMM sample is the one that has the most evidence of Ca^{2+} incorporation into the Na layer, and so most likely to show the improved rate capability typical of Ca doping. So, a 10 mAh g^{-1} higher capacity compared to the 0% Ca P2-NCMM at 5C and 20 mAh g^{-1} higher at C/2 and 1C is further evidence of successful incorporation of Ca^{2+} into the Na layer. Worth noting here is that larger particle sizes lead to worse rate capability because of the longer Na^{+} diffusion pathways [63], and so the improvement in rate capability here are a result of Ca doping, not of the increased particle size.

In the case of 2% Ca P2-NCMM, the capacity at higher C-rates is lower than both 0% and 1% Ca P2-NCMM. The higher capacity retention of the 2% Ca P2-NCMM was thought to be a result of the impurity phase identified in the XRD analysis. Examining the results of the same test on solid state P3-NMMO (with a similar impurity) show that it delivers lower capacity than the biotemplated P2-NMMO. It is likely also due to the impurity phase(s) in the solid state P3-NMMO. This factor may be at play here as well; a similar impurity is present in the 2% Ca P2-NCMM to that present in the solid state P3-NMMO. It

is possible that this impurity affects the rate capability of the cell by hindering diffusion pathways within the cathode material. Introduction of a second phase can improve the rate capability of a cathode [87], but not always [81], [86].

Here, at C/5 there is a large (35 mAh g^{-1}) difference in capacity between 1% Ca and 2% Ca P2-NCMM. This contrasts with the galvanostatic cycling experiment (shown in Figure 4-13), wherein the capacity of the two materials remains within 5 mAh g^{-1} of each other throughout the test. There is variation in the capacity within repeats of the same sample, and so some level of discrepancy is expected. However, this level of difference between the capacity of the two samples is significant, and so another factor is likely affecting the capacity of 2% Ca P2-NCMM, beyond simple variance.

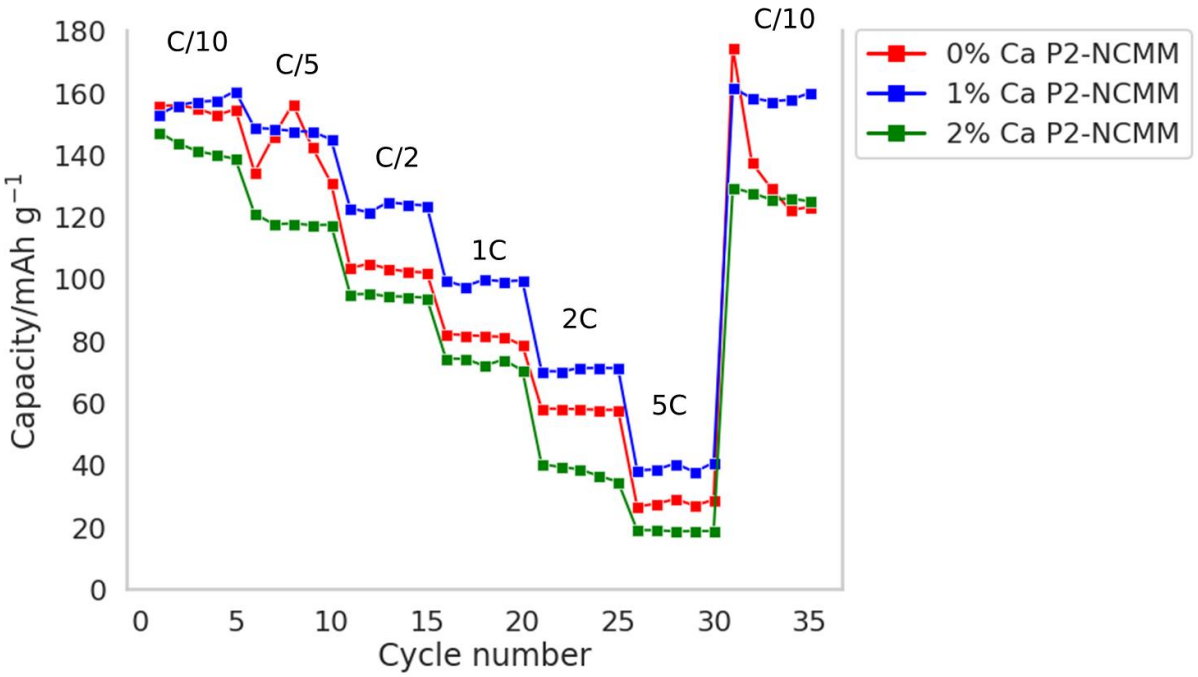

Figure 4-17: Discharge capacity of each P2-NCMM sample. Cycled between 1.5 – 4.0 V at a given C-rate as marked on the graph for 5 cycles each.

4.4 Conclusion

Doping cathode materials with Ca^{2+} is a tactic to increase capacity retention by suppressing phase transitions that undermine the stability of the crystal structure. Due to the similarity in the size of the Ca^{2+} and Na^{+} ions, the Ca^{2+} is expected to occupy vacancies in the Na^{+} layer of the layered structure. In the case of P3-NCMM, the Ca^{2+} instead appears to occupy a tetragonal interstitial site in the MO_2 layer. This leads to no change in electrochemical performance. The capacity retention values show little change (a range of 6%) compared to the P2-NCMM (a range of 10%). The capacity of the 1% Ca-P3-NCMM is the highest of the three (121 mAh g^{-1} compared to 114 mAh g^{-1} from 0% Ca P3-NCMM after 50 cycles), but not by enough that successful Ca^{2+} doping can be assumed.

For P2-NCMM, 1% Ca^{2+} appears to successfully dope the Na^{+} layer, as evidenced by the XRD, SEM, and 10% increase in capacity retention. However, the impurities seen in the 2% Ca P2-NCMM sample suggest the substitution limit for Ca^{2+} is between 1% and 2%. The 1% and 2% Ca P2-NCMM samples exhibit increased capacity retention; with 19 mAh g^{-1} and 16 mAh g^{-1} more capacity delivered in the 50^{th} cycle than the undoped P2-NCMM, respectively. However, the mechanisms by which capacity retention increases is likely to be different for each sample. The 2% Ca P2-NCMM may be improved by the presence of an electrochemically active impurity phase, rather than through Ca doping.

Rate capability tests show that 1% Ca P2-NCMM exhibits superior discharge capacity to the other P2-NCMM samples and outperforms all P3-NCMM samples. Whether this outcome is a result of the anomalously large particle sizes or Ca pillaring is unclear, and it remains possible that these two factors are simultaneously caused by Ca doping.

The results demonstrate the difficulty in doping the Na^{+} layer in P3-NMMO, owing to the absence of Na sites that are edge-sharing on both sides, as is the case in P2 phases. Doping P2-NMMO is possible because of these sites, and although the Ca doping limit is 1-2%, this leads to increased capacity retention and enhanced rate capability. This work highlights again the improvements in performance possible of the established, high-capacity NMMO cathode.

4.5 Further work

The exact position of the Ca ion within the structure of P3-NCMM should be confirmed. This may be possible using solid state NMR, or the X-ray atomic pair distribution function (PDF) method. Similarly, an investigation into higher doping levels could be conducted if the Ca can be placed selectively into the Na sites. The reason that Ca does not appear to occupy the Na should be explored too, as this means it does not cause the pillaring effect that raises the NMMO materials capacity retention. If the Jahn-Teller activity of the Mn^{3+} creates distortions for the Ca^{2+} to occupy, then further Mg doping can mitigate this. Doping with another transition metal such as Cu [88] or Ni [89] could increase the covalency of the bond hybridisation within the TMO_2, similarly to how additional Mg^{2+} stabilises O redox [24].

The 5% Ca P2-NCMM could be tested. The tunnel-type structure, $Na_{0.44}MnO_2$, is a known electrochemically active material [59]–[61]. In Chapter 3, the sample that contained an impurity with the same structure (solid state synthesised P3-NMMO) displayed a lower capacity than the other materials tested (95 mAh g^{-1}), but a much higher capacity retention (95%). It is worth revisiting this material to see if a similar capacity retention can be achieved here. Similar tactics to those suggested to improve Ca doping in the P3 phase could be used to increase the Ca doping level in the P2 phase.

4.6 References

[1] R. D. Shannon and C. T. Prewitt, "Effective ionic radii in oxides and fluorides," *Acta Crystallogr. Sect. B Struct. Crystallogr. Cryst. Chem.*, vol. 25, no. 5, pp. 925–946, 1969,

doi: 10.1107/S0567740869003220.

[2] S. C. Han, H. Lim, J. Jeong, D. Ahn, W. B. Park, K. S. Sohn, and M. Pyo, "Ca-doped Na_xCoO_2 for improved cyclability in sodium ion batteries," *J. Power Sources*, vol. 277, pp. 9–16, 2015, doi: 10.1016/j.jpowsour.2014.11.150.

[3] M. Matsui, F. Mizukoshi, and N. Imanishi, "Improved cycling performance of P2-type layered sodium cobalt oxide by calcium substitution," *J. Power Sources*, vol. 280, pp. 205–209, 2015, doi: 10.1016/j.jpowsour.2015.01.044.

[4] S. Guo, Y. Sun, P. Liu, J. Yi, P. He, X. Zhang, Y. Zhu, R. Senga, K. Suenaga, M. Chen, and H. Zhou, "Cation-mixing stabilized layered oxide cathodes for sodium-ion batteries," *Sci. Bull.*, vol. 63, no. 6, pp. 376–384, 2018, doi: 10.1016/j.scib.2018.02.012.

[5] P. F. Wang, Y. You, Y. X. Yin, Y. S. Wang, L. J. Wan, L. Gu, and Y. G. Guo, "Suppressing the P2–O2 Phase Transition of $Na_{0.67}Mn_{0.67}Ni_{0.33}O_2$ by Magnesium Substitution for Improved Sodium-Ion Batteries," *Angew. Chemie - Int. Ed.*, vol. 55, no. 26, pp. 7445–7449, 2016, doi: 10.1002/anie.201602202.

[6] J. Y. Hwang, S. T. Myung, D. Aurbach, and Y. K. Sun, "Effect of nickel and iron on structural and electrochemical properties of O3 type layer cathode materials for sodium-ion batteries," *J. Power Sources*, vol. 324, pp. 106–112, 2016, doi: 10.1016/j.jpowsour.2016.05.064.

[7] J. Sun, J. Shen, and T. Wang, "Electrochemical study of $Na_{0.66}Ni_{0.33}Mn_{0.67-x}Mo_xO_2$ as cathode material for sodium-ion battery," *J. Alloys Compd.*, vol. 709, pp. 481–486, 2017, doi: 10.1016/j.jallcom.2017.02.200.

[8] H. Yoshida, N. Yabuuchi, and S. Komaba, "$NaFe_{0.5}Co_{0.5}O_2$ as high energy and power positive electrode for Na-ion batteries," *Electrochem. commun.*, vol. 34, pp. 60–63, 2013, doi: 10.1016/j.elecom.2013.05.012.

[9] L. Zheng, J. Li, and M. N. Obrovac, "Crystal Structures and Electrochemical Performance of Air-Stable $Na_{2/3}Ni_{1/3-x}Cu_xMn_{2/3}O_2$ in Sodium Cells," *Chem. Mater.*, vol. 29, no. 4, pp. 1623–1631, 2017, doi: 10.1021/acs.chemmater.6b04769.

[10] L. Zheng and M. N. Obrovac, "Investigation of O3-type $Na_{0.9}Ni_{0.45}Mn_xTi_{0.55-x}O_2$ ($0 \leq x \leq 0.55$) as positive electrode materials for sodium-ion batteries," *Electrochim. Acta*, vol. 233, pp. 284–291, 2017, doi: 10.1016/j.electacta.2017.03.033.

[11] Q. Wang, S. Chu, and S. Guo, "Progress on multiphase layered transition metal oxide cathodes of sodium ion batteries," *Chinese Chem. Lett.*, vol. 31, no. 9, pp. 2167–2176, 2020, doi: 10.1016/j.cclet.2019.12.008.

[12] J. Xu, D. H. Lee, R. J. Clément, X. Yu, M. Leskes, A. J. Pell, G. Pintacuda, X.-Q. Yang, C. P. Grey, and Y. S. Meng, "Identifying the Critical Role of Li Substitution in P2–$Na_x[Li_yNi_zMn_{1-y-z}]O_2$ ($0 < x, y, z < 1$) Intercalation Cathode Materials for High-energy Na-Ion Batteries," *Chem. Mater.*, vol. 26, no. 2, pp. 1260–1269, Jan. 2014, doi: 10.1021/cm403855t.

[13] S. Chu, C. Zhang, H. Xu, S. Guo, P. Wang, and H. Zhou, "Pinning Effect Enhanced Structural Stability toward a Zero-Strain Layered Cathode for Sodium-Ion Batteries," *Angew. Chemie*, vol. 133, no. 24, pp. 13478–13483, 2021, doi:

10.1002/ange.202100917.

[14] S. Chu, D. Kim, G. Choi, C. Zhang, H. Li, W. K. Pang, Y. Fan, A. M. D'Angelo, S. Guo, and H. Zhou, "Revealing the Origin of Transition-Metal Migration in Layered Sodium-Ion Battery Cathodes: Random Na Extraction and Na-Free Layer Formation," *Angew. Chemie*, vol. 3168, 2023, doi: 10.1002/ange.202216174.

[15] M. S. Whittingham, "Lithium batteries and cathode materials," *Chem. Rev.*, vol. 104, no. 10, pp. 4271–4301, 2004, doi: 10.1021/cr020731c.

[16] S.-M. Oh, S.-T. Myung, J.-Y. Hwang, B. Scrosati, K. Amine, and Y. Sun, "High Capacity O3-Type $Na[Li_{0.05}(Ni_{0.25}Fe_{0.25}Mn_{0.5})_{0.95}]O_2$ Cathode for Sodium Ion Batteries," *Chem. Mater.*, vol. 26, no. 21, pp. 6165–6171, Nov. 2014, doi: 10.1021/cm502481b.

[17] Y. Wang, X. Yu, S. Xu, J. Bai, R. Xiao, Y. S. Hu, H. Li, X. Q. Yang, L. Chen, and X. Huang, "A zero-strain layered metal oxide as the negative electrode for long-life sodium-ion batteries," *Nat. Commun.*, vol. 4, pp. 1–8, 2013, doi: 10.1038/ncomms3365.

[18] G. Ceder and A. Van der Ven, "Phase diagrams of lithium transition metal oxides: investigations from first principles," *Electrochim. Acta*, vol. 45, no. 1–2, pp. 131–150, Sep. 1999, doi: 10.1016/S0013-4686(99)00199-1.

[19] M. Tang, W. C. Carter, and Y.-M. Chiang, "Electrochemically Driven Phase Transitions in Insertion Electrodes for Lithium-Ion Batteries: Examples in Lithium Metal Phosphate Olivines," *Annu. Rev. Mater. Res.*, vol. 40, no. 1, pp. 501–529, Jun. 2010, doi: 10.1146/annurev-matsci-070909-104435.

[20] R. J. Clément, J. Billaud, A. Robert Armstrong, G. Singh, T. Rojo, P. G. Bruce, and C. P. Grey, "Structurally stable Mg-doped P2-$Na_{2/3}Mn_{1-y}Mg_yO_2$ sodium-ion battery cathodes with high rate performance: insights from electrochemical, NMR and diffraction studies," *Energy Environ. Sci.*, vol. 9, no. 10, pp. 3240–3251, 2016, doi: 10.1039/C6EE01750A.

[21] Y. N. Zhou, J. L. Yue, E. Hu, H. Li, L. Gu, K. W. Nam, S. M. Bak, X. Yu, J. Liu, J. Bai, E. Dooryhee, Z. W. Fu, and X. Q. Yang, "High-Rate Charging Induced Intermediate Phases and Structural Changes of Layer-Structured Cathode for Lithium-Ion Batteries," *Adv. Energy Mater.*, vol. 6, no. 21, Nov. 2016, doi: 10.1002/aenm.201600597.

[22] T. Ohzuku, A. Ueda, and N. Yamamoto, "Zero-Strain Insertion Material of $Li[Li_{1/3}Ti_{5/3}]O_4$ for Rechargeable Lithium Cells," *J. Electrochem. Soc.*, vol. 142, no. 5, pp. 1431–1435, 1995, doi: 10.1149/1.2048592.

[23] N. Yabuuchi, K. Kubota, M. Dahbi, and S. Komaba, "Research development on sodium-ion batteries," *Chem. Rev.*, vol. 114, no. 23, pp. 11636–11682, 2014, doi: 10.1021/cr500192f.

[24] N. Tapia-Ruiz, W. M. Dose, N. Sharma, H. Chen, J. Heath, J. W. Somerville, U. Maitra, M. S. Islam, and P. G. Bruce, "High voltage structural evolution and enhanced Na-ion diffusion in P2-$Na_{2/3}Ni_{1/3-x}Mg_xMn_{2/3}O_2$ ($0 \le x \le 0.2$) cathodes from diffraction, electrochemical and *ab initio* studies," *Energy Environ. Sci.*, vol. 11, no. 6, pp. 1470–1479, 2018, doi: 10.1039/c7ee02995k.

[25] K. Kubota, Y. Yoda, and S. Komaba, "Origin of Enhanced Capacity Retention of P2-

Type $Na_{2/3}Ni_{1/3-x}Mn_{2/3}Cu_xO_2$ for Na-Ion Batteries," *J. Electrochem. Soc.*, vol. 164, no. 12, pp. A2368–A2373, 2017, doi: 10.1149/2.0311712jes.

[26] Y. Wen, J. Fan, C. Shi, P. Dai, Y. Hong, R. Wang, L. Wu, Z. Zhou, J. Li, L. Huang, and S. G. Sun, "Probing into the working mechanism of Mg versus Co in enhancing the electrochemical performance of P2-Type layered composite for sodium-ion batteries," *Nano Energy*, vol. 60, no. January, pp. 162–170, 2019, doi: 10.1016/j.nanoen.2019.02.074.

[27] Y. Shi, S. Li, A. Gao, J. Zheng, Q. Zhang, X. Lu, L. Gu, and D. Cao, "Probing the Structural Transition Kinetics and Charge Compensation of the P2-$Na_{0.78}Al_{0.05}Ni_{0.33}Mn_{0.60}O_2$ Cathode for Sodium Ion Batteries," *ACS Appl. Mater. Interfaces*, vol. 11, no. 27, pp. 24122–24131, 2019, doi: 10.1021/acsami.9b06233.

[28] P. Hou, Y. Sun, F. Li, Y. Sun, X. Deng, H. Zhang, X. Xu, and L. Zhang, "A high energy-density P2-$Na_{2/3}[Ni_{0.3}Co_{0.1}Mn_{0.6}]O_2$ cathode with mitigated P2-O2 transition for sodium-ion batteries," *Nanoscale*, vol. 11, no. 6, pp. 2787–2794, 2019, doi: 10.1039/c8nr09601e.

[29] Y. Shi, Z. Zhang, P. Jiang, A. Gao, K. Li, Q. Zhang, Y. Sun, X. Lu, D. Cao, and X. Lu, "Unlocking the potential of P3 structure for practical Sodium-ion batteries by fabricating zero strain framework for Na^+ intercalation," *Energy Storage Mater.*, vol. 37, no. February, pp. 354–362, 2021, doi: 10.1016/j.ensm.2021.02.020.

[30] H. Fu, Y.-P. Wang, G. Fan, S. Guo, X. Xie, X. Cao, B. Lu, M. Long, J. Zhou, and S. Liang, "Synergetic stability enhancement with magnesium and calcium ion substitution for Ni/Mn-based P2-type sodium-ion battery cathodes," *Chem. Sci.*, vol. 13, no. 3, pp. 726–736, 2022, doi: 10.1039/D1SC05715D.

[31] Q. Zhu, H. Cheng, X. Zhang, L. He, L. Hu, J. Yang, Q. Chen, and Z. Lu, "Improvement in electrochemical performance of $Na_3V_2(PO_4)_3$/C cathode material for sodium-ion batteries by K-Ca co-doping," *Electrochim. Acta*, vol. 281, pp. 208–217, 2018, doi: 10.1016/j.electacta.2018.05.174.

[32] Q. Mao, Y. Yu, J. Wang, L. Zheng, Z. Wang, Y. Qiu, Y. Hao, and X. Liu, "Mitigating the P2-O2 transition and Na^+/vacancy ordering in $Na_{2/3}Ni_{1/3}Mn_{2/3}O_2$ by anion/cation dual-doping for fast and stable Na+insertion/extraction," *J. Mater. Chem. A*, vol. 9, no. 17, pp. 10803–10811, 2021, doi: 10.1039/d1ta01433a.

[33] I. Lee, G. Oh, S. Lee, T. Y. Yu, M. H. Alfaruqi, V. Mathew, B. Sambandam, Y. K. Sun, J. Y. Hwang, and J. Kim, "Cationic and transition metal co-substitution strategy of O3-type $NaCrO_2$ cathode for high-energy sodium-ion batteries," *Energy Storage Mater.*, vol. 41, no. June, pp. 183–195, 2021, doi: 10.1016/j.ensm.2021.05.046.

[34] L. Zheng, J. C. Bennett, and M. N. Obrovac, "Stabilizing $NaCrO_2$ by Sodium Site Doping with Calcium," *J. Electrochem. Soc.*, vol. 166, no. 10, pp. A2058–A2064, 2019, doi: 10.1149/2.1041910jes.

[35] T. Y. Yu, J. Kim, J. Y. Hwang, H. Kim, G. Han, H. G. Jung, and Y. K. Sun, "High-energy O3-$Na_{1-2x}Ca_x[Ni_{0.5}Mn_{0.5}]O_2$ cathodes for long-life sodium-ion batteries," *J. Mater. Chem. A*, vol. 8, no. 27, pp. 13776–13786, 2020, doi: 10.1039/d0ta04847j.

[36] L. Sun, Y. Xie, X. Z. Liao, H. Wang, G. Tan, Z. Chen, Y. Ren, J. Gim, W. Tang, Y. S. He, K. Amine, and Z. F. Ma, "Insight into Ca-Substitution Effects on O3-Type

$NaNi_{1/3}Fe_{1/3}Mn_{1/3}O_2$ Cathode Materials for Sodium-Ion Batteries Application," *Small*, vol. 14, no. 21, pp. 1–7, 2018, doi: 10.1002/smll.201704523.

[37] M. Matsui, F. Mizukoshi, H. Hasegawa, and N. Imanishi, "Ca-substituted P3-type $Na_xNi_{1/3}Mn_{1/3}Co_{1/3}O_2$ as a potential high voltage cathode active material for sodium-ion batteries," *J. Power Sources*, vol. 485, no. September 2020, p. 229346, 2021, doi: 10.1016/j.jpowsour.2020.229346.

[38] Y. Ishado, H. Hasegawa, S. Okada, M. Mizuhata, H. Maki, and M. Matsui, "An experimental and first-principle investigation of the Ca-substitution effect on P3-type layered Na_xCoO_2," *Chem. Commun.*, vol. 56, no. 58, pp. 8107–8110, 2020, doi: 10.1039/d0cc01675f.

[39] H. Hasegawa, Y. Ishado, S. Okada, M. Mizuhata, H. Maki, and M. Matsui, "Stabilized Phase Transition Process of Layered Na_x CoO_2 *via* Ca-Substitution," *J. Electrochem. Soc.*, vol. 168, no. 1, p. 010509, 2021, doi: 10.1149/1945-7111/abd451.

[40] Y. Ono, N. Kato, Y. Ishii, Y. Miyazaki, and T. Kajitani, "Crystal Structure and Transport Properties of γ-Na_xCoO_2 (x = 0.67-0.75)," *J. Japan Soc. Powder Powder Metall.*, vol. 50, no. 6, pp. 469–474, 2003, doi: 10.2497/jjspm.50.469.

[41] R. Berthelot, D. Carlier, and C. Delmas, "Electrochemical investigation of the P2–Na_xCoO_2 phase diagram," *Nat. Mater.*, vol. 10, no. 1, pp. 74–80, 2011, doi: 10.1038/nmat2920.

[42] M. Nishijima, T. Ootani, Y. Kamimura, T. Sueki, S. Esaki, S. Murai, K. Fujita, K. Tanaka, K. Ohira, Y. Koyama, and I. Tanaka, "Accelerated discovery of cathode materials with prolonged cycle life for lithium-ion battery," *Nat. Commun.*, vol. 5, pp. 1–7, 2014, doi: 10.1038/ncomms5553.

[43] R. Zhou, X. Guo, Z. Li, S. Luo, and M. Luo, "More Ca^{2+}, Less Na^{+}: Increase the Desalination Capacity and Performance Stability of $Na_xCa_yCoO_2$," *ACS Sustain. Chem. Eng.*, vol. 7, no. 17, pp. 14561–14568, 2019, doi: 10.1021/acssuschemeng.9b02157.

[44] Q. Wang, S. Mariyappan, J. Vergnet, A. M. Abakumov, G. Rousse, F. Rabuel, M. Chakir, and J.-M. Tarascon, "Reaching the Energy Density Limit of Layered O3-$NaNi_{0.5}Mn_{0.5}O_2$ Electrodes via Dual Cu and Ti Substitution," *Adv. Energy Mater.*, vol. 9, no. 36, p. 1901785, Sep. 2019, doi: 10.1002/aenm.201901785.

[45] W. M. Haynes, D. R. Lide, and T. J. Bruno, *CRC Handbook of Chemistry and Physics*, 95th ed. CRC Press, 2014. doi: 10.1201/b17118.

[46] D. Larcher and J.-M. Tarascon, "Towards greener and more sustainable batteries for electrical energy storage," *Nature Chemistry*, vol. 7, no. 1. pp. 19–29, 2015. doi: 10.1038/nchem.2085.

[47] M. Titirici, P. Adelhelm, and Y. Hu, *Sodium-Ion Batteries: Materials, Characterization, and Technology, Volume 1*, vol. 23, no. 8. Wiley, 2022. doi: 10.1002/9783527825769.

[48] K. Kubota, S. Kumakura, Y. Yoda, K. Kuroki, and S. Komaba, "Electrochemistry and Solid-State Chemistry of $NaMeO_2$ (Me = 3d Transition Metals)," *Advanced Energy Materials*, vol. 8, no. 17. Wiley-VCH Verlag, Jun. 15, 2018. doi:

10.1002/aenm.201703415.

[49] D. Walsh, S. C. Wimbush, and S. R. Hall, “Use of the Polysaccharide Dextran as a Morphological Directing Agent in the Synthesis of High-T_c Superconducting $YBa_2Cu_3O_{7-\delta}$ Sponges with Improved Critical Current Densities,” *Chem. Mater.*, vol. 19, no. 4, pp. 647–649, 2007, doi: 10.1021/cm0626684.

[50] S. Zilinskaite, A. J. R. Rennie, R. Boston, and N. Reeves-McLaren, “Biotemplating: a sustainable synthetic methodology for Na-ion battery materials,” *J. Mater. Chem. A*, vol. 6, no. 13, pp. 5346–5355, 2018, doi: 10.1039/C7TA09260A.

[51] R. Boston, A. Carrington, D. Walsh, and S. R. Hall, “Synthesis of spherical superconductors,” *CrystEngComm*, vol. 15, no. 19, p. 3763, 2013, doi: 10.1039/c3ce40269j.

[52] S. Zilinskaite, N. Reeves-McLaren, and R. Boston, “Xanthan gum as a water-based binder for P3-$Na_{2/3}Ni_{1/3}Mn_{2/3}O_2$,” *Front. Energy Res.*, vol. 10, no. August, pp. 1–11, Aug. 2022, doi: 10.3389/fenrg.2022.909486.

[53] Z. Zhang, S. C. Wimbush, A. Kursumovic, H. Suo, and J. L. MacManus-Driscoll, “Detailed study of the process of biomimetic formation of YBCO platelets from nitrate salts in the presence of the biopolymer dextran and a molten NaCl flux,” *Cryst. Growth Des.*, vol. 12, no. 11, pp. 5635–5642, 2012, doi: 10.1021/cg301143r.

[54] L. J. Vera Stimpson, S. Ramos, G. B. G. Stenning, M. Jura, S. Parry, G. Cibin, and D. C. Arnold, “Investigation of the role of morphology on the magnetic properties of $Ca_2Mn_3O_8$ materials,” *Dalt. Trans.*, vol. 46, no. 41, pp. 14130–14138, 2017, doi: 10.1039/c7dt03053c.

[55] B. H. Toby, “ R factors in Rietveld analysis: How good is good enough? ,” *Powder Diffr.*, vol. 21, no. 1, pp. 67–70, 2006, doi: 10.1154/1.2179804.

[56] X. Li, Y. Wang, D. Wu, L. Liu, S. H. Bo, and G. Ceder, “Jahn-Teller assisted Na diffusion for high performance Na ion batteries,” *Chem. Mater.*, vol. 28, no. 18, pp. 6575–6583, 2016, doi: 10.1021/acs.chemmater.6b02440.

[57] P. F. Wang, Y. You, Y. X. Yin, and Y. G. Guo, “Layered Oxide Cathodes for Sodium-Ion Batteries: Phase Transition, Air Stability, and Performance,” *Adv. Energy Mater.*, vol. 8, no. 8, pp. 1–23, 2018, doi: 10.1002/aenm.201701912.

[58] N. Yabuuchi, R. Hara, M. Kajiyama, K. Kubota, T. Ishigaki, A. Hoshikawa, and S. Komaba, “New O2/P2-type Li-Excess Layered Manganese Oxides as Promising Multi-Functional Electrode Materials for Rechargeable Li/Na Batteries,” *Adv. Energy Mater.*, vol. 4, p. 1031453, 2014, doi: 10.1002/aenm.201301453.

[59] M. S. Chae, A. Chakraborty, S. Kunnikuruvan, R. Attias, S. Maddukuri, Y. Gofer, D. T. Major, and D. Aurbach, “Vacancy-Driven High Rate Capabilities in Calcium-Doped $Na_{0.4}MnO_2$ Cathodes for Aqueous Sodium-Ion Batteries,” *Adv. Energy Mater.*, vol. 10, no. 37, pp. 1–7, 2020, doi: 10.1002/aenm.202002077.

[60] G. Ma, Y. Zhao, K. Huang, Z. Ju, C. Liu, Y. Hou, and Z. Xing, “Effects of the starting materials of $Na_{0.44}MnO_2$ cathode materials on their electrochemical properties for Na-ion batteries,” *Electrochim. Acta*, vol. 222, pp. 36–43, 2016, doi: 10.1016/j.electacta.2016.11.048.

[61] R. Qiao, K. Dai, J. Mao, T. C. Weng, D. Sokaras, D. Nordlund, X. Song, V. S. Battaglia, Z. Hussain, G. Liu, and W. Yang, "Revealing and suppressing surface Mn(II) formation of $Na_{0.44}MnO_2$ electrodes for Na-ion batteries," *Nano Energy*, vol. 16, pp. 186–195, 2015, doi: 10.1016/j.nanoen.2015.06.024.

[62] M. Kalapsazova, P. Markov, K. Kostov, E. Zhecheva, D. Nihtianova, and R. Stoyanova, "Controlling at Elevated Temperature the Sodium Intercalation Capacity and Rate Capability of P3-$Na_{2/3}Ni_{1/2}Mn_{1/2}O_2$ through the Selective Substitution of Nickel with Magnesium," *Batter. Supercaps*, vol. 3, no. 12, pp. 1329–1340, 2020, doi: 10.1002/batt.202000137.

[63] L. G. Chagas, D. Buchholz, C. Vaalma, L. Wu, and S. Passerini, "P-type $Na_xNi_{0.22}Co_{0.11}Mn_{0.66}O_2$ materials: linking synthesis with structure and electrochemical performance," *J. Mater. Chem. A*, vol. 2, no. 47, pp. 20263–20270, 2014, doi: 10.1039/C4TA03946G.

[64] J. Billaud, G. Singh, A. R. Armstrong, E. Gonzalo, V. Roddatis, M. Armand, T. Rojo, and P. G. Bruce, "$Na_{0.67}Mn_{1-x}Mg_xO_2$ ($0 \leq x \leq 0.2$): a high capacity cathode for sodium-ion batteries," *Energy Environ. Sci.*, vol. 7, no. 4, pp. 1387–1391, 2014, doi: 10.1039/C4EE00465E.

[65] N. Yabuuchi, R. Hara, K. Kubota, J. Paulsen, S. Kumakura, and S. Komaba, "A new electrode material for rechargeable sodium batteries: P2-type $Na_{2/3}[Mg_{0.28}Mn_{0.72}]O_2$ with anomalously high reversible capacity," *J. Mater. Chem. A*, vol. 2, no. 40, pp. 16851–16855, 2014, doi: 10.1039/C4TA04351K.

[66] L. G. Chagas, D. Buchholz, L. Wu, B. Vortmann, and S. Passerini, "Unexpected performance of layered sodium-ion cathode material in ionic liquid-based electrolyte," *J. Power Sources*, vol. 247, pp. 377–383, 2014, doi: 10.1016/j.jpowsour.2013.08.118.

[67] M. H. Han, E. Gonzalo, N. Sharma, J. M. López Del Amo, M. Armand, M. Avdeev, J. J. Saiz Garitaonandia, and T. Rojo, "High-Performance P2-Phase $Na_{2/3}Mn_{0.8}Fe_{0.1}Ti_{0.1}O_2$ Cathode Material for Ambient-Temperature Sodium-Ion Batteries," *Chem. Mater.*, vol. 28, no. 1, pp. 106–116, 2016, doi: 10.1021/acs.chemmater.5b03276.

[68] J. Hong, S. Xiao, L. Deng, T. Lan, and G. He, "Li-free P2/O3 biphasic $Na_{0.73}Ni_{0.4}Mn_{0.4}Ti_{0.2}O_2$ as a cathode material for sodium-ion batteries," *Ionics (Kiel).*, vol. 26, no. 8, pp. 3911–3917, 2020, doi: 10.1007/s11581-020-03560-2.

[69] C. Chen, W. Hang, Y. Li, M. Zhang, K. Nie, J. Wang, W. Zhao, R. Qi, C. Zuo, Z. Li, H. Yi, and F. Pan, "P2/O3 biphasic Fe/Mn-based layered oxide cathode with ultrahigh capacity and great cyclability for sodium ion batteries," *Nano Energy*, vol. 90, no. PA, p. 106504, 2021, doi: 10.1016/j.nanoen.2021.106504.

[70] D. Buchholz, C. Vaalma, L. G. Chagas, and S. Passerini, "Mg-doping for improved long-term cyclability of layered Na-ion cathode materials - The example of P2-type $Na_xMg_{0.11}Mn_{0.89}O_2$," *J. Power Sources*, vol. 282, pp. 581–585, 2015, doi: 10.1016/j.jpowsour.2015.02.069.

[71] E. J. Kim, L. A. Ma, D. M. Pickup, A. V. Chadwick, R. Younesi, P. Maughan, J. T. S. Irvine, and A. R. Armstrong, "Vacancy-enhanced oxygen redox reversibility in P3-type

magnesium-doped sodium manganese oxide $Na_{0.67}Mg_{0.2}Mn_{0.8}O_2$," *ACS Appl. Energy Mater.*, vol. 3, no. 11, pp. 10423–10434, 2020, doi: 10.1021/acsaem.0c01352.

[72] S. F. Linnell, M. Hirsbrunner, S. Imada, G. Cibin, A. B. Naden, A. V. Chadwick, J. T. S. Irvine, L. C. Duda, and A. R. Armstrong, "Enhanced Cycling Stability in the Anion Redox Material P3-Type Zn-Substituted Sodium Manganese Oxide," *ChemElectroChem*, vol. 9, no. 11, 2022, doi: 10.1002/celc.202200240.

[73] C. Liu, Z. G. Neale, and G. Cao, "Understanding electrochemical potentials of cathode materials in rechargeable batteries," *Mater. Today*, vol. 19, no. 2, pp. 109–123, 2016, doi: 10.1016/j.mattod.2015.10.009.

[74] T. Risthaus, L. Chen, J. Wang, J. Li, D. Zhou, L. Zhang, D. Ning, X. Cao, X. Zhang, G. Schumacher, M. Winter, E. Paillard, and J. Li, "P3 $Na_{0.9}Ni_{0.5}Mn_{0.5}O_2$ Cathode Material for Sodium Ion Batteries," *Chem. Mater.*, vol. 31, no. 15, pp. 5376–5383, 2019, doi: 10.1021/acs.chemmater.8b03270.

[75] M. Sathiya, K. Hemalatha, K. Ramesha, J.-M. Tarascon, and A. S. Prakash, "Synthesis, structure, and electrochemical properties of the layered sodium insertion cathode material: $NaNi_{1/3}Mn_{1/3}Co_{1/3}O_2$," *Chem. Mater.*, vol. 24, no. 10, pp. 1846–1853, 2012, doi: 10.1021/cm300466b.

[76] S. Komaba, N. Yabuuchi, T. Nakayama, A. Ogata, T. Ishikawa, and I. Nakai, "Study on the reversible electrode reaction of $Na_{1-x}Ni_{0.5}Mn_{0.5}O_2$ for a rechargeable sodium-ion battery," *Inorg. Chem.*, vol. 51, no. 11, pp. 6211–6220, 2012, doi: 10.1021/ic300357d.

[77] S. Maddukuri, P. Valerie, and V. V. Upadhyayula, "Synthesis and Electrochemical Study of New P3 Type Layered $Na_{0.6}Ni_{0.25}Mn_{0.5}Co_{0.25}O_2$ for Sodium-Ion Batteries," *ChemistrySelect*, vol. 2, no. 20, pp. 5660–5666, 2017, doi: 10.1002/slct.201700376.

[78] J. Li, S. Jeong, R. Kloepsch, M. Winter, and S. Passerini, "Improved electrochemical performance of $LiMO_2$ (M=Mn, Ni, Co)-Li_2MnO_3 cathode materials in ionic liquid-based electrolyte," *J. Power Sources*, vol. 239, pp. 490–495, 2013, doi: 10.1016/j.jpowsour.2013.04.015.

[79] Y. Terada, Y. Nishiwaki, I. Nakai, and F. Nishikawa, "Study of Mn dissolution from $LiMn_2O_4$ spinel electrodes using *in situ* total reflection X-ray fluorescence analysis and fluorescence XAFS technique," *J. Power Sources*, vol. 97–98, pp. 420–422, Jul. 2001, doi: 10.1016/S0378-7753(01)00741-8.

[80] S. Guo, P. Liu, H. Yu, Y. Zhu, M. Chen, M. Ishida, and H. Zhou, "A layered P2- and O3-type composite as a high-energy cathode for rechargeable sodium-ion batteries," *Angew. Chemie - Int. Ed.*, vol. 54, no. 20, pp. 5894–5899, 2015, doi: 10.1002/anie.201411788.

[81] M. Bianchini, E. Gonzalo, N. E. Drewett, N. Ortiz-Vitoriano, J. M. Lopez Del Amo, F. J. Bonilla, B. Acebedo, and T. Rojo, "Layered P2-O3 sodium-ion cathodes derived from earth abundant elements," *J. Mater. Chem. A*, pp. 3552–3559, 2018, doi: 10.1039/C7TA11180K.

[82] M. Tang, J. Yang, H. Liu, X. Chen, L. Kong, Z. Xu, J. Huang, and Y. Xia, "Spinel-Layered Intergrowth Composite Cathodes for Sodium-Ion Batteries," *ACS Appl. Mater. Interfaces*, vol. 12, no. 41, pp. 45997–46004, 2020, doi: 10.1021/acsami.0c12280.

[83] J. Li, T. Risthaus, J. Wang, D. Zhou, X. He, N. Ehteshami, V. Murzin, A. Friesen, H. Liu, X. Hou, M. Diehl, E. Paillard, M. Winter, and J. Li, "The effect of Sn substitution on the structure and oxygen activity of $Na_{0.67}Ni_{0.33}Mn_{0.67}O_2$ cathode materials for sodium ion batteries," *J. Power Sources*, vol. 449, no. November 2019, p. 227554, 2020, doi: 10.1016/j.jpowsour.2019.227554.

[84] B. Sambandam, M. H. Alfaruqi, S. Park, S. Lee, S. Kim, J. Lee, V. Mathew, J. Y. Hwang, and J. Kim, "Validating the structural (In)stability of P3- and P2-$Na_{0.67}Mg_{0.1}Mn_{0.9}O_2$-Layered cathodes for sodium-ion batteries: A time-decisive approach," *ACS Appl. Mater. Interfaces*, vol. 13, no. 45, pp. 53877–53891, 2021, doi: 10.1021/acsami.1c15394.

[85] S. Guo, Y. Sun, J. Yi, K. Zhu, P. Liu, Y. Zhu, G. Zhu, M. Chen, M. Ishida, and H. Zhou, "Understanding sodium-ion diffusion in layered P2 and P3 oxides *via* experiments and first-principles calculations: a bridge between crystal structure and electrochemical performance," *NPG Asia Mater.*, vol. 8, p. e266, 2016, doi: 10.1038/am.2016.53.

[86] Y. N. Zhou, P. F. Wang, Y. Bin Niu, Q. Li, X. Q. Yu, Y. X. Yin, S. Xu, and Y. G. Guo, "A P2/P3 composite layered cathode for high-performance Na-ion full batteries," *Nano Energy*, vol. 55, no. September 2018, pp. 143–150, 2019, doi: 10.1016/j.nanoen.2018.10.072.

[87] G. L. Xu, R. Amine, Y. F. Xu, J. Liu, J. Gim, T. Ma, Y. Ren, C. J. Sun, Y. Liu, X. Zhang, S. M. Heald, A. Solhy, I. Saadoune, W. L. Mattis, S. G. Sun, Z. Chen, and K. Amine, "Insights into the structural effects of layered cathode materials for high voltage sodium-ion batteries," *Energy Environ. Sci.*, vol. 10, no. 7, pp. 1677–1693, 2017, doi: 10.1039/c7ee00827a.

[88] S. F. Linnell, A. G. Manche, Y. Liao, M. Hirsbrunner, S. Imada, A. B. Naden, J. T. S. Irvine, L. C. Duda, and A. R. Armstrong, "Effect of Cu substitution on anion redox behaviour in P3-type sodium manganese oxides," *JPhys Energy*, vol. 4, no. 4, 2022, doi: 10.1088/2515-7655/ac95cc.

[89] K. Luo, M. R. Roberts, N. Guerrini, N. Tapia-Ruiz, R. Hao, F. Massel, D. M. Pickup, S. Ramos, Y. S. Liu, J. Guo, A. V. Chadwick, L. C. Duda, and P. G. Bruce, "Anion Redox Chemistry in the Cobalt Free 3d Transition Metal Oxide Intercalation Electrode $Li[Li_{0.2}Ni_{0.2}Mn_{0.6}]O_2$," *J. Am. Chem. Soc.*, vol. 138, no. 35, pp. 11211–11218, 2016, doi: 10.1021/jacs.6b05111.

5 Combining P3- and P2-$Na_{0.67}Mn_{0.9}Mg_{0.1}O_2$ phases

5.1 Introduction

Multiphase composite structures have long been established as a route to increased capacity and capacity retention in NIB cathode materials [1]. The need for composite phases arises because of the distinct benefits and drawbacks of the different crystal structures possible in layered oxide cathode materials. For example, prismatic (P-type) compounds exhibit higher rate capability and lower energy barriers than octahedral (O-type) ones [2]. This is as result of the face-sharing nature of the trigonal prismatic Na^+ sites, which allows facile transport through the structure. By comparison, the Na^+ in octahedral sites diffuse *via* an intermediate tetrahedral site, which is unfavourable and sluggish due to the size discrepancy between the Na^+ and the tetrahedral site [3]; the Na^+ is too large, meaning diffusion is slow. However, the O-type structures form when Na^+ content is high ($x > 0.9$), as opposed the P-type which form in Na^+ deficient conditions ($x \sim 0.67$). Therefore, the O-type phases are said to act as a Na^+ reservoir, particularly in full cells [1]. The formula for determining theoretical capacity is correlating with the number of moles of electrons that transfer during charge or discharge, and therefore the number of Na^+ that can be extracted. Thus various combinations are available to create these multiphase structures; such as the P2/O3 [2], [4]–[7] and P2/P3 biphases [8]–[12], and the P2/P3/O3 triphase [13], [14].

These composites are generated using a range of techniques: cation doping (for example, Li [2], [4], or a transition metal [7], [15]), quenching [13], varying Na^+ content [6], and adjusting calcination temperature [8], [16], [17]. Calcination temperature is the technique used to generate a P2/P3 biphase in this chapter. Since both the P2 and P3 phases are sodium deficient compared to the O3 phases ($x \approx 0.67$ *vs* $x \approx 1$), the two phases can be grown simultaneously as the two phases use the same ratio of starting materials, but different calcination temperatures. Previous work notes that P2 phases form at higher temperatures than the P3 phase [18]–[20]. The reason this occurs at high temperatures is that the transition involves a 60° rotation of all the TMO_2 octahedra in alternate layers [21], as well as a layer glide, shown in Figure 5-1. Unlike the P-type to O-type transitions, which is achieved *via* only layer gliding at certain Na^+ occupancies, the transition between P-type structures involves the breaking of TM-O bonds. The result is a grain made up of both P2 and P3 phases [17]. These multiphase composites are shown to be topotactic intergrowths [12], [22]–[24], made possible by the 3D structural similarity between the different layered oxides phases [4], [13], [25], and occurs when the multiphase is generated *via* adjusting the calcination temperature [16], [17].

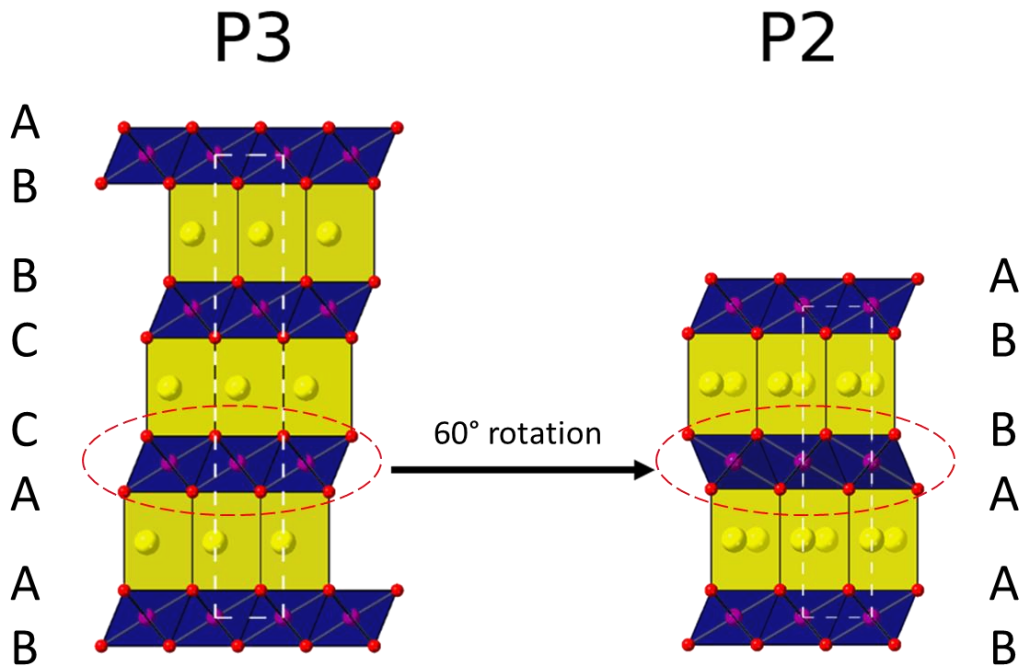

Figure 5-1: Schematic of the P3 and P2 phases. Note the change in relative orientation of the TMO_2 layers.

Doping the TMO_2 layer can also generate composite phases. It is suggested that when doping with Sn the preferred structure of the $Na_{0.67}Ni_{0.33}Mn_{0.66-x}Sn_xO_2$ cathode changes [26]. It lowers the pH of the initial solution during the precipitation synthesis (as well as annealing temperature) as it is a Lewis acid, which leads to formation of the P3 phase [27]. The undoped material forms a P3/P2 biphase that is majority P2 when calcined at 800 °C. However, when doping with increasing amounts of Sn^{4+} (x = 1, 3, and 5%) the P3 phase becomes more dominant as the Sn^{4+} decreases the pH of the initial solution. A similar effect was seen in generating a P2/O3 biphase of the same material at 1000 °C instead [15]: increasing Sn^{4+} doping leading to higher phase fraction of O3 over the P2 phase. In both cases, 1% Sn doping is enough to increase initial discharge capacity over 50 cycles at 200 mA g^{-1} (1C) or over 30 cycles at a current density of 15 mA g^{-1}, respectively. In both cases an improvement in capacity at higher C-rates was observed.

Neither study deconvolutes the effects of doping on the cell performance from the effects of having a composite material acting as the cathode. Thus, the multiphase materials generated *via* doping cannot be said to be better than the single phases. One study does acknowledge this convolution and proposes that the neighbouring phases stabilise each other *via* an interlocking interface reaction mechanism [28] – resulting in a hetero-epitaxial structure that reduces strain energy at the phase boundary. This is results in a smaller volume change and translates to less damage permanently done to the structure during cycling, despite the composite sample displaying a more complex phase progression during cycling as observed in *operando* XRD.

Smaller volume changes during cycling are particularly relevant to Mn-rich cathodes. These cathodes utilise the Mn^{3+}/Mn^{4+} redox couple, and are susceptible to Mn^{2+} dissolution as a capacity fading mechanism [29]. Using biphasic compounds to reduce lattice mismatch during phase transitions has been shown to reduce Mn^{2+} dissolution in P2/O3-$Na_{0.7}Li_{0.11}Fe_{0.36}Mn_{0.36}Ti_{0.17}O_2$, which utilises the Mn^{3+}/Mn^{4+} redox couple, by reducing micro-cracks in the material during cycling [5].

Using biphasic materials, as with doped materials, can also prevent harmful phase transitions. In $Na_{0.67}Li_{0.18}Mn_{0.8}Fe_{0.2}O_2$ [30], the addition of Li to the host material leads to formation of a P2 and O3 phase. The O3 phase is an electrochemically inactive minor phase which the authors suggest is suppressing the P2↔OP4 transition. Although this could also be caused by Li substitution, it is more likely to be a result of the biphase as it displays higher capacity (125 mAh g^{-1}) than the equivalent phase-pure P2 material [31]. This supports the above study, wherein the biphases are thought to be interlocked and prevent detrimental phase transitions (displayed in Figure 5-2).

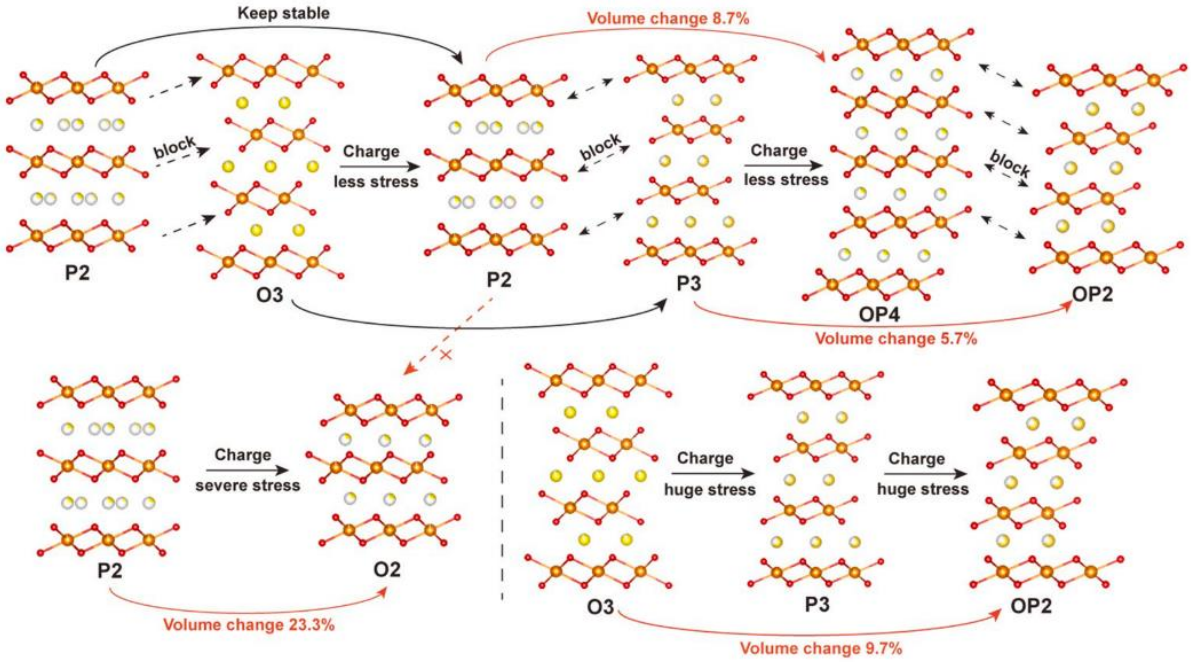

Figure 5-2: Schematic of the suppression of volume change in P2/O3 biphases (top) as opposed to P2 and O3 single phases (bottom). Adapted from [28].

At C/10 the capacity of 125 mAh g^{-1} is low compared to other compared to other biphases described here. The capacity falls to 100 mAh g^{-1} after <25 cycles before levelling off – overall, the capacity retention is <70% over 100 cycles between 1.5 – 4.2 V vs Na/Na^+ at C/10. This capacity fade was investigated *via* cyclic voltammetry (CV) and it identified increasing polarisation and reduced intensities of the redox peaks, which was attributed to polarisation at the electrode interface [32], [33].

It is unlikely the Mn^{2+} dissolution is the cause of capacity fading here, as the material shows increased capacity after 100 cycles when ball milled. Doing this reduced the aggregate size from 3 – 30 µm to 0.5 µm – 3 µm [30]. Decreasing the particle size of the

material led to an increase in the electrochemical activity after 20 cycles, although after this there was a more rapid fade in capacity. The authors suggest that reducing particle size increases the surface exposed to SEI formation, which reduces Na^+ mobility. This is offset by the increased electrochemical activity of the material and the O3 phase prevents rapid capacity fading over the first 20 cycles by prevent the P2↔OP4 transition.

As mentioned, biphases can be generated by selection of calcination temperature. P3/P2-$Na_{0.45}Ni_{0.22}Co_{0.11}Mn_{0.66}O_2$ [8] was produced *via* calcining at a mid-point temperature between the P3 and P2 phase transition. Analysis *via* SEM revealed that the material consists of nano-sized particles, surrounding larger, micron-sized flakes, which are attributed to the P3 and P2 phase, respectively. This may be based on the particle size of each phase after synthesis of the single phases, which follow the pattern of the P2 particles being larger than the P3. The resulting composite exhibited a higher initial discharge capacity than the pure P2 phase, although its capacity retention is worse. The P3/P2 biphase delivers 146.8 mA g^{-1} in the first cycle, and 94.5 mAh g^{-1} after 150 cycles, compared to the P2 phase which delivers 130.4 mAh g^{-1} and 111.6 mAh g^{-1} for the same cycles. In this case, the use of a biphase did not produce better electrochemical performance overall than the single phase P2 material.

It is suggested that the increased capacity retention is due to increasing particle size from 0.1 μm to 2 μm, which can be controlled using biotemplating [34], [35]. The cause of lower capacity retention of the smaller particles is manganese dissolution. According to the authors, this position is supported by the combination of capacity fade and high cycle efficiency, and mitigated in later work by changing the electrolyte [29]. Comparing to the previous paper, in which reducing particle size improved capacity retention, increasing particle size seems counterintuitive. However, examination of the original particle sizes (3 – 30 μm [30] and 0.05 – 0.15 μm [8]) reveals that both are converging on a similar particle size range (0.5 – 3 μm in both studies) where the best cycling performance is achieved.

In the same study of P3/P2-$Na_{0.45}Ni_{0.22}Co_{0.11}Mn_{0.66}O_2$, the voltage profiles of the P3 and P2 single phases and the P3/P2 biphase were compared and found to be visually similar. Key features in the discharge profile were a voltage step between 4.1 and 3.6 V vs Na/Na^+ followed by a plateau at 3.6 V vs Na/Na^+, and then two plateaux at 3.2 V and 2.3 V vs Na/Na^+. The features below 3.5 V vs Na/Na^+ were attributed to sodium vacancy ordering at specific sodium contents [36]. Mn^{3+}/Mn^{4+} redox activity occurs between 2.1-2.4 V, meaning that this redox couple caused the plateau at 2.3 V vs Na/Na^+. The features are better defined in the P2 samples; one calcined at 800 °C, the other at 900 °C. This is possibly due to the larger particle sizes (0.5 μm – 3 μm, and 1 μm – 4 μm) compared to the P3 (0.05 μm – 0.15 μm) or P3/P2 phase (~ 1 μm). The capacity fading was indicated by the shortening and increasing gradient of voltage plateaux at 4.2 V and 3.6 V vs Na/Na^+, which represent phase transitions to O-type structures from the P-type. The feature at 2.3 V, although not mentioned, also shortens to a degree – supporting the case for Mn^{2+} dissolution in smaller particles due to the higher surface area.

The rate capability of the materials is also tested, and it is found that larger particle size can be detrimental to the capacity at high C-rates [8]. The longer diffusion pathways in the bulk material limits the capacity that can be extracted; the two P2 phases with different calcination temperatures, and thus particle sizes, show this. It is also worth noting that although the P2 phase with the smaller particle size still outperforms the lower temperature samples. The P3 and P3/P2 lose capacity as the voltage plateau is raised at higher C-rates, to a level above the upper cut-off voltage. However, the P3/P2 materials shows some improvement over the single P3 phase – likely die to the presence of the P2 phase.

Other studies on P3/P2 biphases, beyond demonstrating that the biphase outperforms the P3 phase [16] or both the P3 and P2 phases [17], also show the nature of these phases to be intergrowth structures. In both cases, TEM shows that the two P-type phases are growing next to each other in topotactic layers [4]. An example is shown in Figure 5-3 of a scanning transmission electron microscopy (STEM) image using high-angle annular dark field (HAADF) to show to show the P3 and P2 phases growing next to each other [11]. In the former, the P3/P2 $Na_{0.6}Ni_{0.17}Co_{0.17}Mn_{0.66}O_2$ [16] biphase outperforms the P3 phase only slightly, with a capacity retention after 50 cycles of 57.5% and 54.1%, respectively, cycling between 1.5 – 4.5 V vs Na/Na^+ at C/5. However, the capacity is approximately 20 mAh g^{-1} higher than the P3 phase per cycle throughout the test.

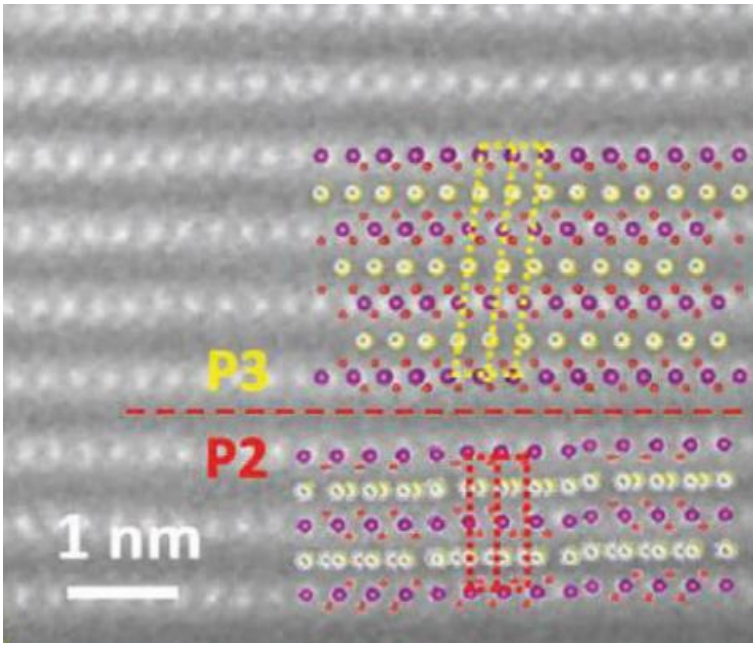

Figure 5-3: STEM-HAADF image of P2/P3–$Na_{0.67}Mn_{0.64}Co_{0.30}Al_{0.06}O_2$ [11].

Both samples are in turn outperformed by a triphasic sample, made up of the P2, P3, and an O'3 phase. The O'3 phase is generated by doping with Li and is in fact a Li layered material, shown by EXAFS in previous work by the same group [37]. This gives the material a nominal formula of $Na_{0.6}Li_{0.18}Ni_{0.17}Co_{0.17}Mn_{0.66}O_2$, consisting of Na-P2, Na-P3, and Li-O'3 phases. The CV shows that the Li-doped triphasic material has a much smoother voltage profile with fewer, and less intense redox peaks than either single P3

phase or the P3/P2 biphase sample. The Li is thought to disrupt Na^+/vacancy ordering, or rather induce disorder; simultaneously promoting higher capacity retention and higher rate capability [38], [39]. The material has a capacity retention of 78%, and at 5C delivers 110 mAh g^{-1}, rather than 73 and 80 mAh g^{-1} for the P3 and P3/P2 phases, respectively.

In the latter case the biphasic P3/P2-$Na_{0.7}Li_{0.06}Mg_{0.06}Ni_{0.22}Mn_{0.67}O_2$ [17] outperforms the pure P3 and P2 phase, and a mixed P3 and P2 material. The biphase had a capacity of 80mAh g^{-1} after 100 cycles at C/5. The capacity after 100 cycles at C/5 of the single phase P3 material is 65 mAh g^{-1}, and 55 mAh g^{-1} for the P2. This study is one of the few [14] to report a comparison to a post-synthesis mixture of the two phases– the mixed phase has a capacity of only 40 mAh g^{-1} after 100 cycles. The results follow a similar pattern: the biphase outperforms the single phases, which outperform the mixed phase. The explanations for the differences in performance are like other studies described here: the formation of the OP4 phase over the O2 phase promotes reversibility, and an avoidance of a phase transition from P3 to a distorted P''3 phase. The latter improvement is achieved *via* Li doping, as the biphasic P3/P2-$Na_{0.66}Ni_{0.33}Mn_{0.67}O_2$ sample performed worse than the doped sample. In rate capability testing the undoped P3/P2-$Na_{0.66}Ni_{0.33}Mn_{0.67}O_2$ performed much worse the single phase P3- and P2-$Na_{0.66}Ni_{0.33}Mn_{0.67}O_2$, where the capacity drops to zero at 2C. The rapid capacity fade is likely to be caused by the P2↔O2 phase transition, which occurs as the samples are all cycled with an upper cut-off voltage of 4.4 V vs Na/Na^+. The cause of the poor capacity retention relative to P2-$Na_{0.66}Ni_{0.33}Mn_{0.67}O_2$ is, however, unclear. There is no consideration of particle size in the study, but since the biphase is synthesised *via* an intermediate temperature it possible that the rapid capacity fade is due to the smaller particle size of the biphase compared to the P2 phase. This results in higher surface area, likely meaning greater initial electrochemical activity which fades rapidly due to the P2↔O2 transition already discussed. This would mean the biphasic material does not prevent the phase transition and resulting strain and micro-cracks that occur [5]. If true, this highlights the importance of material selection to not be compromised by the particle size reduction when synthesising composite by calcining at intermediate temperatures, and when synthesising using methods such as biotemplating.

In these hetero-epitaxy structures, proximity of the P2 phase to P3 is suggested to stabilise the P3 phase and suppress the P3↔O3 phase transition [4], which coincides with reducing strain energy at the material interface. For example, multiphasic P2/O3/O'3/P3-$Na_{0.7}Li_{0.3}Ni_{0.5}Mn_{0.5}O_2$, transforms into a biphasic P3/P2 structure during first charge. It briefly transitions into a P2/O''3 at the beginning of discharge before it returns to the P2/P3 and remains in that configuration until the end of discharge – the O3 phase does not reappear after discharge (Figure 5-4). The lack of energy cost of repeat transitions is what the authors credit for the high rate performance of the multiphase material over the pure O3 analogue (although this contained no Li), which undergoes repeat O3 – O'3 – P3 transitions in the same voltage range [40].

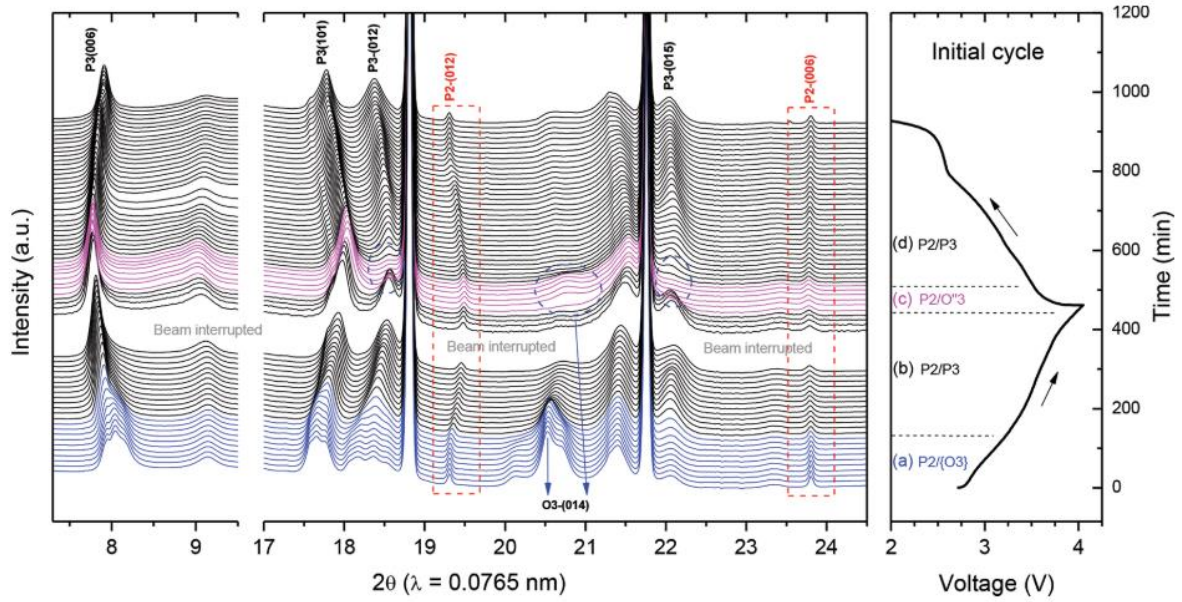

Figure 5-4: $Na_{0.7}Li_{0.3}Ni_{0.5}Mn_{0.5}O_2$ during initial charge–discharge. {O3} denotes a combination of O3, O'3 and P3 phases [4].

The disappearance of the O-type phase avoids the high energy barrier for Na^+ diffusion in those materials, and so throughout the range of Na contents the rapid diffusion of the P3 material can be utilised. The reason the P3 phase does not transition back into the O3 is that the presence of the P2 phase influences the crystal structure: interlocking of the P3 phase stabilises the P2 and reduces strain at the interface. This is likely made possible by the close match of the two prismatic Na^+ sites, as opposed to the octahedral and prismatic sites present in the P2/O3 system initially. This also results in a smoothed voltage profile compared to the $Na_{1-x}Li_xNi_{0.5}Mn_{0.5}O_2$ with lower Li contents, caused by a disruption in Na^+/vacancy ordering, meanwhile enhancing the rate capability and capacity retention.

Conversely, a multiphase material can undergo a more complex phase progression while having a better capacity retention than a single phase [13]. P2/O3/O1-$NaNi_{0.33}Co_{0.33}Mn_{0.33}O_2$ undergoes several phase transitions throughout the first and second charge-discharge cycles between 2.0 – 4.4 V vs Na/Na^+ at C/10 and recovers the same phases afterwards. This triphasic material displayed higher capacities than the P2/O3 material, and P2 material (135 mAh g^{-1}, 100 mAh g^{-1}, and 55 mAh g^{-1}, respectively) after 50 cycles between 2.0 – 4.4 V at C/10, as well as better rate capability. The P2/O3 material undergoes a similar phase progression to the triphase, but on discharge cannot recover the O3 phase and remains as a P2/P3 biphase. The resulting biphase still performs well (100 mAh g^{-1} after 50 cycles), particularly since almost all the capacity loss occurs during the first five cycles and then remains steady. The triphase performs better as it suffers very little capacity loss throughout the procedure and so still delivers a higher capacity after 50 cycles.

The interlocking of phases is likely to be the reason multiphases outperform the single phase counterparts. It prevents irreversible or harmful phase transitions that would have

occurred *via* formation of a hetero-epitaxy structure. Although the production of multiphases is often achieved in conjunction with doping a host material, leading to difficulty in identifying its specific effects, its prevention of harmful phase transitions extends the life of the cathode by reducing the strain and energy expenditure of the transition [41].

The overall effect of composites then is the increased capacity retention of the cathode [5], [16], [28]. The capacity fading in cathodes has numerous origins, but commonly occur during phase transitions. The increased capacity retention of multiphase composites comes from the prevention of harmful phase transitions, either by promoting more reversible ones (such as formation of OP4 over O2) or the avoidance of a transition altogether. This results in a reduction of strain on the crystal structure and a better maintenance of it during cycling through the prevention of micro-crack formation. The prevention of micro-cracks can also reduce the Mn^{2+} dissolution into the electrolyte by prevent increases in electrode surface area.

The behaviour of the different P-type NMMO phases has been established both in this and previous work [42]–[46]. The capacity fading mechanism of the material is likely to be caused by Mn^{2+} dissolution, as with other Mn-rich cathodes. There are also several phase transitions that occur within each material that can reduce the capacity retention. This work then is to use a combination of P3- and P2-NMMO phases to reduce the capacity loss seen so far in this work.

The P3-NMMO phase has been explored [45], [46], and as seen in Chapter 3 it has the potential to outperform its P2 analogue, but still suffers from capacity decay. Similarly, P2-NMMO is a well-studied material [42]–[45] that has been shown in this thesis to suffer from capacity fading. With this context, the exploration of the P3/P2-NMMO biphase is warranted, both to stabilise the P3-NMMO phase against the transition to the O3/OP4 phases, and to unlock the potential of the P2-NMMO cathode material.

5.2 Aims

To fully elucidate the effects of phases on the electrochemistry on NMMO, a range of phase fractions were targeted, along with the phase-pure compounds. Expressed as a ratio of the P3 to P2 phase, these fractions were: 9:1, 7:3, 1:1, 3:7: 1:9. These ratios were chosen to give a more complete overview of the effect of composite phases. Minor phases [16], [30] have been shown to have an effect on battery performance, as have ratios closer to 1:1 [8], [17]. Different ratios of the phases have not been explored, and the ratios explored here provide good coverage of the range of phase fractions possible.

As shown in the HTXRD results of Chapter 3, the phase progression from P3 to P2 evolves without the presence of any intermediate phases. Each target phase fraction can be obtained via a biotemplating synthesis by varying calcination temperature. As a comparison, these *in situ* generated biphases were compared against the same phase fractions prepared by simply mixing two phase-pure P3-NMMO and P2-NMMO samples

together. the mixed phases are also referred to as the *ex situ* samples. The single phase P3- and P2-NMMO are also used here for comparison.

To characterise the materials, the XRD patterns of the mixed phases are examined, and phase fractions of each are found *via* Rietveld. This is used to provide a comparison with which to compare and verify the phase fractions of the biphases. Further, each sample is examined *via* SEM to determine whether particle size is likely to play a role in the electrochemical performance, as has been seen in earlier chapters, and studies already discussed. Galvanostatic tests and C-rate cycling are conducted to determine any differences between the mixed phases and the biphases. The mixed phases should perform more similarly to the single phase P3- and P2-NMMO, but there should be differences between the these and biphases as it is expected that the intergrowth nature of them should suppress various harmful modifications to the structure.

XRD is used in this and previous chapters to show the progression at high temperature from P3-NMMO to P2-NMMO. The transformation does not happen immediately; the phase fraction of P2-NMMO increases with temperature, so specific phase fractions can be targeted by calcining with a specific temperature.

The separately mixed P3/P2-NMMO phases are produced from P3-NMMO and P2-NMMO calcined for 2 h at 650 °C and 900 °C, respectively. This gives a total heat treatment time of 4 h and 5 h, respectively. This mirrors the conditions used in Chapter 4 to produce P3- and P2-NCMM. The mixed cathode materials produced *via* calcination (referred to throughout this chapter as biphases) were calcined using a range of temperatures from 720 °C – 820 °C, all for 2 h at 10 °C min^{-1}. This gives a range of total heat treatment times of 4 h 20 min to 4 h 40 min. The different temperatures are used as the P3 and P2 phases are produced at different temperatures, as shown in Chapter 3. Therefore producing a biphase in which one is grown from the other is necessitates the use of different temperatures to obtain a range of phase fractions.

In this chapter, the sample powders are synthesised and examined by XRD once, examined by SEM once, and one sample powder is used to make the cathode material. From the cathode material, three cells are made to test the discharge capacity over 50 cycles, and one is used to test the rate capability.

5.3 Results and discussion

5.3.1 XRD

5.3.1.1 Single phase P3- and P2-NMMO

Synthesis of the P3-NMMO phases requires a biotemplating synthesis, as does the synthesis of biphases without the presence of unwanted side products, as established in Chapter 3. Phase pure materials were synthesised during Chapter 4 and serve as a baseline to allow us to identify the origins of the electrochemical process within the

mixed electrode. This provides a baseline structure profile to use when determining *via* Rietveld refinement the phase fractions present.

The XRD patterns in Figure 5-5 show that the phase pure P3- and P2-NMMO can be synthesised at 650 °C and 900 °C, respectively. The ideal crystal structures of each phase form ($R3m$ and $P6_3/mmc$, respectively) without any visible impurities. There is a minor ordering peak in the P2-NMMO at 22 °2θ corresponding to the $(\frac{1}{3}\frac{1}{3}1)$ plane [47]. Visually, the refinement fit for both samples is good, except for the peaks at 16 °2θ. These correspond to the (003) and (002) peaks in P3- and P2-NMMO, respectively. The position of these peaks is correct, but not the intensity. This discrepancy is likely due to preferred orientation of the planes in question [34] but has not been modelled for here. The refinement values are displayed in

Table 5-1. Lattice parameters match well with previously reported values for these phases [42]–[46]. The R_{wp} is high for both samples [48], but typical of the machine used, and the low GOF and good visual fit using established space groups for the refinement mitigate this.

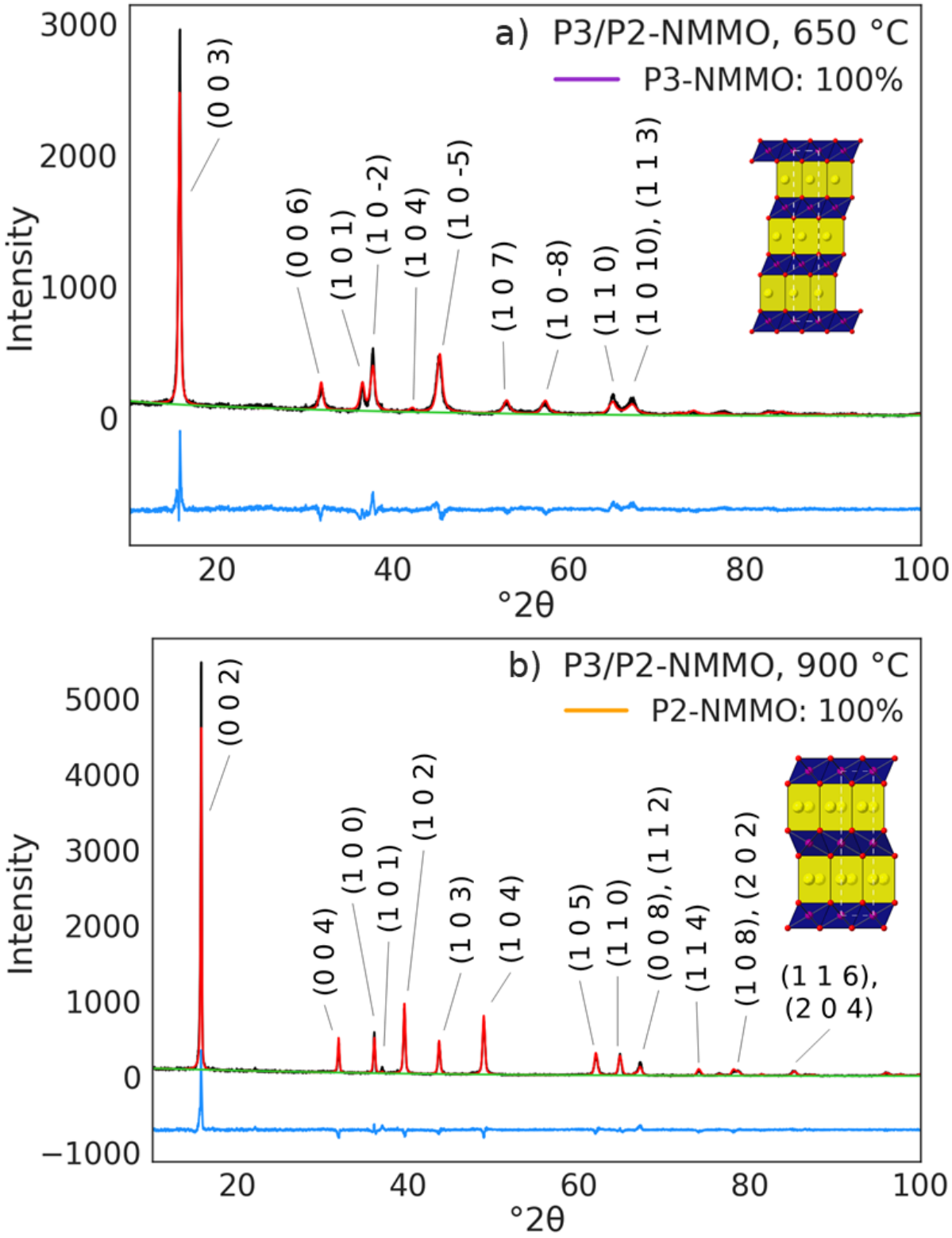

Figure 5-5: XRD patterns and Rietveld refinement results of phase pure a) P3- and b) P2-NMMO.

Table 5-1: Refined structural parameters of P3- and P2-NMMO.

Sample	Space group	*a* (Å)	*c* (Å)	R_{wp} (%)	GOF
P3-NMMO	R3m	2.867(1)	16.843(5)	17.3	1.48
P2-NMMO	$P6_3/mmc$	2.8760(1)	11.2316(5)	16.4	1.37

5.3.1.2 *Ex situ* mixed samples

To generate the biphases targeted, a reference for the phase fraction was made using phase pure P3- and P2-NMMO. The two phases were ground together in the target ratios by mass and examined *via* XRD. This meant that the phase fractions calculated from the *in situ* biphase generation can be checked against the results of the *ex situ* samples, in case of error in the calculated phase fraction in the Rietveld refinement. The XRD patterns of the mixed phases, the target ratio, and the phase fractions derived from Rietveld refinements are displayed in Figure 5-6. Further Rietveld detail can be found in the Appendix.

The phase fractions obtained by the Rietveld refinement show some deviation from the expected value from the masses used. The molar mass of the P3 and P2 phase should be equal, save for Na loss during calcination (10% excess Na was used during synthesis to counteract this). The difference in Na loss between 650 °C and 900 °C 2 h calcination should be small. As such, the molar ratio of P3/P2 should be equal to the mass ratio. The difference between the calculated and Rietveld refinement derived phase fraction is 9% either way.

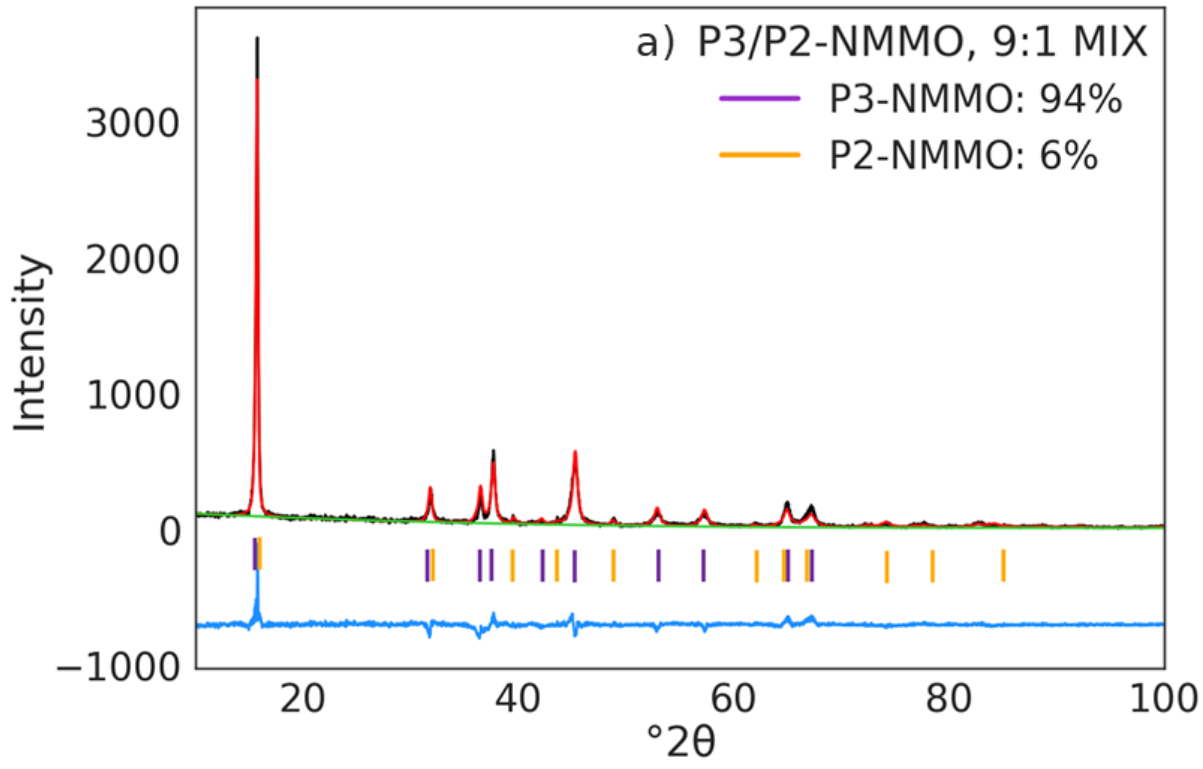
a) P3/P2-NMMO, 9:1 MIX
P3-NMMO: 94%
P2-NMMO: 6%
Intensity
3000
2000
1000
0
−1000
20
40
60
80
100
°2θ

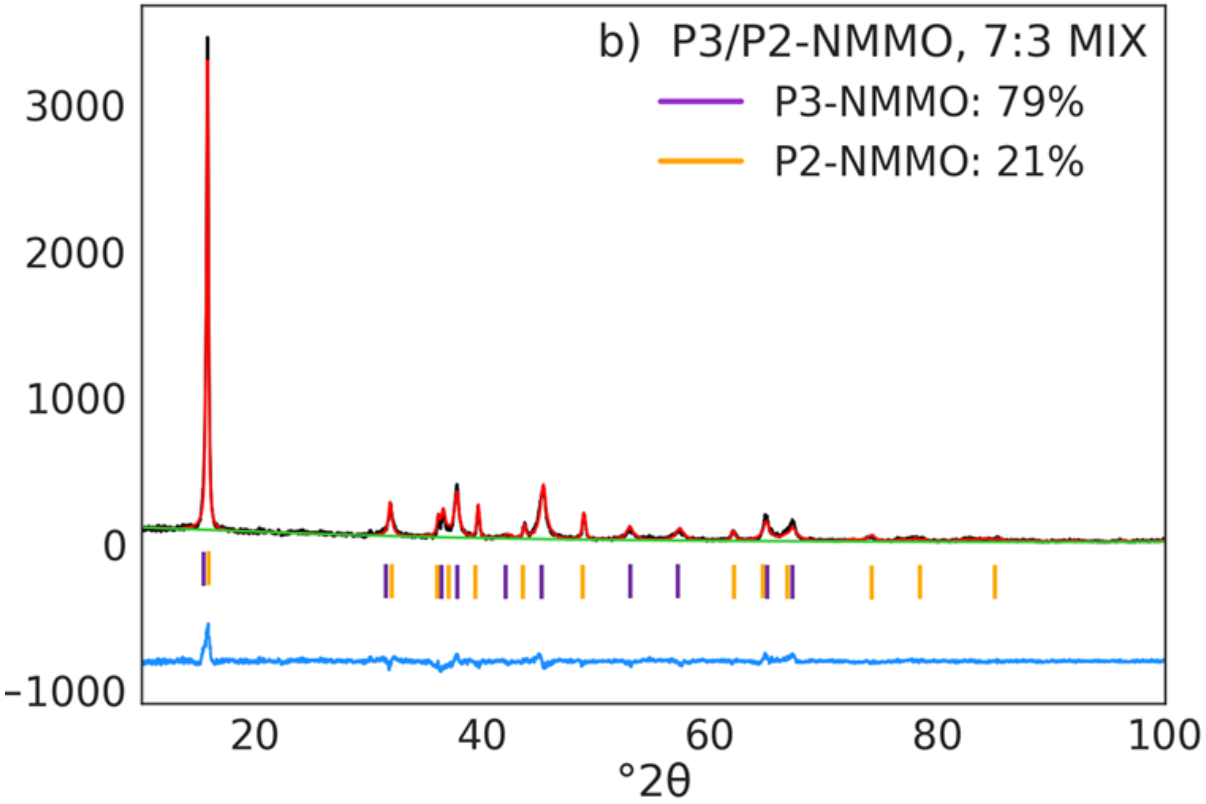
b) P3/P2-NMMO, 7:3 MIX
P3-NMMO: 79%
P2-NMMO: 21%
3000
2000
1000
0
−1000
20
40
60
80
100
°2θ

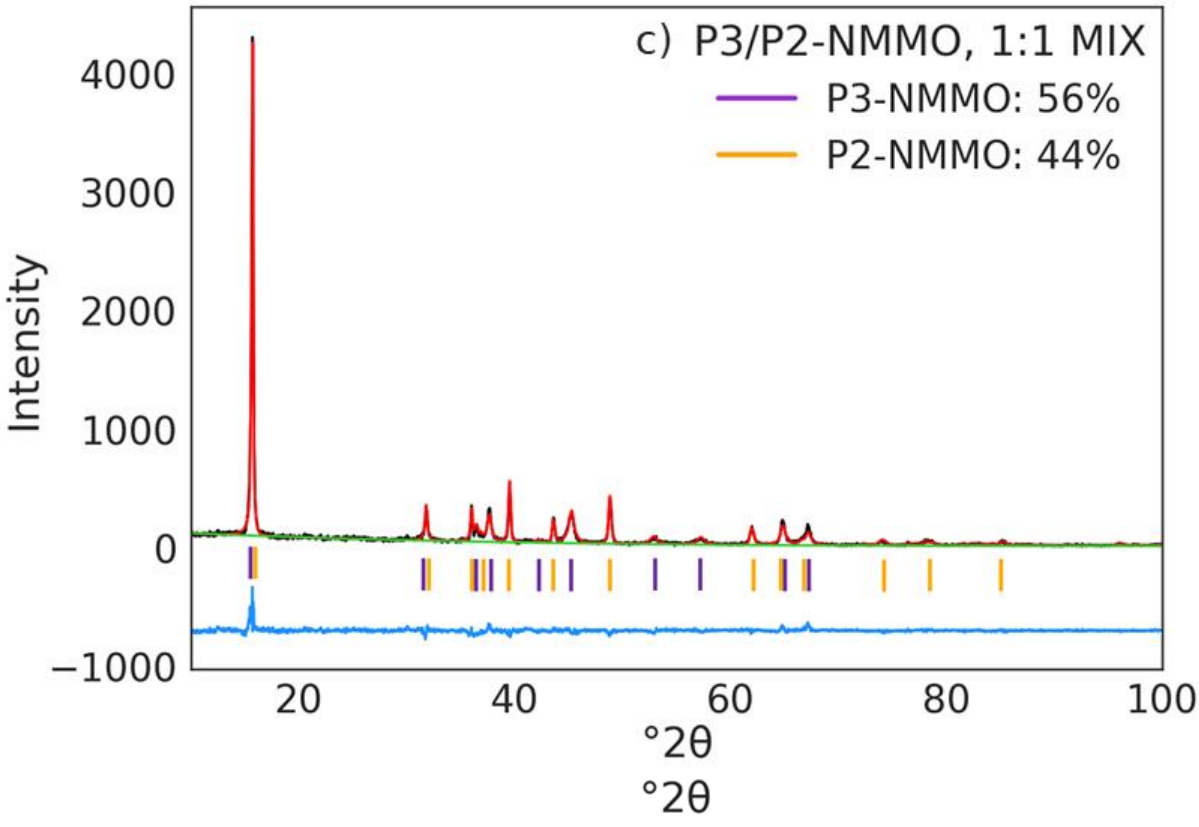
c) P3/P2-NMMO, 1:1 MIX
P3-NMMO: 56%
P2-NMMO: 44%
Intensity
4000
3000
2000
1000
0
−1000
20
40
60
80
100
°2θ

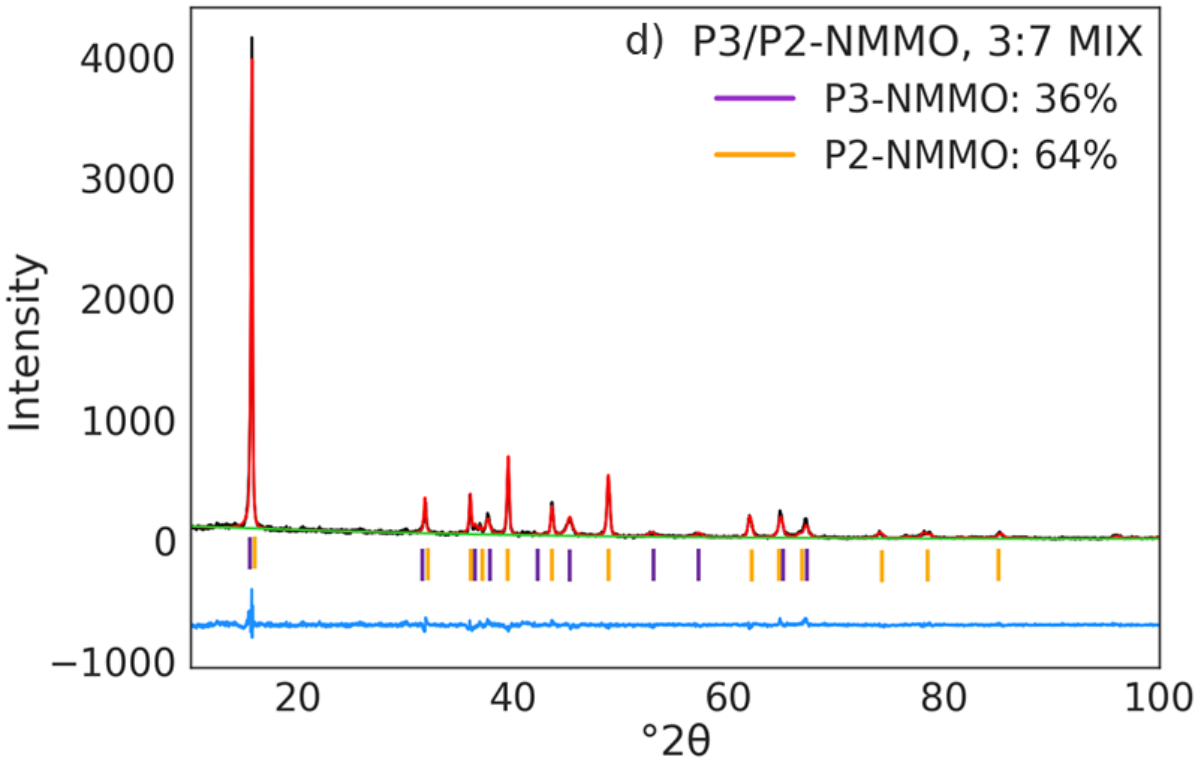
d) P3/P2-NMMO, 3:7 MIX
P3-NMMO: 36%
P2-NMMO: 64%
Intensity
4000
3000
2000
1000
0
−1000
20
40
60
80
100
°2θ

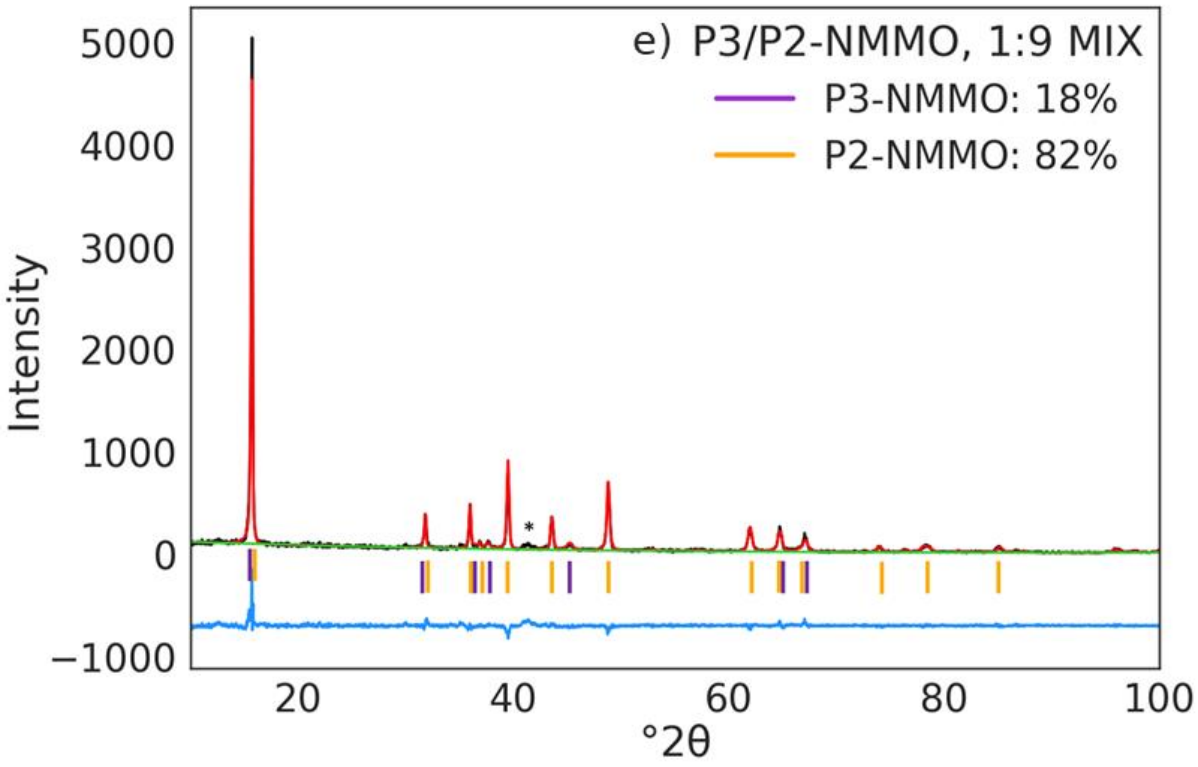

Figure 5-6: XRD patterns of P3/P2-NMMO synthesised separately at 650 °C and 900 °C, respectively, and mixed in the ratios indicated on the pattern. Annotated to show phase fraction determined by Rietveld refinement. Peaks arising from each phase are marked on the patterns (P3-NMMO in purple, P2-NMMO in orange).

Overall, the results demonstrate the ability to determine phase fraction using Rietveld refinement, with an error of ±9% from the analysis. This data is used when generating the *in situ* biphases; the phase fractions of the P3/P2-NMMO biphases when synthesised by varying temperature are afforded an error of 9% away from the targeted phase fraction. The initial exploration of this, determining the temperature at which phase fractions form, was conducted with HTXRD.

5.3.1.3 *In situ* biphases

This investigation into the phase progression from P3-NMMO to P2-NMMO shows that the phase formation is temperature dependent (Figure 5-7). Only the P3-NMMO phase is present at 650 °C. By 750 °C, the P3 phase is barely visible as it has been steadily disappearing since 670 °C and is being replaced by the P2 phase. In the HTXRD results only showing the 30 – 50 °2θ range (Figure 5-8), the P2-NMMO phase is first visible at 670 °C, and remains visible until the end of the experiment at 750 °C. The P3-NMMO phase is already present at 650 °C, and is still visible at 750 °C, but only as a minor phase, as shown by the Rietveld refinements, shown in Figure 5-9. The HTXRD results do not show an intermediate phase, in agreement to the Chapter 3 HTXRD, and so the biotemplated P3/P2-NMMO biphases are assumed to contain no impurity phases when synthesised *ex situ*.

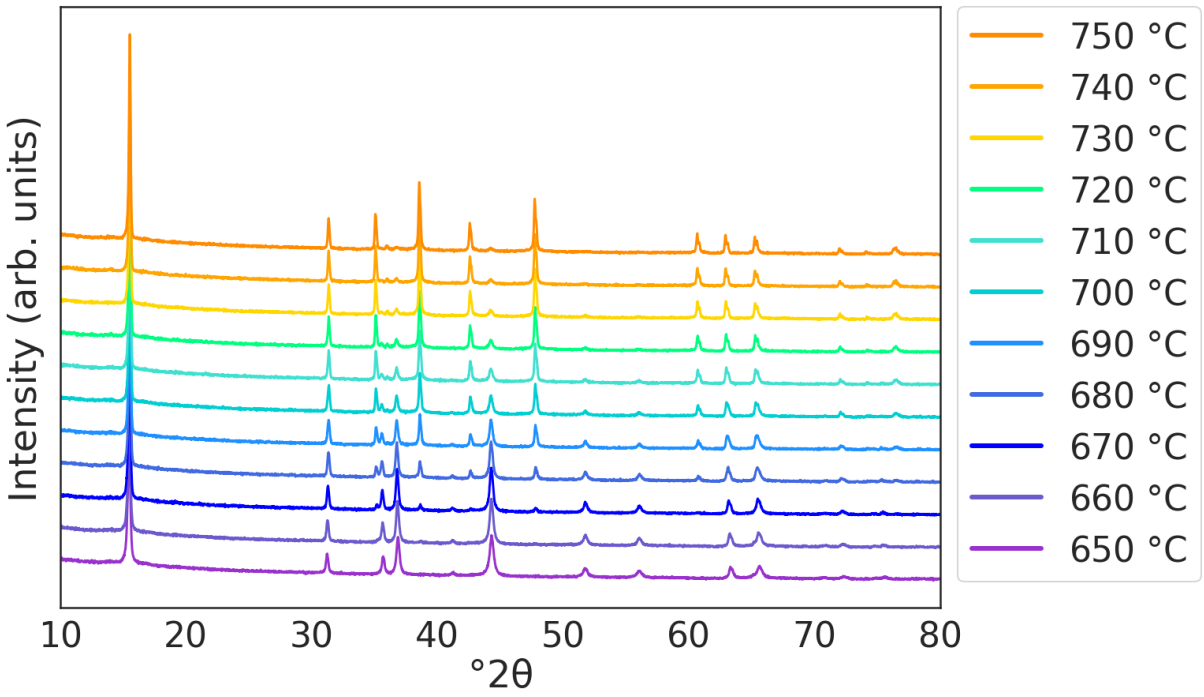

Figure 5-7: HTXRD of NMMO from 650 °C to 750 °C in 10 °C intervals.

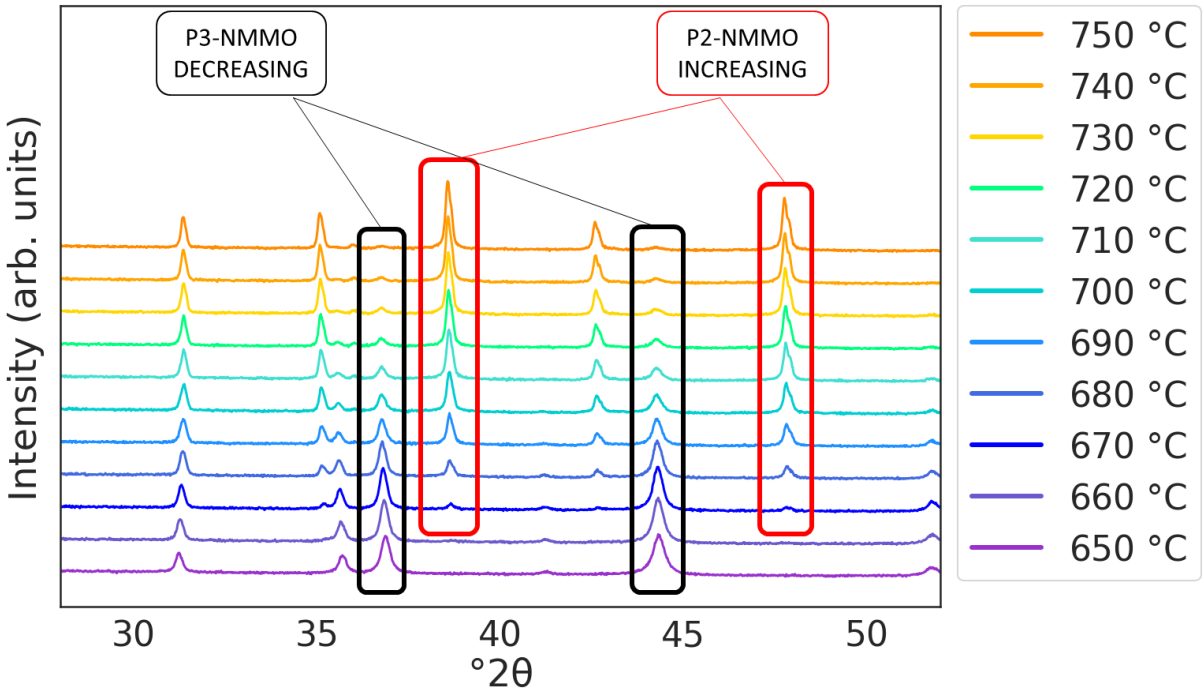

Figure 5-8: HTXRD of NMMO from 650 °C to 750 °C in 10 °C intervals, only the 30 – 50 °2θ range is shown. A selection of P3-NMMO and P2-NMMO peaks are highlighted to show their waning and waxing, respectively.

The Rietveld refinement results of the HTXRD patterns show the phase fractions change with temperature and are displayed in Figure 5-9. They show that one the P2 phase forms that the phase progression (from 670 °C to 710 °C) is mostly linear, with the approximate midpoint of the two phases occurring at 695 °C. The progression then slows as the P3

phase reaches 0%, from 710 °C to 750 °C, showing that synthesis of the near-end members of the P3/P2-NMMO series may be less straightforward. The error derived from the Rietveld is 1% (expect when the phase fraction is 100%).

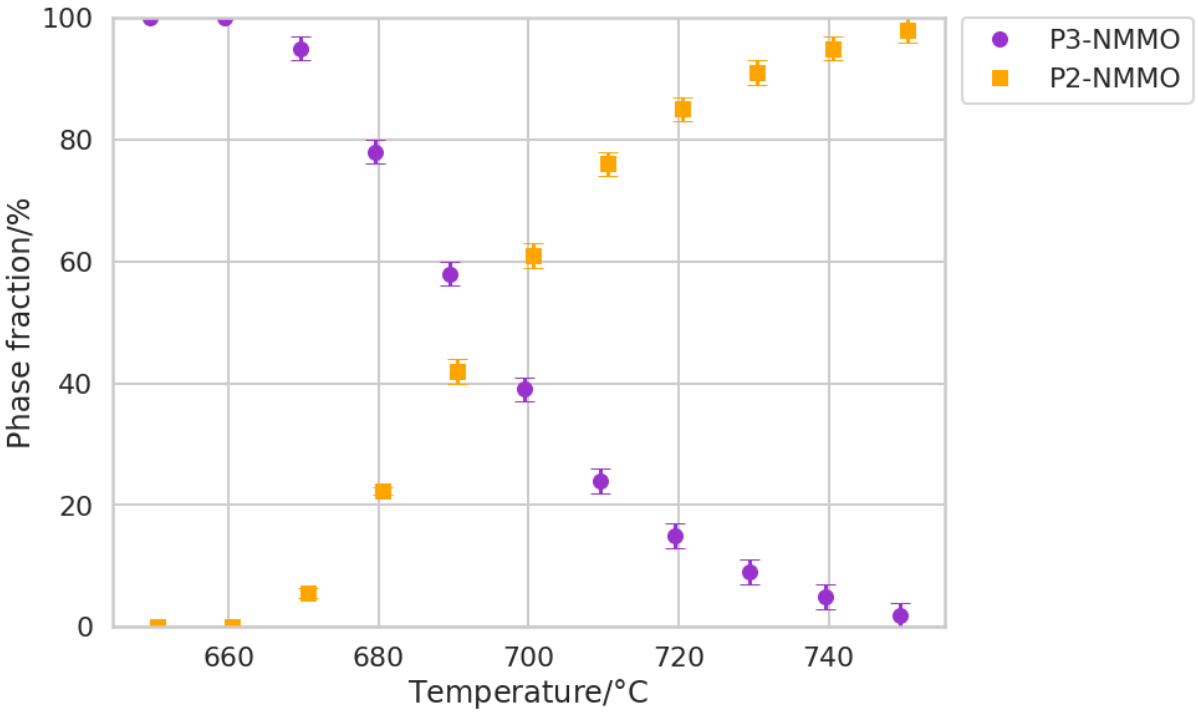

Figure 5-9: Phase fractions of P3- and P2-NMMO calculated from Rietveld refinement results of the HTXRD patterns of NMMO.

The pattern of phase progression is used herein as a guide to choose calcination temperature to synthesise *in situ* biphases. The samples calcined in the lab muffle furnace generate the biphases at different (nominal) temperatures than in the HTXRD. The *in situ* biphases from the muffle furnace are generated at higher temperatures, and with a wider range. The XRD results of the target biphases are shown with in Figure 5-10, annotated to show the calcination temperature. Further Rietveld detail can be found in the Appendix. Shown in Figure 5-10a, an *ex situ* calcination temperature of 720 °C results in a mix of 91% P3-NMMO and 9% P2-NMMO, as opposed to the 15% P3-NMMO, 85% P2-NMMO composition that the HTXRD would suggest. This discrepancy likely arises from a difference between either the HTXRD furnace or muffle furnace nominal temperature and the actual temperature, or both.

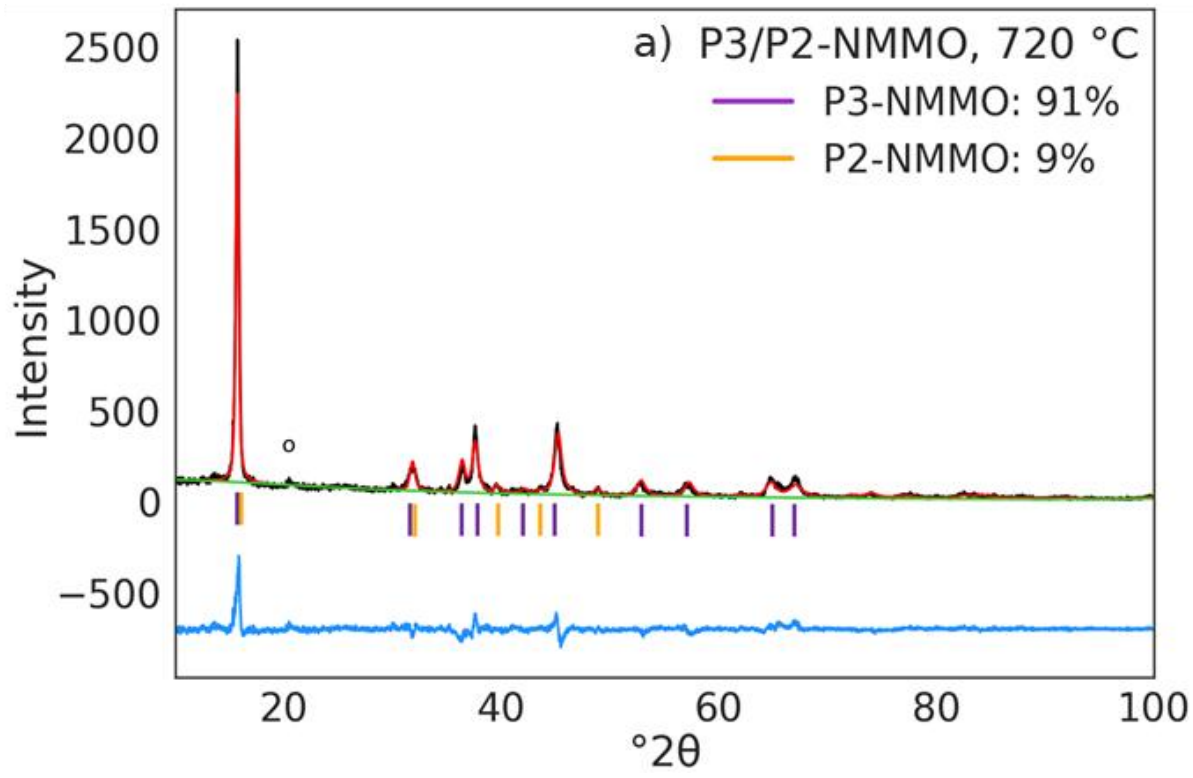
a) P3/P2-NMMO, 720 °C
P3-NMMO: 91%
P2-NMMO: 9%
Intensity
2500
2000
1500
1000
500
0
−500
20
40
60
80
100
°2θ

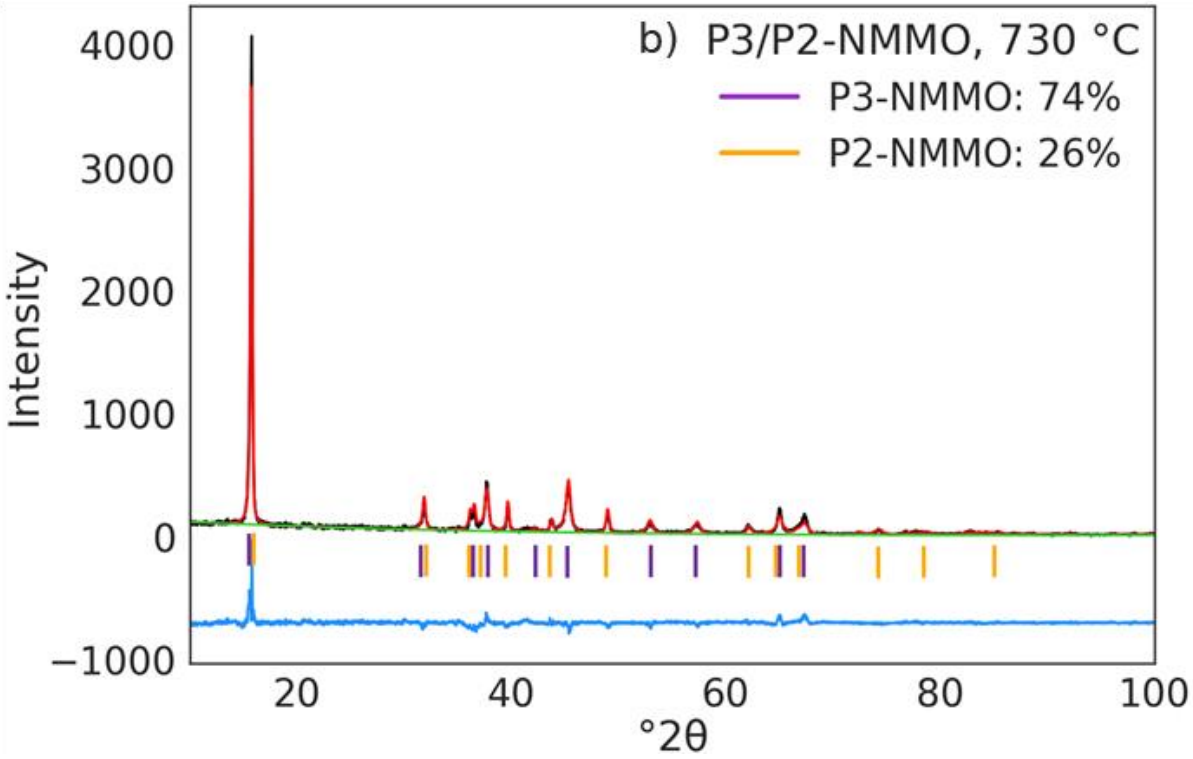
b) P3/P2-NMMO, 730 °C
P3-NMMO: 74%
P2-NMMO: 26%
Intensity
4000
3000
2000
1000
0
−1000
20
40
60
80
100
°2θ

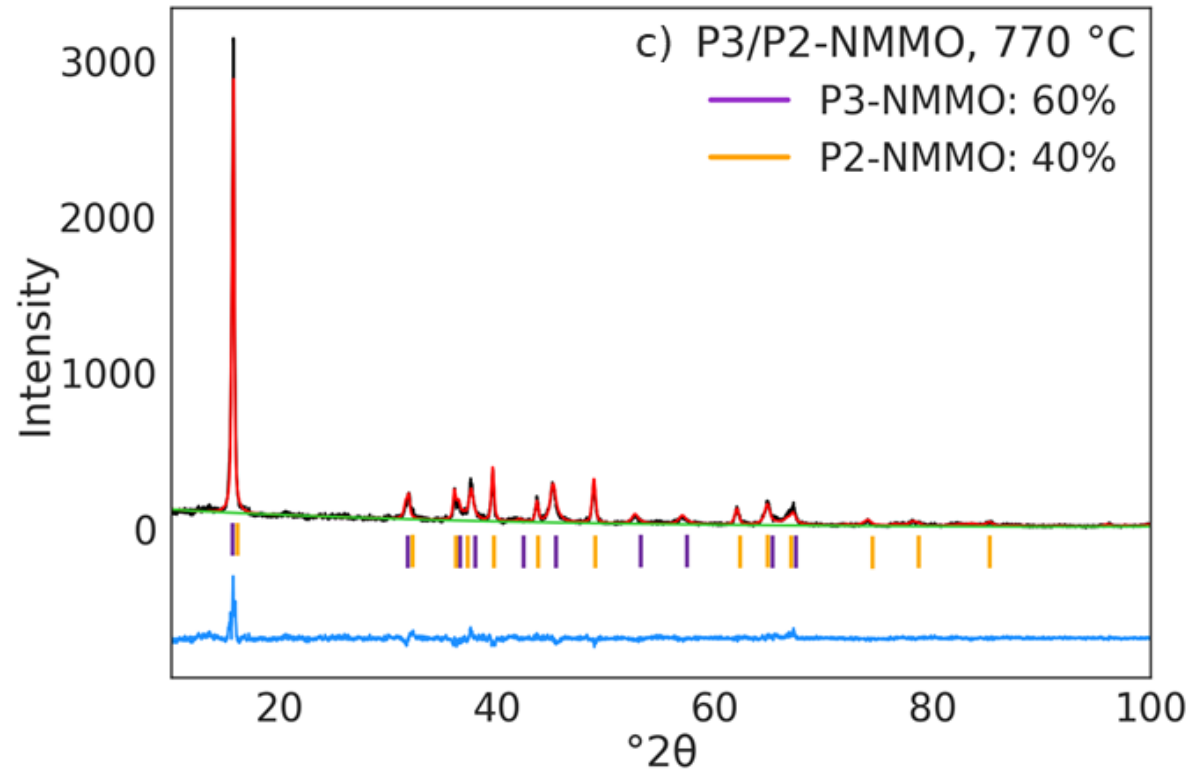
c) P3/P2-NMMO, 770 °C
P3-NMMO: 60%
P2-NMMO: 40%
Intensity
3000
2000
1000
0
20
40
60
80
100
°2θ

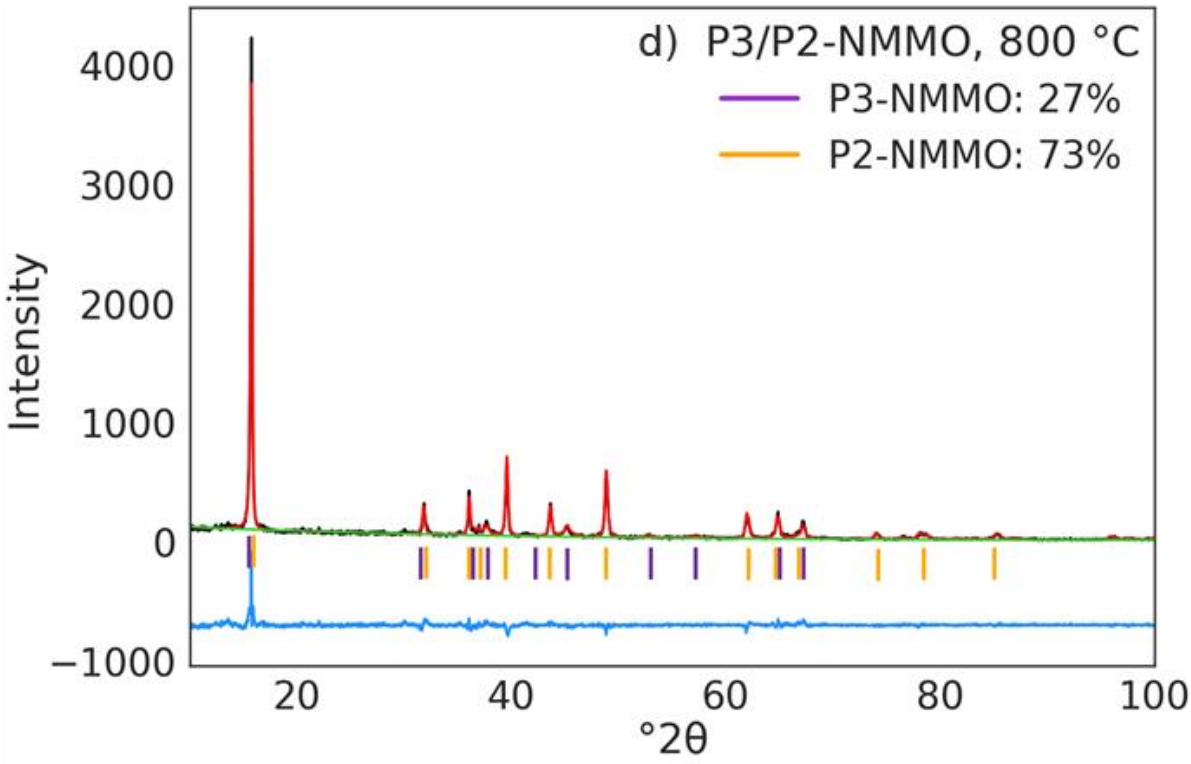
d) P3/P2-NMMO, 800 °C
P3-NMMO: 27%
P2-NMMO: 73%
Intensity
4000
3000
2000
1000
0
−1000
20
40
60
80
100
°2θ

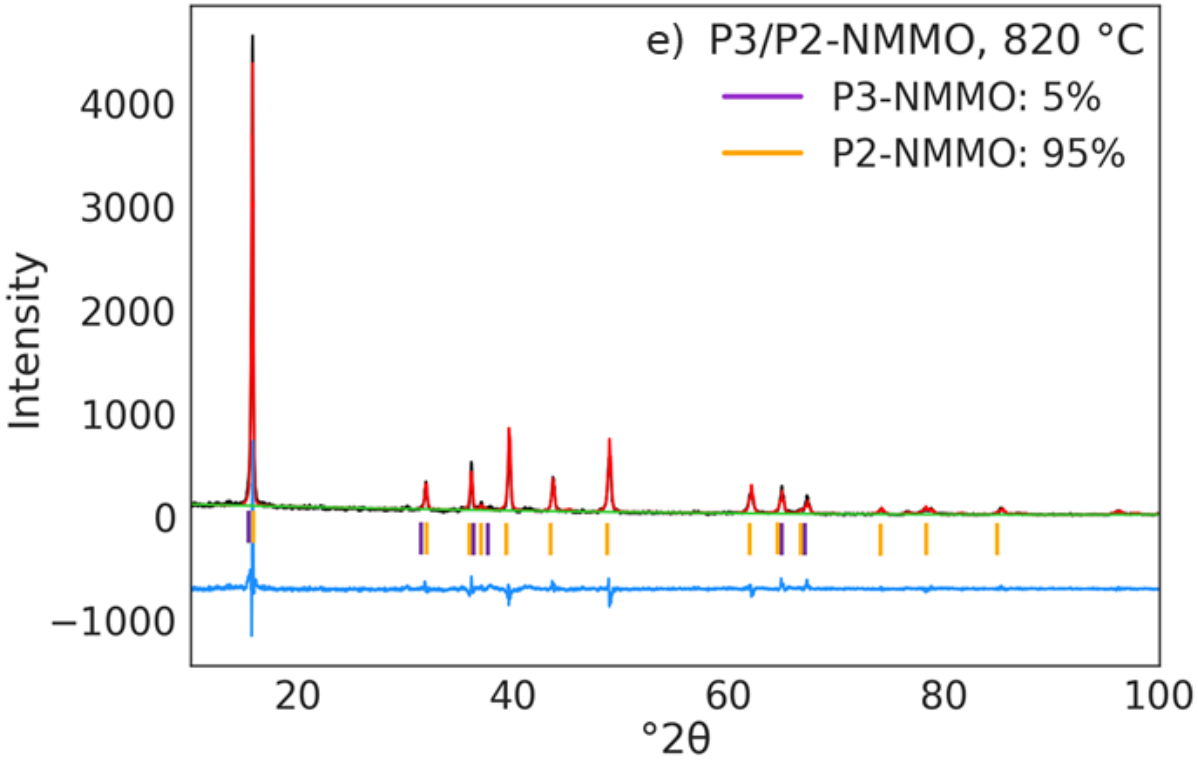

Figure 5-10: XRD patterns of P3/P2-NMMO biphases synthesised at different calcination temperatures. Annotated to show calcination temperature and phase fraction determined by Rietveld refinement. Peaks arising from each phase are marked on the patterns (P3-NMMO in purple, P2-NMMO in orange). o = transition metal ordering [49], or $Na_{0.44}MnO_2$ [50].

From the XRD patterns of the *ex situ* mixed phases (Figure 5-6), the Rietveld-derived phase fractions vary from the expected value (based on the masses of the phases) by 8%. Furthermore, the *ex situ* biphases are a known quantity with respect to the quantity of P3- and P2-NMMO in the sample. Therefore, since the Rietveld-derived phase fractions from the HTXRD patterns had an error of 1%, the Rietveld-derived phase fractions of the *in situ* biphases were allowed a 9% margin of error from the *ex situ* phase fractions.

Along with the phase-pure end members, both *in situ* and *ex situ* biphases are produced. Specific phase fractions of P3- and P2-NMMO can be targeted with the biotemplating synthesis. In the 9:1, 720 °C sample, there is a peak at 20 °2θ. This peak has two potential sources; transition metal ordering [49], or $Na_{0.44}MnO_2$ [50]. This will be explored further during the discussion of SEM, but it is possible that $Na_{0.44}MnO_2$ is generated at these temperatures, but there is no evidence of it during electrochemical testing, and so the peak is assumed to originate from transition metal ordering.

5.3.2 SEM

The particle size and shape of all samples were examined *via* SEM. The measurements of particle sizes in this chapter were made challenging by a large degree of agglomeration across the range of samples. This made distinguishing being specific particles challenging.

As a result, the minimum number of particles measured to obtain an average and standard deviation was lowered from 500 to 200. The data obtained from particle size measurements are used to identify trends on particle size as the proportion of P2-NMMO increases. Correlations between changes in particle size and electrochemical performance are drawn but not claims regarding specific values as these will have more errors than acceptable for this.

Figure 5-11 shows the SEM images of P3/P2-NMMO prepared by mixing the two separately calcined phases. P2-NMMO has a larger size than the P3-NMMO, as seen by the increasing average size as the phase fraction of the P2 phase increases. This is to be expected from the higher calcination temperature of the P2-NMMO, and previous work into the two phases (including Chapter 3), and other work into P3 and P2 phases. Since the average particle size is increasing without making any modifications to the separately prepared P3- and P2-NMMO phases, the P2 phase must be larger than the P3 phase.

Histograms of the particle size measurements (Figure 5-12) show the distribution of particle size show the decrease in relative frequency of <1.0 μm particles as the proportion of P3-NMMO decreases. In the *ex situ* samples, the particle size increased from 1.25 μm ± 0.87 μm in 9:1 P3/P2-NMMO mixed sample, to 2.54 μm ± 1.20 μm for the 1:9 P3/P2-NMMO. This trend was expected, given that the calcination temperature is increasing which leads to larger particle sizes, and the particle sizes reported for each phase. The standard deviation of the particle sizes is high, as there are two different phases with different sizes. The proportion of P3-NMMO [8], [14] can be seen decreasing as the fraction of particle with a size of <1.0 μm decrease through the series, and conversely particles with a size of 1-4 μm increase [8], [14], [30].

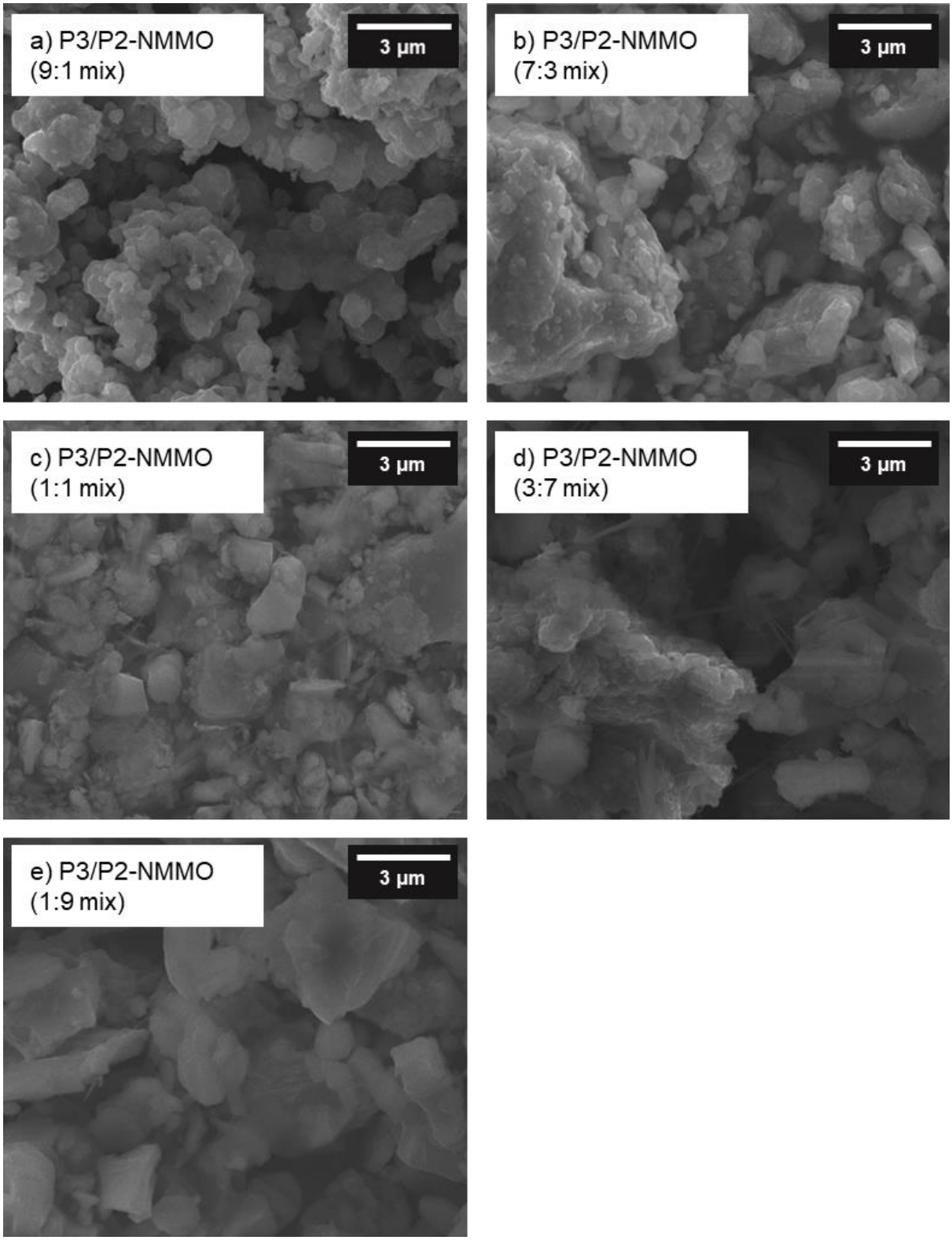

Figure 5-11: SEM images of P3/P2-NMMO biphases generated via mixing.

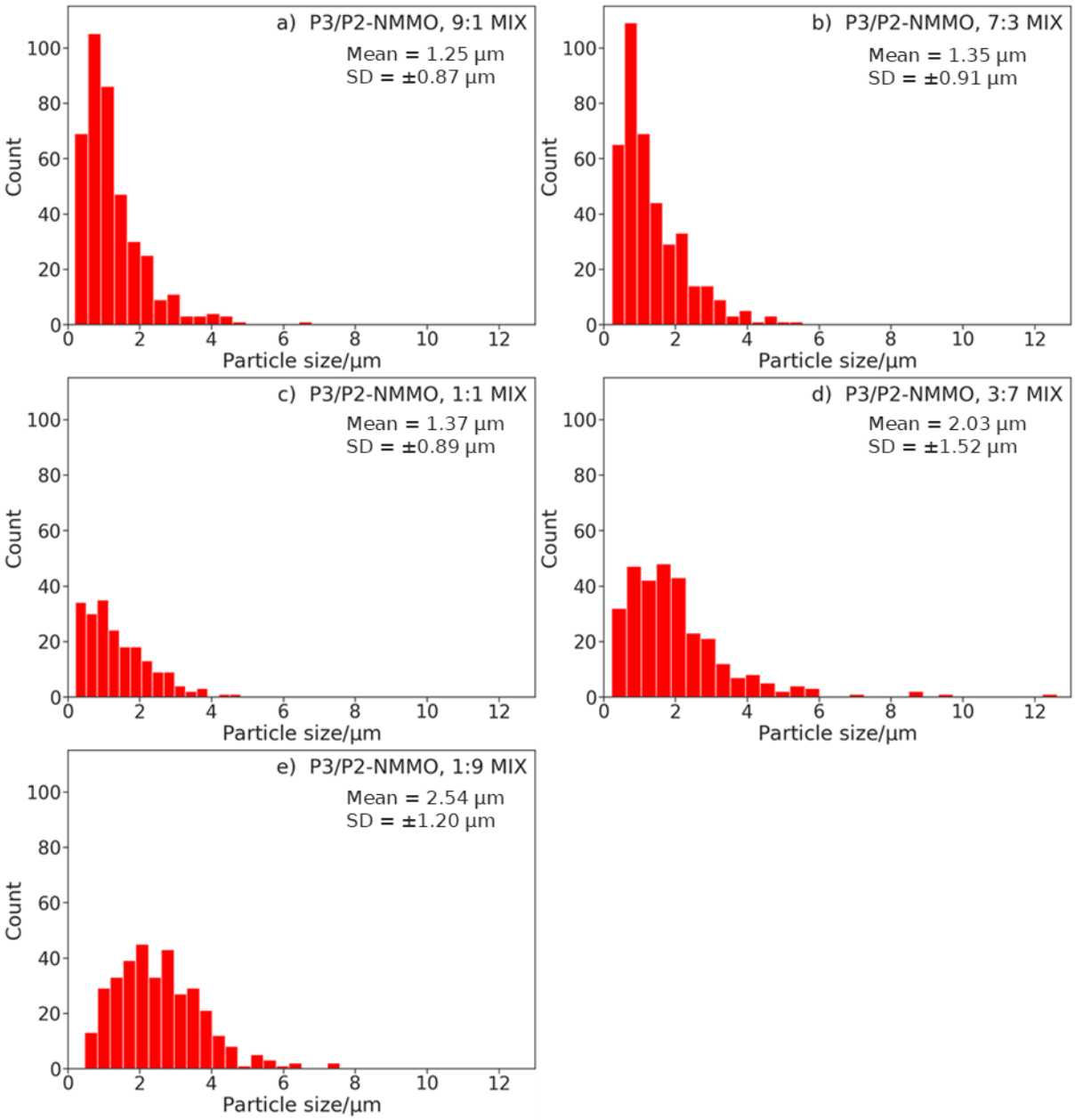

Figure 5-12: Histograms of the particle size of P3/P2-NMMO biphases generated via mixing.

The SEM images of the P3/P2-NMMO biphase calcined at different temperatures (Figure 5-13) and show the changing particle sizes. The *in situ* biphases follow the same pattern as the *ex situ* mixed phases: as the calcination temperature increases the average particle size increases too. This correlates with an increase in proportion of the P2 phase. There is a difference in the morphology between the two series, however.

In Figure 5-13a and c there are several rod-shaped particles present in the sample, 0.25 µm wide, and up to 3 µm long. These have not been present in other images of P3- or P2-NMMO, only in the biphasic samples. There is evidence that the rod-shaped particles are orthorhombic $Na_{0.44}MnO_2$. The XRD for the 720 °C sample (which contains these rod-shaped particles) may contain this as a minor phase, with the main peak of this noted by *o*. This impurity peak matches an impurity peak seen in P3-NMMO synthesised *via* solid

state methods in Chapter 3. The rod-shaped particles, characteristic of $Na_{0.44}MnO_2$ [50]–[53], are absent in the solid state P3-NMMO sample, and so it appears that the minor impurity phase there is not $Na_{0.44}MnO_2$. However, the phase could not be matched *via* Rietveld refinements, and there is little evidence of the $Na_{0.44}MnO_2$ phase in the electrochemical testing of these samples [54]. These rods may be showing the transition from P3- to P2-NMMO; the small (<1.0 μm) P3-NMMO particles growing in one direction, before adopting the more plate-like morphology typical of P2-NMMO [42]. It has been seen that P3 and P2 can display different morphologies even while generated together using an intermediate temperature [8].

Other than the rods, there are no obvious differences in particle morphology between the two preparation methods. It is possible given the small size of the P3-NMMO particles (0.65 μm ± 0.41 μm) that during calcination, the P3-NMMO transforms rapidly into the P2-NMMO. The transformation may propagate through the particles too quickly to form the hetero-epitaxial structures seen in successful intergrowth studies.

The sizes of the particles and standard deviations are given on the histograms in Figure 5-14. The distribution of particle size changes in a similar pattern to the mixed samples; the frequency of particles <1.0 μm decreases, relative to that of larger (1-4 μm) ones. The average size increases from 1.07 μm ± 1.20 μm to 1.70 μm ± 0.98 μm in the 9:1 and 1:9 P3/P2-NMMO samples, respectively. The abundance of the <1.0 μm particles in the sample calcined at 720 °C (Figure 5-14a) is higher than that of the equivalent *ex situ* sample (Figure 5-12a). At 720 °C the P2-NMMO will likely have smaller particles than if it was calcined at 900 °C. For the 7:3, 1:1, and 3:7 *in situ* samples, the particle size and standard deviation are the same as in the corresponding *ex situ* sample. The final sample in the series, 1:9 P3/P2-NMMO, has an average size less than its *ex situ* equivalent, and lower than the samples calcined at lower temperatures.

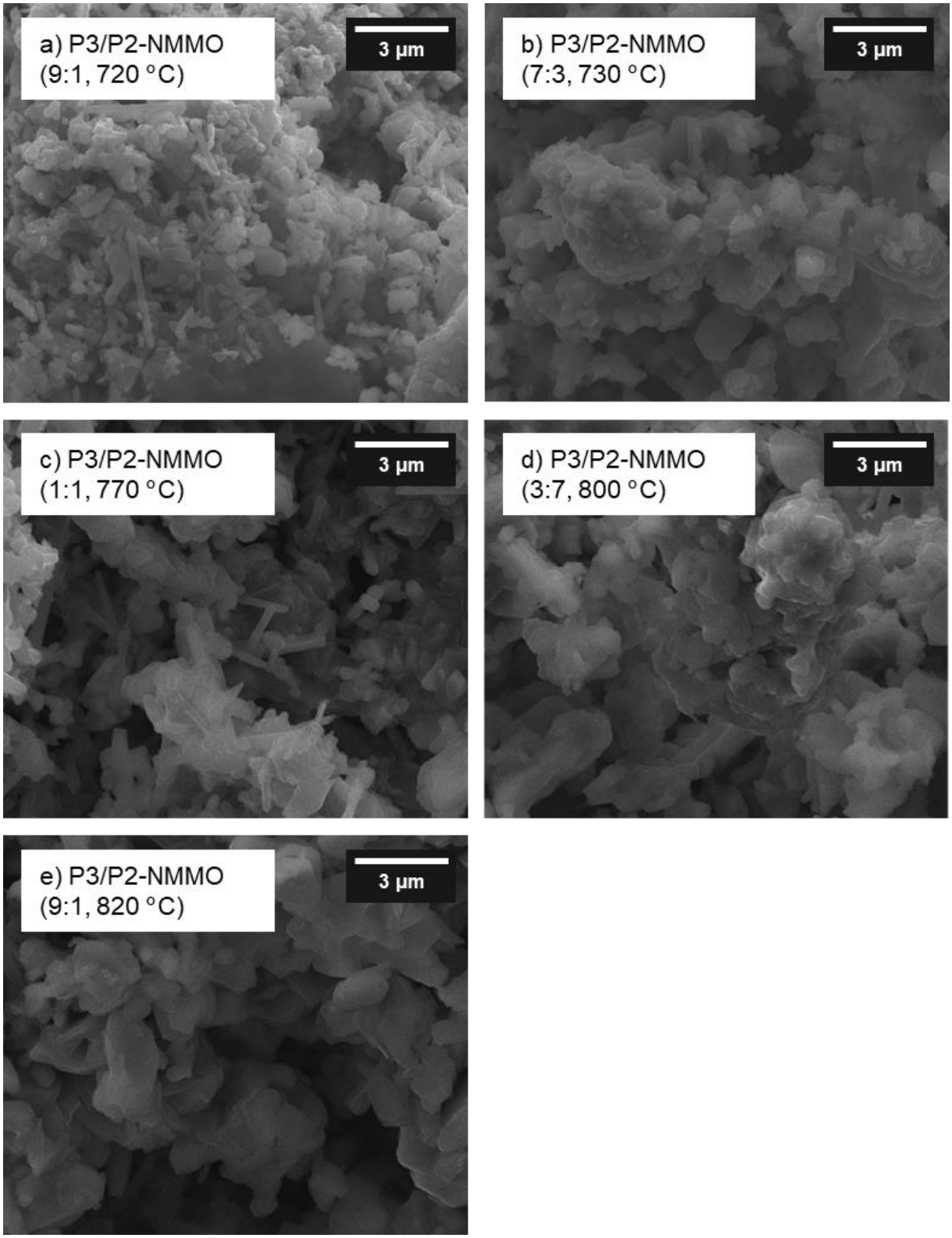

Figure 5-13: SEM images of P3/P2-NMMO biphases generated via calcination.

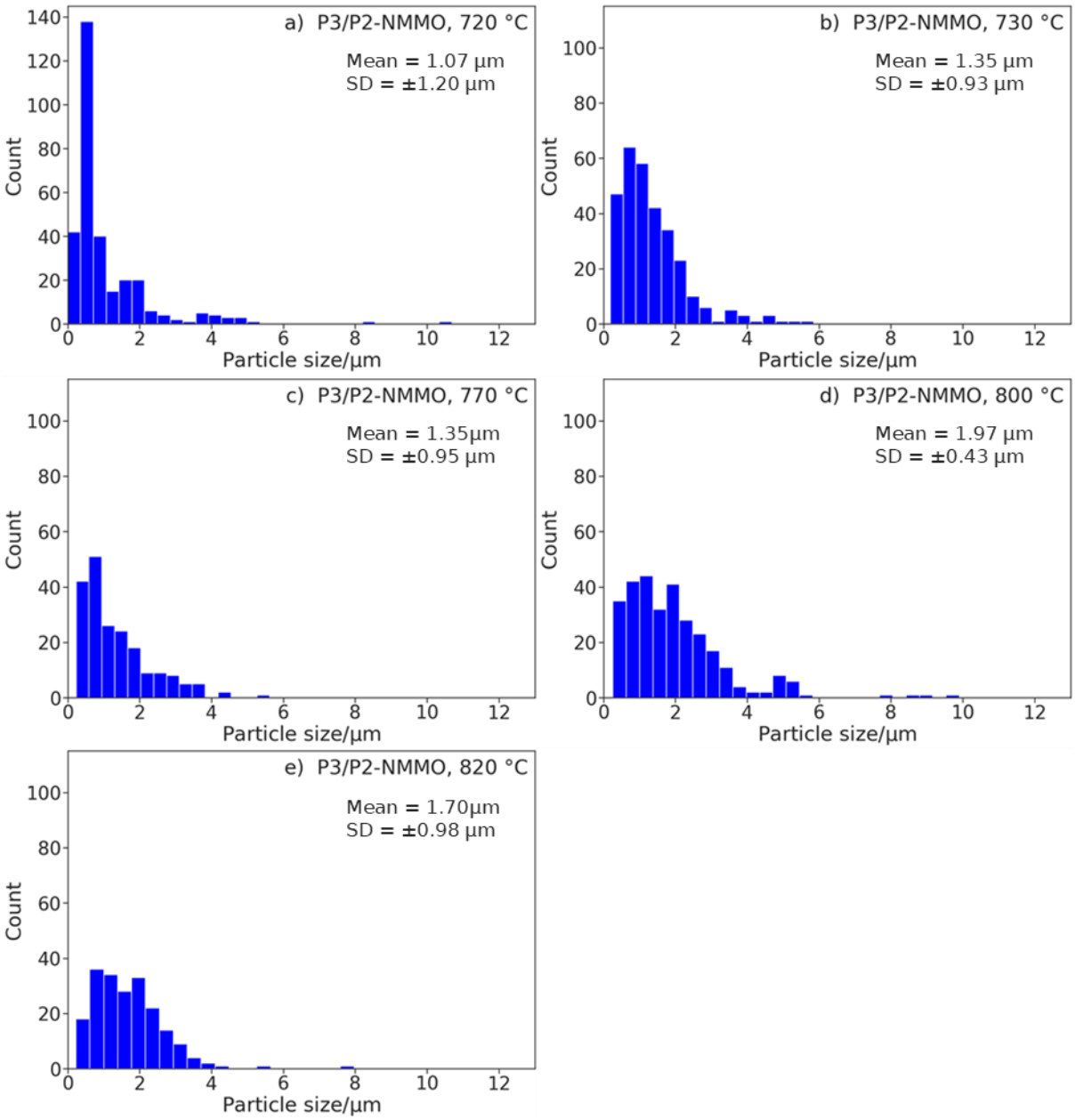

Figure 5-14: Histograms of particle sizes of P3/P2-NMMO biphases generated via calcination.

It is likely that the average sizes of the *in situ* biphases are smaller than their equivalent *ex situ* phases due to the lower calcination temperatures compared to 900 °C used for single phase P2-NMMO. The higher the phase fraction of P2-NMMO, the higher the expected difference between particle size between the two series. Due to the large standard deviation in the average size, it is difficult to confirm that this is the case. This is displayed more clearly in Figure 5-15.

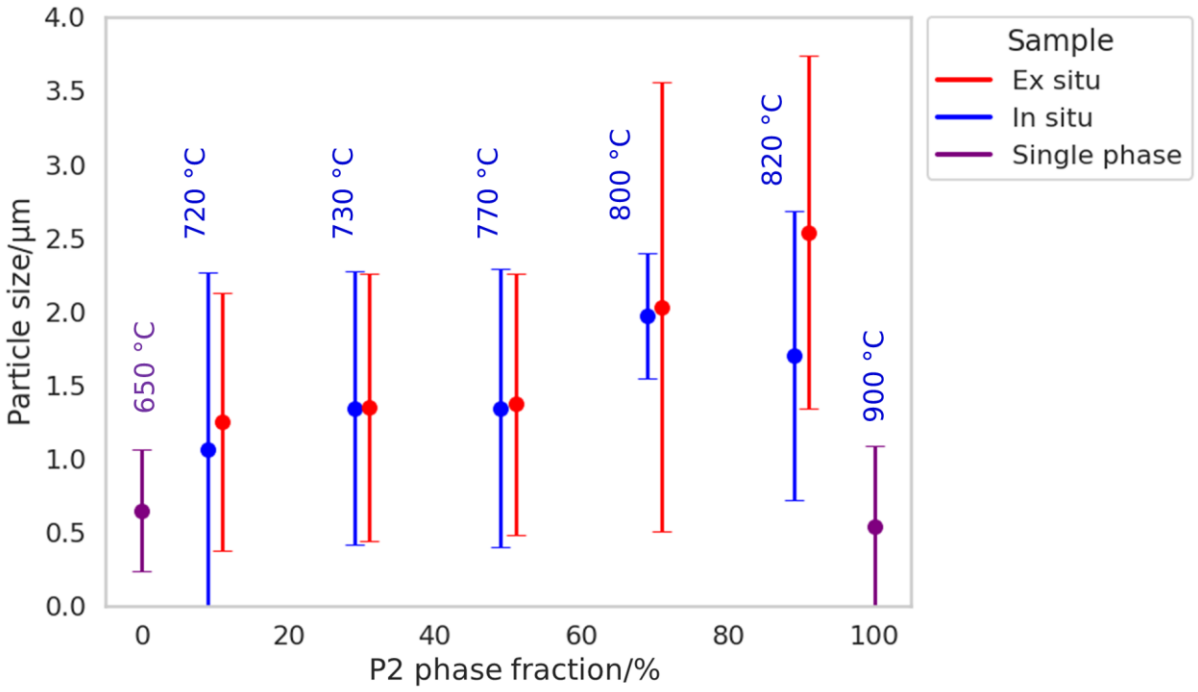

Figure 5-15: Average particle size of P2/P3-NMMO samples for each method as the phase fraction of P2-NMMO increases (ex situ: red; in situ: blue; single phase: purple) with the standard deviation as the error bars. Phase pure and biphasic samples are labelled with the relevant calcination temperature. All samples were calcined for 2 h.

5.3.3 Electrochemistry

The electrochemical performance of all biphase samples was tested, as were the single phases. A summary of the calcination conditions of the samples is given in Table 5-2. This allows for a comparison of the various phase fractions of P3/P2-NMMO to determine which, if any, offer greater capacity or improved capacity retention. It also allows a comparison across synthesis method to determine if the effect arises from the proximity of the two phases as the P3 grows into the P2 phase. The previous work suggests that the biphases generated by calcination should perform better (at least with respect to capacity retention) than those generated by mixing.

Table 5-2: Summary of the calcination conditions of each material tested throughout the chapter.

P3/P2 ratio	Calcination conditions	
	Mixed phases	Biphases
9:1	Mixing the appropriate fractions (by weight) of the P3- and P2-NMMO produced with: P3: 650 °C, 2h, 10 °C min^{-1} P2: 900 °C, 2h, 10 °C min^{-1}	720 °C, 2h, 10 °C min^{-1}
7:3		730 °C, 2h, 10 °C min^{-1}
1:1		770 °C, 2h, 10 °C min^{-1}
3:7		800 °C, 2h, 10 °C min^{-1}
1:9		820 °C, 2h, 10 °C min^{-1}

The tests used were the same as that of the previous chapters: galvanostatic testing within a potential window of 1.5 V – 4.0 V vs Na/Na^+ at C/5 (1C = 184 mAh g^{-1}) for 50 cycles. At the end of charge, the voltage is held at 4.0 V vs Na/Na^+ until the current reaches C/10. Rate capability was also used with the same potential window, with 5 cycles each of C/10, C/5, C/2, 1C, 2C, 5C, followed by another 5 cycles of C/10.

5.3.3.1 Single phase P3- and P2-NMMO

The electrochemical characteristics of the single phase materials are examined so that they can be compared to the mixed and composite phases. Figure 5-16 shows the voltage profiles and differential capacity graphs of the single phase materials. The discharge curves show the capacity fade of the material. Much of the capacity loss in both materials occurs below approximately 2.1 V vs Na/Na^+. This is particularly evident in the discharge curve of the differential capacity graph, as the intensity of the reduction peak there decreases significantly as the cycle number increases. In the case of the P3-NMMO, the oxidation peak also decreases in intensity, and main oxidation peak in both P3- and P2-NMMO increases in potential (starting at 2.3 V, moving to 2.5 V vs Na/Na^+).

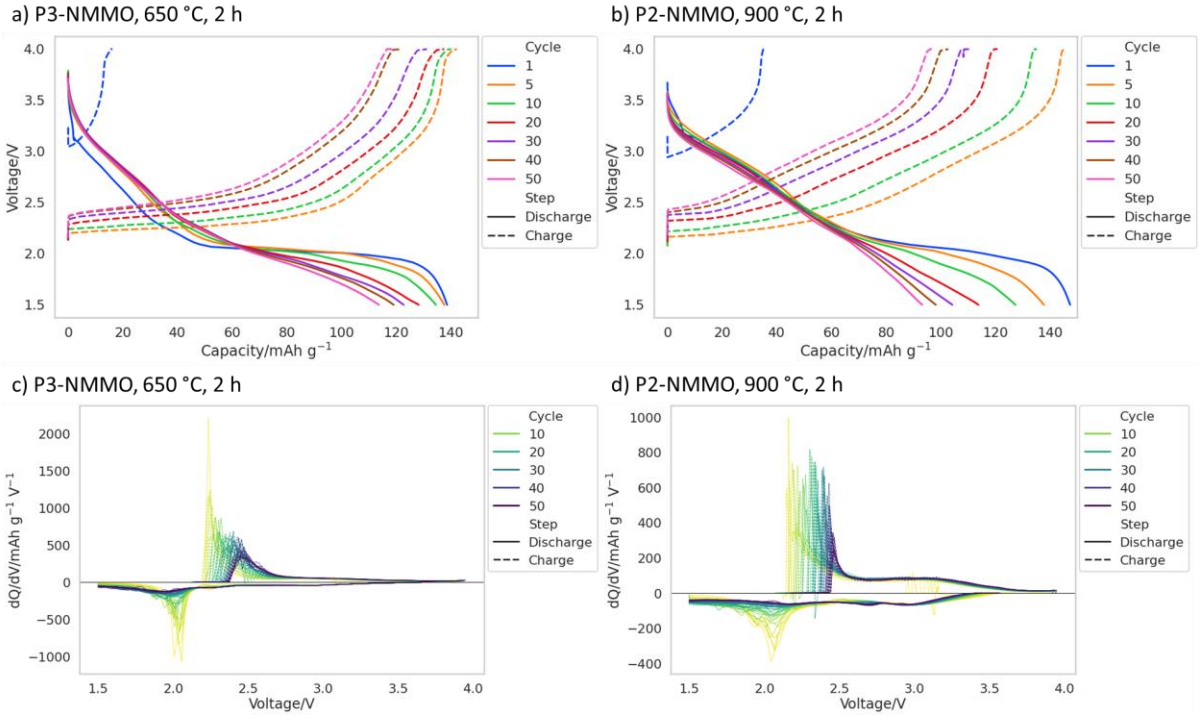

Figure 5-16: Voltage profiles of a) P3-NMMO and b) P2-NMMO, and the differential capacity graphs of c) P3-NMMO and d) P2-NMMO. 50 cycles between 1.5 – 4.0 V vs Na/Na^+ at C/5. The plateau at the top of each charge step is when the cell was held at a constant voltage. For the differential capacity graph, the curve fades from yellow to green to blue as the cycle number increases.

The exact discharge capacity values are detailed in Table 5-3. They show the P2-NMMO has a high initial discharge capacity of 147 mAh g^{-1}, but a low capacity retention of 63%.

Although the P3-NMMO starts with a lower initial discharge capacity (139 mAh g^{-1}), the higher capacity retention (83%) means that after 50 cycles it has a higher capacity than the P2-NMMO by 19 mAh g^{-1}.

Table 5-3: Discharge capacities of the 1st, 10th, and 50th cycle of single phase P3- and P2-NMMO.

Sample	Discharge capacity/mAh g^{-1}				Capacity retention over 50 cycles
	1st cycle	10th cycle	50th cycle	Avg. 50th cycle and std. dev.	
P3-NMMO	139	135	114	111.3 ∓ 2.2	82%
P2-NMMO	147	127	93	94.6 ∓ 0.9	63%

Greater detail can be seen in the differential capacity graph when looking beyond the major redox pair at 2.1 V/2.3 V (Figure 5-17). The P3 phase in this graph has a reduction (discharge) peak at 2.3 V, with a shoulder in the oxidation (charge) curve at 2.4 V that likely corresponds to it. There are two further redox pairs at 2.8 V and 3.0 V vs Na/Na^+. The larger redox peak at 2.1 V, and the corresponding voltage plateau, are a result of Mn^{3+}/Mn^{4+} redox [42], [49], [55] and a likely simultaneous P-type to O-type phase transition [27], [33], [40], [56], [57], or formation of distorted P-type phases [58]. The redox pairs at higher voltages, however, may instead be distortions of the P3 phase, for instance to P'3 or P3' [57]. Without *operando* XRD, exact determination of the structure changes that accompany the redox peaks is not possible, as there are several candidate phase transitions that can occur.

The P2 phase shows two redox peaks associated with Na^+ insertion and extraction (and the corresponding Mn^{3+}/Mn^{4+} redox) [42] at 2.1 V/2.3 V and 3.1 V/3.0 V vs Na/Na^+. There are few other obvious features of the differential capacity graph that can be used to infer the structural changes of the material. Overall, the two p-type phases appear similar to each other in the voltage profile and differential capacity plots. The main redox peaks are at 2.1 V/2.3 V, and other peaks are relatively minor – almost indistinguishable in the voltage profiles.

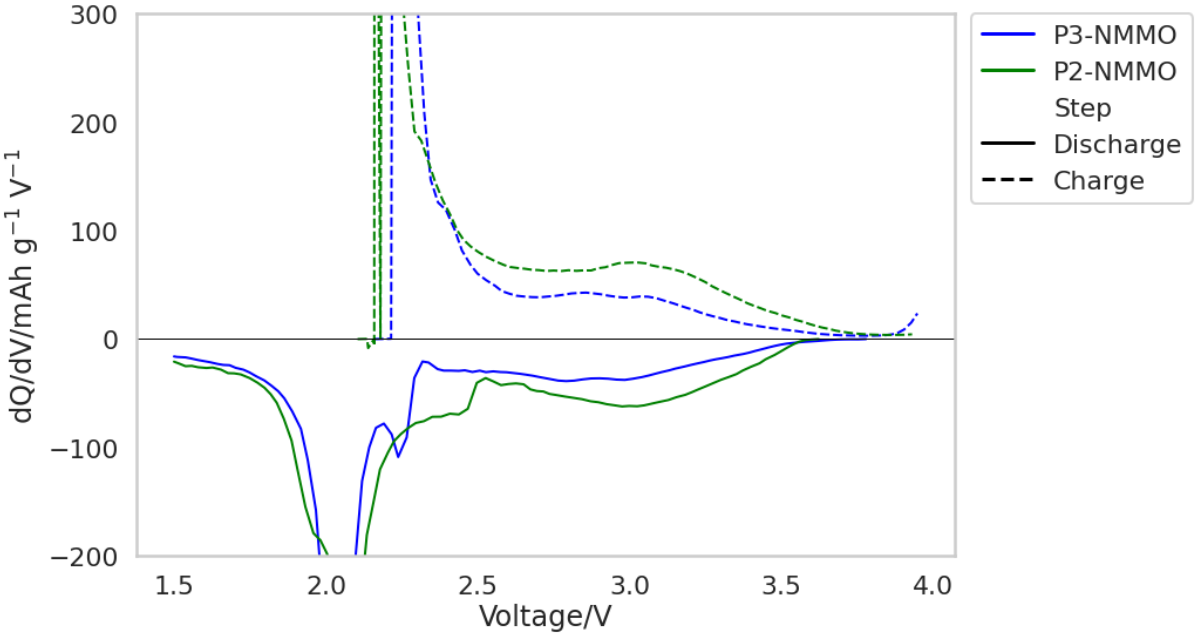

Figure 5-17: Differential capacity graph of P3-NMMO (blue) and P2-NMMO (green). Only the 2nd cycle is shown.

5.3.3.2 Discharge capacity

The capacity of each mixed sample decreases with each cycle (Figure 5-18), as seen in previous results for P3- and P2-NMMO in this work. First examining the samples generated *via* mixing. The 7:3 P3/P2-NMMO delivered the highest capacity throughout the procedure, with good capacity retention of 83% [2]. Its first cycle has a discharge capacity of 138 mAh g^{-1}, falling to 130 mAh g^{-1} after 10 cycles, and 115 mAh g^{-1} after 50. These results, and the results of the other samples in that series, are displayed in Table 5-4. The capacity values of the P3/P2-NMMO biphases are lower than the equivalent mixed phase. As shown in Table 5-4, the best capacity retention of these samples is from the 9:1 P3/P2-NMMO biphase. Compared to the mixed samples, a capacity retention of 73% is close to the lowest value. Initial capacities of the 9:1 and 1:9 P3/P2-NMMO biphase are 120 mAh g^{-1} and 166 mAh g^{-1}, respectively. These, along with the similarly performing 1:9 P3/P2-NMMO mixed phase (117 mAh g^{-1}) are the lowest initial capacities of the materials under investigation here. The initial capacities of the remaining P3/P2-NMMO biphases (7:3, 1:1, 3:7) are all close to the mixed phases, but the capacity fading is much worse, due to the inferior capacity retention. After 50 cycles, the range of capacities of the biphases is 14 mAh g^{-1}. This suggests that the performance of these biphases is relatively unaffected by the phase fractions of P3- and P2-NMMO.

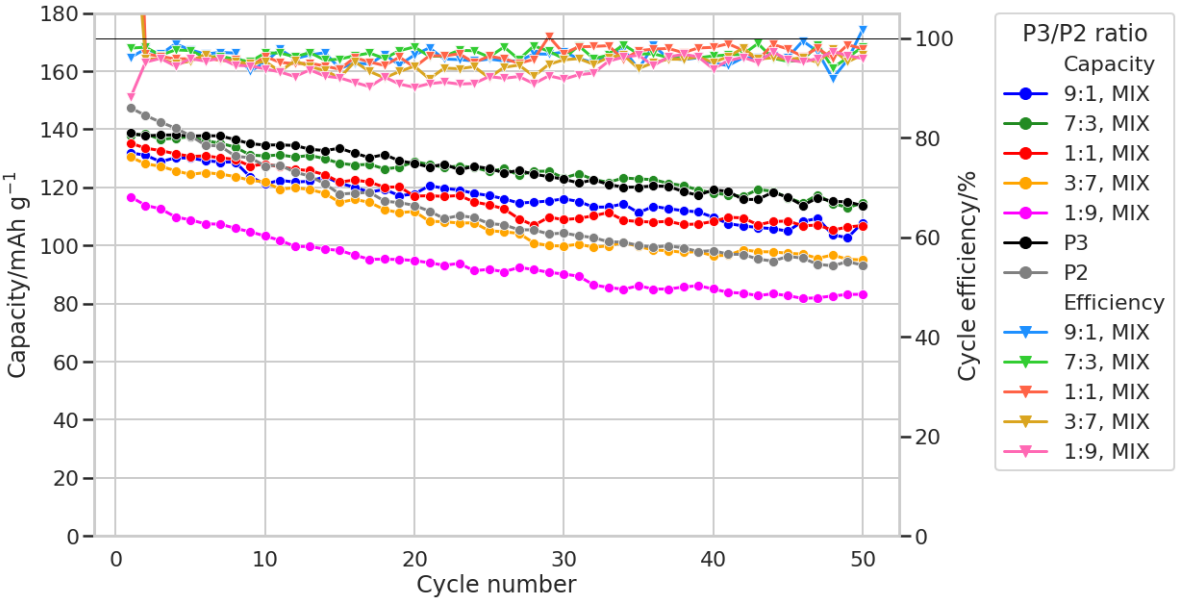

Figure 5-18: Discharge capacities and cycle efficiencies of P3/P2-NMMO mixed phases generated via mixing, and the discharge capacities of single phase P3- and P2-NMMO.

The capacities of the 9:1 and 1:1 mixed P3/P2-NMMO are similar across the test procedure: delivering 132 mAh g^{-1} and 135 mAh g^{-1} respectively, after the first cycle, and 108 mAh g^{-1} and 107 mAh g^{-1}, respectively, after 50 cycles. As the phase fraction of P2-NMMO is increased from 50%, the capacity decreases. Although the initial capacity of the 3:7 P3/P2-NMMO is 130 mAh g^{-1}, like the 9:1 mixed sample, it falls to 95 mAh g^{-1} after 50 cycles. The capacity of 1:9 mixed P3/P2-NMMO is lowest of this series; the initial capacity is 117 mAh g^{-1}, and after 50 cycles is 83 mAh g^{-1}.

Throughout this work, P3-NMMO has delivered higher capacities than the P2 phase, at least beyond the initial cycles. Therefore, it is expected that the samples with higher P2 content have lower capacity. However, when comparing these mixed samples to the phase pure P3- and P2-NMMO, the P2-NMMO delivers a higher capacity than 1:9 P3/P2-NMMO. The singe phase P2-NMMO loses capacity rapidly, falling from 147 mAh g^{-1} to 93 mAh g^{-1} over 50 cycles – a 63% loss of capacity. So, although the mixed phases all have lower initial capacities than single phase P2-NMMO, by 50 cycles the capacity of single phase P2-NMMO has fallen to the same value as 3:7 P3/P2-NMMO. This is supported by the falling capacity retention across the sample range; from 82-83% in majority P3 mixes, falling to 71% in the 1:9 mix and 63% in the single phase P2-NMMO. This pattern shows the increased stability of the P3 phase over P2 within this voltage range.

The capacity values of the P3/P2-NMMO biphases are lower than their mixed equivalents. As shown in Table 5-4, the best capacity retention of these samples is from the 9:1 P3/P2-NMMO biphase. Compared to the mixed samples, a capacity retention of 73% is close to the lowest value. Initial capacities of the 9:1 and 1:9 P3/P2-NMMO biphase are 120 mAh g^{-1} and 166 mAh g^{-1}, respectively. These, along with the similarly performing 1:9 P3/P2-NMMO mixed phase (117 mAh g^{-1}) are the lowest initial capacities of the materials under investigation here. The initial capacities of the remaining P3/P2-NMMO biphases (7:3,

1:1, 3:7) are all close to the mixed phases, but the capacity fading is much worse, due to the inferior capacity retention. After 50 cycles, the range of capacities of the biphases is 14 mAh g^{-1}. This suggests that the performance of these biphases is relatively unaffected by the phase fractions of P3- and P2-NMMO.

Table 5-4: Discharge capacities of the 1st, 10th, and 50th cycle and capacity retention after 50 cycles of P3/P2-NMMO mixed and composite phases.

P3/P2-NMMO ratio	Discharge capacity/mAh g^{-1}				
	1st cycle	10th cycle	50th cycle	Avg. 50th cycle and std. dev.	Capacity retention
9:1, mixed	132	121	108	105.6 ∓ 3.4	82%
7:3, mixed	138	130	115	110.9 ∓ 2.7	83%
1:1, mixed	135	128	107	100.7 ∓ 4.7	79%
3:7, mixed	130	122	95	93.6 ∓ 1.4	73%
1:9, mixed	117	103	83	77.5 ∓ 4.0	71%
9:1, 720 °C	120	125	88	86.4 ∓ 2.3	73%
7:3, 730 °C	132	119	85	86.7 ∓ 1.4	64%
1:1, 770 °C	134	126	93	91.6 ∓ 0.9	69%
3:7, 800 °C	132	116	83	79.1 ∓ 3.5	63%
1:9, 820 °C	116	100	79	76.9 ∓ 2.6	68%

These biphases also have lower capacity retention than the single phases, demonstrated in Figure 5-19. The P3-NMMO displays better capacity and retention than the biphases. In comparison, the P2-NMMO has a capacity retention of 63%, equal to the lowest capacity of the biphases (3:7 P3/P2-NMMO). However, since P2-NMMO starts with a higher initial capacity it finishes with a discharge capacity of 93 mAh g^{-1}, equal to the highest of the biphases (1:1 P3/P2-NMMO).

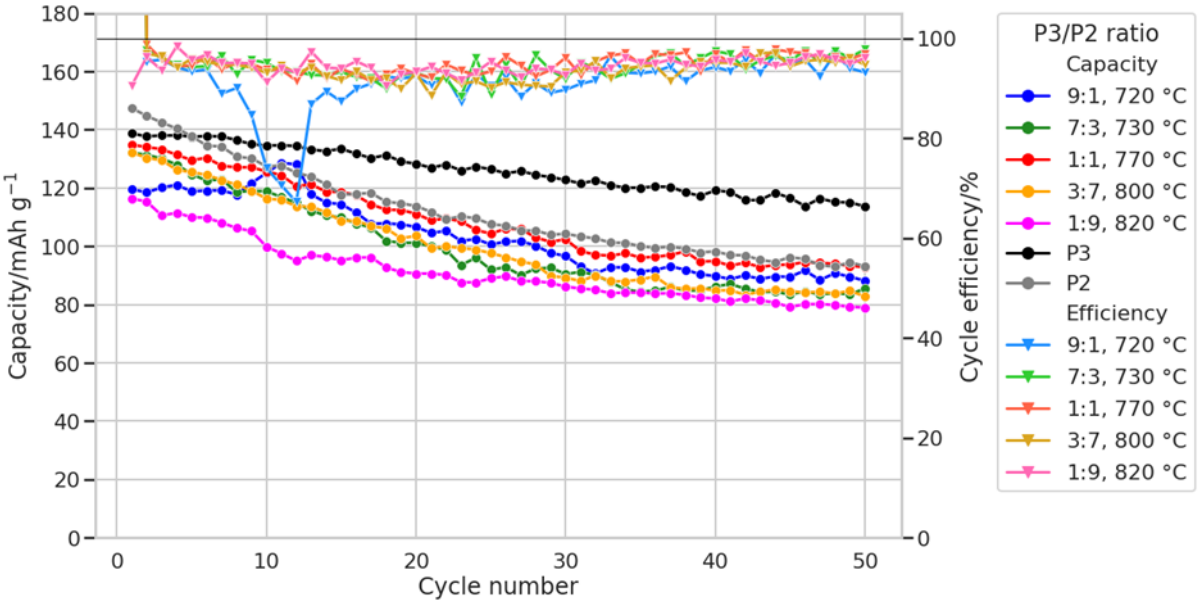

Figure 5-19: Discharge capacities and cycle efficiencies of P3/P2-NMMO biphases generated via calcination, and the discharge capacities of single phase P3- and P2-NMMO.

As seen in previous chapters, the cycle efficiency of the samples is lowest between cycles 10-30, approximately 90%, but in the first 10 and final 20 cycles it is 95% and often higher. The 10-30 cycle range is where much of the capacity loss occurs and in this material the likely cause is Mn^{2+} dissolution from the active material into the cathode [6], [8], [29], [32], [59]–[64]. This is a common occurrence in Mn-rich cathodes such as NMMO. This can be exasperated by excess carbon in the cathode composite, as well as smaller particle size [65].

This does not explain why the capacity retention of the single phase P3-NMMO is much higher than that of P2-NMMO. This is in contrast to previous work showing the structural stability, and thus cycle life, of P3-NMMO to be worse than P2-NMMO [45]. The difference in this work is the voltage range of the galvanostatic testing, avoiding anionic redox at high voltage (>4.2 V vs Na/Na^+) and promoting more reversible phase transitions at low voltages (~2.0 V vs Na/Na^+). This should improve the cycle life of the P3 phase. Limiting the voltage to 4.0 V should also prevent the P2↔O2 transition, which is harmful to the cycle life of P2 cathodes. Indeed, there is no evidence of this phase transition, as can be seen in the differential capacity graphs.

It is possible that P2-NMMO is more susceptible to Mn^{2+} dissolution than P3-NMMO, and that its generally better electrochemical performance compared to the P3 phase is masked by its larger particle size as it is calcined at higher temperatures. It also has a shorter calcination time in this work owing to the biotemplating synthesis route. This is a pattern that can be seen in the mixed P3/P2-NMMO phases: the capacity retention of the mixed phases decreases with increase phase fraction of P2-NMMO.

The 1:9 P3/P2-NMMO biphase (calcined at 820 °C) here performs worse than the biotemplated P2-NMMO in Chapter 3 with respect to its capacity retention. The capacity

after 50 cycles is lower (79 mAh g^{-1} *vs*. 98 mAh g^{-1} in P2-NMMO calcined for 20 h), as is the initial capacity (116 mAh g^{-1} *vs*. 127 mAh g^{-1}). This is consistent with the difference in average particle size between the two samples. The P2-NMMO calcined for 20 h had an average particle size of 3.39 μm ± 2.04 μm, whereas calcination for 2 h led to an average particle size of 1.70 μm ± 0.98 μm. What this suggests is that smaller particle sizes for P2-NMMO are not necessarily beneficial and lead to increased capacity fading, possibly caused by Mn^{2+} dissolution which is exacerbated by having a higher surface area/volume ratio.

Regarding the 1:9 P3/P2-NMMO mixture, it has a lower capacity than single phase P2-NMMO, although a higher capacity retention. It is possible that this is just variation in the performance of the material, not solved by testing three times, as opposed to the addition of 10% P3-NMMO causing the capacity to fall by 10 mAh g^{-1}.

The reason for the poor performance of the biphases compared to both the mixed phases and the single phases may also be a result of Mn^{2+} dissolution. The process of transitioning from P3 to the P2 phase involves the growth of grains at the expense of another. Since the P3 and P2 phases do not perfectly align with each other, this is likely to cause defects in the crystal structure. These defects could lead to increased surface area in the material through which Mn^{2+} can dissolve into the electrolyte. This would explain the low capacity retention of the all the biphases compared to the other samples under investigation here, despite the often high (~130 mAh g^{-1}) initial discharge capacity.

Several hypotheses have been discussed here as reasons for the poor performance: Mn^{2+} dissolution, harmful P2↔O2 phase transitions, and crystal defects on the biphases. There are ways to test these hypotheses. For Mn^{2+} dissolution, inductively coupled plasma-optical emission spectroscopy (ICP-OES, or ICP) can be conducted on the electrolyte post-cycling. If Mn^{2+} was continually dissolving into the electrolyte, ICP would show the increasing presence of it at various points in the cycle procedure. Cells could be stopped and disassembled at given cycle numbers and have the electrolyte examined to show the presence of Mn^{2+} over time.

The P2↔O2 transition can be observed by XRD, either *in operando* or *ex situ*. For *operando* XRD, the experimental setup is well-established both in the wider literature and discussed in this work. *Ex situ* XRD would require disassembly of the cell at various states of charge and washing and examining the cathode. Although slightly more involved, *ex situ* should give better data than *operando* XRD; less beam attenuation and testing the cell in a regular coin cell rather than a cell designed for *operando* XRD experiments, which are not completely sealed. Equally, transmission XRD could be conducted on a pouch cell if the material cost is of less importance.

The crystal defects and grain growth would have to be examined with HRTEM or HAADF-STEM. This would reveal the interaction of the two phases at the grain boundary. As well as identifying again defects in the crystal structure and any potential sources of strain,

this would also confirm whether the biphases are indeed biphases as described in the introduction.

5.3.3.3 Voltage profile

In the P3/P2-NMMO mixes, the voltage profiles do not change dramatically as the P2-NMMO phase faction increases. As expected from the P3- and P2-NMMO single phase graphs, which behave similarly to each other, the major plateau in each mixture does not change position, although it does fade faster as the phase fraction of P2-NMMO increases. The shape of the voltage curve (Figure 5-20) after 50 cycles is more linear in the 3:7 and 1:9 P3/P2-NMMO mixed samples than the others, which fits with the faster capacity fade. It is clear here that the capacity fading occurs below 2.1 V. The discharge curves all overlay very closely with each other, providing a visual demonstration that the process in the 2.1 V – 4.0 V vs Na/Na^+ range are reversible. This is in keeping with the evidence that the Mn^{3+}/Mn^{4+} redox is the cause of the plateau, and that Mn^{2+} dissolution is the cause of the capacity fade in this material.

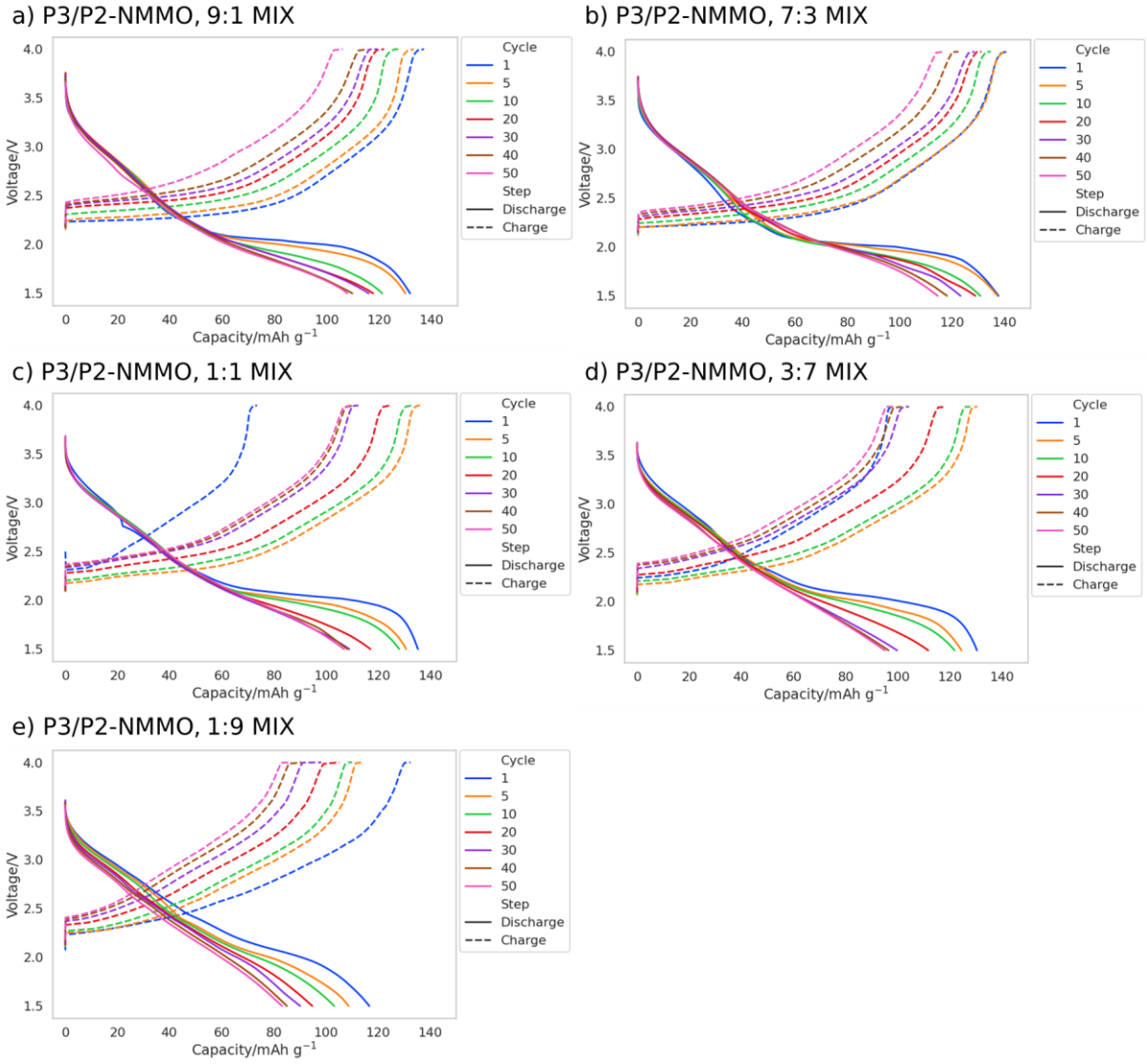

Figure 5-20: Voltage profiles of P3/P2-NMMO mixed phases generated via mixing. The plateau at the top of each charge step is when the cell was held at a constant voltage.

An examination of the differential capacity graphs can reveal more about the internal processes of the material. The plots of the second cycle of the five mixed phases Figure 5-21) show that there are several processes that occur in the P2-NMMO material and not in P3-NMMO. It is also notable that these are not all apparent in the single phase P2-NMMO differential capacity graph. Most clear, in terms of intensity and the progression as the P2 phase fraction increases, is the redox pair at 2.4 V/2.6 V vs Na/Na^+. There is also one at 2.8 V/2.9 V, two peaks during charge at 3.2 V and 3.5 V that have no obvious counterpart. The peak at 3.5 V has previously been identified as the P2↔OP4 transition [44], [66], and similarly appears in the P2-NMMO synthesised *via* solid state methods.

The other minor peaks are not identified, at least commonly in previous work. Even with *operando* XRD, it is likely that these peaks would arise from minor structural changes that would not be discernible from the background or more major reflection peaks, or manifest as peak shifts only. It may be possible to identify them using *ex situ* techniques that examine more short-range interactions, such as NMR or Raman spectroscopy. Regardless, because of the increase in intensity with increase in phase fraction of P2-NMMO they can be used to identify P2-NMMO electrochemical behaviour in the biphases generated *via* calcination.

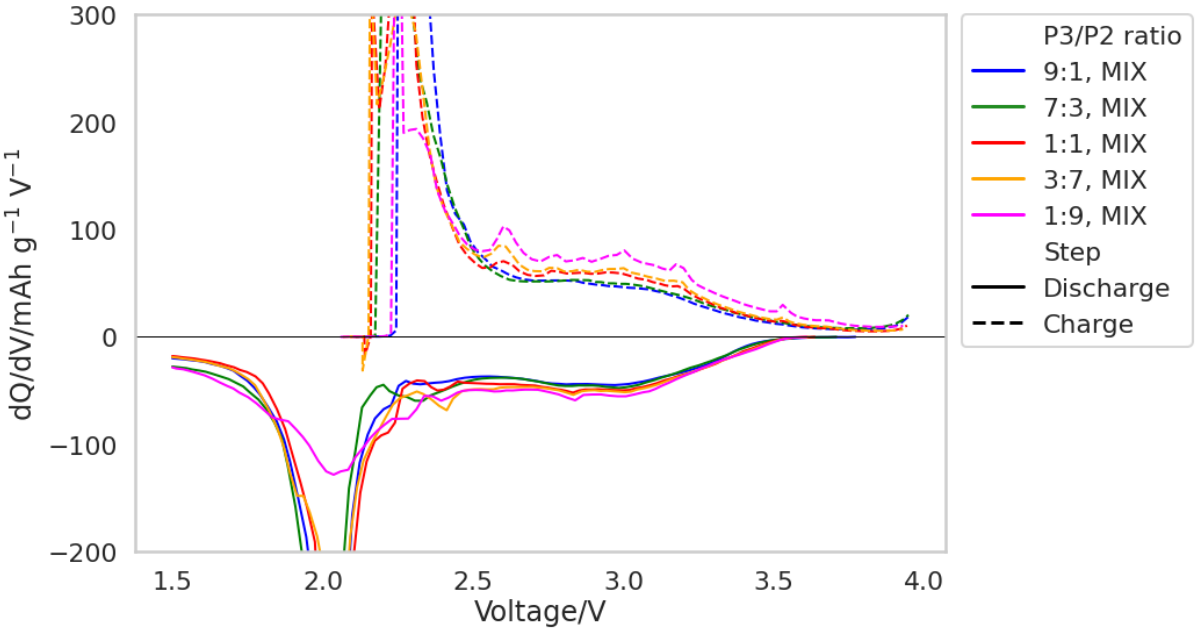

Figure 5-21: Differential capacity graph of P3/P2-NMMO mixed phases generated via mixing. Only the 2nd cycle is shown.

The voltage profiles of the biphases follow the same pattern as the mixed phases (Figure 5-22). The plateau at 2.1 V vs Na/Na^+ in the discharge step fades throughout the test procedure, becoming more linear and decreasing the capacity delivered. As seen in Table 5-4, the capacity decay is more rapid than in the mixed phases, but in both cases the

capacity decay seems to originate from Mn^{2+} dissolution, suggested by the shortening of the voltage plateaux meaning a reduction in Mn^{3+}/Mn^{4} redox. No major other features are present in the plots, showing that the electrochemical features of the biphases and mixed phases are identical, save for some possible minor structural changes revealed under close examination of the differential capacity graphs.

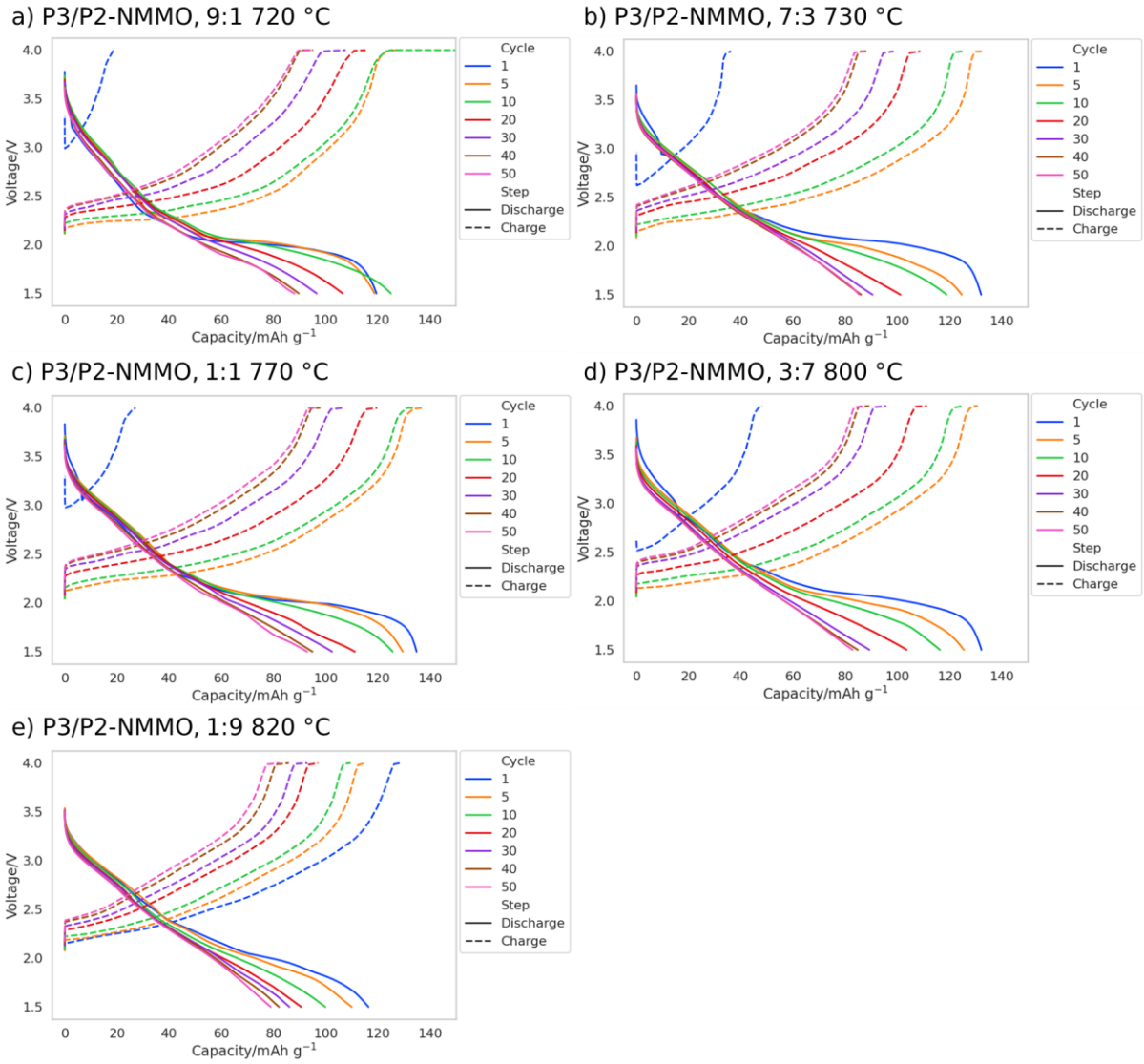

Figure 5-22: Voltage profiles of P3/P2-NMMO biphases generated via calcination. The plateau at the top of each charge step is when the cell was held at a constant voltage.

The differential capacity graphs show similar redox peaks and positions for the biphases as the mixed phases. The most significant different seems to be the prevalence of redox peaks that appears at higher P2 phase fractions. For example, the reduction peak at 2.6 V vs Na/Na^{+} that is only visible from the 1:1 P3/P2-NMMO mixed phase, is visible in all the biphase samples. This is true for the other minor peaks in the graphs. The 2nd cycles of each biphase sample are shown in Figure 5-23. They show that the redox peaks that seem to only relate to the P2 phase are present in throughout the series, suggesting greater redox activity of the P2-NMMO material when generated this way. Greater redox activity

in the P2-NMMO may explain the worse capacity fading of the biphases samples compared to the mixed samples. The P2-NMMO has worse capacity retention than the single phase P3-NMMO, and samples have worsening capacity retention as the P2 phase fraction increases.

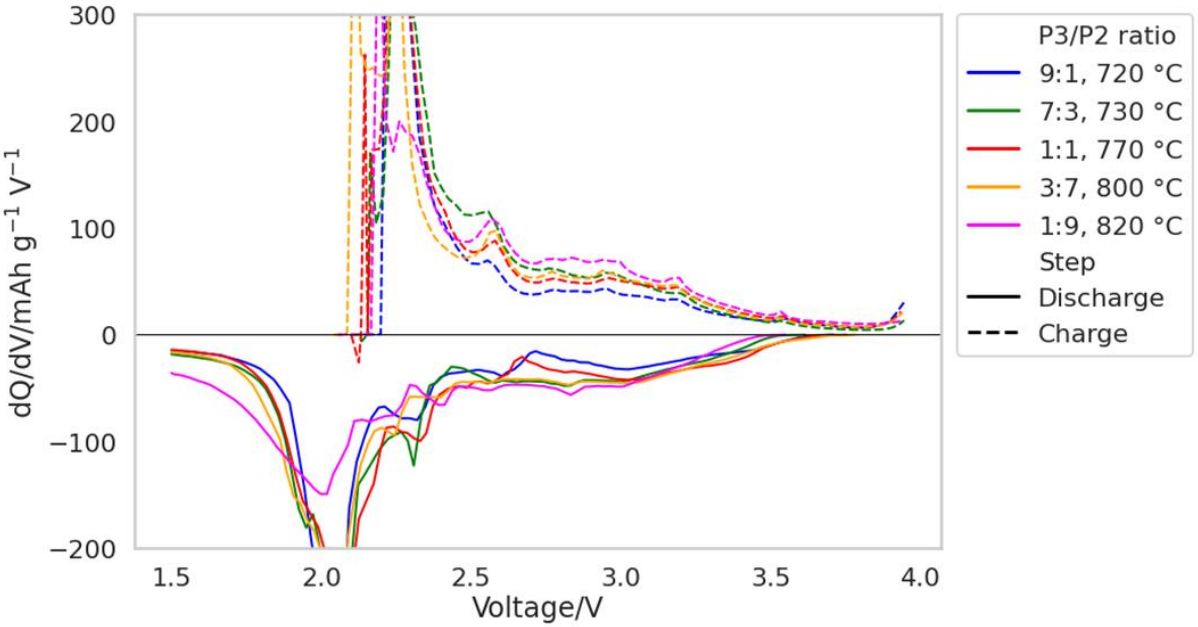

Figure 5-23: Differential capacity graph of P3/P2-NMMO biphases generated via calcination. Only the 2nd cycle is shown.

In the differential capacity plot of the single phase P3-NMMO (Figure 5-17) a peak on discharge at 2.3 V which is replicated here more intensely than in the mixed phases. It persists until the 3:7 P3/P2-NMMO biphase sample. It is posited that the breakdown of the P3 phase to form the P2 phase creates additional surface area of the P2-NMMO, and so it may have the same effect on the P3-NMMO. the result of this would be the exposure of more surface area and thus greater electrochemical activity and more rapid capacity fade.

Over 50 cycles, as seen in the voltage profiles, the peaks in the differential capacity curves broaden because of degradation in the cell which has been seen in previous chapters. The likely origin of this degradation is the dissolution of Mn^{2+} into the electrolyte because of the disproportionation of Mn^{3+}. This is the case for a wide number of biphases studied that are Mn-rich and can be seen in the reduction in the intensity of the voltage plateau at 2.1 V vs Na/Na^{+} in the discharge curve. Overall, there appears to be more electrochemical process that are occurring in the cathode. This is not necessarily detrimental to the lifetime of the cell [13], as long as they are reversible. Examination of the voltage profiles shows that the main capacity loss comes from the Mn^{3+}/Mn^{4+} redox, the other processes either are unaffected throughout cycling, or suffer the same degradation in the mixed phase as they do in the biphase (such as those in 1:9 P3/P2-NMMO samples). The biphases do not show any prevention of the degradation of the NMMO cathode, with their capacity retention being worse for each sample.

Comparing the different ratios of P3/P2-NMMO reveals the differences between the two preparation methods. Shown in Figure 5-24 are the differential capacity graphs of each ratio of P3/P2-NMMO made by each method. Viewed this way, two peaks in the charge step can be seen at 2.1 and 2.3 V vs Na/Na^+ with changing intensity as the phase fraction of P2-NMMO increases. The peak at 2.1 V increases and the peak at 2.3 V decreases. The peaks in this voltage range (2.0 – 2.4 V vs Na/Na^+) correspond to Mn^{3+}/Mn^{4+} redox as Na^+ is extracted on charge. This shows that Na^+ extraction from the P3 material happens a higher potential than from the face-sharing Na site (Na_f) in P2-NMMO – there are two in P2 phases and extraction from the edge-sharing site (Na_e) occurs at ~3.0 V vs Na/Na^+ [42].

When the phase fraction of P2 is more than 50%, the differential capacity graphs appear the same in the mixed samples and biphase samples. However, at lower P2 phase fractions the oxidation peaks in charge step of the mixed samples disappear but persist in the biphasic samples. For the 1:1 sample, the charge step appears the same regardless of preparation method, but the not the discharge step. The small oxidation peaks above 2.5 V likely result from ordering or phase transformations as opposed to Mn^{3+}/Mn^{4+} redox. The likely origin of the peaks is the P2-NMMO, as they appear in the P2-rich mixed samples. The reason that P2 phases are more likely to undergo ordering steps is the presence of two Na sites that are filled at different potentials; coulombic repulsion of Na^+ leads to specific distributions, independent of the material composition [36], [67]–[70].

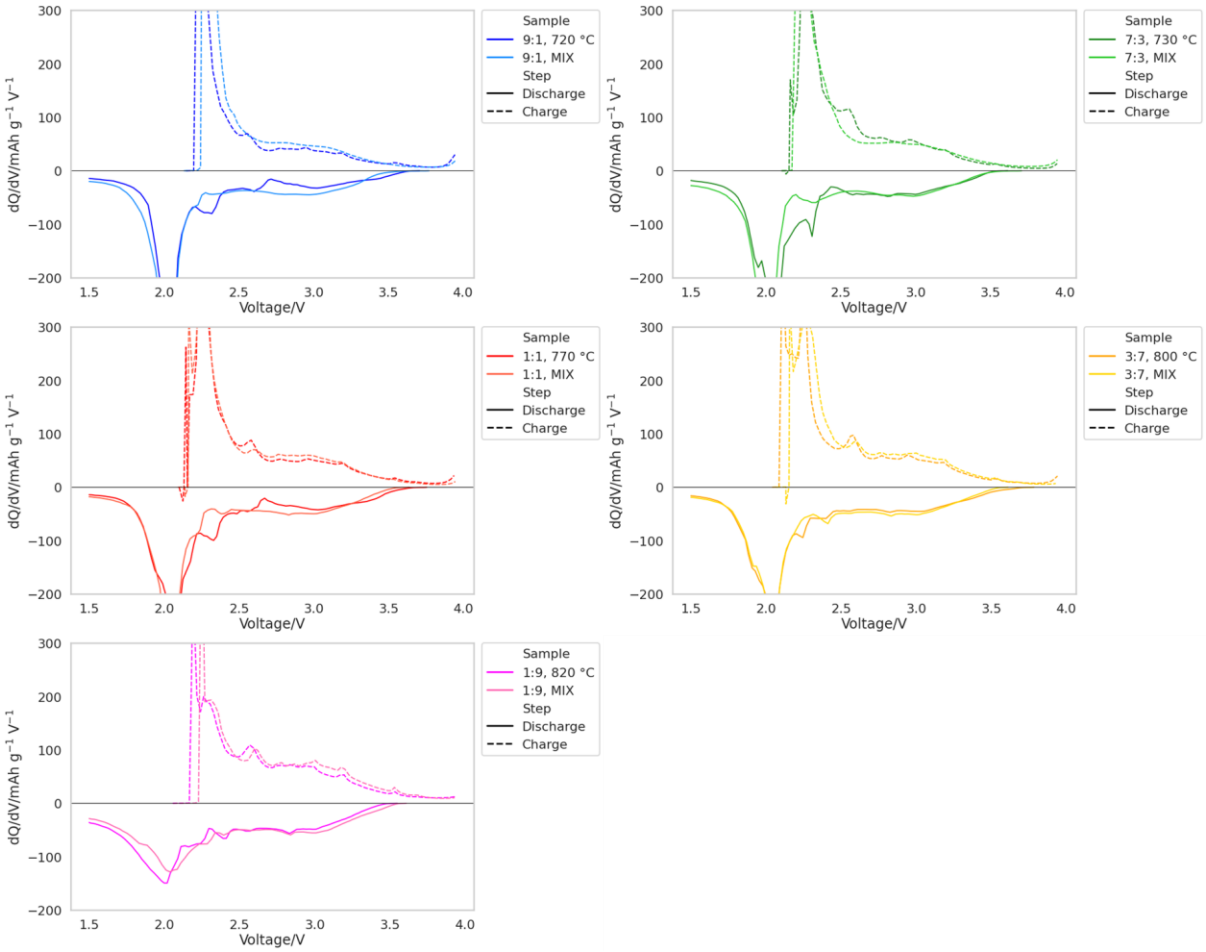

Figure 5-24: Differential capacity graphs of P3/P2-NMMO biphases generated via calcination and via *mixing. Only the 2nd cycle between -200 – 300 mAh g-1 V-1 is shown.*

The reason the P2 phase may have greater redox activity at low phase fractions may be due to its size. The calcination synthesis means that the P2-NMMO crystallites are small as it is only just forming at the temperatures used. This translates to a higher surface area/volume ratio than the P2-NMMO present in the mixed phases which are calcined at 900 °C instead. This could also contribute to the lower capacity retention as a higher surface area of the P2-NMMO allows for more Mn^{2+} dissolution, as suggested earlier.

The single phase P2-NMMO does not exhibit these peaks in its differential capacity graph. This raises the possibility that there is some interaction between the P2 and P3 phases that activates the Na^+/vacancy ordering within the P2 structure. So the interaction of the P3 and P2 phases in the material increases the capacity retention of the P2-NMMO. however, when prepared *via* calcination P2-NMMO particles are smaller and so suffer rapid capacity fading. This explains why the capacity retention of the biphases is lower overall than the mixed phase but greater than (or equal to) the capacity retention of the single phase P2-NMMO.

The low capacity retention of single phase P2-NMMO is likely due to its small particle size (Figure 5-25), compared to the biotemplated P2-NMMO in Chapter 3, and the size of P2-NMMO in the mixed samples. The size of P2-NMMO in the mixed samples is apparent from

the size increase as the phase fraction of P2-NMMO increases (Figure 5-15). The size of the P2-NMMO here is smaller than other reported cases of P2 phases, which are commonly 1-4 μm in size. The reason the P2 is smaller than the other P2 samples in this chapter is unclear. The synthesis method of single phase P2-NMMO and the P2-NMMO used in the mixed phases was identical. The P2-NMMO used in the mixed phases was made in a larger batch than the single phase P2-NMMO. this could lead to incomplete combustion of the dextran and higher particle sizes [71].

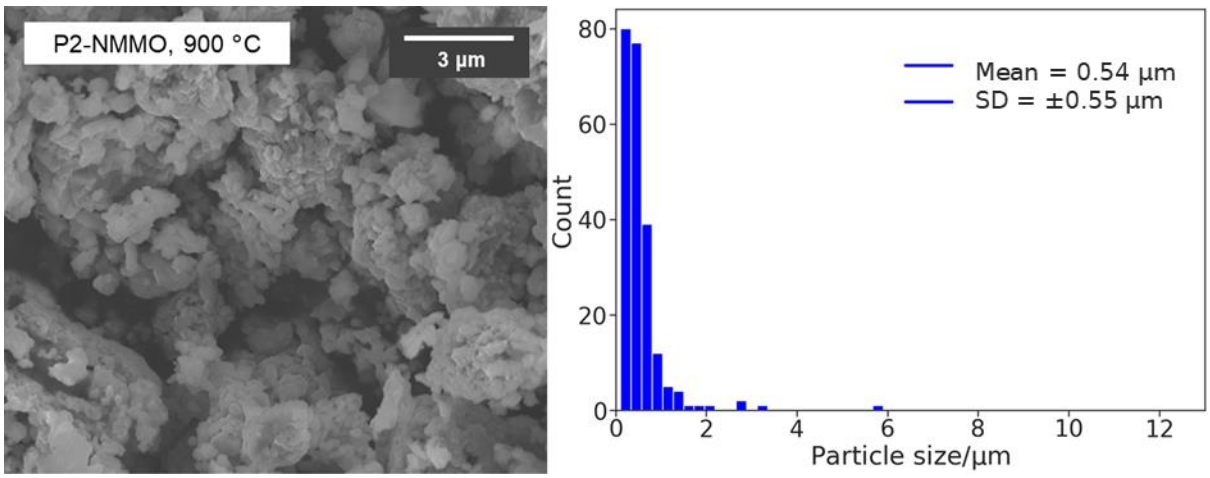

Figure 5-25: SEM image of single phase P2-NMMO calcined at 900 °C for 2 h, and a histogram of particle sizes.

5.3.3.4 Rate capability

Testing the capacity of the samples at different C-rates was conducted to test for evidence of enhances performance of the biphases over the mixed phases. The C-rates tested are C/10, C/5, C/2, 1C, 2C, and 5C. The cells are cycled five times at each C-rate, before cycling again at C/10 for final five cycles. Seen in previous chapters, the P3- and P2-NMMO phases do not display good rate capability. At 5C, the capacity extracted is approximately 30 mAh g^{-1}. This is caused by high internal resistance in the cell. There are several explanations for this, such as poor mixing of the active material with the C65 and PVDF, creating points in the cathode with longer Na^+ diffusion pathways. It could also be that exposure to air hydrated the active material to a degree, although this is not apparent in the XRD.

The mixed phases display the same behaviour. The 9:1 P3/P2-NMMO mixed phase has the lowest capacity of the 5 in the series, consistently 10 mAh g^{-1} lower than the others for each different C-rate. The 7:3 P3/P2-NMMO, the next along in the series performs the best, although only when cycling at C/10, C/5, C/2 and 1C. at 2C and 5C, it has the same capacity as the rest of the samples (expect 9:1 P3/P2-NMMO). The capacity values of the other samples are similar to each other; 137 mAh g^{-1}, 121 mAh g^{-1},94 mAh g^{-1}, 72 mAh g^{-1}, 51 mAh g^{-1}, and 25 mAh g^{-1} at each C-rate (Figure 5-26). Each sample recovers its capacity to approximately its original value, indicating that the low capacity at high C-rates is not due to degradation of the material, but more likely to high internal resistance.

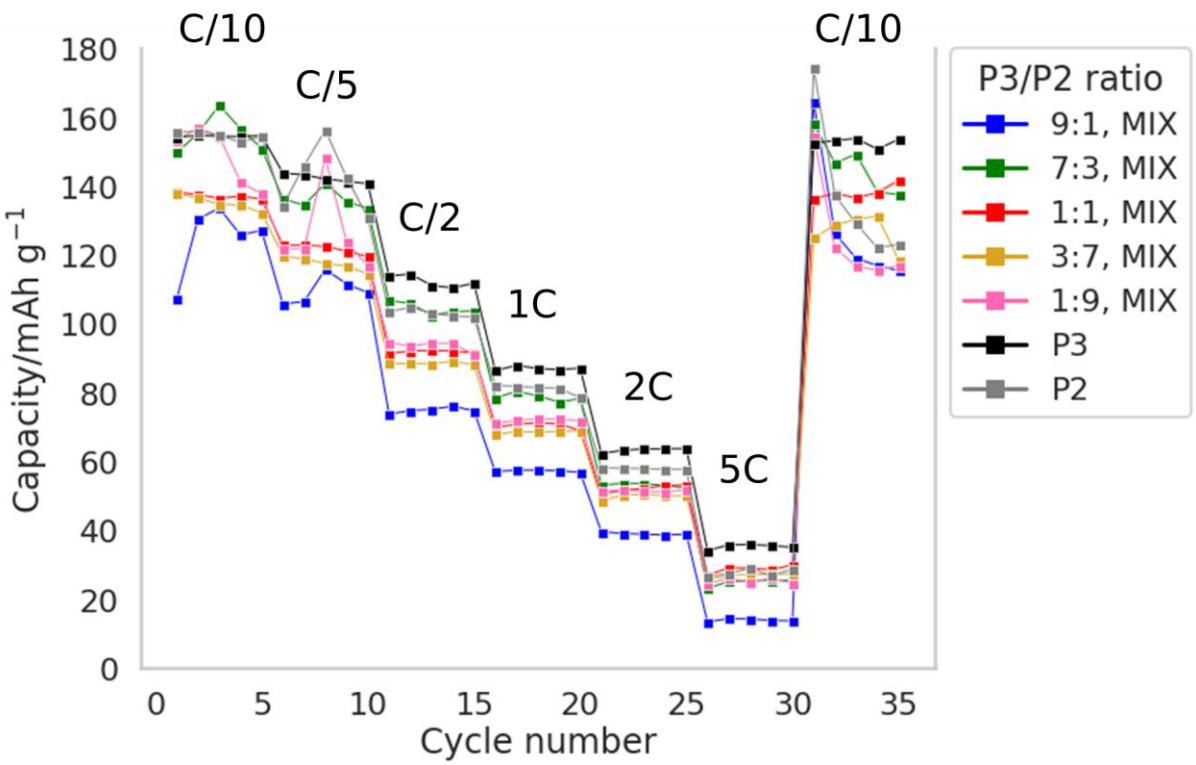

Figure 5-26: Capacity at various C-rates of P3/P2-NMMO mixed phases generated via mixing. C-rates are marked on the plot.

The performance of the biphases is very similar to that of the mixed phases. The biphase samples all have very similar capacity values to each other at almost every cycle. The exception is the 9:1 P3/P2-NMMO sample which, similar to the galvanostatic cycling test, shows an increase in capacity within the first 10 cycles but it follows the rest of the series for the remainder of the procedure. The capacity of the biphases is lower at each cycle number, as with the galvanostatic cycling, and shows no improvement in performance at elevated C-rates or with increasing P2 phase fraction. The capacities progress from 142 mAh g^{-1} at C/10 to 19 mAh g^{-1} at 5C (Figure 5-27). The capacity values, although lower, are within 10 mAh g^{-1} of the mixed phases, and so it is likely that the performance of both samples is the same, and that if a biphase is being formed it is not having the effect on the materials that has been seen in other intergrowth studies.

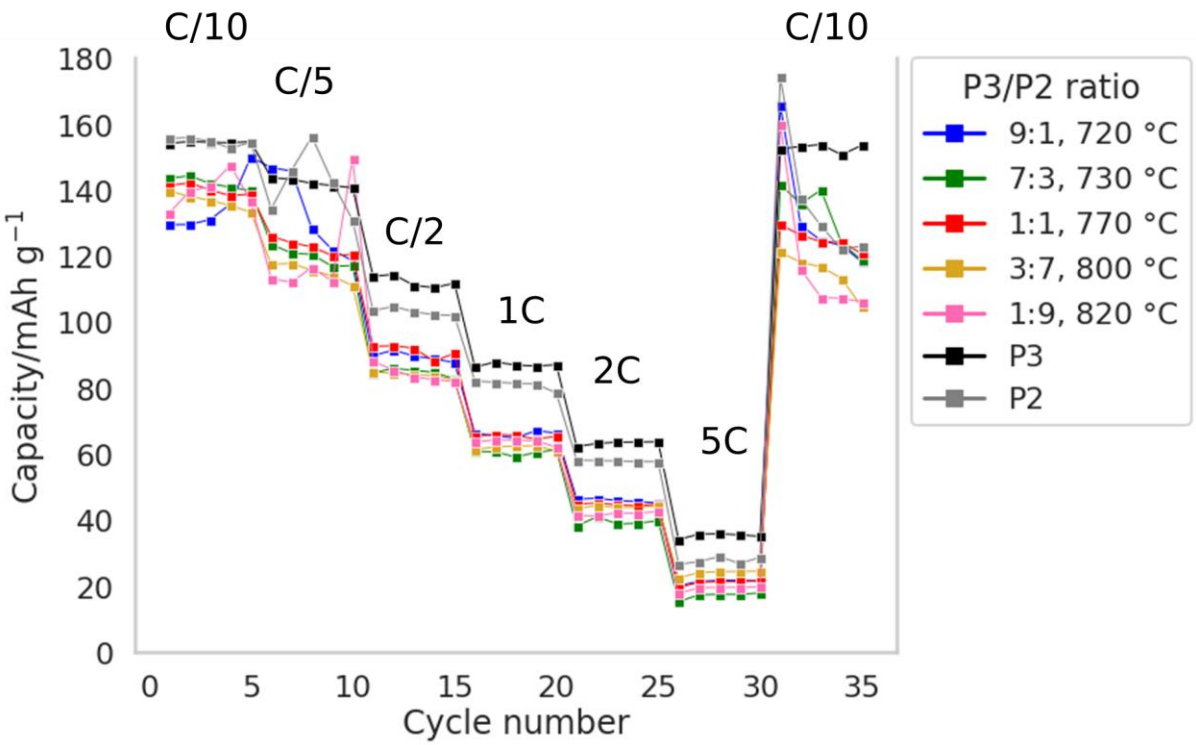

Figure 5-27: Capacity at various C-rates of P3/P2-NMMO biphases generated via calcination. C-rates are marked on the plot.

The benefit of intergrowth structures is often that they greatly improve on the rate capability of the separate materials. This is not always the case [17], [30], even where intergrowth material is present and has a marked effect on the phase progression throughout cycling, such as preventing the P2↔OP4 phase transition [30]. In that case, the material was made up of a P2-$Na_{0.67}Li_{0.18}Mn_{0.8}Fe_{0.2}O_2$ and only a minor O3 phase growing on its surface. The effects of different phase ratios are not explored, though it does display a higher capacity over 50 cycles than the pure P2 equivalent [31].

The rate capability of all the samples being so similar to each other suggests that the samples are not interacting in a way typical of intergrowth phases. Intergrowth materials typically exhibit much improved rate capability and capacity retention, but these do not. The P3 phase does seem to have a stabilising effect on the P2-NMMO, causing it to have a higher capacity retention that the single phase P2-NMMO – or at least activating certain ordering steps. This effect is more pronounced in the biphases than the mixed phases.

The negligible effect on the rate capability suggests that the interaction is not truly that of an intergrowth structure. Similarly, the changing particle size, both within each series and between series, should result in changing rate capability, but it doesn't.

5.4 Conclusion

From these results there is no apparent benefit to synthesising a mixed P3/P2-NMMO phase *via* calcination at an intermediate temperature between those used to generate pure P3 and P2 phases. Particle size or morphology is the same across synthesis method

for the same phase ratios. Aside from the unexpected small size of the phase pure P2-NMMO, there is an increase in size with increase P2 phase fraction, as expected [8]. There are some differences with respect to the electrochemical performance, but these differences show the *ex situ* mixed phases to perform better than the biphases, owing to the superior capacity retention. It is possible that the P3-NMMO, given their size (0.65 μm ± 0.41 μm) transform too rapidly into the P2-NMMO to maintain the hetero-epitaxial structure. It's possible that through quenching the material at a midpoint temperature that the intergrowth structure could be obtained.

It is likely that the dominant capacity fading mechanism present in all samples is Mn^{2+} dissolution, resulting from Mn^{3+} disproportionation. This occurs often in Mn-rich cathodes and is exacerbated by a higher surface area to volume ratio [8], [29], [60], [63]–[65], as there is a higher surface area through which the Mn^{2+} can dissolve into the electrolyte. To test for this, ICP on the electrolyte post-cycling could be conducted, as well as on the Na metal anode.

The lower capacity retention of the biphases, relative to the mixed phases, does suggest that the surface area is higher. This difference could be explained by the lower calcination temperature of the P2-NMMO phase as the P2-NMMO in the mixed phases was calcined at 900 °C. Though it is hard to accurately determine the size of the P2-NMMO particles *via* SEM (in part because of the degree of agglomeration), it is likely the case that the P2-NMMO particles in the biphases are smaller than the mixed phases.

As a general point, the pure P2-NMMO does display a lower capacity retention compared to all the P3/P2-NMMO samples tested, just as the P3-NMMO displays a higher capacity retention. This could be a result of the P2-NMMO having smaller particle sizes, as it was noted that the pure P2-NMMO had smaller particle sizes in the SEM than would be expected. However, the as the phase fraction of the P2-NMMO increases, the capacity retention of the materials decreases – particularly in the mixed phases. As such, it is likely that the P2-NMMO suffers from a capacity fading mechanism more severely than the P3-NMMO does. It would be interesting to determine the degree of Mn^{2+} dissolution from each sample, as well as from a P2-NMMO synthesised a different way, such as solid state synthesis, to determine whether the 2 h calcination used in biotemplating has a detrimental effect on the P2 phase, but seemingly not on the P3 phase. This would show if the P3-NMMO material performs better than the P2 phase when the particle sizes are smaller and discover whether the P3 phase is less susceptible to Mn^{2+} dissolution, as these results suggest.

Without HRTEM and/or HAADF-STEM, the nature of the samples that have been generated *via* calcination is unknown. They have been referred to as biphases throughout the chapter, partly to distinguish them from the mixed phases. These experiments are not always conducted in studies into intergrowth structures, even when there are multiple particle morphologies present in SEM images of the two phases [8]. In that case the benefit of the composite phase is shown over the single phase. Future work is therefore needed to confirm the presence of an intergrowth structure as there seems to be little

difference in performance; the biphases may even have lower capacity retention than the mixed phases. the interaction of the two phases may explain this behaviour and HRTEM would show the differences in proximity of the two phases.

What is shown in this work is an investigation into the different phase ratios of the mixed-phase cathode, as well as a comparison of these samples to the equivalent phase ratio when mixed post-synthesis. The comparison of different phase ratio is done occasionally, often in work that generates biphases *via* doping the host material. The comparison to post-synthesis mixed phases is much less commonly done. The lack of improvement both in the capacity, capacity retention, and rate capability of the biphases over their mixed phase equivalents suggests that there is at least no interlocking of the P3 and P2 phases *via* a hetero-epitaxial structure to reduce the microstrain by preventing phase transitions. That there are no major differences in the differential capacity graphs suggests that there is no avoidance of phase transitions, although this would have to be confirmed *via operando* XRD.

It may be the case that raising the upper voltage limit on charging would reveal differences between the two series. This has been avoided in previous chapters as it can lead to irreversible P2↔O2 transitions, or oxygen redox, which are both detrimental to the life of the material. However, it is reported that intergrowth structures suppress this transition, and the P2↔OP4 as well. There are instances of enhanced oxygen activity in intergrowth studies, but this is often related to dopants or changes in particle sizes as opposed to the intergrowth structure itself [5], [26].

The only sample to display a higher capacity retention than either of the phase pure P3- and P2-NMMO was the 7:3 P3/P2-NMMO mixed phase. This improvement is only 1% (from 82% to 83%) and so likely not a significant difference. The biphases all display a lower capacity retention than the equivalent mixed phase ratio, despite the initial capacities being close in value. The size of the P2-NMMO in the biphase is likely the reason for the low capacity retention, given that the calcination temperature was higher in the mixed phases. Similarly, the capacity retention for P2-NMMO in Chapter 3, the capacity retention of P2-NMMO was 73% when calcined for 20 h. There have not been differences in the rate capabilities across the whole sample range (expect for lower capacity at across all C-rates for the 9:1 P3/P2-NMMO mixed phase). Overall, the improvements in capacity retention and rate capability that were achieved in previous work by generating biphases are not achieved here.

5.5 Further work

The relationship between the two phases in both the biphasic and mixed phase samples can be elucidated using high-resolution TEM. None of the samples within the range of phase fractions tested resulted in the increased capacity retention and rate capability that was predicted. This suggests that the phase transition mechanism is different to the previous work on intergrowth structures. It is worth probing the resultant powders to

determine how they are different from the mixed phases as the electrochemistry results suggest there is little difference.

Although the biphases did not have capacity retentions than the mixed phases, the solid state synthesised P3-NMMO in Chapter 3 did. The impurity phase was a tunnel-type cathode, likely based on $Na_{0.44}MnO_2$ [53], [72], [73]. The solid state P3-NMMO had a higher capacity retention (95%) than all the mixed and *in situ* phases, but a lower initial capacity (95 mAh g^{-1}). An exploration into that relationship between the P3 phase and this tunnel-type phase in solid state P3-NMMO, and subsequent comparison with the biphases here may reveal why the difference in capacity retention is so great. Synthesising the biphases using solid state methods could also achieve this.

The capacity retention of the samples in both series decreases as the phase fraction of P2-NMMO is increased. The proposed reason for this is that the P2 phase degrades more rapidly than the P3 phase when the particle sizes are the same. The particle size can be increased by increasing the calcination time [34], which should lead to higher capacity retention.

5.6 References

[1] Q. Wang, S. Chu, and S. Guo, "Progress on multiphase layered transition metal oxide cathodes of sodium ion batteries," *Chinese Chem. Lett.*, vol. 31, no. 9, pp. 2167–2176, 2020, doi: 10.1016/j.cclet.2019.12.008.

[2] S. Guo, P. Liu, H. Yu, Y. Zhu, M. Chen, M. Ishida, and H. Zhou, "A layered P2- and O3-type composite as a high-energy cathode for rechargeable sodium-ion batteries," *Angew. Chemie - Int. Ed.*, vol. 54, no. 20, pp. 5894–5899, 2015, doi: 10.1002/anie.201411788.

[3] S. P. Ong, V. L. Chevrier, G. Hautier, A. Jain, C. Moore, S. Kim, X. Ma, and G. Ceder, "Voltage, stability and diffusion barrier differences between sodium-ion and lithium-ion intercalation materials," *Energy Environ. Sci.*, vol. 4, no. 9, p. 3680, 2011, doi: 10.1039/c1ee01782a.

[4] E. Lee, J. Lu, Y. Ren, X. Luo, X. Zhang, J. Wen, D. Miller, A. DeWahl, S. Hackney, B. Key, D. Kim, M. Slater, and C. S. Johnson, "Layered P2/O3 intergrowth cathode: Toward high power Na-ion batteries," *Adv. Energy Mater.*, vol. 4, no. 17, pp. 1–8, 2014, doi: 10.1002/aenm.201400458.

[5] C. Chen, W. Hang, Y. Li, M. Zhang, K. Nie, J. Wang, W. Zhao, R. Qi, C. Zuo, Z. Li, H. Yi, and F. Pan, "P2/O3 biphasic Fe/Mn-based layered oxide cathode with ultrahigh capacity and great cyclability for sodium ion batteries," *Nano Energy*, vol. 90, no. PA, p. 106504, 2021, doi: 10.1016/j.nanoen.2021.106504.

[6] J. Hong, S. Xiao, L. Deng, T. Lan, and G. He, "Li-free P2/O3 biphasic $Na_{0.73}Ni_{0.4}Mn_{0.4}Ti_{0.2}O_2$ as a cathode material for sodium-ion batteries," *Ionics (Kiel).*, vol. 26, no. 8, pp. 3911–3917, 2020, doi: 10.1007/s11581-020-03560-2.

[7] J. Zhai, H. Ji, W. Ji, R. Wang, Z. Huang, T. Yang, C. Wang, T. Zhang, Z. Chen, W. Zhao, A. Tayal, L. Jin, J. Wang, and Y. Xiao, "Suppressing the irreversible phase transition from P2 to O2 in sodium-layered cathode *via* integrating P2- and O3-type

structures," *Mater. Today Energy*, vol. 29, p. 101106, 2022, doi: 10.1016/j.mtener.2022.101106.

[8] L. G. Chagas, D. Buchholz, C. Vaalma, L. Wu, and S. Passerini, "P-type $Na_xNi_{0.22}Co_{0.11}Mn_{0.66}O_2$ materials: linking synthesis with structure and electrochemical performance," *J. Mater. Chem. A*, vol. 2, no. 47, pp. 20263–20270, 2014, doi: 10.1039/C4TA03946G.

[9] X. Chen, X. Zhou, M. Hu, J. Liang, D. Wu, J. Wei, and Z. Zhou, "Stable layered P3/P2 $Na_{0.66}Co_{0.5}Mn_{0.5}O_2$ cathode materials for sodium-ion batteries," *J. Mater. Chem. A*, vol. 3, no. 41, pp. 20708–20714, 2015, doi: 10.1039/c5ta05205j.

[10] P. Hou, J. Yin, X. Lu, J. Li, Y. Zhao, and X. Xu, "A stable layered P3/P2 and spinel intergrowth nanocomposite as a long-life and high-rate cathode for sodium-ion batteries," *Nanoscale*, vol. 10, no. 14, pp. 6671–6677, 2018, doi: 10.1039/c8nr00650d.

[11] N. Jiang, Q. Liu, J. Wang, W. Yang, W. Ma, L. Zhang, Z. Peng, and Z. Zhang, "Tailoring P2/P3 Biphases of Layered Na_xMnO_2 by Co Substitution for High-Performance Sodium-Ion Battery," *Small*, vol. 2007103, pp. 1–9, 2021, doi: 10.1002/smll.202007103.

[12] M. M. Rahman, J. Mao, W. H. Kan, C.-J. Sun, L. Li, Y. Zhang, M. Avdeev, X.-W. Du, and F. Lin, "An Ordered P2/P3 Composite Layered Oxide Cathode with Long Cycle Life in Sodium-Ion Batteries," *ACS Mater. Lett.*, vol. 1, no. 5, pp. 573–581, 2019, doi: 10.1021/acsmaterialslett.9b00347.

[13] G. L. Xu, R. Amine, Y. F. Xu, J. Liu, J. Gim, T. Ma, Y. Ren, C. J. Sun, Y. Liu, X. Zhang, S. M. Heald, A. Solhy, I. Saadoune, W. L. Mattis, S. G. Sun, Z. Chen, and K. Amine, "Insights into the structural effects of layered cathode materials for high voltage sodium-ion batteries," *Energy Environ. Sci.*, vol. 10, no. 7, pp. 1677–1693, 2017, doi: 10.1039/c7ee00827a.

[14] M. Keller, D. Buchholz, and S. Passerini, "Layered Na-Ion Cathodes with Outstanding Performance Resulting from the Synergetic Effect of Mixed P- and O-Type Phases," *Adv. Energy Mater.*, vol. 6, no. 3, pp. 1–11, 2016, doi: 10.1002/aenm.201501555.

[15] R. Li, Y. Liu, Z. Wang, and J. Li, "A P2/O3 biphasic cathode material with highly reversibility synthesized by Sn-substitution for Na-ion batteries," *Electrochim. Acta*, vol. 318, pp. 14–22, 2019, doi: 10.1016/j.electacta.2019.06.020.

[16] Q. Huang, S. Xu, L. Xiao, P. He, J. Liu, Y. Yang, P. Wang, B. Huang, and W. Wei, "Improving the Electrochemical Properties of the Manganese-Based P3 Phase by Multiphasic Intergrowth," *Inorg. Chem.*, vol. 57, no. 24, pp. 15584–15591, 2018, doi: 10.1021/acs.inorgchem.8b02931.

[17] Y. N. Zhou, P. F. Wang, Y. Bin Niu, Q. Li, X. Q. Yu, Y. X. Yin, S. Xu, and Y. G. Guo, "A P2/P3 composite layered cathode for high-performance Na-ion full batteries," *Nano Energy*, vol. 55, no. September 2018, pp. 143–150, 2019, doi: 10.1016/j.nanoen.2018.10.072.

[18] Y. Lei, X. Li, L. Liu, and G. Ceder, "Synthesis and stoichiometry of different layered sodium cobalt oxides," *Chem. Mater.*, vol. 26, no. 18, pp. 5288–5296, 2014, doi:

10.1021/cm5021788.

[19] S. Guo, Y. Sun, J. Yi, K. Zhu, P. Liu, Y. Zhu, G. Zhu, M. Chen, M. Ishida, and H. Zhou, "Understanding sodium-ion diffusion in layered P2 and P3 oxides *via* experiments and first-principles calculations: a bridge between crystal structure and electrochemical performance," *NPG Asia Mater.*, vol. 8, p. e266, 2016, doi: 10.1038/am.2016.53.

[20] S. Y. Lee, J. H. Kim, and Y. C. Kang, "Electrochemical properties of P2-type $Na_{2/3}Ni_{1/3}Mn_{2/3}O_2$ plates synthesized by spray pyrolysis process for sodium-ion batteries," *Electrochim. Acta*, vol. 225, pp. 86–92, 2017, doi: 10.1016/j.electacta.2016.11.141.

[21] C. Delmas, J.-J. Braconnier, C. Fouassier, and P. Hagenmuller, "Electrochemical intercalation of sodium in Na_xCoO_2 bronzes," *Solid State Ionics*, pp. 165–169, 1981, doi: 10.1016/0167-2738(88)90351-7.

[22] C. N. R. Rao and J. M. Thomas, "Intergrowth structures: The chemistry of solid-solid interfaces," *Trends Chem. Mater. Sel. Res. Pap. C N R Rao*, vol. 60, no. 1970, pp. 58–64, 2008, doi: 10.1142/9789812833846_0004.

[23] D. Wang, H. Chen, X. Zheng, L. Qiu, J. Qu, Z. Wu, Y. Zhong, W. Xiang, B. Zhong, and X. Guo, "Simultaneous Component Ratio and Particle Size Optimization for High-Performance and High Tap Density P2/P3 Composite Cathode of Sodium-Ion Batteries," *ChemElectroChem*, vol. 6, no. 19, pp. 5155–5161, 2019, doi: 10.1002/celc.201901211.

[24] M. Tang, J. Yang, H. Liu, X. Chen, L. Kong, Z. Xu, J. Huang, and Y. Xia, "Spinel-Layered Intergrowth Composite Cathodes for Sodium-Ion Batteries," *ACS Appl. Mater. Interfaces*, vol. 12, no. 41, pp. 45997–46004, 2020, doi: 10.1021/acsami.0c12280.

[25] A. R. West, *Solid state chemistry and its applications*. Wiley, 2014. doi: 10.1107/s0108768185002476.

[26] J. Li, T. Risthaus, J. Wang, D. Zhou, X. He, N. Ehteshami, V. Murzin, A. Friesen, H. Liu, X. Hou, M. Diehl, E. Paillard, M. Winter, and J. Li, "The effect of Sn substitution on the structure and oxygen activity of $Na_{0.67}Ni_{0.33}Mn_{0.67}O_2$ cathode materials for sodium ion batteries," *J. Power Sources*, vol. 449, no. November 2019, p. 227554, 2020, doi: 10.1016/j.jpowsour.2019.227554.

[27] T. Risthaus, L. Chen, J. Wang, J. Li, D. Zhou, L. Zhang, D. Ning, X. Cao, X. Zhang, G. Schumacher, M. Winter, E. Paillard, and J. Li, "P3 $Na_{0.9}Ni_{0.5}Mn_{0.5}O_2$ Cathode Material for Sodium Ion Batteries," *Chem. Mater.*, vol. 31, no. 15, pp. 5376–5383, 2019, doi: 10.1021/acs.chemmater.8b03270.

[28] L. Yu, Z. Cheng, K. Xu, Y. X. Chang, Y. H. Feng, D. Si, M. Liu, P. F. Wang, and S. Xu, "Interlocking biphasic chemistry for high-voltage P2/O3 sodium layered oxide cathode," *Energy Storage Mater.*, vol. 50, no. May, pp. 730–739, 2022, doi: 10.1016/j.ensm.2022.06.012.

[29] L. G. Chagas, D. Buchholz, L. Wu, B. Vortmann, and S. Passerini, "Unexpected performance of layered sodium-ion cathode material in ionic liquid-based electrolyte," *J. Power Sources*, vol. 247, pp. 377–383, 2014, doi: 10.1016/j.jpowsour.2013.08.118.

[30] M. Bianchini, E. Gonzalo, N. E. Drewett, N. Ortiz-Vitoriano, J. M. Lopez Del Amo, F. J. Bonilla, B. Acebedo, and T. Rojo, "Layered P2-O3 sodium-ion cathodes derived from earth abundant elements," *J. Mater. Chem. A*, pp. 3552–3559, 2018, doi: 10.1039/C7TA11180K.

[31] D. Kim, S. H. Kang, M. Slater, S. Rood, J. T. Vaughey, N. Karan, M. Balasubramanian, and C. S. Johnson, "Enabling sodium batteries using lithium-substituted sodium layered transition metal oxide cathodes," *Adv. Energy Mater.*, vol. 1, no. 3, pp. 333–336, 2011, doi: 10.1002/aenm.201000061.

[32] J. B. Goodenough and K. S. Park, "The Li-ion rechargeable battery: A perspective," *J. Am. Chem. Soc.*, vol. 135, no. 4, pp. 1167–1176, 2013, doi: 10.1021/ja3091438.

[33] C. Liu, Z. G. Neale, and G. Cao, "Understanding electrochemical potentials of cathode materials in rechargeable batteries," *Mater. Today*, vol. 19, no. 2, pp. 109–123, 2016, doi: 10.1016/j.mattod.2015.10.009.

[34] S. Zilinskaite, A. J. R. Rennie, R. Boston, and N. Reeves-McLaren, "Biotemplating: a sustainable synthetic methodology for Na-ion battery materials," *J. Mater. Chem. A*, vol. 6, no. 13, pp. 5346–5355, 2018, doi: 10.1039/C7TA09260A.

[35] B. L. Cushing, V. L. Kolesnichenko, and C. J. O'Connor, "Recent Advances in the Liquid-Phase Syntheses of Inorganic Nanoparticles," *Chem. Rev.*, vol. 104, no. 9, pp. 3893–3946, 2004, doi: 10.1021/cr030027b.

[36] R. Berthelot, D. Carlier, and C. Delmas, "Electrochemical investigation of the P2–Na_xCoO_2 phase diagram," *Nat. Mater.*, vol. 10, no. 1, pp. 74–80, 2011, doi: 10.1038/nmat2920.

[37] Q. Huang, J. Liu, L. Zhang, S. Xu, L. Chen, P. Wang, D. G. Ivey, and W. Wei, "Tailoring alternating heteroepitaxial nanostructures in Na-ion layered oxide cathodes via an in-situ composition modulation route," *Nano Energy*, vol. 44, pp. 336–344, Feb. 2018, doi: 10.1016/j.nanoen.2017.12.014.

[38] P. F. Wang, H. R. Yao, X. Y. Liu, Y. X. Yin, J. N. Zhang, Y. Wen, X. Q. Yu, L. Gu, and Y. G. Guo, "Na^+/vacancy disordering promises high-rate Na-ion batteries," *Sci. Adv.*, vol. 4, no. 3, pp. 1–10, 2018, doi: 10.1126/sciadv.aar6018.

[39] J. Xu, D. H. Lee, R. J. Clément, X. Yu, M. Leskes, A. J. Pell, G. Pintacuda, X.-Q. Yang, C. P. Grey, and Y. S. Meng, "Identifying the Critical Role of Li Substitution in P2–$Na_x[Li_yNi_zMn_{1-y-z}]O_2$ ($0 < x, y, z < 1$) Intercalation Cathode Materials for High-energy Na-Ion Batteries," *Chem. Mater.*, vol. 26, no. 2, pp. 1260–1269, Jan. 2014, doi: 10.1021/cm403855t.

[40] S. Komaba, N. Yabuuchi, T. Nakayama, A. Ogata, T. Ishikawa, and I. Nakai, "Study on the reversible electrode reaction of $Na_{1-x}Ni_{0.5}Mn_{0.5}O_2$ for a rechargeable sodium-ion battery," *Inorg. Chem.*, vol. 51, no. 11, pp. 6211–6220, 2012, doi: 10.1021/ic300357d.

[41] S. Guo, Y. Sun, P. Liu, J. Yi, P. He, X. Zhang, Y. Zhu, R. Senga, K. Suenaga, M. Chen, and H. Zhou, "Cation-mixing stabilized layered oxide cathodes for sodium-ion batteries," *Sci. Bull.*, vol. 63, no. 6, pp. 376–384, 2018, doi: 10.1016/j.scib.2018.02.012.

[42] D. Buchholz, C. Vaalma, L. G. Chagas, and S. Passerini, "Mg-doping for improved long-term cyclability of layered Na-ion cathode materials - The example of P2-type $Na_xMg_{0.11}Mn_{0.89}O_2$," *J. Power Sources*, vol. 282, pp. 581–585, 2015, doi: 10.1016/j.jpowsour.2015.02.069.

[43] R. J. Clément, J. Billaud, A. Robert Armstrong, G. Singh, T. Rojo, P. G. Bruce, and C. P. Grey, "Structurally stable Mg-doped P2-$Na_{2/3}Mn_{1-y}Mg_yO_2$ sodium-ion battery cathodes with high rate performance: insights from electrochemical, NMR and diffraction studies," *Energy Environ. Sci.*, vol. 9, no. 10, pp. 3240–3251, 2016, doi: 10.1039/C6EE01750A.

[44] J. Billaud, G. Singh, A. R. Armstrong, E. Gonzalo, V. Roddatis, M. Armand, T. Rojo, and P. G. Bruce, "$Na_{0.67}Mn_{1-x}Mg_xO_2$ ($0 \leq x \leq 0.2$): a high capacity cathode for sodium-ion batteries," *Energy Environ. Sci.*, vol. 7, no. 4, pp. 1387–1391, 2014, doi: 10.1039/C4EE00465E.

[45] B. Sambandam, M. H. Alfaruqi, S. Park, S. Lee, S. Kim, J. Lee, V. Mathew, J. Y. Hwang, and J. Kim, "Validating the structural (In)stability of P3- and P2-$Na_{0.67}Mg_{0.1}Mn_{0.9}O_2$-Layered cathodes for sodium-ion batteries: A time-decisive approach," *ACS Appl. Mater. Interfaces*, vol. 13, no. 45, pp. 53877–53891, 2021, doi: 10.1021/acsami.1c15394.

[46] S. F. Linnell, A. G. Manche, Y. Liao, M. Hirsbrunner, S. Imada, A. B. Naden, J. T. S. Irvine, L. C. Duda, and A. R. Armstrong, "Effect of Cu substitution on anion redox behaviour in P3-type sodium manganese oxides," *JPhys Energy*, vol. 4, no. 4, 2022, doi: 10.1088/2515-7655/ac95cc.

[47] N. Yabuuchi, R. Hara, M. Kajiyama, K. Kubota, T. Ishigaki, A. Hoshikawa, and S. Komaba, "New O2/P2-type Li-Excess Layered Manganese Oxides as Promising Multi-Functional Electrode Materials for Rechargeable Li/Na Batteries," *Adv. Energy Mater.*, vol. 4, p. 1031453, 2014, doi: 10.1002/aenm.201301453.

[48] B. H. Toby, " R factors in Rietveld analysis: How good is good enough? ," *Powder Diffr.*, vol. 21, no. 1, pp. 67–70, 2006, doi: 10.1154/1.2179804.

[49] E. J. Kim, L. A. Ma, D. M. Pickup, A. V. Chadwick, R. Younesi, P. Maughan, J. T. S. Irvine, and A. R. Armstrong, "Vacancy-enhanced oxygen redox reversibility in P3-type magnesium-doped sodium manganese oxide $Na_{0.67}Mg_{0.2}Mn_{0.8}O_2$," *ACS Appl. Energy Mater.*, vol. 3, no. 11, pp. 10423–10434, 2020, doi: 10.1021/acsaem.0c01352.

[50] X. Ju, H. Huang, H. Zheng, P. Deng, S. Li, B. Qu, and T. Wang, "A facile method to hunt for durable high-rate capability $Na_{0.44}MnO_2$," *J. Power Sources*, vol. 395, no. May, pp. 395–402, 2018, doi: 10.1016/j.jpowsour.2018.05.086.

[51] X. He, J. Wang, B. Qiu, E. Paillard, C. Ma, X. Cao, H. Liu, M. C. Stan, H. Liu, T. Gallash, Y. S. Meng, and J. Li, "Durable high-rate capability $Na_{0.44}MnO_2$ cathode material for sodium-ion batteries," *Nano Energy*, vol. 27, pp. 602–610, 2016, doi: 10.1016/j.nanoen.2016.07.021.

[52] D. Su, H. J. Ahn, and G. Wang, "β-MnO_2 nanorods with exposed tunnel structures as high-performance cathode materials for sodium-ion batteries," *NPG Asia Mater.*, vol. 5, no. 10, pp. e70-7, 2013, doi: 10.1038/am.2013.56.

[53] M. S. Chae, A. Chakraborty, S. Kunnikuruvan, R. Attias, S. Maddukuri, Y. Gofer, D. T.

Major, and D. Aurbach, “Vacancy-Driven High Rate Capabilities in Calcium-Doped $Na_{0.4}MnO_2$ Cathodes for Aqueous Sodium-Ion Batteries,” *Adv. Energy Mater.*, vol. 10, no. 37, pp. 1–7, 2020, doi: 10.1002/aenm.202002077.

[54] V. Dall’Asta, D. Buchholz, L. G. Chagas, X. Dou, C. Ferrara, E. Quartarone, C. Tealdi, and S. Passerini, “Aqueous Processing of $Na_{0.44}MnO_2$ Cathode Material for the Development of Greener Na-Ion Batteries,” *ACS Appl. Mater. Interfaces*, vol. 9, no. 40, pp. 34891–34899, 2017, doi: 10.1021/acsami.7b09464.

[55] S. F. Linnell, M. Hirsbrunner, S. Imada, G. Cibin, A. B. Naden, A. V. Chadwick, J. T. S. Irvine, L. C. Duda, and A. R. Armstrong, “Enhanced Cycling Stability in the Anion Redox Material P3-Type Zn-Substituted Sodium Manganese Oxide,” *ChemElectroChem*, vol. 9, no. 11, 2022, doi: 10.1002/celc.202200240.

[56] M. Sathiya, K. Hemalatha, K. Ramesha, J.-M. Tarascon, and A. S. Prakash, “Synthesis, structure, and electrochemical properties of the layered sodium insertion cathode material: $NaNi_{1/3}Mn_{1/3}Co_{1/3}O_2$,” *Chem. Mater.*, vol. 24, no. 10, pp. 1846–1853, 2012, doi: 10.1021/cm300466b.

[57] T. Y. Yu, H. H. Ryu, G. Han, and Y. K. Sun, “Understanding the Capacity Fading Mechanisms of O3-Type $Na[Ni_{0.5}Mn_{0.5}]O_2$ Cathode for Sodium-Ion Batteries,” *Adv. Energy Mater.*, vol. 10, no. 37, pp. 1–8, 2020, doi: 10.1002/aenm.202001609.

[58] S. Kumakura, Y. Tahara, K. Kubota, K. Chihara, and S. Komaba, “Sodium and Manganese Stoichiometry of P2-Type $Na_{2/3}MnO_2$,” *Angew. Chemie - Int. Ed.*, vol. 55, no. 41, pp. 12760–12763, 2016, doi: 10.1002/anie.201606415.

[59] M. H. Han, E. Gonzalo, N. Sharma, J. M. López Del Amo, M. Armand, M. Avdeev, J. J. Saiz Garitaonandia, and T. Rojo, “High-Performance P2-Phase $Na_{2/3}Mn_{0.8}Fe_{0.1}Ti_{0.1}O_2$ Cathode Material for Ambient-Temperature Sodium-Ion Batteries,” *Chem. Mater.*, vol. 28, no. 1, pp. 106–116, 2016, doi: 10.1021/acs.chemmater.5b03276.

[60] Y. Terada, Y. Nishiwaki, I. Nakai, and F. Nishikawa, “Study of Mn dissolution from $LiMn_2O_4$ spinel electrodes using *in situ* total reflection X-ray fluorescence analysis and fluorescence XAFS technique,” *J. Power Sources*, vol. 97–98, pp. 420–422, Jul. 2001, doi: 10.1016/S0378-7753(01)00741-8.

[61] N. Sabi, S. Doubaji, K. Hashimoto, S. Komaba, K. Amine, A. Solhy, B. Manoun, E. Bilal, and I. Saadoune, “Layered P2-$Na_{2/3}Co_{1/2}Ti_{1/2}O_2$ as a high-performance cathode material for sodium-ion batteries,” *J. Power Sources*, vol. 342, pp. 998–1005, 2017, doi: 10.1016/j.jpowsour.2017.01.025.

[62] Y. Zhang, R. Zhang, and Y. Huang, “Air-stable Na_xTMO_2 cathodes for sodium storage,” *Front. Chem.*, vol. 7, no. MAY, pp. 1–15, 2019, doi: 10.3389/fchem.2019.00335.

[63] C. Zhan, T. Wu, J. Lu, and K. Amine, “Dissolution, migration, and deposition of transition metal ions in Li-ion batteries exemplified by Mn-based cathodes-A critical review,” *Energy Environ. Sci.*, vol. 11, no. 2, pp. 243–257, 2018, doi: 10.1039/c7ee03122j.

[64] W. Zuo, J. Qiu, X. Liu, B. Zheng, Y. Zhao, J. Li, H. He, K. Zhou, Z. Xiao, Q. Li, G. F. Ortiz, and Y. Yang, “Highly-stable P2–$Na_{0.67}MnO_2$ electrode enabled by lattice tailoring

and surface engineering," *Energy Storage Mater.*, vol. 26, no. November 2019, pp. 503–512, Apr. 2020, doi: 10.1016/j.ensm.2019.11.024.

[65] D. H. Jang, Y. J. Shin, and S. M. Oh, "Dissolution of Spinel Oxides and Capacity Losses in 4 V $Li/Li_xMn_2O_4$ Cells," *J. Electrochem. Soc.*, vol. 143, no. 7, pp. 2204–2211, Jul. 1996, doi: 10.1149/1.1836981.

[66] N. Yabuuchi, M. Kajiyama, J. Iwatate, H. Nishikawa, S. Hitomi, R. Okuyama, R. Usui, Y. Yamada, and S. Komaba, "P2-type $Na_x[Fe_{1/2}Mn_{1/2}]O_2$ made from earth-abundant elements for rechargeable Na batteries," *Nat. Mater.*, vol. 11, no. 6, pp. 512–517, 2012, doi: 10.1038/nmat3309.

[67] I. Hasa, D. Buchholz, S. Passerini, B. Scrosati, and J. Hassoun, "High Performance $Na_{0.5}[Ni_{0.23}Fe_{0.13}Mn_{0.63}]O_2$ Cathode for Sodium-Ion Batteries," *Adv. Energy Mater.*, vol. 4, no. 15, pp. 2–8, 2014, doi: 10.1002/aenm.201400083.

[68] D. Buchholz, L. G. Chagas, C. Vaalma, L. Wu, and S. Passerini, "Water sensitivity of layered P2/P3-$Na_xNi_{0.22}Co_{0.11}Mn_{0.66}O_2$ cathode material," *J. Mater. Chem. A*, vol. 2, no. 33, pp. 13415–13421, 2014, doi: 10.1039/c4ta02627f.

[69] Z. Lu and J. R. Dahn, "*In Situ* X-Ray Diffraction Study of P2-$Na_{2/3}[Ni_{1/3}Mn_{2/3}]O_2$," *J. Electrochem. Soc.*, vol. 148, no. 11, p. A1225, 2001, doi: 10.1149/1.1407247.

[70] Z. Lu and J. R. Dahn, "The Effect of Co Substitution for Ni on the Structure and Electrochemical Behavior of T2 and O2 Structure $Li_{2/3}[Co_xNi_{1/3-x}Mn_{2/3}]O_2$," *J. Electrochem. Soc.*, vol. 148, no. 3, p. A237, 2001, doi: 10.1149/1.1350016.

[71] J. J. Li, J. Yu, Y. Y. Wu, J. Lee, Y. B. Wang, and W. L. Zhou, "Effect of pyrolysis atmosphere on ferroelectric properties of $Bi_{3.25}La_{0.75}Ti_3O_{12}$ films prepared by sol-gel method," *Chinese Phys. Lett.*, vol. 26, no. 3, pp. 12–17, 2009, doi: 10.1088/0256-307X/26/3/037702.

[72] G. Ma, Y. Zhao, K. Huang, Z. Ju, C. Liu, Y. Hou, and Z. Xing, "Effects of the starting materials of $Na_{0.44}MnO_2$ cathode materials on their electrochemical properties for Na-ion batteries," *Electrochim. Acta*, vol. 222, pp. 36–43, 2016, doi: 10.1016/j.electacta.2016.11.048.

[73] R. Qiao, K. Dai, J. Mao, T. C. Weng, D. Sokaras, D. Nordlund, X. Song, V. S. Battaglia, Z. Hussain, G. Liu, and W. Yang, "Revealing and suppressing surface Mn(II) formation of $Na_{0.44}MnO_2$ electrodes for Na-ion batteries," *Nano Energy*, vol. 16, pp. 186–195, 2015, doi: 10.1016/j.nanoen.2015.06.024.

6 Conclusions and further work

6.1 Conclusions

The aims of this work were to improve the sustainability of NIBs. One method to achieve this is the reduction in energy cost of cathode production *via* the use of biotemplating without sacrificing performance. This has been achieved particularly in P3-$Na_{0.67}Mn_{0.9}Mg_{0.1}O_2$ (NMMO), where the use of a 2 h calcination increases the capacity retention by 9% compared to 20 h calcination. Although this is difficult to compare against the solid state synthesis as it could not produce phase pure P3-NMMO. The second is to use various techniques to improve the capacity retention of NIB cathode. These have had more limited success, but the use of 1% Ca doping did increase the capacity retention of P2-NMMO biotemplated 10%. Combining phases (either *in situ* or post-synthesis mix) did not improve capacity or retention compared to single phase P3-NMMO.

In Chapter 3, the P3 and P2 phases of NMMO were synthesised *via* solid state methods and, for the first time, biotemplating; creating four samples for testing and comparison. For the sake of comparing the two methods, the calcination times in this chapter were consistent across both synthesis methods. *Via* XRD, solid state synthesis successfully produced single phase P2-NMMO after 20 h at 900 °C but not the P3 phase. Both single phase P3- and P2-NMMO were successfully synthesised *via* biotemplating, using dextran as the template. P3 samples both measured 0.3 μm particle sizes compared to 3 μm for P2.

Biotemplated P3-NMMO displayed 142 mAh g^{-1}, the highest initial capacity of the four samples with capacity retention of 73%. Solid state P3-NMMO displays the lowest capacity with the highest capacity retention: losing 5 mAh g^{-1} over 50 cycles 94 mAh g^{-1}. The sample contained only 64% of the desired P3 phase, but the major (17%) impurity is argued to be $Na_{0.44}MnO_2$, which is redox active. Therefore, the total proportion of electrochemically active material in the sample was 81%. The capacities of the solid state and biotemplated P2-NMMO samples are initially 124 mAh g^{-1} and 134 mAh g^{-1}, 95 mAh g^{-1} and 98 mAh g^{-1} after 50 cycles, respectively. The difference in performance is not major. The high capacity retention in solid state P3-NMMO is thought to be caused by the tunnel-type impurity phase. As with the intergrowth studies reviewed in Chapter 5, it prevents the cathode from undergoing phase transitions. The presence of a second phase at the surface of the layered oxide crystal may prevent layer gliding and thus the formation of a new phase. This provides structural stability; meaning fewer phase transitions which prevents degradation of the material. Overall, the biotemplated materials exhibit higher capacities than the solid state synthesised equivalents, as well as better rate capability. This highlights the efficacy with which biotemplating can generate single phase cathodes with better performance metrics than standard solid state synthesis.

When compared to the literature values, detailed in Table 3-1, the capacities of the materials are low. They are low in comparison to the study on which this work is based, which reported an initial capacity of 170 mAh g^{-1} [1]. There are lower reported

capacities of P2-NMMO [2] but generally, and particularly more recently, P3- and P2-NMMO has been shown to exhibit higher capacity than achieved here, although the capacity retention is similar [3], [4], approximately 1% capacity loss per cycle. However, there will be differences between the synthesis conditions of reported P-type NMMO materials and those described herein, despite effort to keep them the same or comparable. Reasons for this could the absorption of water from the atmosphere during the XRD analysis or slurry curing. Greater optimisation of the cell construction process could have been carried out. For example, the viscosity of the slurry (and mixing order of the PVDF, NMP and carbon), the thickness of the drawdown, and densification of the cathode during calendaring could have altered to test the effects on capacity and capacity retention.

The variety in synthesis conditions during the cell making process and the effect it can have on the cell performance are part of the reason why solid state NMMO was investigated in this chapter. With these samples as a baseline, the effect of biotemplating on cell performance can be compared with like samples and more valid conclusion can be drawn. These conclusions are that for P2-NMMO biotemplating leads to an increase in rate capability above 1C, but not necessarily an increase in capacity below it (shown for C/5). For P3-NMMO biotemplating shows the same increase in rate capability, as well as an increase in capacity at C/5. The increase in capacity is (only) in part caused by the impurities present in the solid state P3-NMMO which reduces the proportion of electrochemically active material. The presence of these impurities could be causing the rest of the drop in capacity by passivating the NMMO surface and preventing some de/insertion of Na^+.

This shows the ability of biotemplating syntheses to produce phase pure materials that are inaccessible when using solid state methods, which is a very commonly used technique. This makes it worth exploring as a method to produce new battery materials, especially in conjunction with the easier processing and dissolution of the metal ions, leading to atomic level mixing. As shown in Chapters 4 and 5, the calcination time can be shortened from 20 h to 2 h, reducing the total heat treatment time by at least threefold. In addition to significant energy savings during production, it also allows for some finer control over particle size by controlling calcination time. In comparison, solid state methods take longer to form as the metal ions must migrate further and so the control of particle size is less.

For Chapters 4 and 5, the only synthesis method used to generate the cathodes was biotemplating with calcinations times of 2 h. This reduced energy cost of production without sacrificing performance benefits already gained from biotemplating. In Chapter 4, the P3 and P2 phases of NMMO were doped with Ca to prevent phase transitions and other structural distortions in the cathode material that cause material degradation and contribute to capacity loss. P3-NCMM showed small increases in lattice expansion. Shown in the lattice spacing of the (101) plane, 1% Ca doping caused an increase of 0.0016 Å and 2% Ca caused an increase of 0.0062 Å. The values of lattice parameters across the three samples were within 3 standard deviations of each other and thus not significant. This indicates that Ca^{2+} did not occupy the Na site, further evidenced by the

unchanged electrochemical performance. 0% Ca, 1% Ca, and 2% Ca P3-NCMM had discharge capacities 114 mAh g^{-1}, 121 mAh g^{-1}, and 109 mAh g^{-1} after 50 cycles. There was little difference between samples in the differential capacity plots and rate capability tests. Biotemplated P3-NMMO in this chapter, using a 2 h calcination at 650 °C demonstrated a higher capacity retention (82%) than the biotemplated P3-NMMO in Chapter 3 using a 20 h calcination at 580 °C (73%). This comparison highlights the benefits of the biotemplating synthesis that were predicted from previous work and contributes to the increasing performance and sustainability of this material.

1% Ca P2-NCMM decreased the *c* lattice parameter compared to 0% Ca P2-NCMM, as did 2% Ca but to a lesser degree, but not enough to be significant. However, there was a significant increased in the size of the *a* lattice parameter. 2% Ca P2-NCMM showed evidence of a tunnel-type impurity phase suggesting the doping limit of Ca in P2-NMMO to be 1-2%. 1% Ca P2-NCMM displayed a larger particle size than all other samples in the chapter. Ca doping may stabilise the structure and allow larger particles to form and preventing capacity fade. Although the small particle size of 0% Ca P2-NCMM is likely an outlier. The particle sizes of 2% Ca P2-NCMM are the same as the 0% Ca P2-NCMM. After 50 cycles, 0% Ca, 1% Ca, and 2% Ca P2-NCMM had discharge capacities of 93 mAh g^{-1}, 112 mAh g^{-1}, and 109 mAh g^{-1}, respectively. This is a larger difference than in the P3 samples, indicating successful doping. Doped samples had capacity retentions 10% higher than undoped P2-NMMO. 2% Ca doping may lead to improved capacity retention but be counteracted by smaller average particle size. It is worth considering that the impurity phase assists the capacity retention similarly to solid state P3-NMMO. The smaller particle size of 2% Ca P2-NCMM may be caused by the impurity phase disrupting grain growth. While Ca doping improved capacity retention, its effects on rate capability were negligible. Capacity retention of 1% Ca P2-NCMM was still lower than all Ca-doped P3 samples.

This is the first time that NMMO materials have been doped with Ca^{2+}. However, the effects on capacity retention that Ca^{2+} doping has had in the literature are not seen here. Table 4-1 details previous works into Ca doping, and shows that it commonly results in capacity retention of >85% in both P3 and P2 materials, with increases of 10-25% compared to the undoped material [5]–[8]. Here an increase in capacity retention of 10% is seen in the P2-NCMM, but only to 73%. The capacity retention increase in P3-NCMM is from 80% to 86% with 1% Ca doping, but it drops to 82% with 2% Ca doping, calling into doubt that improvements in capacity retention are caused by Ca doping. The explanation for this is that the Ca^{2+} is not being integrated into the layered structure.

Also in this chapter, the P3- and P2-NMMO are synthesised *via* biotemplating using the 2 h calcination. The outcome of this is a 10% increase in capacity retention over 50 cycles at C/5 compared to the 20 h calcination for P3-NMMO, but a 10% reduction in capacity retention for P2-NMMO. It was suggested in the discussion that the P3 phase performs better when the particle size is comparatively smaller, and vice versa for P2-NMMO. This observation is novel as very little work is done in comparing synthesis conditions for battery materials, or P3 phases generally, or comparing them to the P2 analogue.

Combining NMMO phases in Chapter 5 was also done with the aim of improving capacity retention by avoiding structural distortions. Material characterisation of the different ratios of P3/P2-NMMO phases was the similar regardless of synthesis route. Smaller particle sizes were observed for the 1:9 P3/P2-NMMO *in situ* sample, as the calcination temperature is lower than in the *ex situ* samples, leading to smaller particle sizes, which is more noticeable at higher P2 phase fractions. Although single phase P2-NMMO has smaller particle sizes than any P2-rich samples. The biphases perform exhibit worse electrochemical performance than mixed phases. Initial discharge capacity is usually comparable to the mixed phases for each ratio but the capacity retention at is lower. Retention worsens as P2 phase fraction increases as with Chapter 4, where capacity retention of 0% Ca P2-NCMM is lower than 0% Ca P3-NCMM. Several peaks in the differential capacity plots are more pronounced in the biphases than in the mixed phases that do not appear in other chapters. The peaks are more pronounced in the biphase samples, suggesting some structural changes in the P2 phase are activated, contributing to more rapid capacity fade.

This study into multiphase P-type cathodes is the first to examine NMMO. Similarly, its approach in producing and comparing a wider range of phase fractions sets it apart from the other intergrowth studies in this matter. It is rare that the intergrowth material is compared to a separately prepared mixed of the same fraction of the two phases studied, which was undertaken here. In most cases only one mixed phase is selected for reporting, usually 1:1 (depending on the intergrowth technique). However, in this study a range of phase fractions of P3/P2-NMMO was synthesised, characterised, and tested. It also produced the biphases *via* biotemplating, where solid state could not due the presence of the $Na_{0.44}MnO_2$ impurity phase during the P3↔P2 transition shown in Chapter 3.

Again, the aim of this work was to improve the capacity retention of both P3- and P2-NMMO by restricting phase transitions as the intergrowth structures should provide external pressure to prevent layer gliding – just as Ca^{2+} was meant to provide internal pressure *via* pillaring. As with the Ca^{2+} doping work, the capacity retention did not increase. In fact, the P3/P2-NMMO produced in a one-step mid-point temperature calcination had approximately 10% lower capacity retention than the equivalent mixed phase P3/P2-NMMO. It was shown that the capacity retention decreased as the phase fraction of P2-NMMO increased in both sample series, which lends further credence to the suggestions that P2-NMMO performs less well when calcined for only 2 h than 20 h, and less well than P3-NMMO.

Shown in Table 5-4, the capacity retention of both the P3- and P2-NMMO simply decreases as the phase fraction of P2-NMMO increases in both the mixed and biphase samples. The one exception is a 1% capacity retention increase in the 7:3 mixed P3/P2-NMMO over the single phase P3-NMMO. In comparison, many of the intergrowth structures reported in the literature show an improvement in capacity retention over (at least one of) the single phases of at least 10% [9], [10], or an increase in capacity of at least 15 mAh g^{-1} [11]. These figures are taken after 50 cycles. In this work we do not see the same improvements in either capacity or capacity retention.

Despite the lack of improving in performance, it is important that the work is carried out. It shows the promise of using biotemplating synthesis, which allows for the more rapid calcination of P3-NMMO, which can outperform its P2-NMMO analogue. This superior capacity and capacity retention runs counter to much of the research seen in literature, in the few studies where the two phases are directly compared.

Biotemplated P3-NMMO delivered higher capacity retention, if not also higher capacity, than P2-NMMO, regardless of the synthesis method of P2-NMMO. it should be noted that P2-NMMO using a 2 h biotemplating synthesis delivered the highest initial capacities of the cathodes tested in this chapter. Shorter calcination times, leading to smaller particle sizes, increases its capacity retention but decreases it for the P2 phase. It possible that a longer calcination would be more effective in encouraging Ca doping, further increasing the capacity retention. Particle size certainly plays a role in capacity retention, more so in P2-NMMO. The biotemplating synthesis can be adapted, as shown by the results here, to produce larger particles of P2 phases, and so optimisation could be done to balance capacity retention against energy cost. Except for solid state P3-NMMO, there is not much variation in initial capacity of the materials tested. Where these is variation, it is often correlated to particle size.

If NIBs are to be used in large-scale energy storage, then both P3- and P2-NMMO are worthy candidates. The low cost, molar mass, and toxicity of the materials make for cathodes with high capacity and sustainability. Using a biotemplated synthesis, the production of these materials also becomes more sustainable, as (in the case of P3-NMMO) it reduces the energy cost while increasing its capacity retention. For P2-NMMO, the shorter synthesis reduces the particle size, increasing the capacity at the expense of capacity retention. Using the (Ca doping) strategies detailed here, and further investigation of the calcination procedure, the P2-NMMO cathode can be optimised. The same is true of P3-NMMO, and so both materials can be made suitable for large-scale production.

The materials chosen in this work were done so for their sustainability. However, there are a wide range of energy storage materials, including cathodes, anodes, and LIBs. Most, if not all, of the materials have the same problems that biotemplating can solve: long, high temperature calcinations, and particle sizes that are challenging to selectively target. The using of biotemplating in these materials could lead to the same benefits as the ones achieved here: increased capacity and retention, and reduced cost of production.

6.2 Further work

Chapters 4 and 5 in this thesis were attempts to improve the performance and sustainability of P-type NMMO. The 2 h calcination time has improved the capacity retention of P3-NMMO by 9%. The capacity retention was lower than solid state P3-NMMO in Chapter 3, likely assisted by the impurity phase. Although the calcination temperature was 70 °C higher, the shorter calcination time reduced the energy cost of cathode production. Changing the calcination procedure did not affect the particle size.

Perhaps longer calcination times for biotemplated P3-NMMO cause volatilisation of active material since the particle size does not change, causing lower capacity retention. Further investigation into optimising the calcination procedure could be done, as it will affect the particle size which in turns informs the electrochemical properties.

The opposite was true of P2-NMMO, where shorter calcination times reduced the particle size and capacity retention. Capacity fade was likely to be caused by dissolution if Mn^{2+} which can occur during phase transitions and is limited by surface area. The small particle size of P2-NMMO measured in Chapter 4 should be investigated and replicated as it was lower than expected from other results. Longer calcination times (6-8 h) would increase the particle size of P2-NMMO, whilst maintaining a lower energy cost of synthesis than solid state methods. This may lead to a calcination procedure that more reliably generates 2-3 μm particles.

Further characterisation of the materials could reveal important information. HAADF-STEM would reveal the relationship between the P3- and P2-NMMO in the biphase samples, and whether their proximity to each other is likely to be affecting their electrochemical performance. This information can be contrasted against solid state P3-NMMO and the impurity phase. There is some interaction as P2-NMMO activity changes, but the expectation was that structural changes would be prevented but instead seem more prevalent. Impedance spectroscopy of both the active material and cathode itself could also reveal the materials proximity; whether a grain boundary exists between the two phases. NMR and pair distribution function (PDF) analysis could be used to locate the Ca^{2+} in Ca-doped P3-NCMM. This may reveal why the strategy to improve the capacity retention of P3-NMMO did not work. Either Ca^{2+} is absent from the structure entirely or occupies an unexpected site, and this information may answer why it did not occupy the Na site. Generally, further exploration of generating Ca-doped P3-NMMO could be done. Longer calcination times could result in a properly doped structure if the charge density of Ca^{2+} prevents it from migrating through the structure.

Overall, NMMO is resistant to Ca doping. Whether a different synthesis regime or material doping (higher levels of Mg^{2+}) could overcome this should be explored. Longer calcination times may allow the Ca to migrate into the P2-NMMO structure if (a derivative of) $Na_{0.44}MnO_2$ is preferentially forming and preventing the integration of Ca into P2-NMMO – if the Ca^{2+} are trapped in the impurity phase. Based on Chapter 3, dwelling at high temperatures should cause the impurity to break down and release any Ca^{2+} to further dope the P2 structure. In conjunction with predicted larger particle sizes, this could produce the higher capacity retention that this work attempted.

Mn^{2+} dissolution is thought to be the primary cause of capacity fade throughout the work. This can be confirmed *via* elemental analysis of either the electrolyte or scrapings of the anode post-cycling. This was not possible so far due to being unable to disassemble cells. The presence of Mn in the electrolyte would provide evidence of dissolution. Higher proportion of Mn in the electrolyte would be expected in cells with low capacity retention than cells with high capacity retention, as this indicates more Mn^{2+} dissolution.

The dissolution process usually occurs during phase transitions which are expected in NMMO from previous work. The nature of the phase transitions (such as P3↔O3 or P2↔O2) can be confirmed and linked to activity in the voltage profile using *operando* XRD. Using this information, the voltage range can be altered to avoid transitions, identifying which cause more capacity fading and perhaps why. This would be particularly useful in analysis of the biphases: more structural changes are suspected to occur in this material than single phase P2-NMMO. Knowing which phase transitions occur may explain why the capacity fade is so rapid compared to the mixed phases, and strategies to prevent them can be developed.

The impurity phase present in solid state P3-NMMO is the likely causing its high (95%) capacity retention. Attempts to combine P3- and P2-NMMO do not replicate this effect. Further investigation into this impurity and whether higher capacity retention can be replicated in other electrodes is warranted. So too is study into different phase ratios, or combinations with multiple phases. As shown in Chapter 3, the impurity appears as an intermediate phase between P3- and P2-NMMO. As such, it should be possible to combine the impurity phase with P2-NMMO, or with both P3 and P2 phases. One reason that a 20 h calcination was chosen was to drive the solid state P3-NMMO reaction to completion at low temperature, as higher temperatures would form the impurity phase. As the aim is not to obtain a single phase material, a calcination of this length may not be required. It is important to be mindful of this effect this may have on the particle sizes, but reduction to 12-15 h is likely to produce similar sizes.

The effect that biotemplating has on cathode materials, particularly the P3 phase, is to increase its discharge capacity when calcinations are 20 h. A 90% reduction in calcination time achieved higher capacity retention in biotemplated P3-NMMO, which represents huge promise for the sustainability of energy materials production. However, a 2 h synthesis for biotemplated P3-NMMO led to lower capacity retention than longer synthesis, so there is scope for improvement. The calcination can be made longer whilst retaining an advantage in energy cost over solid state synthesis. Similarly, having fewer processing steps pre-calcination compared to solid state synthesis make it an ideal synthesis to use for rapid prototyping of different energy materials. It could be used for larger-scale production too, but biotemplating has clear benefits for synthesising and testing many different materials.

With this context and the ease of selection of phase during of synthesis, biotemplating can be applied to many different materials. Doping materials with a range or combination of metal ions becomes easier when using biotemplating, allowing for the testing and development of cathodes much faster and with less waste than solid state methods. In turn, the development of energy materials to allow a transition to renewable energy sources becomes more feasible.

6.3 References

[1] J. Billaud, G. Singh, A. R. Armstrong, E. Gonzalo, V. Roddatis, M. Armand, T. Rojo, and P. G. Bruce, "$Na_{0.67}Mn_{1-x}Mg_xO_2$ ($0 \leq x \leq 0.2$): a high capacity cathode for sodium-ion batteries," *Energy Environ. Sci.*, vol. 7, no. 4, pp. 1387–1391, 2014, doi:

10.1039/C4EE00465E.

[2] J. Li, J. Wang, X. He, L. Zhang, A. Senyshyn, B. Yan, M. Muehlbauer, X. Cao, B. Vortmann-Westhoven, V. Kraft, H. Liu, C. Luerenbaum, G. Schumacher, E. Paillard, M. Winter, and J. Li, "P2-Type $Na_{0.67}Mn_{0.8}Cu_{0.1}Mg_{0.1}O_2$ as a new cathode material for sodium-ion batteries: Insights of the synergetic effects of multi-metal substitution and electrolyte optimization," *J. Power Sources*, vol. 416, no. December 2018, pp. 184–192, 2019, doi: 10.1016/j.jpowsour.2019.01.086.

[3] B. Sambandam, M. H. Alfaruqi, S. Park, S. Lee, S. Kim, J. Lee, V. Mathew, J. Y. Hwang, and J. Kim, "Validating the structural (In)stability of P3- and P2-$Na_{0.67}Mg_{0.1}Mn_{0.9}O_2$-Layered cathodes for sodium-ion batteries: A time-decisive approach," *ACS Appl. Mater. Interfaces*, vol. 13, no. 45, pp. 53877–53891, 2021, doi: 10.1021/acsami.1c15394.

[4] E. J. Kim, L. A. Ma, D. M. Pickup, A. V. Chadwick, R. Younesi, P. Maughan, J. T. S. Irvine, and A. R. Armstrong, "Vacancy-enhanced oxygen redox reversibility in P3-type magnesium-doped sodium manganese oxide $Na_{0.67}Mg_{0.2}Mn_{0.8}O_2$," *ACS Appl. Energy Mater.*, vol. 3, no. 11, pp. 10423–10434, 2020, doi: 10.1021/acsaem.0c01352.

[5] S. C. Han, H. Lim, J. Jeong, D. Ahn, W. B. Park, K. S. Sohn, and M. Pyo, "Ca-doped Na_xCoO_2 for improved cyclability in sodium ion batteries," *J. Power Sources*, vol. 277, pp. 9–16, 2015, doi: 10.1016/j.jpowsour.2014.11.150.

[6] Y. Shi, S. Li, A. Gao, J. Zheng, Q. Zhang, X. Lu, L. Gu, and D. Cao, "Probing the Structural Transition Kinetics and Charge Compensation of the P2-$Na_{0.78}Al_{0.05}Ni_{0.33}Mn_{0.60}O_2$ Cathode for Sodium Ion Batteries," *ACS Appl. Mater. Interfaces*, vol. 11, no. 27, pp. 24122–24131, 2019, doi: 10.1021/acsami.9b06233.

[7] Y. Ishado, H. Hasegawa, S. Okada, M. Mizuhata, H. Maki, and M. Matsui, "An experimental and first-principle investigation of the Ca-substitution effect on P3-type layered Na_xCoO_2," *Chem. Commun.*, vol. 56, no. 58, pp. 8107–8110, 2020, doi: 10.1039/d0cc01675f.

[8] H. Hasegawa, Y. Ishado, S. Okada, M. Mizuhata, H. Maki, and M. Matsui, "Stabilized Phase Transition Process of Layered Na_xCoO_2 via Ca-Substitution," *J. Electrochem. Soc.*, vol. 168, no. 1, p. 010509, 2021, doi: 10.1149/1945-7111/abd451.

[9] C. Chen, W. Hang, Y. Li, M. Zhang, K. Nie, J. Wang, W. Zhao, R. Qi, C. Zuo, Z. Li, H. Yi, and F. Pan, "P2/O3 biphasic Fe/Mn-based layered oxide cathode with ultrahigh capacity and great cyclability for sodium ion batteries," *Nano Energy*, vol. 90, no. PA, p. 106504, 2021, doi: 10.1016/j.nanoen.2021.106504.

[10] Y. N. Zhou, P. F. Wang, Y. Bin Niu, Q. Li, X. Q. Yu, Y. X. Yin, S. Xu, and Y. G. Guo, "A P2/P3 composite layered cathode for high-performance Na-ion full batteries," *Nano Energy*, vol. 55, no. September 2018, pp. 143–150, 2019, doi: 10.1016/j.nanoen.2018.10.072.

[11] M. Keller, D. Buchholz, and S. Passerini, "Layered Na-Ion Cathodes with Outstanding Performance Resulting from the Synergetic Effect of Mixed P- and O-

Type Phases," *Adv. Energy Mater.*, vol. 6, no. 3, pp. 1–11, 2016, doi: 10.1002/aenm.201501555.

7 Appendix

7.1 Chapter 3 Rietveld data

7.1.1 Solid state P2-NMMO

R (profile)/ %	4.93919
R (weighted profile)/ %	6.28128
GOF	0.95787
Space group (No.)	P 63/m m c (194)
Lattice parameters	
a/ Å	2.8891(2)
b/ Å	2.8891(2)
c/ Å	11.2686(4)
alpha/ °	90
beta/ °	90
gamma/ °	120
V/ 10^6 pm^3	81.45389
V ESD/ 10^6 pm^3	0.0076207

Atom	Wyck.	s.o.f.	x	y	z	B/ 10^4 pm^2
Na	2b	0.180(5)	0.000000	0.000000	0.250000	0.500000
Na	2c	0.292(5)	0.333333	0.666667	0.250000	0.500000
Mn	2a	0.89(1)	0.000000	0.000000	0.000000	0.500000
Mg	2a	0.11(1)	0.000000	0.000000	0.000000	0.500000
O	4f	1.000000	0.333333	0.666667	0.5857(3)	0.500000

7.1.2 Biotemplated P2-NMMO

R (profile)/ %	5.83712
R (weighted profile)/ %	7.76987
GOF	1.20714
Space group (No.)	P 63/m m c (194)
Lattice parameters	
a/ Å	2.8781(1)
b/ Å	2.8781(1)
c/ Å	11.2447(3)
alpha/ °	90
beta/ °	90
gamma/ °	120
V/ 10^6 pm^3	80.66392
V ESD/ 10^6 pm^3	0.0032708

Atom	Wyck.	s.o.f.	x	y	z	B/ 10^4 pm^2
Na	2b	0.258(3)	0.000000	0.000000	0.250000	0.500000
Na	2c	0.402(3)	0.333333	0.666667	0.250000	0.500000
Mn	2a	0.90(1)	0.000000	0.000000	0.000000	0.500000
Mg	2a	0.10(1)	0.000000	0.000000	0.000000	0.500000
O	4f	1.000000	0.333333	0.666667	0.5816(3)	0.500000

7.1.3 Solid state P3-NMMO

R (profile)/ %	5.18195
R (weighted profile)/ %	6.71888
GOF	1.00567
Space group (No.)	R 3 m (160)
Lattice parameters	
a/ Å	2.879(1)
b/ Å	2.879(1)
c/ Å	16.828(1)
alpha/ °	90
beta/ °	90
gamma/ °	120
V/ 10^6 pm^3	120.81990
V ESD/ 10^6 pm^3	0.0410043

Atom	Wyck.	s.o.f.	x	y	z	B/ 10^4 pm^2
Na	3a	0.37(1)	0.000000	0.000000	0.161(2)	0.500000
Mn	3a	0.90(4)	0.000000	0.000000	0.000000	0.500000
Mg	3a	0.10(4)	0.000000	0.000000	0.000000	0.500000
O	3a	1.000000	0.000000	0.000000	0.390(5)	0.500000
O	3a	1.000000	0.000000	0.000000	-0.390(5)	0.500000

7.1.4 Biotemplated P3-NMMO

R (profile)/ %	4.97151
R (weighted profile)/ %	6.52325
GOF	1.00857
Space group (No.)	R 3 m (160)
Lattice parameters	
a/ Å	2.8650(3)
b/ Å	2.8650(3)
c/ Å	16.8296(9)
alpha/ °	90
beta/ °	90
gamma/ °	120
V/ 10^6 pm^3	119.63350
V ESD/ 10^6 pm^3	0.0135455

Atom	Wyck.	s.o.f.	x	y	z	B/ 10^4 pm^2
Na	3a	0.558(6)	0.000000	0.000000	0.1626(6)	0.500000
Mn	3a	0.90(2)	0.000000	0.000000	0.000000	0.500000
Mg	3a	0.10(2)	0.000000	0.000000	0.000000	0.500000
O	3a	1.000000	0.000000	0.000000	0.394(1)	0.500000
O	3a	1.000000	0.000000	0.000000	-0.391(1)	0.500000

7.2 Chapter 4 Rietveld data

7.2.1 0% Ca P3-NCMM

R (profile)/ %	13.49629

R (weighted profile)/ %	17.39047
GOF	1.48206
Space group (No.)	R 3 m (160)
Lattice parameters	
a/ Å	2.867(1)
b/ Å	2.867(1)
c/ Å	16.835(5)
alpha/ °	90
beta/ °	90
gamma/ °	120
V/ 10^6 pm^3	119.80780
V ESD/ 10^6 pm^3	0.0358151

Atom	Wyck.	s.o.f.	x	y	z	B/ 10^4 pm^2
Na	3a	0.670000	0.000000	0.000000	0.1611(5)	0.500000
Mn	3a	0.900000	0.000000	0.000000	0.000000	0.500000
Mg	3a	0.100000	0.000000	0.000000	0.000000	0.500000
O	3a	1.000000	0.000000	0.000000	0.389(1)	0.500000
O	3a	1.000000	0.000000	0.000000	-0.388(1)	0.500000

7.2.2 1% Ca P3-NCMM

R (profile)/ %	14.52530
R (weighted profile)/ %	18.77260
GOF	1.60145
Space group (No.)	R 3 m (160)
Lattice parameters	
a/ Å	2.869(1)
b/ Å	2.869(1)
c/ Å	16.848(6)
alpha/ °	90
beta/ °	90
gamma/ °	120
V/ 10^6 pm^3	120.08810
V ESD/ 10^6 pm^3	0.0438329

Atom	Wyck.	s.o.f.	x	y	z	B/ 10^4 pm^2
NA1	3a	0.650000	0.000000	0.000000	0.163040	0.500033
CA1	3a	0.010000	0.000000	0.000000	0.163040	0.500033
MN1	3a	0.899154	0.000000	0.000000	0.000000	0.500033
MG1	3a	0.100846	0.000000	0.000000	0.000000	0.500033
O1	3a	1.000000	0.000000	0.000000	0.389888	0.500033
O2	3a	1.000000	0.000000	0.000000	0.612068	0.500033

7.2.3 2% Ca P3-NCMM

R (profile)/ %	14.54395
R (weighted profile)/ %	18.77871
GOF	1.58845
Space group (No.)	R 3 m (160)
Lattice parameters	

a/ Å	2.868(1)
b/ Å	2.868(1)
c/ Å	16.862(7)
alpha/ °	90
beta/ °	90
gamma/ °	120
V/ 10^6 pm^3	120.15270
V ESD/ 10^6 pm^3	0.0484225

Atom	Wyck.	s.o.f.	x	y	z	B/ 10^4 pm^2
NA1	3a	0.630000	0.000000	0.000000	0.1645(6)	0.500033
CA1	3a	0.020000	0.000000	0.000000	0.1645(6)	0.500033
MN1	3a	0.899154	0.000000	0.000000	0.000000	0.500033
MG1	3a	0.100846	0.000000	0.000000	0.000000	0.500033
O1	3a	1.000000	0.000000	0.000000	0.389716	0.500033
O2	3a	1.000000	0.000000	0.000000	0.6101(5)	0.500033

7.2.4 0% Ca P2-NCMM

R (profile)/ %	13.05911
R (weighted profile)/ %	16.38472
GOF	1.36958
Space group (No.)	P 63/m m c (194)
Lattice parameters	
a/ Å	2.8760(1)
b/ Å	2.8760(1)
c/ Å	11.2316(5)
alpha/ °	90
beta/ °	90
gamma/ °	120
V/ 10^6 pm^3	80.45195
V ESD/ 10^6 pm^3	0.0038833

Atom	Wyck.	s.o.f.	x	y	z	B/ 10^4 pm^2
Na	2b	0.250000	0.000000	0.000000	0.250000	0.500000
Na	2c	0.420000	0.333333	0.666667	0.250000	0.500000
Mn	2a	0.900000	0.000000	0.000000	0.000000	0.500000
Mg	2a	0.100000	0.000000	0.000000	0.000000	0.500000
O	4f	1.000000	0.333333	0.666667	0.585704	0.500000

7.2.5 1% Ca P2-NCMM

R (profile)/ %	11.52449
R (weighted profile)/ %	15.12812
GOF	1.23609
Space group (No.)	P 63/m m c (194)
Lattice parameters	
a/ Å	2.8799(2)
b/ Å	2.8799(2)
c/ Å	11.2276(6)
alpha/ °	90

beta/ °	90
gamma/ °	120
V/ 10^6 pm^3	80.64413
V ESD/ 10^6 pm^3	0.0051745

Atom	Wyck.	s.o.f.	x	y	z	B/ 10^4 pm^2
Na	2b	0.250002	0.000000	0.000000	0.250000	0.500000
Na	2c	0.399995	0.333333	0.666667	0.250000	0.500000
Mn	2a	0.900000	0.000000	0.000000	0.000000	0.500000
Mg	2a	0.100000	0.000000	0.000000	0.000000	0.500000
O	4f	1.000000	0.333333	0.666667	0.584235	0.500000
Ca	2c	0.010002	0.333333	0.666667	0.250000	0.500000

7.2.6 2% Ca P2-NCMM

R (profile)/ %	12.90882
R (weighted profile)/ %	16.53436
GOF	1.37334
Space group (No.)	P 63/m m c (194)
a/ Å	2.8797(2)
b/ Å	2.8797(2)
c/ Å	11.2306(6)
alpha/ °	90
beta/ °	90
gamma/ °	120
V/ 10^6 pm^3	80.65413
V ESD/ 10^6 pm^3	0.0049047

Atom	Wyck.	s.o.f.	x	y	z	B/ 10^4 pm^2
Na	2b	0.250000	0.000000	0.000000	0.250000	0.500000
Na	2c	0.380000	0.333333	0.666667	0.250000	0.500000
Mn	2a	0.900000	0.000000	0.000000	0.000000	0.500000
Mg	2a	0.100000	0.000000	0.000000	0.000000	0.500000
O	4f	1.000000	0.333333	0.666667	0.586583	0.500000
Ca	2c	0.020000	0.333333	0.666667	0.250000	0.500000

7.3 Chapter 5 Rietveld data

7.3.1 9:1, mixed P3/P2-NMMO

R (profile)/ %	10.88464
R (weighted profile)/ %	14.12184
GOF	1.21059
P3-NMMO	
Space group (No.)	R 3 m (160)
Lattice parameters	
a/ Å	2.8687(3)
b/ Å	2.8687(3)
c/ Å	16.831(1)
alpha/ °	90
beta/ °	90

gamma/ °	120
V/ 10^6 pm^3	119.95320
V ESD/ 10^6 pm^3	0.0139598

Atom	Wyck.	s.o.f.	x	y	z	B/ 10^4 pm^2
Na	3a	0.468(9)	0.000000	0.000000	0.1640(7)	0.500000
Mn	3a	0.90(2)	0.000000	0.000000	0.000000	0.500000
Mg	3a	0.10(2)	0.000000	0.000000	0.000000	0.500000
O	3a	1.000000	0.000000	0.000000	0.392(2)	0.500000
O	3a	1.000000	0.000000	0.000000	-0.394(2)	0.500000

P2-NMMO

Space group (No.)	P 63/m m c (194)
Lattice parameters	
a/ Å	2.871(2)
b/ Å	2.871(2)
c/ Å	11.2758(9)
alpha/ °	90
beta/ °	90
gamma/ °	120
V/ 10^6 pm^3	80.46296
V ESD/ 10^6 pm^3	0.0362838

Atom	Wyck.	s.o.f.	x	y	z	B/ 10^4 pm^2
Na	2b	0.05(5)	0.000000	0.000000	0.250000	0.500000
Na	2c	0.40(5)	0.333333	0.666667	0.250000	0.500000
Mn	2a	0.9(1)	0.000000	0.000000	0.000000	0.500000
Mg	2a	0.1(1)	0.000000	0.000000	0.000000	0.500000
O	4f	1.000000	0.333333	0.666667	0.570(4)	0.500000

7.3.2 7:3, mixed P3/P2-NMMO

R (profile)/ %	10.43541
R (weighted profile)/ %	13.61921
GOF	1.16751

P3-NMMO

Space group (No.)	R 3 m (160)
Lattice parameters	
a/ Å	2.8727(5)
b/ Å	2.8727(5)
c/ Å	16.848(2)
alpha/ °	90
beta/ °	90
gamma/ °	120
V/ 10^6 pm^3	120.40650
V ESD/ 10^6 pm^3	0.0210580

Atom	Wyck.	s.o.f.	x	y	z	B/ 10^4 pm^2
Na	3a	0.44(1)	0.000000	0.000000	0.1628(8)	0.500000
Mn	3a	0.90(2)	0.000000	0.000000	0.000000	0.500000
Mg	3a	0.10(2)	0.000000	0.000000	0.000000	0.500000
O	3a	1.000000	0.000000	0.000000	0.390(2)	0.500000

O	3a	1.000000	0.000000	0.000000	-0.394(2)	0.500000

P2-NMMO

Space group (No.)	P 63/m m c (194)
Lattice parameters	
a/ Å	2.8735(4)
b/ Å	2.8735(4)
c/ Å	11.245(2)
alpha/ °	90
beta/ °	90
gamma/ °	120
V/ 10^6 pm^3	80.41411
V ESD/ 10^6 pm^3	0.0159313

Atom	Wyck.	s.o.f.	x	y	z	B/ 10^4 pm^2
Na	2b	0.18(2)	0.000000	0.000000	0.250000	0.500000
Na	2c	0.40(3)	0.333333	0.666667	0.250000	0.500000
Mn	2a	0.89(4)	0.000000	0.000000	0.000000	0.500000
Mg	2a	0.11(4)	0.000000	0.000000	0.000000	0.500000
O	4f	1.000000	0.333333	0.666667	0.584(2)	0.500000

7.3.3 1:1, mixed P3/P2-NMMO

R (profile)/ %	9.29512
R (weighted profile)/ %	12.56128
GOF	1.08354

P3-NMMO

Space group (No.)	R 3 m (160)
Lattice parameters	
a/ Å	2.8712(5)
b/ Å	2.8712(5)
c/ Å	16.852(3)
alpha/ °	90
beta/ °	90
gamma/ °	120
V/ 10^6 pm^3	120.31230
V ESD/ 10^6 pm^3	0.0265437

Atom	Wyck.	s.o.f.	x	y	z	B/ 10^4 pm^2
Na	3a	0.41(2)	0.000000	0.000000	0.163(1)	0.500000
Mn	3a	0.90(3)	0.000000	0.000000	0.000000	0.500000
Mg	3a	0.10(3)	0.000000	0.000000	0.000000	0.500000
O	3a	1.000000	0.000000	0.000000	0.392(3)	0.500000
O	3a	1.000000	0.000000	0.000000	-0.391(3)	0.500000

P2-NMMO

Space group (No.)	P 63/m m c (194)
Lattice parameters	
a/ Å	2.8744(2)
b/ Å	2.8744(2)
c/ Å	11.2365(9)

alpha/ °	90
beta/ °	90
gamma/ °	120
V/ 10^6 pm^3	80.39815
V ESD/ 10^6 pm^3	0.0076291

Atom	Wyck.	s.o.f.	x	y	z	B/ 10^4 pm^2
Na	2b	0.166(9)	0.000000	0.000000	0.250000	0.500000
Na	2c	0.31(1)	0.333333	0.666667	0.250000	0.500000
Mn	2a	0.89(2)	0.000000	0.000000	0.000000	0.500000
Mg	2a	0.11(2)	0.000000	0.000000	0.000000	0.500000
O	4f	1.000000	0.333333	0.666667	0.5878(7)	0.500000

7.3.4 3:7, mixed P3/P2-NMMO

R (profile)/ %	9.63004
R (weighted profile)/ %	12.73830
GOF	1.06611
P3-NMMO	
Space group (No.)	R 3 m (160)
Lattice parameters	
a/ Å	2.8733(8)
b/ Å	2.8733(8)
c/ Å	16.841(4)
alpha/ °	90
beta/ °	90
gamma/ °	120
V/ 10^6 pm^3	120.41080
V ESD/ 10^6 pm^3	0.0410751

Atom	Wyck.	s.o.f.	x	y	z	B/ 10^4 pm^2
Na	3a	0.50(2)	0.000000	0.000000	0.160(1)	0.500000
Mn	3a	0.90(5)	0.000000	0.000000	0.000000	0.500000
Mg	3a	0.10(5)	0.000000	0.000000	0.000000	0.500000
O	3a	1.000000	0.000000	0.000000	0.395(3)	0.500000
O	3a	1.000000	0.000000	0.000000	-0.389(3)	0.500000

P2-NMMO	
Space group (No.)	P 63/m m c (194)
Lattice parameters	
a/ Å	2.8754(2)
b/ Å	2.8754(2)
c/ Å	11.2389(6)
alpha/ °	90
beta/ °	90
gamma/ °	120
V/ 10^6 pm^3	80.47058
V ESD/ 10^6 pm^3	0.0055213

Atom	Wyck.	s.o.f.	x	y	z	B/ 10^4 pm^2
Na	2b	0.157(7)	0.000000	0.000000	0.250000	0.500000
Na	2c	0.274(9)	0.333333	0.666667	0.250000	0.500000

Mn	2a	0.89(2)	0.000000	0.000000	0.000000	0.500000
Mg	2a	0.11(2)	0.000000	0.000000	0.000000	0.500000
O	4f	1.000000	0.333333	0.666667	0.5899(5)	0.500000

7.3.5 1:9, mixed P3/P2-NMMO

R (profile)/ %	9.69703
R (weighted profile)/ %	13.31316
GOF	1.14275
P3-NMMO	
Space group (No.)	R 3 m (160)
Lattice parameters	
a/ Å	2.874(2)
b/ Å	2.874(2)
c/ Å	16.883(7)
alpha/ °	90
beta/ °	90
gamma/ °	120
V/ 10^6 pm^3	120.80750
V ESD/ 10^6 pm^3	0.0756705

Atom	Wyck.	s.o.f.	x	y	z	B/ 10^4 pm^2
Na	3a	0.32(5)	0.000000	0.000000	0.156(4)	0.500000
Mn	3a	0.9(1)	0.000000	0.000000	0.000000	0.500000
Mg	3a	0.1(1)	0.000000	0.000000	0.000000	0.500000
O	3a	1.000000	0.000000	0.000000	0.411(2)	0.500000
O	3a	1.000000	0.000000	0.000000	-0.356(2)	0.500000

P2-NMMO	
Space group (No.)	P 63/m m c (194)
Lattice parameters	
a/ Å	2.8785(1)
b/ Å	2.8785(1)
c/ Å	11.2299(7)
alpha/ °	90
beta/ °	90
gamma/ °	120
V/ 10^6 pm^3	80.58284
V ESD/ 10^6 pm^3	0.0055479

Atom	Wyck.	s.o.f.	x	y	z	B/ 10^4 pm^2
Na	2b	0.163(6)	0.000000	0.000000	0.250000	0.500000
Na	2c	0.269(8)	0.333333	0.666667	0.250000	0.500000
Mn	2a	0.89(1)	0.000000	0.000000	0.000000	0.500000
Mg	2a	0.11(1)	0.000000	0.000000	0.000000	0.500000
O	4f	1.000000	0.333333	0.666667	0.5874(5)	0.500000

7.3.6 9:1, 720 °C P3/P2-NMMO

R (profile)/ %	11.30170
R (weighted profile)/ %	14.71425

GOF	1.25373
P3-NMMO	
Space group (No.)	R 3 m (160)
Lattice parameters	
a/ Å	2.8784(6)
b/ Å	2.8784(6)
c/ Å	16.847(2)
alpha/ °	90
beta/ °	90
gamma/ °	120
V/ 10^6 pm^3	120.88120
V ESD/ 10^6 pm^3	0.0234309

Atom	Wyck.	s.o.f.	x	y	z	B/ 10^4 pm^2
Na	3a	0.33(1)	0.000000	0.000000	0.163(1)	0.500000
Mn	3a	0.90(2)	0.000000	0.000000	0.000000	0.500000
Mg	3a	0.10(2)	0.000000	0.000000	0.000000	0.500000
O	3a	1.000000	0.000000	0.000000	0.391(3)	0.500000
O	3a	1.000000	0.000000	0.000000	-0.395(3)	0.500000

P2-NMMO

Space group (No.)	P 63/m m c (194)
Lattice parameters	
a/ Å	2.871(2)
b/ Å	2.871(2)
c/ Å	11.350(8)
alpha/ °	90
beta/ °	90
gamma/ °	120
V/ 10^6 pm^3	81.04331
V ESD/ 10^6 pm^3	0.0677721

Atom	Wyck.	s.o.f.	x	y	z	B/ 10^4 pm^2
Na	2b	0.37(6)	0.000000	0.000000	0.250000	0.500000
Na	2c	0.93(9)	0.333333	0.666667	0.250000	0.500000
Mn	2a	0.9(1)	0.000000	0.000000	0.000000	0.500000
Mg	2a	0.1(1)	0.000000	0.000000	0.000000	0.500000
O	4f	1.000000	0.333333	0.666667	0.563(3)	0.500000

7.3.7 7:3, 730 °C P3/P2-NMMO

R (profile)/ %	10.52154
R (weighted profile)/ %	13.65731
GOF	1.16624
P3-NMMO	
Space group (No.)	R 3 m (160)
Lattice parameters	
a/ Å	2.8643(4)
b/ Å	2.8643(4)
c/ Å	16.816(2)
alpha/ °	90

beta/ °	90
gamma/ °	120
V/ 10^6 pm^3	119.48410
V ESD/ 10^6 pm^3	0.0172597

Atom	Wyck.	s.o.f.	x	y	z	B/ 10^4 pm^2
Na	3a	0.39(2)	0.000000	0.000000	0.1629(9)	0.500000
Mn	3a	0.90(3)	0.000000	0.000000	0.000000	0.500000
Mg	3a	0.10(3)	0.000000	0.000000	0.000000	0.500000
O	3a	1.000000	0.000000	0.000000	0.398(2)	0.500000
O	3a	1.000000	0.000000	0.000000	-0.389(2)	0.500000

P2-NMMO

Space group (No.)	P 63/m m c (194)
Lattice parameters	
a/ Å	2.8644(4)
b/ Å	2.8644(4)
c/ Å	11.201(2)
alpha/ °	90
beta/ °	90
gamma/ °	120
V/ 10^6 pm^3	79.58937
V ESD/ 10^6 pm^3	0.0151210

Atom	Wyck.	s.o.f.	x	y	z	B/ 10^4 pm^2
Na	2b	0.18(2)	0.000000	0.000000	0.250000	0.500000
Na	2c	0.39(3)	0.333333	0.666667	0.250000	0.500000
Mn	2a	0.89(4)	0.000000	0.000000	0.000000	0.500000
Mg	2a	0.11(4)	0.000000	0.000000	0.000000	0.500000
O	4f	1.000000	0.333333	0.666667	0.579(1)	0.500000

7.3.8 1:1, 770 °C P3/P2-NMMO

R (profile)/ %	9.64431
R (weighted profile)/ %	12.88165
GOF	1.09377

P3-NMMO

Space group (No.)	R 3 m (160)
Lattice parameters	
a/ Å	2.8781(6)
b/ Å	2.8781(6)
c/ Å	16.961(3)
alpha/ °	90
beta/ °	90
gamma/ °	120
V/ 10^6 pm^3	121.67670
V ESD/ 10^6 pm^3	0.0299675

Atom	Wyck.	s.o.f.	x	y	z	B/ 10^4 pm^2
Na	3a	0.39(1)	0.000000	0.000000	0.161(1)	0.500000
Mn	3a	0.90(4)	0.000000	0.000000	0.000000	0.500000
Mg	3a	0.10(4)	0.000000	0.000000	0.000000	0.500000

O	3a	1.000000	0.000000	0.000000	0.395(3)	0.500000
O	3a	1.000000	0.000000	0.000000	-0.393(3)	0.500000

P2-NMMO

Space group (No.)	P 63/m m c (194)
Lattice parameters	
a/ Å	2.8731(3)
b/ Å	2.8731(3)
c/ Å	11.219(1)
alpha/ °	90
beta/ °	90
gamma/ °	120
V/ 10^6 pm^3	80.20108
V ESD/ 10^6 pm^3	0.0097649

Atom	Wyck.	s.o.f.	x	y	z	B/ 10^4 pm^2
Na	2b	0.16(1)	0.000000	0.000000	0.250000	0.500000
Na	2c	0.29(1)	0.333333	0.666667	0.250000	0.500000
Mn	2a	0.89(2)	0.000000	0.000000	0.000000	0.500000
Mg	2a	0.11(2)	0.000000	0.000000	0.000000	0.500000
O	4f	1.000000	0.333333	0.666667	0.5806(7)	0.500000

7.3.9 3:7, 800 °C P3/P2-NMMO

R (profile)/ %	9.54937
R (weighted profile)/ %	12.78262
GOF	1.08528

P3-NMMO

Space group (No.)	R 3 m (160)
Lattice parameters	
a/ Å	2.876(1)
b/ Å	2.876(1)
c/ Å	16.933(3)
alpha/ °	90
beta/ °	90
gamma/ °	120
V/ 10^6 pm^3	121.31050
V ESD/ 10^6 pm^3	0.0538876

Atom	Wyck.	s.o.f.	x	y	z	B/ 10^4 pm^2
Na	3a	0.08(4)	0.000000	0.000000	0.12(1)	0.500000
Mn	3a	0.90(8)	0.000000	0.000000	0.000000	0.500000
Mg	3a	0.10(8)	0.000000	0.000000	0.000000	0.500000
O	3a	1.000000	0.000000	0.000000	0.39(2)	0.500000
O	3a	1.000000	0.000000	0.000000	-0.39(2)	0.500000

P2-NMMO

Space group (No.)	P 63/m m c (194)
Lattice parameters	
a/ Å	2.8750(2)
b/ Å	2.8750(2)

c/ Å	11.2393(6)
alpha/ °	90
beta/ °	90
gamma/ °	120
V/ 10^6 pm^3	80.45440
V ESD/ 10^6 pm^3	0.0057837

Atom	Wyck.	s.o.f.	x	y	z	B/ 10^4 pm^2
Na	2b	0.208(6)	0.000000	0.000000	0.250000	0.500000
Na	2c	0.302(8)	0.333333	0.666667	0.250000	0.500000
Mn	2a	0.89(2)	0.000000	0.000000	0.000000	0.500000
Mg	2a	0.11(2)	0.000000	0.000000	0.000000	0.500000
O	4f	1.000000	0.333333	0.666667	0.5860(5)	0.500000

7.3.10 1:9, 820 °C P3/P2-NMMO

R (profile)/ %	12.53758
R (weighted profile)/ %	16.20655
GOF	1.38710
P3-NMMO	
Space group (No.)	R 3 m (160)
Lattice parameters	
a/ Å	2.887(5)
b/ Å	2.887(5)
c/ Å	16.69845(9)
alpha/ °	90
beta/ °	90
gamma/ °	120
V/ 10^6 pm^3	120.56720
V ESD/ 10^6 pm^3	0.1356417

Atom	Wyck.	s.o.f.	x	y	z	B/ 10^4 pm^2
Na	3a	0.670000	0.000000	0.000000	0.159672	0.500000
Mn	3a	0.900000	0.000000	0.000000	0.000000	0.500000
Mg	3a	0.100000	0.000000	0.000000	0.000000	0.500000
O	3a	1.000000	0.000000	0.000000	0.39(1)	0.500000
O	3a	1.000000	0.000000	0.000000	-0.32(1)	0.500000

P2-NMMO	
Space group (No.)	P 63/m m c (194)
Lattice parameters	
a/ Å	2.8647(1)
b/ Å	2.8647(1)
c/ Å	11.1868(5)
alpha/ °	90
beta/ °	90
gamma/ °	120
V/ 10^6 pm^3	79.50327
V ESD/ 10^6 pm^3	0.0039324

Atom	Wyck.	s.o.f.	x	y	z	B/ 10^4 pm^2
Na	2b	0.128(7)	0.000000	0.000000	0.250000	0.500000

Na	2c	0.215(7)	0.333333	0.666667	0.250000	0.500000
Mn	2a	0.89(2)	0.000000	0.000000	0.000000	0.500000
Mg	2a	0.11(2)	0.000000	0.000000	0.000000	0.500000
O	4f	1.000000	0.333333	0.666667	0.5857(5)	0.500000